europhysics
conference
abstracts

11th European Conference on

Controlled Fusion and Plasma Physics

Aachen, 5–9 September 1983

Contributed Papers
Part II

by: European Physical Society

Editor: Prof. S. Methfessel, Bochum

Editor: G. Thomas, Geneva

VOLUME 7D Part II

EUROPEAN PHYSICAL SOCIETY
PLASMA PHYSICS DIVISION

Max-Planck-Institut für Plasmaphysik
5000 5861
03. NOV. 1983
Bibliothek

11th European Conference on

Controlled Fusion and Plasma Physics

Aachen, 5–9 September 1983

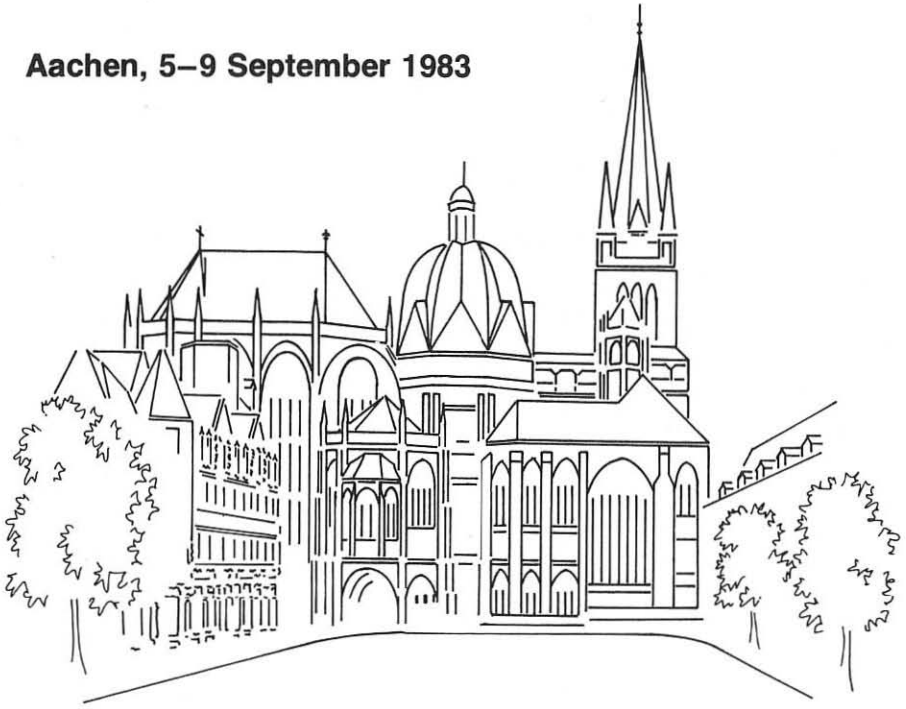

Contributed Papers
Part II

A859-83

EUROPHYSICS CONFERENCE ABSTRACTS is published by the
European Physical Society, ©1983
Reproduction rights reserved

This volume is published under the copyright of the European Physical Society. We want to inform the authors that the transfer of the copyright to EPS should not prevent an author to publish an article in a journal quoting the original first publication or to use the same abstract for another conference. This copyright is just to protect EPS against using the same material in similar publications.

Printing WEKA-Druck GmbH, Linnich

The 11th European Conference on Controlled Fusion and Plasma Physics will be held at Aachen, Federal Republic of Germany, from 5-9 September 1983. The conference will take place in the Kármán-Auditorium of the University of Aachen. It is being organized by the Nuclear Research Centre Jülich for the Plasma Physics Division of the European Physical Society.

The conference will cover the following topics:

Magnetic confinement
Inertial confinement
Plasma heating
Reactor concepts
Theory, processes and methods related to fusion research

The conference programme will include 24 invited papers presented in oral sessions and about 300 contributed papers. The majority of the contributed papers will be presented in poster sessions.

Programme Committee

E. Hintz, Jülich, FRG (Chairman)
A. Gibson, Culham, UK
J. Jacquinot, Culham, UK
H. Ringler, Garching, FRG
D.D. Ryutov, Novosibirsk, USSR
F. Troyon, Lausanne, CH
H.A. Claassen, Jülich, FRG (Scientific Secretary)

Organizing Committee

G.H. Wolf, Jülich, (Chairman)
G. Ecker, Bochum
E. Hintz, Jülich
B. Krahl-Urban, Jülich
G. Mohl, Jülich
W. Schilling, Aachen
H. Tuczek, Essen
J. Uhlenbusch, Düsseldorf

Local Committee

G.H. Wolf (Chairman)
B. Krahl-Urban (Vice-Chairman)
H.A. Claassen (Scientific Secretary)
H. Gerhauser
H. Gresser
G. Mohl

Conference Secretary

Helga Bongartz
KFA Jülich GmbH
Conference Secretariat
P.O. Box 1913
D-5170 Jülich
Fed. Rep. of Germany
Tel.: (02461) 613008
Telex: 833556-70 kf d

Invited Papers

The book of invited papers will be published by Pergamon Press as Special Supplement 1984 of the journal "Plasma Physics" and sent free of charge to each registered participant.

Correspondence List

O01 - O04	Tokamaks
O05 - O06	Plasma-Wall Interaction, Divertors
O07 - O09	Laser Plasma Interaction
O10	Tokamaks
O11 - O16	Magnetic Confinement Theory
O17 - O20	Stellarators, Bumpy Tori
O21	Plasma-Wall Interaction, Divertors
O22	Magnetic Confinement Theory
O23 - O28	Plasma Focus Devices
O29 - O31	Reversed Field Pinches, Compact Tori
O32	Heating and Current Drive
O33	Tokamaks
A01 - A11	Tokamaks
A12 - A21	Transport Codes
A22 - A31	Heating and Current Drive
A31 - A42	Plasma-Wall Interaction, Divertors
A43 - A48	Reversed Field Pinches, Compact Tori
B01 - B14	Tokamaks
B15 - B23	Transport Codes
B24 - B31	Heating and Current Drive
B32 - B4O	Plasma-Wall Interaction, Divertors
B41 - B54	Magnetic Confinement Theory
C01 - C04	Tokamaks
C05 - C16	Heating and Current Drive
C17 - C24	Stellarators, Bumpy Tori
C25 - C36	Plasma-Wall Interaction, Divertors
C37 - C49	Magnetic Confinement Theory
D01 - D10	Reactor Aspects
D12 - D17	Stellarators, Bumpy Tori
D17 - D22	Mirrors
D23 - D33	Heating and Current Drive
D34 - D44	Plasma Focus Devices, Theta-and Z-Pinches
D45 - D51	Magnetic Confinement Theory
E01 - E13	Plasma Focus Devices
E14 - E25	Diagnostics
E26 - E36	Heating and Current Drive
E37 - E45	Laser-Plasma Interaction, Inertial Confinement
E46 - E53	Magnetic Confinement Theory

Contents

Part I

Correspondence List ..... **IV**
Oral Presentations ..... **VII**
Poster Presentations ..... **IX**

Tokamaks 1
O 01 - O 04
O 10
O 33
A 01 - A 11
B 01 - B 14
C 01 - C 04

Reversed Field Pinches, Compact Tori 137
O 29 - O 31
A 43 - A 48

Stellarators, Bumpy Tori 175
O 17 - O 20
C 17 - C 24
D 12 - D 17

Mirrors 247
D 18 - D 22

Heating and Current Drive 267
O 32
A 22 - A 31
B 24 - B 31
C 05 - C 16
D 23 - D 33
E 26 - E 36

Plasma Focus Devices, Theta-and Z-Pinches 467
O 23 - O 28
D 34 - D 44
E 01 - E 13

Author Index 579

Part II

Correspondence List ..... **IV**
Oral Presentations ..... **VII**
Poster Presentations ..... **IX**

Laser-Plasma Interaction, Inertial Confinement 1
O 07 - O 09
E 37 - E 45

Diagnostics 51
E 14 - E 25

Magnetic Confinement Theory 101
O 11 - O 16
O 22
B 41 - B 54
C 37 - C 49
D 45 - D 51
E 46 - E 53

Transport Codes 289
A 12 - A 21
B 15 - B 23

Plasma-Wall Interaction, Divertors 367
O 05
O 06
O 21
A 32 - A 42
B 32 - B 40
C 25 - C 36

Reactor Aspects 505
D 01 - D 10

Author Index 547

Oral Presentations

O 1 Scott S.D., Isler R.C., Murakami M., Bell J.D., Bush C.E., et al.
ORNL, Oak Ridge, Tennessee, USA
Carnevali[1] A., Murray L.E.
University of Tennessee, Knoxville, Tennessee, USA
[1]Harding University, Searcy, Arkansas, USA
Neutral injection experiments on the ISX-B tokamak

O 2 Greenwald M., Parker J., Besen M., Fiore C.L., Foord M., et al.
Plasma Fusion Center, MIT, Cambridge, Massachusetts, USA
Milora S., Schuresco D.
ORNL, Oak Ridge, Tennessee, USA
Hydrogen pellet injection into ALCATOR-C

O 3 Burrell K.H., Doublet III Physics, Operations and Neutral Beam Groups
GA-Technologies, Inc., San Diego, Ca.,USA
A regime of improved energy and particle confinement in neutral beam heated divertor discharges in DOUBLET III

O 4 Ellis J.J., Morris A.W.
Culham Laboratory, Abingdon, Oxon, UK
Instability control with active saddle coils on TOSCA

O 5 Dobrokhotov E.J., Dremin M.M., Pavlov Yu.D., Petrov D.P., Solntsev A.M., Stefanovskij A.M., Terebkov A.L., Shcherbak A.F.
I.V.Kurchatov Institute of Atomic Energy, Moscow, USSR
Bolometer measurements of the energy losses in the graphite wall tokamak

O 6 Fußmann G., Behringer K., Bernhardi K., Haas G., Poschenrieder W., et al.
MPI für Plasmaphysik, Garching, FRG
Kissel[1] S., Szymanski[2] Z.,
[1]on leave from MIT, Cambridge, Massachusetts, USA
[2]on leave from Institute of Fundamental Technological Research, Warsaw, Poland
Impurity retainment in the divertor of ASDEX

O 7 Meyer-ter-Vehn J., Arnold R., Metzler N., Schmalz R., Unterseer K., Witkowski S.
MPI für Quantenoptik, Garching, FRG
ICF-target research at MPQ/Garching

O 8 Yoshida K., Miyanaga N., Kitagawa Y., Kato Y., Nishihara K., et al.
Institute of Laser Engineering, Osaka University, Osaka, Japan
Efficient and uniform compression to high density with 1.052μm GM-II laser

O 9 Rockett P.D., Tarvin J.A., Busch Gar. E., Charatis G., Johnson R.R., et al.
KMS Fusion, Inc., Ann Arbor, Michigan, USA
The impact of quality diagnostics on ICF research at KMS-Fusion, Inc.

O 10 Kaye S.M. Bell M., Bol K., Boyd D., Brau K., et al.
PPPL, Princeton University, Princeton, NJ, USA
High confinement discharges in PDX with neutral beam injection

O 11 Degtyarev L.M., Poshekhonov Yu.Yu.
Keldysh Institute of Applied Mathematics
Shafranov V.D.
I.V. Kurchatov Institute of Atomic Energy, Moscow, USSR
Comparative characteristics of various plasma systems

O 12 Chance M.S., Chen L., Furth H.P., Goldston R., Grimm R.C., et al.
PPPL, Princeton University, Princeton, NJ, USA
Dewar R.L.
Research School of Physical Sciences, A.N.U., Australia
Todd A.
Grumman Aerospace Corporation, Princeton, New Jersey, USA
Bean-shaped tokamak configurations

O 13 Berk H.L, Rosenbluth M.N.
Institute for Fusion Studies, University of Texas at Austin, USA
Shohet J.L., Hitchon W.N.G.
University of Wisconsin, Torsatron/Stellerator Laboratory, Madison, Wisconsin, USA
Ballooning mode calculations in stellarators

O 14 Rogister A., Hasselberg G., Waelbroeck F.
IPP, KFA Jülich GmbH, Jülich, FRG
On the origin of sawtooth relaxations and plasma disruptions

O 15 Goedbloed[1] J.P., Freidberg J.P., Rohatgi R.
Plasma Fusion Center, MIT, Cambridge, Ma., USA
[1]On leave from FOM-Instituut voor Plasmafysica, Rijnhuizen, Nieuwegein, The Netherlands
Influence of a limiter on the stability of external kink modes

O 16 Faulconer D.W.
Laboratoire de Physique des Plasmas, Ecole Royale Militaire, Brussels, Belgium
Electrostatic shield fringe field interaction with plasma in rf heating

O 17 Swain D.W., Colchin R.J., Baity F.W., Cobble J.A., Davis W.A., et al.
ORNL, Oak Ridge, Tennessee , USA
The EBT experiment

O 18 Lyon J.F., Carreras B.A., Cooper W.A., Dory R.A., Garcia L., et. al.
ORNL, Oak Ridge , Tennessee, USA
Charlton L.A., Fowler R.H., Hicks H.R., Holmes, J.A., Lynch V.E., Masden B.F.
Union Carbide Corporation Nuclear Division, Computer Sciences
ATF-1 torsatron studies

O 19 Uo K., Iiyoshi A., Obiki T., Motojima O., Morimoto S., et al.
Plasma Physics Laboratory, Kyoto University, Kyoto, Japan
Recent results of nbi and ecr heating experiments on HELIOTRON E

O 20 Andryukhina Eh.D., Agapov L.N., Batanov G.M., Berezhetskij M.S., Blokh M.A.. et al.
General Physics Institute, USSR Academy of Sciences, Moscow, USSR
Initial experiments on electron cyclotron plasma heating in the L-2 stellarator

O 21 Nedospasov A.V., Tokar M.Z.
Institute of High Temperatures, USSR Academy of Sciences, Moscow, USSR
Recycling influence on plasma of a tokamak periphery

O 22 Bernard L.C., Bhadra D.K., Helton F.J., Lao L.L.
GA Technologies, Inc., San Diego, California, USA
Todd T.N.
Culham Laboratory, Abingdon, Oxon, UK
Ideal MHD beta limits: scaling laws and comparison with DOUBLET III high-beta plasmas

O 23 Czekaj S., Denus S., Kasperczuk A., Miklaszewski R., Paduch M., et al.
S. Kaliski Institute of Plasma Physics and Laser Microfusion, Warsaw, Poland
Investigation of connections between the plasma column evolution and the neutron emission in the plasma focus device

O 24 Yokoyama M., Yamamoto Y., Kisoda A., Yamada Y., Kitagawa Y., Yamanaka M., Yamanaka C. et al.
Institute of Laser Engineering, Osaka University, Osaka, Japan
Dense plasma focus research in ILE, Osaka

O 25 Herold H., Bertalot L., Jäger U., Schmidt H., Schmidt R., Shakhatre M.
Institut für Plasmaforschung, Universität Stuttgart, FRG
Plasma dynamics, neutron and ion emission of the POSEIDON plasma focus

O 26 Brzosko[1] J.S., Conrads[2] H., Rager[3] J.P., Robouch B.V., Steinmetz[4] K.
Association EURATOM-ENEA, Frascati (Rome), Italy
[1]University of Warsaw, Bialystok Branch, Poland
[2]IPP, KFA Jülich GmbH, Jülich, FRG
[3]DG- 12-Fusion (Meeus), CCE Brussels, Belgium
[4]MPI für Plasmaphysik, Garching, FRG
Characteristics of high energy deuterons in the Frascati 1-MJ plasma focus

O 27 Jerzykiewicz A., Bielik M., Jankowicz Z., Kociecka K., Kocinski L., et al.
Institute for Nuclear Studies, Swierk, Poland
Borowiecki M., Czekaj S., Denus S., Skrzeczanowski W.
Institute of Plasma Physics and Laser Microfusion, Warsaw, Poland
Preliminary investigations of 360 kJ plasma-focus device

O 28 Nardi V., Bostick[1] W.H., Powell C., Prior W.
Stevens institute of Technology, Hoboken, N.J., USA
[1]Physics Department, University of New Mexico, Albuquerque, New Mexico, USA
Ion imaging and energy spectrum from the plasma-focus ion emission

O 29 Tuszewski M., Armstrong W.T., Barnes Cris W., Barnes D.C., Bartsch R.R., et al.
Los Alamos Natl. Lab., Los Alamos, NM., USA
Gladd N.T.
Jaycor, Inc., Del Mar, California, USA
Shestakov A.I.
Lawrence Livermore Natl. Lab., Livermore, California, USA
Recent results in the Los Alamos compact torus program

O 30 Antoni V., Buffa A., Giudicotti L., Martini S., Ortolani S., Puiatti M.E., Scarin P.
Istituto Gas Ionizzati del C.N.R., Padova, Italy
Reversed field pinch experiments at various currents in ETA-BETA II

O 31 Watt R.G., Jacobson A.R., Massey R.S., Mondt J.P. and the ZT-40M Team
Los Alamos Natl. Lab., Los Alamos, New Mexico, USA
Recent results from the ZT-40M reversed field pinch program

O 32 Porkolab M., Lloyd B., Schuss J.J., Takase Y., Texter S., et al.
Plasma Fusion Center , MIT, Cambridge, Ma., USA
Lower hybrid current drive and heating experiments at the 1MW rf power level on ALCATOR-C

O 33 Nagayama Y., Tsuji S., Miyamoto K.
Department of Physics, University of Tokyo, Tokyo, Japan
Kawahata K., Noda N., Tanahashi S., Fujita J.
Institute of Plasma Physics, Nagoya University, Nagoya, Japan
A study of tokamak disruptions in JIPP T-II using soft X-ray imaging

Poster Presentations

Tokamaks

Part I, p. 1 -136

A 1 FT Group: Alladio F., Barbato E., Bardotti G., Bartiromo R., Bracco G. et al.
CRE, Frascati, Italy
Iacono R., Mazzitelli G.
ENEA guests
Low-q discharges in FT tokamak

A 2 FT Group
CRE, Frascati, Italy
Mazzitelli G.
ENEA guest
Decrease of central iron concentration in Ih-heated FT discharges

A 3 Barsukov A.G., Gorshkov A.V., Kovrov P.E., Levchenko Yu.M., Leonov V.M. et al.
I.V. Kurchatov Institute of Atomic Energy, Moscow, USSR
Low-q discharges in the T-11 tokamak

A 4 Nakamura Y., Itoh S., Hiraki N., Nakamura K., Tanaka M., Nagao A.,Kikuchi[1] M.
Research Institute for Applied Mechanics, Kyushu University, Fukuoka, Japan
[1]JAERI, Tokai, Naka, Ibaraki, Japan
High-field tokamak TRIAM-1M with superconducting toroidal magnets

A 5 Niedermeyer H., Behringer K., Bernhardi K., Eberhagen A., Fußmann G.
MPI für Plasmaehysikc Garching, FRG
Kissel[1]S., Szymanski[2] Z.,
[1] On leave from MIT, Cambridge, Massachusetts, USA
[2]On leave from Institute of Fundamental Technological Research, Warsaw. Poland
Change of plasma properties prior to high density disruptions in ASDEX

A 6 Müller E.R., Niedermeyer H., Behringer K., Bernhardi K., Eberhagen A., et al.
MPI für Plasmaphysik, Garching, FRG
Bein[1] B.K., Kissel[2] S., Szymanski[3] Z.,
[1]Institut für Experimentalphysik VI, Ruhruniversität Bochum, FRG
[2]On leave from MIT, Cambridge, Massachusetts, USA
[3]On leave from Institute of Fundamental Technological Research, Warsaw, Poland
Total radiation losses and global energy balance in neutral beam-heated ASDEX discharges

A 7 Steinmetz K. , Rapp H., Behringer K., Bernhardi K., Eberhagen A., et.al.
MPI für Plasmaphysik, Garching, FRG
Hübner K., Malek K.,Kissel[1] S., Szymanski[2] Z.
Institut für Angewandte Physik II, Universität Heidelberg, FRG
[1]On leave from MIT, Cambridge, Massachusetts, USA
[2]On leave from Institute of Fundamental Technological Research, Warsaw, Poland
Non-thermonuclear neutron production in hydrogen-beam- heated ASDEX plasmas

A 8 Shoji T., Funahashi A., Hoshino K., Kasai S., Kawakami T. et al.
JAERI, Tokai, Naka, Ibaraki, Japan
Okta[1] K., Tamai[2] H., Yanagisawa[3] I.,
[1]On leave from Mitsubishi Electrical Corp.
[2]On leave from Mitsubishi Atomic Power Industries
[3]On leave from University of Tsukuba
Results from the JFT-2M experiments

A 9 Strait E.J., Bernard L.C., Lee J.K., Moore R.W., Stambaugh R.D. and Doublet III Physics Operations, Neutral Beam and Theory Groups (presented by Keith H. Burrell)
GA Technologies Inc. San Diego, California, USA
MHD stability of high-beta plasmas in Doublet III

A 10 Karger F., Klüber O., Niedermeyer H.
MPI für Plasmaphysik, Garching, FRG
Schüller F., Thomas P.,
JET Joint Undertaking, Abingdon, Oxon UK
Experimental studies of current ramp rates in ASDEX

A 11 Strachan J.D.,Soltwisch[1] H.,
PPPL, Princeton, New Jersey, USA
[1]IPP, KFA Jülich GmbH, Jülich, FRG
The correlation of some parameters on PLT neutral beam heated plasmas

B 1 Leonov V.M.
I.V. Kurchatov Institute of Atomic Energy, Moscow , USSR
Charge-exchange spectra in T-11 tokamak with neutral beam injection

B 2 Gentle K.,Brower[1] D.L, Bravenec R., Kochanski T., Luhmann[1] N.C.Jr.,Peables[1] W.A., Phillips P., Richards B., Rowan W., Savagu[1] R., Yu[1] C.X.
University of Texas at Austin
Fusion Research Center, Austin, USA
[1]University of California, Los Angeles, USA
The spectrum of density fluctuations in TEXT

B 3 Atkinson D., Blewett S., Dalton A., Edlington T., Goldsmith P., Hall K., Parham B., Rabbett H., Robinson D.C., Todd T.N.
Culham Laboratory, Abingdon, Oxon, UK
Experimental studies of low-q tokamak discharges in the CLEO apparatus

B 4 Cheetham A.D., Hamberger S.M.,Hogg[1] G.R., How J.A., Kuwahara H., Morton A.H., Sharp L.E., Vance C.F.,
Plasma Research Laboratory, Australian National University, Canberra, Australia
[1]AAEC Lucas Heights Research Laboratories, Sutherland, NSW, Australia
MHD activity and disruptions in the LT-4 tokamak

B 5 Simonet F., TFR Group
Département de Recherches sur la Fusion Contrôlée
CEN, Fontenay-aux-Roses, France
Measurements of electron density profile and local density fluctuations by microwave reflectometry on TFR

B 6 Platz P.,Bombarda F., TFR Group
Département de Recherches sur la Fusion Contrôlée
CEN, Fontenay-aux-Roses, France
Highly ionized argon in TFR plasmas

B 7 TFR Group
Département de Recherches sur la Fusion Contrôlée,
CEN, Fontenay-aux-Roses, France
Grésillon D., Hémon A., Truc A.,
Laboratoire PMI, Ecole Polytechnique, Palaiseau, France
How to measure drift wave propagation along the torus of a tokamak

B 8 Dubois M.A., TFR Group
Département de Recherches sur la Fusion Contrôlée
CEN, Fontenay-aux-Roses, France
Low-q MHD activity studies on TFR

B 9 Luxon J.L., Brooks N.H., Davis L.G., Fisher R.K., Helton F.J., Mahdavi M.A. et al.
GA Technologies Inc., San Diego, California, USA
The big DEE upgrade of Doublet III

B 10 Waidmann G.
IPP, KFA Jülich GmbH, Jülich, FRG
Electron cyclotron emission diagnostics on TEXTOR

B 11 Golant V.E., Goncharov S.G.,Gornostaev[1] S.V. Grigorjev A.V., Gryaznevich M.P. et al.[2]
A.F. Ioffe Physico-Technical Institute, Leningrad, USSR
[1]D.V. Efremov Scientific Research Institute for Electrophysical Equipment, Leningrad, USSR
[2]I.V. Kurchatov Institute of Atomic Energy, Moscow, USSR
The investigation of plasma minor radius compression in TUMAN-3 tokamak

B 12 Golant V.E., Bender[1] S.E.,Gornostaev[1] S.V., Grigoriev A.V., Gryaznevich M.-P. et al.
A.F. Ioffe Physico-Technical Institute, Leningrad, USSR
[1]D.V. Efremov Scientific Research Institute for Electrophysical Equipment, Leningrad, USSR
The experiments with compressed plasma column on TUMAN-3 tokamak

B 13 Nagami M., Kasai[1] M., Aikawa H., Kitsunezaki A., Kobayashi[2] T. et al.
JAERI, Tokai, Naka, Ibaraki, Japan
[1]On leave from Mitsubishi Atomic Power Industries
[2]On leave from Hitachi, Ltd.
Angel T., Armentrout C., Blau F., Bramson G., Brooks N., et.al.
GA Technologies, Inc., San Diego, USA
High temperature and high density plasmas in beam heated divertor discharges in Doublet III

B 14 Montvai A., Pócs L., Vályi L., Zoletnik S.
Central Research Institute for Physics Budapest, Hungary,
Phenomenology of the internal disruption in MT-1 tokamak

C 1 Soltwisch H.
IPP, KFA Jülich GmbH, Jülich, FRG
Measurement of electron and current density profiles in TEXTOR by means of a far-infrared laser interferometer/polarimeter

C 2 Vlases[1] G., Büchl K., Campbell[2] D.,
MPI für Plasmaphysik, Garching, FRG
[1]University of Washington, Seattle, Washington, USA
[2]Culham Laboratory Abingdon, Oxon, UK
Studies of tokamak transport based on pellet injection

C 3 Chang C.T.
Risö National Laboratory, Roskilde, Denmark
Some considerations of pellet injections in JET and INTOR

C 4 Mercurio S.
Istituto di Fisica dell Università, Palermo, Italy
Electrostatic shielding of pellets in plasmas of controlled fusion experiments

Reversed Field Pinches, Compact Tori
Part I, p. 137 - 174

A 43 Hutchinson I.H.
Culham Laboratory, Abingdon, Oxon, UK
Plasma resistance studies in HBTX1A reversed field pinch

A 44 Bunting C.A., Carolan P.G., Muir[1] D.G.
Culham Laboratory, Abingdon, Oxon, UK
[1]Royal Holloway College, Egham, London, UK
Total radiation measurements from the HBTX1A experiment

A 45 Long[1] J.W., Newton A.A., Gimblett C.G.
Culham Laboratory, Abingdon , Oxon, UK
[1]Oxford Polytechnic, Oxford, UK
Predictions of relaxation models in reversed field pinches

A 46 Edenstrasser J.W.
Institut für Theoretische Physik, Universität Innsbruck, Austria
Nalesso G.F.
University of Padova, Italy
F-O diagrams of ETA-BETA II RFPs with β and the safety factor an axis as parameters

A 47 Kaligin A.G., Kochan W.J., Kretchuk A.P., Kurtmullaev R.Kh., Proshletsov A.P.
I.V. Kurchatov Institute of Atomic Energy, Moscow, USSR
Compact torus with combined magnetic structure ($B_\varphi \neq 0$): Compression, heating, relaxation features

A 48 Es'kov A.G., Korshunov V.K., Krylov S.F., Kurtmullaev R.Kh., Laukhin Ya. et al.
I.V. Kurchatov Institute of Atomic Energy, Moscow, USSR
Principles of compact torus equilibrium and translation in profiled magnetic field

Stellarators, Bumpy Tori
Part I, p. 175 - 246

C 17 Ringler H., W VII-A Team, NI Group
MPI für Plasmaphysik, Garching, FRG
Energy and particle confinement in currentless W VII-A discharges

C 18 Weller A., W VII-A Team, NI Group
MPI für Plasmaphysik, Garching, FRG
Impurity confinement studies in the Wendelstein W VII-A stellarator

C 19 Müller G., W VII-A Team, NI Group
MPI für Plasmaphysik, Garching, FRG
Plasma fluctuation measurements in the W VII-A stellarator

C 20 Renner H., W VII-A Team, NI Group
MPI für Plasmaphysik, Garching, FRG
Effect of the rotational transform on plasma behaviour in the W VII-A stellarator

C 21 Maaßberg H., Wobig H.
MPI für Plasmaphysik, Garching, FRG
Monte-Carlo simulation of particle and energy confinement in stellarators at low collision frequency

C 22 Fujiwara M., Shoji T., Hosokawa M., Iguchi H., Takasugi K. et al.
Institute of Plasma Physics, Nagoya University, Nagoya, Japan
[1]Research Institute for Applied Mechanics, Kyushu University, Fukuoka, Japan
Plasma heating and confinement in Nagoya Bumpy Torus (NBT-1M)

C 23 Sbitnikova I.S., Blokh M.A., Voronov G.S., Gippius E.F., Donskaya N.P. et al.
Lebedev Institute of Physics, Moscow, USSR
Profiles of diffusion coefficient of impurity ions in L-2 stellarator plasma

C 24 McLenithan K.D., Shohet J.L.
University of Wisconsin, Torsatron/Stellarator Laboratory, Madison, Wisconsin, USA
Grieger G.
MPI für Plasmaphysik , Garching, FRG
Runaway current generation by cyclotron resonance in the Wendelstein VII-A stellarator

D 12 Miyawaki S., Nagao S., Okajima S., Sasaki[1] N., Abe[2] Y.
Chubu Institute of Technology, Kasugai, Japan
[1]Faculty of Engineering, Tohoku University, Sendai, Japan
[2]Institute of Plasma Physics, Nagoya University, Nagoya, Japan
Helical axis torsatron

D 13 Funato Y.,Kitajima S., Sakamoto I., Watanabe H., Nagao[1] S.
Tohoku University, Sendai, Japan
[1]Chubu Institute of Technology, Kasugai, Japan
Experiments on the non-planar torus: Asperator NP-4

D 14 Treffert J.D., Shohet J. L.
University of Wisconsin, Torsatron/Stellarator Laboratory, Madision, Wisconsin, USA
Measurement of self-generated Pfirsch-Schlüter and bootstrap currents in the PROTO-CLEO stellarator

D 15 Anderson D.T., Anderson F.S.B., Shohet J.L., University of Wisconsin, Torsatron/Stellarator Laboratory, Madison, Wisconsin, USA
Design, fabrication and initial operation of IMS

D 16 Kawahata K., Fujita J., Mase[2] A., Nishizawa A., Noda N., Sakai[1] T. et al.
Institute of Plasma Physics, Nagoya University, Nagoya, Japan
[1]Faculty of Engineering, Nagoya University, Nagoya, Japan
[2]Plasma Research Center, University of Tsukuba, Iberaki, Japan
Confinement and density fluctuations on JIPP T-II plasma

D 17 Perepelkin N.F., Suprunenko V.A., Volkov E.D., Arsen'ev A.V., Burchenko P. Ya. et al.
Institute of Physics and Technology, Ukrainian Academy of Sciences, Kharkhov, USSR
Restriction and suppression of electron runaway in a stellarator during ohmic heating of a magnetized plasma

Mirrors
Part I, p. 247 - 266

D 18 Konstantinov S.G., Bocharov V.N., Kudryavtsev A.M., Myskin O.K., Panasyuk V.M. et al.
Institute of Nuclear Physics, Novosibirsk, USSR
The study of the radial density and velocity profiles of plasma rotation on the SVIPP device

D 19 Bocharov V.N., Konstantinov S.G., Kudryavtsev A.M., Myskin O.K., Panasyuk V.M. et al.
Institute of Nuclear Physics, Novosibirsk, USSR
Stabilizing plasma layer for rotating plasmas

D 20 Zhitlukhin A.M., Safronov V.M., Sidnev V.V., Skvortsov Yu.V.
I.V. Kurchatov Institute of Atomic Energy, Moscow, USSR
Magnetic mirrors effect on confinement of plasma produced through the collision of streams with $\beta \sim 1$

D 21 Ioffe M.S., Kanaev B.I., Pastukhov V.P., Pitersky V.V., Chistyakov R.R. et al.
I.V. Kurchatov Institute of Atomic Energy, Moscow, USSR
Studies on nature of anomalous electron diffusion in ATOLL magneto-electrostatic trap

D 22 McVey B.D., Post R.S., Blackfield D.T., Gerver M., Irby J. et al.
MIT, Cambridge, Massachusetts, USA
TARA tandem mirror

Heating and Current Drive
Part I, p. 267 - 466

A 22 Zhang[1] Z.X., Wobig H.
MPI für Plasmaphysik, Garching, FRG
[1]Institute of Physics, Peking, Academia Sinica, Guest of Alexander von Humboldt Stiftung
Ecrh calculations for the stellarator W-VII A

A 23 FT Group
CRE, Frascati, Italy
Behaviour of electron cyclotron emission during heating at $\omega > \omega_{ln}$ in the Frascati tokamak (FT)

A 24 FT Group
CRE, Frascati, Italy
Mazzitelli G., ENEA-guest
Parametric decay instabilities observed in FT tokamak

A 25 Barbato E. Santini F.,
CRE, Frascati, Italy
Features of lower hybrid wave trajectories in low and high density FT discharges

A 26 T-10 Group
I.V. Kurchatov Institute of Atomic Energy, Moscow USSR
Andreev A.P., Kuteev B.V., Skoblikov S.V., Umov A.P., M.I. Kalinin Polytechnical Institute, Leningrad, USSR
Usov V.G., Flyagin V.A.,
Institute of Applied Physics, Gorki, USSR
Piekaar H.W., Sillen R.M.J., Oyevaar Th.
FOM-Instituut voor Plasmafysica, Rijnhuizen, Nieuwegein, The Netherlands
Cavallo A.
University of Maryland, USA
Transport of plasma energy in T-10 at ecrh with the resonance zone displaced from plasma center

A 27 Hansen F.R., Lynov J.P., Michelsen P.
Risö National Laboratory, Roskilde, Denmark
Ecrh of a high density plasma

A 28 Bures, M.
Royal Institute of Technology, Department of Plasma Physics and Fusion Research, Stockholm, Sweden
Alfvén wave heating of a plasma surrounded by a cold gas-mantle

A 29 Keller R., Appert K., Behn R., de Chambrier A., Collins G.A. et al.
CRPP-EPFL, Lausanne , Switzerland
Experimental determination of ω/ω_{ci} effects in shear Alfvén wave excitation in TCA tokamak

A 30 Appert K.,Vaclavik J., Villard L.
CRPP-EPFL, Lausanne, Switzerland
Global modes in the Alfvén wave heating scheme

A 31 Dorokhov V.V., Elfimov A.G., Lozovsky S.N.
Institute of Physics and Technology, Sukhumi, USSR
Alfvén heating of axial uniform current-carrying plasma

B 24 Tanaka S., Kubo S., Nakamura M., Cho T., Nakao S. et al.
Department of Physics, Kyoto University, Kyoto, Japan
Toroidal plasma current start-up and sustainment by rf in the WT-2 tokamak

B 25 Petrzilka V.A., Klima R., Pavlo P.
Institute of Plasma Physics Czechoslovak Academy of Sciences, Prague, Czechoslovakia
Nonlinear variations of the reflection coefficient at the lower hybrid heating

B 26 Surjalal, Sharma A., Mohna M.
Physical Research Laboratory, Ahmedabad, India
Plasma heating by mode-conversion of lower-hybrid to electron-acoustic mode

B 27 Canobbio E., Croci R.
MPI für Plasmaphysik, Garching, FRG
On the interpretation of the lh current drive experiments

B 28 Gormezano C., Bibet P., Blanc P., Briand P., Briffod G. et al.
Département de Recherches sur la Fusion Contrôlée, CEN, Grenoble, France
Lower hybrid heating and current drive in the PETULA-B tokamak

B 29 Appert K., Kritz[1] A.H., Succi S., Vaclavik J.
CRPP-EPFL, Lausanne, Switzerland
[1]Department of Physics, Hunter College, CUNY
Numerical studies of the influence of runaways on current drive

B 30 Faillon G.
THOMSON-CSF, Boulogne-Bilancourt, France
Recent progress in plasma- heating klystrons

B 31 Breizman B.N., Erofeev V.I.
Institute of Nuclear Physics, Novosibirsk, USSR
Electron beam relaxation in a magnetically confined plasma with random density inhomogeneities

C 5 Anderson D., Lisak M.
Institute for Electromagnetic Field Theory, Chalmers University of Technology, Göteborg, Sweden
Effects of icrh on fast ion containment in tokamaks

C 6 Lisak M., Anderson D.
Institute for Electromagnetic Field Theory, Chalmers University of Technology, Göteborg, Sweden
Anomalous alpha-particle losses and generation of a plasma current due to thermonuclear cone instabilities in tokamaks

C 7 Brambilla M., Ottaviani M.
MPI für Plasmaphysik, Garching, FRG
Ion cyclotron minority heating of a hydrogen plasma

C 8 Boehmer H., Barter J.,Dandl[1] R., Goede H., Lazar N. et al.
TRW Energy Research Center Redondo Beach CA, USA
[1]Applied Microwave Plasma Concepts, Encinitas, Ca., USA
Ion cyclotron resonance heating in the symmetric tandem mirror

C 9 Scharer J., Romero H., Sund R.
University of Wisconsin, Madison, Wisconsin, USA
Tokamak wave coupling and heating in the Icrf

C 10 Olivain J., TFR Group
Déartement de Recherches sur la Fusion Contrôlée, CEN, Fontenay-aux-Roses, France
Truc A.
PMI, Ecole Polytechnique, Palaiseau, France
Observation of fast and slow modes during icrf heating in TFR by CO_2 coherent scattering-comparison between rf excitations on the inner and the outer side of the torus

C 11 Gambier D. J., Samain A.
Département de Recherches sur la Fusion Contrôlée, CEN, Fontenay-aux-Roses, France
Variational modelling of ion cyclotron resonance heating

C 12 Evrard M.P., Bhatnagar V.P., Faulconer D.W., Koch R., Messiaen A.M. et al.
Laboratoire de Physique des Plasmas, Ecole Royale Militaire, Brussels, Belgium
Theoretical study of the JET trombone antenna loading at the IC frequency

C 13 Bhatnagar V.P., Koch R., Weynants R.R., Geilfus P., Kirkpatrick R.
Laboratoire de Physique des Plasmas, Ecole Royale Militaire, Brussels, Belgium
Power deposition profile of the ion-cyclotron resonance heating of large tokamaks by ray-tracing technique

C 14 Sbitnikova I.S., Batyuk V.A., Blokh M.A., Grebenshchikov S.E., Kovan[1] T.A. et al.
Lebedev Institute of Physics, Moscow, USSR
[1]I.V. Kurchatov Institute of Atomic Energy, Moscow, USSR
Heating of hydrogen plasma on the first harmonic of ion-cyclotron frequency in L-2 stellarator

C 15 Grekov D.L., Stepanov K.N.
Institute of Physics and Technology, Ukrainian Academy of Sciences, Kharkov, USSR
RF plasma heating in DRACON devices

C 16 Pavlenko V.N., Panchenko V.G., Revenchuk[1] S.M.
Institute of Physics and Technology and
[1]Institute of Nuclear Research, Ukrainian
Academy of Sciences, Kharkov, USSR
Anomalous absorption of electromagnetic wave energ near the lower hybrid resonance

D 23 Bornatici M., Crestani M., Ferri P., Ruffina U.
Departement of Physics' A. Volta, University of
Pavia, Italy
Electron cyclotron absorption and emission in anisotropic plasmas

D 24 Airoldi A.C., Argenti L., Cirant S., Orefice A.,
Ramponi G.
Istituto di Fisica del Plasma, CNR, Milano, Italy
Numerical simulation of the electron cyclotron absorption in THOR plasma

D 25 Argenti L., Bonizzoni G.,Carretta[1] U., Cima G.,
Cirant S. et al.[2]
Istituto di Fisica del Plasma, CNR, Milano, Italy
[1]Centro Studi sulla Propulsione e l'Energetica,
CNR-Politecnico di Milano, Italy
[2]Istituto di Fisica dell Università di Milano, Italy
The ecrh experiment in the THOR tokamak

D 26 Scharer J., Lam N.T., Audenaerde K.,
Electrical and Computer Engineering Department,
University of Wisconsin, Madison, Wisconsin, USA
Electron cyclotron resonance heating in realistic tandem mirror configuratrons

D 27 Pesic S.
Laboratory for Physics, Institute of Nuclear
Sciences 'Boris Kidric'-Vince, Beograd, Yugoslavia
Extraordinary wave absorption near the electron cyclotron frequency

D 28 Alcock M.W., Atkinson D., Blewett S.,
Collins P.R., Dalton A. et al.
Culham Laboratory, Abingdon, Oxon, UK
Preliminary gyrotron heating results on CLEO

D 29 Nakamura K., Itoh S., Nakamura Y., Hiraki N.,
Kikuchi[1] M., Nagao A., Watanabe T.
Research Institute for Applied Mechanics, Kyushu
University, Fukuoka, Japan
[1]JAERI, Tokai, Japan
Acceptable turbulent heating for large tokamak devices

D 30 Tortur-Team: de Kluiver H., Yousef N.,
de Groot B., Barth C.J., van der Meiden H.J. et al.[1]
ECE Team: Piekaar H.W., Sillen R.M.J. Oyevaar T.,
Tubbing B.J.D., Niestadt R.M.
FOM Instituut voor Plasmafysica, Rijnhuizen,
Nieuwegein, The Netherlands
[1]On leave from Chubu Institute of Technology,
Kasugai, Japan
High temperature plasma heating by weak turbulence in the TORTUR tokamak

D 31 Edenstrasser J.W.,de Kluiver[1] H.,
Schuurman[1] W.
University of Innsbruck, Austria
[1]FOM Instituut voor Plasmafysica, Rijnhuizen,
Nieuwegein, The Netherlands
Time-evolution of the turbulent heating experiment TORTUR II

D 32 Ikezawa S., Takeda S.,
Chubu Institute of Technology, Kasugai, Japan
Mechanism of rf confinement of a plasma

D 33 Peneva I.H., Kirchev S.D., Dukov I.V.,
Kondratenko[1] A.N.,Sarhad I.Ibn
Higher Pedagogical Institute, Shumen, Bulgaria
[1]Kharkov University, Kharkov, USSR
The kinetic theory of nonsymmetric waves in bounded plasma

E 26 Ainsworth N.R., Alcock M.W., Collins P.R.,
Morris W.A., Morris[1] A.W., Robinson D.C.
Culham Laboratory, Abingdon, Oxon, UK
[1]University of Oxford, UK
High β and lower q studies on TOSCA using ecrh

E 27 O'Brien M.R., Start D.F.H., Grace[1] P.M.V.
Culham Laboratory, Abingdon, Oxon, UK
[1]St. John's College, Cambridge, UK
The effects of the relativistic correction to the electron mass on ecrh current drive

E 28 Riviere A.C.
Culham Laboratory, Abingdon, Oxon, UK
An assessment of tokamak ecrh experiments

E 29 Charbit P., Faillon G., Garin P., Mourier G., Perre Y.
Thomson-CSF, Electron Tube Division Boulogne-
Bilancourt, France
Studies on high-power 100 GHz gyrotron

E 30 Cap F.
Plasma Physics Group, Institut für Theoretische
Physik, University of Innsbruck, Innsbruck, Austria
Propagation of electromagnetic low frequency waves in inhomogeneous toroidal plasmas

E 31 Takamura S., Ushigusa K., Okuda T.
Department of Electrical Engineering, Nagoya
University, Nagoya, Japan
Internal structure on energetic electrons and waves in radio frequency current-driven tokamak plasma

E 32 Da Costa Cabral J.A.
Centro de Electrodinamica, Instituto Superior
Técnico, Lisboa, Portugal
Transformation of a Trivelpiece-Gould wave with $F \sim F_{ce}$ into an electromagnetic wave in an inhomogeneous plasma column

E 33 W VII-A Team: Junker J., Cattanei G., Dorst D., Elsner A.,
Erckmann V. et al.
NI Group: Freudenberger K., Lister G.G., Ott W.,
Penningsfeld F.P., Speth E.
MPI für Plasmaphysik, Garching, FRG
Ion heating in the stellarator W VII-A

E 34 Bulyginsky D.G., Gusev V.K., Djachenko V.V.,
Irzak M.A., Kantor M.Yu. et al.
A.F. Ioffe Physico-Technical Institute, Leningrad,
USSR
Ecr - heating of plasma in FT-1 tokamak and its influence on the ion component

E 35 Levin L.S. Dyachenko V.V., Larionov M.M.
Lebedev A.D., Serebreny G.A.,
A.F. Ioffe Physico-Technical Institute, Leningrad,
USSR
Poloidal rotation of the tokamak plasma and asymmetry of the charge exchange atoms flux

E 36 Subbarao D., Uma R.
Fusion Energy Cell, Centre of Energy Studies
Indian Institute of Technology, New Delhi, India
Stochastic heating of charged particles during reflection of em-waves from inhomogeneous plasmas

Plasma Focus Devices, Theta- and Z-Pinches
Part I, p. 467 - 578

D 34 Bourham M.A., El Gamal H.A., Abu El Nasr[1] T.Z.
Nuclear Research Centre, Cairo, Egypt
[1]Physics Department, Faculty of Science, Al Azhar University, Cairo, Egypt
Electromagnetic radiation from a turbulent plasma of a straight thetatron discharge

D 35 Kucínski J., Rabinski M.
Institute of Nuclear Studies, Swierk-Otwock, Poland
Investigation of heat transfer to the anode of the plasma-focus device at elevated repetition rate

D 36 Gacek A., Farynski A.
S. Kaliski Institute of Plasma Physics and Laser Microfusion, Warsaw, Poland
A diode model of high-energy charged particle emission in the plasma-focus device

D 37 Decker G., Jäger[1] U. Kies W., Pross G., Rybach J.
Physikalisches Institut I, Universität Düsseldorf, FRG
[1]Institut für Plasmaforschung, Universität Stuttgart, FRG
SPEED 1: A high impedance, high voltage driven fast plasma focus of improved performance

D 38 Khautiev E.Yu., Krauz V.I., Salukvadze R.G.
I.N. Vekua Institute of Physics and Technology, Sukhumi, USSR
Some features of ion beam formation in a plasma focus

D 39 Burtsev V.A., Bardinov A.A., Zhukov A.P.
Kozhevin V.M., Kuznetsov V.S. et al.
D.V. Efremov Scientific Research Institute of Electrophysical Apparatus, Leningrad, USSR
Laser theta-pinch heating of dense plasma in pulsed magnetic systems

D 40 Gryzinski M.
Institute for Nuclear Studies, Swierk-Otwock, Poland
Fusion energy production at the ordered motion of ions

D 41 Gryzinski M., Baranowski J., Gebalksi S.,
Langner J. et al.
Institute for Nuclear Studies, Swierk-Otwock, Poland
Structure of ion beams generated in RPI imploders

D 42 Konkashbaev I.K., Nikandrov L.B., Ryltseva T.V.,
I.V. Kurchatov Institute of Atomic Energy, Moscow, USSR
Z-pinch-liner acceleration

D 43 Gryukanov M.F., Konkashbaev I.K.
I.V. Kurchatov Institute of Atomic Energy Moscow, USSR
Heat waves in a dense plasma

D 44 Alikhanov S.G., Novikov V.P.
I.V. Kurchatov Institute of Atomic Energy, Moscow, USSR
The toroidal intertial system with magnetogas-kinetic confinement of plasma

E 1 Sinman S.
Middle East Technical University, Plasma Engineering Laboratory, Ankara, Turkey
Sinman A.
Ankara Nuclear Research and Training Center, Electron Physics Laboratory, Ankara, Turkey
A conceptual design study of a new DPF system for an alternative heating scheme

E 2 Sinman S.
Middle East Technical University, Plasma Engineering Laboratory Ankara, Turkey
Sinman A.
Ankara Nuclear Research and Training Center
Electron Physics Laboratory, Ankara, Turkey
Optimization of REB generators employing in collective ion acceleration

E 3 Denus S., Czekaj S., Szydlowski A.
S. Kaliski Institute of Plasma Physics and Laser Microfusion, Warsaw, Poland
Measurement of fast deuteron emission from a plasma focus device

E 4 Czekaj S., Borowiecki M., Denus S.,
Koziarkiewicz W., Skrzeczanowski W. et al.
S. Kaliski Institute of Plasma Physics and Laser Microfusion, Warsaw, Poland
The dynamics and plasma sheath structure in the plasma-focus device

E 5 Sadowski M., Chyrczakowski S., Komar W.
Rydygier E., Zebrowski J.
Institute for Nuclear Studies, Swierk-Otwock, Poland
Investigation of ion beams generated in a plasma focus

E 6 Hirano K., Shimoda K., Yamamoto T., Sato M.
Kobayashi K. et al.
Dept. of Electronic Engineering, Gunma University, Kiryu, Gunma, Japan
Plasma dynamics and charged particle emission in the plasma focus

E 7 Challis, C.D., Dangor A.E., Wyndham E.S.,
Mosher[1] D., Bessell W.G. et al.
Imperical College , University of London, UK
[1]Office of Navel Research, London, Branch Office
X-ray production in a gas-puff Z-pinch

E 8 Dangor A.E., Favre M., Psimopoulos M.
Imperial College, London, UK
Mateev E.S.
Sofia University, Sofia, Bulgary
Transformation of a gas-embedded Z-pinch into a Helix

E 9 Zukakishvili G.G., Ryzhkov V.N., Salukvadze R.G.,
Tikhanov E.K., Chkuaseli Z.D.,
I.N. Vekua Institute of Physics and Technology, Sukhumi, USSR
Restriction of end losses in a linear theta-pinch by means of corrugated magnetic mirrors

E 10 Panarella E., Savic P.
National Research Council, Ottawa, Canada
Scaling laws for the REXIMPLO spherical pinch

E 11 Orlov M.M., Terentiev A.R., Khrabrov V.A.
I.V. Kurchatov Institute of Atomic Energy, Moscow, USSR
Plasma dynamics in plasma focus

E 12 Forrest M.J., Peacock N.J.
Culham Laboratory Abingdon, Oxon, UK
Kirk R.E., Muir D.G.
On attachment from Royal Holloway College, London, UK
The significance of new measurements of density fluctuations and the current distribution in the Culham plasma focus

E 13 Gorbulin Yu.M., Gordeev E.M., Zlotnikov D.M., Kalinin Yu.G., Kuksov P.V. et al.
I.V. Kurchatov Institute of Atomic Energy, Moscow, USSR
Study of intense relativistic electron beam self-focusing dynamics

Laser-Plasma Interaction, Intertial Confinement
Part II, p. 1 - 50

E 37 Atzeni S., Caruso A.
CRE, Frascati, Italy
Ignition criterion for dense, isobaric D-T plasmas and consequences on ICF target design

E 38 Heikkinen J.A., Karttunen S.J.,Salomaa[1] R.R.E.,
Technical Research Centre of Finland,
Nuclear Engineering Laboratory, Helsinki, Finland
[1]Helsinki University of Technology, Espoo, Finland
Nonlinear ion waves in absolute Brillouin scattering

E 39 Yoshida K., Kato Y., Nakatsuka M., Jitsuno T., Nowada S. et al.
Institute of Laser Engineering, Osaka University, Suita, Osaka, Japan,
GEKKO XII glass laser system for laser fusion research

E 40 Hora H., Lalousis P., Ghatak A.K., Jones[1] D.A. Talapaga-Rosenberger S.
Department of Theoretical Physics, University of New South Wales, Kensington, Australia
[1]Materials Research Labs., Ascot Vale, Victoria
High electrostatic fields and oscillations in expanding inhomogeneous plasmas without external fields or with laser irradiation

E 41 Sternlieb A.
Soreq Nuclear Research Centre, Yavne, Israel
Scaling laws for the resistive longitudinal instability in finite charged beams

E 42 Nicolas J.A., Sanmartin J.R.
ETSI Aeronáuticos, Universidad Politécnica de Madrid, Spain
Inverse Bremsstrahlung effects on the coronae of laser- irradiated pellets and slabs

E 43 Barrero A., Rosety L.,Sanz[1] J.
ETSI Industriales, Universidad de Sevilla, Spain
ETSI Aeronáuticos, Universidad de Politecnica de Madrid, Spain
Spherical expansion plasmas in ion beam impinged pellets

E 44 Wooding E.R., Brown D.A., Marchington P.S., Sayed N., Sudera Y.
Royal Holloway College, University of London, UK
Density profiles and fluctuations in CO_2 laser produced plasmas

E 45 Murusidze I.G., Tsintsadze N.L. Tskhakaya D.D.,
Institute of Physics, Academy of Sciences of the Georgian SSR, Tbilisi, USSR
Radiation of Alfvén waves by the accelerating Langmuir soliton

Diagnostics
Part II, p. 51 - 100

E 14 Mori I.
Technical College of Tokushima University, Tokushima, Japan
Ion temperature measurement with neutral beams

E 15 Alladio F., Crisanti F.
CRE, Frascati, Italy
Equilibrium magnetic measurements by toroidal multipolar method for FTU tokamak

E 16 Lehner Th.
Laboratoire de Physique des Milieux Ionisés, Ecole Polytechnique, Palaiseau, France
Ion Bernstein modes fluctuations as a measure of the magnetic field orientation

E 17 von Hellermann M., Gülker H.J., Hasse O.R.,
FB Physik, Universität Essen, FRG
Observation of plasma turbulence by coherent far forward scattering using a multi channel detector array at 10 microns

E 18 Airoldi A.C., Orefice A., Ramponi G.
Istituto di Fisica del Plasma, CNR Milano, Italy
Ece simulation for a toroidal plasma and its applications to JET

E 19 Hallock G.A., Hickok R.L., Jennings W.C., Connor K.A., Forester J.C. et al.
Rensselaer Polytechnic Institute, Troy, NY., USA
Haste G.R., Wootton A.J.
ORNL, Oak Ridge, Tennessee, USA
Space potential measurements on EBT-S and ISX-B

E 20 Tonetti G.
CRPP-EPFL, Lausanne, Switzerland
Measurement of the plasma magnetic field with an ion beam probe

E 21 Woskoboinikow P., Mulligan W.J., Machuzak J., Cohn D.R., Temkin R.J. et al.
Plasma Fusion Center, MIT, Cambridge, USA
385μm D_2O Laser collective Thomson scattering ion temperature diagnostic

E 22 Gimzewski J.K., Veprek S.
Institute of Inorganic Chemistry, University of Zürich, Zürich, Switzerland
A new method for the determination of impurity ion energies and their implantation depths in collection probes exposed to the scrape-off layer

E 23 Lisitano G., Baretich[1] F., Gammino[1] G., Bazzo I., Cassamagnaghi C. et al.
MPI für Plasmaphysik, Garching, FRG
[1]Cise, Department of Acoustical Diagnostics, Milano, Italy
Millimeter wave Schlieren diagnostics for fusion plasma

E 24 W VII-A Team: Tutter M., Cattanei G., Dorst D., Elsner A. Erckmann V. et al.
NI-Group: Freudenberger K., Lister G.G., Ott W., Penningsfeld F.-P., Speth E.
MPI für Plasmaphysik, Garching, FRG
Effect of suprathermal electrons on Ece-spectra in W VII-A

E 25 Filippov V.N., Komissarova I.I., Ostrovskaya G.V., Shedova E.N.
A.F. Ioffe Physico-Technical Institute, Leningrad, Academy of Sciences, USSR
The prospects to enhance the sensitivity of holographic interferometry plasma diagnostics in IR-region

Magnetic Confinement Theory

Part II, p. 101 - 288

B 41 Ming-Lun Xue
Institute of Mechanics, Chinese Academy of Sciences, Beijing, People's Republic of China
Advanced concept of adiabatic compression of tokamak and self-compression of compact torus

B 42 Khait V.D., Kolesnikov V.K.
Institute of High Temperatures, USSR Academy of Sciences, Moscow, USSR
Solution of the tokamak plasma equilibrium at high betas by the variational method

B 43 Casci F., Kaleck[1] A., Zehrfeld H.P.
MPI für Plasmaphysik, Garching, FRG
[1]IPP, KFA Jülich GmbH, Jülich, FRG
Quasistatic evolution of ideal MHD equilibria in INTOR and ASDEX-UG

B 44 Bernardin M.P., Tataronis J.A.
University of Wisconsin, Madison, Wisconsin, USA
Force-free MHD equilibria in non-axisymmetric toroidal geometry

B 45 Kovrizhnykh L.M., Shchepetov S.V.
Institute of General Physics, Moscow, USSR
Condition for the stability of dissipative modes in a stellarator

B 46 Rem J., Galvao[1] R.M.O., Goedbloed J.P., Sakanaka[2] P.H.
FOM-Instituut voor Plasmafysica, Rijnhuizen, Nieuwegein, The Netherlands
[1]Centro Tecnico Aerospacial, Sao Paulo, Brazil
[2]Universidade Estadual de Campinas, Sao Paulo, Brazil
Ideal MHD stability of a tokamak in the high-beta tokamak ordering

B 47 Nührenberg J. Großmann R., Herrnegger F.
MPI für Plasmaphysik, Garching, FRG
Evaluation of Mercier's criterion in 3D HELIAC equilibria

B 48 Pogutse O.P., Yurchenko E.I.
I.V. Kurchatov Institute of Atomic Energy, Moscow, USSR
Critical plasma pressure provided by the ballooning modes of helical instability in tokamak

B 49 Pogutse O.P., Chudin N.V.
I.V. Kurchatov Institute of Atomic Energy, Moscow, USSR
Radial structure of resistive ballooning modes

B 50 Rosenau Ph.
Faculty of Mechanical Engineering, Israel Institute of Technology, Haifa, Israel
On tearing modes in a resistive medium

B 51 Saramito B., Maschke E.K.
Département de Recherches sur la Fusion Contrôlée, CEN, Fontenay-aux-Roses, France
Bifurcation theory for tearing modes

B 52 Dnestrovskij[1] Yu.N., Kosomarov D.P., Popov A.M., Shagirov E.A.
M.V. Lomonosov State University, Moscow, USSR
[1]I.V. Kurchatov Institute of Atomic Energy, Moscow, USSR
Non-linear evolution of helical modes in a tokamak with low q

B 53 Samain A.
Département de Recherches sur la Fusion Contrôlée, CEN, Fontenay-aux-Roses, France
Diamagnetic destabilization of magnetic islands in the non-linear regime

B 54 Nedospasov A.V.
Institute of High Temperatures, USSR Academy of Sciences, Moscow, USSR
Current-convective turbulence and anomalous diffusion in tokamaks

C 37 Evangelidis E.A.
Plasma Physics Division, NUCOR-Pelindaba Pretoria, South Africa
On the solution of the equation of plasma equilibrium in a toroidal configuration

C 38 Mikhailov M.I.
"Energiya" Scientific Manufacturing Association
Shafranov V.D.
I.V. Kurchatov Institute of Atomic Energy, Moscow, USSR
Variational principle in flux variables for the toroidal plasma equilibrium

C 39 Wahlberg C., Arora[1] A.K., Ring. R.
Institute of Technology, Uppsala, Sweden
[1]Department of Physics, University of Rajasthan, Jaipur, India
Z-Pinch Equilibria in an External Magnetic Multipole Field

C 40 Grauer R., Rebhan, E.
Institut für Theoretische Physik II, Universität Düsseldorf, Düsseldorf, FRG
Semianalytical calculation of equilibrium and axisymmetric stability of finite aspect ratio tokamaks with elliptic cross-section

C 41 Kratzsch, K.A., Rebhan E.
Institut für Theoretische Physik II, Universität Düsseldorf, Düsseldorf, FRG
Calculation of growth rates from the marginal mode

C 42 Rewoldt G., Johnson[1] J.L., Anania[2] G.,
Chance M.S., Manickam J. et al.
PPPL Princeton University, New Jersey, USA
[1]On loan from Westinghouse Research & Development Center
[2]At Booz Allen and Hamilton, Management Consultants
Application of the stellarator expansion to equilibrium and stability studies of three-dimensional toroidal configurations

C 43 Kammash T., Nguyen K.,
University of Michigan, Ann Arbor, Michigan, USA
Beta limit for ballooning instabilities in EBT

C 44 Cheng C.Z., Chen L., Chance M.S., Rewoldt G.,Tang W.M.
PPPL Princeton University, Princeton, New Jersey, USA
Shear Alfvén waves and ballooning modes in tokamaks

C 45 Sundaram A.K., Sen A., Kaw P.K.
Physical Research Laboratory, Ahmedabad, India
Resistive ballooning modes in a high-temperature plasma

C 46 Storer R.G.
The Flinders University of South Australia, Bedford Park, South Australia
Resistive magnetohydrodynamic spectrum for toroidal plasmas

C 47 Tagger M., Frey M.
Departement de Recherches sur las Fusion Contrôlée, CEN, Fontenay-aux-Roses, France
Pellat R.
Ecole Polytechnique, Palaiseau, France
Quasi-linear evolution of tearing modes

C 48 Gribkov V.M., Kadomtsev B.B., Pogutse O.P.
I.V. Kurchatov Institute of Atomic Energy, Moscow, USSR
Plasma pressure drops produced by the ballooning modes

C 49 Lee J.K., Chu M.S., Helton F.J.
GA Technologies, Inc., San Diego, California, USA
Park W.
PPPL, Princeton University, Princeton, New Jersey, USA
Magnetic fluctuations in high-β tokamak plasmas

D 45 Klieb L., Schep T.J., Venema M.
FOM-Instituut voor Plasmafysica, Rijnhuizen, Nieuwegein, The Netherlands
Pegoraro F.
Scuola Normale Superiore, Pisa, Italy
Collisional and kinetic effects on electomagnetic modes in toroidal geometry

D 46 Schep T.J., Venema M.
FOM-Institut voor Plasmafysica, Rijnhuizen, Nieuwegein, The Netherlands
Drift modes in toroidal geometry

D 47 Pegoraro F., Coppi[1] B., Ramos J.
Scuola Normale Superiore, Pisa, Italy
[1]MIT, Cambridge, Massachusetts, USA
Electromagnetic ion cyclotron modes in a plasma with polarized nuclear spins

D 48 Hasselberg G., Rogister A.
IPP, KFA Jülich GmbH, Jülich, FRG
Drift wave spectra, energy fluxes and impurity transport in tokamak plasmas

D 49 Andersson P.
Institute for Electromagnetic Field Theory, Chalmers University of Technology, Göteborg, Sweden
The effects of temperature gradients on the curvature driven trapped electron mode

D 50 Hamnén H., Bondeson A., Anderson D., Lisak M.,
Core [1] W.G.F.
Institute for Electromagnetic Field Theory, Chalmers University of Technology, Göteborg, Sweden
[1]JET Joint Undertaking, Abingdon, Oxon, UK
Ripple-induced radial diffusion of fast ions in tokamaks

D 51 Weiland J.
Institute for Electromagnetic Field Theory, Chalmers University of Technology, Göteborg, Sweden
A nonlinear gyrokinetic equation obtained by integration along unperturbed orbits

E 46 Nocentini A., De Meio L.,
Istituto di Meccanica dell' Università Trieste, Italy
A new pseudo-classical transport theory for tokamak plasmas

E 47 Thyagaraja A., Haas F.A.
Culham Laboratory, Abingdon, Oxon, UK
A novel test-particle approach to anomalous transport in tokamaks

E 48 Gurevich A.V., Dimant Ya.S., Dnestrovskij[1] Yu.M.,
Kostomarov[2], D.P., Smirnov[2] A.P.
Lebedev Institute of Physics, Moscow, USSR
[1]I.V. Kurchatov Institute of Atomic Energy, Moscow, USSR
[2]M.V. Lomonosov State University, Moscow, USSR
Simulation of convective electron transport in T-10 tokamak

E 49 Dnestrovskij Yu.N., Neudatchin S.V. Pereverzev G.V.,
Polevoj A.R.
I.V. Kurchatov Institute of Atomic Energy, Moscow, USSR
Anomalous pinching and particle balance in tokamak

E 50 Yushmanov P.N.
I.V. Kurchatov Institute of Atomic Energy, Moscow, USSR
Generalized ripple-banana transport in tokamak

E 51 Yushmanov P.N.
I.V. Kurchatov Institute of Atomic Energy, Moscow, USSR
High energy ion confinement in tokamaks with local divertor

E 52 Avinash K.
Physical Research Laboratory, Navrangpura, Ahmedabad, India
Is motion of charged particle in mirror of true Markovian nature?

E 53 Riedler J.M., Heindler M., Miley[1] G.H.
Institut für Theoretische Physik, TU Graz, Austria
[1]Nuclear Engineering Laboratory, Urbana, Illinois, USA
Coulomb scattering between Maxwellian plasma and monoenergetic beam

Transport codes
Part II, p. 289 - .366

A 12 Rau F., Chodura R., Kisslinger J., Lotz W., Wobig H.
MPI für Plasmaphysik, Garching, FRG
Some effects of finite plasma pressure in the advanced stellarator WENDELSTEIN VII-AS

A 13 Nicolai A., Reiter D.
IPP, KFA Jülich GmbH, Jülich, FRG
Two-dimensional computer modelling of JET as a specific example of D-shaped tokamak plasmas

A 14 Becker G., Behringer K., Bernhardi K., Ebernhagen A., Fußmann G., et al.
MPI für Plasmaphysik, Garching, FRG
Kissel[1] S., Szymanski[2] Z.,
[1]On leave from MIT, Cambridge, Massachusetts, USA
[2]On leave from Institute of Fundamental Technological Research, Warsaw, Poland
Transport modelling of neutral beam heated l and h discharges in ASDEX

A 15 Watkins M.L.
JET Joint Undertaking, Abingdon, Oxon, UK
Abels van Maanen A.E.P.M.
On attachment from FOM-Instituut voor Plasmafysica Rijnhuizen, Nieuwegein, The Netherlands
Tokamak transport calculations for JET with different limiter materials

A 16 Sidorov V.P., Minenko V.P., Komoshvilli K.G.,
Vekua Institute of Physics and Technology, Sukhumi, USSR
Favorsky A.P., Dmitrieva M.V., Tishkin V.F.
Keldysh Institute of Applied Mathematics, Moscow, USSR
Numerical calculations of plasma parameters for a steady-state Alfvén-wave tokamak

A 17 Pavlichenko D.S., Besedin N.T., Pyatov V.N.,
Slavny A.S., Shvets O.M.
Institute of Physics and Technology, Ukrainian Academy of Sciences, Kharkov, USSR
Neoclassical equilibrium of plasma during ion heating in stellarator

A 18 Core W.G.F.
Jet Joint Undertaking, Abingdon, Oxon, UK
A 2-d model for the calculation of neutral transport in tokamaks with non-circular magnetic surfaces

A 19 Nicolai A., Wolf G.H.,
IPP, KFA Jülich GmbH, Jülich, FRG
Modelling of tokamak discharges based on transport processes along oblique magnetic field lines

A 20 Lister G.G.,Penningsfeld F.P., Ott W., Speth E.
MPI für Plasmaphysik, Garching , FRG
Neutral beam injection studies for W VII AS using the 3-d computer code FAFNER

A 21 Watkins M.L., Düchs D.F., Noll P.
JET Joint Undertaking, Abingdon, Oxon, UK
Is additional edge transport beneficial?

B 15 Sano F., Obiki T., Hanatani K., Zushi H.,
Sudo S. et al.
Plasma Physics Laboratory, Kyoto University, Gokasho, Uji, Kyoto, Japan
Ion and electron energy balance analysis of neutral-beam-heated Heliotron E plasmas

B 16 Martínez-Val J.M., Velarde G., Aragonès J.M.,
Arroyo R., Gago J.A. et al.
Departamento de Energia Nuclear E.T.S.I. Industriales Universidad Politécnica de Madrid, Spain
Analysis of charged- particle energy deposition for ICF calculations with the NORCLA Code

B 17 Minardi E.
Istituto di Fisica del Plasma, Associazione EUR-CNR, Milano, Italy
Plasma circuit instability and current disruption

B 18 Tendler M., Neuhauser[1] J.,Wunderlich[1] R.
Royal Institute of Technology, Stockholm, Sweden
[1]MPI für Plasmaphysik, Garching, FRG
Numerical simulations of the oxygen impurity transport at the plasma periphery in a tokamak

B 19 Tendler M.
Royal Institute of Technology, Stockholm, Sweden
EXTRAP in the quasi-stationary regime

B 20 Lindmann[1] E.L., Rickard G., Haines M.G.
Blackett Laboratory, Imperial College, London, UK
[1]On leave from Los Alamos National Laboratory, New Mexico, USA
An implicit "quasineutral" plasma simulation method which includes sheath and vacuum regions

B 21 Hitchon W.N.G., Mynick H.E.
Torsatron / Stellarator Lab. University of Wisconsin, Madison, Wisconsin, USA
A model for the magnetic field strength along a stellarator field line and its application to particle orbit calculations

B 22 Turner M.F.
Culham Laboratory, Abingdon, Oxon, UK
Wesson J.A.
JET Joint Undertaking, Abingdon, Oxon, UK
JET simulation

B 23 Sykes A., Turner M.F., Patel S.
Culham Laboratory, Abingdon, Oxon, UK
β-limits in tokamaks due to high-n ballooning modes

Plasma-Wall Interaction, Divertors
Part II, p. 367 - 504

A 32 Krüger H., Rödiger K., Schulz V., Stampa A.
FB Physik, Universität Essen, FRG
Experiments on plasma-induced arcs

A 33 Ertl K., Behrisch R., ASDEX Team and PWW Team
MPI für Plasmaphysik, Garching, FRG
Jüttner, B.
Zentralinstitut für Elektronenphysik, Akademie der Wissenschaften der DDR, Berlin, GDR
Investigation of electric arcs in the divertor of the tokamak experiment ASDEX

A 34 Heifetz[1] D., Lackner K., Rauh K.G., Schneider W.
MPI für Plasmaphysik, Garching, FRG
[1]PPPL, Princeton, New Jersey, USA
Simulation of ASDEX divertor action using a realistic neutral gas model

A 35 Wienhold P., Waelbroeck F., Winter J., Rota E., Banno T.
IPP, KFA Jülich GmbH, Jülich FRG
In situ measurement of the hydrogen recycling constant of the TEXTOR liner

A 36 Igitkhanov Yu.L., Kukushkin A.S., Pigarov A.Yu., Pistunovich V.I.,
I.V. Kurchatov Institute of Atomic Energy, Moscow, USSR
Two-dimensional calculations of near-wall plasma dynamics for a tokamak with a poloidal divertor

A 37 Petrov V.G.
Institute of High Temperatures, USSR Academy of Sciences, Moscow, USSR
The characteristics of stationary plasma flow in the tokamak scrape-off layer

A 38 Zykova N.M., Ikonnikov A.O., Kabanov V.N., Nedospasov A.V.
Institute of High Temperatures, USSR Academy of Sciences, Moscow, USSR
Arcing study in disruptive tokamak discharges

A 39 Fidel'man G.N., Ivanov R.S., Stotsky G.J.,
Institute of High Temperatures, USSR Academy of Sciences, Moscow, USSR
On longitudinal transport of charged particles to tokamak limiter

A 40 Samm U.
IPP, KFA Jülich GmbH, Jülich, FRG
Results from infrared-thermography on limiters in TEXTOR

A 41 Pospieszczyk A., Bogen P., Samm U.
IPP, KFA Jülich GmbH, Jülich, FRG
Neutral particle fluxes emitted from the TEXTOR limiter

A 42 Betz G., Husinsky W., Viehböck, F.
Institut für Allgemeine Physik, TU Wien, Wien, Austria
Influence of oxygen coverage on the sputtering of chromium

B 32 Sugai H.
Department of Electrical Engineering, Nagoya University, Nagoya, Japan
Radio-frequency divertor for impurity pump-out

B 33 Harbour P.J., Morgan J.G.
Culham Laboratory, Abingdon, Oxon, UK
The transport of impurity ions in a scrape-off plasma

B 34 Braams B.J.
FOM-Instituut voor Plasmafysica. Rijnhuizen. Nieuwegein. The Netherlands
Numerical studies of the two-dimensional scrape-off plasma

B 35 Fielding S.F., Mc Cracken G.M.
Culham Laboratory, Abingdon. Oxon. UK
A comparison of impurity levels in JET with nickel, carbon and beryllium limiters

B 36 Harrison M.F.A., Hotston E.S.
Culham Laboratory, Abingdon, Oxon. UK
Exhaust of helium and impurity release in INTOR with a divertor or a pumped limiter

B 37 Gruber O., Lackner K.
MPI für Plasmaphysik, Garching, FRG
Poloidal field requirements for divertor and pump limiter design

B 38 Daybelge U.
Marmara Research Institute, Department of Applied Mathematics, Gebze, Kocaeli-Turkey
Asymmetry of plasma scrape-off in limiter and divertor tokamaks

B 39 Clark W.H.M., Fielding S.J., Goodall D.H.J., Hugill J., Johnson P.C. et al.
Culham Laboratory, Abingdon, Oxon, UK
Energy and power balances in DITE tokamak

B 40 Fielding S.J., Goodall D.H.J., Hugill J., Johnson P.C.
Culham Laboratory, Abingdon, Oxon, UK
Characteristics of the particle and energy exhaust into the DITE bundle divertor

C 25 Shimada M., Sengoku S., Kobayashi T., Miya N. Kasai M. and the JAERI Team
JAERI, Tokai, Japan
Kahn C.L., Burrell K.H. and the GA Doublet III Groups
GA Technologies, Inc., San Diego, California, USA
Experimental observation of a dense and cold divertor plasma in D-III beam-heated divertor discharges and its numerical simulation

C 26 Gimzewski[1] J.K.,Veprek[1] S., Hofmann F., Lister J.B., Pochelon A.,Groner[2] P.
CRPP-EPFL, Lausanne, Switzerland
[1]Institute of Inorganic Chemistry, University of Zürich, Switzerland
[2]Federal Institute for Reactor Research Würenlingen, Switzerland
Impurity fluxes in the scrape-off layer of the TCA tokamak: effects of rf heating

C 27 Behringer K., Fußmann G., Poschenrieder W., Taglauer E., Bernhardi K., et al.
MPI für Plasmaphysik, Garching, FRG
Kissel[1] S., Szymanski[2] Z.,
[1]On leave from MIT, Cambridge, Massachusetts, USA
[2]On leave from Institute of Fundamental Technological Research, Warsaw, Poland
Production and transport of impurities in the ASDEX tokamak plasma

C 28 Joye B., Behn R., Hofmann F., Hollenstein Ch. Lister J.B. et al.[1]
CRPP-EPFL, Lausanne, Switzerland
[1]University of Fribourg, Switzerland
Peacock N.J., Stamp M.F.,
Culham Laboratory, Abingdon, Oxon, UK
A comparison betwen steel, carbon and TiC-coated limiters in the TCA tokamak

C 29 Neuhauser J., Schneider W., Wunderlich R.
MPI für Plasmaphysik, Garching, FRG
Impurity flow in the tokamak scrape-off layer

C 30 Chodura R.
MPI für Plasmaphysik, Garching, FRG
Plasma transport to the wall through the electrostatic sheath

C 31 Winter J., Waelbroeck F., Wienhold P., Esser H.G., Könen L. et al.[1]
IPP, KFA Jülich GmbH, Jülich, FRG
[1]ORNL, Oak Ridge, Tennessee, USA
Surface conditioning of the TEXTOR liner and limiters by plasmachemical carbon deposition

C 32 Artemenkov L.J., Gurov A.A., Kovan J.A., Maltsev S.G., Melikhov P.J. et al.
I.V. Kurchatov Institute of Atomic Energy, Moscow, USSR
Experiments in TO-2-tokamak with toroidal divertor

C 33 Alexander K.F., Grote H., Hildebrandt D., Laux M. Kotai[1] E. et al.
Zentralinstitut für Elektronenphysik, Akademie der Wissenschaften der DDR, Berlin, GDR
[1]Central Research Institute for Physics, Hungarian Academy of Sciences, Budapest, Hungary
Deuterium and impurity fluxes in the limiter shadow of T-10:indication for time-dependent local sources

C 34 Grosman A., TFR Group
Département de Recherches sur la Fusion Contrôlée, CEN, Fontenay-aux-Roses, France
Plasma edge measurements during additional heating in the TFR tokamak

C 35 Kever H.
IPP, KFA Jülich GmbH, Jülich, FRG
Scaling of plasma scrape-off layers in tokamaks

C 36 Johnson P.C., Mudford B.S.,Cordey[1] J.G.
Culham Laboratory, Abingdon, Oxon, UK
[1]JET Joint Undertaking
Neutral beam injection modelling for DITE with the MKII bundle divertor

Reactor Aspects

Part II, p. 505 - 546

D 1 Brunelli B., Zampaglione V.
CRE, Frascati, Italy
Avanzini P.G., Raia G., Rosatelli F.
NIRA - C.P. Genoa, Italy
HTMR- a hybrid toroidal magnet tokamak reactor study

D 2 Dabiri A.E., Glancy J.E.,
Science Application, Inc., La Jolla, California, USA
d-d compact reversed field pinch reactor technology assessment

D 3 Gill R.D.,
JET Joint Undertaking, Abingdon Oxon, UK
Empirical determination of the parameters of ignition and reactor tokamaks

D 4 Sternlieb A.,
Soreq Nuclear Research Centre, Yavne, Israel
The Mirrotron – a compact disposable tandem mirror fusion reactor

D 5 Lodder, J.,
FOM-Instituut voor Plasmafysica, Rijnhiuzen, Nieuwegein, The Netherlands
Nuclear spin depolarization by classical mixing in fusion reactor plasmas

D 6 Kernbichler W., Niederl K., Heindler M.
Technische Universität Graz, Austria
Physics and engineering constraints on the feasibility of advanced fuel fusion reactors

D 7 Carretta, U.,
CNR-Politecnico di Milano, Italy
Farina D., Lontano M., Minardi E., Pozzoli R.,
Istituto di Fisica del Plasma, CNR-Milano, Italy
Burn optimization in a thermonuclear reactor

D 8 Wobig H., Brossmann U., Gorenflo H., Harmeyer E., Kisslinger J.et al.
MPI für Plasmaphysik, Garching, FRG
Some aspects of an advanced stellarator reactor

D 9 Bobbio S., Coccorese V., Fabricatore G.,
[1]Martone R., Rubinacci G.,
Istituto di Electrotecnica, University of Naples, Italy
[1]Dipartimento Elettrico, University of Calabria, Italy
Passive stabilization in INTOR reactor

D 10 [1]Brzosko J., Ingrosso L., Robouch B.V.
EURATOM-ENEA, Frascati, Rome, Italy
[1]On leave from Warsaw University, Biacystik Branch, Poland
Depression of the nuclear properties of fusion reactor breeding blankets by nonhomogeneities

Laser-Plasma Interaction, Inertial Confinement

O07 - O09

E37 - E45

ICF-Target Research at MPQ/Garching

J. Meyer-ter-Vehn, R. Arnold, N, Metzler, R. Schmalz,
K. Unterseer, S. Witkowski
Max-Planck-Institut für Quantenoptik,
D-8046 Garching, FRG

Theoretical work on physics and design of ICF targets driven by laser or heavy ion beams is reported. It is related to laser plasma experiments at the MPQ iodine laser and to the German feasibility study on heavy ion fusion guided by the Gesellschaft für Schwerionenforschung (GSI) in Darmstadt. Results of a parameter study on target gain, simulations of heavy ion target implosions and laser driven plane foils, and a proposal for dense plasma experiments with high energy ion beams at GSI are presented.

1. Target Energy Gain

A key function for ICF power production is target gain versus beam energy. A gain model has been developed (for details see ref. /1/) that reproduces

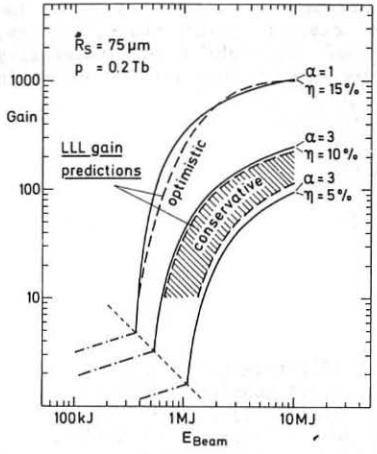

Fig. 1 Fit of the present gain model to the 'conservative' and 'optimistic' gain predictions obtained at Livermore on the basis of extensive code simulations. The LLL results correspond to a central pressure of p = 0.2 Tbar; the 'conservative' band is well reproduced with an isentrope α=3 and an hydroefficiency ranging between 5% < η 10%, whereas the optimistic curve corresponds to α = 1 and η = 15%.

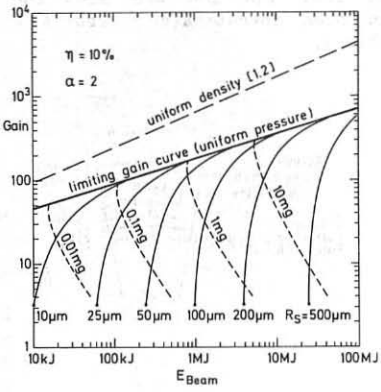

Fig. 2 Gain curves for fixed isentrope α and hydroefficiency η, but increasing spark radius R_s. Lines of equal fuel mass M_F (short dashes) are labelled by the mass value. Limiting gain curves (max. gain at given E_{Beam} for any R_s) are shown for the present model assuming uniform pressure (fat solid line) as well as for the Kidder model with uniform density (long dashed line).

results of complex computer codes in terms of three free parameters characterizing the DT fuel at ignition: (1) the hydrodynamic efficiency η which is the fraction of beam energy E_{Beam} transferred into internal fuel energy, (2) the radius R_s of the igniting spark in the centre of the highly compressed fuel (R_s is limited by implosion symmetry!), (3) the isentrope parameter α giving the deviation from pure degeneracy pressure ($p = \alpha\, p_{deg}$, α is a measure for preheat). Fig. 1 shows a fit of the present model to Livermore gain predictions and Fig. 2 the gain dependence on spark radius. High gain for $E_{Beam} < 100$ kJ would require $R_s \cong 10$ µm; a possible regime for ICF power production is $R_s \cong 100$ µm with $1\ MJ < E_{Beam} < 10$ MJ, 1 mg < fuel mass < 10 mg, and Gain ≅ 100.

2. Reactor-size target for heavy ion beam fusion

Heavy ion beams are presently considered as a promising driver for ICF power production. This is due to the high efficiency and high repetition rate of heavy ion accelerators. Within the German feasibility study of heavy ion fusion and the HIBALL reactor study /2/, reactor-size targets for heavy ion drivers have been investigated at MPQ/Garching /2,3/ and KfK/Karlsruhe /2,3/. A target sector is shown Fig. 3. The shell radius is given by the multi-beam focal spots of about 3 mm, the shell thickness by the range of 10 GeV Bi-ions, the fuel mass by a 1 GJ output limit. 10 GeV ion energy is found as an optimum for this target. Implosion hydrodynamics /4/, the relation between pulse shape, shocks, and fuel ignition and also the growth of Rayleigh-Taylor instability has been investigated. Results of a typical implosion run is given in Table 1.

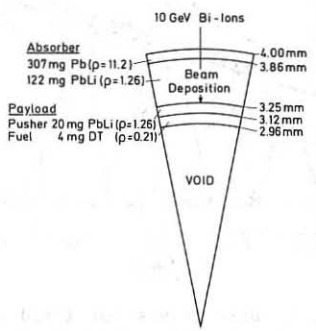

Fig. 3 HIBALL target sector. The spherical shell consists of three material layers: (1) PbLi deposition and pusher layer in the middle, (3) cryogenic DT layer inside. 10 GeV Bi-Ions are stopped in the Pb and part of the PbLi layer.

Table 1: Heavy ion driven implosion of target (Fig. 1) with box shape pulse 10 ns long; results of implosion and burn.

pulse energy	pulse power	hydro-efficiency	implosion velocity	ignition $(\rho R)_{Fuel}$	Gain
5 MJ	500 TW	8 %	$3 \cdot 10^7$ cm/sec	1.2 g/cm^2	140

3. Laser acceleration of plane foils

A 1D-Lagrangian hydrodynamic code with laser energy deposition and flux-limited electron heat conduction has been developed to simulate laser impact on thin foils. (The original version of this code has been written by P. Mulser and G. Spindler.) A typical result is shown in Fig. 4. With laser intensities of 10^{12}-10^{15} W/cm^2, maximum pressures of 1-50 Mbar are obtained in the compressed part of the foil and velocities of 10^6-10^8cm/s. These values are calculated with a heat flux limit (2% of free streaming limit). They agree well with experiments made at the MPQ Asterix laser /5/. Material velocities above $2 \cdot 10^7$ cm/s have to be achieved in spherical implosions of ICF targets for DT ignition. Theoretical work on equation-of-state and transport properties of such foils is now in progress to further study the potential of the Asterix laser for hot, dense matter research. In colliding foil experiments, pressures above 300 Mbar, the atomic pressure unit, should be achievable and effects from squashing inner atomic shells are expected.

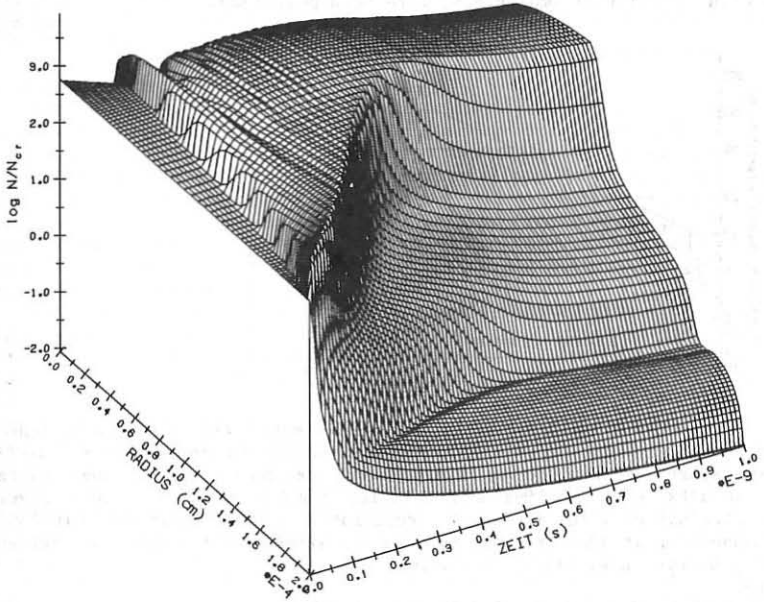

Fig. 4 Laser irradiation (pulse: $P(t) = 10^{15}$ W/cm$^2 \cdot \sin^2(\pi t/600$ ps)) from front side on a 2 µm plane plastic foil. Density in units of critical density ($N_{crit}=6.4 \cdot 10^{20}$ cm^{-3} for $\lambda = 1.3$ µm iodine laser) is plotted versus Lagrangian space coordinate (foil depth at t=0) and time. Three distinct regions are seen: (1) the unperturbed foil to the left, (2) the high density region to the rear between the shock front at the left and the ablation front at the right, and (3) the laser heated ablation region (right front side) with a density jump near the critical density. A heat flux limit of f = 0.02 was used in the simulation.

4. Proposal for ICF experiments with heavy ion beams at GSI

A proposal has been worked out to use the heavy ion synchrotron planned at GSI/Darmstadt for basic atomic and nuclear research also for investigating accelerator and target problems of heavy ion fusion. The advantage of using very energetic (even relativistic) heavy ion beams for this purpose is that they have low emittance and can be focussed on very small spots (radii of 100 μm and below) to produce high power density. We have studied corresponding target physics /7/. The beam heats needle-like cylinders of solid target material to temperatures of 10 - 100 eV. In Fig. 5, temperatures are plotted versus specific power deposition, and regions which may be attained with different accelerator options now under discussion are indicated. In addition to beam-target coupling, target hydrodynamics including instabilities (e.g. Rayleigh-Taylor inst.) and energy transport mechanisms crucial for ICF target behaviour can be investigated. Detailed 1D and 2D simulations of structured targets (e.g. with different material, and hollow targets with cylindrical implosions) have been performed.

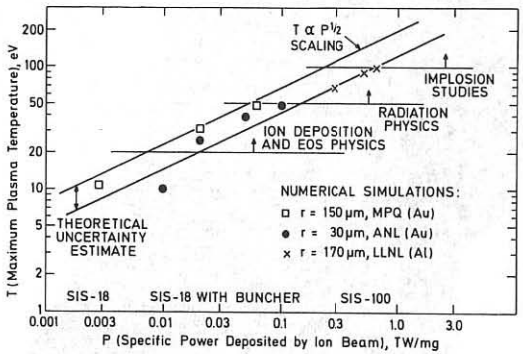

Fig. 5 Temperatures achievable in ion beam heated cylinders as a function of specific beam deposition. For the beams considered here, maximum temperature is limited by hydrodynamic expansion rather than pulse energy. Results from scaling and detailed simulations are shown. Power regions attainable with different accelerator options (SIS 18, SIS 100) under discussion at GSI as well as physics areas and temperature regions where they become interesting are indicated.

References

/1/ J. Meyer-ter-Vehn, Nucl. Fusion 22, 561 (1982).
/2/ B. Badger et al., HIBALL - A Conceptual Heavy Ion Beam Driven Fusion Reactor Study, Kernforschungszentrum Karlsruhe, Report KfK-3202 (June 1981).
/3/ Proc. Symp. Accelerator Aspects of Heavy Ion Fusion, March 29-April 22, 1982, Ed. D. Böhne, Report GSI-82-8, p. 514 and p. 598.
/4/ J. Meyer-ter-Vehn, C. Schalk, Z. Naturforsch. 37a, 955 (1982) and Report MPQ 70 (1983).
/5/ R. Sigel, K. Eidmann et al., MPQ Jahresbericht 1981.
/6/ R. Bock et al., GSI-Report, to appear (1983).
/7/ R. Arnold, J. Meyer-ter-Vehn, Report MPQ 73 (1983).

EFFICIENT AND UNIFORM COMPRESSION TO HIGH DENSITY WITH 1.052 μm GM-II LASER

N. Miyanaga, Y. Kitagawa, Y. Kato, K. Nishihara, T. Yabe, M. Nakatsuka, T. Jitsuno, K. Yoshida and C. Yamanaka

Institute of Laser Engineering, Osaka University
Suita, Osaka 565, Japan

1. INTRODUCTION

We present Cannonball implosion of a double shell target with holes. This target structure has been studied with one-dimensional model calculation[1] and with two-dimensional simulation calculations[2], and also tested by using a double-foil target with a hole[3]. In these works several advantages of this target have been noted, such as high laser absorption efficiency, high hydrodynamic efficiency and excellent uniform compression. In this paper we report the implosion experiments on the several types of cannonball targets, and discuss their implosion characteristics comparing with the results from the computer simulation.

2. TARGET STRUCTURE AND PLASMA DIAGNOSTICS

The cannonball target was composed of an outer shell (tamper) made of parylene and an inner glass microshell (pusher) filled with DT gas. The two beams from GEKKO M-II[4] glass laser were injected into a cavity, which was formed between the shells, generating the hot plasma and the thermal radiation. The laser was operated at the output energy of ~450J in the pulse width of 100ps. The tamper coated with gold on its inner surface was also examined on the contribution by the thermal radiation to the implosion of the pusher. The effect of the gold coating on the outer surface of the pusher was also studied for the preheat suppression.

The implosion characteristics dramatically changed with the different target materials and sizes, these were investigated by using the several diagnostic instruments; eg. the pinhole cameras for observation of the implosion uniformity, an X-ray streak photograph with one-dimensional spatial resolution and a fast X-ray diode for the implosion dynamics, an X-ray crystal spectrometer for temperature and density measurements, S→1streak camera for the backscattered and sidescattered lights, neutron detectors (plastic scintillator-photomultiplier, silver activation counter) for the neutron yield, an α particle zone plate camera, an X-ray URA camera[5], ion charge collectors and a transmission-grating soft X-ray spectrometer.

3. IMPLOSION UNIFORMITY

We first discuss the implosion uniformity based on the pinhole camera observation. Figure 2(b),(c) show the typical X-ray images of the imploded cannonball targets. It is remarkable that the spherically symmetric compressions were obtained in spite of the irradiation by only two beams of the relatively large F number (f/2.75). This is quite different from the exploding pusher compression driven by the same laser (Fig.2(a)). The implosion uniformity of the fuel can be evaluated from the ratio $\Delta r_f/r_f$, where the deformation amplitude Δr_f and the average radius r_f are defined as $\Delta r_f = (r_2-r_1)/2$ and $r_f=(r_1+r_2)/2$, respectively, by using the minimum radius of the fuel-pusher interface r_1 and the maximum radius r_2. It is useful to evaluate Δr_f as a function of the volume compression ratio R_v and the nonuniformity of the implosion velocity $\Delta v/v$ or the nonuniformity of the compress-

ed fuel $\Delta r_f/r_f$. The nonuniformity Δr_f normalized to the initial radius $r_{p,0}$ is expressed as $\Delta r_f/r_{p,0}=(1-(R_v)^{-1/3})\cdot(\Delta v/v)$ or $\Delta r_f/r_{p,0}=(\Delta r_f/r_f)(R_v)^{-1/3}$. These relations are plotted in Fig. 3 for the different parameters $\Delta v/v$ and $\Delta r_f/r_f$ by the solid lines and the dashed lines, respectively. The measured data show the significant uniform compression of $8\% \lesssim \Delta r_f/r_f \lesssim 20\%$ and $1\% \lesssim \Delta v/v \lesssim 4\%$. The observed uniformity is satisfactory, since only two beams have been used in this experiment. This great advantage for high density compression is also predicted from the 2-D computer simulation /2/.

4. IMPLOSION EFFICIENCY

The implosion efficiency η_h which is defined here as the ratio between the kinetic energy of the accelerated pusher and the incident laser energy, depends on both the pusher-tamper aspect ratio ($\zeta_{c,0}=r_{p.0}/r_t$) and the material of the tamper as shown in Fig. 4.

The low Z (parylene) tamper shows that the implosion efficiency in-

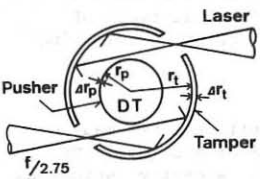

$r_{p,0}=(60\text{-}115)\,\mu m$
$\Delta r_p=(1.2\text{-}1.3)\,\mu m$
$r_t=(185\text{-}285)\,\mu m$
$\Delta r_t=(10\text{-}15)\,\mu m$
DT: (4,16) atm

Fig. 1.
Schematic illustration
of a cannonball target.

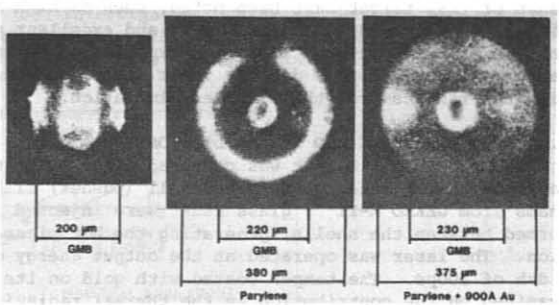

(a) (b) (c)

Fig. 2. Typical X-ray images of (b) a low-Z tamper cannonball target and (c) a high-Z tamper cannonball target which are quite different from (a) the explosive pusher compression.

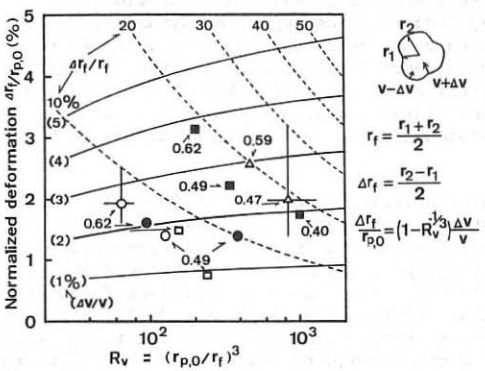

	Tamper	Pusher
△	Parylene	Glass micro-balloon(GMB)
▲	Solid Al	GMB
×	Thin parylene	GMB
○	Parylene	GMB
●	Parylene	Au-coated GMB
□	Au-coated parylene	GMB
■	Au-coated parylene	Au-coated GMB

Fig. 3. The core deformation normalized to the initial pusher radius ($\Delta r_f/r_{p,0}$) as a function of the volume compression ratio R_v. The numbers for the data points are initial aspect ratio of the cannonball targets.

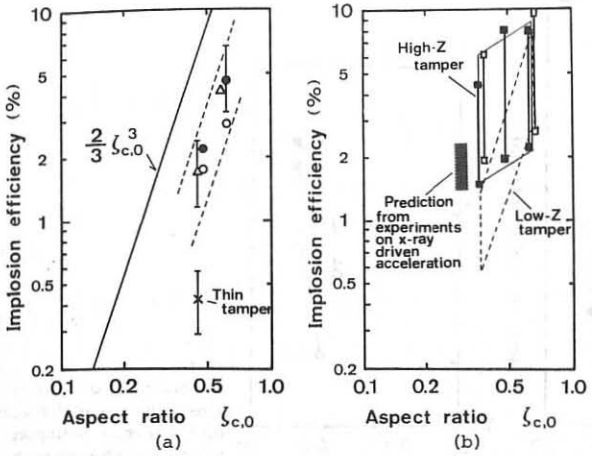

Fig. 4.
Dependence of the implosion efficiency on the aspect ratio of the target in the cases of (a) low-Z tamper and (b) high-Z tamper.

creases with $\zeta_{c,0}$ is expected from the model calculation. The application of the adiabatic cannonball model [1] to the spherical geometry gives a simple scaling on the aspect ratio as $\eta_i=\eta_{abs}\cdot\eta_h=\eta_{abs}\cdot\eta_c\cdot\{1-[(1-\zeta_{c,0}^3)/(1-\zeta_c^3)]^{2/3}\}$ $\simeq(2/3)\cdot\eta_{abs}\cdot\eta_c\cdot\zeta_{c,0}^3$, where the product of the absorption and the cavity coupling efficiencies can be estimated to be 0.15-0.4. This implosion scheme, in which the pusher acceleration is driven by the pressure of the confined plasma, does not raise the decrease in the hydrodynamic efficiency even if the thicker pusher is used. The decrease of the sound velocity of the cavity plasma, which affects the pusher acceleration to limit the pusher velocity, was not so serious because of the temperature of higher than 2keV and the pusher velocity of $(2\text{-}4)\times10^7$cm/s.

On the other hand the gold-coated tamper shows the relatively weak dependence of the implosion efficiency on the aspect ratio. The ablative acceleration driven by the thermal radiation from the tamper is expected to have the implosion efficiency scaled as $\zeta_{c,0}^{\alpha}$ ($\alpha\leq2$). The factor $\zeta_{c,0}^2$ corresponds to the simple geometrical coupling of the radiation from the tamper to the pusher. Therefore the higher efficiency is obtained at the higher aspect ratio and the high-Z coated tamper. Furthermore it is noteworthy that the efficiency does not so decrease at the lower aspect ratio. This is promising for the high density compression because of the improvement of implosion uniformity at the lower aspect ratio as is shown in Fig.3.

5. FUEL CORE DENSITY AND NEUTRON YIELD

The core density and the neutron yield depended on the aspect ratio as shown in Fig.5. The fuel density was determined from the volume compression ratio. The maximum neutron yield of 1.7×10^8/shot was observed in the case of the low-Z tamper, and 2.4×10^8/shot in the case of the high-Z tamper. These neutron yields were obtained at the higher aspect ratio of $\zeta_{c,0}=0.62$ which also gave the maximum implosion efficiencies. On the other hand the higher core density was obtained with the lower aspect ratio target and with the gold-coated pusher, because the less preheating of the fuel pellet improves the compression density. In the present experiment the compression densities up to 1.4 g/cm^3 (low-Z tamper) and 3.9 g/cm^3 (high-Z tamper) have been achieved.

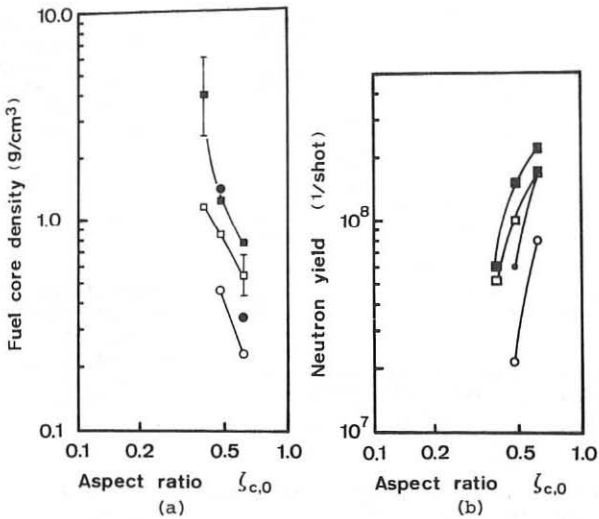

Fig. 5. Dependence of (a) the fuel core density and (b) the neutron yield on the aspect ratio.

6. CONCLUSION

We have demonstrated that the cannonball target satisfies both the high compression density and the high neutron yield, arising from high implosion efficiency and good implosion uniformity. The cannonball target presents a new concept of pellet implosion which would be regarded as alternative to the isentropic and explosive compressions. Another properties, such as the hot electron generation, the preheating of the fuel pellet and the laser absorption efficiency, will be also reported.

ACKNOWLEDGEMENT

We would like to thank Prof. Y. Izawa, Dr. T. Norimatsu, M. Yoshida, K. Yata and M. Nishi for providing cannonball targets, and greatly appreciate cooperations by T. Kanabe, S. Arinaga, E. Toide, T. Yamada, T. Otani, M. Miyazaki and M. Umewaka for laser-system operations.

REFERENCES

/1/ H. Azechi, N. Miyanaga, S. Sakabe, Y. Yamanaka and C. Yamanaka: Japan. J. Appl. Phys. 20 (1981) L477.

/2/ K. Nishihara, K. Mima, T. Yabe, S. Ido and C. Yamanaka: Report on IAEA Technical Meeting on Advances in Inertial Confinement Systems, Takarazuka, Japan, Oct.29-Nov.1,1979, Rev. Laser Eng. 8 (1980) No.1 special issue, p.70. ; Proc. Japan-US seminar on Theory and Application of Multiplly-Ionized Plasmas Produced by Laser and Particle Beams, Nara, Japan, May 3-7,1982, Rev. Laser Eng. 10 (1982) supplement, p.183.

/3/ K. Yamada, M. Yagi, H. Nishimura, F. Matsuoka, H. Azechi, T. Yamanaka and C. Yamanaka: J. Phys. Soc. Japan 51 (1982) 280.

/4/ Y. Kato, K. Yoshida, J. Kuroda and C. Yamanaka: Appl. Phys. Lett. 38 (1981) 72.

/5/ M. Yamanaka: ILE Progress Report on Inertial Fusion Program, Inst. of Laser Engineering, Osaka Univ. (1983) No.1, p.5.

THE IMPACT OF QUALITY DIAGNOSTICS ON ICF RESEARCH AT KMS FUSION, INC.

P. D. Rockett, J. A. Tarvin, Gar. E. Busch, G. Charatis, R. R. Johnson, R. J. Schroeder, C. L. Shepard, J. D. Simpson, D. C. Slater, D. Sullivan and C. R. Bird*

KMS Fusion, Inc., Ann Arbor, Michigan 48106, USA

INTRODUCTION

The progress of inertial confinement fusion (ICF) research has been paced by the development of sophisticated, high quality diagnostics. As our emphasis at KMSF has shifted from studies of laser absorption to energy transport in laser fusion targets, our diagnostic requirements for improved spectral, spatial, and temporal resolution have grown. Efforts in experiment design and diagnostic instrument design have been merged to optimize the amount of data extracted from experiments. The targets have become a part of the diagnostic, providing temporal and spectral fiducials on streaked and dispersed records, respectively. Most instruments have been upgraded via temporal, spectral, and intensity calibrations. This applies not only to optical detectors, but to x-ray diagnostics as well. Improvements in instrument resolution and sensitivity have brought dramatic results, in particular in the area of holographic interferometry. The detailed data we have recovered from laser-target experiments have allowed scrupulous comparisons between theoretical models of energy transport and hydrodynamic phenomena in dense plasmas.

THERMAL TRANSPORT DIAGNOSTICS

Electron energy transport experiments at KMSF provide an excellent example of the power of thorough diagnostic measurements. Our study of thermal transport in spherical geometry involved measurements of energy burnthrough from plastic to aluminum layers of varied depth in 73 to 105 μm diameter targets.[1] Burnthrough times were used to infer mass ablation rates in spherical geometry. A square 1 ns pulse of 1.05 μm laser radiation illuminated parylene-on-aluminum coated glass Microshell® targets with absorbed intensities varying from 4×10^{13} to 4×10^{14} W/cm^2. An outer target coating of 0.01 μm titanium provided a diagnostic x-ray timing fiducial. Streaked x-ray pinhole imaging (Lawrence Livermore National Laboratory soft x-ray streak camera on loan to KMSF) with a CsI photocathode clearly identified the initial titanium fiducial, and at later times observed strong emission as energy was transported to the aluminum layer. A densitometer trace from one such streak record appears in Figure 1. The late time x-ray emission from the transport targets was spectrally examined by replacing the x-ray streak camera pinhole with a 3000 line per mm transmission grating (on loan from LLNL). Streaked spectra showed the burnthrough emission to be primarily composed of Al XII resonance radiation. The streak camera maintained 20 ps resolution and contained a demountable photocathode. We fabricated a 1000 Å CsI photocathode evaporated on 250 Å Au and standing on a 3000 Å carbon substrate.[2] (The gold was found to stabilize the alkali halide for long times.) In comparative studies at KMSF, normal density CsI sensitivity was found to be $\sim$ 5 times that of gold at 1-2 keV. The camera was temporally calibrated with a series of 100 ps x-ray pulses

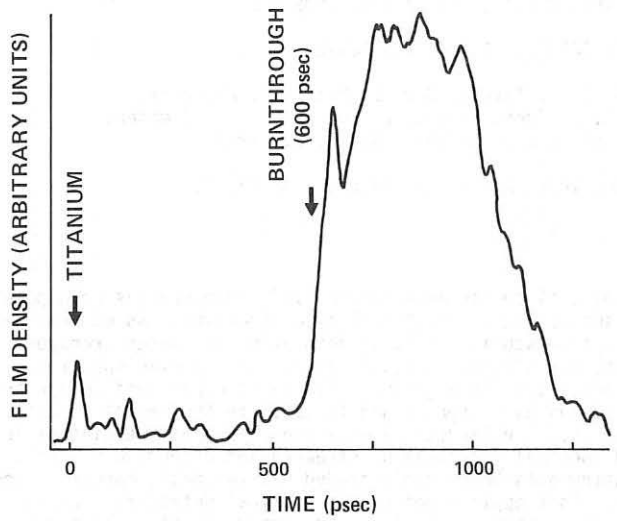

Figure 1. X-ray streak signature

spaced 100 ps apart. The corresponding set of laser pulses was readily generated in our coherent pulse stacker.

Coronal electron density profiles were measured to 2 x n_{crit} with 80 ps 0.264 μm holographic interferometry. By recording interferograms at different times into the laser pulse, we were able to confirm the establishment of a static density profile after the first 300 ps. This permitted theoretical modeling of the experiment with a steady state transport model. Brilliant, high-data-content interferograms were obtained by long-path spatial filtering of the ultraviolet (UV) beam and by low f/number collection optics. One such interferogram can be seen in Figure 2. Collection efficiency was optimized by the design of an f/2.0 catadioptric imaging optic, which placed an image of the target plane near the recording plate.[3] Timing of the probe pulse was established by merging the 0.264 μm probe pulse and the second harmonic of the main 1.05 μm laser pulse on a Hamamatsu S-20 streak camera with 10 ps resolution.

(Recent improvements to the holographic probe pulse have reduced its pulse length to $\lesssim$ 20 ps by use of a regenerative amplifier. This has dramatically improved our ability to record high velocity plasma events. Fringe contrast has remained high by careful attention to temporal beam overlap.)

Additional diagnostic measurements included absorption calorimetry and hard x-ray spectrometry. A KMSF-designed thermistor flake calorimeter (TFC) differentially measured plasma energy to determine the laser absorption fraction. The TFC is smaller and more sensitive than a thermoelectric module, and can be readily calibrated *in situ* with an electrical self-heating pulse.[4] Hard x-ray analysis was performed with a conventional array of K-edge filtered

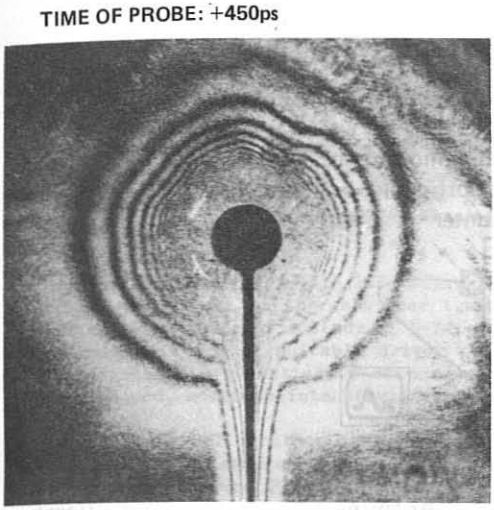

Figure 2. UV interferogram of laser-irradiated microballoon target.

PIN diodes and scintillator photomultiplier tubes. Data were recorded in charge integrators and computer analyzed on-line.

The results of this well-diagnosed thermal transport experiment supported a model of strongly flux-limited transport. They showed mass-ablation rates higher than planar-target experiments at absorbed intensities above 10^{14} W/cm^2. Finally, the data were all internally consistent.

SUPRATHERMAL TRANSPORT DIAGNOSTICS AND CALIBRATIONS

A separate experimental series studied the transport of suprathermal electron energy at laser intensities around 5 x 10^{15} W/cm^2. These experiments utilized x-ray spectroscopy with crystal spectrographs calibrated for absolute intensity measurements. The targets consisted of a glass Microshell® target coated with 0.5 μm V, 1-3 μm Al, 0.5 μm Ti, and 2.9 μm of parylene. Ti and V Kα yields were measured with two convex curved crystal spectrographs. From knowledge of the absorbed incident energy and hard x-ray yield, one could infer the absolute spectrum of fast electrons. Energy transported to the fluorescing layers was modeled theoretically by multi-group diffusion and by an analytical electron range model. Comparison of calculated Kα yields to experimental data required an intensity calibration of both spectrographs at Ti Kα (4.51 keV) and V Kα (4.95 keV).

To meet this need and other x-ray calibration needs, we have constructed an x-ray test facility. The facility is based upon a Manson point soft x-ray source and low energy proportional counter. The test chamber is shown in Figure 3 and has operated on many characteristic lines from C Kα (283 eV) to Ti Kβ (4.93 keV). Manson's source is a 5 W radiatively-cooled, open Coolidge-type tube with Wehnelt electrostatic focusing. Our x-ray pinhole photographs show a 350 μm diameter spot size. The proportional counter operates with

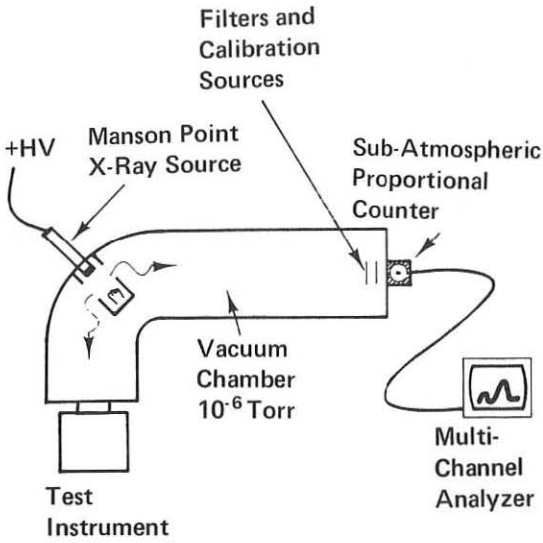

Figure 3. KMSF X-ray calibration facility.

either a 1500 Å VYNS window or a 5000 Å parylene window and is operated sub-atmospheric. Calibrations are based on photon counting, and a multichannel analyzer records and integrates the dispersed source flux in real time. Vacuum in the test chamber is maintained at 10^{-6} Torr with a trapped diffusion pump. The x-ray test facility was inexpensive to set up and can be a model for small laboratory x-ray calibration systems. It is capable of absolute calibration of x-ray diodes, filters, spectrographs, and photocathodes.

Calibration of the LiF and PET spectrographs proceeded with a Ti-coated Cu anode. The source produced both Ti Kα and Ti Kβ lines, which proved adequate to complete the spectrograph calibrations. This work revealed that laser-target Kα emission was an order of magnitude lower than theoretical models would predict. This suggested strong flux inhibition of suprathermal energy transport, a result never directly experimentally observed. Again, sufficient data of high quality yielded an internally consistent, albeit perplexing, physical picture.

REFERENCES

/1/ J. A. Tarvin, W. B. Fechner, J. T. Larsen, P. D. Rockett and D. C. Slater, submitted to Physical Review Letters.
/2/ P. D. Rockett, submitted to Applied Optics.
/3/ G. E. Busch and G. Charatis, SPIE Proceedings of the 15th International Congress on High Speed Photography 348 (1982), 650.
/4/ J. D. Simpson, Rev. Sci. Instrum. 53 (1982), 0057.

---

*Work prepared for the U.S. Dept. of Energy under Contract DE-AC08-82DP40152.

IGNITION CRITERION FOR DENSE, ISOBARIC D-T PLASMAS AND CONSEQUENCES ON ICF TARGET DESIGN

S. Atzeni and A. Caruso

Associazione EURATOM-ENEA sulla Fusione, Centro di Frascati, C.P. 65, 00044 Frascati, Rome, Italy

The design of high-gain ICF targets is strongly influenced by the efficient attainment of thermonuclear ignition. In this connection we have applied the results of a study of D-T ignition in plasmas relevant to ICF, to envisage a set of suitable driver and target parameters. We have then investigated the potentiality of a class of double-shell targets, requiring unshaped, moderate intensity laser pulses.

To study D-T ignition in conditions close to those achieved in hollow-shell implosions, we have analyzed the evolution of a system initially at uniform pressure P_o, and consisting of a cold, dense D-T plasma at density ρ_c, containing a hot-spot of radius R_o at temperature $T_o \geq 3$ keV and density $\rho_o \ll \rho_c$. In the analysis that follows we will use the equation of state of a perfect gas for the hot-spot, and that of a partially degenerate electron gas for the cold fuel, namely, $\varepsilon_o = C_v T_o$; $\varepsilon_c = \alpha\varepsilon_d$; $\varepsilon_d = 3.1 \cdot 10^{12}\, \rho_c^{2/3}$(erg/g), and $P = (2/3)\,\rho\varepsilon$ everywhere; here α_c is the isentrope parameter; other symbols are of standard use; subscript o indicates quantities at time t = 0.

Ignition occurs if the energy that the α particles deliver to the hot-spot (whose mass is increased by cold fuel ablation) is larger than the losses due to thermal conduction, radiation emission and mechanical work. Four stages of this process have been identified [1]. 1) At first the hot-spot quantities evolve in order to have $\tau = R/\ell \cong 0.6$ [2] (ℓ [cm] $\cong 0.02\,(T\ [\mathrm{keV}])^{3/2}/\rho$ is the α-particle range); 2) The hot-spot self-heats; 3) When $T \gtrsim 10$ keV a self-similar burn-wave develops at constant τ. This is a deflagration, substained by fusion (α) energy and propagated by α-particles, thermal conduction and radiative transfer; all of them heat and ablate the cold fuel just out of the burning region (see Fig. 1 of ref. [1]); 4) When the pressure $P \gg P_o$, then the burning is propagated hydrodynamically (detonation).

When radiative losses, neutron heating and hot-spot inertia are negligible, i.e. if $T_o \gtrsim 7$ keV, $\rho_c R_c \lesssim 2$ gcm^{-2} and $\rho_o \ll \rho_c$, the system is described by the dimensionless quantities τ, $\gamma_\alpha = W_{\alpha o} t_s/\varepsilon_o \rho_o$, and $\gamma_e = W_{eo} t_s/\varepsilon_o \rho_o$ [2]. Here W_α and W_e are the power density produced as α-particles, and lost via thermal conduction, respectively, and $t_s = R_o (\rho_c/\rho_o)^{1/2}/(2C_v T_o)^{1/2}$ is the relevant time scale. The factor $(\rho_c/\rho_o)^{1/2}$ accounts for the tamping action of the dense fuel, opposing hot-spot expansion.

Recent numerical simulations have shown that the results of refs. [1,2] apply to the wider temperature range $4 \leq T_o \leq 15$ keV. In particular, rapidity of ignition depends only on the values of γ_α and γ_e, and an

ignition criterion can be approximately written as

$$\rho_o R_o \ (\rho_c/\rho_o)^{1/3} \geq 5\cdot10^{-16} \ T_o^{19/12} \ / \ \langle\sigma v\rangle_o^{5/6} \qquad (g/cm^2); \qquad 4 \leq T_o \leq 15 \text{ keV}. \quad (1)$$

The RHS on eq. (1) is below 0.5 if $6.5 \leq T_o \leq 30$ keV and is a minimum (0.35) at $T_o = 14$ keV. These results have been obtained by an upgraded version of the 1-D IMPLO Code [3], now a 3-T code, including radiation, neutron and charged fusion product energy diffusion [4] (the latter by either a simple model or a multigroup package; both are valid at $T \lesssim 100$ keV [4]).

By using eq. (1) and imposing isobaricity we can write the minimum hot-spot energy required for ignition as $E_o = E_o(P_o, T_o, \alpha)$, and the fuel gain of targets which are isobaric at ignition as $GF = GF(M, T_o, P_o, \alpha)$ or $GF = GF(E, T_o, P_o, \alpha)$ [5,6]; here M is the D-T mass and E its internal energy just before ignition. We have $E_o\,[kJ] = 0.8\cdot Q'(T_o)\ \alpha^{3/5}/(P_o\,[Tbar])^{8/3}$, where $Q'(T_o) \geq 1$ is a weak function of T_o in the range $6 \div 15$ keV; $Q'(9 \text{ keV}) = 1$.

The fuel gain is practically independent on T_o ($5 \leq T_o \leq 15$ keV), and its limiting value, and the corresponding pressure are

$$\overset{*}{GF} = 1150\ (E\ [kJ])^{1/3}/\alpha = 4300\ (M\ [mg])^{4/15}/\alpha^{4/5}$$

$$P_o^*\,[Tbar] = 8.3\ (E[kJ])^{-2/3}\ \alpha^{3/5} = 0.6\ (M\ [mg])^{-8/15}\alpha^{1/5} \qquad (2)$$

"Optimal working points" [6] could instead be those corresponding to the minimum energy E^+ required to ignite a fuel mass M: $E^+\,[kJ] = 43\ \alpha^{3/5}\ (M[mg])^{4/5}$. Indeed $\overset{+}{GF}(M, \alpha)$ is close to limiting gain ($\overset{+}{GF} \cong 0.8\ \overset{*}{GF}$), but $P_o^+ \cong 0.4\ P_o^*$, and $R_o^+ \cong 2.2\ R_o^*$, thus relaxing pressure and symmetry requirements.

From the gain curves of fig. 1 and eq. (2), we infer that, for "realistic" values of $\alpha \cong 2 \div 4$ and $P_o \cong 0.1 \div 0.4$ Tbar, values of $GF \gtrsim 10^3$ require that energies in the range $E \sim 100 \div 300$ kJ (corresponding to absorbed driver energy $E_L \sim 1 \div 4$ MJ) are delivered to a D-T mass $M \sim 1 \div 5$ mg, and that ignition is effectively triggered.

These results are being applied to the design of thermonuclear laser-fusion targets, imploded by unshaped laser pulses in a moderate intensity regime (i.e. $10^{12}\ I \lesssim 10^{14}$ W/cm^2), in which plasma instabilities are not expected to occur (they should be important at $I\lambda^2 > 10^{14}$ W/cm^2). Also, if $I \leq I_S = 1.1\cdot10^{16}\ \lambda^{-7/2}\ R_a^{3/4}\ (Z/A)^{3/8}\ f$ W/cm^2, heat flow should not be saturated [7], making simulation results independent on the value chosen for the flux limiting parameter f (R_a is the ablation radius, λ [μ] is the wavelenght).

With the regard to the choice of the wavelenght, it has been pointed out [8] that while shorter wavelenghts yield higher ablation pressures (P_a scales as $I^{7/9}/\lambda^{2/9}$ in the inverse-bremsstrahlung regime [9], i.e. if $I \ll I_b = 5\cdot10^{14}\ R\ Z/\lambda^4$ W/cm^2 [10], as $I^{2/3}/\lambda^{2/3}$, if $I_b \ll I < I_S$ [11], and as $\sim I^{1/2}/\lambda$, if $I > I_S$ and $f \ll 1$ [7]), they result in lower thermal conductivity smoothing of illumination non-uniformity.

Intensities can be kept in the above range if thin hollow-shells are used [12]; an upper limit to their aspect ratio A could be set by Raleigh--Taylor instability. Furthermore the implosion velocity has to be larger than some ignition velocity $\sim 3 \cdot 10^7$ cm/s. In the attempt to satisfy both of these conditions we consider double shell targets, which exploit the velocity multiplication (up to a factor $\cong 2$), that occurs when a larger mass collides elastically with a smaller one.

Preliminary results show that medium gain ($G \sim 100$) targets with fuel mass $M = 2 \div 6$ mg, outer-shell radius $R_1 = 0.4 \div 0.6$ cm, inner-shell radius $\sim R_1/3$, aspect ratio $40 \leqq A \leqq 80$, require $2 \div 2.5$ MJ in a $25 \div 50$ ns triangular pulse, with $0.53 \div \lambda \leqq 2\mu$ (we have taken $0.04 \leqq f \leqq 0.4$; lower mass and higher aspect ratio correspond to longer wavelenght and/or lower f). A reference target is shown in Fig. 2. The gap between the shells is filled with low pressure gas, to make the collision elastic; the Al layer is a thermal shield.

Work is in progress to improve the design of this kind of targets (in particular to attain higher hydrodynamic efficiency) and to explore the potentiality of other concepts.

REFERENCES

[1] Atzeni, S., and Caruso, A.: "Inertial confinement fusion: ignition of isobarically compressed D-T targets", Rep. ENEA 82.61 p (1982), sub. to Nuovo Cimento.

[2] Atzeni, S., and Caruso, A.: "An ignition criterion for isobarically compressed, inertially confined D-T plasmas", Phys. Lett. 85A (1981) 345.

[3] Atzeni, S., Caruso, A., Giupponi, P., and Pais, V.A.: "A 1-dimensional numerical code for laser driven implosion and ignition", Rep. CNEN 80.40 (1980).

[4] Atzeni, S., in preparation.

[5] Atzeni, S., and Caruso, A.: "On the energy gain of D-T targets for inertial confinement fusion", Rep. ENEA 82.51 p (1982), to appear in Nucl. Fusion.

[6] Meyer ter Vehn, J.: "On the energy gain of fusion targets: the model of Kidder and Bodner improved", Nucl. Fusion 22 (1982) 561.

[7] Max, C.E., Mc Kee, C.F., and Mead, W.C.: "A model for laser driven ablative implosions", Phys. Fluids 23 (1980) 1620.

[8] Gardner, J.H., and Bodner, S.E.: "Wavelenght scaling for reactor size laser-fusion targhets", Phys. Rev. Lett. 47 (1981) 1137.

[9] Caruso, A., Gratton, R.,: "Some properties of the plasmas produced by irradiating light solids by laser pulses", Plasma Phys. 10 (1968) 867.

[10] Mora, P.: "Theoretical model of absorption of laser light by a plasma", Phys. Fluids, 25 (1982) 1051.

[11] Sanz, J., Linan,A., Rodriguez, M., and Sanmartin, J.R.: "Quasi-steady expansion of plasma ablated from laser-irradiated pellets, Phys. Fluids 24 (1981) 2098.

[12] Afanas'ev, Yu.V., Basov, N.G., Volosevich, P.P., Gamalii, E.G., Krokhin, O.N., Kurdymov, S.P., Levanov, E.I., Rozanov, V.B., Samarskii, and Tikhonov, A.N.: "Laser initiation of thermonuclear reaction in inhomogeneous spherical targets", JETP Lett. 21 (1975) 68.

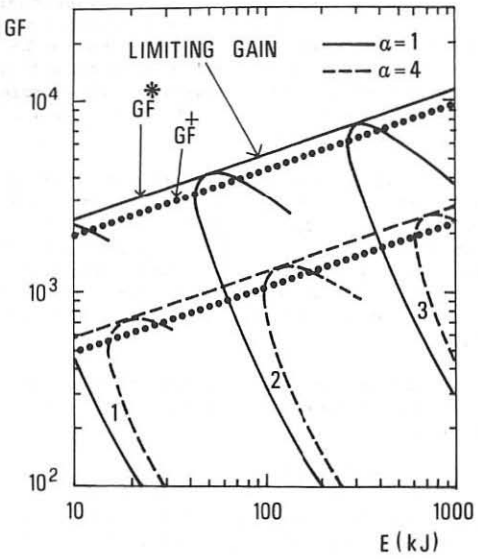

Fig. 1 - Fuel gain GF versus the energy E delivered to the D-T fuel, for different fuel masses M.
1) M = 10^{-1} mg; 2) M = 1 mg; 3) M = 10 mg.

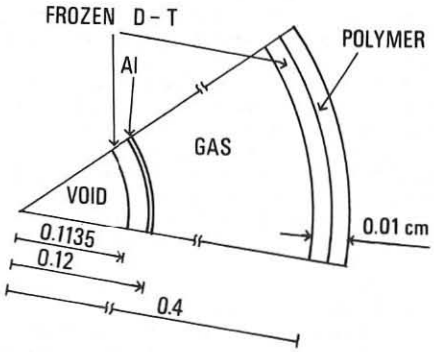

Fig. 2 - Reference double-shell target (not to scale). E_L = 2.3 MJ; Δt = 25 ns; λ = 1.06 μ.

NONLINEAR ION WAVES IN ABSOLUTE BRILLOUIN SCATTERING

J.A. Heikkinen, S.J. Karttunen, and R.R.E. Salomaa*)
Technical Research Centre of Finland
Nuclear Engineering Laboratory
P.O.B. 169, SF-00181 Helsinki 18, Finland

Absolute growth of stimulated Brillouin scattering (SBS) occurs in the regime of weak linear damping of ion waves. In laser-plasmas mainly electrons are heated so that the conditions for weak ion wave damping (i.e. $ZT_e/T_i \gg 1$) are likely at the early stage of Brillouin scatter. In absolute Brillouin process the backscattered wave grows from zero level and no electromagnetic noise source is required for the onset of the instability. To prevent high SBS-reflectivities the damping of ion acoustic waves must strongly increase during the evolution of Brillouin process. This can be obtained by nonlinear ion heating (i.e. tail-heating) [1] or by subharmonics [2] and higher harmonics generation of ion waves [3].

In this paper we study the effects of higher ion wave harmonics on the absolute Brillouin backscattering using a time and space dependent WKB-model. For simplicity the plasma is taken homogeneous because a weak density gradient was not shown any essential new features in our study. By including higher harmonics of the SBS-excited ion wave $e_1(k_1, \omega_1)$ we obtain the normalized equations [4]

$$\frac{\partial e_0}{\partial \xi} = -e_- e_1 , \tag{1}$$

$$\frac{\partial e_-}{\partial \xi} = -e_0 e^*_1 , \tag{2}$$

$$\frac{\partial e_n}{\partial \tau} + \alpha_n \frac{\partial e_n}{\partial \xi} + (\beta_n + i\Delta_n) e_n = e_0 e^*_- \delta_{n,1}$$

$$+ \kappa n \left[\frac{1}{2} \sum_{p=1}^{n-1} e_p e_{n-p} - \sum_{p=1}^{\infty} e^*_p e_{n+p} \right] , \tag{3}$$

where e_0 is the pump, e_- the backscattered amplitude and e_n ($n = 1,2,\ldots$) is the nth harmonic of the ion wave. The normalized damping β_n, detuning Δ_n and group velocity α_n depend on the mode number n as: $\beta_n = nL_g\Gamma_1/c_s$ and $\Delta_n = n(n^2-1)k_1 L_g k_1^2\lambda_D^2/2$ and $\alpha_n = (1+n^2k_1^2\lambda_D^2)^{-1}$ where $L_g = 2\sqrt{2}(c/v_0)\lambda_D$ is the basic gain length of SBS. The length is in units of L_g and time is normalized to L_g/c_s where c_s is the ion sound velocity. Due to the large group velocity ratio $c^2k_0/\omega_0 c_s$ the time derivatives in Eqs. (1) and (2) are neglected. The efficiency of the ion harmonics generation is described by the coefficient $\kappa = 4k_0^2c^2/\omega_p^2$ which depends on plasma density. The electromagnetic modes e_0 and e_- couple resonantly to the primary ion wave e_1 only. Thus the excitation of higher harmonics represent a loss mechanism i.e. a nonlinear damping for the SBS-generated ion wave.

The task remains to solve numerically Eqs. (1)-(3) with the boundary and initial conditions: $|e_0(0,\xi)| = |e_0(\tau,0)| = 1$, $|e_-(0,\xi)| = |e_-(\tau,L/L_g)| = 0$, $|e_n(0,\xi)| = |e_n(\tau,0)| = 0$, for $n > 1$ and $|e_1(\tau,0)| = 0$ where L is the plasma length. To start the instability we assume the initial condition $|e_1(0,\xi)| = \varepsilon \neq 0$ which affect the initial transient stage only. Due to the boundary conditions the phases are locked at $\xi = 0$ and L/L_g. The time dependent SBS-reflectivity $r(\tau)$ is defined by the boundary condition $|e_-(\tau,0)| = \sqrt{r(\tau)}$.

Higher harmonics appear after the excitation of the primary ion mode e_1 so that they have no effect on the onset of Brillouin scattering. This means that the condition for the absolute SBS is same as for the pure three-wave case i.e. $\beta_1 < 2$ [5,6].

Fig. 1 shows SBS-reflectivity as a function of time with harmonic number n = 2,6 and 10. The parameters are $L/L_g = 6.9$, $\beta_1 = 0.73$, $\kappa = 23$ $(n/n_{cr} \simeq 0.15)$ and $\Delta_n = n(n^2-1)\times 0.024$. In the cases n = 2 (second harmonic) and n = 6 (six harmonics) the reflectivity approaches a limit cycle after the initial

transient and no steady-state exists. The period 5.5 is of the order of the acoustic transit time $\tau_{tr} = 6.9$ but no simple relationship between the two characteristic times was found when the parameters were varied. When ten harmonics (n = 10) are included the time structure disappears and a proper steady-state is reached. The steady-state reflectivity $r \approx 0.31$ is considerably smaller than the corresponding three-wave value [6]: $r = 1-\beta_1^2/4 \approx 0.87$.

When the plasma length or the pump intensity (i.e. L/L_g) is increased the steady-state reflectivity approaches the three-wave limit $1-\beta_1^2/4$. This is illustrated in Fig. 2 which shows the reflectivity as a function of L/L_g for n = 1 (no harmonics) and n = 6 with the parameters $\kappa = 36$ ($n/n_{cr} = 0.1$), $\Delta_n = n(n^2-1)\times 0.12$ and $\beta_1 = 1$. Due to the larger detuning than in previous case (Fig. 1) a proper steady-state is obtained with six harmonics. In the region $L/L_g < 20$ harmonics generation dominates the linear damping leading to well reduced reflectivities as compared to the three-wave value.

In the limit of small damping and detuning (β_r, $\Delta_n \to 0$) the amplitudes oscillates strongly when only few harmonics are included. The convergence with the harmonic number n is slow and large values of n are required to describe the process properly. When the damping and detuning are increased the time behaviour relaxes and typically 6 - 10 harmonics are needed ($\beta_n \sim n$ and $\Delta_n \sim n^3$). For a large damping or detuning the excitation of higher harmonics is quenched and the process behaves according to three-wave equations.

The harmonics generation of ion waves reduces SBS most strongly in well underdense plasma $n/n_{cr} < 0.2$ where SBS-growth is rather weak (recall the density dependence of κ).

Qualitatively results remain same for inhomogeneous plasmas where the absolute growth takes place if the condition $\beta_1 < 2$ can be met locally in the high density region (β_1 decreases

with increasing density). This expands the parameter range for absolute Brillouin scatter in comparison with the homogeneous case.

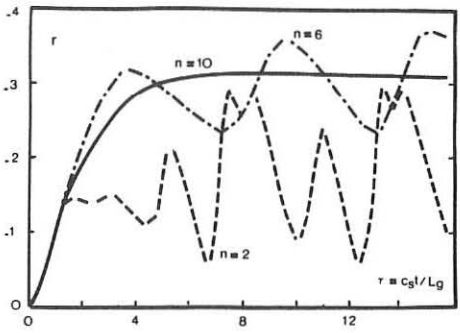

Fig. 1. SBS-reflectivity versus time. Parameters given in text.

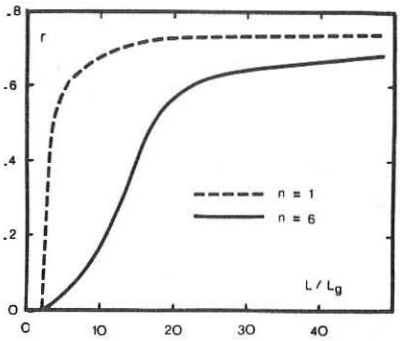

Fig. 2. SBS-reflectivity as a function of normalized plasma length. Parameters given in text.

1. D.W. Phillion et al., Phys. Rev. Lett. 39, 1529 (1977).
2. S.J. Karttunen and R.R.E. Salomaa, Phys. Lett. 72A, 336 (1979).
3. J.M. Dawson et al., in Dynamics of Ionized Gases, Tokyo 1973; V.P. Silin and V.T. Tikhonchuk, JETP Lett. 34, 365 (1981); S.J. Karttunen and R.R.E. Salomaa, Phys. Lett. 88A, 350 (1982).
4. J.A. Heikkinen et al., to be published.
5. D.W. Forslund et al., Phys. Fluids 18, 1002 (1975).
6. V. Fuchs, Phys. Fluids 19, 1554 (1976).

*)Permanent address: Helsinki University of Technology,
Department of Technical Physics,
Espoo, Finland

GEKKO XII GLASS LASER SYSTEM FOR LASER FUSION RESEARCH

K. Yoshida, Y. Kato, M. Nakatsuka, T. Jitsuno, S. Nowada, J. Kuroda, Y. Goto, H. Azechi, N. Miyanaga, S. Sakabe, T. Mochizuki, T. Yamanaka, S. Nakai and C. Yamanaka

INSTITUTE OF LASER ENGINEERING, OSAKA UNIVERSITY
SUITA, OSAKA 565, JAPAN

1. INTRODUCTION

The GEKKO XII (G-XII) system is designed and constructed in order to perform high-density compression experiment. System assembly of G-XII were completed in March 1983 and initial testing is going. The target experiment will start in December 1983 following the completion of the target irradiation system.

The conceptional view of G-XII is shown in Fig. 1. The laser beam from the master oscillator room on the first floor is guided to the steel optical bench on the second floor of the laser bay, and then is divided into twelve-beams.

Passing through the main amplifier chains fixed to the steel space frames, laser beams are guided into the gear room. The beams are switched to either a symmetric or a two directional irradiation target room.

The main oscillator is located in the oscillator room of 382m^2 clean room of class 1,000. The areas of the laser, the gear room, the target room I and II are respectively 2,250m^2, 900m^2, 900m^2 and 600m^2, which are class 10,000.

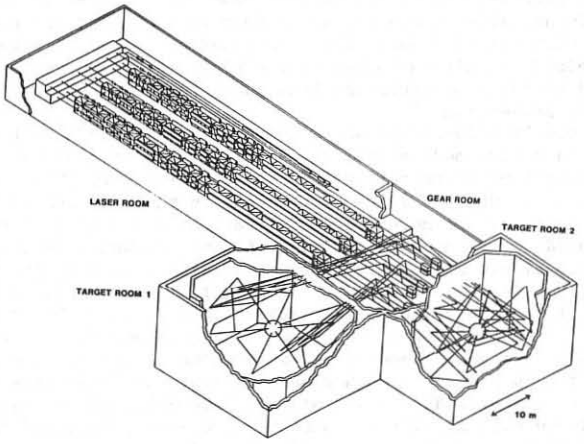

Fig. 1. Conceptional design of GEKKO XII glass laser system.

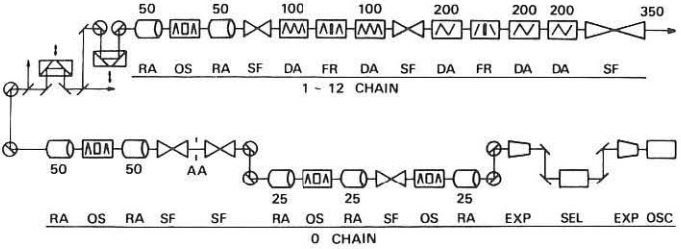

Fig. 2. Layout of the GEKKO XII system.
OSC:oscillator, EXP:expander, SEL:pulse selector,
RA:rod amplifier, OS:optical shutter, SF:spacial filter,
FR:Faraday rotator, DA:disk amplifier, AA:hard aperture

2. SYSTEM DESCRIPTIONS

The layout of G-XII is shown in Fig. 2. The design is similar to the GM-II system[1] (which is a prototype of G-XII) except for several modifications. The laser system consists of a preamplifier section, a beam-splitting section, and twelve main amplifier chains. In the preamplifier section a spatially shaped laser pulse is generated to obtain a high filling factor, amplified and expanded to the beam diameter of 44mm. In the beam-splitting section, the laser pulse is split into twelve beams. The optical path lengths of the twelve beams are adjusted in this section. In each main amplifier chain the laser beam is amplified and expanded to the output diameter of 340mm. Each component is connected with beam tubes for dust-shield and air-turbulence protection. Nitrogen gas without dust is supplied to the components and beam tubes for the cooling of amplifiers and humidity prevention.

An actively mode-locked and Q-switched oscillator[2] with a Nd:YLF crystal as an active medium provides a pulse train at 1.053μm. Table 1 shows the operating characteristics of this oscillator. The pulsewidth is variable between 90ps and 1.2ns by changing intracavity etalons and a modulation depth of the mode-locker. Wavefront distortion of the laser beam, measured by the Mach-Zhender interferometer, was less than $\lambda/10$ (λ=1.053μm). Single pulse energy from the pulse selector with triple Pockels cells which is activated by electronically triggered avalanche transistor circuits provides ∿11μJ with variation of ±1.9 percent in 1,000 shots. The selected pulse is expanded to 22mm diameter. After amplification, the beam diameter is expanded to triple in size and the central 10.5mm is passed through a hard aperture AA. The beam diameter is then successively expanded to 44, 94, 190, and 340mm by the spatial filters. These spatial filters completely relay the image of the hard aperture AA to the target lens in order to reduce intensity nonuniformity due to Fresnel diffraction. The optical shutters prevent coupling between the amplifiers and reduce background emission reaching the target before the main pulse. The Faraday rotators prevent the damage of optical

components from the laser beam reflected from or transmitted through the target.

Table 2 lists the measured transmission wavefront distortions of the major optical components of the G-XII laser. Nd : phosphate glass LHG-8 was adopted as a laser glass of the G-XII system. All the components have wavefront distortions less than $\lambda/7$ (λ=632.8nm). In assembling the disk amplifiers and Faraday rotators, optical components are arranged to cancel the wavefront distortions each other. All laser components are assembled in a clean room of class 100 adjacent to the laser bay.

A block diagram of the control system is shown in Fig. 3. It monitors the flashlamp current, the Faraday rotator current, the nitrogen flow rate, the purity of the cooling water, and the vacuum of the spatial filters. The functions of the beam diagnostics controller are to monitor the laser beam, the optical shutter and the oscillator.

Table 1. Operating characteristics of the oscilltaor.

Output energy	11.1 μJ
Reproducibility	±1.9%(In1000 shots)
Pulsewidth	90ps - 1.2ns
Beam divergence	<15 μrad
Prepulse ratio	$<3\times10^{-8}$
Wavefront distortion	$<\lambda/10$ (λ=1.053 μm)
Repetition rate	6pps

Table 2. Measured transmission wavefront distortion of the optical components.

Item	Number of components	Wavefront distortion at 632.8nm(average value)
1. Laser glass		
RA 25$^{\phi}$	3	$\lambda/18.3$
50$^{\phi}$	26	$\lambda/8.2$
DA 100$^{\phi}$	144	$\lambda/10.4$
200$^{\phi}$	108	$\lambda/7.6$
2. Faraday glass		
FR 100$^{\phi}$	12	$\lambda/16.5$
200$^{\phi}$	12	$\lambda/17.2$

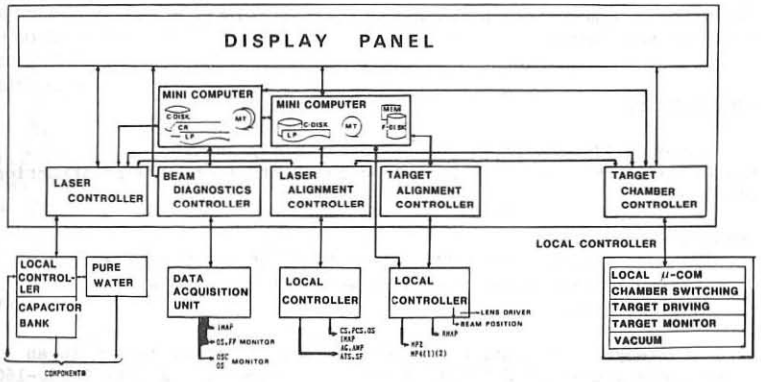

Fig. 3. Block diagram of the control system for GEKKO XII.

Table 3. Laser performance of GEKKO XII.

Beam number	12 beams
Beam diameter	340mm
Output energy	20kJ
Peak power	40TW
Output reproducibility	$< \pm$ 10%
Energy balance	$< \pm$ 5%
Prepulse ratio	$< 3 \times 10^{-8}$
Repetition time	1hour

3. LASER PERFORMANCE

Table 3 shows the laser performances of G-XII. The design performance of G-XII is output energy of 20kJ at 1ns and peak power of 40TW at 0.1ns. These performances are guranteed with sufficient margin.

4. SUMMARY

The GEKKO XII glass laser can deliver 20kJ in 1ns and 40TW in 0.1ns. Twelve-beams with the final output diameter of 340mm are switched to the target room I or II depending on the experimental program. Target rooms I and II have a symmetric and two directional irradiation target chambers respectively.

ACKNOWLEDGEMENT

We should like to thank the G-Project Group and the Optical-Technology Group for their laborious efforts to the construction of G-XII.

REFERENCES

/1/ C. Yamanaka et al. : Nd-DOPED PHOSPHATE GLASS LASER SYSTEMS FOR LASER-FUSION RESEARCH, IEEE J. Quantum Electron. QE-17, (1981) 1639-1649.

/2/ D.J. Kuizenga : Generation of short pulses for laser fusion in an actively mode-locked Nd:YAG laser, Opt. Commun., 22 (1977) 156-160.

HIGH ELECTROSTATIC FIELDS AND OSCILLATIONS IN EXPANDING INHOMOGENEOUS PLASMAS WITHOUT EXTERNAL FIELDS OR WITH LASER IRRADIATION

H. Hora, P. Lalousis, A.K. Ghatak, D.A. Jones* and S. Talapaga-Rosenberger
Department of Theoretical Physics, The University of New South Wales,
Kensington, 2033, Australia

This paper reports on the numerical discovery and the analytical formulation of the fact that all plasmas with inhomogeneities in the plasma density and/or the temperatures have high electrostatic fields. These fields are important for inertial confinement as a reason for strongly reduced thermal transport or by suppression of energetic electron penetration by electrostatic double layers, or for magnetic confinement when causing **E** × **B**-drifts not generally recognized before.

The motivation was to study the nonthermal direct electrodynamic interaction of lasers with plasmas by nonlinear forces[1] where the optical fields act at the plasma electrons dragging along the ions electrostatically. While the two-fluid plasma theory was so successful for explaining very many phenomena (including the ponderomotive effects of the nonlinear forces), the restriction to small local non-neutrality prevented the treatment of the electrostatic effects. In order to overcome these difficulties, a numerical code with one spatial dimension x for two genuine fluids (for electrons and ions) was established where detailed nonlinear optical and dynamical effects were included and time steps much less than the plasma oscillation time was necessary. Though advanced programming led to several reductions - especially a matrix procedure for exact solutions of the wavefields with reflection - nevertheless, only long computer runs led to the first results[2].

Without any external magnetic or laser fields, Fig. 1 shows the electrostatic fields up to some 10^6 V/cm in the real plasma slab of 10 μm thickness of about keV temperature and about 10^{21} cm^{-3} density. After 40 periods, the fine ripple of the oscillations has decayed by Coulomb collisions (seen as faster decay for lower temperature) and the monotonous slope of the strong electrostatic field remains.

While the numerical results deserve full generality, the following analytical model includes some simplifications. Differing from the two-fluid model, the two genuine fluid model does not run into difficulties with the Poisson equation[3] but can actively use it unrestrictedly. After temporal differentiation, substitution by the equation of continuity and spatial integration, Poisson's equation for the electric field strength **E** in the x-direction of the plasma

$$\frac{\partial}{\partial t} E = 4\pi e \, (n_e v_e - Z v_i n_i) \qquad (1)$$

where Z is the ion charge number. Further temporal differentiation and substitution of the terms on the r.h.s. by the equations of motion and assuming - only at this point of the analytical model - $n_e \approx Z n_i$ for adding viscosity terms with the Coulomb collision frequency ν, we arrive at

$$\frac{\partial^2}{\partial t^2} E + 2\gamma \frac{\partial E}{\partial t} + \omega_{po}^2 E = 4\pi e \left(\frac{3Zk}{m_i} \frac{\partial T_i n_i}{\partial x} - \frac{3k}{m_e} \frac{\partial T_e n_e}{\partial x} \right) \qquad (2)$$

where

$$\gamma = \frac{\nu}{2} \left(1 + \frac{Z m_e}{m_i} \right); \quad \omega_{po}^2 = 4\pi e^2 \left(\frac{n_e}{m_e} + \frac{Z^2 n_i}{m_i} \right); \quad \text{if } \omega_p > \frac{\nu}{2}$$

using the plasma frequency $\omega_p \approx \omega_{po}$. Simplifications in the interpretation of the partial differentiations lead to the local solution of Eq. (2)

$$E = \frac{4\pi e}{\omega_p^2}\left(\frac{1}{m_i}\frac{\partial p_i}{\partial x} - \frac{1}{m_e}\frac{\partial p_e}{\partial x}\right)\left[1 - e^{-\nu t}\left(\cos\left[\left(\omega_p^2 - \nu^2\right)^{\frac{1}{2}} t\right] + \frac{\nu \sin\left[\left(\omega_p^2 - \nu^2\right)^{\frac{1}{2}} t\right]}{\left(\omega_p^2 + \nu^2\right)^{\frac{1}{2}}}\right)\right] \quad (3)$$

well explaining that fast oscillations with the plasma frequency $(\omega_p^2 - \nu^2)^{\frac{1}{2}} \approx \omega_p$ are decaying by the collisions. What remains is an electrostatic field, determined by the first bracket in Eq.(3) where the ion and electron pressures are $p_i = n_i k T_i$ and $p_e = n_e k T_e$. This remaining field is approximately

$$E = -\frac{4\pi e}{\omega_p^2 m_e}\frac{\partial}{\partial x}\left(3\, n_e k T_e\right) \quad (4)$$

For the example of Fig. 1, the temperatures and the densities have not changed much from the initial values at x = 0, with the result $E = 2.58 \times 10^6$ V/cm from Eq. (4) in agreement with the numerical values.

For the case with laser irradiation, Fig. 2 represents the numerical result of 10^{16} W/cm^2 neodymium glass laser irradiation, where electrostatic fields up to 2×10^8 V/cm are produced after 1.5 psec. The nonlinear force requires an additional term in the equation of motion for the electrons

$$f_{NL} = (\partial/\partial x)\ (\underline{E}^2 + \underline{H}^2)/8\pi \quad (5)$$

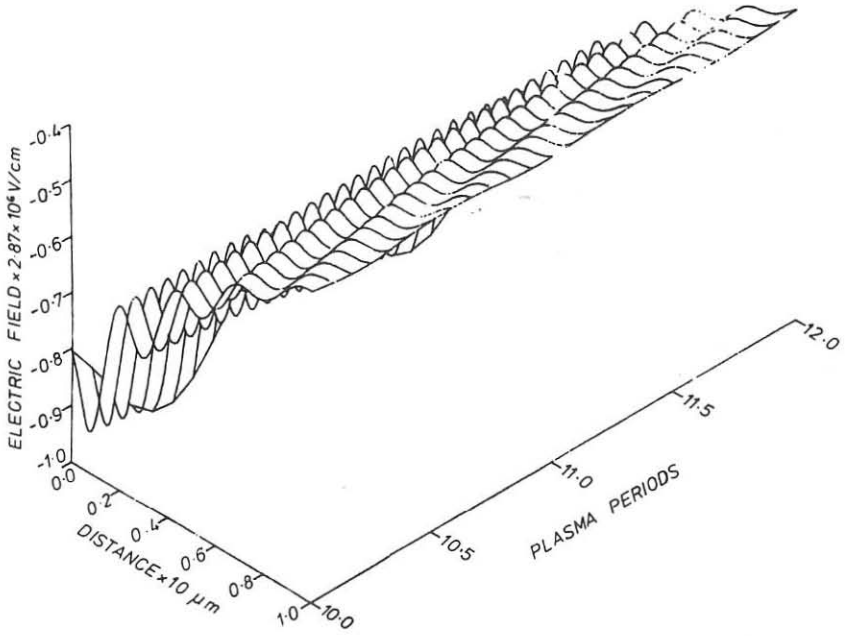

Fig. 1. Starting from a linear initial density profile of a 10 μm thick slab of $n_e(x = 0) = 5 \times 10^{20}$ cm^{-3} up to 10^{21}cm^{-3} densities $n_e = n_i$ for a real hydrogen plasma with initial electron and ion velocities v_e and v_i being zero, and the initial electron and ion temperatures $T_e = T_i = 10^7$ °K, the initial electric field E is then zero. Developing in time in numbers of plasma oscillation periods of 5×10^{20} cm^{-3} density, an electrostatic field of some 10^6 V/cm is appearing with oscillations.

where **E** and **H** are the electric and the magnetic field strength of the laser in the plasma. Further terms are not effective for this geometry as long as we consider the monochromatic wave interaction. The question what additional terms are to be used[5, Eq. (10)] was clarified before [1] since 1969: only all these terms and no others produce the necessary shearfreeness of the forces at oblique incidence of laser radiation on plasma. The electron density between x = 0 and the caviton at 4 μm has been increased by the dynamics from low initial values up to densities above the critical density $n_{ec} = 10^{21}$ cm^{-3} which, at this time step, prevents the penetration of light to the plasma. This self-shutting of laser irradiation by the plasma was observed before from one-fluid computations[1] if the exact wave field with reflection was included. The result confirms the driving mechanisms of the electrons by the nonlinear forces. Electrostatic oscillations are generated at each change of the driving of the electrons by the laser field and have been followed up within the laser field oscillations.

The result of Eq. (4) has very general validity for plasmas: **Any inhomogeneity in a plasma produces electrostatic fields**, any gradient in the electron density and/or any temperature gradient. For laser-fusion, these fields lead to a reduction of thermal conduction current C. The double layer in a DT plasma reduces C to the pure ion conduction (smaller by $(m_e/m_i)^{1/2}$ = 1/68), or explained from the kinetic theory from

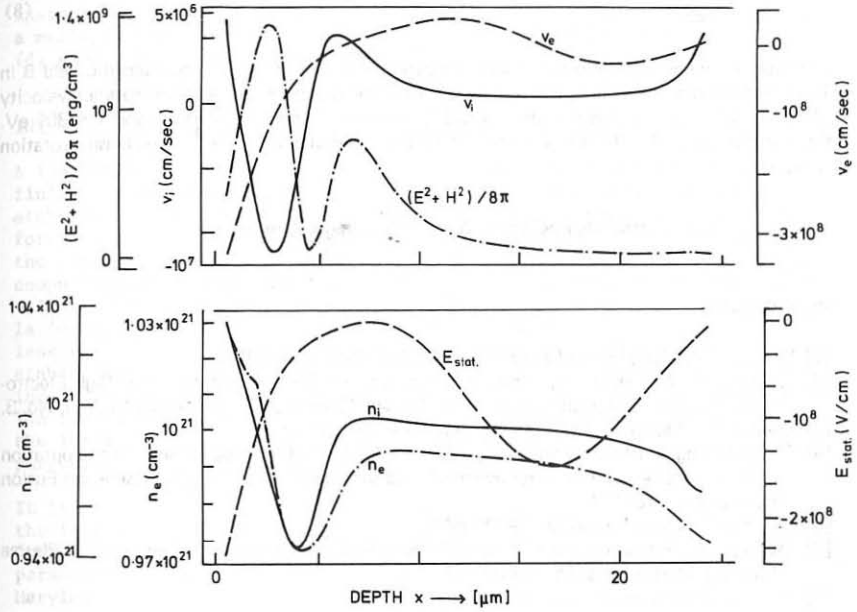

Fig. 2. 10^{16} W/cm^2 neodymium glass laser irradiation from the left side on a 25 μm thick hydrogen layer at 1.5 psec. Initially at t = 0, a parabolic density profile $n_e = n_i$ of $T_e = T_i$ = 1 keV at rest $v_i = v_e = 0$ was thermally expanding and developing during the first 0.5 psec without laser irradiation damping out electrostatic oscillations due to the initial conditions. When the laser is switched on, producing an electromagnetic field density $(E^2 + H^2)/8\pi$, the nonlinear force driven motion produced a density minimum (caviton) at 4 μm producing ion velocities up to 10^7 cm/sec and electrostatic fields up to 2×10^8 V/cm.

$$C = -\frac{4\pi m_e}{6}\int_0^\infty v^5 \ell \left(\frac{\partial f^\circ}{\partial x} - \frac{e}{2m_e} E \frac{\partial f^\circ}{\partial (v^2)} \right) dv \qquad (6)$$

(v ~ kinetic electron velocity, f° ~ equilibrium distribution function; ℓ ~ mean free path) what has been concluded indirectly[4] from pellet fusion gains which agree with the measurements only if C is taken 100 times smaller.

For cases of magnetic fusion confinement, one has to generalize Eq. (4) by a magnetic pressure term

$$E = -\frac{4\pi e}{\omega_p^2 m_e} \frac{\partial}{\partial x} (p - H_s^2/8\pi) \qquad (7)$$

where the interpretation of internal and external fields has to be given[6]. Assuming the confining magnetic field $\mathbf{H}_s$ in a similar way as the wall limitation by a probe, the static electric field of Eq. (7) will cause an $\mathbf{E} \times \mathbf{B}$ drift with a velocity v_d in a cylindrical or toroidal plasma column of approximately

$$v_d = \frac{3T}{rB} \qquad (8)$$

in m/sec, if the average plasma electron temperature T is given in eV, the magnetic field B in Tesla, and the radius r of the plasma in meter. This would explain the observed rotation velocity of 3×10^4 m/sec of theta-pinch plasmas[7] taking r = 1 cm, B = 3 Tesla, and T = 300 eV. For a stellarator of B = 3 Tesla, T = 1 keV, r = 3 cm, v_d results in 3×10^4 m/sec plasma rotation velocities.

* Now at Materials Res. Labs., Ascot Vale 3032, Victoria.

REFERENCES

[1] Hora, H.: Physics of Laser Driven Plasmas. Wiley, New York 1981.
[2] Lalousis, P., and Hora, H., Direct Electron and Ion Fluid Computation of High Electrostatic Fields in Dense Inhomogeneous Plasmas, Laser and Particle Beams **1** (1983) No. 3.
[3] Chen, F.F.: Plasma Physics. Plenum, New York 1975, p. 66.
[4] Ding Le-Ming, Tai Wei Hai, and Wang Run-Wen, Analysis of the mechanism and computation of similar modes in laser compression of glass shell pellets with DT gas, Plasma and Fusion (China) **1** (1982) 187.
[5] Peratt, A.L., Phys. Rev. **A20**, (1979) 2555.
[6] Bobin, J.L., Ponderomotive Pressure Effects in Laser-Driven High-Temperature Plasma Flows, J. Plasma Phys. **25**, (1981) 193.
[7] Kronast, B. (private communication).

SCALING LAWS FOR THE RESISTIVE LONGITUDINAL INSTABILITY IN FINITE CHARGED BEAMS*

Abraham Sternlieb
Soreq Nuclear Research Centre
Yavne 70600, Israel

ABSTRACT

Heavy ion beams are considered as possible drivers in an inertial confinement fusion scheme /1/. The high required intensities introduce space-charge effects. It has been shown analytically that a finite cold beam is longitudinally stable when a small resistive term is present /2,3/. This is confirmed by our simulations /4/ which show that for resistivities causing less than one e-folding of a perturbation over the bunch length, the beam is stable (unlike a coasting beam), probably due to end reflections. However, for resistivities causing more than three e-foldings, the beam is unstable (emittance deteriorated exponentially). We discuss the implication of this instability threshold for a few cases: (a) a full-scale driver model; (b) a multiple-beam driver; (c) single beam transport experiment-SBTE (LBL); (d) slow e-beam experiment (Maryland).

INTRODUCTION

A 1-d particle simulation code /5/ is used to investigate the stability of finite charged beams in a resistive transport line. Linear theory shows stability for resistive force values to be small compared to space-charge forces /2,3/. It was suggested that this occurs when the e-folding length of the perturbation is long compared to bunch length. To check this, particle computer simulations have been performed /4/ including various resistive force values. The line charge density distribution was parabolic /3/. The simulation results indicate clearly that for a resistive force corresponding to less than one e-folding of the perturbation over the beam length, the beam is stable, while for a resistive force corresponding to more than three e-foldings, the beam is unstable and the longitudinal emittance grows uncontrollably. The simulation results both confirm and extend the theoretical results beyond the linear regime. It seems that for low enough resistive force terms, the perturbation is stabilized during reflection from the bunch ends.

It is calculated that the resistance of typical one beam driver model is in the instability range. Stability may be achieved, e.g. using a multiple beam driver /6/. We also calculate the resistive threshold values for the design parameters of SBTE /7/ at LBL and for the slow e-beam experiment /8/ at Maryland.

The longitudinal resistive threshold is a pure computer simulation result. No coupling to the transverse modes is assumed. Therefore a 2-d or 3-d simulation code is desirable. The resistance is assumed to be frequency independent and the beam velocity constant. Coasting beam results /9/ indicate

(*) Part of this work was performed during the author's stay at Lawrence Berkeley Lab.

that longer wave length modes are more active. This result seems to complement a more detailed investigation /10/.

Finally, we suggest that results obtained from computer simulation may provide input for a possible active feedback stabilization of the longitudinal resistive instability.

THEORETICAL AND SIMULATION MODEL

The simulation follows in a self-consistent manner the non-linear longitudinal behavior of a bunched beam in the presence of a resistive wall. The distribution function is given by /3/:

$$f_o(x,v) = (3N/2\Pi x_o v_o)(1 - x^2/x_o^2 - v^2/v_o^2)^{\frac{1}{2}} \qquad (1)$$

where x_o, v_o are the maximum values for x and v. The resultant linear density is:

$$n(x) = (3N/4x_o)(1 - x^2/x_o^2) \ , \qquad (2)$$

where N is total number of particles in the bunch. The forces acting on the bunch are:

(a) Space-charge defocussing force: $-e\partial n(x)/\partial x$ (long bunch).

(b) Resistive force: $-eRn(x)$, where $R = R'v_o$. R' is the average wall resistance per unit length, and V_o is the beam velocity.

(c) Focussing forces to balance (a) and (b): $-kx + eRn(x, t = 0)$, where K is a constant.

We study a cold finite beam moving with the simulation system. For a cold beam we require: $v_{th} << v_p$, where v_{th} is thermal spread and v_p is the phase velocity of the perturbation, given by: $v_p = q(n/m)^{\frac{1}{2}}$, where q is the particle charge and m is the particle mass. For comparison purposes, we use cold coasting beam formulae for growth rate γ_k and real frequency ω_R:

$$\gamma_k = \pm \frac{1}{2} v_p \frac{R}{g} \ ; \quad \omega_R = \pm v_p k \ , \qquad (3)$$

where g is a geometric factor taken as 1 and k is the wavenumber of the perturbed mode. Relations (3) hold to good accuracy for $R/kg \lesssim 1$, which in our computer model becomes $R \lesssim 0.1$ ($k \gtrsim 0.1$). This condition is equivalent to the small resistive term approximation, which predicts stability /2/.

We use dimensionless code units, explained in Ref (5), and take: L_s (system length) = 128; L_B (bunch length at t=o)=64; v_p(maximum)=13; $v_{th}(t=o)$=2.2; R=0,0.03,0.1.

The e-folding time of the perturbation is defined as $\gamma_k \tau = 1$, and the e-folding length l is defined as: $l = v_p \tau = v_p/\gamma_k = 2/R$. For R=0.03 we have τ=5 and l=66(L_B). For R=0.1 we have τ=1.7 and $l \simeq 20$ ($L_B/3$). We have not checked whether R=0 ($l=\infty$) means stability, irrespective of initial perturbation amplitude. This should be further investigated.

SIMULATION RESULTS AND APPLICATIONS

The simulation results can be summarized as follows:

(1) For $R \lesssim 0.03$ ($R=0.03$ corresponds to one e-folding of the perturbation over the bunch length), the bunch is stable. This regime corresponds to the linear theoretical analysis /2/.

(2) For $R \gtrsim 0.1$ (more than 3 e-foldings), the bunch is destroyed by the growing waves.

It is desirable to check this non-linear threshold behavior in experiments. The translation from code units to MKS-C unit (or vice-versa) is performed by using the following relationship:

$$\bar{R}^1 = (L_B/4\pi\bar{\varepsilon}_o)(\bar{m}/2\bar{E}\bar{\tau}_B)R \ , \qquad (4)$$

where the barred quantities are in MKS-C units, the unbarred are in code units, $\bar{R}^1$ is resistance per unit length, $L_B=64$, $\bar{\varepsilon}_o=8.85\times10^{-12}$ (MKS), $\bar{m}$ is particle mass, $\bar{E}$ is particle energy, $\bar{\tau}_B$ is pulse length, and $R=R'v_B$ ($R=\bar{R}\bar{v}_B$). In obtaining eq. (4) we have used Ref. (5), $\bar{E} = \bar{m}\bar{v}_B^2/2$, and $\bar{L}_B = \bar{v}_B\cdot\bar{\tau}_B$. We also require a minimum accelerator length which permits at least one end reflection. This can be formulated as: $\bar{L}_A \gtrsim (\bar{L}_B\cdot\bar{v}_B/\bar{v}_p)$, where L_A is the accelerator length. We use the following relationships (MKS-C) to find how to change the beam parameters in order to permit a practical $\bar{L}_A$ value, when necessary: $\bar{L}_B = \bar{v}_B\cdot\bar{\tau}_B$, $\bar{v}_p = \bar{q}(\bar{n}/4\pi\bar{\varepsilon}_o\bar{m})^{\frac{1}{2}}$, $\bar{m}\bar{v}_B^2/2 = \bar{E}$, $\bar{n} = \bar{I}/\bar{e}\bar{v}_B$. Then we get:

$$\frac{2\cdot 2^{1/4}\sqrt{4\pi\bar{\varepsilon}_o}}{\sqrt{\bar{m}}\ \bar{m}^{1/4}\sqrt{q}} \quad \frac{\bar{E}^{5/4}\cdot\bar{\tau}_B}{\sqrt{\bar{I}}} \leq \bar{L}_A \qquad (5)$$

Next, we calculate the threshold behavior for some proposed or existing experiments:

(1) A typical HIF driver design includes: $\bar{R}^1=100\Omega/m$, $\bar{v}_B=10^8$m/sec, $\bar{L}_B=10$m, $\bar{N}=10^{15}$, Cs^{+1}. Using eq. (4), we obtain $R=0.2$, which is unstable.

(2) An approach has been proposed for a HIF driver which uses a multitude of low current beamlets /6/. This permits a larger current to be transported through the same aperture as compared to a single beam, so one can use shorter bunches to transport the same charge. When $1(=v_p/\gamma_k)$, $\bar{R}^1$ and $\bar{v}_B$ are kept constant, shorter bunches tend to be more stable.

(3) The single beam transport experiment (SBTE) at LBL has: Cs^{+1} ions, $\bar{E}$=200 keV, $\bar{I}$=20mA, $\bar{\tau}_B \gtrsim 5\mu$sec, $\bar{v}_B=5.36\times10^5$ m/sec, $\bar{L}_B=2.68$m. To have instability, one uses eq. (4) with $R\gtrsim0.1$, which gives: $\bar{R}^1 \gtrsim 40K\Omega/m$. Below 13 k$\Omega$/m we expect stability. However, from eq. (5) we get $\bar{L}_A>93$m which is much longer than in reality. We can reduce $\bar{E}$, $\bar{\tau}_B$ and/or increase $\bar{I}$. E.g., $\bar{E}\cdot\bar{\tau}_B$ can be reduced by a factor of 10 and eq. (4) should then be used again e.g. $\bar{R}^1$ 0.5 MΩ/m, if we desire instability ($R=0.1$) .

(4) The slow e-beam experiment at U. of Maryland has: $\bar{E}$=1-10 keV (we take 5 keV), $\bar{\tau}_B=5\mu$sec, $\bar{I}$=200mA, $\bar{v}_B=4.18\times10^7$m/sec, $\bar{v}_p=2.75\times10^4$m/sec. One gets: $\bar{L}_B = \bar{v}_B\cdot\bar{\tau}_B=209$m and $\bar{L}_A \gtrsim 300$km. To have practical $\bar{L}_B$ and $\bar{L}_A$ values, one may, e.g., reduce $\bar{E}$ and $\bar{\tau}_B$ by two orders of magnitude each and increase $\bar{I}$ by

two orders of magnitude (eq. 5). This will decrease $\bar{L}_B$ by three orders of magnitude, to 21cm, $\bar{v}_p$ will be increased by $\sqrt{10^3}\approx 30$, to 8×10^5m/sec, and $\bar{L}_A$ will become: $\bar{L}_A \gtrsim 1$m. Then we have: $\bar{E}$=50eV, $\bar{\tau}_B$=50msec, $\bar{I}$=20A. From eq. (4) we find (R=0.1) that $\bar{R}^I$=50kΩ/m should cause instability.

In summary, by inserting known artificial resistances in existing experiments, one can check the validity of the computer-found threshold for the resistive longitudinal instability in finite charged beams.

REFERENCES

/1/ Proceedings of the HIF workshop, Oct. 29 - Nov. 9, 1979, LBL-10301, Sept. 1980.
/2/ Channel, P. J., Sessler, A. and Wurtele, J., LBL-11367, July 1980; LBL-12107, Feb. 1981.
/3/ Neuffer, D., Part. Accel. 11 (1980) 23-26.
/4/ Sternlieb, A.: Longitudinal resistive instability in finite charged beams: A computer simulation study, in Proceedings of the 1982 Int. Conf. on Plasma Physics, Gotebord, Sweden, June 9-15, 1982.
/5/ Sternlieb, A., Smith, L., Laslett, L. J., Bisognano, J. and Haber, I., LBL-12205, 1981.
/6/ Hermannsfeldt, W. B. and Keefe, D., HI-FAN-149 (1981), HIF-LBL Report.
/7/ Kim, C.: Single Beam Transport Experiment Reference Parameters, HI-FAN-160, Haevy Ion Fusion Report., Lawrence Berkeley Lab.
/8/ Reiser, M. in: Proceedings of 1981 Linear Acc. Conf., Santa-Fe, NM, Oct. 19-23, 1981.
/9/ Sternlieb, A., LBL-12878, June 1981.
/10/ Bisognano, J. in: these Proceedings (1983 Particle Acc. Conf.).

INVERSE BREMSSTRAHLUNG EFFECTS IN THE CORONAE OF LASER-IRRADIATED PELLETS AND SLABS

J.A. Nicolás and J.R. Sanmartín
E.T.S.I.Aeronáuticos, Universidad Politécnica de Madrid
Ciudad Universitaria, Madrid-3, Spain

In recent, quasi-steady analyses of the spherical, ablative corona of a laser-irradiated pellet, absorption was assumed to occur at the critical density n_{cr} /1/-/4/. Both classical and saturated heat-flux, and ion-electron energy exchange where taken into account. If the ion charge number Z_i and mass per unit charge $\bar{m} \equiv m_i/Z_i$, the instantaneous pellet radius r_a and laser power W_L, and its wavelength (or equivalently n_{cr}), are given, one can obtain quantities of interest such as the ablation pressure P_a, the critical radius r_{cr}, and the mass ablation rate $4\pi\bar{m}\mu$, as dimensionless functions ($\bar{P}_a \equiv P_a/\rho_{cr}V^2$, r_{cr}/r_a, and $\bar{\mu} \equiv \mu/r_a^2 n_{cr} V$) of the parameters Z_i, $\hat{W} \equiv W_L/r_a^2\rho_{cr}V^3$, and heat-flux limit factor f. We have introduced $\rho_{cr} \equiv \bar{m}n_{cr}$, a convenient speed $V \equiv (r_a n_{cr}/\bar{m}^{5/2}\bar{K})^{1/4}$, and the factor $\bar{K}$ of Spitzer's classical heat-flux ($\equiv -\bar{K}T^{5/2}\,dT/dr$, the electron temperature T being in energy units).

Lately the search for more ablative conditions in laser-irradiation of targets has moved the interest into shorter wavelengths (larger n_{cr}) and larger pellet radii. For such conditions inverse Bremsstrahlung absorption in the underdense flow can be substantial /5/. Here we attempt to quantitatively determine that absorption using the model of Refs. /3/ and /4/. Inverse Bremsstrahlung introduces into the model the electron mass m_e and the light speed c, and is found here to be parametrized by the ratio $\bar{m}V/m_e c$, which lies close to unity for all cases of interest. Large values of n_{cr} and r_a lead to relatively low $\hat{W}$ ($1\text{-}10^4$ typically). Recently Sanmartín et al. have considered effects due to a suprathermal electron population generated by resonant absorption, at higher values of $\hat{W}$ ($10^5\text{-}10^8$); it was found that hot-electron effects are parametrized by the ratio $\bar{m}V/m_e c$ too /6/.

Using the continuity equation $nvr^2 = \mu$ (independent of r), the momentum and energy equations for the quasineutral ion-electron fluid read

$$\bar{m}v\,\frac{dv}{dr} = \frac{T}{r}\,\frac{2 - d\ln T/d\ln r}{1 - T/\bar{m}v^2} \quad , \tag{1}$$

$$\frac{\mu}{r^2}\left(\frac{1}{2}\bar{m}v^2 + \frac{5}{2}T\right) - \bar{K}T^{5/2}\,\frac{dT}{dr} = 0 \quad , \qquad r < r_{cr} \tag{2a}$$

$$= I \quad , \qquad r > r_{cr} \tag{2b}$$

where v is the ion velocity and I the laser irradiance, which is given by

$$\frac{1}{r^2}\,\frac{d}{dr}\,r^2 I = K I \quad ; \tag{3}$$

here K is the absorption coefficient /7/. Equations (1)-(3) can be solved for $v(r)$, $T(r)$, and $W(r) \equiv 4\pi r^2 I(r)$, and the eigenvalues μ, r_{cr}, and P_a, by using the conditions

$$T = 0 \quad , \qquad v/T = \mu/r_a^2 P_a \qquad \text{at} \quad r_a$$

$$T \to 0 \ , \quad W \to W_L \qquad \text{as} \quad r \to \infty$$

$$vr^2 = \mu / n_{cr} \qquad \text{at} \quad r_{cr}$$

$$\text{either } r = r_{cr} \quad \text{or} \quad 2 = d \ln T / d \ln r \quad \text{where} \quad \bar{m} v^2 = T .$$

In Eqs. (2b) and (3) we assumed that the light power W_{cr} reaching the critical surface is absorbed there by some unspecified anomalous process. We also assumed that $Z_i \gg 1$; in this way the ion temperature is uncoupled (ion pressure and internal energy are negligible) and the problem is simplified. We use classical heat-flux everywhere, an approximation justified, for the $\hat{W}$ values of interest, in Refs. /4/ and /6/.

The ratio r_{cr}/r_a decreases as $\hat{W}$ decreases with $\bar{m}V/m_e c$ fixed. We find that for $r_{cr} > 1.215\ r_a$ the flow at r_{cr} is supersonic (the sonic speed is reached at $r \equiv 1.215\ r_a$); the solution for the range $r_a < r < r_{cr}$ is the same one given in Ref. /3/. The flow at r_{cr} is sonic if $\eta^* r_a < r_{cr} < 1.215\ r_a$; here η^* is a function of $\bar{m}V/m_e c$, and lies within the range 1--1.215. For $r_a < r_{cr} < \eta^* r_a$ the flow at r_{cr} is subsonic. When $(r_{cr} - r_a)/r_a$ is small heat conduction is restrictied to a thin layer surrounding the pellet.

If $(r_{cr}/r_a) - 1 = O(1)$, the results of Ref. /3/ are recovered for $\bar{m}V/m_e c$ small. If $(r_{cr}/r_a) - 1 \ll 1$, those results are recovered when $10^2 \times (\bar{m}V/m_e c)/\hat{W}$ is small. The ratio $(\bar{m}V/m_e c)/\hat{W}$ is proportional to the quantity $I\lambda^4/r_a$ ($\lambda \equiv$ wavelength) introduced by Mora /5/.

In Fig. 1(a) we have represented the fraction of laser power absorbed by inverse Bremsstrahlung, as a function of $\hat{W}$ for several values of $\bar{m}V/m_e c$; also shown is the ratio r_{cr}/r_a. In Fig. 1(b) we represented the ablation pressure P_a normalized to its value for $\hat{W} \to 0$, $\bar{m}V/m_e c \to 0$. The curves change behaviour when $r_{cr}/r_a = 1.215$, and again when $r_{cr}/r_a = \eta^*(\bar{m}V/m_e c)$. Numerical data for $r_{cr}/r_a < \eta^*$ are not shown in the figure. Asymptotic results for low $\hat{W}$ ($r_{cr}/r_a \to 1$) are also presented. The mass ablation rate $4\pi\bar{m}\mu$ is the same of Ref. /3/ for $r_{cr}/r_a > 1.215$.

We have also considered large focal-spot irradiation of slabs, leading to one-dimensional, unsteady problems. We approximated the irradiance I in the rising-half of the laser pulse by a law $I(t) \simeq I_0 (t/\tau)^s$. For large Z_i and classical heat-flux one has the equations ($x > 0$, $t > 0$)

$$\frac{\partial n}{\partial t} + \frac{\partial}{\partial x} nv = 0 \ , \qquad \bar{m} n \left(\frac{\partial v}{\partial t} + v \frac{\partial v}{\partial x} \right) = - \frac{\partial}{\partial x} nT$$

$$nT \left(\frac{\partial}{\partial t} + v \frac{\partial}{\partial x} \right) \ln \frac{T^{3/2}}{n} - \frac{\partial}{\partial x} \bar{K} T^{5/2} \frac{\partial T}{\partial x} = \frac{\partial I}{\partial x} = K I \ .$$

There are two dimensionless parameters, as in the spherical case,

$$\hat{I} \equiv \frac{I_0}{\rho_{cr} U^3} \ , \qquad \frac{\bar{m} U}{m_e c} \ ,$$

where $U \equiv (\tau n_{cr} / \bar{K} \bar{m}^{5/2})^{1/3}$. If $\hat{I} \ll 1$, conduction is restricted to a thin deflagration layer, which is quasisteady /8/. If, in addition, $s = 3/2$ the flow outside that layer is self-similar. We have determined all quantities for $\hat{I} \ll 1$ and $(\bar{m}U/m_e c)^{3/2}/\hat{I}$ large and small (when the results of Ref. /8/ are recovered). The ratio $(\bar{m}U/m_e c)^{3/2}/\hat{I}$ is proportional to $I_0 \lambda^5 / \tau^{3/2}$ a quantity

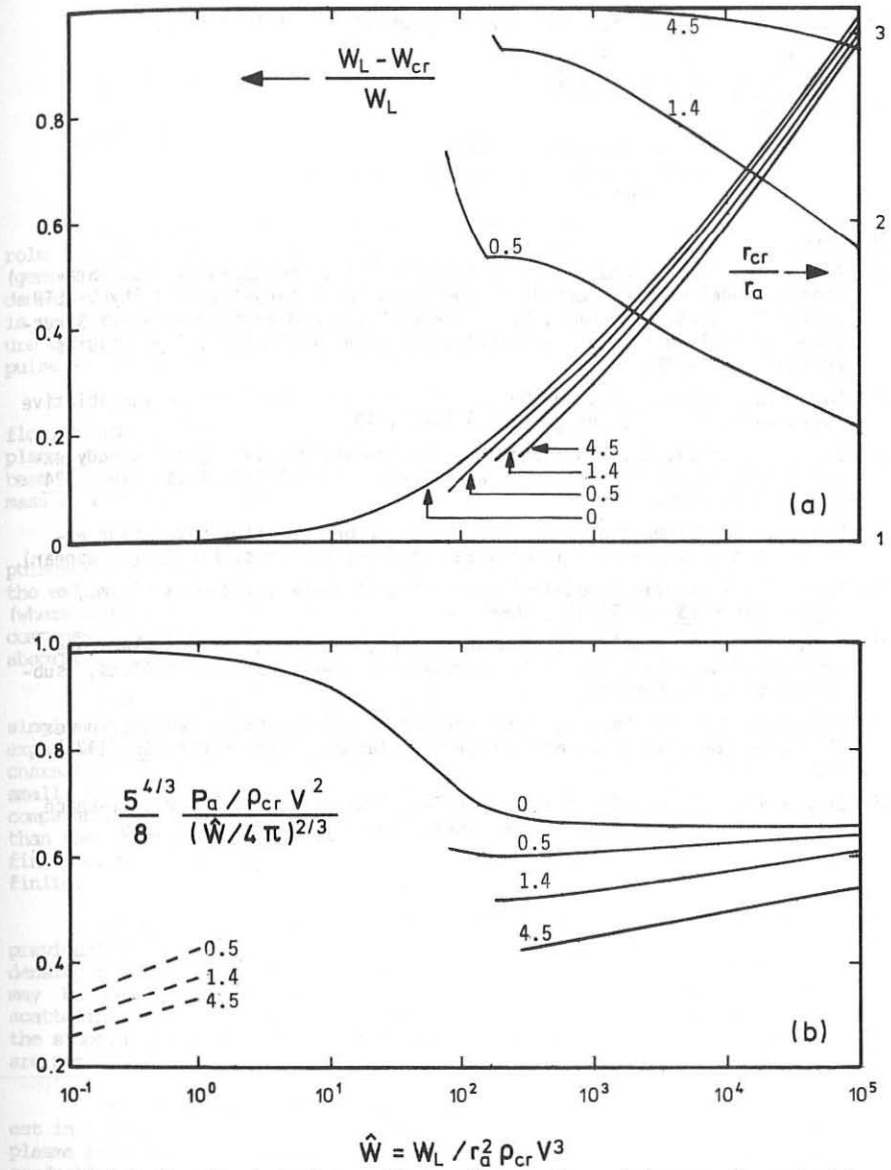

Fig.1(a) Ratio of critical to pellet radius r_{cr}/r_a and inverse Bremsstrahlung absorption $(W_L-W_{cr})/W_L$, and (b) ablation pressure P_a (normalized), versus laser power W_L (in dimensionless form), for values of $\bar{m}V/m_e c$ indicated; ---, behaviour at low power.

introduced by Mora /5/. For the ablation pressure P_a at $t = \tau$ we get

$$\frac{P_a}{\rho_{cr}^{1/3} I_o^{2/3}} = \frac{8}{5^{4/3}}, \quad \frac{\bar{m}U/m_e c}{\hat{I}^{2/3}} << 1$$

$$= 0.45 \left(\frac{\hat{I}^{2/3}}{\bar{m}U/m_e c} \right)^{1/8}, \quad \frac{\bar{m}U/m_e c}{\hat{I}^{2/3}} >> 1 .$$

References

/1/ Afanas'ev, Yu.V., Gamalii, E.G., Krokhin, O.N., and Rozanov, V.B.: Stationary model of the "corona" of spherical laser targets, Sov. Phys. JETP 44 (1977) 311-316; Gitomer, S.J., Morse, R.L., and Newberger, B.S.: Structure and scaling laws of laser-driven ablative implosions, Phys. Fluids 20 (1977) 234-238.

/2/ Max, C.E., McKee, C.F., and Mead, W.C.: A model for laser driven ablative implosions, Phys. Fluids 23 (1980) 1620-1645.

/3/ Sanz, J., Liñán, A., Rodríguez, M., and Sanmartín, J.R.: Quasi-steady expansion of plasma ablated from laser-irradiated pellets, Phys. Fluids 24 (1981) 2098-2106.

/4/ Sanz, J. and Sanmartín, J.R.: Ion charge number and flux saturation effects in the corona of a laser-irradiated pellet, Phys. Fluids (to appear).

/5/ Mora, P.: Theoretical model of absorption of laser light by a plasma, Phys. Fluids 25 (1982) 1051-1056.

/6/ Sanmartín, J.R., Ramis, R., Montañés, J.L., and Sanz, J.: Hot electrons and heat-flux inhibition in the coronae of laser-irradiated pellets, (submitted to Nucl. Fusion).

/7/ Johnston, T.W. and Dawson, J.M.: Correct values for high-frequency power absorption by inverse bremsstrahlung in plasmas, Phys. Fluids 16 (1973) 722.

/8/ Sanmartín, J.R. and Barrero, A.: Self-similar motion of laser half-space plasmas. I. Deflagration regime. Phys. Fluids 21 (1978) 1957-1966.

SPHERICAL EXPANSION PLASMAS IN ION BEAM IMPINGED PELLETS

A. Barrero and L. Rosety
E.T.S.I.Industriales. Universidad de Sevilla, Sevilla. Spain.

J. Sanz
E.T.S.I.Aeronáuticos. Universidad Politécnica de Madrid, Madrid.Spain

Hydrodynamics of the ion beam plasma interaction plays an essential role for achieving break-even conditions in ion beam fusion, since entropy (generated in the energy absorption process) should be kept low inside the dense pellet while mass and energy should inflow efficiently. Clearly, this is only possible if the pressure at the pellet surface (the ablation pressure P_a) depends on time in a spherical manner and therefore ion beam energy pulse and ion beam current should be appropriately shaped.

Our purpose is to obtain, by means of an analysis of the corona flow, simple analytical scaling laws relating the ablation pressure and the plasma mass ablated rate to the beam energy and other parameters such as the beam current (or beam mass rate), the pellet radius r_a and the plasma ion mass m_i and charge number Z_i.

The planar problem has recently been studied assuming ion beam pulses for which self-similar solutions are possible /1/. The results showed the existence of an ablation regime with a well-defined surface ablation (where density peaks and temperature goes to zero) separating an isentropic compression region from a much wider expansion flow where the energy beam absorption occurs.

Here we consider a spherical quasi-neutral expansion flow of a single ion-species plasma under the irradiation of an intense ion beam. This expansion flow may be assumed steady ($\partial/\partial t << v\partial/\partial r$) if the pellet/corona characteristic velocity ratio (and therefore the characteristic time) is small. Since the momentum fluxes produced by P_a in pellet and corona are comparable, the characteristic density in the expansion must be much smaller than the density pellet, so that the density in the corona should go to infinity at the pellet surface while temperature vanishes there since P_a remains finite.

We have also assumed that the beam is both cold and neutralized previously by electrons, and beam density is so small compared with plasma density that ion beam backward flow occurring after the release of its energy may be neglected; beam and plasma interact through the classical Coulomb scattering /2/, but we only consider low Z_i targets since modifications to the stopping power due to collective plasma and atomic ionization processes are not taken into account /3/.

In addition, it is easy to prove that for the conditions of interest in ion beam fusion 1) the momentum transferred from the beam to the plasma is negligible compared with the isotropic energy deposition, 2) heat conduction is small as against energy convection and 3) ion-electron energy exchange is so efficient that the ion and electron temperatures become equal. Then, for a spherical steady flow the continuity and momentum equation for the beam and continuity,momentum and total energy equations for the plasma

may be written

$$n_b\, v_b\, r^2 = \mu_b \quad ,$$

$$m_b\, n_b\, v_b\, dv_b/dr = R \quad ,$$

$$n\, v\, r^2 = \mu \quad ,$$

$$m_i\, n\, v\, dv/dr = -(Z_i+1) Z_i^{-1}\, d(n\, k\, T)/dr \quad ,$$

$$\mu\left[5(Z_i+1)\, k\, T/2\, Z_i + m_i\, v^2/2\, Z_i\right] = \mu_b\, m_b\, v_b^2/2 \quad ,$$

$$R = 4\pi\, e^4\, \ln\Lambda\, n\, n_b (m_e\, v_b^2)^{-1}\, \Phi\left[v_b/(2\, k\, T/m_e)^{1/2}\right] \quad ,$$

$$\Phi(y) = 2\pi^{-1/2}\left[\int_o^y \exp(-t^2)dt - y\, \exp(-y^2)\right] \quad ,$$

where n, v and T are density, velocity and temperature respectively (subcripts b, e and i referring to beam, electrons and ions) and e, k and $\ln\Lambda$ are the electron charge, Boltzmann's constant and Coulomb logarithms. Both the beam and the ablated plasma flow rates $4\pi\, m_b\, \mu_b$ and $4\pi\, m_i\, \mu/Z_i$ are independent of the radius r.

Since μ and P_a are unknown we must have two additional boundary conditions, then

$$T = 0 \quad , \quad \text{and} \quad \mu\, k\, T/v\, r^2 = P_a \quad \text{at} \quad r = r_a \quad ,$$

$$T \to 0 \quad , \quad \text{and} \quad m_b\, v_b^2/2 = E_b \quad \text{as} \quad r \to \infty \quad .$$

Now defining the dimensionless variables

$$\Omega = \alpha^{-2/5}\, \beta^{1/5}\, \eta^{2/5}\, m_b\, v_b^2/2E_b \quad , \quad \Theta = \alpha^{-2/5}\, \beta^{-4/5}\, \eta^{2/5}\, T/T_r \quad ,$$

$$Y = \alpha^{-2/5}\, \beta^{-4/5}\, \eta^{2/5}\, m_i\, v^2/Z_i\, k\, T_r \quad , \quad \eta = r/r_a \quad ,$$

choosing

$$k\, T_r = \frac{Z_i}{m_i}\left[\frac{Z_i}{Z_i+1}\right]^2 \frac{P_a^2\, r_a^4}{\mu^2} \quad , \quad \beta = \frac{\mu_b\, E_b}{\mu\, k\, T_r} \quad ,$$

$$\alpha = \frac{2\pi\, e^4\, \ln\Lambda\, m_b\, \mu}{m_e\, E_b^2\, r_a (Z_i k\, T_r/m_i)^{1/2}} \quad , \quad \beta^* = \frac{m_e\, E_b}{m_b k\, T_r} \quad ,$$

and introducing them into the above equations we arrive (after some manipulation) to the following phase plane equations

$$\frac{d\Omega}{dY} = \frac{\left[2\Omega^2 Y^{1/2} + 5\Phi(X)\right](2Y - \Omega)}{Y^{1/2}\left[6Y\, \Omega(3\Omega - Y) - 10 Y^{1/2}\Phi(X)\right]} \quad , \quad (1)$$

$$\frac{1}{\eta}\frac{d\eta}{dY} = \frac{5\Omega(2Y-\Omega)}{6Y\,\Omega(3\Omega-Y)-10Y^{1/2}\Phi(X)} \quad , \qquad (2)$$

where

$$X = \left[\frac{5\beta^*(Z_i+1)}{2\beta\,Z_i}\,\frac{\Omega}{\Omega-Y/2}\right]^{1/2} \quad ;$$

the boundary conditions are:

$$\Omega = \frac{5(Z_i+1)Y^{1/2}}{2Z_i\alpha^{1/2}\beta^{2/5}} \quad , \text{ and } \eta = 1 \quad \text{at} \quad Y = 0 \quad ,$$

$$\Omega = Y/2 \quad \text{and} \quad \eta = \alpha\,\beta^{-2}(Y/2)^{5/2} \quad \text{at} \quad Y \to \infty \quad .$$

The solution to equation (1) near the nodal point Y=0, Ω=0, is $\Omega=C\,Y^{1/2}$ (the constant C being related to the eingenvalues α and β through the boundary conditions) and since Ω=Y/2, for large Y, we must have Ω=2Y in a certain point of the interval $0 \leq Y \leq \infty$. In addition, dY/dη must remain finite to avoid a multivalued solution, so that the numerator on the right hand side of equation (2) must vanish if Ω=2Y. This condition leads to

$$6Y_s^{5/2} = \Phi(X_s) \quad , \quad X_s = \left[10(Z_i+1)\beta^*/3Z_i\beta\right]^{1/2} \quad ,$$

which gives the singular point coordinates $(Y_s, 2Y_s)$ as a function of β^*/β; Y_s ranges from 0, for $\beta^*/\beta \to 0$, to .488, for $\beta^*/\beta \to \infty$.

For a given value of β^*/β we may determine Y_s and find that there exists a value of C (call it C^*) that allows to reach the saddle (sonic) point $(Y_s, 2Y_s)$. Starting from this point and integrating backward to the node we numerically find C^* for each β^*/β (see fig. 1). The numerical integration of equations (1) and (2) beyond Y_s yields the value of $C_1 = \eta^{2/5}/Y$ (for Y large) which is related to the eingenvalues α and β through the boundary conditions.

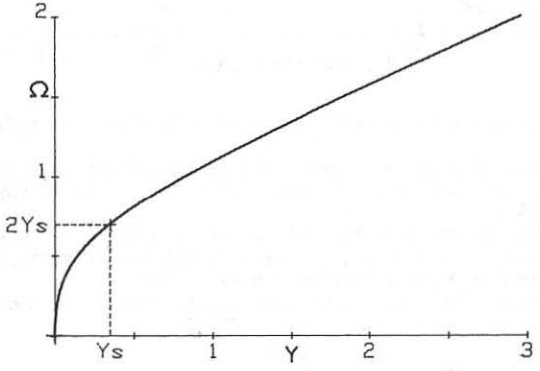

Fig. 1. Integral curve solution to equation (1)

Once α and β are determined from the calculated values of C^* and C_1, we may obtain the profiles of beam density and velocity and plasma density, velocity and temperature respectively, and from the expressions of α , β and β^* we arrive at the following simple analytical laws that related the beam energy E_b and beam mass rate μ_b with the ablation pressure

$$E_b = f(2\pi\, e^4\, \ln\Lambda)\,(m_e/m_b)^{2/3}(P_a\, r_a)^{1/3} \quad ,$$

$$\mu_b = g(2\pi\, e^4\, \ln\Lambda)^{-1/6}(m_e/m_b)^{5/6}(Z_i/m_i)^{1/2} P_a^{5/6}\, r_a^{11/6} \quad ,$$

where $f = C_1(5/2C^*)^{1/3}(\beta^*/\beta)^{1/3}$ and $g = (5/2C^*)^{5/6}(\beta/\beta^*)^{2/3}$, that depend weakly on Z_i are given in fig. 2 as functions of $m_e\mu/m_b\mu_b$.

Then, for a given target, one may determine the ablation pressure $P_a(t)$ that generates an optimal compression; this problem has been studied elsewhere /4/ and its solution also determines the pellet radius $r_a(t)$. Our solution yields, for given instantaneous P_a and r_a, the required beam energy E_b and the mass beam rate μ_b , for each value of the ablated plasma mass rate.

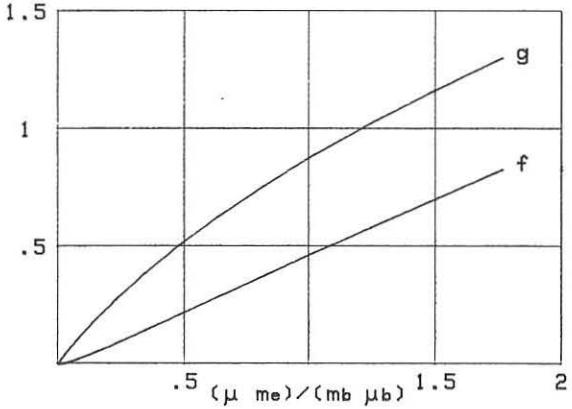

Fig.2. Numerical values of f and g as a function of $\mu m_e/m_b\mu_b$

/1/ Barrero,A.,Fernandez,A.:One-dimensional motion of ion beam fusion plasmas, in Proceedings of the 1982 International Conference on Plasma Physics , Göteborg 1982 p.280.
/2/ Miyamoto,K.:Plasma Physics for Nuclear Fusion,MIT Press Cambridge 1980.
/3/ Nardi,E.,Peleg,E.,and Zinamon,Z.:Energy deposition by fast protons in pellet fusion targets,Phys. Fluids 21 (1978) 574-579.
/4/ Kidder,R.E.:Theory of homogeneous isentropic compression and its applications to laser fusion,Nucl. Fusion 14(1974) 53-60.

DENSITY PROFILES AND FLUCTUATIONS IN CO_2 LASER PRODUCED PLASMAS

D A BROWN, P S MARCHINGTON, N SAYED, Y SUDERA & E R WOODING
ROYAL HOLLOWAY COLLEGE, UNIVERSITY OF LONDON,
EGHAM, SURREY, TW20 0EX, UK.

Electron densities have been determined by holographic interferometry of plasmas produced when CO_2 laser radiation was incident on plane solid targets. Soft X-ray emission was recorded simultaneously by means of a pinhole camera. From these measurements it is seen that the density profile steepened near the target but also developed fine structure. These results are compared with theory and simulations of profile modification /1,2/ .

The TEA CO_2 laser had an unstable cavity and produced pulses of 10.6 μm radiation with energies of 15 to 20 J. The temporal pulse profile had a rise time of 20 ns, a fall time of 40 ns, and a tail of 200 ns. In these pulses, partial mode locking resulted in intensity fluctuations of about 30% on a 5 ns time scale. The output beam was focussed to a spot diameter of 200 μm by a germanium lens of 120 mm focal length and aperture f2.5, producing irradiance up to $2 \times 10^{16} Wm^{-2}$.

The plasma density was determined by using a double exposure holographic interferometer with a ruby laser of 3 ns (fwhm) duration. From published work it appeared to be preferable to use the infinite fringe technique as this required no movement of the reference beam for the second exposure. This method also permitted the fringe shift in the lower density regions to be determined by linear extrapolation and is less likely to show Moiré artefacts. The X-ray pinhole camera carried a 0.75 μm aluminium filter foil and produced an image magnified twice.

Electron densities determined after Abel inversion from the fringe shift in the holograms are shown in fig. 1. These values are subject to an error of ± 20% which results from refraction and the minimum fringe shift of 0.1λ that could be estimated.

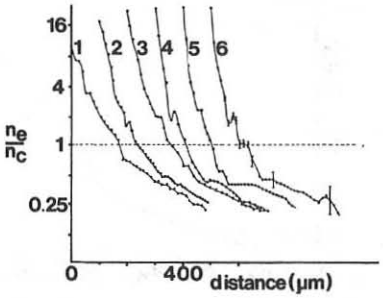

Fig.1 Density profiles at (1)10ns(2)25ns(3)35ns(4)65ns(5)90ns and (6)115 ns after the onset of the laser pulse. Profiles stepped 100 μm to right.

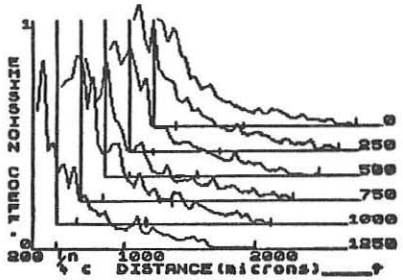

Fig.2 X-ray emission coefficient (arb. units) varying with distance from the surface of a plane carbon target.

In the results now reported the target was carbon and the laser irradiance was $10^{16} Wm^{-2}$. Successive profiles obtained from separate plasma shots are displaced 100 μm. Development of profile steepening can be seen to occur over the first 50 ns in which time the irradiance has reached its peak value and is falling. The plateau at 0.3 n_c is predicted by the theory of Lee et al /1/ but the plateau at 0.5 n_c has yet to be explained. Further information on the underdense plasma is obtained from the spatially resolved X-ray emission shown in fig.2. A peak exists in this emission where the density is $n_c/4$, a region where parametric processes such as two plasmon decay occur. There is also a peak in emission near to the $n_c/2$ region which could be related to the density plateau there. There are marked periodic variations in emission along the axis and in a radial direction, showing that fluctuations extend well into the underdense plasma and must represent a structure that persists for most of the plasma lifetime.

Another feature of the density profile is a bump which occurs between $1.6n_c$ and $2.2n_c$ with a density modulation of about 30%. This feature resembles the rarefaction wave predicted by Max et al /3/. In the expanding plasma there is a rarefaction or compression front depending on the Mach number being less than:-

$$(1-P_f/\rho_1 c_1^2)^{\frac{1}{2}}$$

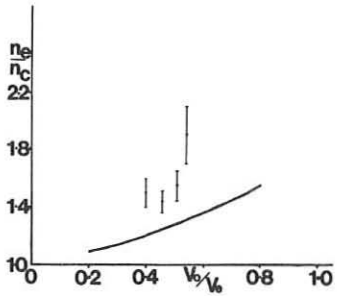

Fig.3 Dependence of density at upper plateau on irradiance. The line shows the density expected for a plasma temperature of 200 eV.

where **E** and **H** are the electric and the magnetic field strength of the laser in the plasma. Further terms are not effective for this geometry as long as we consider the monochromatic wave interaction. The question what additional terms are to be used [5, Eq. (10)] was clarified before [1] since 1969: only all these terms and no others produce the necessary shearfreeness of the forces at oblique incidence of laser radiation on plasma. The electron density between x = 0 and the caviton at 4 μm has been increased by the dynamics from low initial values up to densities above the critical density $n_{ec} = 10^{21}$ cm^{-3} which, at this time step, prevents the penetration of light to the plasma. This self-shutting of laser irradiation by the plasma was observed before from one-fluid computations [1] if the exact wave field with reflection was included. The result confirms the driving mechanisms of the electrons by the nonlinear forces. Electrostatic oscillations are generated at each change of the driving of the electrons by the laser field and have been followed up within the laser field oscillations.

The result of Eq. (4) has very general validity for plasmas: **Any inhomogeneity in a plasma produces electrostatic fields**, any gradient in the electron density and/or any temperature gradient. For laser-fusion, these fields lead to a reduction of thermal conduction current C. The double layer in a DT plasma reduces C to the pure ion conduction (smaller by $(m_e/m_i)^{1/2}$ = 1/68), or explained from the kinetic theory from

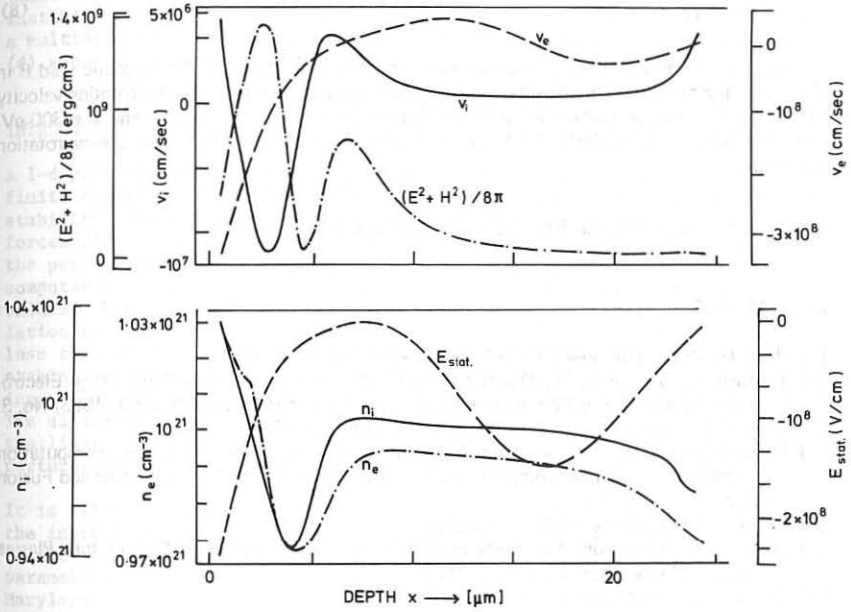

Fig. 2. 10^{16} W/cm^2 neodymium glass laser irradiation from the left side on a 25 μm thick hydrogen layer at 1.5 psec. Initially at t = 0, a parabolic density profile $n_e = n_i$ of $T_e = T_i$ = 1 keV at rest $v_i = v_e = 0$ was thermally expanding and developing during the first 0.5 psec without laser irradiation damping out electrostatic oscillations due to the initial conditions. When the laser is switched on, producing an electromagnetic field density $(E^2 + H^2)/8\pi$, the nonlinear force driven motion produced a density minimum (caviton) at 4 μm producing ion velocities up to 10^7 cm/sec and electrostatic fields up to 2×10^8 V/cm.

$$C = -\frac{4\pi m_e}{6}\int_0^\infty v^5 \ell \left(\frac{\partial f^\circ}{\partial x} - \frac{e}{2m_e} E \frac{\partial f^\circ}{\partial (v^2)} \right) dv \qquad (6)$$

($v \sim$ kinetic electron velocity, $f^\circ \sim$ equilibrium distribution function; $\ell \sim$ mean free path) what has been concluded indirectly[4] from pellet fusion gains which agree with the measurements only if C is taken 100 times smaller.

For cases of magnetic fusion confinement, one has to generalize Eq. (4) by a magnetic pressure term

$$E = -\frac{4\pi e}{\omega_p^2 m_e} \frac{\partial}{\partial x} (p - H_s^2/8\pi) \qquad (7)$$

where the interpretation of internal and external fields has to be given[6]. Assuming the confining magnetic field $\mathbf{H}_s$ in a similar way as the wall limitation by a probe, the static electric field of Eq. (7) will cause an $\mathbf{E} \times \mathbf{B}$ drift with a velocity v_d in a cylindrical or toroidal plasma column of approximately

$$v_d = \frac{3T}{rB} \qquad (8)$$

in m/sec, if the average plasma electron temperature T is given in eV, the magnetic field B in Tesla, and the radius r of the plasma in meter. This would explain the observed rotation velocity of 3×10^4 m/sec of theta-pinch plasmas[7] taking r = 1 cm, B = 3 Tesla, and T = 300 eV. For a stellarator of B = 3 Tesla, T = 1 keV, r = 3 cm, v_d results in 3×10^4 m/sec plasma rotation velocities.

* Now at Materials Res. Labs., Ascot Vale 3032, Victoria.

REFERENCES

[1] Hora, H.: Physics of Laser Driven Plasmas. Wiley, New York 1981.
[2] Lalousis, P., and Hora, H., Direct Electron and Ion Fluid Computation of High Electrostatic Fields in Dense Inhomogeneous Plasmas, Laser and Particle Beams **1** (1983) No. 3.
[3] Chen, F.F.: Plasma Physics. Plenum, New York 1975, p. 66.
[4] Ding Le-Ming, Tai Wei Hai, and Wang Run-Wen, Analysis of the mechanism and computation of similar modes in laser compression of glass shell pellets with DT gas, Plasma and Fusion (China) **1** (1982) 187.
[5] Peratt, A.L., Phys. Rev. **A20**, (1979) 2555.
[6] Bobin, J.L., Ponderomotive Pressure Effects in Laser-Driven High-Temperature Plasma Flows, J. Plasma Phys. **25**, (1981) 193.
[7] Kronast, B. (private communication).

SCALING LAWS FOR THE RESISTIVE LONGITUDINAL INSTABILITY IN FINITE CHARGED BEAMS*

Abraham Sternlieb
Soreq Nuclear Research Centre
Yavne 70600, Israel

ABSTRACT

Heavy ion beams are considered as possible drivers in an inertial confinement fusion scheme /1/. The high required intensities introduce space-charge effects. It has been shown analytically that a finite cold beam is longitudinally stable when a small resistive term is present /2,3/. This is confirmed by our simulations /4/ which show that for resistivities causing less than one e-folding of a perturbation over the bunch length, the beam is stable (unlike a coasting beam), probably due to end reflections. However, for resistivities causing more than three e-foldings, the beam is unstable (emittance deteriorated exponentially). We discuss the implication of this instability threshold for a few cases: (a) a full-scale driver model; (b) a multiple-beam driver; (c) single beam transport experiment-SBTE (LBL); (d) slow e-beam experiment (Maryland).

INTRODUCTION

A 1-d particle simulation code /5/ is used to investigate the stability of finite charged beams in a resistive transport line. Linear theory shows stability for resistive force values to be small compared to space-charge forces /2,3/. It was suggested that this occurs when the e-folding length of the perturbation is long compared to bunch length. To check this, particle computer simulations have been performed /4/ including various resistive force values. The line charge density distribution was parabolic /3/. The simulation results indicate clearly that for a resistive force corresponding to less than one e-folding of the perturbation over the beam length, the beam is stable, while for a resistive force corresponding to more than three e-foldings, the beam is unstable and the longitudinal emittance grows uncontrollably. The simulation results both confirm and extend the theoretical results beyond the linear regime. It seems that for low enough resistive force terms, the perturbation is stabilized during reflection from the bunch ends.

It is calculated that the resistance of typical one beam driver model is in the instability range. Stability may be achieved, e.g. using a multiple beam driver /6/. We also calculate the resistive threshold values for the design parameters of SBTE /7/ at LBL and for the slow e-beam experiment /8/ at Maryland.

The longitudinal resistive threshold is a pure computer simulation result. No coupling to the transverse modes is assumed. Therefore a 2-d or 3-d simulation code is desirable. The resistance is assumed to be frequency independent and the beam velocity constant. Coasting beam results /9/ indicate

(*) Part of this work was performed during the author's stay at Lawrence Berkeley Lab.

that longer wave length modes are more active. This result seems to complement a more detailed investigation /10/.

Finally, we suggest that results obtained from computer simulation may provide input for a possible active feedback stabilization of the longitudinal resistive instability.

THEORETICAL AND SIMULATION MODEL

The simulation follows in a self-consistent manner the non-linear longitudinal behavior of a bunched beam in the presence of a resistive wall. The distribution function is given by /3/:

$$f_o(x,v) = (3N/2\pi x_o v_o)(1 - x^2/x_o^2 - v^2/v_o^2)^{\frac{1}{2}} \qquad (1)$$

where x_o, v_o are the maximum values for x and v. The resultant linear density is:

$$n(x) = (3N/4x_o)(1 - x^2/x_o^2) \ , \qquad (2)$$

where N is total number of particles in the bunch. The forces acting on the bunch are:

(a) Space-charge defocussing force: $-e\partial n(x)/\partial x$ (long bunch).

(b) Resistive force: $-eRn(x)$, where $R = R'v_o$. R' is the average wall resistance per unit length, and V_o is the beam velocity.

(c) Focussing forces to balance (a) and (b): $-kx + eRn$ (x, t = 0), where K is a constant.

We study a cold finite beam moving with the simulation system. For a cold beam we require: $v_{th} << v_p$, where v_{th} is thermal spread and v_p is the phase velocity of the perturbation, given by: $v_p = q(n/m)^{\frac{1}{2}}$, where q is the particle charge and m is the particle mass. For comparison purposes, we use cold coasting beam formulae for growth rate γ_k and real frequency ω_R:

$$\gamma_k = \pm \frac{1}{2} v_p \frac{R}{g} \ ; \ \omega_R = \pm v_p k \ , \qquad (3)$$

where g is a geometric factor taken as 1 and k is the wavenumber of the perturbed mode. Relations (3) hold to good accuracy for $R/kg \lesssim 1$, which in our computer model becomes $R \lesssim 0.1$ ($k \gtrsim 0.1$). This condition is equivalent to the small resistive term approximation, which predicts stability /2/.

We use dimensionless code units, explained in Ref (5), and take: L_s (system length) = 128; L_B (bunch length at t=o)=64; v_p(maximum)=13; $v_{th}(t=o)$=2.2; R=0,0.03,0.1.

The e-folding time of the perturbation is defined as $\gamma_k \tau = 1$, and the e-folding length l is defined as: $l = v_p \tau = v_p/\gamma_k = 2/R$. For R=0.03 we have τ=5 and l=66(L_B). For R=0.1 we have $\tau \simeq 1.7$ and $l \simeq 20$ ($L_B/3$). We have not checked whether R=0 ($l=\infty$) means stability, irrespective of initial perturbation amplitude. This should be further investigated.

SIMULATION RESULTS AND APPLICATIONS

The simulation results can be summarized as follows:

(1) For $R \lesssim 0.03$ ($R=0.03$ corresponds to one e-folding of the perturbation over the bunch length), the bunch is stable. This regime corresponds to the linear theoretical analysis /2/.

(2) For $R \gtrsim 0.1$ (more than 3 e-foldings), the bunch is destroyed by the growing waves.

It is desirable to check this non-linear threshold behavior in experiments. The translation from code units to MKS-C unit (or vice-versa) is performed by using the following relationship:

$$\bar{R}^1 = (L_B/4\pi\bar{\varepsilon}_o)(\bar{m}/2\bar{E}\bar{\tau}_B)R \ , \qquad (4)$$

where the barred quantities are in MKS-C units, the unbarred are in code units, $\bar{R}^1$ is resistance per unit length, $L_B=64$, $\bar{\varepsilon}_o=8.85\times10^{-12}$ (MKS), $\bar{m}$ is particle mass, $\bar{E}$ is particle energy, $\bar{\tau}_B$ is pulse length, and $R=R'v_B(R=\bar{R}\bar{v}_B)$. In obtaining eq. (4) we have used Ref. (5), $\bar{E} = \bar{m}\bar{v}_B^2/2$, and $\bar{L}_B = \bar{v}_B\cdot\bar{\tau}_B$. We also require a minimum accelerator length which permits at least one end reflection. This can be formulated as: $\bar{L}_A \gtrsim (\bar{L}_B\cdot\bar{v}_B/\bar{v}_p)$, where L_A is the accelerator length. We use the following relationships (MKS-C) to find how to change the beam parameters in order to permit a practical $\bar{L}_A$ value, when necessary: $\bar{L}_B = \bar{v}_B\cdot\bar{\tau}_B$, $\bar{v}_p = \bar{q}(\bar{n}/4\pi\bar{\varepsilon}_o\bar{m})^{\frac{1}{2}}$, $\bar{m}\bar{v}_B^2/2 = \bar{E}$, $\bar{n} = \bar{I}/\bar{e}\bar{v}_B$. Then we get:

$$\frac{2\cdot 2^{1/4}\sqrt{4\pi\bar{\varepsilon}_o}}{\sqrt{\bar{m}}\ \bar{m}^{1/4}\sqrt{q}} \quad \frac{\bar{E}^{5/4}\cdot\bar{\tau}_B}{\sqrt{\bar{I}}} \leq \bar{L}_A \qquad (5)$$

Next, we calculate the threshold behavior for some proposed or existing experiments:

(1) A typical HIF driver design includes: $\bar{R}^1=100\Omega/m$, $\bar{v}_B=10^8$m/sec, $\bar{L}_B=10$m, $\bar{N}=10^{15}$, Cs^{+1}. Using eq. (4), we obtain $R=0.2$, which is unstable.

(2) An approach has been proposed for a HIF driver which uses a multitude of low current beamlets /6/. This permits a larger current to be transported through the same aperture as compared to a single beam, so one can use shorter bunches to transport the same charge. When $1(=v_p/\gamma_k)$, $\bar{R}^1$ and $\bar{v}_B$ are kept constant, shorter bunches tend to be more stable.

(3) The single beam transport experiment (SBTE) at LBL has: Cs^{+1} ions, $\bar{E}$=200 keV, $\bar{I}$=20mA, $\bar{\tau}_B \gtrsim 5\mu$sec, $\bar{v}_B=5.36\times10^5$ m/sec, $\bar{L}_B=2.68$m. To have instability, one uses eq. (4) with $R\gtrsim0.1$, which gives: $\bar{R}^1 \gtrsim 40K\Omega/m$. Below 13 kΩ/m we expect stability. However, from eq. (5) we get $\bar{L}_A>93$m which is much longer than in reality. We can reduce $\bar{E}$, $\bar{\tau}_B$ and/or increase $\bar{I}$. E.g., $\bar{E}\cdot\bar{\tau}_B$ can be reduced by a factor of 10 and eq. (4) should then be used again e.g. $\bar{R}^1$ 0.5 MΩ/m, if we desire instability ($R=0.1$) .

(4) The slow e-beam experiment at U. of Maryland has: $\bar{E}$=1-10 keV (we take 5 keV), $\bar{\tau}_B=5\mu$sec, $\bar{I}$=200mA, $\bar{v}_B=4.18\times10^7$m/sec, $\bar{v}_p=2.75\times10^4$m/sec. One gets: $\bar{L}_B = \bar{v}_B\cdot\bar{\tau}_B=209$m and $\bar{L}_A \gtrsim 300$km. To have practical $\bar{L}_B$ and $\bar{L}_A$ values, one may, e.g., reduce $\bar{E}$ and $\bar{\tau}_B$ by two orders of magnitude each and increase $\bar{I}$ by

two orders of magnitude (eq. 5). This will decrease $\bar{L}_B$ by three orders of magnitude, to 21cm, $\bar{v}_p$ will be increased by $\sqrt{10^3}\approx 30$, to 8×10^{5}m/sec, and $\bar{L}_A$ will become: $\bar{L}_A \gtrsim 1$m. Then we have: $\bar{E}$=50eV, $\bar{\tau}_B$=50msec, $\bar{I}$=20A. From eq. (4) we find (R=0.1) that $\bar{R}^I$=50kΩ/m should cause instability.

In summary, by inserting known artificial resistances in existing experiments, one can check the validity of the computer-found threshold for the resistive longitudinal instability in finite charged beams.

REFERENCES

/1/ Proceedings of the HIF workshop, Oct. 29 - Nov. 9, 1979, LBL-10301, Sept. 1980.
/2/ Channel, P. J., Sessler, A. and Wurtele, J., LBL-11367, July 1980; LBL-12107, Feb. 1981.
/3/ Neuffer, D., Part. Accel. 11 (1980) 23-26.
/4/ Sternlieb, A.: Longitudinal resistive instability in finite charged beams: A computer simulation study, in Proceedings of the 1982 Int. Conf. on Plasma Physics, Gotebord, Sweden, June 9-15, 1982.
/5/ Sternlieb, A., Smith, L., Laslett, L. J., Bisognano, J. and Haber, I., LBL-12205, 1981.
/6/ Hermannsfeldt, W. B. and Keefe, D., HI-FAN-149 (1981), HIF-LBL Report.
/7/ Kim, C.: Single Beam Transport Experiment Reference Parameters, HI-FAN-160, Haevy Ion Fusion Report., Lawrence Berkeley Lab.
/8/ Reiser, M. in: Proceedings of 1981 Linear Acc. Conf., Santa-Fe, NM, Oct. 19-23, 1981.
/9/ Sternlieb, A., LBL-12878, June 1981.
/10/ Bisognano, J. in: these Proceedings (1983 Particle Acc. Conf.).

INVERSE BREMSSTRAHLUNG EFFECTS IN THE CORONAE OF LASER-IRRADIATED PELLETS AND SLABS

J.A. Nicolás and J.R. Sanmartín
E.T.S.I.Aeronáuticos, Universidad Politécnica de Madrid
Ciudad Universitaria, Madrid-3, Spain

In recent, quasi-steady analyses of the spherical, ablative corona of a laser-irradiated pellet, absorption was assumed to occur at the critical density n_{cr} /1/-/4/. Both classical and saturated heat-flux, and ion-electron energy exchange where taken into account. If the ion charge number Z_i and mass per unit charge $\bar{m} \equiv m_i/Z_i$, the instantaneous pellet radius r_a and laser power W_L, and its wavelength (or equivalently n_{cr}), are given, one can obtain quantities of interest such as the ablation pressure P_a, the critical radius r_{cr}, and the mass ablation rate $4\pi\bar{m}\mu$, as dimensionless functions ($\bar{P}_a \equiv P_a/\rho_{cr}V^2$, r_{cr}/r_a, and $\bar{\mu} \equiv \mu/r_a^2 n_{cr} V$) of the parameters Z_i, $\hat{W} \equiv W_L/r_a^2\rho_{cr}V^3$, and heat-flux limit factor f. We have introduced $\rho_{cr} \equiv \bar{m} n_{cr}$, a convenient speed $V \equiv (r_a n_{cr}/\bar{m}^{5/2}\bar{K})^{1/4}$, and the factor $\bar{K}$ of Spitzer's classical heat-flux ($\equiv -\bar{K}\,T^{5/2}\,dT/dr$, the electron temperature T being in energy units).

Lately the search for more ablative conditions in laser-irradiation of targets has moved the interest into shorter wavelengths (larger n_{cr}) and larger pellet radii. For such conditions inverse Bremsstrahlung absorption in the underdense flow can be substantial /5/. Here we attempt to quantitatively determine that absorption using the model of Refs. /3/ and /4/. Inverse Bremsstrahlung introduces into the model the electron mass m_e and the light speed c, and is found here to be parametrized by the ratio $\bar{m}V/m_e c$, which lies close to unity for all cases of interest. Large values of n_{cr} and r_a lead to relatively low $\hat{W}$ ($1\text{-}10^4$ typically). Recently Sanmartín et al. have considered effects due to a suprathermal electron population generated by resonant absorption, at higher values of $\hat{W}$ ($10^5\text{-}10^8$); it was found that hot-electron effects are parametrized by the ratio $\bar{m}V/m_e c$ too /6/.

Using the continuity equation $nvr^2 = \mu$ (independent of r), the momentum and energy equations for the quasineutral ion-electron fluid read

$$\bar{m}v\frac{dv}{dr} = \frac{T}{r}\frac{2 - d\ln T/d\ln r}{1 - T/\bar{m}v^2} \quad , \tag{1}$$

$$\frac{\mu}{r^2}\left(\frac{1}{2}\bar{m}v^2 + \frac{5}{2}T\right) - \bar{K}T^{5/2}\frac{dT}{dr} = 0 \quad , \qquad r < r_{cr} \tag{2a}$$

$$= I \quad , \qquad r > r_{cr} \tag{2b}$$

where v is the ion velocity and I the laser irradiance, which is given by

$$\frac{1}{r^2}\frac{d}{dr}r^2 I = K I \quad ; \tag{3}$$

here K is the absorption coefficient /7/. Equations (1)-(3) can be solved for $v(r)$, $T(r)$, and $W(r) \equiv 4\pi r^2 I(r)$, and the eigenvalues μ, r_{cr}, and P_a, by using the conditions

$$T = 0 \quad , \quad v/T = \mu/r_a^2 P_a \qquad \text{at} \quad r_a$$

$$T \to 0\ , \quad W \to W_L \qquad \text{as} \quad r \to \infty$$

$$v r^2 = \mu / n_{cr} \qquad \text{at} \quad r_{cr}$$

$$\text{either } r = r_{cr} \quad \text{or} \quad 2 = d \ln T / d \ln r \quad \text{where} \quad \bar{m} v^2 = T .$$

In Eqs. (2b) and (3) we assumed that the light power W_{cr} reaching the critical surface is absorbed there by some unspecified anomalous process. We also assumed that $Z_i \gg 1$; in this way the ion temperature is uncoupled (ion pressure and internal energy are negligible) and the problem is simplified. We use classical heat-flux everywhere, an approximation justified, for the $\hat{W}$ values of interest, in Refs. /4/ and /6/.

The ratio r_{cr}/r_a decreases as $\hat{W}$ decreases with $\bar{m}V/m_e c$ fixed. We find that for $r_{cr} > 1.215\ r_a$ the flow at r_{cr} is supersonic (the sonic speed is reached at $r \equiv 1.215\ r_a$); the solution for the range $r_a < r < r_{cr}$ is the same one given in Ref. /3/. The flow at r_{cr} is sonic if $\eta^* r_a < r_{cr} < 1.215\ r_a$; here η^* is a function of $\bar{m}V/m_e c$, and lies within the range 1--1.215. For $r_a < r_{cr} < \eta^* r_a$ the flow at r_{cr} is subsonic. When $(r_{cr}-r_a)/r_a$ is small heat conduction is restrictied to a thin layer surrounding the pellet.

If $(r_{cr}/r_a) - 1 = O(1)$, the results of Ref. /3/ are recovered for $\bar{m}V/m_e c$ small. If $(r_{cr}/r_a) - 1 \ll 1$, those results are recovered when $10^2 \times (\bar{m}V/m_e c)/\hat{W}$ is small. The ratio $(\bar{m}V/m_e c)/\hat{W}$ is proportional to the quantity $I\lambda^4/r_a$ ($\lambda \equiv$ wavelength) introduced by Mora /5/.

In Fig. 1(a) we have represented the fraction of laser power absorbed by inverse Bremsstrahlung, as a function of $\hat{W}$ for several values of $\bar{m}V/m_e c$; also shown is the ratio r_{cr}/r_a. In Fig. 1(b) we represented the ablation pressure P_a normalized to its value for $\hat{W} \to 0$, $\bar{m}V/m_e c \to 0$. The curves change behaviour when $r_{cr}/r_a = 1.215$, and again when $r_{cr}/r_a = \eta^*(\bar{m}V/m_e c)$. Numerical data for $r_{cr}/r_a < \eta^*$ are not shown in the figure. Asymptotic results for low $\hat{W}$ ($r_{cr}/r_a \to 1$) are also presented. The mass ablation rate $4\pi\bar{m}\mu$ is the same of Ref. /3/ for $r_{cr}/r_a > 1.215$.

We have also considered large focal-spot irradiation of slabs, leading to one-dimensional, unsteady problems. We approximated the irradiance I in the rising-half of the laser pulse by a law $I(t) \simeq I_0 (t/\tau)^s$. For large Z_i and classical heat-flux one has the equations ($x > 0$, $t > 0$)

$$\frac{\partial n}{\partial t} + \frac{\partial}{\partial x} nv = 0 \ , \quad \bar{m} n \left(\frac{\partial v}{\partial t} + v \frac{\partial v}{\partial x} \right) = - \frac{\partial}{\partial x} nT$$

$$nT \left(\frac{\partial}{\partial t} + v \frac{\partial}{\partial x} \right) \ln \frac{T^{3/2}}{n} - \frac{\partial}{\partial x} \bar{K} T^{5/2} \frac{\partial T}{\partial x} = \frac{\partial I}{\partial x} = K I \ .$$

There are two dimensionless parameters, as in the spherical case,

$$\hat{I} \equiv \frac{I_0}{\rho_{cr} U^3} \ , \quad \frac{\bar{m} U}{m_e c} \ ,$$

where $U \equiv (\tau n_{cr} / \bar{K} \bar{m}^{5/2})^{1/3}$. If $\hat{I} \ll 1$, conduction is restricted to a thin deflagration layer, which is quasisteady /8/. If, in addition, $s = 3/2$ the flow outside that layer is self-similar. We have determined all quantities for $\hat{I} \ll 1$ and $(\bar{m}U/m_e c)^{3/2}/\hat{I}$ large and small (when the results of Ref. /8/ are recovered). The ratio $(\bar{m}U/m_e c)^{3/2}/\hat{I}$ is proportional to $I_0 \lambda^5 / \tau^{3/2}$ a quantity

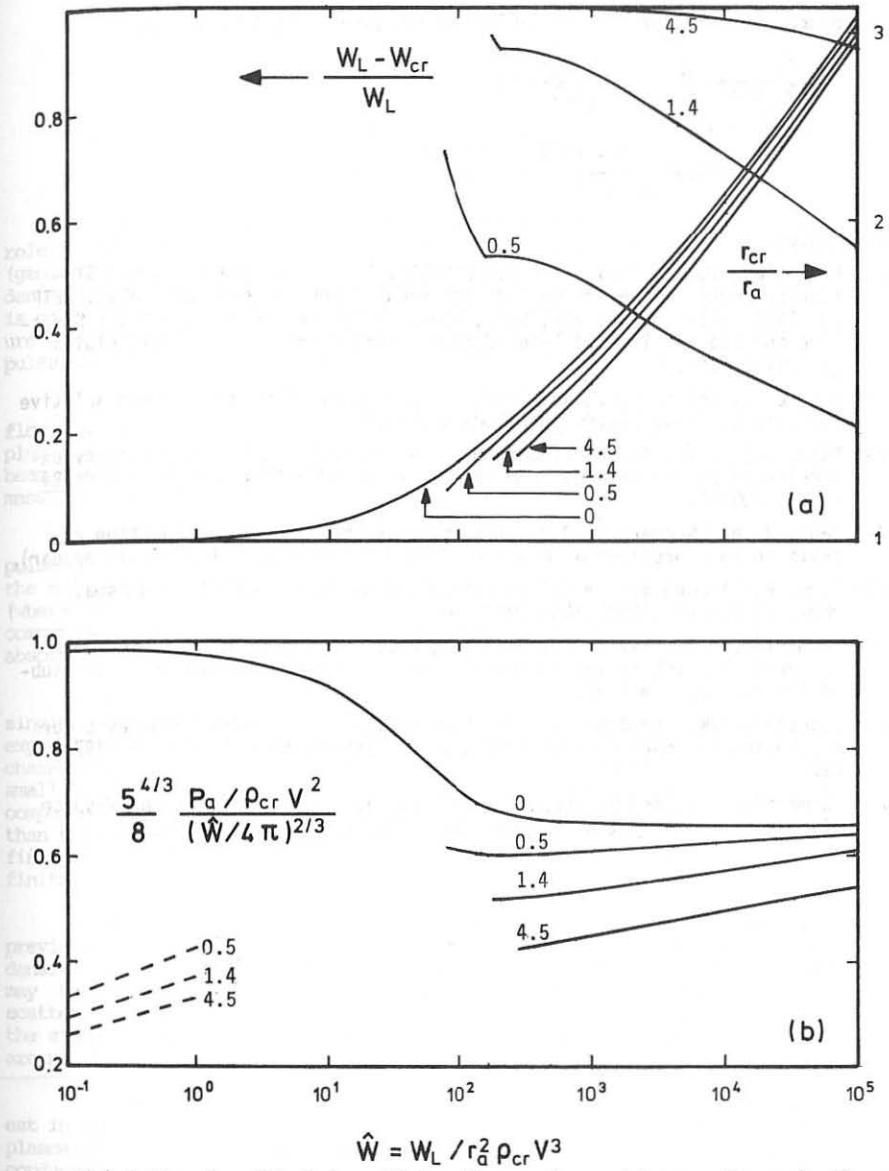

Fig.1(a) Ratio of critical to pellet radius r_{cr}/r_a and inverse Bremsstrahlung absorption $(W_L-W_{cr})/W_L$, and (b) ablation pressure P_a (normalized), versus laser power W_L (in dimensionless form), for values of $\bar{m}V/m_e c$ indicated; ---, behaviour at low power.

introduced by Mora /5/. For the ablation pressure P_a at $t = \tau$ we get

$$\frac{P_a}{\rho_{cr}^{1/3} I_o^{2/3}} = \frac{8}{5^{4/3}}, \quad \frac{\bar{m}U/m_e c}{\hat{I}^{2/3}} << 1$$

$$= 0.45 \left(\frac{\hat{I}^{2/3}}{\bar{m}U/m_e c} \right)^{1/8}, \quad \frac{\bar{m}U/m_e c}{\hat{I}^{2/3}} >> 1 .$$

References

/1/ Afanas'ev, Yu.V., Gamalii, E.G., Krokhin, O.N., and Rozanov, V.B.: Stationary model of the "corona" of spherical laser targets, Sov. Phys. JETP 44 (1977) 311-316; Gitomer, S.J., Morse, R.L., and Newberger, B.S.: Structure and scaling laws of laser-driven ablative implosions, Phys. Fluids 20 (1977) 234-238.

/2/ Max, C.E., McKee, C.F., and Mead, W.C.: A model for laser driven ablative implosions, Phys. Fluids 23 (1980) 1620-1645.

/3/ Sanz, J., Liñán, A., Rodríguez, M., and Sanmartín, J.R.: Quasi-steady expansion of plasma ablated from laser-irradiated pellets, Phys. Fluids 24 (1981) 2098-2106.

/4/ Sanz, J. and Sanmartín, J.R.: Ion charge number and flux saturation effects in the corona of a laser-irradiated pellet, Phys. Fluids (to appear).

/5/ Mora, P.: Theoretical model of absorption of laser light by a plasma, Phys. Fluids 25 (1982) 1051-1056.

/6/ Sanmartín, J.R., Ramis, R., Montañés, J.L., and Sanz, J.: Hot electrons and heat-flux inhibition in the coronae of laser-irradiated pellets, (submitted to Nucl. Fusion).

/7/ Johnston, T.W. and Dawson, J.M.: Correct values for high-frequency power absorption by inverse bremsstrahlung in plasmas, Phys. Fluids 16 (1973) 722.

/8/ Sanmartín, J.R. and Barrero, A.: Self-similar motion of laser half-space plasmas. I. Deflagration regime. Phys. Fluids 21 (1978) 1957-1966.

SPHERICAL EXPANSION PLASMAS IN ION BEAM IMPINGED PELLETS

A. Barrero and L. Rosety
E.T.S.I.Industriales. Universidad de Sevilla, Sevilla. Spain.
J. Sanz
E.T.S.I.Aeronáuticos. Universidad Politécnica de Madrid, Madrid.Spain

Hydrodynamics of the ion beam plasma interaction plays an essential role for achieving break-even conditions in ion beam fusion, since entropy (generated in the energy absorption process) should be kept low inside the dense pellet while mass and energy should inflow efficiently. Clearly, this is only possible if the pressure at the pellet surface (the ablation pressure P_a) depends on time in a spherical manner and therefore ion beam energy pulse and ion beam current should be appropriately shaped.

Our purpose is to obtain, by means of an analysis of the corona flow, simple analytical scaling laws relating the ablation pressure and the plasma mass ablated rate to the beam energy and other parameters such as the beam current (or beam mass rate), the pellet radius r_a and the plasma ion mass m_i and charge number Z_i.

The planar problem has recently been studied assuming ion beam pulses for which self-similar solutions are possible /1/. The results showed the existence of an ablation regime with a well-defined surface ablation (where density peaks and temperature goes to zero) separating an isentropic compression region from a much wider expansion flow where the energy beam absorption occurs.

Here we consider a spherical quasi-neutral expansion flow of a single ion-species plasma under the irradiation of an intense ion beam. This expansion flow may be assumed steady ($\partial/\partial t << v\partial/\partial r$) if the pellet/corona characteristic velocity ratio (and therefore the characteristic time) is small. Since the momentum fluxes produced by P_a in pellet and corona are comparable, the characteristic density in the expansion must be much smaller than the density pellet, so that the density in the corona should go to infinity at the pellet surface while temperature vanishes there since P_a remains finite.

We have also assumed that the beam is both cold and neutralized previously by electrons, and beam density is so small compared with plasma density that ion beam backward flow occurring after the release of its energy may be neglected; beam and plasma interact through the classical Coulomb scattering /2/, but we only consider low Z_i targets since modifications to the stopping power due to collective plasma and atomic ionization processes are not taken into account /3/.

In addition, it is easy to prove that for the conditions of interest in ion beam fusion 1) the momentum transferred from the beam to the plasma is negligible compared with the isotropic energy deposition, 2) heat conduction is small as against energy convection and 3) ion-electron energy exchange is so efficient that the ion and electron temperatures become equal. Then, for a spherical steady flow the continuity and momentum equation for the beam and continuity,momentum and total energy equations for the plasma

may be written

$$n_b v_b r^2 = \mu_b \quad ,$$

$$m_b n_b v_b \, dv_b/dr = R \quad ,$$

$$n v r^2 = \mu \quad ,$$

$$m_i n v \, dv/dr = -(Z_i+1) Z_i^{-1} \, d(n k T)/dr \quad ,$$

$$\mu\left[5(Z_i+1) k T/2 Z_i + m_i v^2/2 Z_i\right] = \mu_b m_b v_b^2/2 \quad ,$$

$$R = 4\pi e^4 \ln\Lambda \, n n_b (m_e v_b^2)^{-1} \Phi\left[v_b/(2 k T/m_e)^{1/2}\right] \quad ,$$

$$\Phi(y) = 2\pi^{-1/2}\left[\int_0^y \exp(-t^2)dt - y \exp(-y^2)\right] \quad ,$$

where n, v and T are density, velocity and temperature respectively (subcripts b, e and i referring to beam, electrons and ions) and e, k and $\ln\Lambda$ are the electron charge, Boltzmann's constant and Coulomb logarithms. Both the beam and the ablated plasma flow rates $4\pi m_b \mu_b$ and $4\pi m_i \mu/Z_i$ are independent of the radius r.

Since μ and P_a are unknown we must have two additional boundary conditions, then

$$T = 0 \quad , \quad \text{and} \quad \mu k T/v r^2 = P_a \quad \text{at} \quad r = r_a \quad ,$$

$$T \to 0 \quad , \quad \text{and} \quad m_b v_b^2/2 = E_b \quad \text{as} \quad r \to \infty \quad .$$

Now defining the dimensionless variables

$$\Omega = \alpha^{-2/5} \beta^{1/5} \eta^{2/5} m_b v_b^2/2E_b \quad , \quad \Theta = \alpha^{-2/5} \beta^{-4/5} \eta^{2/5} T/T_r \quad ,$$

$$Y = \alpha^{-2/5} \beta^{-4/5} \eta^{2/5} m_i v^2/Z_i k T_r \quad , \quad \eta = r/r_a \quad ,$$

choosing

$$k T_r = \frac{Z_i}{m_i}\left[\frac{Z_i}{Z_i+1}\right]^2 \frac{P_a^2 r_a^4}{\mu^2} \quad , \quad \beta = \frac{\mu_b E_b}{\mu k T_r} \quad ,$$

$$\alpha = \frac{2\pi e^4 \ln\Lambda \, m_b \mu}{m_e E_b^2 r_a (Z_i k T_r/m_i)^{1/2}} \quad , \quad \beta^* = \frac{m_e E_b}{m_b k T_r} \quad ,$$

and introducing them into the above equations we arrive (after some manipulation) to the following phase plane equations

$$\frac{d\Omega}{dY} = \frac{\left[2\Omega^2 Y^{1/2} + 5\Phi(X)\right](2Y - \Omega)}{Y^{1/2}\left[6Y\,\Omega(3\Omega - Y) - 10Y^{1/2}\Phi(X)\right]} \quad , \quad (1)$$

$$\frac{1}{\eta}\frac{d\eta}{dY} = \frac{5\Omega(2Y-\Omega)}{6Y\,\Omega(3\Omega-Y)-10Y^{1/2}\Phi(X)} \quad , \qquad (2)$$

where

$$X = \left[\frac{5\beta^*(Z_i+1)}{2\beta\,Z_i}\,\frac{\Omega}{\Omega-Y/2}\right]^{1/2} \quad ;$$

the boundary conditions are:

$$\Omega = \frac{5(Z_i+1)Y^{1/2}}{2Z_i\alpha^{1/2}\beta^{2/5}} \quad , \text{ and } \eta = 1 \quad \text{at} \quad Y = 0 \quad ,$$

$$\Omega = Y/2 \quad \text{and} \quad \eta = \alpha\,\beta^{-2}(Y/2)^{5/2} \quad \text{at} \quad Y \to \infty \quad .$$

The solution to equation (1) near the nodal point Y=0, Ω=0, is $\Omega = C\,Y^{1/2}$ (the constant C being related to the eingenvalues α and β through the boundary conditions) and since Ω=Y/2, for large Y, we must have Ω=2Y in a certain point of the interval $0 \le Y \le \infty$. In addition, dY/dη must remain finite to avoid a multivalued solution, so that the numerator on the right hand side of equation (2) must vanish if Ω=2Y. This condition leads to

$$6Y_s^{5/2} = \Phi(X_s) \quad , \quad X_s = \left[10(Z_i+1)\beta^*/3Z_i\beta\right]^{1/2} \quad ,$$

which gives the singular point coordinates $(Y_s, 2Y_s)$ as a function of β^*/β; Y_s ranges from 0, for $\beta^*/\beta \to 0$, to .488, for $\beta^*/\beta \to \infty$.

For a given value of β^*/β we may determine Y_s and find that there exists a value of C (call it C^*) that allows to reach the saddle (sonic) point $(Y_s, 2Y_s)$. Starting from this point and integrating backward to the node we numerically find C^* for each β^*/β (see fig. 1). The numerical integration of equations (1) and (2) beyond Y_s yields the value of $C_1 = \eta^{2/5}/Y$ (for Y large) which is related to the eingenvalues α and β through the boundary conditions.

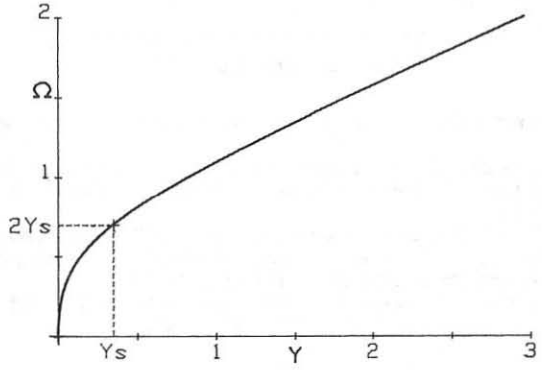

Fig. 1. Integral curve solution to equation (1)

Once α and β are determined from the calculated values of C^* and C_1, we may obtain the profiles of beam density and velocity and plasma density, velocity and temperature respectively, and from the expressions of α , β and β^* we arrive at the following simple analytical laws that related the beam energy E_b and beam mass rate μ_b with the ablation pressure

$$E_b = f(2\pi e^4 \ln\Lambda)(m_e/m_b)^{2/3}(P_a r_a)^{1/3} ,$$

$$\mu_b = g(2\pi e^4 \ln\Lambda)^{-1/6}(m_e/m_b)^{5/6}(Z_i/m_i)^{1/2}P_a^{5/6} r_a^{11/6} ,$$

where $f = C_1(5/2C^*)^{1/3}(\beta^*/\beta)^{1/3}$ and $g = (5/2C^*)^{5/6}(\beta/\beta^*)^{2/3}$, that depend weakly on Z_i are given in fig. 2 as functions of $m_e\mu/m_b\mu_b$.

Then, for a given target, one may determine the ablation pressure $P_a(t)$ that generates an optimal compression; this problem has been studied elsewhere /4/ and its solution also determines the pellet radius $r_a(t)$. Our solution yields, for given instantaneous P_a and r_a, the required beam energy E_b and the mass beam rate μ_b , for each value of the ablated plasma mass rate.

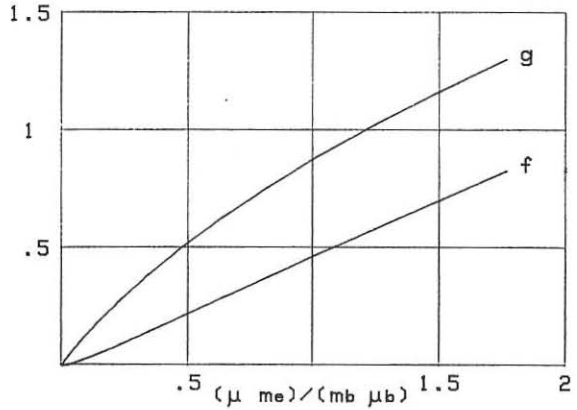

Fig.2. Numerical values of f and g as a function of $\mu m_e/m_b\mu_b$

/1/ Barrero,A.,Fernandez,A.:One-dimensional motion of ion beam fusion plasmas, in Proceedings of the 1982 International Conference on Plasma Physics , Göteborg 1982 p.280.
/2/ Miyamoto,K.:Plasma Physics for Nuclear Fusion,MIT Press Cambridge 1980.
/3/ Nardi,E.,Peleg,E.,and Zinamon,Z.:Energy deposition by fast protons in pellet fusion targets,Phys. Fluids 21 (1978) 574-579.
/4/ Kidder,R.E.:Theory of homogeneous isentropic compression and its applications to laser fusion,Nucl. Fusion 14(1974) 53-60.

DENSITY PROFILES AND FLUCTUATIONS IN CO_2 LASER PRODUCED PLASMAS

D A BROWN, P S MARCHINGTON, N SAYED, Y SUDERA & E R WOODING
ROYAL HOLLOWAY COLLEGE, UNIVERSITY OF LONDON,
EGHAM, SURREY, TW20 0EX, UK.

Electron densities have been determined by holographic interferometry of plasmas produced when CO_2 laser radiation was incident on plane solid targets. Soft X-ray emission was recorded simultaneously by means of a pinhole camera. From these measurements it is seen that the density profile steepened near the target but also developed fine structure. These results are compared with theory and simulations of profile modification /1,2/ .

The TEA CO_2 laser had an unstable cavity and produced pulses of 10.6 μm radiation with energies of 15 to 20 J. The temporal pulse profile had a rise time of 20 ns, a fall time of 40 ns, and a tail of 200 ns. In these pulses, partial mode locking resulted in intensity fluctuations of about 30% on a 5 ns time scale. The output beam was focussed to a spot diameter of 200 μm by a germanium lens of 120 mm focal length and aperture f2.5 producing irradiance up to $2 \times 10^{16} Wm^{-2}$.

The plasma density was determined by using a double exposure holographic interferometer with a ruby laser of 3 ns (fwhm) duration. From published work it appeared to be preferable to use the infinite fringe technique as this required no movement of the reference beam for the second exposure. This method also permitted the fringe shift in the lower density regions to be determined by linear extrapolation and is less likely to show Moiré artefacts. The X-ray pinhole camera carried a 0.75 μm aluminium filter foil and produced an image magnified twice.

Electron densities determined after Abel inversion from the fringe shift in the holograms are shown in fig. 1. These values are subject to an error of ± 20% which results from refraction and the minimum fringe shift of 0.1λ that could be estimated.

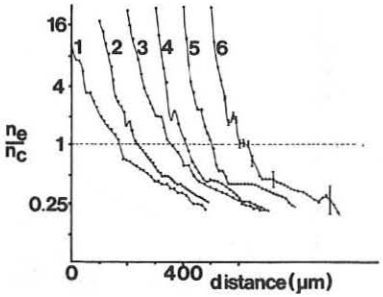

Fig.1 Density profiles at (1)10ns(2)25ns(3)35ns(4)65ns(5)90ns and (6)115 ns after the onset of the laser pulse. Profiles stepped 100 μm to right.

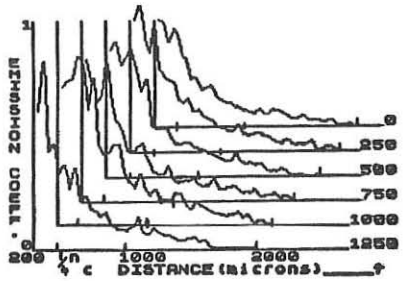

Fig.2 X-ray emission coefficient (arb. units) varying with distance from the surface of a plane carbon target.

In the results now reported the target was carbon and the laser irradiance was $10^{16} Wm^{-2}$. Successive profiles obtained from separate plasma shots are displaced 100 μm. Development of profile steepening can be seen to occur over the first 50 ns in which time the irradiance has reached its peak value and is falling. The plateau at 0.3 n_c is predicted by the theory of Lee et al /1/ but the plateau at 0.5 n_c has yet to be explained. Further information on the underdense plasma is obtained from the spatially resolved X-ray emission shown in fig.2. A peak exists in this emission where the density is $n_c/4$, a region where parametric processes such as two plasmon decay occur. There is also a peak in emission near to the $n_c/2$ region which could be related to the density plateau there. There are marked periodic variations in emission along the axis and in a radial direction, showing that fluctuations extend well into the underdense plasma and must represent a structure that persists for most of the plasma lifetime.

Another feature of the density profile is a bump which occurs between $1.6n_c$ and $2.2n_c$ with a density modulation of about 30%. This feature resembles the rarefaction wave predicted by Max et al /3/. In the expanding plasma there is a rarefaction or compression front depending on the Mach number being less than:-

$$(1-P_f/\rho_1 c_1^2)^{\frac{1}{2}}$$

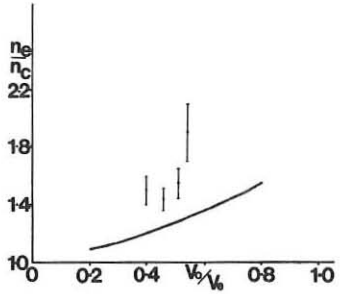

Fig.3 Dependence of density at upper plateau on irradiance. The line shows the density expected for a plasma temperature of 200 eV.

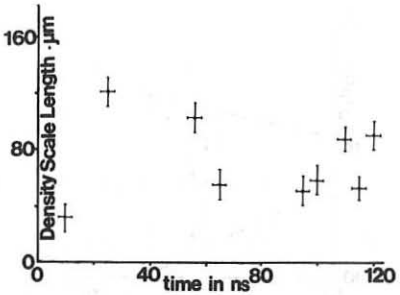

Fig.4 Variation of scale length with time. Irradiance was $2.10^{16}Wm^{-2}$

or greater than:- $(1+P_f/\rho_1 c_1^2)^{\frac{1}{2}}$

where P_f is the ponderomotive pressure, ρ_1 is the plasma ion density and c_1 is the ion speed on the low density side of the front. Virmont et al/4/ have carried out simulations on radially symmetric plasma and find such bumps at the critical density. The width of the bump varies with the position of n_c and as the square of the ratio of radiation pressure to thermal pressure. For a temperature of 200 eV and an absorption coefficient of 0.4 the width calculated is 25 µm, which agrees with experimental values of 30 to 40 µm. The scale length L_c in the vicinity of n_c shown in fig.4 , varies from 30 to 120 µm over the duration of the plasma, but these values were obtained from successive shots. Since this is the region of the plasma where resonance absorption occurs, its parameters are likely to be very sensitive to fluctuations in the laser pulse. The existence of more than one scale length at any time could explain why the $2\omega_0$ harmonic intensity passes through more than one maximum as the angle of incidence of the laser beam on the target is varied. The first two maxima shown in fig.5 correspond to scale lengths of 20 µm and 150 µm. /5/.

The variation of scale length with irradiance shown in fig.6 falls below the value predicted by the self consistent model of Montes /6/ which omits the ponderomotive force. However, still lower values are derived from the capacitor model of Estabrook et al /7/ which includes ponderomotive forces.

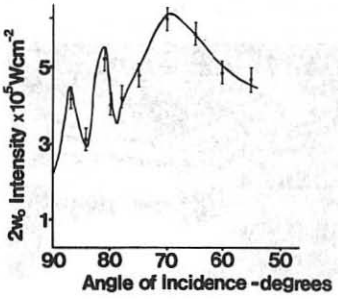

Fig.5 Variation of $2\omega_0$ intensity with angle of incident radiation. Irradiance $6.6\ 10^{15}Wm^{-2}$

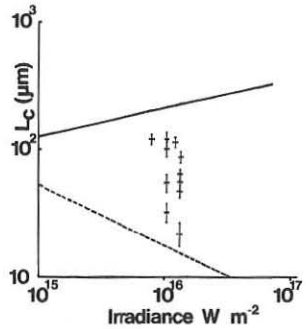

Fig.6 Scale length dependence on irradiance. Solid line - no ponderomotive force. Broken line - Estabrook model.

From measurements of density at various times, it was found that the n_c region is accelerated in the first 20 ns to a velocity of 5.10^4m/s. Baker /8/ shows that an exponential density gradient with an antiparallel acceleration can develop Rayleigh Taylor instabilities. Holograms such as that shown in fig.7 give some evidence of instabilities. There are also ripples across the surface and some regions of higher density. In some instances, a regular modulation of the electron density is seen in the axial direction.

Detailed analysis of this structure requires more data, particularly on temperature distributions and magnetic fields. In addition, methods of initiating instabilities are being studied.

1. Lee,K. Forslund,D.W. Kindel,J.M. & Lindman,E.L. Phys.Fluids (1977) 17,51
2. Estabrook,K. Valeo,E. & Kruer,W.L. Phys.Lett. (1974) 49A,109
3. Max,C.E. & McKee,C.F. Phys.Rev.Lett. (1977) 39, 1336
4. Virmont,J. Pellat,R. & Mora,A. Phys.Fluids (1978) 21, 567
5. Ginzburg,V.L. (1970) The propagation of electromagnetic waves in plasmas, Pergamon, Oxford.
6. Montes,A. PhD Thesis, Oxford University, (1980)
7. Estabrook,K. & Kruer,W.L. Phys.Rev.Lett. (1978) 40, 42
8. Baker,L. Phys.Fluids (1983) 26, 391

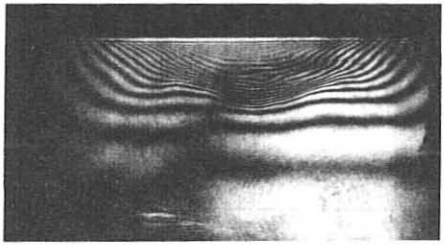

Fig.7 Hologram of plasma from plane target showing instabilities that have developed after 180 ns - irradiance 1.3 10^{12}Wcm^{-2}.

RADIATION OF ALFVÉN WAVES BY THE ACCELERATING LANGMUIR SOLITON

I.G.Murusidze, N.L.Tsintsadze

D.D.Tskhakaya

Institute of Physics, Academy of Sciences of the Georgian SSR, Tbilisi, USSR

It has been shown in/1/that Langmuir soliton radiates ion--acoustic waves being accelerated due to plasma inhomogeneity. In the present paper the possibility of the radiation of Alfvén waves by the accelerating Langmuir soliton is demonstrated. Langmuir waves in the homogeneous magnetoactive plasma have been investigated in a number of papers /2-3/ taking into account only the plasma density perturbation under the action of high frequency (HF) Langmuir wave ponderomotive force. In the present paper we take into account the low--frequency (LF) perturbation of the magnetic field, as well.

We consider HF Langmuir wave with the dispersion $\omega = \omega_{Pe} + \frac{3}{2}(kr_D)^2\omega_{Pe} + \frac{\Omega_e^2}{2\omega_{Pe}}\frac{k_z^2}{k^2}$ which causes both plasma density and magnetic field LF perturbations penetrating at a certain angle with the weak external magnetic field $\left(\left(\frac{eB_0}{m_e c}\right)^2 \equiv \Omega_e^2 \ll \omega_{Pe}^2\right)$ directed along z-axis. Considering the plasma which is weakly inhomogeneous along z-axis, we assume that the plasma drift velocity due to the heterogeneity is lower than the ionic sound velocity C_S and Alfvén velocity C_A , while the characteristic inhomogeneity length greatly exceeds the spatial scale of LF motion. Taking all that into account and substituting the HF wave amplitude in the following form

$$\vec{E} = -\nabla\left(\psi(z,t)e^{i\vec{k}\vec{r}}\right), \quad \vec{k} = (k_x, 0, k_z), \quad |\nabla\psi| \ll |\vec{k}\psi|, \left|\frac{\partial\psi}{\partial t}\right| \ll \omega|\psi|$$

we obtain for ψ :

$$i\frac{\partial\psi}{\partial t} + ig\frac{\partial\psi}{\partial z} + q\omega_{Pe}r_D^2\frac{\partial^2\psi}{\partial z^2} - \frac{\omega_{Pe}}{2}\Delta n(z)\psi - \frac{\omega_{Pe}}{2}\delta v\psi + \frac{\Omega_e^2}{\omega_{Pe}}\frac{k_x k_z}{k^2}\delta B_x\psi = 0 \qquad (1)$$

where $$q \equiv \frac{\partial \omega}{\partial k_z} = \left(\frac{3 V_{Te}^2}{\omega_{Pe}} - \frac{\Omega_e^2}{\omega_{Pe}} \frac{k_x^2}{k^4} \right) k_z$$

$$\gamma = \frac{3}{2} + 6 \frac{k_z^2}{k^2} - \frac{\Omega_e^2}{2\omega_{Pe}^2} \frac{k_x^2}{k^2} \frac{1}{(k r_D)^2}$$

$\Delta n(z)$ determines the plasma inhomogeneity profile, and δv and δB_x normalized to the corresponding equilibrium values represent the particle concentration and the magnetic field perturbations. We describe these perturbations by magnetohydrodynamic system of equations. In the linear approximation, the following is valid:

$$\left(\frac{\partial^2}{\partial t^2} - c_s^2 \frac{\partial^2}{\partial z^2} \right) \delta v = - \frac{1}{m_i n_0} \frac{\partial F_z}{\partial z} \qquad (2)$$

$$\left(\frac{\partial^2}{\partial t^2} - c_A^2 \frac{\partial^2}{\partial z^2} \right) \delta B_x = \frac{1}{m_i n_0} \frac{\partial F_x}{\partial z} \qquad (3)$$

F_x and F_z being the components of the ponderomotive force/4,5/ expressed by the potential Ψ :

$$\vec{F} = - \frac{\kappa^2}{16\pi} \nabla |\Psi(z,t)|^2 + \frac{\kappa^2}{8\pi} \frac{\vec{\kappa}}{\omega_{Pe}} \frac{\partial |\Psi(z,t)|^2}{\partial t} \qquad (4)$$

Note that the magnetic field perturbation has no component along $\vec{B}_0$, the quadratic approximation for HF wave amplitude. Eqns (1), (2) and (3) represent a closed system describing the interaction of HF Langmuir waves with LF perturbations of density and magnetic field. In case of homogeneous plasma ($\Delta n(z) = 0$), the solution of this system has the form of stationary solitons, both δv and δB_x being concentrated within the soliton localization region. However, taking into account the soliton acceleration due to inhomogeneity, the radiation of Alfvén waves occurs, side by side with the ionic sound. We represent δv and δB_x as sums

$$\delta v = \delta v_0 + \delta v_s = \frac{\kappa^2}{16\pi m_i n_0} \cdot \frac{\psi_0^2(z - \bar{z}(t))}{\ddot{\bar{z}}^2(t) - c_s^2} + \delta v_s \qquad (5)$$

$$\delta B_x = \delta B_{x0} + \delta B_A = -\frac{\kappa^2}{8\pi m_i n_0}\frac{\kappa_x}{\omega_{pe}}\dot{\bar{z}}(t)\frac{\psi_0^2(z-\bar{z}(t))}{\dot{\bar{z}}^2(t)-c_A^2} + \delta B_A \qquad (6)$$

where $\psi_0(z-\bar{z}(t)) \equiv |\psi|$, $\bar{z}(t)$ and $\dot{\bar{z}}(t) = d\bar{z}/dt$ are the coordinate and the velocity of the soliton center, δV_s and δB_A - perturbations due to the radiation. Assuming $|\delta V_s| \ll |\delta V_0|$ and $|\delta B_A| \ll |\delta B_{x0}|$, we neglect the reaction of the radiation on the soliton. In case of "subsonic" regime $\dot{\bar{z}}^2(t) \ll c_s, c_A$ and under the conditions $\Omega_e^2 \ll \omega_{ie}^2$, the contribution of δB_x into Eqn(1) is smaller than that of δV. Then, according to (5) and (6), we obtain a system of Eqs.

$$i\frac{\partial\psi}{\partial t} + ig\frac{\partial\psi}{\partial z} + q\omega_{pe}r_D^2\frac{\partial^2\psi}{\partial z^2} - \frac{\omega_{pe}}{2}\Delta n(z)\psi + \frac{\omega_{pe}\kappa^2|\psi|^2}{32\pi n_e T_e}\psi = 0 \qquad (7)$$

$$\left(\frac{\partial^2}{\partial t^2} - c_A^2\frac{\partial^2}{\partial z^2}\right)\delta B_A = -\ddot{\bar{z}}(t)\frac{3\kappa^2\kappa_x}{2B_0^2\omega_{pe}}\frac{\partial|\psi|^2}{\partial t} \qquad (8)$$

Since the Eqn for δV_s coincides (as it should be) with the corresponding Eqs in /1/, we omit the former. Solving Eqn(7), we obtain

$$|\psi| = \psi_0(z-\bar{z}(t)) = \psi_{0m}\,\mathrm{sech}\frac{z-\bar{z}(t)}{\Delta\ell} \qquad (9)$$

where $\Delta\ell = \left(\sqrt{4q\,16\pi n_e T_e}\, r_0\right)/\kappa\psi_{0m}$ (supposing $q>0$), while $\bar{z}(t)$ is defined using Eqn (10)/6/:

$$\ddot{\bar{z}}(t) = -qV_{Te}^2\left(\frac{\partial\Delta n(z)}{\partial z}\right)\Big|_{z=\bar{z}(t)} \qquad (10)$$

Since the acceleration change during the time $\frac{\Delta\ell}{c_A}$ is small, the solution of Eqn(8) is the following:

$$\delta B_A(z,t) = -\frac{3}{4C_A^2}\left(\frac{\kappa\psi_{0m}}{B_0}\right)^2\frac{\kappa_x\Delta\ell}{\omega_{pe}}\left\{\dot{\bar{z}}(t')\ddot{\bar{z}}(t')\Big|_{t'=t-\frac{z-\bar{z}(t)}{c_A}}\left[\mathrm{th}\frac{z-\bar{z}(t)}{\Delta\ell} - \right.\right. \qquad (11)$$

$$\left.\left. - \mathrm{th}\frac{z-c_At-\bar{z}(0)}{\Delta\ell}\right] + \dot{\bar{z}}(t')\ddot{\bar{z}}(t')\Big|_{t'=t+\frac{z-\bar{z}(t)}{c_A}}\left[\mathrm{th}\frac{z-\bar{z}(t)}{\Delta\ell} - \mathrm{th}\frac{z+c_At-\bar{z}(0)}{\Delta\ell}\right]\right\}$$

E.g., consider the case of $\Delta n(z) = \frac{\alpha^2 z^2}{2}$. In such case the soliton "oscillates" within the density well with the frequency $\omega_0 = \sqrt{q}\,\alpha V_{Te}^2$, radiating Alfvén waves:

$$\delta B_A(z,t) = -\frac{3}{8}\left(\frac{k\Psi_{0m}}{B_0}\right)^2 \frac{k_x \Delta\ell\, \omega_0}{\omega_{pe}} \frac{V_0^2}{C_A^2}\left\{\sin 2\omega_0\left(t - \frac{z-\bar{z}(t)}{C_A}\right)\left[th\,\frac{z-\bar{z}(t)}{\Delta\ell} - th\,\frac{z-C_A t-\bar{z}(0)}{\Delta\ell}\right] + \right. \tag{12}$$

$$\left. + \sin 2\omega_0\left(t + \frac{z-\bar{z}(t)}{C_A}\right)\left[th\,\frac{z-\bar{z}(t)}{\Delta\ell} - th\,\frac{z+C_A t-\bar{z}(0)}{\Delta\ell}\right]\right\}$$

Here V_0 is the maximum soliton velocity.

We obtain the following estimation for the energy density (Poynting's vector) averaged over the period $T = 2\pi/\omega_0$:

$$\bar{S} = C_A \frac{9}{64}\left(\frac{k\Psi_{0m}}{B_0}\right)^4 \cdot (k_x \Delta\ell)^2 \cdot \left(\frac{\omega_0 V_0^2}{\omega_{pe} C_A^2}\right)^2 \cdot \frac{B_0^2}{8\pi} \tag{13}$$

References

1. R.K.Kow, N.L.Tsintsadze, D.D.Tskhakaya. Journal Experim. i Teor. Fiziki, 1982, 82, 1449.
2. K.B.Dysthe, E.Mjølhus, H.L.Pecseli, L.Stenflo. Plasma Phys., 1978, 20, 1087.
3. P.Rolland, S.G.Tagare. J.Plasma Phys., 1982, 28, 19.
4. V.I.Karpman, A.G.Shagalov. J.Plasma Phys., 1982, 27, 215.
5. D.D.Tskhakaya. J.Plasma Phys., 1981, 25, 233.
6. H.H.Chen, C.S.Liu. Phys.Fluids, 1978, 21, 377.

Diagnostics

E14 - E25

Ion Temperature Measurement with Neutral Beams

Ichiro MORI
Technical College of Tokushima University
Tokushima, 770 JAPAN

Abstract: A new method with an elastic scattering of neutral beam is proposed for ion temperature measurement in thermo-nuclear plasmas. Model calculation based on this method is performed by employing plasma parameters of the Tokamak device JT-60.

1. Introduction The first trial to measure a plasma temperature with fast neutrals was done by Aleksandrov et al./1/ on the basis of Abramov's theory/2/. In the theory, Born approximation and Rutherford cross-section were utilized. However, it can be shown that even in the high energy range such as 100KeV, phase shift of quantum mechanical wave function, η_0, has the value about 4 radian, which means that the Born approximation breaks down because the approximation is accurate only when $\eta_n \ll 1$ is fulfilled/3/. Conversely, in this paper, we use the approximation which is adequate to large η_n and calculate a cross-section of H^0-H^+ elastic scattering. With the cross-section, width of broadening in velocity distribution is obtained. From the width, we can estimate the plasma temperature. As an example, the width is evaluated when H^0 passes through the thermo-nuclear plasma in Tokamak device JT-60. Distinctive point of our method is the fact that interacting length of scattering is much larger, 20 times, than that of above experiment. This is quite profitable from the point of view that we must get large particle flux as much at measuring point, because injected neutral flux will be damped out quickly by charge exchange with plasma ions.

2. Cross-section Differential cross-section is described as

$$\sigma(\vec{k},\theta)=(1/4k^2)\sum_{nm}\sum(2n+1)(2m+1)[\cos 2\eta_n-1][\cos 2\eta_m-1]P_n(\cos\theta)P_m(\cos\theta)$$
$$+(1/4k^2)\sum_{nm}\sum(2n+1)(2m+1)\sin 2\eta_n\cdot\sin 2\eta_m\cdot P_n(\cos\theta)P_m(\cos\theta), \qquad (1)$$

where $k=|\vec{k}|$, θ and η_n are wave number, scattering angle and phase shift respectively. The wave number is related to relative velocity $\vec{u}$ with the formula $\vec{k}=m\vec{u}/\hbar$. If we express the cross-section with kinetic energy $E(=mu^2/2)$, and integrate it with solid angle, then it becomes

$$\sigma(E)=(4\pi/k^2)\sum_n(2n+1)\sin^2\eta_n=(2\pi\hbar^2/mE)\sum_n(2n+1)\sin^2\eta_n \qquad (2)$$

Let's calculate the phase shift η_n in the approximation for large η_n by making use of a H^0-potential

$$V(r)=(e^2/4\pi\varepsilon_0)\cdot(1/r+1/a_0)\cdot\exp(-2r/a_0). \qquad (3)$$

With the normalized distance by Bohr radius a_0, $(x=2r/a_0)$, one obtains

$$\eta_n=\int_{x_1}^{\infty}\left\{\frac{k^2a_0^2}{4}-\frac{m}{h^2}\cdot\frac{e^2a_0}{4\pi\varepsilon_0}\left(\frac{1}{x}+\frac{1}{2}\right)\exp(-x)-\frac{(n+\frac{1}{2})^2}{x^2}\right\}^{1/2}dx$$
$$-\int_{x_2}^{\infty}\left\{\frac{k^2a_0^2}{4}-\frac{(n+\frac{1}{2})^2}{x^2}\right\}^{1/2}dx \qquad (4)$$

where x_1 and x_2 are zeros of each integrand /3/.

Taking account of the fact that only small value of x contributes to the integral, we expand the exponential term in power series and use till second term and then use the formula (for a>0, c<0),

$$\int\sqrt{ax^2+bx+c}\cdot dx/x=\sqrt{ax^2+bx+c}+(b/2\sqrt{a})\cdot\ln\left|2ax+b+2\sqrt{a(ax^2+bx+c)}\right| - \sqrt{|c|}\cdot\sin^{-1}\{(bx+2c)/x\sqrt{b^2-4ac}\} \qquad (5)$$

and we get finally

$$\eta_n=\sqrt{\frac{1}{4}\left(\frac{E}{2E_c}-1\right)\left(\frac{m_p}{m_e}\right)-(n+\tfrac{1}{2})^2}-\sqrt{\frac{E}{8E_c}\left(\frac{m_p}{m_e}\right)-(n+\tfrac{1}{2})^2} - \frac{\sqrt{\frac{m_p}{m_e}}}{4\sqrt{\frac{E}{2E_c}+1}}\cdot\ln\left[\frac{\frac{E}{4E_c}+\sqrt{\left(\frac{E}{2E_c}+1\right)\left(\frac{m_p}{m_e}\right)\left\{\frac{1}{4}\left(\frac{E}{2E_c}-1\right)\left(\frac{m_p}{m_e}\right)-(n+\frac{1}{2})^2\right\}}}{\sqrt{\frac{1}{4}\left(\frac{m_p}{m_e}\right)^2+\left(\frac{E}{2E_c}-1\right)\left(\frac{m_p}{m_e}\right)(n+\frac{1}{2})^2}}\right] -(n+\tfrac{1}{2})\cdot\left[\sin^{-1}\left\{\frac{-\frac{1}{2}\left(\frac{m_p}{m_e}\right)-2(n+\frac{1}{2})^2}{\sqrt{\frac{1}{4}\left(\frac{m_p}{m_e}\right)^2+\left(\frac{E}{2E_c}-1\right)\left(\frac{m_p}{m_e}\right)(n+\frac{1}{2})^2}}\right\}-\sin^{-1}\left\{\frac{-2(n+\frac{1}{2})}{\sqrt{\frac{E}{2E_c}\cdot\left(\frac{m_p}{m_e}\right)}}\right\}\right] \qquad (6)$$

where a relation $\hbar^2=e^2a_0m_e/4\pi\varepsilon_0=E_c.m_ea_0^2$ was used. From the Eqs.(2) and (6), The cross-section is obtained as shown in Fig.1.

3. Diffusion Coefficient in Velocity Space for Uniform Plasma

Diffusion coefficient of H^0particle in velocity space can be obtained with similar method studied by Rosenbluth et al./4/

$$\langle\Delta v_\mu\Delta v_\nu\rangle=\int d\vec{v}'f_b(\vec{v}')\int d\vec{\Omega}\cdot\sigma(\vec{u},\vec{\Omega})u\Delta v_\mu\Delta v_\nu \qquad (7)$$

where $\langle\Delta v_\mu\Delta v_\nu\rangle$ represents the diffusion coefficient per unit time, and $f_b(\vec{v}')$ and $\vec{\Omega}$ show an ion distribution function and solid angle respectively.
For the calculation, it is convenient to introduce a local Cartesian coordinate in which the changes of each velocity component undergone the collision are expressed as follows.

$$\left.\begin{aligned}\Delta u_1^L&=-2u\cdot\sin^2(\theta/2)\\ \Delta u_2^L&=2u\cdot\sin(\theta/2)\cdot\cos(\theta/2)\cdot\cos\phi\\ \Delta u_3^L&=2u\cdot\sin(\theta/2)\cdot\cos(\theta/2)\cdot\sin\phi\end{aligned}\right\} \qquad (8)$$

Now,we denote the average of product of velocity change $\Delta u_\mu^L\Delta u_\nu^L$ as

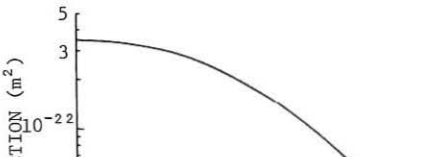

Fig.1
Calculated cross-section
of H^0-H^+ elastic scattering

$$\{\Delta u_\mu^L \Delta u_\nu^L\} = \int d\vec{\Omega}\sigma(\vec{u},\vec{\Omega}) u \Delta u_\mu^L \Delta u_\nu^L \ , \qquad (\mu,\nu = 1\sim3) \tag{9}$$

Then the transformation of this quantity from local Cartesian coordinate to laboratory system becomes

$$\{\Delta v_\mu \Delta v_\nu\} = \left(\frac{m_b}{m_a+m_b}\right)^2 \left[\frac{u_\mu u_\nu}{(u)^2}\{\Delta u_1^L \Delta u_1^L\} + \{\delta_{\mu\nu} - \frac{u_\mu u_\nu}{(u)^2}\}\{\Delta u_2^L \Delta u_2^L\}\right] \tag{10}$$

where the subscription 1 means direction of relative velocity and 2 its perpendicular direction. Multiplying Eq.(10) by Maxwellian

$$f_b(\vec{v}') = n_b (m_b/2\pi kT)^{3/2} \cdot \exp\{-m_b(\vec{v}')^2/2kT\} \tag{11}$$

and integrating with $\vec{v}'$-space, we can finally obtain the diffusion coefficients. For example, $<\Delta v_1 \Delta v_1>$ becomes

$$<\Delta v_1 \Delta v_1> = 2\sqrt{\pi} a_0^2 n_b \frac{E_c m_e}{m_p^2} \left(\frac{2kT}{m_p}\right)^{1/2} [2e^{-x} - 2x^{-1}e^{-x} + 2\sqrt{\pi}\sqrt{x}\Phi(\sqrt{x}) - \frac{\sqrt{\pi}}{\sqrt{x}}\Phi(\sqrt{x}) + \frac{\sqrt{\pi}}{\sqrt{x}^3}\Phi(\sqrt{x})] \sum_n K_1$$
$$+ \sqrt{\pi} a_0^2 n_b \frac{E_c m_e}{m_p^2} \left(\frac{2kT}{m_p}\right)^{1/2} [2x^{-1}e^{-x} + 2\frac{\sqrt{\pi}}{\sqrt{x}}\Phi(\sqrt{x}) - \frac{\sqrt{\pi}}{\sqrt{x}^3}\Phi(\sqrt{x})] \cdot \sum_n K_2 \tag{12}$$

$$K_1 = \{(2n+1) + \frac{n^2}{2n-1} + \frac{(n+1)^2}{2n+3}\}\sin^2\eta_n - 2n\sin\eta_n \sin\eta_{n-1}\cos(\eta_n - \eta_{n-1})$$
$$-2(n+1)\sin\eta_n \sin\eta_{n+1}\cos(\eta_n - \eta_{n+1}) + \frac{(n-1)n}{2n-1}\sin\eta_n \sin\eta_{n-2}\cos(\eta_n - \eta_{n-2})$$
$$+\frac{(n+1)(n+2)}{2n+3}\sin\eta_n \sin\eta_{n+2}\cos(\eta_n - \eta_{n+2}) \tag{13}$$

$$K_2 = \{(2n+1) - \frac{n^2}{2n-1} - \frac{(n+1)^2}{2n+3}\}\sin^2\eta_n - \frac{(n-1)n}{2n-1}\sin\eta_n \sin\eta_{n-2}\cos(\eta_n - \eta_{n-2})$$
$$-\frac{(n+1)(n+2)}{2n+3}\sin\eta_n \sin\eta_{n+2}\cos(\eta_n - \eta_{n+2}) \tag{14}$$

where $x = E/kT$ and $\Phi(x)$ represents error function $\Phi(x) = (2/\sqrt{\pi})\int_0^x \exp(-y^2)dy$.

4. Calculation for JT-60(Non-Uniform Plasma including Magnetic Field)

Schematic drowing of proposed system is shown in Fig.2. Ionized component from the plasma are removed beforehand by deflector. Neutrals are ionized when they pass through the gas cell, then their orbit are bent by magnet. In the model, following parameters are used: ion density in center $N_p = 10^{20} m^{-3}$, plasma radius a=95 cm, flux density B=5T, distance between the magnet and detector L=10 m.

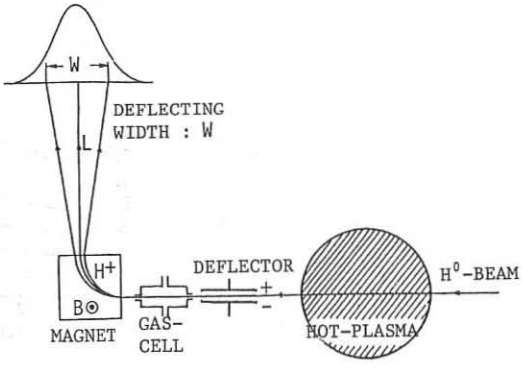

Fig.2
Schematic drawing of experimental arrangement for proposed method

We assume that the plasma density and the temperature are expressed as quadratic function $N(R)=Np\{1-(R/a)^2\}$ and $T(R)=T_p\{1-(R/a)^2\}$ and also assume that the function $f_b(\vec{v}')$ are maxwellian in a basic principle

$$f_b(\vec{v}')=N(R)\{m_b/2\pi kT(R)\}^{3/2}\exp\{-m_b/2kT(R)\cdot(v_x'^2+v_y'^2+v_z'^2)\} \qquad (15)$$

where R represents the position of guiding center and is expressed by cyclotron frequency ω_c and the actual position of ions (x,y).

$$R^2=\{x+(v_y'/\omega_c)\}^2+\{y-(v_x'/\omega_c)\}^2 \leq a^2 \qquad (16)$$

Calculation is performed by dividing the plasma diameter in n-th section. In the each section, the ion density and the temperature are assumed to be constant. If we denote an injecting velocity of particles as v, the time which is required to pass through one section becomes (2a/nv), so that the deflecting width W expressed in Fig.2 becomes

$$W\simeq(2L/v)\cdot\sqrt{(2a/nv)\cdot\sum_{i=1}^{n}<\Delta v_1\Delta v_1>_i}\ . \qquad (17)$$

From W, one can estimate the plasma temperature. We used here n=21 sections, however the result does not depend almost on number of n. Figure 3 shows the temperature dependence of W in which the parameter shows injecting energy.

References:
/1/ E.V.Aleksandrov, V.V.Afrosimov and E.L.Berezovskii, JETF Lett. 29 1(1979)
/2/ V.G.Abramov, V.V.Afrosimov, I.P.Gladkovskii, A.I.Kislyakov and V.I.Perel, Sov.Phys.-Tech.Phys. 16 1520(1972)
/3/ N.F.Mott, H.S.W.Massey, Theory of Atomic Collisions, Second ed. Oxford Univ. Press(1949) p.127,191
/4/ M.N.Rosenbluth, W.M.MacDonald and D.L.Judd, Phys.Rev. 107 1(1957)

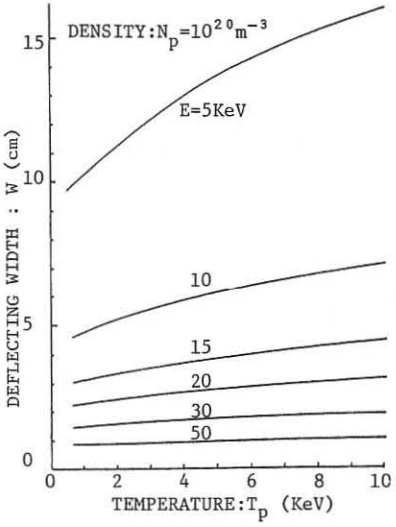

Fig.3
Deflecting width calculated by using longitudinal diffusion coefficient

EQUILIBRIUM MAGNETIC MEASUREMENTS BY TOROIDAL MULTIPOLAR METHOD FOR FTU TOKAMAK

F. Alladio and F. Crisanti
Associazione EURATOM-ENEA sulla Fusione, Centro di Frascati
C.P. 65 - 00044 Frascati, Rome, Italy

The circular cross section of FTU [1] vacuum vessel indicates as a natural choice the use of fully toroidal coordinates $(\theta, \tilde{\omega}, \phi)$ (see Fig. 1) for equilibrium magnetic measurements. They are connected with the cylindrical coordinates (r, z, ϕ) by

$$r = \frac{R_o \, sh\theta}{ch\theta - cos\tilde{\omega}} \quad ; \qquad z = \frac{R_o \, sin\tilde{\omega}}{ch\theta - cos\tilde{\omega}} \tag{1}$$

where R_o is determined by the major and minor radius R_{pr} and a_{pr} of the torus $\theta = \theta_{pr}$ on which the measuring probes are sitting:

$$ch\theta_{pr} = R_{pr}/a_{pr} \quad ; \qquad R_o = \sqrt{R_{pr}^2 - a_{pr}^2} \tag{2}$$

In axial symmetry the equation for the flux function $\psi = 2\pi r A_\phi$ is (j_ϕ being the current density)

$$\frac{\partial^2\psi}{\partial\theta^2} + \frac{\partial^2\psi}{\partial\tilde{\omega}^2} - \frac{1 - ch\theta cos\tilde{\omega}}{sh\theta\,(ch\theta - cos\tilde{\omega})}\frac{\partial\psi}{\partial\theta} + \frac{sin\tilde{\omega}}{ch\theta - cos\tilde{\omega}}\frac{\partial\psi}{\partial\omega} = -\frac{2\pi\mu_o R_o^3 sh\theta}{(ch\theta - cos\tilde{\omega})^3} j_\phi \tag{3}$$

The homogeneous equation admits (almost) separable solutions ("harmonics") expressible in terms of the Fock functions [2] $f_m(ch\theta)$ and $g_m(ch\theta)$. These correspond to the flux functions of internal and external current multipole fields (see Fig. 2).

$$i\,\{^{s}_{c}\,\psi_m = \frac{f_m(ch\theta)}{\sqrt{ch\theta - cos\tilde{\omega}}}\,\{^{sin\,(m\tilde{\omega})}_{cos\,(m\tilde{\omega})} \quad ; \qquad e\,\{^{s}_{c}\,\psi_m = \frac{g_m(ch\theta)}{\sqrt{ch\theta - cos\tilde{\omega}}}\,\{^{sin\,(m\tilde{\omega})}_{cos\,(m\tilde{\omega})} \tag{4}$$

The normalization of the Fock functions has been decided as

$$g_m(ch\theta) = -\,sh\theta\,\frac{d}{d\theta}\,Q^{\circ}_{m-\frac{1}{2}}(ch\theta) \quad ; \qquad f_m(ch\theta) = sh\theta\,\frac{d}{d\theta}\,P^{\circ}_{m-\frac{1}{2}}(ch\theta)$$

where the half integer order Legendre functions Q and P are the ones given by Morse and Feshbach.

The solution of the inhomogenous equation by Green's function method is: ($\varepsilon_o = 2$; $\varepsilon_m = 1$ for $m \neq 0$)

$$\Psi(\theta,\tilde{\omega}) = \frac{\mu_o R_o^3}{\sqrt{ch\theta - cos\tilde{\omega}}} \iint d\tilde{\omega}_o d\theta_o \frac{j(\theta_o, \tilde{\omega}_o)}{(ch\theta_o - cos\tilde{\omega}_o)^{5/2}} \left[\sum_{m=0}^{\infty} \varepsilon_m \frac{\Gamma(m-\frac{1}{2})}{\Gamma(m+\frac{1}{2})} \right.$$

$$\left. [\cos(m\tilde{\omega}) \cos(m\tilde{\omega}_o) + \sin(m\tilde{\omega}) \sin(m\tilde{\omega}_o)] \right. \begin{cases} f_m(ch\theta)\, g_m(ch\theta_o); & \text{if } \theta < \theta_o \\ g_m(ch\theta)\, f_m(ch\theta_o); & \text{if } \theta_o < \theta \end{cases} \quad 5)$$

This naturally leads to define the following multipolar current density moments (the internal ones being generated by the plasma and the external ones by the poloidal windings)

$$M_m^{i\,\{c}_{s} = \int_0^{2\pi} d\tilde{\omega}_o \int_{\theta_{pr}}^{\infty} d\theta_o \mu_o R_o^3 \frac{\varepsilon_m j(\theta_o,\tilde{\omega}_o)}{(ch\theta_o - cos\tilde{\omega}_o)^{5/2}} \frac{\Gamma(m-\frac{1}{2})}{\Gamma(m+\frac{1}{2})} g_m(ch\theta_o) \begin{cases} \cos(m\tilde{\omega}_o) \\ \sin(m\tilde{\omega}_o) \end{cases} \quad 6)$$

$$M_m^{e\,\{c}_{s} = \int_0^{2\pi} d\tilde{\omega}_o \int_0^{\theta_{pr}} d\theta_o \mu_o R_o^3 \frac{\varepsilon_m j(\theta_o,\tilde{\omega}_o)}{(ch\theta_o - cos\tilde{\omega}_o)^{5/2}} \frac{\Gamma(m-\frac{1}{2})}{\Gamma(m+\frac{1}{2})} f_m(ch\theta_o) \begin{cases} \cos(m\tilde{\omega}_o) \\ \sin(m\tilde{\omega}_o) \end{cases} \quad 7)$$

Between the probe position θ_{pr} and the plasma surface it is

$$\psi(\theta,\tilde{\omega}) = \frac{1}{\sqrt{ch\theta - cos\tilde{\omega}}} \sum_{m=0}^{\infty} [E_m(\theta) \sin(m\tilde{\omega}) + F_m(\theta) \cos(m\tilde{\omega})] + C$$

$$\text{where } \begin{cases} E_m(\theta) = M_m^{e,s}\, g_m(ch\theta) + M_m^{i,s}\, f_m(ch\theta) \\ F_m(\theta) = M_m^{e,c}\, g_m(ch\theta) + M_m^{i,c}\, f_m(ch\theta) \end{cases} \quad 8)$$

In order to measure the multipolar moments it is convenient to use discrete $B_{\tilde{\omega}}$ coils and B_θ saddles equally spaced in the correct poloidal angle $\tilde{\omega}$. The constant C can be determined by a toroidal voltage loop. Performing the Fourier analysis of the saddles signal

$$S_1(\tilde{\omega}) = \sqrt{ch\theta_{pr} - cos\tilde{\omega}}\, \Psi(\theta_{pr},\tilde{\omega}) \quad 9)$$

and of the combination signal

$$S_3(\tilde{\omega}) = \left[S_2(\tilde{\omega}) + \frac{1}{2} \frac{sh\theta_{pr} S_1(\tilde{\omega})}{(ch\theta_{pr} - cos\tilde{\omega})^{3/2}} \right] \sqrt{ch\theta_{pr} - cos\tilde{\omega}} \quad 10)$$

(being $S_2(\tilde{\omega}) = -\frac{2\pi R_o^2\, sh\theta_{pr}}{(ch\theta_{pr} - cos\tilde{\omega})^2} B_{\tilde{\omega}}$ the coils signal)

one can obtain

$$M_m^{e\{_s^c} = -\left.\frac{S_{3m}^{\{_s^c} f_m - S_{1m}^{\{_s^c} \frac{\partial f_m}{\partial\theta}}{(m+\frac{1}{2})(m-\frac{1}{2})\,sh\theta}\right|_{\theta_{pr}} \quad ; \quad M_m^{i\{_s^c} = -\left.\frac{S_{1m}^{\{_s^c} \frac{\partial g_m}{d\theta} - S_{3m}^{\{_s^c} g_m}{(m+\frac{1}{2})(m-\frac{1}{2})\,sh\theta}\right|_{\theta_{pr}} \tag{11}$$

The coordinates $(\theta_c, \tilde{\omega}_c)$ of the weighted centre of the current in the plasma can be found from the internal m = 0 and m = 1 multipolar moments by

$$\frac{g_1(ch\theta_c)}{g_o(ch\theta_c)} = -\frac{3}{2}\frac{\sqrt{(M_1^{i,c})^2 + (M_1^{i,s})^2}}{M_o^{i,c}} \quad ; \quad tg\tilde{\omega}_s = \frac{M_1^{i,s}}{M_1^{i,c}} \tag{12}$$

As in this expression the external multipolar moments are absent the current weighted centre cannot be controlled externally in a proper way. If a circular limiter at $\theta = \theta_L$ is used, it appears fron Eq. 8) that the only nontrivial way to obtain $\Psi(\theta_L, \tilde{\omega}) = \text{const}$ on the limiter is to impose $E_m(\theta_L) = F_m(\theta_L) = 0$; i.e. the external windings must provide external moments proportional to the internal ones

$$M_m^{e\{_c^s} = -M_m^{i\{_c^s} \frac{f_m(ch\theta_L)}{g_m(ch\theta_L)} \tag{13}$$

In such a case simple expressions for relevant plasma parameters can be obtained.

The safety factor q_ψ at the limiter is: (B_o being the toroidal field at R_o)

$$q_\psi = \frac{d\phi}{d\psi} = \frac{B_o R_o^2}{sh\theta_L}\int_o^{2\pi} \frac{d\tilde{\omega}}{\sqrt{ch\theta_L - cos\tilde{\omega}}\ \{\Sigma_m\ [\left.\frac{\partial F_m}{\partial\theta}\right|_{\theta_L} cos(m\tilde{\omega}) + \left.\frac{\partial E_m}{\partial\theta}\right|_{\theta_L} sin(m\tilde{\omega})]\}} \tag{14}$$

neglecting terms of the second order this becomes

$$q_\psi = \frac{2\sqrt{2}\ B_o R_o^2}{sh\theta_L \left.\frac{\partial F_o}{\partial\theta}\right|_{\theta_L}} \left.\{[2ch\theta + (\frac{\partial F_1}{\partial\theta}/\frac{\partial F_o}{\partial\theta})]\, g_o - [1 + ch\theta\,(\frac{\partial F_1}{\partial\theta}/\frac{\partial F_o}{\partial\theta})]\, g_1\}\right|_{\theta_L} \tag{15}$$

Following Shafranov [3] with $\alpha = 1 + (1+\delta)\, ch\theta_L/sh\theta_L$, where $\delta = (R_t - R_o)/R_o$ (R_T being the weight centre of the total plasma pressure), it is possible to obtain

$$\beta_p + \frac{l_i}{2} = \frac{1}{32\pi\mu_o^2 R_o^2 I_p^2} \{ 3\alpha\left(\frac{\partial F_o}{\partial\theta}\ \frac{\partial F_1}{\partial\theta}\right) + \alpha \sum_{m=1}^{\infty} [\frac{\partial F_m}{\partial\theta} \left(\frac{\partial F_{m-1}}{\partial\theta} + \frac{\partial F_{m+1}}{\partial\theta}\right)$$

$$+ \frac{\partial E_m}{\partial\theta} \left(\frac{\partial E_{m-1}}{\partial\theta} + \frac{\partial E_{m+1}}{\partial\theta}\right) - \frac{2(\alpha-1)}{ch\theta} \sum_{m=o}^{\infty} [\left(\frac{\partial E_m}{\partial\theta}\right)^2 + \left(\frac{\partial F_m}{\partial\theta}\right)^2]\} \Big|_{\theta_L} \qquad 16)$$

REFERENCES

[1] Frascati Tokamak Upgrade, Frascati report 82.49 (1982);
[2] V.A. Fock, Fiz. Zh. Sovietunion 1 (1932) 215 - 236
[3] V. D. Shafranov, Plasma Phys., 13 (1971) 757 - 764

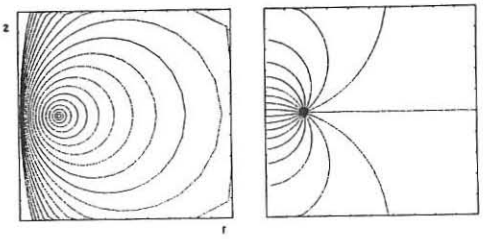

Fig. 1 - Poloidal projections of θ = const (tori) and $\tilde{\omega}$ = const (spheres) surfaces

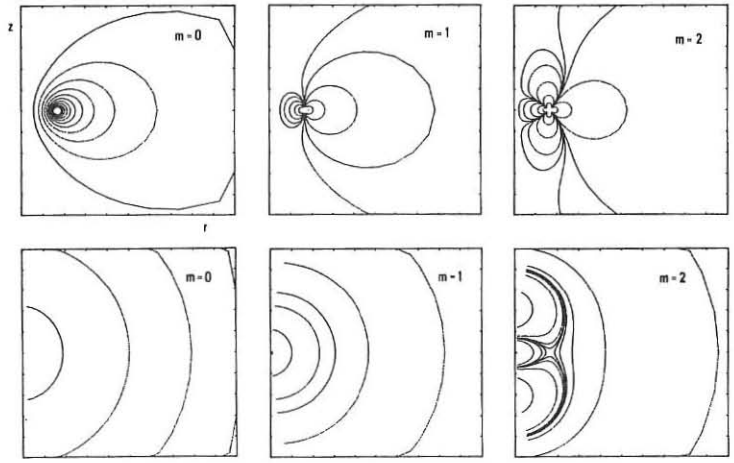

Fig. 2 - Poloidal projections of m = 0,1,2 flux surfaces of internal (upper line) and external toroidal "harmonics"

ION BERNSTEIN MODES FLUCTUATIONS AS A MEASURE OF THE MAGNETIC FIELD ORIENTATION

Th. LEHNER

Laboratoire de Physique des Milieux Ionisés
Groupe de Recherche 29 du C.N.R.S.
Ecole Polytechnique, 91128 Palaiseau Cedex (France)

INTRODUCTION.

It is a crucial point in magnetically confined fusion plasmas to get the local magnetic field direction of the medium. A previous method using the modulation of the scattering form factor of electron density fluctuations $S(k, \omega)$ with the angle θ of the wave number k with the magnetic field (B) at electron cyclotron harmonics has been performed /1-3/. Another currently proposed diagnosis consists in selecting the polarisation of transition lines presenting the Zeeman effect /4/.

We suggest a new method in the low frequency (ion) range. In this last region of the spectrum the fluctuations perpendicular to the B field arise from ion Bernstein modes in homogeneous plasmas.

ION BERNSTEIN WAVES.

We remind the existence of two extreme kind of modes depending on the magnitude of cos θ, /5/,

$$\text{for : } 0 \leq \cos\theta \leq \frac{2\pi}{k\rho_i}\frac{V_i}{V_e} = \delta, \quad \left(\delta \simeq \left(\frac{m_e}{m_i}\right)^{\frac{1}{2}} \text{ if } k\rho_i \simeq 1, \frac{T_e}{T_i} \simeq 1\right)$$

we are dealing with pure ion Bernstein modes (PBM). (V_s is the thermal velocity of either electron or ion particules, ρ_i is the ion Larmor radius). For these waves the wave phase velocity parallel to the B field is well above the electron thermal velocity : $V_{\varphi//} = \omega/k_{//} >> V_e$. As a consequence electrons are frozen along the B field and they don't answer to the ion fluctuations /6-7/.

$$\text{For } \delta << \cos\theta << \min\left(1, \frac{2\pi}{k\rho_i}\right)$$

we have the quasi-neutralized Bernstein modes (QNBM). For those waves on the opposite we have $V_{\varphi//} << V_e$: electrons can be considered as Boltzmanian and there is no electron Landau damping.

DENSITY FLUCTUATIONS FORM FACTOR SHAPE.

In this last cos θ range $S(k,\omega)$ is deeply modulated in θ /8/. But the behavior of $S(k,\omega)$ is different in the first θ range : because of the progressive freezing of all the electrons the spectrum narrows and for $\theta = \pi/2$ it shrinks to its zero frequency component where all the power lies there. We propose the study of the migration of the power towards $\omega = 0$ as a function of the θ angle as a diagnosis for determining the B field direction.

We have already studied the form factor, whose expression is well known in a warm, collisionless, infinite, homogeneous plasma to give a ion tempera-

ture diagnosis by looking at the spectrum shape in the ion cyclotron (QNBM) frequency range /9/.

Figure 1 shows the smearing out of the cyclotron resonance of quasi-neutralized waves as one looks nearer and nearer to a perpendicular of the B field.

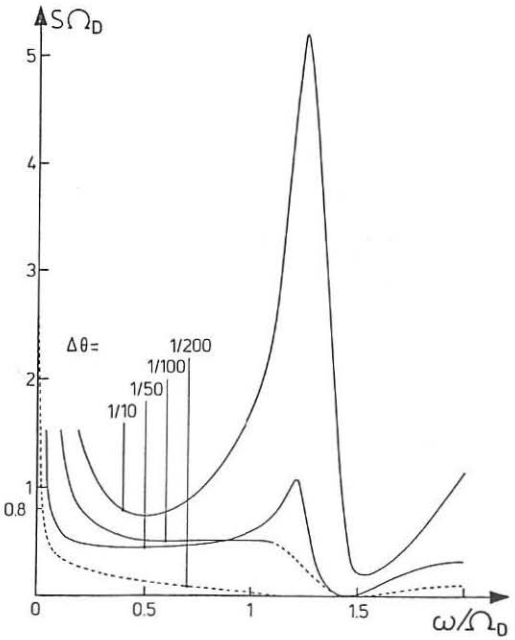

Fig. 1 : $S(k,\omega)$ for fixed $k_{\perp_o}$ ($k_{\perp_o}\rho_i = 1.3$) and various θ angle of $\bar{k}$ with the magnetic field $\underline{B}$ near the perpendicular position : $\Delta\theta = \pi/2 - \theta$. $S(k,\omega)$ is plotted as function of frequency. Ω_o is the ion (deuterium) gyrofrequency. As $\Delta\theta$ goes to zero the cyclotron resonance disapears and the spectrum shifts to low frequencies.

When $(\pi/2) - \theta$ becomes smaller than δ the resonance vanishes as reminded above. One could notice the progressive correspondant enhancement of the zero frequency amplitude. The total power

$$S_\infty(k) = \int_{-\infty}^{+\infty} S\ (k,\omega)\ d\omega$$

is given by a sum rule which is a consequence of the fluctuation dissipation theorem, for an equilibrium plasma /10/ ($T_e/T_i = 1$, and $S_\infty(k) = 2\pi$ for $k \ll k_d$, k_d being the Debye wave number, and semi-analytical expressions are available for $T_e/T_i \neq 1$, /11-12/.

Figure 2 gives the integrated power $A = \int_o^{\Delta\omega} S(k,\omega)\, d\omega$, for different angles of the wavevector k with the plane perpendicular to B. $\Delta\omega$ is a low pass filter cut-off chosen equal to half the ion cyclotron gyro-frequency

($\Delta\omega = \Omega_{ci}/2$). The half width (1/e points) of the spectrum provides the precision of the experiment. One sees that for instance, for Te/Ti = 2 (a common temperature ratio in Tokomaks), we get $\underline{2}\ \delta_1 = 1/10\ (m_e/m_i)^{\frac{1}{2}}$, a precision on θ of 0.05° is then indicated for a deuterium plasma.

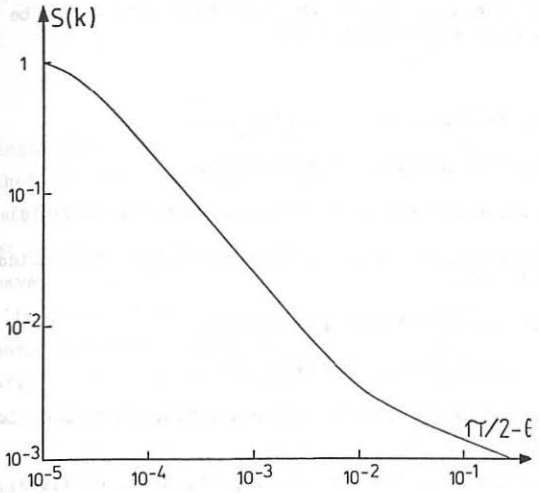

Fig. 2 : Integrated power $S'(k) = 2/S_\infty(k) \int_0^{\Delta\omega} S(k,\omega)\, d\omega$, as a function of the angle θ near $\pi/2$. S' and θ each being plotted on a logarithmic scale.

Let us now discuss the application to a Tokamak plasma. The B field is mainly the sum of two contributions : the toroidal field B running along the torus lines and the poloïdal field B_p which causes the helicoïdal (shear) structure of the total field.

In a real measurement by electromagnetic wave scattering one must cope with a finite $k_{//}$ resolution. $\Delta k_{//}$ should be low enough (for $\Delta k_{//}/k_o < \delta$ to avoid the Bernstein resonance). Besides the form factor is not sensitive to the central k_o value. For infrared light Thomson scattering, the laser wavelength is much smaller than the wavelength of fluctuations and one should use a tangential sight, with respect to the toroïdal direction. The $k_{//}$ resolution mainly arises from two terms :

$$\frac{\Delta k_{//}}{k_o} = \frac{2w}{L_s(r)} + \frac{1}{4k_o\sqrt{R\,w}}$$

(where w is the laser beam waist, R the mean large radius, L_s the shear length, r the radial small radius distance), the first term is due to shear, the second one to the geometry due to the lack of resolution, this could be minimized by matching w.

One need to perform two experiments in different perpendicular directions with respect to $\underline{B}$ in order to get the local absolute B direction. A preliminary try in the equatorial plane where B reduces to its toroïdal component could test the method.

In conclusion, by using the scattering of light on pure ion Bernstein modes, we have shown that a measurement of the B field direction can be performed with a good precision of the order 0.05°.

/1/ Sheffield J., Plasma Phys., 14 (1972) 385.

/2/ Carolan P.G., Plasma Phys., 19 (1977) 757.

/3/ Forrest M.J., Carolan P.G., Peacock N.J., Nature, 27 (1978) 718.

/4/ Fujita J., McCormick F., Int. Conf. on Controlled and Nuclear Fusion, Vienna, (1976) 191.

/5/ Schmitt J.P.M., Thèse d'Etat, Paris (1973).

/6/ Fejer J.A., Can. J. Phys., 39 (1961) 716.

/7/ Farley D.T., Dougherty J.P., Barron D.W., Proc. Roy. Soc. London, 263 (1961, 238.

/8/ Dougherty J.P., Farley D.T., J. of Geophys. Res., 68 (1963), 5473.

/9/ Schmitt J.P.M., Lehner T., Phys. Rev. Letters, 45 (1980), 1185.

/10/ Sitenko A.G., Fluctuations and Nonlinear wave interactions in plasmas, Pergamon Press, (1982).

/11/ Farley D.T., J. of Geophys. Res., 71 (1966), 4091.

/12/ Fejer J.A., Kohl H., J. of Geophys. Res., 85 (1980), 781.

Observation of Plasma Turbulence by Coherent Far Forward Scattering Using a Multi Channel Detector Array at 10 Microns

M. von Hellermann, H.J.Gülker, O.R.Hasse
FB Physik, Universität Essen, 43 Essen 1, FRG

Long wavelength electron density fluctuations in a plasma can be determined by the method of far-forward-scattering [1] i.e. scattering experiments where the scattering angle is comparable to the divergence of the probing beam. Experiments in the IR at 10.6μ [2], [3] in the FIR at 1.2 mm [4] and with microwaves at 8mm have been reported [5].

The method is based on a Fourier optics approach to plasma scattering of electromagnetic radiation which leads to an analytical description of the spatial profile of the resulting scattered fields and that of the undeviated probe beam. For small scattering angles the fields of the scattered light and of the probe beam overlap spatially and lead to intermediate frequency signals. The spatial profile of the intermediate frequency scattering signal contains information on the wavelength, the location, the fluctuation level and the direction of propagation of the investigated waves. To make use, however, of the full potential of this diagnostic technique, the spatial profile of the amplitude and the phase of the scattered signal has to be recorded simultaneously by several detectors.

The spatial and temporal development of fluctuation parameters can be constructed in a wide range of frequencies during one single plasma discharge. This might especially useful for turbulent plasmas with non reproducible fluctuation frequency spectra.

The range of fluctuation wavelength which can be analysed by this method is $w_o < \Lambda < 30\ w_o$ where w_o is the 1/e-radius of the probe beam waist in the plasma. The observable frequency range is mainly limited by the sampling rate and temporal window of the ADC's recording the detector signals. The method is equivalent to a time resolved holographic diagnostic of electron density fluctuations and may be especially suitable for plasma heating experiments.

In this paper we describe results from a turbulent plasma experiment where a dispersion of electron density waves is obtained by this method from one

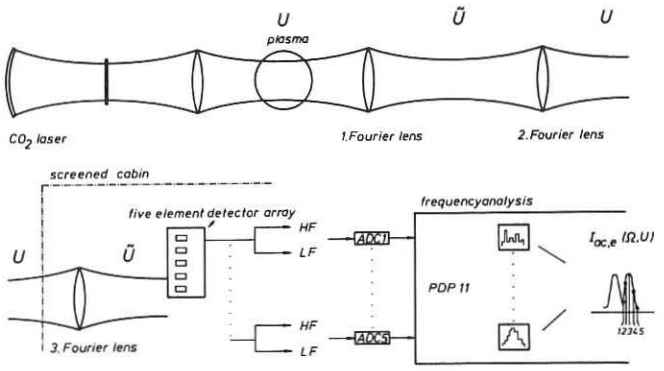

Fig.1 Scattering arrangement using a five element detector array

single plasma discharge.

The plasma is excited in a travelling wave assembly [6] where an external high power, high frequency pulse (100 MWatt, 1 MHz, 12μsec) is fed into a linear transmission line , the inductances of which are the magnetic field coils surrounding the plasma vessel. This leads to the excitation of cylinder symmetrical compressional Alfvén waves which are strongly enhanced in the case of resonant eigenmodes. Up to 90% of the high frequency power is dissipated in this case.

The scattering arrangement schematically in fig. 1. The scattered signals are detected by an array of five Ge:Hg (SBRC) detector elements in the front focal plane of the fourier transforming lens.

Two regimes of operation are investigated. In the first regime of operation ($B_{axial} \approx 0.03$ Tesla), where $\Omega_{pump} \sim 2\Omega_{ci}$ and $v_{Alfvén} \approx v_{ionacoustic}$ strong fluctuations in the direction perpendicular to the magnetic field are found.

The amplitude frequency spectra are nearly monochromatic. The wavelengths are in the order of 5 cm and $K_{\perp}\rho_{ci} \sim 1$. In the second representative regime of operation (B_{oz}=0.12 Tesla), where the axial magnetic field, the mean electron density and temperature show high spatial and temporal gradients, a broad fluctuation frequency spectrum is observed with wavelength in the order of a few mm . An example of the resulting wavelengths and density levels as a function of the observed frequencies are displayed in fig.2. The number of the evaluated frequency channels is limited in this case mainly by the sampling rate of the ADC's . The signal level are approximately two orders of magnitude above the shot noise level of the detector-amplifier system.

The observed wavelength in the order of a few mm and the observed density level correspond to electrical fields which are enhanced with respect to the first regime of operation. The broad frequency spectra are quantitatively

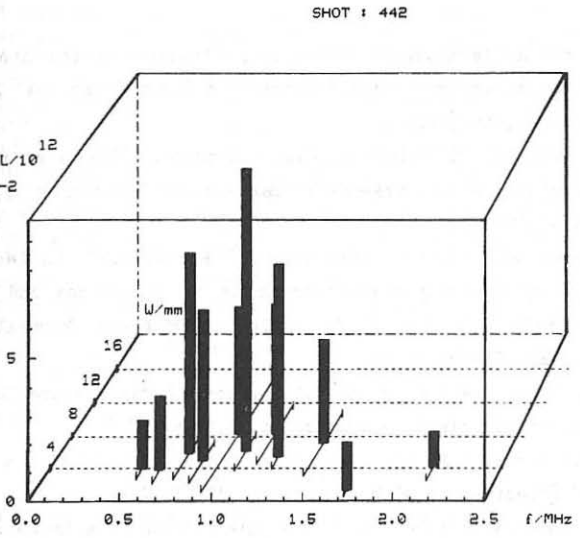

Fig. 2 Fluctuation spectra observed in the direction perpendicular to the axial magnetic field in the turbulent plasma regime. The plot shows fluctuation level $\tilde{n}_e \cdot L$ and wavelength versus frequency.

not reproducible at discharges with identical external parameters. The enhanced electrical fields and the erratic spectra indicate a turbulent plasma state.

In an earlier incoherent ruby laser scattering experiment [7] in the same regime of operation distinctive deviations from a maxwellian distribution were found. The fluctuation wavelengths in the order of a few mm observed in the present experiment confirm the former assumption that the observed distortion in the incoherent maxwellian spectra were due to fluctuation wavelength wavelengths comparable to the dimensions of the scattering volume .

A quantity which has been hitherto neglected in scattering experiments is the phase of the scattered signal. It is verified that it gives immediate information on the direction of propagation. In the first regime of operation where nearly monochromatic and reproducible spectra are observed the spatial profiles of the phase of the scattered signal are smooth wheras in the turbulent regime the phase profiles display erratic non reproducible jumps. This is a further indication for the turbulent plasma state.

[1] D.E.Evans, M.v.Hellermann, E. Holzhauer, "Fourier Optics Approach to Far Forward Scattering and Related Refractive Index Phenomena" . Plasma Physics 24,819 (1982),

[2] D.E.Evans, E.Doyle, D. Frigione, M.v.Hellermann, "Measurement of Long Wavelength Turbulence in a Tokamak by Far Forward Scattering." Plasma Physics 7(1983),

[3] M.v.Hellermann, H.J.Gülker, E.Holzhauer, " Far Forward Scattering from Plasma Fluctuations Using a Detector Array at 10 Microns and Coherent Data Processing". VII. Int. Conf. on IR and MM Waves, Marseille 1983, submitted to IEEE Plasma Sciences,

[4] B.W.James , C.X.Yu, W.A.Peebles, N.C.Luhmann, " Far Forward Scattering at Millimeter Wavelength." Bull.Amer.Soc.27,1098(1982)

[5] Y.Sonoda, A.Sakurai, K.Muraoka, M.Akazaki, "Measuremt of Plasma Waves by Fraunhofer diffraction ." Jap.J.Phys. 21,372(1982),

[6] K.H.Finken, A.Stampa, H.Tuczek, " The Interaction of a Large Amplitude Travelling Wave a Cylindrical Plasma." Z.Natf.30A,195(1975)

[7] M.v.Hellermann, A.Stampa, "Correlation Analysis of of the Electron distribution Function in a Turbulent Plasma:" Phys.Lett. 68A, 333(1978)

ECE SIMULATION FOR A TOROIDAL PLASMA AND ITS APPLICATIONS TO JET (*)

A.C.Airoldi, A. Orefice, G. Ramponi

Istituto di Fisica del Plasma - EURATOM/CNR
Fusion Association - Via Bassini,15, 20133 Milano (Italy)

(*) Work done under JET contract n. JB2/9005

In toroidal plasmas in thermal regimes, an important tool for the diagnostics of the electron temperature T_e profiles is given by the analysis of the electron cyclotron emission (ECE). In the JET facility, T_e profiles shall be obtained both in the equatorial plane and normally to it /1/, by using a set of 10 antennas located in a port on the low magnetic field side at different distances and inclination angles with respect to the equatorial plane. Physically important features to be taken into account in the model simulating the emitted spectra are those due to refraction, toroidal and poloidal magnetic field, and finite relativistic line width, as imposed by the substantial perpendicularity to the magnetic field $\underline{B}$ of the antenna lines of sight. We have developed a numerical code keeping all these features into account in the computation of the single pass emitted intensities in thermal regimes, both for the case of circular concentrical and D-shaped magnetic equilibrium surfaces /2/. We refer to a moderate temperature regime ($T < 10$ Kev) where the cyclotron radiation spectrum is basically in the low harmonic range, and a separate description of different harmonic contributions is possible. By using Kirchhoff's law and the well know integral solution of the radiative transfer equation /3/, the radiation intensity leaving the plasma at a given frequency ω and in a given polarization mode is computed along the ray trajectory, obtained by solving the relevant Hamiltonian system of geometrical optics equations in toroidal geometry /4/. While the use of the cold dispersion relation is both convenient and allowable /5/ for the ray tracing, the absorption coefficient must be calculated by using a relativistic warm plasma theory, even for not strictly perpendicular propagation angles with respect to $\underline{B}$. In our code we make use of the exact expression of the weakly relativistic plasma dispersion functions in terms of the Fried and Conte Z-function as given in Ref./6/. The warm dispersion relation may be always written in the form:

$$C_o\, n_\perp^4 - C_1\, n_\perp^2 + C_2 = 0 \qquad (1)$$

where $n_\perp$ is the component of the refractive index normal to the total magnetic field and the coefficients C_o, C_1 and C_2 depend on $n_\perp$ for harmonic numbers $\ell > 1$. By iterating the "cold" $n_\perp$ value in these coefficients, as allowed when $|I_m(n_\perp)| \ll |R_e(n_\perp)|$, eq.(1) may be treated in any case as a biquadratic. We simulate the finite pattern of each antenna by considering a set of entering rays characterized by their divergence angles with respect to the antenna axis. In Fig. 1 we show the unrefracted beams of 9 antennas in the poloidal

plane for circular concentrical magnetic surfaces. After a suitable choice of radial positions along each unrefracted beam, the code determines, for each assigned harmonic number, the relevant resonant frequencies at which the ray trajectory and the emission intensity are computed. In the computations illustrated in Figs. 2 and 3 we have assumed parabolic profiles for the safety factor q the electron density n and temperature T_e with:

$$q(0) = 1 \; ; \quad q(a) = 3 \; ; \quad n(0) = 5 \times 10^{19} m^{-3} \; ; \quad T_e(0) = 1 \text{ keV} .$$

Fig. 2 shows the refracted beams of 3 antennas for different frequencies and polarization modes. The width of the emission layer is represented by two vertical bars, the one with the arrow indicating the resonant position. The label (a) indicates the case of an ordinary mode resonating as second harmonic in the region 2 and as first harmonic in the region 1. In this overlapping case the contribution to the total emitted intensity due to the first harmonic turns out to be quite stronger than the one due to the second harmonic. The code takes properly into account both of them including reabsorption. Labels (b) and (c) refer to refracted beams of antennas whose lines of sight are oblique with respect to the equatorial plane, in the case of a second harmonic X-mode. In the last two cases the computed optical depths are large enough to ensure black-body emission. In Fig. 3 we show a typical example of simulated intensity (normalized to the black-body central intensity) obtained at the second harmonic along a vertical line in the low field half of the poloidal plane. Dots (·) represent the O-mode intensities and crosses (+) the X-mode intensities. Each dot or cross refers to a different antenna. The continous line represents the assumed temperature profile. The plasma, for the considered parameters, is optically thick for the X-mode, while it is optically thin, as expected, for the O-mode. It is seen that a minimum (rather than a maximum) of O-mode intensity characterizes the central region of the plasma. This is due to the fact that the absorption (and emission) of the O-mode at the second harmonic has an "oblique" optimal angle of propagation, as pointed out also in Ref /7/. Owing to the fact that, in our geometry, $n_{\parallel}$ depends also on the poloidal magnetic field, a larger contribution to the O-mode intensity is to be expected for antennas whose line of sight encounters resonant regions with higher poloidal magnetic field.

References

/1/ Costley A.E., Baker E.A.M., Bartlett D.V., Clark W.H.M., Kiff M.G., Neill G.F. : Feasibility of Diagnosing the JET Plasma Using ECE , Report 19.1, Contract B-EH395, NPL (Teddington, U.K., 1980)

/2/ Airoldi A.C., Orefice A., Ramponi G. : ECE Simulation Code for JET, Report EURATOM-CNR FP 83/5 (Milan,Italy,1983)

/3/ Bekefi G., Radiation Processes in Plasmas, Wiley and Sons, 1966

/4/ Stix T.H., The Theory of Plasma Waves, McGraw-Hill, 1962

/5/ Weitzner H., Batchelor D.B., Phys. Fluids 23 (1980), 1359

/6/ Krivenski V., Orefice A., to appear on J. Plasma Physics

/7/ Hui B., Chu K.R., Ott E., Antonsen T., Phys. Fluids 23 (1980), 822

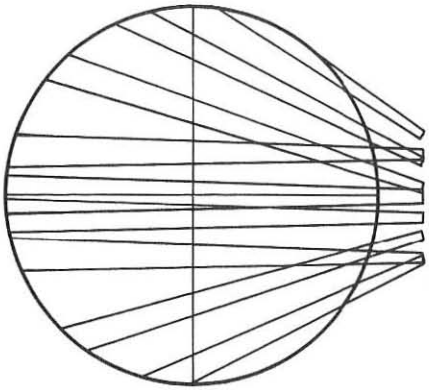

Fig.1

Unrefracted beams of the antennas, in a poloidal section.

Fig. 2

Refracted beams for 3 antennas.

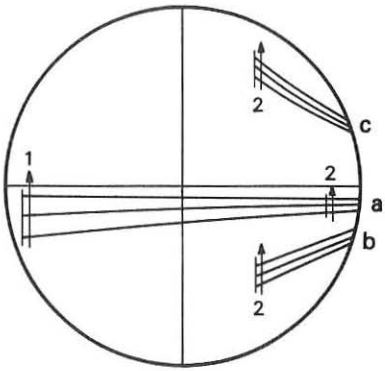

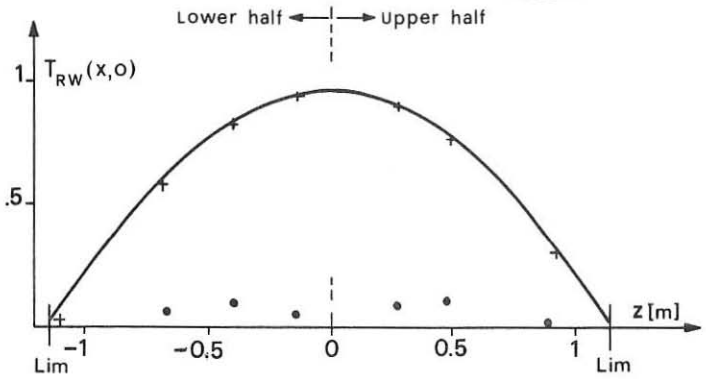

Fig. 3 Radiative temperature for 2^{nd} harmonic X-mode (+) and O-mode (·) along a vertical chord. The continuous line represents the assumed T_e profile.

Space Potential Measurements on EBT-S and ISX-B

G.A. Hallock, R.L. Hickok, W.C. Jennings, K.A. Connor
J.C. Forester, J.R. Goyer, J. Mathew, L. Solensten
Rensselaer Polytechnic Institute, Troy, NY 12181
G.R. Haste, A.J. Wootton
Oak Ridge National Laboratory, Oak Ridge, TN 37830

Direct measurements of the plasma space potential are obtained using heavy ion beam probes. On EBT, a cesium ion beam, 5 KeV < E_{beam} < 40 Kev, is directed into the plasma on the midplane of cavity E6. The beam follows a curved trajectory through the cavity, determined by injection parameters and the magnetic field. Within the plasma beam ions undergo impact ionization and generate a flux of multiply charged secondaries, $C_s^+ + e \rightarrow C_s^{+n} + (n+1)e$. A parallel plate electrostatic energy analyzer measures the energy of secondaries created within a small sample volume (typically ~ 1 cm^3), defined as the volume element along the beam where secondaries have trajectories such as to enter the analyzer. The plasma potential within the sample volume is given by the energy increase of the secondary ions, $ne\phi = E_s - eV_{beam}$.

The heavy ion beam probe on EBT has provided detailed steady state profile measurements for a wide range of machine conditions (pressure, power, etc.) /1/. Recently, the system has been upgraded to provide wide bandwidth measurements in order to follow rapid changes in plasma density and potential. This capability will allow detailed fluctuation studies [$\tilde{\phi}$, $\tilde{nf}(\tilde{T_e})$], and measurements during pulsed experiments designed to enhance EBT performance (ex., higher density T-mode operation) and provide diagnostic information (ex., the energy confinement time, τ_e).

Measurements obtained during a microwave power pulsing experiment are shown in Fig. 1. Here the 28 GHz gyrotron, which provides the power input to the plasma, is modulated between 69 and 112 KW, with a duty cycle of 5 ms at the lower power and 12 ms at high power. The EBT fill pressure is $6x10^{-6}$ Torr, providing mid-T mode operation at both power levels. At 0 < t < 1 ms the power is switched from high to low (the uncertainty is in the tube's output response to drive modulation). The power is returned to the high level at approximately 6.3 ms.

Measurements of the plasma potential, ϕ, and the total secondary current, i_{sum}, are shown in the figure. Data are from the core (near the plasma center, r < 4 cm) and in the hot electron ring region, r ~ 13 cm. Ring measurements are sensitive primarily to the bulk plasma, since the ring density is ~ 10% bulk density, and the ionization cross section is low at the high ring temperature (T_r ~ 500 KeV). The secondary current level is proportional to the plasma density and temperature within the sample volume, $i_s \propto n_e f(T_e)$, where $f(T_e)$ is the effective cross section for impact ionization. For electron temperatures below ~ 100 eV, $f(T_e)$ increases strongly with temperature. Above ~ 100 eV the cross section peaks and then slowly decreases, making the secondary current level primarily sensitive to density changes. The repetitive spikes on the signals (0.6 ms period) are from beam chopping to establish the baseline noise level.

When the microwave power is switched low, at t ~ 1 ms, the secondary current level drops ~ 60% at both the core and ring locations. The decay

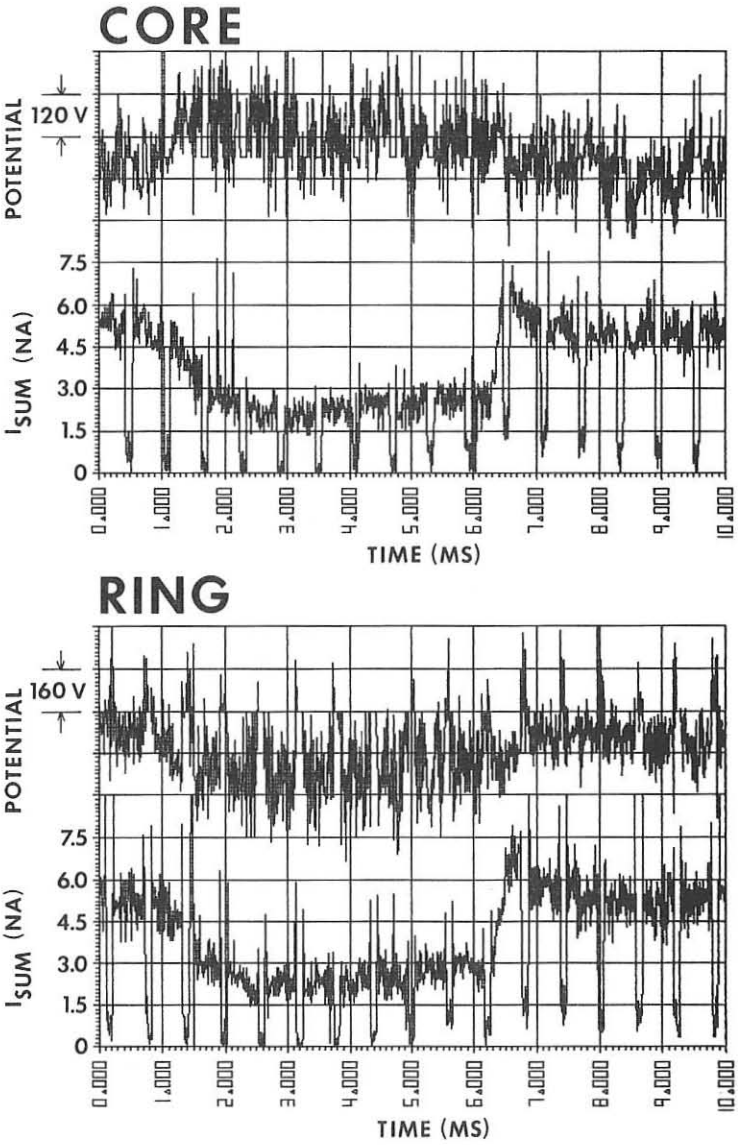

Fig. 1. Space potential and secondary current level measurements in the core and ring region of EBT-S.

time constant is ~ 1 ms. The plasma potential in the core increases, concurrently with a drop in potential in the ring region. The change is ~ 100 V in the core and ~ 150 V at the ring, yielding a net change in the potential well depth of ~ 250 V. This change is consistent with profile measurements during steady state /2/. When the power is returned to the high level, at t ~ 6.3 ms, the potential and total current change faster, with a time constant of ≤ 0.25 ms.

A heavy ion beam probe has recently been installed on the ISX-B Tokamak. A 200 KeV accelerator directs a C_s^+ beam (used at 8 KG and 10 KG toroidal fields) or a Tl^+ beam (used at 12 KG toroidal field) into the plasma at machine sector 13. A parallel plate electrostatic energy analyzer monitors secondary ions. The analyzer contains a 12 channel split plate detector, segmented to provide a dynamic range of > 8 KV and to allow monitoring toroidal deflection of the beam. Toroidal deflection results from the plasma current (typically > 250 KA). The resulting toroidal angle of the secondary ions must be accurately known, since the analyzer measures only the beam energy component along its axis. The analyzer sensitivity is ~ 25 V.

The heavy ion beam probe is capable of probing the upper outside of the ISX plasma, as shown in Fig. 2. This detection grid gives the range of beam injection energy and angle required at 8.8 KG with a cesium ion beam, and can be scaled to other field intensities and ion species by $E_{beam} \propto B^2/m$. The accessable plasma is limited primarily by the injector port size and location. A crossover sweep system may eventually be added to the beamline to allow more complete coverage of the plasma cross section.

Initial analyzer noise measurements have been made, during full ISX operation but with no beam injection. The noise level ranges from ~ 4 nA during low density ohmic discharges ($n_e \sim 2 \times 10^{13}$ cm^{-3}) to ~ 60 nA during high density ($n_e \sim 6 \times 10^{13}$ cm^{-3}) discharges with 2 MW of neutral beam injection. The noise, primarily ultraviolet light entering the detector, is low frequency and should be easily separated from signals by sweeping or chopping the ion beam. Expected signal levels using cesium at 8.8 KG range from 50 nA at the plasma center to > 400 nA near the plasma edge. The signal level is lower in the plasma interior due to beam attenuation.

The accelerator has been voltage tested to 100 KV, and operated at 50 KV. Beam characterization and alignment are in progress. Beam operation during ISX shots is expected by the end of June, followed by initial secondary ion measurements. It is anticipated that we will calibrate the system early in July, and begin our detailed physics study.

The primary objective of initial operation is the measurement of radial space potential profiles during ohmic and neutral beam discharges. ISX-B has three 1.5 MW beamlines, which can be configured for co- or co+counter injection with the plasma current to study the role of induced toroidal angular momentum on plasma confinement. Initial results will be reported at this meeting.

/1/ Bieniosek, F.M.: Study of Plasma Confinement in Elmo Bumpy Torus with a Heavy Ion Beam Probe. Ph.D. Thesis, Rensselaer Polytechnic Institute, Troy, NY 1980.

/2/ Uckan, T., Berry, L.A., Hillis, D.L., Richards, R.K.: Confinement Scaling of Core Plasma Electrons in the ELMO Bumpy Torus Experiment, Phys. Fluids 25(7), 1982 1254-1255.

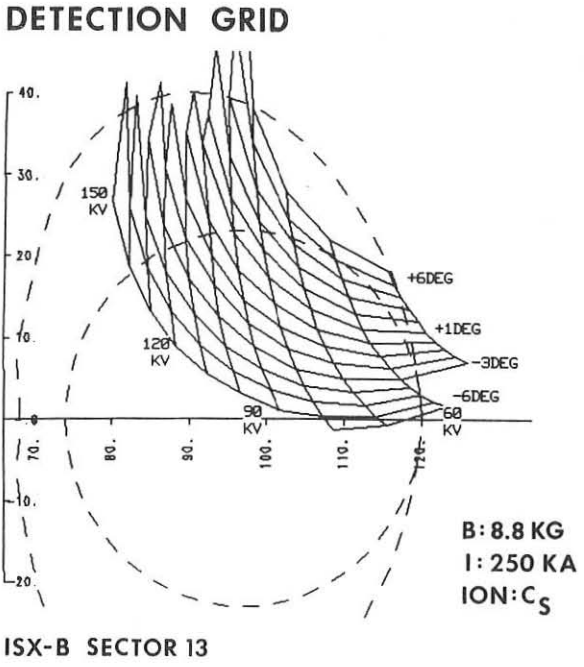

Fig. 2. Energy/angle detection grid for the ISX-B heavy ion beam probe.

MEASUREMENT OF THE PLASMA MAGNETIC FIELD WITH AN ION BEAM PROBE

G. Tonetti

Centre de Recherche en Physique des Plasmas
Association Euratom - Suisse
Ecole Polytechnique federale
21 av. des Bains, CH-1007 Lausanne Switzerland *

There are still no satisfactory methods for measuring the magnetic field structure inside a hot dense plasma. We propose to use an Ion Beam Probe (IBP) for this measurement. The IBP is already a well-established method for obtaining profiles of the plasma electron density and of the electric potential as well as fluctuations of these quantities (ref. 1 - 3).

This technique uses a monoenergetic well-collimated ion beam which is swept across the plasma. Collisions with the hot electrons produce secondary ions without appreciable change of their momentum ($I^{+}+e \rightarrow I^{++} + 2e$). The confining magnetic field separates these secondary ions from the primary beam and, if the energy is high enough, a fraction of them (the secondary beam) can be collected outside the plasma, as shown in fig. 1. The detector therefore ''observes'' a single small plasma volume which can be moved by sweeping the ion beam or changing its energy.

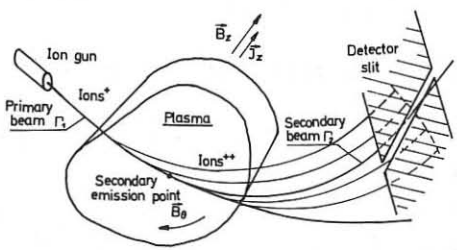

Fig. 1 Principle of the IBP

The secondary ions carry local information out of the plasma. The electron density and temperature are related to the beam current, and the electric potential is given by the change of kinetic energy of the ions [1]. Components of the magnetic potential can be measured if the field structure of the plasma device has an axis of symmetry k [3]. Then, the corresponding component of the canonical momentum of the probing ions $P_k = p_k + qh_k A_k$ is a constant of the motion. ($\vec{p}=m\vec{v}$ is the momentum and q is the charge of the ions, h_k is the metric coefficiant and $\vec{A}$ the magnetic potential). Referring to figure 1 with z as axis of symmetry, we have for the primary and secondary trajectories:

$$\Gamma 1)\ (p_z+qA_z)(\vec{r}_g) = (p_z + qA_z)(\vec{r}_i) \qquad \Gamma 2)\ (p_z+2qA_z)(\vec{r}_d) = (p_z+2qA_z)(\vec{r}_i)$$

where $\vec{r}_g$, $\vec{r}_i$, $\vec{r}_d$ are respectively the position of the ion gun, the secondary emission point and the detector. These relations allow us to derive the internal magnetic potential from the external velocity measured by the detector. We assume the initial condition $v_z(\vec{r}_g) = 0$ and we ignore the constant terms. Then:

$$A_z(\vec{r}_i) = \frac{m}{q} \cdot v_z(\vec{r}_d)$$

This particular component of $\vec{A}$ is the most interesting to measure because it is related to the poloidal field and to the current density. The surfaces A_z = const. are also magnetic surfaces. Similar results are obtained for a tokamak where the toroidal direction is an axis of symmetry.

For tokamak operation, we expect that the beam deflection in the toroidal direction $\delta = v_z/v$ (caused by the magnetic potential) will be of the order of 10-20 mrad. Since the divergence of the ion beam is of the order of 5 mrad, we must find a way to measure much smaller deflection angles than the divergence of the beam. The principle of such a detector is shown in figure 2 and 3. A grid (1) of equally spaced flat wires with a spacing d much smaller than the beam width splits the beam into equal segments. After crossing the drift space l, the beam segments are collected by the grid (2) and the plate (3). By simple geometrical inspection, it is easy to show that if the aperture angle of the detector $\beta = 2d/l$ is larger than the beam divergence γ, then the beam angle δ is given by:

$$\frac{I_2 - I_3}{I_2 + I_3} = \frac{l}{2d} \operatorname{tg} \delta$$

which is unaffected by the divergence (if $\gamma < \beta$ and $|\delta| < \beta - \gamma$) (fig 3 b).

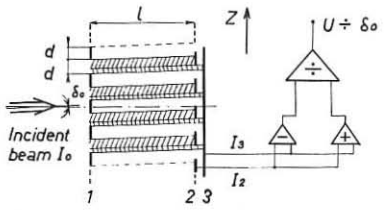

Fig. 2 Principle of the detector for measuring the incident beam angle

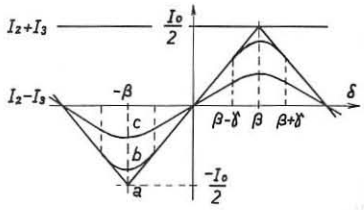

Fig. 3 Characteristic of the detector a) parallel beam b) divergent beam with $\gamma < \beta$ c) with $\gamma > \beta$

We have constructed such a detector as shown in Fig. 4 with d = 0.25 mm and l = 20 mm. Experimental tests have shown that the sensitivity is limited only by noise (amplifier noise and mechanical oscillations of the test bench). Fig.5 shows the output of the detector for an angular variation of the beam of $\pm$ 3.5 10^{-5}rad. The low frequency oscillation is caused by mechanical vibrations.

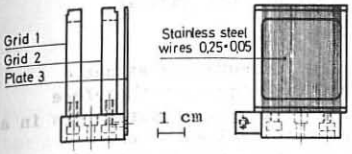

Fig. 4 Schematic of the detector

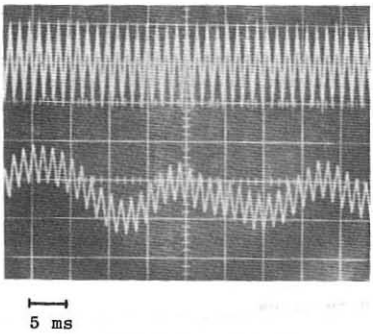

Fig. 5 Response of the detector
Upper sweep voltage
Lower detector response

The feasibility of the IBP technique for magnetic potential measurement has been tested with a 5 kV potassium beam probe on a cylindrically symmetric plasma produced by a DC hollow cathode arc discharge (fig 6) This system has the symmetry requirement for measuring the potential component Az related to the plasma current. However, the plasma diameter was too small to allow spatially resolved measurement of the potential profile. Therefore, we have only been able to measure the potential variations at a fixed point (centre of the plasma) due to a pulsed current of 10 A superposed on the DC plasma current (100A). The resulting calculated angular variations of the beam ($\delta = \Delta v_z/v$) to be measured are about $2 \cdot 10^{-4}$ rad. The result is shown in fig 7 which displays the measured angular variations (middle trace) and the plasma current (lower trace). The top trace is the total current of secondary ions collected by the detector. It is proportional to the plasma density and function of the electron temperature. The measured angular variation was callibrated by applying a known square wave voltage on the horizontal steering plates of the ion gun.

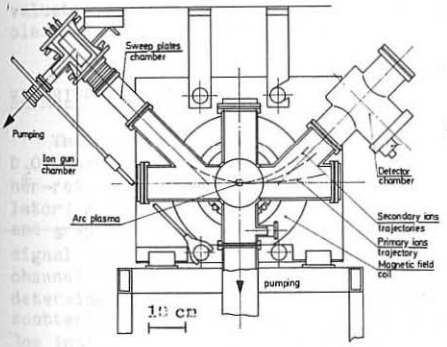

Fig. 6 Diagram of the experiment

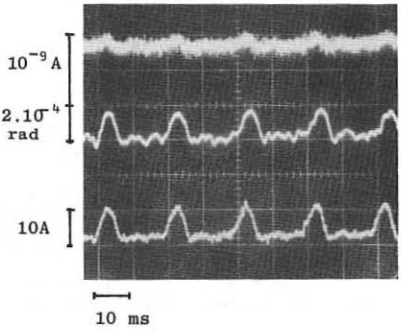

Fig. 7 Plasma Potential Measurement

The major problems encountered in this experiment were caused by the very low current of secondary ions ($\sim 10^{-9}$A) and a high noise level due to unstable plasma conditions. These problems will be much less important for a tokamak, because the current of secondary ions and the angular deflections are 2-orders of magnitude larger.

We have shown that the IBP diagnostic system can measure the magnetic potential related to the plasma current. This technique can therefore produce local and direct measurements of the most important parameters in a tokamak plasma. IBPs are however limited to small devices by the achievable probe beam energy (<500kV) and by the beam attenuation ($\int n_e d_l < 5 \cdot 10^{14} cm^{-2}$).

References

1. Bienosek F.M., Colestock P.L., Connor K.A Hickok R.L.

Elmo Bumpy torus Heavy Ion Probe
Rev. Sc. Inst. 51 (1980) p. 206

2. Hosea J.C., Jobes F.C. Hickok R.L. Dellis A.N.

Rotation and Structure of Low Frequency
Oscillations inside the ST tokamak
Phys. Rev. Lett. 30(1973) p. 839

3. Tonetti G. , Connor K.A.

The Direct Sensitivity of Particle Probes to the Magnetic field of Plasmas
Plasma Physics 22 (1980) p. 361

* Present address : JET Joint Undertaking Abingdon Oxon. England
OX14 3EA

385 μm D_2O Laser Collective Thomson Scattering Ion Temperature Diagnostic

P. Woskoboinikow, W.J. Mulligan, J. Machuzak, D.R. Cohn, R.J. Temkin, T.C.L.G. Sollner, and B. Lax

Plasma Fusion Center
Massachusetts Institute of Technology
Cambridge, MA 02139

ABSTRACT

Thomson scattering from ion thermal fluctuations in a tokamak plasma has been observed for the first time using a 385μm D_2O laser system on Alcator C. The frequency shift of the scattered radiation was consistent with ion temperatures between 0.7 and 1.5 KeV. Experimental accuracy was limited by stray light caused by restricted port access.

INTRODUCTION

Collective Thomson scattering from ion thermal fluctuations can provide a direct measurement of spatially resolved ion temperature /1/. This diagnostic capability can provide an important complement to other ion diagnostic techniques which in general become more limited as plasma size, density, and temperature increase in major fusion confinement experiments. Collective Thomson scattering ion temperature diagnostics have been used in ionospheric studies with radar /2/ and recently, in measurements of laboratory arc plasmas with CO_2 lasers /3/. However, the application to plasma confinement devices of interest for fusion research requires the development of substantially improved sources and receivers in the wavelength range between 10μm-1mm. In this paper we describe the first demonstration of the feasibility of this ion temperature diagnostic on such a device, Alcator C. Although the main goal of the present work is to show feasibility of ion temperature measurements, scattering from thermal level collective fluctuations should be valuable for the study of impurities, local current densities, growth of plasma waves, and turbulence.

EXPERIMENTAL SET UP

The major elements of this diagnostic are: a 200 kW, 1μs pulsed, 385μm D_2O laser /4/; a 20,000K (double side band) heterodyne receiver with a corner-reflector Schottky diode mixer /5/ and a 381μm DCOOD laser local oscillator; a 40dB N_2O gas cell filter for stray laser radiation rejection /4/; and graphite beam and viewing dumps inside the tokamak /6/. The down shifted signal (8.12-10.68 GHz) was frequency analyzed by a 32 channel, 80 MHz per channel filter bank. The scattering geometry on Alcator C was primarily determined by the available access using top and bottom ports resulting in a scattering angle of 20^0 with a scattering volume of a few cubic centimeters 3cm inside of the vacuum chamber axis.

MEASUREMENTS

Most of the scattering measurements were done at a magnetic field on the tokamak axis of 8 Tesla, peak densities > 2 X 10^{14} cm^{-3} and electron and ion temperatures on the order of 1 KeV, resulting in a range for the scattering parameter $\alpha = 1/K\lambda_D$ of 10-25. The receiver system was gated before and after the laser pulse to sample the background noise, mostly electron cyclotron emission. The two background noise samples were averaged and subtracted from the signal sample.

Stray laser radiation caused by the restricted diagnostic port access and diffraction placed the most severe limit on the present measurements. The stray radiation from inside the tokamak was about 60dB above the scattered signals. An N_2O absorption cell in front of the receiver prevented this radiation from saturating the Schottky diode mixer. The stray radiation and N_2O absorption cell effectively blocked from measurement the central $\pm$400 MHz of the scattered spectrum. This placed a lower limit on the measurable ion temperature of about 700eV in hydrogen and 1000eV in deuterium. The stray light problem also prevented observation of effects of impurities on the central part of the thermal spectrum or non-thermal scattering with frequency offsets of less than 400 MHz. At frequency offsets greater than 400 MHz an experimentally determined stray laser radiation level due to the low level D_2O laser linewidth /4/ was subtracted from the plasma scattered signals.

Fig. 1 shows a scattered spectrum for a hydrogen plasma with $\bar{n}_e$ = 3.6 X 10^{14} cm^{-3}. This data represents the average of six identical plasma shots. The error bars correspond to one standard deviation of the data average. The error bars are larger at smaller frequency offsets because of the stronger contribution from the subtracted stray radiation background. Also, there is an error bar on the frequency offset scale because the D_2O laser is tunable and there can be a shot to shot fluctuation or drift in its frequency. Three

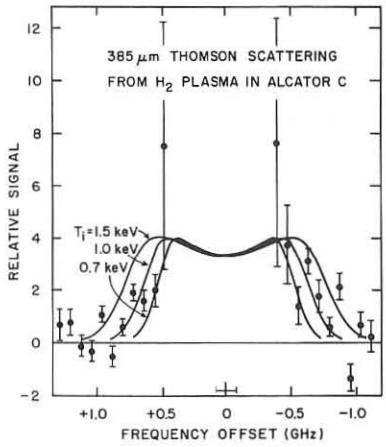

1. Scattered spectrum from a hydrogen plasma at 8 Tesla, $\bar{n}_e$ = 3.6 X 10^{14} cm^{-3}, and plasma current ~ 450KA

theoretical ion thermal spectra for $T_e/T_i = 1.2$ are superimposed over the data. (Small changes in the ratio T_e/T_i does not seriously effect the outer wings of the thermal spectrum.) These curves are normalized to the scattered signal level expected at $T_i = 1.0$ KeV based on the measured laser power, receiver calibration, and plasma density. However, this absolute calibration is uncertain by about a factor of two. It can be seen that the data in Fig. 2 is consistent with scattering from thermal fluctuations in a plasma with ion temperature in the range of 0.7 to 1.5 KeV. This temperature range is consistent with temperatures of about 1 KeV expected in Alcator C.

Fig. 2 shows a scattered spectrum for a deuterium plasma with parameters similar to the hydrogen plasma used for Fig. 1. This data is the average of ten identical plasma shots and therefore has smaller error bars than Fig. 1. The distinct narrowing of the scattered spectrum in deuterium relative to hydrogen is consistent with the interpretation of the scattered signal as originating from thermal ion fluctuations.

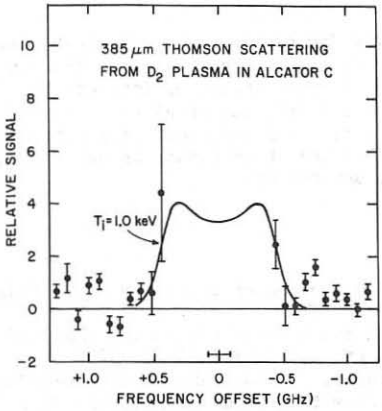

2. Scattered spectrum from a deuterium plasma at 8 Tesla, $\bar{n}_e = 2.5 \times 10^{14}$ cm^{-3}, and plasma current ~ 420KA.

DISCUSSION AND CONCLUSIONS

Although the scatter in the data points leads to a poor ion temperature resolution, the feasibility of scattering from ion thermal fluctuations in a tokamak device is shown for the first time. Significant improvements are possible in these measurements. The set up on Alcator C was not optimum for the following reasons: 1) Restricted diagnostic port apertures, 2.5cm wide, caused a large stray laser radiation background. Port apertures of 7cm or more for beam propagation path lengths of 1 to 2m would reduce the stray background; 2) The scattering geometry was aligned for scattering from fluctuations perpendicular to the magnetic field. With this orientation the scattered spectrum should be modulated at the ion cyclotron frequency which in a hydrogen plasma at 8 Tesla is 122 MHz. This modulation could have contributed to the scatter in the present data; 3) The normal operating values for the magnetic field in Alcator C are too high for thermal level scattering at a wavelength of 385μm. For the present measurements the central magnetic

field of Alcator C was limited to 8 Tesla or less because of strong interference from 3rd and 2nd harmonic electron cyclotron emission and absorption. This limitation prevented the use of the diagnostic at the highest ion temperatures and densities of Alcator C.

For scattering from plasma confinement devices with a combination of high temperature and relatively high field a shorter scattering wavelength is desirable to reduce electron cyclotron emission background levels. A shorter wavelength would also be better for experiments with restricted access. D_2O gas has several high power, 100μm laser transitions /7/ and NH_3 has high power laser lines at 152, 257, and 281μm /8/, at which the present Schottky diode mixer could be usable. The present 385μm scattering system as demonstrated on Alcator C should be useful for ion temperature diagnostics on lower field plasma confinement devices with large access. A 385μm D_2O laser has been operated at energy levels of up to 5 Joules per pulse at ~ 5MW power levels at Princeton /9/, a 20-fold increase over the laser used for the present measurements.

In summary, these results demonstrate, for the first time, the scientific and engineering feasibility of collective Thomson scattering from ion thermal fluctuations in a plasma confinement device of interest for fusion research. With the use of more optimized source and receiver technologies and better access, this technique could become a practical diagnostic tool for the measurement of ion temperature and other plasma properties which are manifest in thermal level collective scattering.

REFERENCES

1. Sheffield, J., Plasma Scattering of Electromagnetic Radiation, Academic Press, New York 1975.
2. Evans, J.V., Theory and practice of ionosphere study by Thomson scatter radar, Proceedings of IEEE 57 (1969) 496-530.
3. Kasparek, W. and Holzhauer, E., CO_2 laser scattering from thermal fluctuations in a plasma with two ion components, Phys. Rev. A 27 (March 1983).
4. Woskoboinikow, P., Mulligan, W.J., and Erickson, R., 385μm D_2O laser linewidth measurements to -60dB, IEEE J. Quantum Electron. QE-19 (1983) 4-7.
5. Fetterman, H.R., Tannenwald, P.E., Clifton, B.J., Parker, C.D., and Fitzgerald, W.D., Far-ir heterodyne radiometric measurements with quasioptical Schottky diode mixers, Appl. Phys. Lett. 33 (1978) 151-154.
6. Woskoboinikow, P., Erickson, R., and Mulligan W.J., Submillimeter-wave dumps for fusion plasma diagnostics, Int. J. IR and MM Waves 4 (1983) to be published.
7. Dodel, G., and Douglas, N.G., New pulsed far infrared laser lines in D_2O, IEEE J. Quantum Electron. QE-19 (1983) 797-798.
8. Hirose, H., Matsuda, H., and Kon, S., High power FIR NH_3 laser using a folded resonator, Int. J. IR and MM Waves 2 (1981) 1165-1176.
9. Semet, A., Johnson, L.C., and Mansfield, D.K., A high energy D_2O submillimeter laser for plasma diagnostics, Int. J. IR and MM Waves 4 (1983) to be published.

A NEW METHOD FOR THE DETERMINATION OF IMPURITY ION ENERGIES AND THEIR IMPLANTATION DEPTHS IN COLLECTION PROBES EXPOSED TO THE SCRAPE-OFF LAYER

J.K. Gimzewski and S. Veprek
Institute of Inorganic Chemistry, University of Zürich,
Winterthurerstrasse 190, CH-8057, Switzerland

EXTENDED ABSTRACT

An understanding of impurity generation, transport and deposition processes in the scrape-off layer (SOL) of Tokamak devices requires information on the impurity fluxes and their energy distribution/1/. This paper concerns the experimental determination of the impact energy of impurity ions using collection probes. The methods developed to date for the determination of ion energies in the SOL suffer inherent problems:

a) Techniques based on the determination of the ion gyroradius require a knowledge of the charge state of the ion /2/ and this is essentially an unknown parameter.

b) The method pioneered by Mohri et al /3/ relies on the accurate determination of the implantation depths of impurities in the target. From this depth the ion impact energy is interpolated using LSS theory /4/. Unfortunately the sputter-etch depth profiling technique employed is, in the experimental sense, fraught with difficulties.

Our method is based on the second approach. Using X-ray photoelectron spectroscopy (XPS) and chemical etching in a hydrogen plasma, we have developed a method for the determination of the implantation depth. In that case the problems associated with conventional sputter etching, such as Ion-induced atomic mixing /5/, selective sputtering /6/ and the essential requirement that the initial etch rate be accurately known, are overcome.

The example considered in this paper is the determination of the impact energy of Fe impurity ions in the SOL of the TCA Tokamak /1/ using carbon probes. However, the technique may be applied also to other metallic ions that do not form volatile hydrides and silicon is an equally suitable target material.

Figure 1. shows the projected range, Rp, of Fe projectiles in a carbon target calculated using LSS theory as a function of projectile energy. This applies for a normal incidence angle to the surface. Other cases are considered elsewhere /7/. For the energy range considered up to 2keV, Rp is similar to the inelastic mean free path, λ, of the photo- (or Auger) electrons from the impurity atoms which are detected in the XPS (or Auger electron spectroscopy, AES) experiment. For the present case, λ =13 Å for Fe2p photoelectrons excited by AlKα radiation in a carbon matrix /7/. Figure 2a. shows a schematic of the impurities implanted into the target; the overlying layer results in attenuation of the Fe2p signal intensity, I_0 . This overlying layer, and consequently the Fe2p signal attenuation, may be removed by selectively etching the probe chemically in a hydrogen plasma. With the sample at a floating

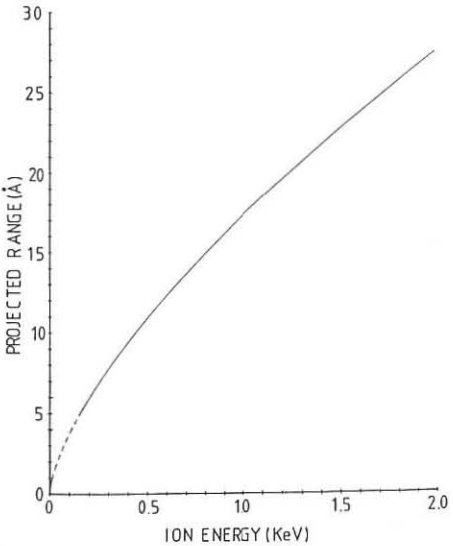

Figure 1. Projected range, Rp, of Fe projectiles in a carbon taget as a function of projectile energy calculated using LSS theory.

potential, carbon but not iron impurities is removed and, as a function of time the signal intensity reaches a saturation value, I_{sat}, which corresponds to the situation depicted in Fig. 2b.

Using several model distributions, including a Gaussian profile, it can be shown that /7/,

$$d = \lambda . \ln (I_{sat} / I_0) \qquad (1)$$

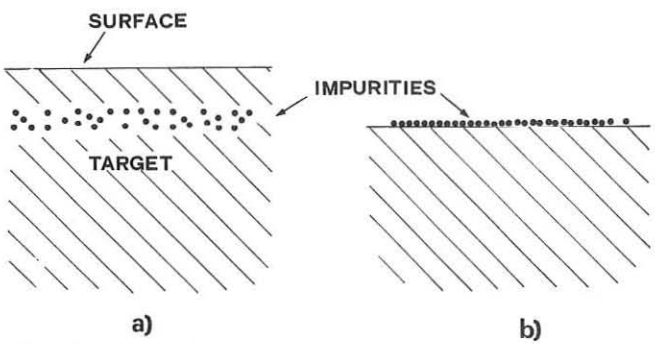

Figure 2. Schematic illustration of the collection probe surface region after implantation, a) and after etching in a hydrogen plasma, b).

Equation (1) is valid for cases where the depth distribution is not too broad ($\delta d/d \leq 0.5$) and for a low concentration of impurity species ,n ($n \leq \sim 10^{15}$ cm^{-2}) /7/. From the value of the experimentally determined implantation depth, d, the ion-impact energy may be readily interpolated using LSS theory (see Fig. 1).

The plasma etching experiments were performed in a custom built plasma etching chamber constructed from UHV components and connects to the XPS system permitting the etching and analysis by XPS to be done under UHV conditions without breaking vacuum /7/. The basic plasma parameters used were:

H_2 pressure = 4×10^{-2}mb and purity = 99.9999%; Substrate Temperature = 180°C; Discharge Current Density = 3 $mA.cm^{-2}$. The etching was done in a DC discharge with the sample at a floating potential and the thermionically heated cathode employed was out-of-line-of-sight of the sample. The electrodes were also electrically isolated from the vessel wall. This set-up essentially excludes physical sputtering of the impurities on the probe and also sputtering at the wall of the experimental chamber.

A typical example of I/I_0 as a function of etch time is shown in Fig.3 for a carbon probe that had been exposed to several shots in the SOL of TCA. Note that etching for extended periods of time does not significantly effect the saturation signal intensity ratio (I_{sat}/I_0) , confirming that possible changes in surface roughness do not contribute to the determined value of d.

Table 1. summarizes the results obtained for collection probes studies in the SOL of TCA. The ion-impact energies fall in the range of 100-160 eV for the data presented. In these experiments the probe was at the potential of the wall and the estimated sheath potential is ~30V. Consequently, the sheath accounts for a significant part of the total energy determined for assumed charge states of the ion of 1-3. Furthermore, sputtering of the deposited impurities during the TCA shots observed in other studies /1/ are consistent with ion energies in the range of 100-200 eV.

In conclusion, plasma chemical etching experiments in conjunction with suitable electron spectroscopic techniques (AES, XPS) may be used to determine the implantation depths and ion energies in the range 100-2000 eV. The method has several advantages over existing techniques used for studies of the SOL and is applicable to carbon or silicon probes and most metallic ions (Fe, Ni, Cr, Mo, Ti, etc).

Table 1.
Ion Impact Energies of Fe Impurities in the Scrape-Off Layer of TCA Tokamak

Drift Side	rf Power (kW)	Implantation Depth (Å)	Ion Energy* (eV)
electron	0	4.6	130
electron	108	5.1	160
ion	108	3.4	90
ion	108	4.2	120

* assuming that projectiles impinge the surface at normal incidence angle.

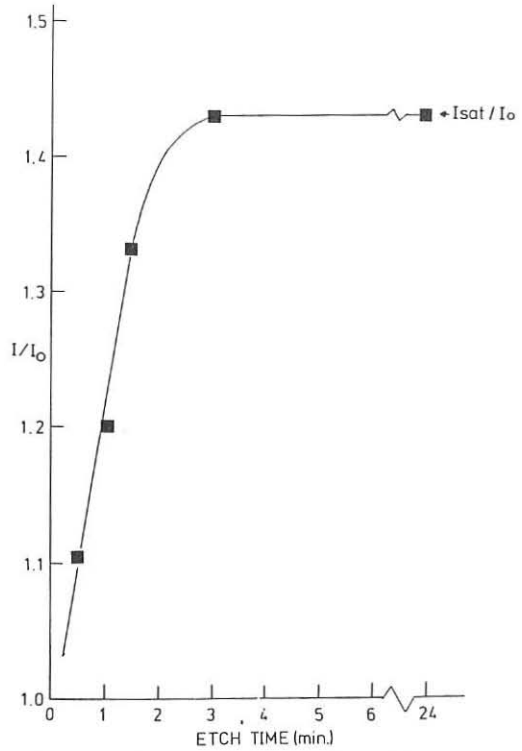

Figure 3. Signal Intensity ratio, I/I_0 , as a function of etch time.

Acknowledgements. The partial support of the National Energy Research Foundation (NEFF) and the Swiss National Science Foundation is acknowledged.

REFERENCES

/1/ J.K. Gimzewski et al.: in these Proceedings.
/2/ G. Staudenmaier and P. Staib: Bull. Am. Phys. Soc., 24 (1979) 1001. and P. Staib, H.F. Dylla and S.M. Rossnagel, J. Nucl. Mater. 93&94 (1980)166.
/3/ M. Mohri et al.: J. Nucl. Mater. 111&112 (1982) 147.
/4/ H.E. Schiott: Rad. Effects, 6 (1970) 107.
/5/ S. Matteson: Appl. Surf. Sci. 9 (1981) 335.
/6/ P. Varga and E. Taglauer: J. Nucl. Mater. 111&112 (1981) 726.
/7/ J.K. Gimzewski and S. Veprek: J. Vac. Sci. Technol. (to be published).

MILLIMETER WAVE SCHLIEREN DIAGNOSTICS FOR FUSION PLASMA

G. Lisitano, +F. Baretich[+,x], G. Gammino[+,x], I. Bazzo[+], C. Cassamagnaghi[+], S. Santicchi
Max-Planck-Insitut für Plasmaphysik, EURATOM-Association, D-8046 Garching

The schlieren diagnostic presented in this paper is based on a finite angular deflection of exploring electromagnetic wave beams, which, for the density of fusion plasmas of $N_e \approx 10^{14} cm^{-3}$, is encountered in the millimeter wavelength range /1/. The plasma is explored by several beams which are deflected in a small region around the intersection of the exploring mm-wave beams with a plane normal to the beams and passing through the center core of the plasma. Besides affording the possibility of calculating the density distribution, the schlieren signals present a direct view of the density gradient transverse to the beams. The amplitude of the schlieren signals is numerically calculated in this paper, from a known density distribution and a known radiation pattern of the mm-wave antenna. The opposite problem of calculating the density distribution form the measured schlieren signals has not jet been faced. It may, however, be solved by imposing some constraint on the numerical results in order to avoid the ambuguity resulting from asymmetric situations. In the following a numerical model for calculating the schlieren signals is applied to several density distributions. In particular, displacement and rotation of the central core reproduces measured schlieren oscillations in the Pulsator tokamak immediately preceding a current disruption.
As well known, the schlieren calculation of a ray path deflected in a dispersive medium is derived from the Fermat law by taking the minimum of the integral $\int_s k dl$, where k is the wave number. Replacing this k with that given by the dispersion relation of an ordinary wave, the radius of curvature R of the deflected ray path is expressed by /2/:

$$\frac{1}{R} = -\frac{\vec{N}}{2} \frac{\nabla V}{1-V} \qquad (1)$$

where $V = N/N_c$; N is the local density and N_c is the cut-off density for the wavelength used; $\vec{N}$ is the unit vector of the normal to the trajectory. From eq. 1) it is seen that the ray deflection is in the direction of decreasing density, is directly proportional to the density gradient and increases for an increasing density.
Assuming a pencil radiation pattern $I(\theta)$ for an exploring electromagnetic wave beam, the unperturbed signal at the receiver is $A = 2\int_0^{\mu} I(\theta) d\theta$ where μ is the angular width of the two undeflected external rays of a wave beam inpinging on the edges of the receiver antenna.

For a perturbed radiation pattern the received signal $\Delta A = \int_{\theta-}^{\theta+} I(\theta) d\theta$ depends on the ray density of the beam inside the two deflected external rays which reach the receiver edges.

+ Thesis, Dip. Energetica, Politechnico di Milano, Milano, Italy
xx Present address: Cise, Department of Acoustical Diagnostic, 20090 Segrate, Milano, Italy

Analytically, these two rays, which are calculated from eq. 1), are identified by the two angles θ^+ and θ^- of the radiation pattern $I(\theta)$ which is approximated by the function

$$I(\theta) = \frac{1}{2}\,(e^{-a\theta^2} + e^{-b\theta^2}). \qquad (2)$$

The amplitude of the normalized schlieren signal is then given by:

$$\Omega = \frac{\Delta A}{A} = \frac{\int_{\theta^-}^{\theta^+} I(\theta)\,d\theta}{2\int_{o}^{\mu/2} I(\theta)\,d\theta} \qquad (3)$$

where the error introduced by the numerically simulated radiation pattern resulted below the uncertainty limit for the experimental data. From eq. 3) one immediately sees the advantage of the schlieren method in comparison with other diagnostics or other models for simulating MHD mode perturbations: the detected signal at the receiver antenna does not need to be integrated along the ray path like the x-ray emissivity or the phase shift of an ordinary wave. Any change in the distribution of the density $V(\xi,\eta)$ deflects the ray path as calculated by eq. 1) to 3) and the signal is that which is not deflected from the edges of the receiver antenna.

Even small variations of the density distributions at any point of the plasma are detected by a sufficient array of exploring wave beams.

In view of the asymmetrical situations that must be faced by the model all the calculations involved by eq. 1), 2) and 3) were referred to orthogonal coordinates ξ,η. Equation 1) is then expressed by:

$$\eta'' = \frac{1}{2\,[1-V(\xi,\eta)]}\,[1 + \eta'^2]\,[-\frac{\partial V}{\partial \xi}\ \eta' - \frac{\partial V}{\partial \eta}] \qquad (4)$$

where the density distribution $V(\xi,\eta)$ is given by: (5)

$$V(\xi,\eta) = Vo\ \{1 - [\frac{(\xi-\tau\cos\Psi_2-\varsigma\cos\Psi_1)^2+(\eta-\tau\sin\Psi_2-\varsigma\sin\Psi_1)^2}{1+\tau^2-2\tau\cos\Psi_2(\xi-\varsigma\cos\Psi_1)-2\tau\sin\Psi_2(\eta-\varsigma\sin\Psi_1)}]^{f}\ \}$$

where $Vo = No/Ne$ is the maximum normalized density value; τ is the radial coordinate of Vo; $\tau\cos\psi_2$ is the vertex abcissa; ψ_2 is the angle of Vo; ψ_1 is the angle of the plasma centre and ς its radial coordinate; f is a profile-flattening index.

Equation 5) represents a generalized density function which, as it will be seen, allows the observed schlieren oscillations of Fig. 1 to be simulated by displacement and rotation of the central peak of the parabolic density funtion.
Figure 2 shows the isodensity lines and the labelling of the density distribution parameters of eq. 5. The geometrical arrangement of the exploring millimeter wave beams of the Pulsator tokamak is also sketched in Fig. 2. For a symmetric and centred density distribution, viz. $\varsigma = o$ and $\tau = o$ in Fig. 2, the results of the numerical model were compared with the Shmoys model /3/ valid for a centred and parabolic radial density distribution only. The result of both models deviated less than 1%. A detailed discription of the numerical programm /4/ of the model will be reported elsewhere, the aim of this work being to show that the schlieren method can give insight

into localized MHD phenomena inside the plasma, as shown in the following application of the model.
Although the numerical method allows the calculation of schlieren effects relating to any radial distribution of density, the following density distributions were chosen in order to simulate some possible physical processes underlying the observed oscillations of schlieren signals. In this contest particular interest is shown in a central density peak radially displaced from the geometrical centre of the discharge tube. The rotation of such a peak density simulates schlieren signals relating to observed MHD perturbations.

The various examples of individual situations are aimed at affording the possibility of combining them in order to get a possible physical understanding of the observed signal.

Figure 3 shows the "kink" effect of the schlieren signals obtained by programming the peak density for: 1) $\varsigma = 0.15$ (asymmetry to the centre); 2) radial displacement $\tau = 0$; 0.25; 0.50; 3) Vo = 0.5; 0.8 and 4) f = 4, corresponding to a large flattening of the radial density distribution.

Rotation of the angle ψ_1 produces the oscillations variety of the schlieren signals in Fig. 3. Some of these oscillations are similar to those detected immediately before a current disruption, shown in Fig. 1.
The $\dot{B}(\phi)$ pick-up coil oscillations of growing amplitude, which are correlated with the observed schlieren oscillation of the millimeter-wave beam, are also shown in Fig. 1. Such oscillations, but of much lower amplitude, are also observed with soft x-rays (not shown in Fig.1). These oscillations have been ascribed to growing magnetic islands external to the hot centre /5,6/. Contrary to the line-integrated soft x-ray signals and the $\dot{B}(\phi)$ oscillations, the local spatial dependence of the schlieren signals describes the evolution of the density center core instant by instant.
This affords the interpretation given in this paper of the rotation of the centre core immediately before the onset of the current disruption, as deduced by comparing the time evolution of the observed schlieren signals with the various individual situations numerically simulated with the model of centre core displacement.
Quantitative details of the radial displacement may be obtained by performing schlieren measurements in several adjacent channels with frequencies optimized for maximum sensitivity of the schlieren signals. Besides the qualitative interpretation of the evolution of the centre core, the oscillations of the schlieren signals presented for the first time in this paper are, however, very promising for studying MHD perturbations of the density centre core of fusion plasmas.

References

/1/ Lisitano, G., in Diagnostics for Fusion Experiments (E. Sindoni and G. Wharton, eds.) Pergamon Press, Oxford, New York (1979) p. 223.
/2/ London, L.D., Lifchitz, E.M., Oxford, Pergamon Press 1975.
/3/ Shmoys, J., I. Appl. Phys. 32 (1961) 689.
/4/ Baretich, F., Gammino, G., Bazzo, I., Cassamagnaghi, G., Santicchi, S., Thesis Politecnico di Milano, Milano, Italy (1980).
/5/ White, R.B., Monticello, D.A. and Rosenbluth, M.N., Phys. Rev. Letters 39 (1977) 1618.
/6/ Sykes, A. and Wesson, I.A., Phys. Rev. Letters 44 (1980) 1215.

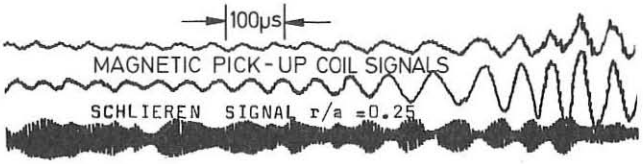

Fig. 1:Observed schlieren signal at r/a = 0.25 and m = 2 oscillations of the $\dot{B}(\phi)$ pick-up coil of a Pulsator tokamak discharge.

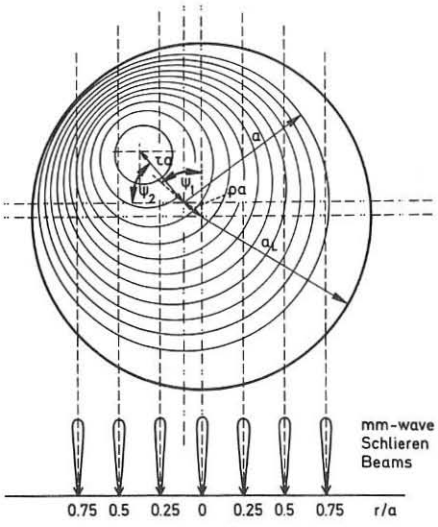

Fig. 2: Isodensity lines of the general density distribution of eq. 5).

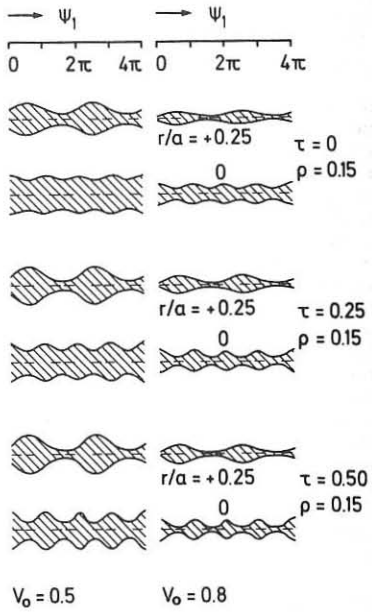

Fig. 3: Simulated "kink" effects of the schlieren signals for a very flat (f = 4) radial density distribution.

EFFECT OF SUPRATHERMAL ELECTRONS ON ECE-SPECTRA IN W VII-A

W VII-A Team[+], Ni Group[++]

Max-Planck-Institut für Plasmaphysik, EURATOM-Association,
D-8046 Garching, FRG

Electron temperature profiles, measured viewing along the larger radius of W VII-A stellarator by means of electron cyclotron emission (ECE) deviate characteristically from those obtained via Thomson scattering. While good agreement is achieved on the high field side, higher values are found with ECE on the low field side. As a reason, a small suprathermal population of electrons in addition to the thermalized main part was supposed. To investigate this possibility, the radiation of suprathermal electrons within the electron cyclotron frequency range was calculated, in the presence of the thermal background plasma, as follows:

The single particle radiation according to the Schottky-Trubnikov formula was summed up considering an energy distribution like exp(-E/EO) starting at the fixed energy ECO /1/. The density, DENS, of the suprathermal distribution is assumed to be homgeneous within a certain radius, RADUT, and zero outside. Besides EO, ECO, DENS, and RADUT the velocity ratio $Q = v_{\parallel}/v_{\perp}$ is introduced as fifth independent parameter. The calculations have been carried out under the following assumptions:

a) density- and temperature-profiles of the background plasma as measured via Thomson scattering;

b) plane geometry due to the small viewing beam diameter; viewing perpendicular to B_z;

c) doppler broadening neglected since both contributions from viewing angle divergence and from maximum electron temperature of the W VII-A plasma are small compared to the resolution of the Michelson interferometer used for the electron temperature profile measurements;

d) the absorption coefficients of individual harmonics, responsible for the optical depth of the thermal emission and for cyclotron absorption of suprathermal radiation in the thermalized main part as well are taken according to the formulas of Bornatici /2/ and Cano et al. /3/ for the first two harmonics and to those of Engelmann and Curatolo /4/ for the higher ones;

+) W VII-A Team: G. Cattanei, D. Dorst, A. Elsner, G. Grieger, P. Grigull, V. Erckmann, H. Hacker, J. Hartfuß, H. Jäckel, R. Jaenicke, J. Junker, N. Kick, H. Kroiss, K. Krusch, G. Kühner, C. Mahn, S. Marlier, G. Müller, W. Ohlendorf, F. Rau, H. Renner, H. Ringler, F. Sardei, M. Tutter, A. Weller, H. Wobig, E. Würsching, M. Zippe.

++) NI Group: K. Freudenberger, G.G. Lister, W. Ott, F.-P. Penningsfeld, E. Speth.

e) radiation damping due to the dispersion of the background plasma, i.e. collision damping and cutoff regions has been considered while multiple reflections at the walls and transitions between directions of polarisation are not included.

The computed spectra fit the measured ones well using one set of the five parameters corresponding to one nonthermal group of electrons. As an example fig. 1 shows in its lower part the radiation spectrum and the corresponding

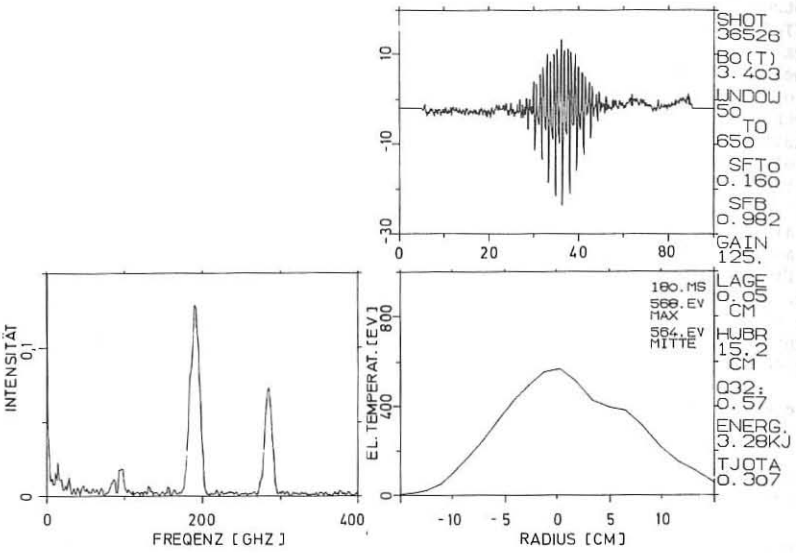

Fig. 1: Experimentally obtained diagrams: Michelson interferogram, spectrum, and temperature profile.

temperature profile measured in a currentless D_2 plasma during the H_2 neutral beam injection pulse while figs. 2 and 3 give computed ones. Included are the parameters of background plasma (lower group) and nonthermal contribution amount (upper group).Considering a density ratio of thermal to nonthermal electrons (DENSTH/DENS) of about 100 within a radius of 2 cm around the torus axis, the small peak at the low frequency side of the 1. harmonic and the bumps at the flanks of 2. and 3. harmonic resp. can be explained. The computed profile given in fig. 3 is based on the 2. harmonic and shows the same bump which should be compared to the measured one, fig. 1.

In rare cases of discharges, the measured spectra are explainable only by the addition of one or two groups of electrons of much higher energy. The generation process of such nonthermal electrons is not yet understood.

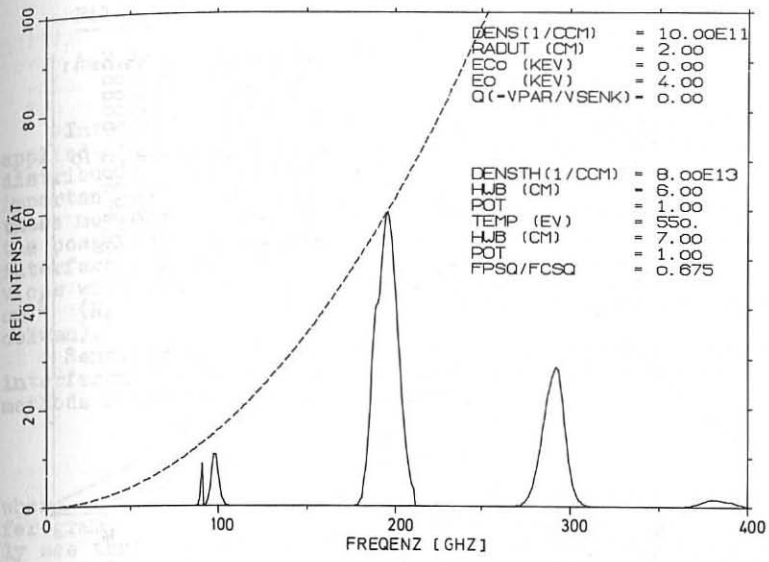

Fig. 2: Computed emission spectrum: The dotted curve is the Rayleigh-Jeans-parabola.

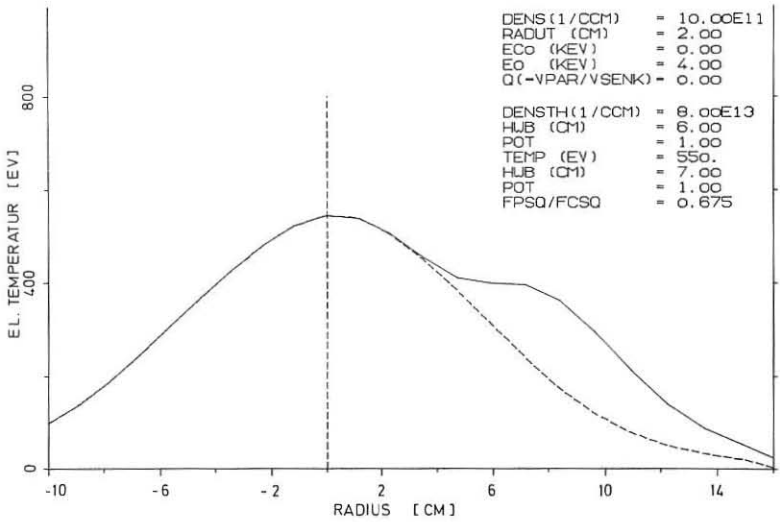

Fig. 3: Computed temperature profile from the 2. harmonic; dotted line is radiation of the thermal plasma only.

References

/1/ Celeta, C.M., Boyd, D.A., Nucl. Fusion 19 (1979), 423-441
/2/ Bornatici, M., FOM-Institut voor Plasmafysica, Rijnhuizen P.P. 80-04 (1980)
/3/ Cano, R., et al., Eur-CEA-FC-983 (1978)
/4/ Engelmann, F., Curatolo, M., Nucl. Fusion 13 (1973), 497-507

THE PROSPECTS TO ENHANCE THE SENSITIVITY OF HOLOGRAPHIC INTERFEROMETRY PLASMA DIAGNOSTICS IN IR REGION

Filippov V.N., Komissarova I.I., Ostrovskaya G.V., Shedova E.N.
A.F.Ioffe Physico-Technical Institute, 194021, Leningrad, Academy of Sciences, USSR

Interferometry and holographic interferometry are widely applied at present for the determination of electron density distribution in comparatively dense plasma. However, for many important cases, as for Tokamak plasmas, the sensitivity of these methods is insufficient. This study aimed to find out the possible ways to increase the sensitivity of holographic interferometry and make possible its application on plasma devices with characteristic N l values in the range $N_e l \approx 5 \times 10^{14}$ cm^{-2} (N_e - electron density, l - length of probing plasma column).

Sensitivity of interferometry and standard holographic interferometry methods such as real time and double exposure methods could be expressed by formula

$$(N_e l)_{min} \approx \frac{\Delta k}{4.46 \cdot 10^{-14} \lambda} \qquad (1)$$

where Δk - accuracy of fringe shift measurements on interferogram, λ - wavelength of probing radiation. One can easily see that the larger the radiation wavelength the higher the attained sensitivity. Thus, application of CO_2 laser (λ = = 10.6 μ) instead of ruby laser (λ = 0.694 μ) permits to enhance the sensitivity 15 times. For registration of holograms we used the pulsed CO_2 laser (gas mixture has been chosen as CO :N :He - 2:2:3, pressure 400 torr, pulse duration 2.5 usec energy $\approx$ 10 J). Hologram recording has been made on TAC film. Experimental set-up is shown in fig.1. Primary laser beam (1) is directed by mirrors (2,3) on Ge plate (4) providing the beam splitting onto subject and reference beams. The investigated phase object was placed near the splitting plate (4) and object image was focused by spherical mirror (6) in recording plane (8). Using the mirror (7) the reference beam was also directed to the same plane (8). (Focusing distance of mirrors (6,7) are about 60 cm). Necessity of spherical mirrors application in the given set up was caused, on the one hand, by the long aperture of primary laser beam (2x4 cm) along with its high divergency and significant losses on optical elements and, on the other hand, by the comparatively high energy density threshold for the used recording materials (E $\approx$ 1 J/cm) Besides, the application of focused images scheme provided at the stage of reconstruction with the He-Ne laser light the obtaining of practically nondistorted images inspite of noticeable difference in wavefront shape and wave length between recorded and reconstructed beams. Using this optical scheme we recorded the interferograms of a.c. arc discharge shown in fig.2. Fringe shifts here reach 0.5, which means that at plas-

ma layer thickness 0.2 the electron density corresponds to 5×10^{16} cm^{-2}. The perfect quality of fringes allows to determine their shifts with accuracy up to 0.1 fringe, which corresponds to the sensitivity $(N_e l)_{min} \approx 2 \times 10^{15}$ cm^{-2}

Aiming to enhance sensitivity furthermore we used the unique opportunities of holographic interferometry, permitting to obtain the phase amplification due to interference of waves, reconstructed in higher orders of nonlinearly recorded hologram /1,2/. These holograms were obtained using the same set up (fig.1), though the angle between interfering beams has been significantly increased. As a result, the spatial frequency of recorded interference structure was about 30 mm^{-1}. With accurate wave front matching of reference and subject beams we registered single-exposure holograms, while interferograms were obtained at the stage of reconstruction under illuminating of holograms two beams formed according Mach-Zender interferometer scheme and directed at some angle to each other. This allows to achieve the superposition of various orders waves and obtain the interferograms possessing different phase amplification (fig.3). The sensitivity of $N_e l$ determination in this procedure will be described by formula

$$(N_e l)_{min} \approx \frac{1}{4{,}46 \cdot 10^{-14} \lambda} \cdot \frac{\Delta k}{C_{n,m}} \qquad (2)$$

where $C_{n,m}$ = /n-m/ - coefficient of sensitivity gain, corresponding to the interferogram obtained at the interference of waves of orders n and m. Optimal conditions for obtaining interferograms would be utilization of high or symmetrical orders /3/.

Another possible way to enhance the sensitivity is application of multi-passage schemes in IR range. However it meets the number of stringent constraints such as troubled alllignment of nontransparent in visible region optical elements, essential light losses at reflection from mirrors that prevents from the application of low sensitive materials with thermal recording mechanism for hologram registration. These disadvantages could be avoided using multi-paasage of radiation through the hologram at the reconstruction stage. Fig.4 shows the reconstruction scheme corresponding to two-fold sensitivity enhancement.

Thus both of considered ways to increase the sensitivity of holographic interferometry allow to reduce significantly the limitation for determination of the electron plasma density and hence made it possible to include in the scope of this diagnostics the measurements of plasma parameters typical for TOKAMAK family.

References

1. Bryngdahl O,, Lohman A.W. Journ.Opt.Soc.Am. 58, 141 (1968).
2. Mystafin K.S., Seleznev V.A., Shtirkov E.I. Opt. and Spectr. (Sov.Phys.Journ.) 28, 1186 (1970).
3. Filippov V.N., Komissarova I.I., Ostrovskaya G.V., Shedova E.N., JTP, 53 (1983).

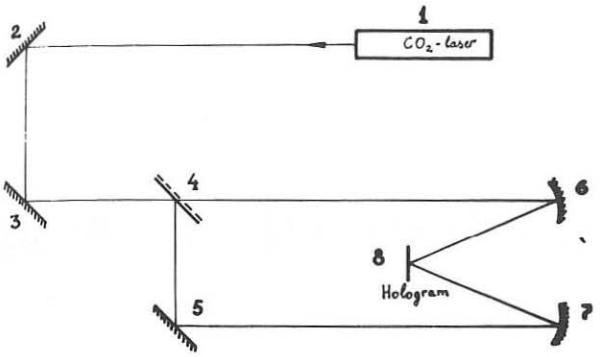
1
CO_2 - laser
2
3
4
5
6
7
8
Hologram

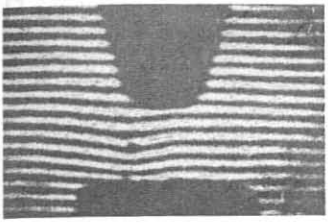

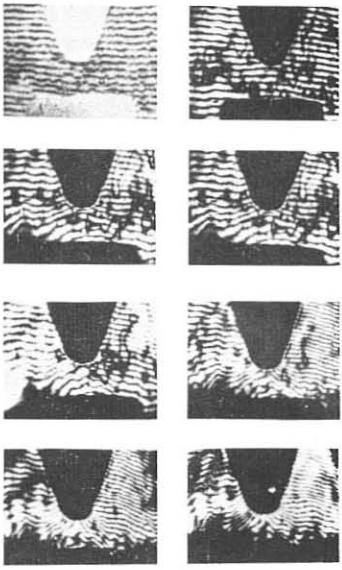

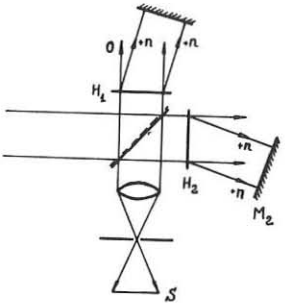
0
+n
+n
H_1
+n
H_2
+n
M_2
S

Magnetic Confinement Theory

O11 - O16

O22

B41 - B54

C37 - C49

D45 - D51

E46 - E53

COMPARATIVE CHARACTERISTICS OF VARIOUS PLASMA SYSTEMS

L.M.Degtyarev, Yu.Yu.Poshekhonov
Keldysh Institute of Applied Mathematics
V.D.Shafranov
I.V.Kurchatov Institute of Atomic Energy,
Moscow, USSR

1. The paper deals with the numerical investigation of two-dimensional axisymmetric tokamak-type configurations or configurations reducible to two-dimensional ones: a stellarator with moderate amplitude of helical fields and a stellarator with a helical axis. The plasma equilibrium in such systems is described by a second order elliptic equation for the poloidal flux function ψ. The configuration is fully determined by assigning a shape of boundary toroidal magnetic surface and by two functions - plasma pressure $p(\psi)$ and toroidal current $J(\psi)$ (or $p(\psi)$ and $q(\psi)$ etc.).

The stability was studied only with respect to local modes [1,2] . In toroidal geometry they are of either ballooning (concentration on the external edge) or quasi-flute (almost uniform along the magnetic field line) type depending on the magnitude and sign of shear. The local modes in tokamaks apparently impose greatest restrictions on the plasma pressure gradient [3]. Required computational accuracy is provided by applying the inverse variable technique [4].

2. Consider a tokamak with the plasma cross-section of the form

$$r(\omega) = R + a(\cos\omega - \delta\sin^2\omega); \quad z(\omega) = ka\sin\omega. \qquad (1)$$

Let $q(\psi) = [(q_s - q_0)\exp\bar{\psi}\sigma + q_0\exp\delta - q_s]\ /(\exp\sigma - 1)$,

$$\bar{\psi} = \frac{\psi - \psi_0}{\psi_s - \psi_0}; \ \sigma = 2\ln(1-\alpha)/\alpha; \ \alpha = \frac{q(\psi^*) - q_0}{q_s - q_0}; \ \frac{\psi^* - \psi_0}{\psi_s - \psi_0} = 0.5.$$

Here k and δ are the plasma elongation and triangularity, q_0 and ψ_0 are the values on the magnetic axis, q_s and ψ_s are the values at the plasma boundary.

Optimization of $p(\psi)$ relative to local mode instabilities leads to the following scaling for the β-limit [5]:

$$\beta_1 = 15\, k q_s^{-0.8} q_0^{-0.7} A^{-0.75}(1+2.6\alpha)^{-1}; \quad (\delta<0.4), \qquad (2)$$

where $A=R/a$ is an aspect ratio. In particular, the limiting value of $\beta=4\%$ is shown to be achieved for the INTOR parameters. At rather high plasma pressure a self-stabilization effect is observed. It is responsible for the second zone of stability as demonstrated in Fig.1. For a circular boundary plasma becomes stable at $\beta > \beta_2 = 13\%$. Both zones tend to unite at $\delta > 1$ (bean-shaped boundary). Unfortunately, this demands rather high current density at the plasma edge.

3. The computational results for an ordinary stellarator with helical windings and a circular axis were obtained by using the two-dimensional description. This can be provided at a sufficiently small amplitude of the helical field by passing over to new variables [2]. The stellarator rotational transform $\iota = 1/q$ is produced by external helical windings and grows, as a rule, monotonically away from the magnetic axis. Therefore,

for stellarators it is typical to have the positive shear $S=V\iota'(V)/\iota= -Vq'(V)/q$, where V is the volume enclosed by the current magnetic surface. On the contrary, for tokamaks there is a monotonic growth of q(necessary to stabilize kink modes) and hence, $S<0$. When the shear is positive, $S<0$, or small ($S \approx 0$), ballooning modes are not formed. Therefore the limiting pressure β_1 in stellarators is higher than that in tokamak at the same magnetic well.

The computations of stability in the ordinary stellarators with circular axis show that plasma can be stable at $\beta<10$ - 12%[2].

4. Now consider the computational results for stellarators with helical axis. The shape of plasma cross-section was described by eq.(1). The helical pitch is characterized by an angle γ between the helical axis and a vertical line on the reference cylinder ($\mathrm{tg}\ \gamma = \lambda/2\pi R$). The selfstabilization effect at plasma pressure growth in such systems is shown in Fig.2. At $k=1$ and $\delta=0$ (a circular cross-section), only the second (rather narrow) stability zone is realized that is bound above by the equilibrium limit. With an increase in δ at $k=1.3$ the stability zone widens. At $k=1.3$ and $\delta=0.6$, there appears a first zone which is separated from the second one by a gap of instability. At some higher elongation($k=1.6$) both zone unite. At $\delta > 0.5$ and $\gamma<50°$, the stability is provided from $\beta=0$ up to the equilibrium limit. Maximally achievable value of $\beta \approx 30\%$ poorly depends here on the plasma shape. There is also no strong dependence on the aspect ratio for $k=1.6$, $\delta=0.5$. Flux surfaces at $k=1.6$ and $\delta=0.3$; 0.9 are shown in Fig.3. Here are also given distributions of longitudinal magnetic field and q. One can see the presence of strong diamagnetism in the longitudinal magnetic field and practically the absence of shear.

5. All stated above allows the following conclusions.

a) The high pressure plasma self-stabilization effect is a dominating factor in a general picture of stability. In all systems the second stability zone due to this effect is revealed. An upper boundary of this zone is determined by violation of equilibrium conditions.

b)The first stability zone will arise, if there is a vacuum magnetic well which depends on the form of the boundary.

c) The stability zones are united in weak-shear systems. In tokamaks there is an instability gap at falling current profile. Thus in realistic cases the limiting pressure in tokamaks is determined by the first zone, and $\beta \lesssim 4\%$ at $A \sim 4$. In stellarators with typical positive shear (as well as in tokamaks with hollow current, which, however, is unstable with respect to tearing modes) the instability gap disappears and the β-limit rises considerably. Specifically, in stellarators with helical axis it reaches the value $\beta=30\%$.

References

/1/ Connor J.W., Hastie R.J., Taylor J.B., Proc.Roy.Soc.Lond., 1979, A365, p.1.

/2/ Zakharov L.E. et al. In Proc.9th Int.Conf. on Plasma Phys. and Contr.Nucl. Fus. Res., Baltimore 1982. IAEA-CN-41/V-5.

/3/ Connor J.W., Hastie R.J., Taylor J.B. In Plasma Phys. and Contr.Nucl.Fus; Res., Innsbruck, 1979, v.1, p.674.

/4/ Vabishchevich P.N., Degtyarev L.M., Drosdov V.V. Preprint IPM im.MV.Keldysha AN SSSR, 1981, No.112.

/5/ Vabishchevich P.N.,Degtyarev L.M.,Medvedev S.Yu.Fizika plasmy 9, 163 (1983).

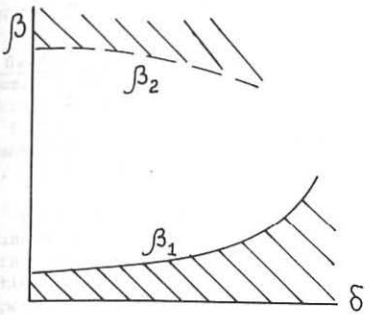

Fig.1 Qualitative dependence of the limiting β on the triangularity δ in tokamaks.

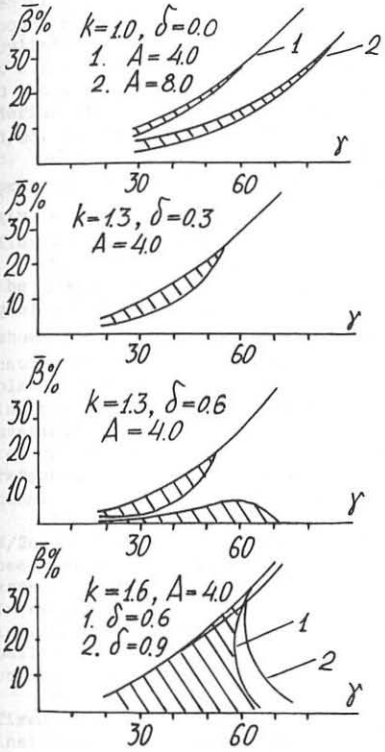

Fig.2 Stability regions in a helical axis stellarator.

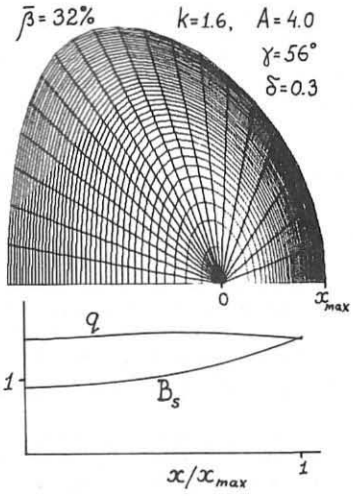

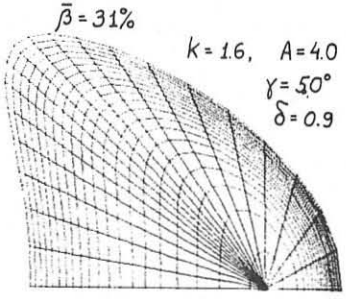

Fig.3 Magnetic surfaces and q, B_s profiles in stable helical axis stellarator.

BEAN-SHAPED TOKAMAK CONFIGURATIONS[a]

M. S. Chance, L. Chen, R. L. Dewar,[b] H. P. Furth, R. Goldston, R. C. Grimm, S. C. Jardin, J. Manickam, D. A. Monticello, M. Okabayashi, F. W. Perkins, M. Reusch, P. H. Rutherford, T. H. Stix, W. M. Tang, A. Todd,[c] and R. B. White
Plasma Physics Laboratory, Princeton University
P.O. Box 451, Princeton, New Jersey 08544, U.S.A.

Previous studies of localized MHD modes /1,2/ have indicated that enhanced stable beta values can be achieved in tokamaks which have their surface at the inner major radius side indented so that a bean-like cross-sectional shape is obtained. We have undertaken an extensive study of the properties of this configuration with a view towards an advanced tokamak with this shape.

Most of the theoretical MHD studies have been carried out for equilibria generated by solving the Grad-Shafranov equation in the fixed boundary mode where we prescribe the shape of the plasma surface. In cylindrical coordinates (X,ϕ,Z) this shape is parameterized by $X = \bar{X} + \rho\cos\gamma$, $Z = E\rho\sin\gamma$, where $\rho = 1 + B\cos t$, $\gamma = C\sin t$, and $0 \leq t \leq 2\pi$. An example of the shape is shown in Fig. 1a, where we also define the aspect ratio, R/a, the elongation, b/a, and the indentation, d/2a, of the plasma. These are generated by appropriate choices for $\bar{X}$, E, B, and C. In a flux conserving sequence of equilibria we choose the pressure and safety factor profiles to be $p(y) = p_o(1-y^2)^2$ and $q(y) = \sum_{i=0}^{3} q_i y^i$ respectively, where $y = \psi/\Delta\psi$, $2\pi\Delta\psi$ being the poloidal flux within the plasma.

The dependence of ballooning mode stability upon the indentation of the plasma is first studied for the case where q_i are chosen such that $q(o) = 1.03$, $q(1) = 4.2$, $q'(o) = 0.84$ and $q'(1) = 9.0$. The result is shown in Fig. 1b. At low indentation an increase of $\beta_{Av}(\equiv 2\int p dv/\int B^2 dv)$ causes the plasma to become unstable, but further increasing the pressure places the plasma in the second stability regime. However, if the indentation is large enough, increasing the pressure by-passes the unstable region completely. Bean shaping thus provides an accessible path to the second region of stability of ballooning modes. The mechanism responsible for this feature is the indentation-enhanced local shear and connection length properties previously discussed in Ref. 3.

The effect of the aspect ratio is shown in Fig. 2 for a plasma with d/2a fixed at 0.304 and for the same p and q profiles as above. There we see that higher stable β values in the first region are obtained with low aspect ratio. However, in that region the second regime becomes increasingly remote. As the aspect ratio is increased the region of instability decreases making it more likely that operation above the ballooning limit should be possible, although it is found that the critical indentation for accessibility moves outwards.

We have repeated the calculations of Fig. 1b for different q(1) but fixed q'(1)/q(1) and found that lower q(1) raises the lower limit of the instability threshold but the upper stability boundary moves rapidly away. The critical indentation for accessibility however decreases.

We have also applied the zeroth order FLR modified ballooning equations of Tang et al. /4/ to these configurations and found a significant stabilizing influence even for $k_\perp \rho_i$ well below unity.

Indenting the plasma shape is also found to be very beneficial

towards stabilizing the n = 1 internal kink mode when q(o) falls below unity. As shown in Fig. 3 the instability region shrinks rapidly to zero as the indentation is increased. The inset in the figure shows that an indentation of ~0.1 is sufficient for complete stabilization. The q profiles used here are the same ones used in Fig. 1b, but scaled by changing the toroidal field at fixed poloidal β. The enhanced stability here is associated with the increased triangularity generated by the indentation.

We have also used the PEST code to study the stability of the free boundary n = 1 kink mode as a function of wall radius. To do this we have examined each of the equilibria in the β-indentation plane of Fig. 1a as a function of the wall position a_w/a. The results are shown in Fig. 4, where contours of marginal stability are shown for various wall positions. At low β these external modes are mostly localized near to the plasma surface and can be described as surface kinks. Indentation is destabilizing in the sense that the wall must be closer to achieve stability as indentation is increased. At modest values of this indentation, $d/2a \lesssim .2$, the modes take on a strong ballooning character as β is increased. Eventually, as the second stable region is approached the advantages associated with more favorable local shear appear and, with the wall at a finite distance, the configuration eventually becomes stable. At strong indentations, finite β effects are seen to stabilize the kink modes, presumably through a variation of the current profile at fixed q. The results shown in this diagram, when considered simultaneously with those of Fig. 1b, indicate that, with a stabilizing wall at 1.3 plasma radii, accessibility to the second stable region without encountering current driven kinks should be achievable, even ignoring the non-ideal stabilizing effects which must be present in current experiments.

Because of the strong shaping the bean configuration is prone to axisymmetric (n = 0) instabilities. We have examined the effect on the stability of judiciously placed conducting plates near the plasma. This was studied with a time dependent resistive MHD code /5/ for a configuration with X = 1.425 m. In this case the conducting plates consisted of surfaces of constant X and Z around the nose areas. When the plates are located further away from the plasma, a plasma initially in equilibrium on the horizontal plane starts to slip with small change in shape as if the plasma is pulled by the separatrix. It was found that surfaces at Z = $\pm$ 0.68 m and X = 0.83 m or Z = $\pm$ 0.75 m and X = 0.9 m would stabilize the plasma motion. However, when the wall was moved to Z = $\pm$ 0.75 m, X = 0.83 m, the plasma became unstable as illustrated in Fig. 5. The mode behavior as well as the conductor locations are in good agreement with those predicted from a PEST analysis.

The magnetic topology of the bean shaped configuration leads to interesting modifications of particle orbits. In addition to the usual outer bananas of conventional tokamaks, for example, there exists a class of inner bananas at the small major radius side which are formed because of the possibility of the presence of a minimum B along a flux surface there. The results of following the particle trajectories with orbit codes shows that the precession of the outer bananas can be in the opposite direction from the usual tokamak case, presumably because of the strong modification of the local shear properties of the bean configuration. Results of the code also indicate that the mechanisms generally accepted to be responsible for the fishbone oscillations are very significantly reduced.

Finally we show in Fig. 6 a schematic of the PDX modifications to

study the effect of bean-shaping in an actual experiment. This was simulated by a free boundary equilibria analysis, assuming that one of the divertor coils is brought to the mid-plane to affect the indentations.

[a]Work supported by U.S. DoE Contract #DE-AC02-76-CHO-3073.
[b]Permanent address: Research School of Physical Sciences, A.N.U., Australia
[c]Grumman Aerospace Corporation, Princeton, New Jersey

REFERENCES

/1/ R. C. Miller and R. W. Moore, Phys. Rev. Lett. 43, 765 (1979).
/2/ C. Mercier, Lectures in Plasma Physics, Research Group of the Association EURATOM-CEA Cen/Fonteney-aux-Roses (France, 1974).
/3/ J. M. Greene and M. S. Chance, Nucl. Fusion 21, 453 (1981).
/4/ W. M. Tang, R. L. Dewar, and J. Manickam, J. Nucl. Fusion 22, 1079 (1982).
/5/ S. C. Jardin and W. Park, Phys. Fluids 24, 679 (1981).

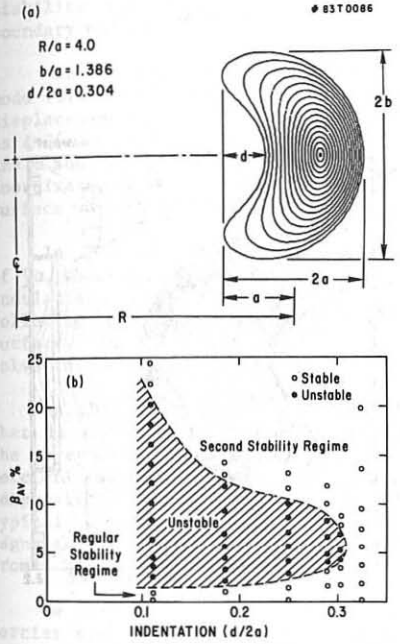

FIG. 1a. Geometry of the bean configuration.
1b. Accessibility to the second region of stability.

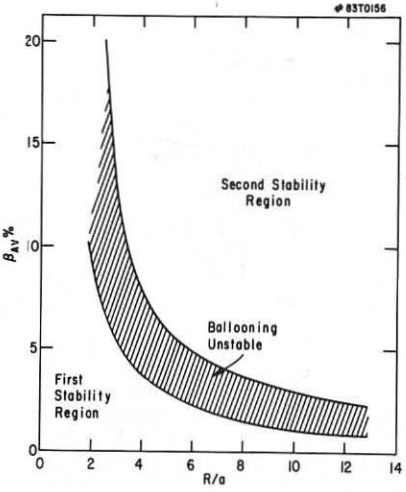

FIG. 2. Effect of the aspect ratio on the balloon stability regions.

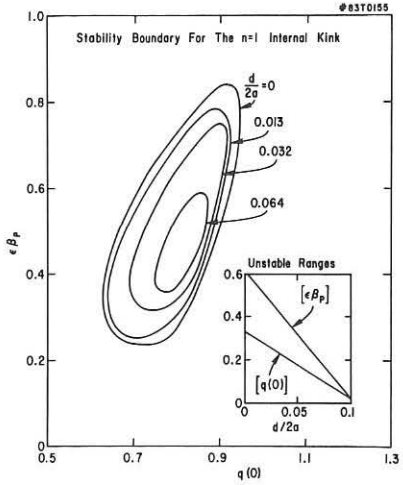

FIG. 3.

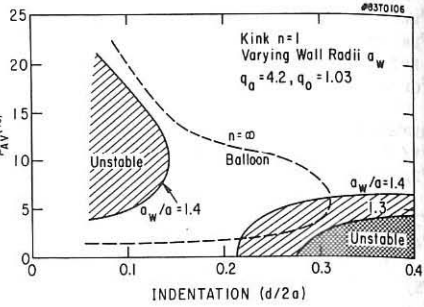

FIG. 4.

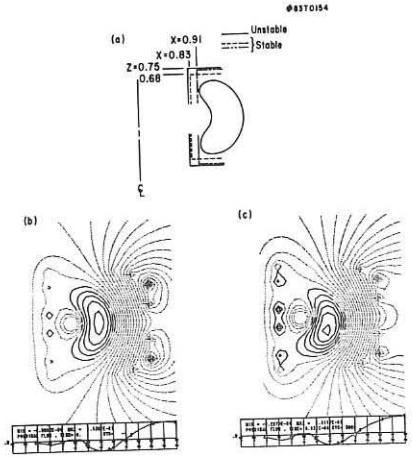

FIG. 5. Effect of conducting plates on the n = 0 mode.

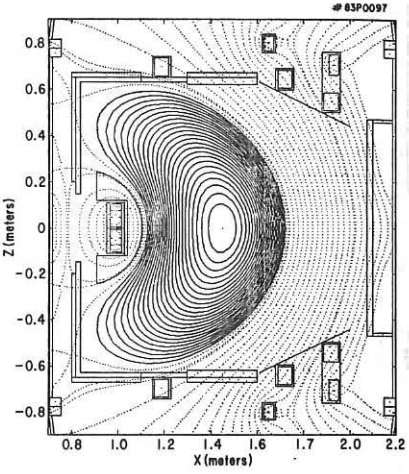

FIG. 6. Schematic of the PDX modification to study bean shaping.

BALLOONING MODE CALCULATIONS IN STELLARATORS

H.L. Berk and M.N. Rosenbluth
Institute for Fusion Studies, The University of Texas at Austin
Austin, TX 78712 (USA)
and
J.L. Shohet and W.N.G. Hitchon
University of Wisconsin, Torsatron/Stellarator Laboratory
Madison, Wisconsin 53706 (USA)

I. Introduction

The problem of MHD plasma stability in a stellarator is complex owing to the intrinsically three-dimensional equilibrium. The analysis simplifies considerably in the ballooning mode limit, where the cross field structure of the mode is assumed localized arbitrarily close to a field line. Analysis of such of modes,[1,2] gives more pessimistic stability conditions than for neighboring modes with larger spatial spread, and hence should yield a conservative figure of merit for the stability properties of a given stellarator except perhaps for free-boundary modes.

In the limit of extreme localization to a field line, the ballooning mode formalism is readily obtained from the eikonal approximation where a displacement ξ, normal to a flux surface, can be written as $\xi=\xi(s)\exp[iS(\alpha,\beta)]$, where s is the distance along a field line and α and β are two surfaces that label a field line. We use Clebsch coordinates α and β where $\underset{\sim}{B}=\underset{\sim}{\nabla}\alpha\times\underset{\sim}{\nabla}\beta$, and α is taken to label a flux surface while β is an angle-like variable.

In general the ballooning mode equation will be given in terms of $\underset{\sim}{\nabla}\alpha$, which is a complicated geometrical function reflecting the complex undulations of the flux surface. We construct $\underset{\sim}{\nabla}\alpha$, as well as $\underset{\sim}{\nabla}\beta$, by following the equations of neighboring field lines on the same flux surface. One then can integrate along the field line and simultaneously solve the ballooning mode equations.

In this paper we: (1) write the ballooning equations in a manner that is readily integrated by a field line following code[4]; (2) analyze the asymptotic properties of the ballooning mode equation to rederive the Mercier condition[5] in a form particularly well suited for our computations; and (3) evaluate the low beta stability properties for three typical configurations, Proto-Cleo, WISTOR-U and Heliac, where the magnetic fields are due to actual vacuum coils plus the currents arising from a localized pressure gradient.

We find if a system has a magnetic well at zero beta, it will be Mercier stable for all beta values consistent with the limitations of the low beta approximation used, a result previously found by Shafranov.[6] However, as ballooning mode stability is more pessimistic than the Mercier criterion, additional ballooning mode stability limitations sometimes arise.

II. Ballooning Mode Equation

The Euler equation of the energy principle, using the eikonal approximation for the variation transverse to the magnetic field, is

$$\frac{d}{ds}\frac{k^2(s)}{B(s)}\frac{d}{ds}\xi(s) + \frac{2}{B^3}(\underset{\sim}{k}\times\underset{\sim}{b}\cdot\nabla p)(\underset{\sim}{k}\times\underset{\sim}{b}\cdot\underset{\sim}{\kappa})\,\xi(s) = 0, \qquad (1)$$

where $\underset{\sim}{b} = \underset{\sim}{B}/|B|$, $\underset{\sim}{\kappa} = (\underset{\sim}{b}\cdot\nabla)\underset{\sim}{b}$. Stability is determined from the condition $\xi(s)$ does not equal zero more than once between $-\infty < s < \infty$. We assume that the lines consist of nested surfaces, labelled by $\alpha \equiv$ const., which can be generated by following a field line.

By applying $\underset{\sim}{B}\times\nabla\alpha\cdot\nabla\times$ to $\nabla\beta$ we obtain

$$\frac{d\Lambda}{ds} = -\frac{B}{|\nabla\alpha|^4}(\underset{\sim}{b}\times\nabla\alpha)\cdot\nabla\times(\underset{\sim}{b}\times\nabla\alpha). \qquad (2)$$

Thus, with an initial condition $\Lambda(s_0)$, we have determined $\nabla\beta$ given $\nabla\alpha$, and Eq. (1) can be integrated from $-\infty < s < \infty$.

We now need a practical way to calculate $\nabla\alpha$. This is done by choosing a convenient third coordinate and examining the covariant and contravariant basis sets. For the covariant bases we have $\nabla\alpha, \nabla\beta$, and say, $\nabla\phi$, where ϕ is the usual toroidal angle so that $\nabla\phi = \underset{\sim}{\phi}/R$, and R is the major radius. The infinitesimal distance, $d\underset{\sim}{r}$ can be expressed in terms of the contravariant basis

set $d\underset{\sim}{r} = d\phi\underset{\sim}{e}_1 + d\alpha\underset{\sim}{e}_2 + d\beta\underset{\sim}{e}_3$, with $\underset{\sim}{e}_1 \equiv \frac{\nabla\alpha\times\nabla\beta}{|\nabla\alpha\times\nabla\beta\cdot\nabla\phi|}$, $\underset{\sim}{e}_2 = \frac{\nabla\beta\times\nabla\phi}{|\nabla\alpha\times\nabla\beta\cdot\nabla\phi|}$, $\underset{\sim}{e}_3 = \frac{\nabla\phi\times\nabla\alpha}{|\nabla\alpha\times\nabla\beta\cdot\nabla\phi|}$

and, similarly, the inverse relations hold, $\nabla\alpha = (\underset{\sim}{e}_3\times\underset{\sim}{e}_1)/|\underset{\sim}{e}_1\times\underset{\sim}{e}_2\cdot\underset{\sim}{e}_3|$, etc. Eqns. (1) and (2) can now be written in terms of $\underset{\sim}{e}_1$, $\underset{\sim}{e}_2$, and $\underset{\sim}{e}_3$.

The advantage of having the equations in this form is that we can determine $\underset{\sim}{e}_3$ and Λ as we generate the equations for a field line. One can show that Eqs. (1) and (2) reduce to the equations derived by Connor, Hastie and Taylor in the symmetric tokamak limit.

III. Mercier Condition and Diamagnetic Shift

We now derive the formal Mercier condition for Eq. (1). We first of all observe that it follows from $\underset{\sim}{j} = \partial p/\partial\alpha[2\lambda\underset{\sim}{B} + (\underset{\sim}{B}\times\nabla\alpha)/B^2]$, and $\nabla\cdot\underset{\sim}{j} = 0$ that $d\lambda/d\phi = R\,\underset{\sim}{e}_3\cdot\underset{\sim}{\kappa}/B_\phi$. Since λ has to be a single-valued function of ϕ space, the integral $\lambda \equiv \int_0^\phi d\phi\frac{R}{B}(\underset{\sim}{e}_3\cdot\underset{\sim}{\kappa})$ cannot be secular if a field line is in a bounded region of ϕ space. We seek a solution, as $\Lambda \to \infty$, of the form $\xi = \Lambda^\nu(\xi_0 + \xi_1/\Lambda + \xi_2/\Lambda^2 + \ldots)$, where ξ_j are non-secular.

Then, with $g \equiv |\underset{\sim}{e}_3\times\underset{\sim}{b}|^2 B_\phi/R$, $\langle\lambda\rangle = \int_0^\infty d\phi\lambda g/\int_0^\infty d\phi g$ $G = \int_0^\phi d\phi g$, $(\frac{\Lambda}{G}) = \lim_{\phi\to\infty}\frac{\Lambda}{G}$, we can obtain a recursion relation $\nu^2+\nu+D = 0$ with

$$D = (\frac{\overline{G}}{\Lambda})\lim_{\phi\to\infty}\frac{1}{\Lambda(\phi)}\{\int_0^\phi d\phi[2\frac{\partial p}{\partial\alpha}(g\frac{\underset{\sim}{e}_3\times\underset{\sim}{b}\cdot\underset{\sim}{\kappa}}{B} + \frac{d\Lambda}{d\phi}(\lambda-\langle\lambda\rangle)) + 4(\frac{\partial p}{\partial\alpha})^2 g(\lambda^2-\langle\lambda\rangle^2)\} \qquad (3)$$

and $D < 1/4$ is required for stability. If we argue that $E = \eta j_{\parallel}$ with η constant, and that $E_{\parallel} = -\partial\Phi/\partial s$, as there is no inductive field (the "zero current" case), then the uniqueness of ϕ demands $\lambda_0 = \int_{-\infty}^{\infty} ds\, B\lambda / \int_{-\infty}^{\infty} ds\, B$.

IV. Numerical Results

We have solved the ballooning mode equations for a variety of existing and proposed experimental devices. In this study we present the results for Proto-Cleo, WISTOR-U, and a Heliac configuration.

The method of computation is essentially the same for each machine. The fields are determined for a given coil structure by the Biot-Savart law. One can then generate magnetic surfaces, shown for Heliac in Fig. 1. The shear parameter Λ is shown in Fig. 2 for Heliac. The average current parameter is shown in Fig. 3.

To find the marginal stability condition we assume that an eigenfunction centered on the outside of the torus will have the most pessimistic stability properties. If we start at the symmetry plane $\phi = \phi_0$ where quantities in Eq. (1) are even in $(\phi - \phi_0)$, we are allowed to consider initial conditions $\xi = 1$ and $d\xi/d\phi = 0$. We then evaluate the Mercier condition. If $D < 0$, we then integrate Eq. (1) in a scan of beta to see if an additional ballooning instability can arise. When ballooning instability is possible, the critical beta is insensitive to the boundary condition $\xi = 0$ at $\phi = \phi_{max}$ as long as $\phi_{max} > 2\pi/\iota$. If $D > 0$, we examine the ballooning mode stability at the Mercier critical beta β_M, to see if more pessimistic ballooning beta can be found. If the eigenfunctioon for $\beta_0 = \beta_M$ indicates an additional intersection, we then search for the critical beta of the ballooning mode.

Our results show that the Proto-Cleo configuration is always stable ($D < 0$ and ballooning modes are not found), whereas WISTOR-U is Mercier unstable, with no additional ballooning mode limits. These results agree with Shafranov's conjecture[7] that if the rotational transformincreases outwardly ballooning mode stability is determined solely by the Mercier condition. However, we find a counter example to Shafranov's conjecture in a Heliac configuration which is Mercier stable, with radially increasing rotational transform, but ballooning limits are found at some radii. In Fig. 4 we show an example of eigenfunction in Heliac which was ballooning unstable with $D < 0$. We note however, that the critical beta is somewhat high, and we may be over-extending the validity of our perturbation method, especially if the pressure gradient is not local to the flux surface. Further study on this aspect is needed.

In conclusion, we have developed a ballooning mode formalism that is amenable to numerical studies. If a magnetic well can be designed at zero beta, there is a strong tendency for the system to be ballooning mode stable for all beta (consistent with the equilibrium beta limitations of our theory) if the rotational transform increases radially, although an exception in a Heliac configuration has been found. Further work is in progress to calculate stellarator equilibrium with global pressure gradients so that ballooning mode stability can be accurately calculated when there are appreciable flux surface shifts due to finite beta.

Acknowledgements

This work was supported in part by DOE Contract #DE-FG05-80ET-53088 and in part by DOE Contract #DEAC02-78-ET53082 and National Science Foundation Grant #ECS-82-06207.

References

/1/ I.B. Bernstein, E.A. Frieman, M.D. Kruskal and R.B. Kulsrud, Proc. Royal Soc. A 17, 244 (1958).
/2/ J.W. Connor, R.J. Hastie, J.B. Taylor, Proc. Royal Soc. A365, 1,(1979).
/3/ R.L. Dewar and A.H. Glasser, "Ballooning Mode Spectrum In General Toroidal Systems," PPL Report 1890, April 1982.
/4/ R.J. Bickerton, A. Gibson, Phys. Fluids 10, 682 (1967).
/5/ C. Mercier, Nuc. Fusion 1, 47 (1960).
/6/ V.D. Shafranov and E.I. Yurchenko, Nuc. Fusion 8, 329 (1968).
/7/ V.D. Shafranov, Phys. Fluids 26, 357 (1983).
/8/ J.M. Greene and M.S. Chance, Nucl. Fusion 21, 453 (1981).
/9/ D.T. Anderson, J.A. Derr and J.L. Shohet, IEEE Trans. on Plasma Science, PS-9, 212 (1981).

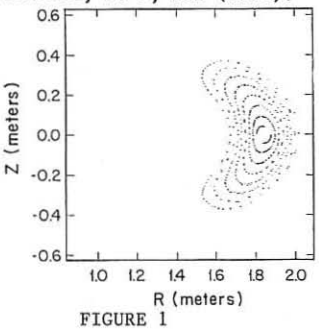

FIGURE 1

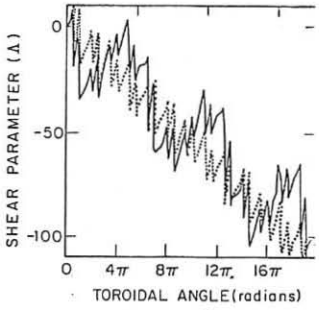

FIGURE 2

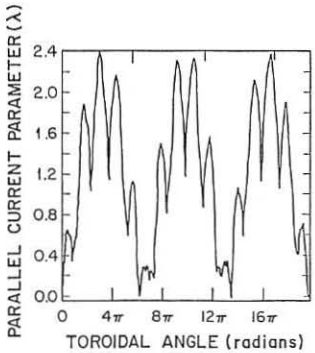

FIGURE 3

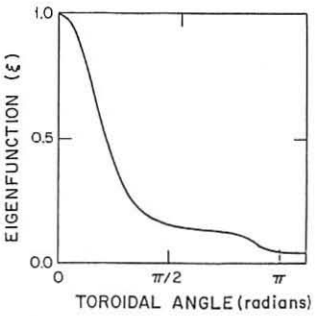

FIGURE 4

On the Origin of Sawtooth Relaxations and Plasma Disruptions

André Rogister, Günter Hasselberg, and François Waelbroeck

Institut für Plasmaphysik Kernforschungsanlage Jülich GmbH,
5170 Jülich, FRG, Association EURATOM/KFA

A. Remarkable points of concurrence of Tokamak experimental results and theory are

(i) that the plasma profiles are not very different from those corresponding to the marginal stability of the dissipative trapped electron mode /1/ and

(ii) that this marginal stability criterion is reminiscent of the empirical law for the high density limit /2/.

(i) suggests that the shear stabilized trapped electron mode is an essential channel of anomalous heat transport; a channel so efficient indeed as to forbid strongly unstable situations to develop. Given the peripheral physics associated with the sawtooth relaxations and the major disruptions, (ii) leads us to relate these phenomena to the anomalous heat flux clamping which results from the quenching of the trapped instability (a) in the plasma core and (b) at high densities (an increased collisionality (v*) stabilizes the mode).

In view of (i), a paradoxical result of the experiment is

(iii) that the measured turbulence spectrum is unable to account, by a full order of magnitude†), for the anomalous losses as deduced from power balance /3/.

The present work aims at giving a theoretical justification of the relaxation of the plasma profiles to a weakly unstable state (point i), at resolving the experimental paradox (point iii) and at supplying arguments which plausibly relate the origin and the mechanism of disruptions (both internal and external) to drift wave transport (point ii). Our theoretical interpretation of the experimental results relies on the conclusions of anomalous transport calculations performed with turbulence spectra which were obtained explicitely from a recent theory of nonlinear saturation of drift instabilities developed from first principles.

B. We have shown /4/ that Compton and induced scattering by ions (nonlinear ion Landau "damping") is the dominant stabilization mechanism of drift instabilities whenever they have a radiative structure à la Pearlstein and Berk. We have thus analysed discharges from TFR (Tokamak Fontenay-aux-Rose) /3/ and FT (Frascati Tokamak) /5/ to verify that the environment is such that shear damping of drift waves prevails and found it to be the case; we have also found, as in Ref. /1/, that the profiles were weakly unstable according to the standard threshold criterion of the dissipative trapped electron mode. Nonlinear ion Landau damping, which connects linear modes of roughly equal frequencies but - in view of the dispersion relation - not necessarily roughly equal mode numbers, yields a splitting of the spectrum

†) The factor 3 by default reported in Ref. /3/ is an underestimate since the radial decoupling of the trapped electrons with the modes was purposefully not taken into consideration in the comparison.

into a long and a short wavelength branch with the latter being excited by nonlinear energy transfer from the long wavelength modes.

The nonlinearly driven short wavelength turbulence spectrum is the key to the transport problem /6/. It provides indeed most of the anomalous electron heat flux (≥ 90 %) while being out of reach of present detection systems; its contribution to the turbulence level $\langle \tilde{n}^2 \rangle$ is not significant ($\lesssim 25$ %). This resolves the paradox (iii). The transport is also found to increase very rapidly with the destabilizing trapped electron term (the ratio of both enhancements can be 10 to 1.5) which explains the relaxation of the profile to a weakly unstable situation*).

C. The rapid increase of the fluxes also provides an incentive to inquire into whether the heat pulses released by the sawtooth relaxations could lower sufficiently the collisionality and hence increase the growth rate of the drift modes to sustain their own transport as they propagate through the plasma /6/ - much as collisionless shock waves excite the instabilities which provide for their dissipation - especially as the Murakami high density limit is reminescent of the threshold criterion of the trapped electron mode. Estimation of the energy released by the core shows that this scenario is indeed plausible; moreover comparison of the drift wave exponentiation time ($\gamma \sim c_s/L_s \sim 10^5$ sec^{-1}; c_s: sound speed; L_s: shear length) and of the observed decay time of the sawteeth ($\sim 10^{-4}$ sec) in TFR indicates that the instability would have the opportunity to fully develop during the passage of the heat pulse.

It is tempting to suggest also that the very origin of the sawtooth activity is the quenching of the trapped electron instability and the clamping of the associated heat flux in the center of the discharge and also to extend the picture to major plasma disruptions /6/. This hypothesis would be consistent with (1) the observed increase of sawtooth amplitude and period with plasma density, (2) an overheating of the core and cooling of the plasma periphery prior to relaxation leading to Mirnov oscillation, and (3) a rapid outflow of the released energy /8/. By introducing a reasonable assumption on the strength of instability quenching for major disruptions to occur, it is possible to show that the theoretical high density limit is given by

$$N_o = 6 \quad 10^{16} \frac{a^{1/2} T_{e,o}^2}{R^{3/2} A_i^{1/2}} \frac{\mu F(a/q_a R)}{1 + Z_{eff}}$$

$$= 4.2 \quad 10^{10} \frac{a^{1/2}}{R^{1/6} A_i^{1/2}} \left(\frac{B_t Z_{eff}}{q_o R V} \right)^{4/3} \frac{F(a/q_a R)}{1 + Z_{eff}}$$

which reminds of Murakami's heuristical result /2/. The subscript "o" re-

*) In view of this nonlinear variation of the flux, a fitting parameter μ was introduced in the expression of the destabilizing electron term in order to fit approximately the theoretical transport with the result from power balance. For the discharges considered, $1 \leq \mu \leq 2.5$ which range can easily be fitted within the theoretical and experimental uncertainties or approximations. What is remarkable is that both the turbulence level and the impurity transport /7/ were in close agreement with experiment for the chosen values of this parameter.

fers to the values on axis. The minor and major radii a and R are in cm; the magnetic field B_t is in Gauss; the temperature T_e in keV; the loop voltage V in volts; A_i is the atomic mass of the working gas; the parameter μ was introduced in the footnote (*/). The functional F depends on the density and temperature profiles; $F(0.1) \cong 1$. Numerically, $N_o = 3 \cdot 10^{14}$ cm^{-3} - if $Z = V = A_i = 2 = \mu$ (the appropriate value of this parameter for high density TFR discharges), $q_a = 3$, $B_t/q_a = 5 \cdot 10^4$, a = 20 and $R = 10^2$ - is fully satisfactory in view of TFR results /9/.

It is finally emphasized that the results on impurity transport, presented at another time of this conference /7/ are in agreement with the well known and poorly understood cleaning action of the sawteeth.

References

/1/ Manheimer, W.M., and Antonsen, T.M.: Phys. Fluids 22 (1979) 957-970
/2/ Murakami, M., Callen, J.D., and Berry, L.A.: Nucl. Fus. 16 (1976) 347-348
/3/ Equipe T.F.R.: in Plasma Physics and Controlled Nuclear Fusion Research (Proc. 8th. Int. Conf. Brussels, 1980) Vol. I., IAEA, Vienna (1981) 425-437 and Rapport EUR-CEA-FC-1113 (1981)
/4/ Rogister, A., and Hasselberg, G., Phys. Rev. Lett. 48 (1982) 249-252 and Phys. Fluids, to appear (June 1983)
/5/ Bartiromo, R., Brusati, M., Buratti, P., Cillocs, F., De Marco, F., Gasparotto, M., Giannella, R., Mazzitelli, G., Pieroni, L., Santini, F., Scovenna, M., Tuccillo, A., Tudisco, O., and Zanza, V.: in Plasma Physics and Controlled Nuclear Fusion Research (Proc. 8th Int. Conf. Brussels, 1980) Vol I., IAEA, Vienna (1981) 43-51
/6/ Rogister, A., Hasselberg, G., and Waelbroeck, F.: submitted to Phys. Rev. Lett. (1983) and Report KFA-JÜL-1829; Hasselberg, G., and Rogister, A.: submitted to Nucl. Fus. (1983) and Report KFA-JÜL-1830
/7/ Rogister, A., and Hasselberg, G., submitted to Nucl. Fus. (1983)
/8/ T.F.R. Group: in Plasma Physics and Controlled Nuclear Fusion Research (Proc. 9th Int. Conf. Baltimore, 1982), paper IAEA-CN
/9/ Equipe T.F.R., Nucl. Fus. 20 (1980) 1227-1245

Influence of a Limiter on the Stability of External Kink Modes

J.P. Goedbloed,* J.P. Freidberg, and R. Rohatgi

Massachusetts Institute of Technology, Plasma Fusion Center

Cambridge, MA 02139 U.S.A.

It is shown that external kink modes are completely stabilized in tokamaks with a poloidal limiter when q at the plasma edge exceeds some critical value, which is only unity for the worst case. Toroidal limiters have a significantly lesser influence.

One of the problems encountered in β optimization studies for tokamaks is the conflicting requirements on the profiles for stability with respect to ballooning modes and external kink modes. In order to obtain high values of β relatively broad current and pressure profiles could be allowed if one only had to worry about internal modes. However, such profiles are extremely unstable with respect to external modes. If, somehow, we could ignore these modes, much higher values of β would be possible. In this paper it is demonstrated that at least one type of limiter is extremely effective in eliminating the external kink modes, so that the latter statement acquires some reality. Also, recall that external kink modes do not seem to play a very decisive role in determining present-day tokamak performance. The stabilizing influence of limiters might be one of the factors involved here.

Consider the following model for a limiter. Let the plasma be in contact with a perfectly conducting rigid ring which is situated in a poloidal or a toroidal cross-section of the plasma column. The electric field along this ring has to vanish so that the ideal MHD Ohm's law $\boldsymbol{E} + \boldsymbol{v} \times \boldsymbol{B} = \boldsymbol{0}$ for the plasma provides the following constraint on the plasma motion at the limiter:

$$\boldsymbol{n} \cdot \boldsymbol{\xi} = 0 \quad \text{at} \quad C. \tag{1}$$

Here, C indicates the intersection of the plasma surface with the poloidal plane $\varphi = 0$ if a poloidal limiter is considered or the intersection with the equatorial plane at $\theta = 0$ in the case of a toroidal limiter.

We will limit the discussion to straight low-β tokamaks since this is most appropriate for the analysis of external kink modes. In that case, the usual helical structure $\exp i(m\theta + n\varphi)$ of the external modes does not lead to nodal curves of the plasma displacement $\boldsymbol{\xi}$ coincident with C. This causes mode coupling of the different harmonics labeled with n in the case of a poloidal limiter (where m remains a good quantum number) and of the different harmonics labeled with m in the case of a toroidal limiter (where n remains a good quantum number). Since, for tokamaks with a particular choice of the plasma parameters, there is only one unstable external mode this coupling presents a stabilizing effect. [The results of a parallel investigation on the stabilization by a sequence of poloidal limiters for a reversed field pinch, where several external modes may be unstable in the absence of a conducting wall, are reported elsewhere.]

A simple variational principle for the investigation of the stability of external kink modes in the presence of the constraint (1) may be formulated as follows:

$$\delta\Lambda = 0, \quad \Lambda \equiv W/N, \tag{2}$$

where W is the usual ideal MHD energy functional consisting of plasma, surface, and vacuum contributions /1/:

$$W = W^p[\boldsymbol{\xi}] + W^s[\boldsymbol{n} \cdot \boldsymbol{\xi}] + W^v[\hat{Q}], \tag{3}$$

and N is a convenient normalization for external modes:

---

*On leave of absence from FOM-Institute for Plasma Physics, Nieuwegein, The Netherlands.

$$N = \frac{1}{4}\rho_0 a \int (\boldsymbol{n}\cdot\boldsymbol{\xi})^2 dS, \tag{4}$$

where ρ_0 is some fixed density, a is some measure of the cross-sectional size (the plasma radius if the cross-section is a circle), and integration is over the plasma surface only. For a poloidal limiter, and fixed poloidal mode number m, the variational principle expressed by the equations (2) and (1) may be simplified to

$$\delta\Lambda = 0, \quad \Lambda \equiv \sum_{n=1}^{N} \lambda_n \xi_n^2 \Big/ \sum_{n=1}^{N} \xi_n^2, \qquad \sum_{n=1}^{N} \xi_n = 0, \tag{5}$$

where the λ_n's are the eigenvalues of the unconstrained system, the ξ_n's are the m, n Fourier harmonics of the radial component of the displacement at the plasma boundary, and summation is extended over a finite range $n = 1, 2, \cdots N$ as a numerical approximation to the infinite dimensional system.

It is a simple matter to compute the λ_n's, which are functions of the parameters n, m, b/a, q_1, and of the shape of the q-profile, i.e., of the current profile. It should be mentioned that the use of the norm (4) implies that the eigenfunctions of the unconstrained system are just the marginal modes considered in Newcomb's theory /2/, which may exhibit a jump in the small solution at the singularities $\boldsymbol{k}\cdot\boldsymbol{B} = 0$. In this manner a complicated problem involving integration over continuum modes is avoided, to the cost of not finding the eigenvalue itself but just a parameter λ determining stability.

The final minimization of (5) may be shown /3/ to be equivalent to finding the lowest eigenvalue of the matrix $\mathbf{L}' \equiv \mathbf{P}\cdot\mathbf{L}\cdot\mathbf{P}$, where $\mathbf{L}$ is the diagonal matrix consisting of the unconstrained eigenvalues λ_n and $\mathbf{P}$ is a projection matrix: $P_{nn'} \equiv \delta_{nn'} - 1/N$. Clearly, the only numerical problem that may arise is poor convergence as $N \to \infty$. This turns out to be a difficulty in the case of toroidal limiters, which are described by equations analogous to Eq. (5) replacing n by m.

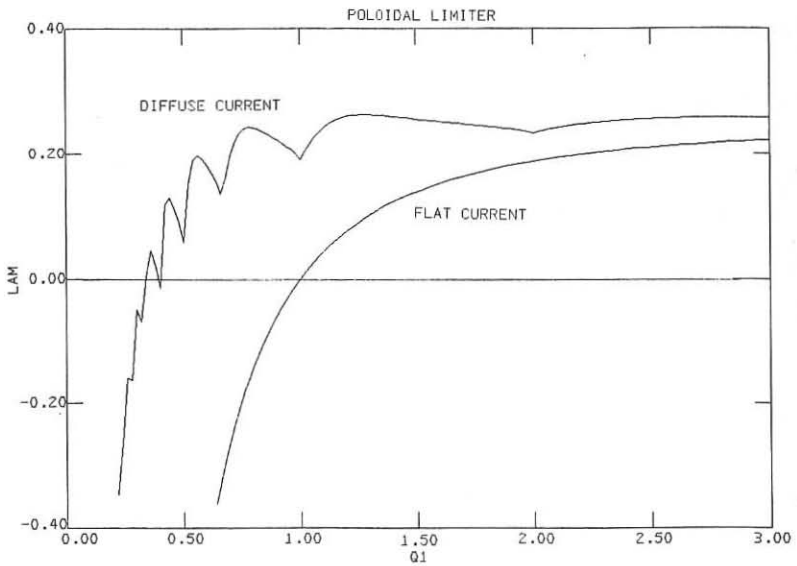

Fig. 1. Stability of $m = 2$ external kink modes in the presence of a poloidal limiter for constant and diffuse toroidal current profiles.

In Fig. 1 the results are shown for the stability of the external $m = 2$ kink mode in the presence of a poloidal limiter for two current profiles. For the flat current profile transition from instability to stability occurs at $q_1 = 1$. This result is actually independent of m for this current profile. In other words: When the Kruskal–Shafranov condition is satisfied the external $m \geq 2$ kink modes become stable as well, just as the external $m = 1$ kink mode in the absence of a limiter. Recall that the low-β tokamak with constant current density represents about the worst case as regards stability of external kink modes: This model is unstable for all values of $q_1 < m$.

For a diffuse current profile the situation even improves: One can surpass the Kruskal–Shafranov limit considerably and still have stability. In Fig. 1 we show results for a current profile $j\varphi = 1 - \psi$, where ψ is the poloidal flux function. The peculiar minima in this curve precisely occur at values $q_1 = m/n = 2/n$. At these values of q_1 singularities start to play a role in the plasma region. For this current profile the situation improves even further for higher m (> 2), so that the worst mode remains the $m = 1$ kink mode (which has a stability diagram that is independent of the current profile).

That a poloidal limiter even affects the $m = 1$ external kink when wall effects are taken into account is shown in Fig. 2. Here, the Kruskal–Shafranov limit is seen to move already significantly to lower values of q_1 when the wall is still relatively far away.

Finally, in Fig. 3 we show results for a toroidal limiter for the same two current profiles as used for Fig. 1. It is already clear from this figure that stability does not improve as dramatically as in the case of a poloidal limiter. Moreover, it should be pointed out that the results of Fig. 3 do not represent valid solutions to the toroidal limiter problem we have posed, since the solutions have not converged. If we keep adding poloidal harmonics the eigenvalue keeps decreasing until it finally comes down to the value for the unconstrained modes. The reason is the extreme localization of the higher-m modes at the plasma

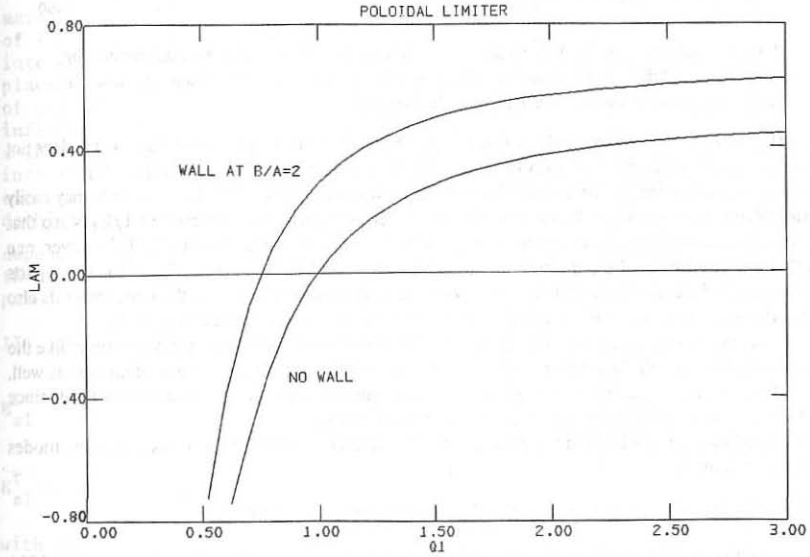

Fig. 2. Effect of the wall on the stability of $m = 1$ external kink modes in the presence of a poloidal limiter for constant current density.

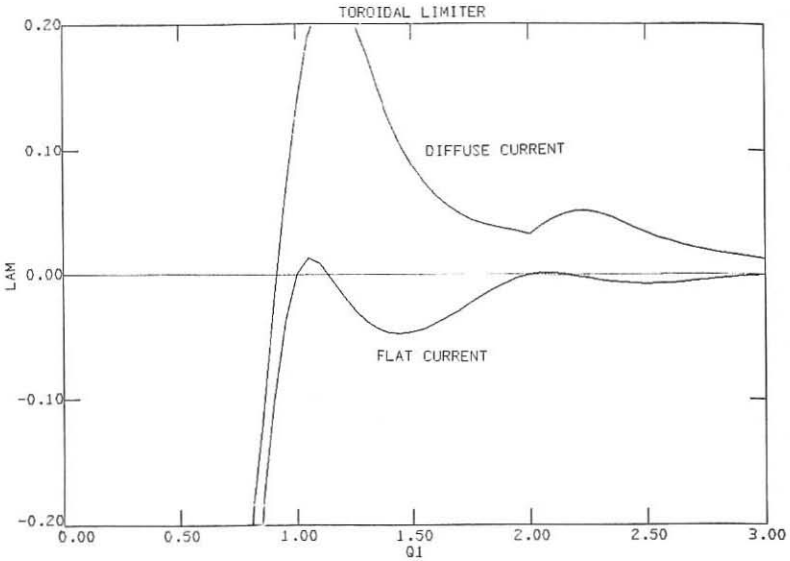

Fig. 3. Stability of $n = 1$ external kink modes in the presence of a toroidal limiter for constant and diffuse toroidal current. These results are not converged. They represent the stability of a constrained system of 60 poloidal harmonics.

surface ($\xi_m \sim r^{|m|-1}$). Consequently, a relatively small contribution of higher–m modes, which does not affect the eigenvalue very much, already has a considerable effect on satisfying the constraint (1).

Whereas convergence in the poloidal limiter case occurs exactly like $1/N$, so that results may easily be extrapolated to $N \to \infty$, in the toroidal limiter case terms appear which behave like $1/\log N$, so that it is virtually impossible to extrapolate from the present numerical results shown in Fig. 3. However, one can prove analytically that the end result for a toroidal limiter will be a curve consisting of the lower parts of the branches of the unconstrained $m = 1, 2, \cdots$ modes. This curve dives below the horizontal axis also for the diffuse current case for $m = 2$ and $m = 3$ just below the values $q_1 = 2$ and $q_1 = 3$.

If some physical mechanism would eliminate the contribution of the higher–m modes, curves like the one shown in Fig. 3 might become relevant to show improvement of stability by toroidal limiters as well. It should be remarked, though, that finite Larmor radius effects do not produce the desired result since their localizations and frequencies do not lead to a different scaling with m.

We conclude that poloidal limiters have a much bigger effect on the stability of external kink modes than toroidal limiters.

This work was supported by the U.S. Department of Energy, FOM, ZWO, and Euratom.

References:

/1/ I.B. Bernstein, E.A. Frieman, M.D. Kruskal, and R.M. Kulsrud, Proc. Roy. Soc. London A224 (1958) 1.

/2/ W.A. Newcomb, Ann. Phys. (N.Y.) 10 (1960) 232.

/3/ G.H. Golub, SIAM Rev. 15 (1973) 318.

ELECTROSTATIC SHIELD FRINGE FIELD INTERACTION WITH PLASMA IN RF HEATING

D.W. FAULCONER

Laboratoire de Physique des Plasmas - Laboratorium voor Plasmafysica
Association "Euratom-Etat belge" - Associatie "Euratom-Belgische Staat"
Ecole Royale Militaire - B 1040 Brussels - Koninklijke Militaire School

I. INTRODUCTION.

Previous studies of ICRF electrostatic shields which incorporate the effect of shield blade discreteness have assumed vacuum to exist in the blade fringe field region [1]. The present model allows plasma to be in contact with the shield blades ; among other effects, this introduces deleterious shield transparency to the TM wave the shield is designed to confine (blades // $\underline{B}_o$). This wave propagates at densities $N < N_{LHR}$; in addition to limiter effect, such low densities in the shield's vicinity are all the more probable in view of heating field ponderomotive effect, and of the sweeping of plasma associated with low frequency fluctuations. Eventual opacity of the shield to the TE (magnetosonic) wave due to plasma-fringe field interaction is also of interest over a broader range of densities [2].

II. MODEL.

Our purpose is to embody the shield-plasma interaction in a matching condition suitable for connecting the nonfringing components of inhomogeneous plasma solutions across the shield region. This interaction being highly localized, we adopt a slab model with a shield placed at the interface of two homogeneous, cold, magnetized plasmas of differing equilibrium characteristics. The shield is modeled as an infinite array of identical, equi-spaced (period=u), z-directed, z-invariant metallic ribbons (width = v, thickness = 0) lying in the interface plane x = 0. The general case of x- wise bidirectional excitation being reduceable to it, we consider the case of unidirectional double-mode excitation from $x < 0$ with $k_{y,inc} = 0$ [exp $i(k_z z - \omega t)$ dependence assumed]. Since the wavelengths of potential interest include the intermediate case, $k_\perp u \sim 2\pi$, we derive a full solution of the posed problem, approaching it in the spirit of Ref. [3].

III. ANALYSIS.

With $(\ )^{r,\ell} \Rightarrow x > 0, < 0$ one has :

$$E^{\ell}_{zl} = a_{inc}\, e^{ik^{\ell}_{xlo}x} + \sum_{n=-\infty}^{\infty} a_n\, e^{i(-k^{\ell}_{xln}x + n\phi)}$$

$$E^{r}_{zl} = \sum_{n=-\infty}^{\infty} b_n e^{i(k^{r}_{xln}x + n\phi)} \qquad (\phi = \frac{2\pi y}{u} \equiv \kappa y) \qquad (1)$$

with the substitutions $1 \to 2$, $a \to c$, $b \to d$ giving the expressions for the second mode ; $k^2_{x\alpha n} = k^2_{\perp\alpha} - n^2\kappa^2$ where $k^2_{\perp\alpha}$, $\underline{E}_\alpha$, $\underline{H}_\alpha$ refer to the α^{th} root of the cold dispersion relation. Sgn $(k_{x\alpha n})$ is chosen with

due respect for the backward nature of certain incident and scattered modes, with scattered modes finite as $|x| \to \infty$. Eqns. (9.163)-(9.166) of Ref. [4], with the substitutions $j \to i$, $\omega \to -\omega$, $\gamma \to -ik_z$, give $\underline{E}^{r,\ell}_{\alpha}$, $\underline{H}^{r,\ell}_{\alpha}$ in terms of $E^{r,\ell}_{z\alpha}$. Choosing the origin at mid-blade and noting $\underline{E}$, $\underline{H} = \underline{E}_1 + \underline{E}_2$, $\underline{H}_1 + \underline{H}_2$, one imposes as boundary conditions at x = 0 : i) the vanishing of $E^{r,\ell}_z$, $E^{r,\ell}_y$ on the respective blade faces ($|\phi| < \frac{v\pi}{u} \equiv \theta$), ii) the continuity of E_z, E_y, H_z, H_y in the gap ($\theta < |\phi| < \pi$). These conditions reduce to a system of the form

$$(|\phi| < \theta): \quad \sum_{\substack{n\neq o \\ -\infty}}^{\infty} \underline{g}^n(I)\, \underline{\Phi}^n e^{in\phi} = \underline{g}^o(I)\, \underline{\Phi}^o + \underline{g}^{inc}(I)\, \underline{\Phi}^{inc} \qquad (2)$$

$(\theta < |\phi| < \pi)$: same with I → II

where $\Phi^n_j(\Phi^o_j\ ,\ \Phi^{inc}_j)$ is a linear combination of $a_n(a_o,\ a_{inc})$ and $b_n(b_o\ ,\ b_{inc})$; $\underline{g}^n(I)$, $\underline{g}^n(II)$ are constant in their respective ϕ domains (denoted by I and II), having finite limits, $\underline{g}^{n\infty/|n|}(I)$, $\underline{g}^{n\infty/|n|}(II)$, as $n \to \pm\infty$. Since we have differentiated the conditions on E_z, H_z in writing Eqn.(2), these conditions are also imposed in undifferentiated form at the blade edge (E_z, H_z are well-behaved there)

$$\sum_{\substack{n\neq o \\ -\infty}}^{\infty} \frac{e^{-in\theta}}{n}\, \underline{\Phi}^n = \underline{g}^o(I,\ II)\, \underline{\Phi}^o + \underline{g}^{inc}(I,\ II)\, \underline{\Phi}^{inc} \qquad (3)$$

where the linear transformations relating a_n, b_n to $\underline{\Phi}_n$ have been expressly chosen to give the identity matrix coefficient of $\underline{\Phi}^n$.

Proceeding in a fashion similar to Ref. [3], one restates the mixed boundary-value problem (2) as a problem of Hilbert type on the unit circle ($t = e^{i\phi}$) of the complex t-plane. Here one writes for $\underline{g}^n(I)$, $\underline{g}^n(II)$ in Eqn. (2) : $\underline{g}^n\underline{\Phi}^n = \underline{g}^{n\infty/|n|}\,\underline{\Phi}^n + [\underline{g}^n - \underline{g}^{n\infty/|n|}]\,\underline{\Phi}^n$ treating the bracketed term's contribution as a given inhomogeneous term. The solution of the resulting 2 x 2 system is known [5]. Projection of this solution on the functions $\exp(-im\phi)$ (m integral) reincorporates the unknowns associated with the aforementioned bracketed term in an infinite algebraic system to which one adds Eqn. (3) with its left member reidentified [3]. The coefficients of this system can be evaluated in terms of known functions. Owing to the bracketed term's dependence $\sim n^{-2}$ as $|n| \to \infty$, the solution of this system converges with truncation at sucessively higher order.

IV. DISCUSSION.

An important aspect of the solution is well-illustrated in the long wavelength limit, $|k_{\perp\alpha}|/\kappa << 1$. Here one can truncate the final alge-

braic system at lowest order and write the solution at x = 0 in terms of that for the Hilbert problem. Though lowest-order in the sense of truncation , the resulting expression accurately describes the field singularities at the blade edges (large n behavior). This is a consequence of the system satisfied by the Hilbert solution being identical to the large n limit of the system satisfied by the full solution. Computed results relative to shield transmission properties are pending, and will be presented at the conference.

REFERENCES.

/1/ Faulconer, D.W. : Proc. 3rd Joint Varenna-Grenoble Internat. Symp., Grenoble, 1982. Commission of the European Communities, Brussels, 1982, Vol. 1, p. 347. To be published in J. Appl. Phys. (1983).
/2/ Weynants, R.R., Lallia, P. : Private communications.
/3/ Agronovich, Z.S., Marchenko, V.A., and Shestopalov, V.P. : Sov. Phys.-Tech. Phys. 7 (1962), 277.
/4/ Allis, W.P., Buchsbaum, S.J., Bers, A. : Waves in Anisotropic Plasmas. M.I.T. Press, Cambridge, Massachusetts 1963.
/5/ Vekua, N.P.: Systems of Singular Integral Equations. Noordhoff, Groningen 1967.

IDEAL-MHD BETA LIMITS: SCALING LAWS AND COMPARISON WITH DOUBLET III HIGH-BETA PLASMAS*

L. C. Bernard, D. K. Bhadra, F. J. Helton, L. L. Lao, and T. N. Todd**
GA Technologies Inc., San Diego, California, U.S.A.

Doublet III (DIII) recently has achieved a value for β, the ratio of volume averaged plasma to magnetic pressure, of 4.5%.[1] This β value is in the range required for an economically attractive tokamak reactor, and also close to the relevant limit predicted by ideal-MHD theory (see Ref. 2 and references therein). It is therefore of great interest to assess the validity of the theory by comparison with experiment and thus to have a basis for the prediction of future reactor performance. A large variety of plasma shapes have been obtained in DIII. These shapes can be divided into two classes: (1) limiter discharges, and (2), diverted discharges, which are of great interest because of their good confinement in the H-mode operation.[3] We derive simple scaling laws from the variation of optimized ideal-MHD beta limits (β_c) with plasma shape parameters. The current profile is optimized for fixed plasma shapes, separately for the high-n (ballooning) and the low-n (kink) modes. Results are presented in the form of suitably normalized curves of β versus poloidal beta, β_p, for both ballooning and kink modes in order to simultaneously compare all the DIII experimental data.

MHD equilibria are obtained with the free-boundary code GAEQ which solves the Grad-Shafranov equation $R^2\nabla\cdot\left(\nabla\psi/R^2\right) = \mu_0 R j_\phi = -\mu_0 R p' - ff'$. The simple "Gaussian profile" p', $ff' \propto \exp(1 - \tilde{\psi}^\alpha) - 1$ is used most often where $\tilde{\psi} = (\psi - \psi_0)/(\psi_s - \psi_0)$ and indices 0 and s refer to the magnetic axis and plasma surface, respectively. For comparison, the safety factor q is specified in some cases instead of ff'. The "q-profile" has the form $q = q_0\{1 + (\tilde{\psi})^\nu[(q_s/q_0)^\nu - 1]\}^{1/\nu}$. In addition to the Gaussian p' profile, a tabular p' profile which is determined by linear interpolation from 12 independently variable values of p' is available.

For the limiter discharges, an analytic expression, $R = R_0 + a\cos\theta$, $z = \kappa a \sin(\theta - \delta' \sin\theta)$, was used to generate limiters with varying ε (inverse aspect ratio), κ (elongation), and δ (triangularity). δ is related to δ' by the expression $\delta' = \sin^{-1}\delta/\cos(\sin^{-1}\delta)$. Equilibria with flux surfaces matching the limiter were generated by specifying a constant flux value on 24 flux loops just outside the limiter. Poloidal field coils were similarly distributed to minimize shaping problems. Experimental plasmas in DIII are slightly up-down asymmetric and the triangularity is defined to be the average of triangularities at the top and bottom. Limiter discharges cover a wide range for ε (0.25 → 0.30), κ (0.9 → 1.7), and δ (−0.05 → 0./4). For simplicity, the equilibria used for the stability analyses were symmetric. $\beta = 2\mu_0 \int pdV/(VB_t^2)$ and $\beta_p = (1/2\pi) \int pdV/ \int (V/V')I'd\psi$, where V, I, and B_t are the volume, the toroidal current, and the vacuum toroidal field at the plasma geometric center, respectively.

Ideal MHD stability in the limit of infinite toroidal mode number was analyzed using the code MBC, which evaluates the ballooning criterion.

*Work supported by U.S. Department of Energy, Contract DE-AT02-76ET51011.
**Permanent Address: EURATOM-UKAEA, Culham Laboratory, United Kingdom.

Stability to low toroidal mode number perturbations was analyzed using the global stability code GATO. GATO computes the eigenfrequencies and eigenmodes using finite hybrid elements to minimize the symmetric form of δW. Determination of β using mesh extrapolation would require too much computer time for optimization studies. Instead, an equilibrium is said to be stable if the growth rate is less than a stability cutoff ($10^{-2}\ \omega_A$), where ω_A is the poloidal Alfvén frequency.

The β limits for the $n=\infty$ ballooning mode are shown in Fig. 1. The solid line refers to the Gaussian profile. Normalized values are used to fit a unique curve through many theoretical data points obtained with a combination of shape parameters. q_0 is chosen to be 0.05 above the critical value for interchange stability. $\hat{\beta}$ and $\hat{\beta}_p$ are the normalized values deduced from the absolute values through the expressions:

$$\hat{\beta} = 0.5\ \beta/[\varepsilon^{1.15}\kappa^{0.5}(1 + 1.55\ \delta)] \quad ; \tag{1}$$

$$\hat{\beta}_p = 4\ \beta_p\varepsilon^{0.9}/[\kappa^{0.5}(1 + 0.33\ \delta)] \quad .$$

These expressions were obtained by fitting to a simple scaling law consisting of a power law variation in ε and κ and a linear variation in δ. The dashed curve of Fig. 1 is obtained for an ε=0.3 circular cross-section by optimizing the q-profile and a 12-parameter pressure profile. This curve shows that high-n β limits are not very sensitive to the functional form of the plasma current.

Figure 2 shows the β limits for the n=1 external kink, which is more restrictive than other low-n modes when no external wall stabilization is assumed.[4] q_0 is held fixed to 1.05 to avoid the n=1 internal kink, potentially unstable for $q_0 < 1$. Suitable normalizations and a Gaussian profile (solid line) are used in Fig. 2, similar to Fig. 1. The use of the q-profile did not yield significant improvement. The scaling $\beta \propto \varepsilon^{1.5}$ was assumed[5] and is supported by the ε=0.42 JET case[4] incorporated in this study. Normalized β values are calculated from the expressions

$$\hat{\beta} = \beta/[3\varepsilon^{1.5}\kappa^{0.95}(1 + 2.6\delta)] \quad ; \qquad \hat{\beta}_p = 2\beta_p\varepsilon^{0.5}\kappa^{0.33} \quad . \tag{2}$$

The dashed curve of Fig. 2 shows the effect of a cool conductive mantle,[6] for an ε=0.3 circular cross-section. The mantle is assumed to be ideally conductive, pressureless and currentless with nonzero density (supposed constant throughout the plasma). The thickness of the mantle, normalized to the minor radius, is 10%. q_s is approximately constant on any straight line through the origin of the plot of Fig. 2. With no mantle, the mode is unstable whenever $q_s < 2$, as found before, and there is a large dip for $2 < q_s < 3$ and a smaller dip for $3 < q_s < 4$. These dips correspond to the occurrence of a rational surface just outside the plasma surface.

Figures 1 and 2 also show the limiter discharge DIII data (solid triangles) normalized with expressions (4) and (5), respectively. Clearly, the high-n β limits are not exceeded significantly by the DIII data so far (excluding the $q_0 \leq 1$ region dominated by sawtooth activity), but the same cannot be said for the kink limits, even with the presence of a mantle. A possible explanation for this discrepancy is the effect of wall stabilization. The vacuum vessel (with a resistive diffusion time τ_v) may effectively appear superconducting if the real frequency of the kink mode is much greater than

$1/\tau_V$. Figure 3 shows the β limit curve for marginal stability to the n=1 kink mode for an ε=0.3 circular cross-section with a superconducting wall located at a constant distance d from the plasma surface of d/a = 0.5. With this plasma-wall separation, the β limit for the n=1 kink is comparable to the ballooning limit. The n=1 kink was determined to be below the n=2 and n=3 kink limits in this case. With a wall closer than d/a = 0.5 or with the combined stabilization of a wall and a mantle, the kink limit would be above the ballooning limit when $q_s < 2$. However, unless the wall is very close, the kink is still unstable when $q_s < 2$. Thus, it is reasonable to postulate a "unified ideal limit" curve, by combining the n=∞ limit line for $q_s > 2$ with the hard q_s=2 limit of the surface kink. This can be written as:

$$\beta_c(\%) = 27\ \varepsilon^{1.3}\kappa^{1.2}(1 + 1.5\delta)q_s^{-1.1} \quad , \qquad q_s > 2 \quad ;$$
$$\beta_c = 0 \quad , \qquad q_s < 2 \quad . \tag{3}$$

Figure 4 shows the goodness of the fit with theoretical points (open circles) for the Gaussian profile (solid line) where the normalization $\hat{\beta}_c = 11\ q_s^{-1.1}$ is used. The coefficient 27 of Eq. (6) is for the q-profile (dashed line) and must be replaced by 23 for the Gaussian profile.

By contrast with the limiter discharges, the disruptive H-mode discharges are all below the theoretical limits, if ε, κ, and δ are defined at the separatrix, assuming up-down symmetry as before. The asymmetry of the H-mode discharges may be important. The effect of asymmetry will be presented at the conference. The presence of an X-point where q goes to infinity may play an important role and will be discussed also.

The scaling law (3) shows that high β values can be reached with tight aspect ratio, high elongation, and high triangularity. All these features are possible in the BIG DEE tokamak (DIII upgrade) where β values in excess of 18% are obtained by optimizing both plasma shape and current profile at peak β (q_s = 2). Such high β values, if achievable in a reactor tokamak, would improve the economics of high power density reactor operation and also make the use of advanced fuels attractive.

REFERENCES

/1/ Burrell, K.H., et al., Nucl. Fusion 23 (1983) 533.
/2/ Bernard, L.C., et al., GA Technologies Report GA-A16981 (1983).
/3/ Wagner, F., et al., Phys. Rev. Lett. 49 (1982) 1408.
/4/ Bernard, L.C., et al., Nucl. Fusion 20 (1980) 1199.
/5/ Bernard, L.C., and Moore, R.W., Phys. Rev. Lett. 46 (1981) 1286.
/6/ Kerner, W., et al., Nucl. Fusion 21 (1981) 1383.

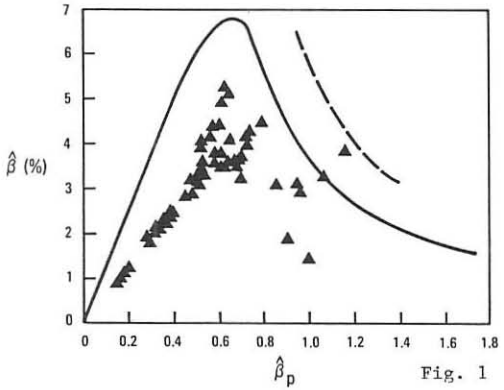

Fig. 1

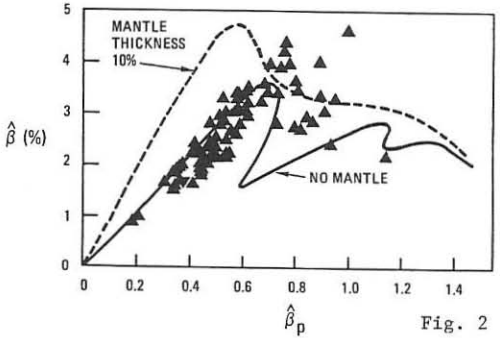

Fig. 2

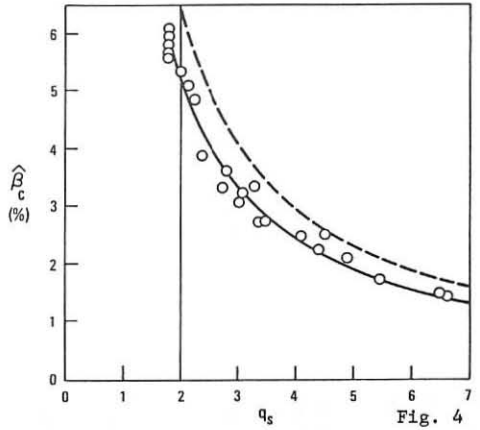

Fig. 4

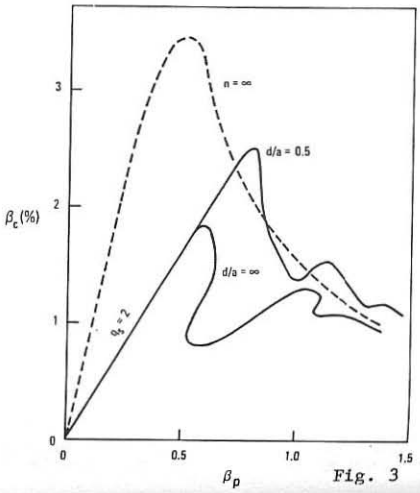

Fig. 3

ADVANCED CONCEPT OF ADIABATIC COMPRESSION OF TOKAMAK & SELF-COMPRESSION OF COMPACT TORUS

MING LUN XUE
Institute of Mechanics, Chinese Acad. of Sci.
Beijing, People's Republic of China

Adiabatic compression may be an inexpensive way to reach the temperature that must be attained in the experimental ignition facilities.[1-5]

It is shown that pure radial compression of tokamak plasma will induce a significant surface current in the same direction to the main plasma current. Furth-Yoshikawa[1] considered two conditions--toroidal and poloidal magnetic flux within the plasma--must be conserved during rapid compression. However, another condition--poloidal magnetic flux outside the plasma must also be conserved. For circular cross section and large aspect ratio, that is $\psi_{out} = \frac{4\pi}{c} R \left(\ln 8 \frac{R}{a} - 2 \right) I_t - \int_0^{R-a} B_\perp 2\pi r dr = const.$

Two limiting cases are considered:

case 1, $B_\perp$ is homogeneous in the whole region and is determined by $B_\perp = \frac{I_t}{cR} \left(\ln 8 \frac{R}{a} + \beta_p - \frac{3}{2} + \frac{l_i}{2} \right)$, then

$$\frac{I_{t2}}{I_{t1}} = \frac{R_1 \left[\ln 8 R_2/a_2 - 2 - \frac{1}{4} \left(\ln 8 R_1/a_1 - 3/2 + \beta_{p1} + l_{i1}/2 \right) (1 - a_1/R_1)^2 \right]}{R_2 \left[\ln 8 R_2/a_2 - 2 - \frac{1}{4} \left(\ln 8 R_2/a_2 - 1/2 + \beta_{p2} + l_{i2}/2 \right) (1 - a_2/R_2)^2 \right]}$$

case2, $B_\perp = 0$ outside the plasma,

then, $\psi_{out} = \frac{4\pi}{c} I_t R \left(\ln 8 \frac{R}{a} - 2 \right) = const.$ $\quad \frac{I_{t2}}{I_{t1}} = \frac{R_1 (\ln 8 R_1/a_1 - 2)}{R_2 (\ln 8 R_2/a_2 - 2)}$

while the result of Furth- Yoshikawa was $I_{t2}/I_{t1} = R_1/R_2$, the difference is owing to the fact that a surface current $I_{tS2} = I_{t2} - I_{tv2}$ must be induced during rapid radial compression. (fig. 1 & 2)

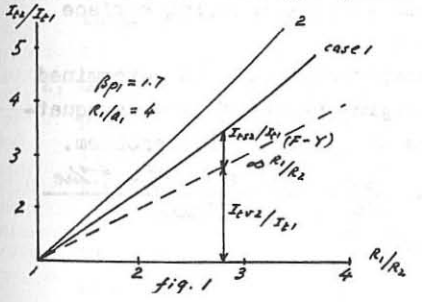

fig. 1

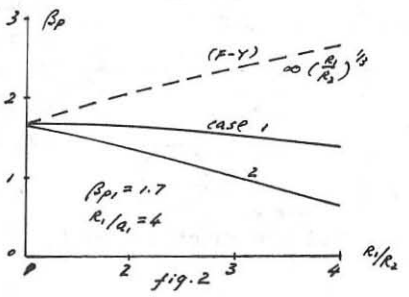

fig.2

Two tokamak tori will be attracted with each other by electmagnetic force, part of the poloidal magnetic energy will be converted to the kinetic energy and finally dissipated to the thermal energy after impact. The total magnetic energy of two mutually interacting tori is (fig.3)

$$W = 2\left(\frac{L}{2c^2} I_t^2\right) + \frac{M}{c^2} I_t^2$$

here L and M are self and mutual inductence.

The equation of momentum is

$$m_p \frac{dV_z}{dt} = \frac{\partial W}{\partial z}\Big|_{I_t} = \frac{I_t^2}{c^2}\frac{\partial M}{\partial z}$$

Since magnetic flux is conserved during acceleration

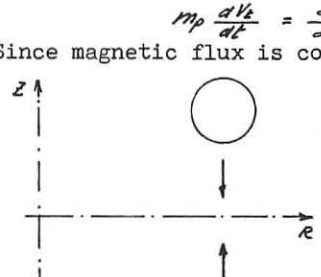

fig. 3

$$(L+M) I_t = \text{const.}$$

after integrating,

$$m_p \frac{V^2}{2} = \frac{I_t^2}{c^2}(L+M_1)^2\left(\frac{1}{L+M_1} - \frac{1}{L+M}\right)$$

M ≈0 for two initially well- separated tori and M ≈L when two tori are one next to another, then,

$$m_p V_2^2/2 \approx I_{t1}^2 L/2c^2$$

and

$$\frac{I_{t2}}{I_{t1}} = \frac{L+M_1}{L+M_2} \approx 1/2$$

Since $q(a)$ is conserved during pure axial acceleration, the total volume current is conserved. If the total current decreased to half of its initial value, then a surface current must be induced in the opposite direction of the main current.

Pure radial compression and pure axial acceleration induce the surface currents in the opposite direction, it is natually to combine these two processes together. (fig.4)

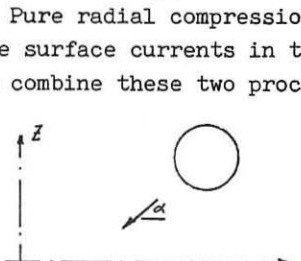

fig. 4

Under certain conditions, it is indeed possible to obtain a dynamic process without inducing surface current.

The compression path is determined by integrating the following equation as an initial value problem.

$$tg\alpha = \frac{dz}{dR} = \frac{(L+M)/R - \frac{dL}{dR} - \partial M/\partial R}{\partial M/\partial z}$$

L,M are functions of R, Z, a

Next, we will see what is happened after a compact torus leaving the coaxial plasma gun without applied toroidal and vertical field[6]. In general, the plasma torus is not in equilibrium, the toroidal magnetic energy is much larger than the poloidal one. The plasma begins to contract along the major as well as the minor radius with the conservation of the toroidal and poloidal magnetic flux. During the compression period, part of the toroidal magnetic energy is transfered to the poloidal magnetic energy, the whole process can be obtained by numerical integration of the following equations

$$\frac{dA_i}{dR} = f_i\,(I_p, I_t, R, a)$$

i=1,2,3,4 correspond to I_t, I_p, p,a

it is proved that the final equilibrium state is reached when

$$\frac{W_t}{W_p} = \frac{\ln 8R/a - 0.5}{2(\ln 8R/a - 2)} \approx 1$$

that is the equipartition of magnetic energy is a consequence of toroidal plasma equilibrium without applied toroidal and vertical field. Typical numerical results show that the temperature ratio could be obtained above four during this self-compression process. (fig. 5)

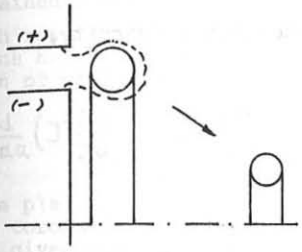

fig. 5

Conclusions:

1, For tokamak plasmas, either pure radial compression or pure axial acceleration with merging will induce a surface current during the compression process, a combined scheme of these two processes is suggested, the surface current could be cancelled completely under certain conditions.

2, Gun-produced plasma torus with different total toroidal and poloidal magnetic energy after leaving the muzzle of the gun is non-equilibrium along major radius. Under certain operating conditions it will contract along major as well as minor radius. The adiabatic self-compression process without a guiding field can raise the plasma temperature to 4 to 5 times its initial value within about one microsecond.

Max-Planck-Institut für Plasmaphysik

3, Magnetic energy equipartition is a consequence of equilibrium of plasma torus without applied toroidal and vertical field.

4, The plasma torus is MHD stable during the whole self-compression process.

References:

/1/ Furth, H.P.,and Yoshikawa, S.: Physics of Fluids,13, (1970) 2593.

/2/ Holmes, J.A., Peng,Y-K.,M.,and Lynch, S.J., Physics of Fluids, 23 (1980) 1874.

/3/ Albert, D.B., Nuclear Fusion, 20 (1980) 939.

/4/ Shafranov, V.D., Nuclear Fusion, 19 (1979) 187.

/5/ Ohyabu, N.,Hsieh, C.L.,and Jensen, T.H., J. of Plasma Physics, 21 (1978) 253.

/6/ Furth, H.P., PPPL Report 1716, Princetion University, (1980).

SOLUTION OF THE TOKAMAK PLASMA EQUILIBRIUM AT HIGH BETAS BY VARIATIONAL METHOD

V.D.Khait, V.K.Kolesnikov

Institute of High Temperatures, USSR Academy of Sciences, Moscow, USSR

Paper /1/ and later independently papers /2,3/ suggested and numerically realized the variational method of solution for plasma equilibrium problem in axially symmetric systems. The geometry of each magnetic surface is supposed to be described by a set of parameters u_i, which are the functions of a surface coordinate a (magnetic surface label). The system of ordinary differential equations can be obtained for the unknown functions $u_i(a)$. Zakharov-Shafranov moments method /5/ promotes the obtaining of the analogous system by averaging two-dimensional equilibrium equation on magnetic surfaces with a set of weight functions, which are the vacuum solutions of the Grad-Shafranov equation. The system of equations for parameters $u_i(a)$ can be obtained otherwise by variation of energy functional $\int(p+B^2/8\pi)dV$ with respect to functions $u_i(a)$. The obtained set of Euler equations has the form which is invariant under the certain selection of parameters

$$\frac{d}{da}\left(J^2\frac{\partial M}{\partial u_i'}\right) - J^2\frac{\partial M}{\partial u_i} + c^2p'\frac{\partial V}{\partial u_i} + II'\frac{\partial L}{\partial u_i} = 0 \ . \qquad (1)$$

Here p(a) is the plasma pressure, J(a) and I(a) are the external toroidal and poloidal currents, $V(u_i)$ is the volume inside the given magnetic surface, $L(u_i)$ is the self-induction coefficient of toroidal solenoid, coinsiding with the given surface. Function $M(u_i,u_i')$ (the prime indicates the derivative with respect to a) is determined by the integral along the meridional contour of cross-section ℓ_a

$$M^{-1} = \oint_{\ell_a} (|\nabla a|/4\pi^2 z)\, d\ell \ .$$

At the practical realization of the method when we have to be restricted by the terminating set of parameters the solution of the problem (if at all) by the variational method is apparently the most accurate among the solutions obtained by the parametrization of the shapes of magnetic surfaces. If there solves a problem for the equilibrium of plasma surrounded by a perfectly conducting casing, then its shape determines the value of parameters at the boundary $u_i = u_i^*$. If the equilibrium is maintained by the external magnetic field then the surface shape of plasma column is determined by multipole harmonics of this field. In this case the equations which should play the role of boundary conditions can be obtained by the following means. The energy of interaction of plasma with external magnetic field, characterized by flux function Ψ_e can be expressed through the values of the plasma column boundary

$$U_e = \frac{MJ}{4\pi^2 c} \oint \frac{\Psi_e |\nabla a|}{r} dl \,. \qquad (2)$$

Generalized forces, acting on the plasma column from the side of the external magnetic field are determined by the derivatives $\partial \tau_e / \partial u_i$.

Forces necessary for the column maintaining in the equilibrium state can be determined by the "virtual casing" method /6/. If the column surface is supposed to be surrounded by an ideal casing, then there should exist no field outside the casing and surface current should flow along it. Inside the casing this current is induced by the field necessary for the maintaining. The field flux function has the form

$$\Psi_m = \frac{MJ}{4\pi^2} \oint_{l_\Sigma} \frac{|\nabla a| \Psi_o}{r} dl \,, \qquad (3)$$

where Ψ_o is flux function of unit current.

To determine the generalized forces necessary for the equilibrium, one can use expression (2), substituting expression (3) for Ψ_m instead of Ψ_e and consider Ψ_m at variation with respect to u_i the function given in space. Thus equalling the obtained forces to those, that influence from the side of the external field, we obtain the conditions which sould be used as boundary ones.

In numerical calculations, which were carried out for the equilibrium problem inside the casing, a four-parametrical metric was used as suggested in /4/. The role of u_i parameters here is played by: R - cross-section centre coordinate of the given surface, η - ellipticity parameter ($e\eta$ - the ratio of cross-section semi-axes), τ_1 and τ_2 - triangularity parameters where τ_1 characterizes the flattening of the surfaces and τ_2 - the sharpening of them.

Equations (7) forming a set of quasi-linear inhomogeneous ones were solved by iterative procedure, the system being solved as a linear one by factorization method for each iteration. The equation coefficients were calculated with the use of solutions obtained from the two previous iterations with a certain weight. As a rule 10 - 15 iterations appeared to be sufficient for the results to be agreeble. The calculations with different number of u_i parameters had been carried out to clear out the role of their number. The numerical code gives an opportunity to single out any of the four parameters R, η , τ_1 and τ_2 to solve practically just a part of the set of equations by a simple method of nullifying the corresponding matrix coefficients. In this case those u_i parameters for which the equations are not solved are fixed equal to their given limiting values.

Table I demonstrated comparative calculation results in three schemes: I - the equation was solved only for R, II - equations for R and η ; III - equations for R, η and τ_2 .

TABLE I

	$\beta_J = 0$			$\beta_J = 2.5$			$\beta_J = 5.0$			β_J^{lim}
	Δ	E	B_p^{π}	Δ	E	B_p^{π}	Δ	E	B_p^{π}	
I	.066	1.00	2.48	.207	1.00	1.41	0.286	1.00	1.04	17.5
II	.080	1.01	2.31	.216	1.05	1.02	.310	1.11	.494	13.0
III	.080	1.01	2.21	.217	1.05	.777	.317	1.12	.048	5.60

Table one gives the following values: Δ is the shift of the magnetic axis rated to the half of the casing size in radial direction; $E = \exp \eta(0)$ is the cross-section ellipticity at the magnetic axis; B_p^{π} is the poloidal magnetic field close to the internal side of the casing, β_J^{lim} are the limiting values of β_J with respect to equilibrium the points with zero values of B_p^{π} being corresponding to these values.

The table illustrates the fact, that for low $\beta_J < A$ the difference of the values in various models is small. However this difference is growing with the increase of β_J and at $\beta_J > A$ it becomes noticable. Values of B_p^{π} differ especially. It is explained by the fact that the model of the nested ellipses (or circles) corresponding to schemes I and II can not adequately describe the zero point of the poloidal field. The significant difference in β_J^{lim} values is also explaned by this fact.

The following distributions of the pressure and azimuth current were given for all cases: $p'(a) = \text{const}$, $J(a) = 5a/(1+4a)$. Calculations were conducted for different values of $\beta_J = 2c^2 \int p\, dS / J_\Sigma^2$. Aspect ratio was equal to A = 3.

REFERENCES

/1/ Khait V.D.: Fizika Plazmy, 6 (1980) 871.

/2/ Lao L.L., Hirshman S.P., Wieland R.M.: Phys.Fluids, 24 (1981) 1431.

/3/ Bhattacharjee A., Wiley J.C.: Phys.Fluids, 26 (1983)520.

/4/ Khait V.D., Kolesnikov V.K.: 10-th Europ.Conf. on Controlled Fusion and Plasma Phys., v.1, report B-8, Moscow, 1981.

/5/ Zakharov L.E., Shafranov V.D.: Preprint, Kurchatov Institute of Atomic Energy, IAE-3075, Moscow (1978).

/6/ Shafranov V.D., Zakharov L.E.: Nucl.Fusion 12 (1972) 599.

Quasistatic Evolution of Ideal MHD Equilibria in INTOR and ASDEX-UG

F. Casci, A. Kaleck+), H.P. Zehrfeld
Max-Planck-Institut für Plasmaphysik, D-8046 Garching
+) Institut für Plasmaphysik, Kernforschungsanlage Jülich, D-5170 Julich

1. Introduction. For studies of plasma equilibrium and stability in some present-day tokamak devices we consider processes of plasma dynamics which evolve fast on the resistive, but slowly on the Alfven time scale. Under such conditions the time evolution of the plasma configuration can be described in terms of a continuous sequence of ideal MHD equilibria which are controlled by appropriate time-dependent external magnetic fields. Such sequences are considered solving the partial differential equation for the poloidal magnetic flux together with the dynamical equations describing the isentropic motion of an ideally conducting plasma. In doing so we self-consistently take account of the instantaneous action on the plasma equilibrium of externally placed passive conductor elements and, by a corresponding adjustment of the loop voltage, provide for a skin-current free formation of the plasma.

2. Theory. In the plasma region we will use the equations for equilibrium

$$\mathrm{rot}\underline{B}\times\underline{B} = \mu_0 \nabla p \qquad (1)$$

with $\mathrm{div}\underline{B} = 0$, the conservation equations for magnetic flux, for mass and for entropy:

$$\partial\underline{B}/\partial t = \mathrm{rot}(\underline{v}\times\underline{B}) \qquad \partial\rho/\partial t + \mathrm{div}\rho\underline{v} = 0 \qquad \partial S/\partial t + \underline{v}.\nabla S = 0 \qquad (2)$$

and an equation of state (more precisely a thermodynamic potential). In these equations all quantities have their usual meaning; we use MKSA-units. With R as the radial distance and with φ the angle about the axis of symmetry in z-direction we will refer to right-handed co-ordinates (R,φ,z). The fluxes of magnetic field and of current density through a surface which is bounded by a field line of the toroidal magnetic field we call Ψ and J, respectively. For the corresponding fluxes through poloidal cross-sectional areas of magnetic surfaces we will use the notations Φ and I. We make the assumption that the temperature is constant on magnetic surfaces. Then the fluxes Ψ and Φ, the currents J and I and the thermodynamic variables p, ρ and T are all surface quantities. The equilibria we are calculating are, besides through the equations (1) and (2), defined by the specification of

(I) a free-boundary equilibrium at an initial time;
(II) the externally produced toroidal and poloidal magnetic vacuum fields controlling and confining the plasma at any time.

By (I) the distribution of the above-mentioned seven quantities

over the different magnetic surfaces is given at an initial time, their values at any time are determined by (II), the three conservation laws, by two equations relating fluxes and currents, the equation of state and by the normal component flux surface average of equation (1). A straightforward elimination procedure leads to a second-order (generalized /4/) ordinary differential equation of the form $F(\psi'',\psi',\psi,V,t) = 0$ for the poloidal flux as function of the volume V (of the magnetic surfaces). This equation is to be solved with the boundary conditions corresponding to a constant flux difference between magnetic axis and plasma boundary and with the side condition that the poloidal current is continuous across the plasma-vacuum interface. This side condition excludes poloidal skin currents; the absence of toroidal ones must be externally controlled keeping constant the poloidal flux at the plasma boundary by an adjustment of the loop voltage. The rest of the problem reveals in (a) (not flux-surface averaged) local equations for $V(R,z,t)$ and $\underline{v}(R,z,t)$ and (b) circuit equations describing the inductive interaction between plasma and external active and passive conductor elements. More details on theory will be given elsewhere /1/.

3. Computational Features. The calculations profit by the fact that for given geometry of the magnetic surfaces the problem amounts to only the solution of ordinary differential equations. Solving it iteratively we start with the geometry of the initial free-boundary equilibrium and then proceed in time changing the currents in the external conductors. In order to find the new self-consistent plasma equilibrium we apply the following iteration scheme: (A) We solve the circuit equations for the external currents with the present plasma current density; (B) Use a fast Buneman solver for the determination of the plasma poloidal flux and superpose the vacuum flux of the external currents; (C) With that flux function calculate the new geometry and on the basis of this geometry a new plasma current density; (D) Repeat steps (A) to (C) until convergence is reached. In some cases acceleration of the procedure is expedient. For this case Newton-like iterations are applied shifting the plasma in about two steps to almost the right new position. Afterwards the cross-section and the exact plasma position is evaluated by iterations of the above scheme. In strongly stable configurations a new equilibrium is reached in 10-15 iterations, weakly stable situations need more iterations (about 30).

4. Application and Results. We considered the vertical stability of two experiments recently in the planning phase: NET/INTOR and ASDEX- UG. As shown in the Fig. INTOR (and similarly ASDEX-UG) have an elongated cross-section and therefore an unstable vertical position unless passive conductors would stabilize it. One easily can prove that in the case of stabilization the plasma displacement is of the following form:

$$\xi_z(t) = \xi_z(0)\exp(t/\tau), \quad \xi_z(0) = F_p/(f_D(\alpha-1)) \qquad (3)$$

where

$$\tau = (\alpha-1)L/R \quad \text{and} \quad \alpha = f_R/f_D \tag{4}$$

ξ_z is a small deviation from the equilibrium position, F_P is a perturbation force (here produced by a radial magnetic field), $F_D = f_D\xi_z$ is the driving force due to an unstable vertical field index, $F_R = f_R\xi_z$ is the restoring force due to the induced currents in the passive coils and L/R is the time constant of the passive coil system in the absence of a plasma. For stability it is necessary that $\alpha > 1$, and the larger α the smaller are the energy requirements on a feed-back system. As $\alpha \sim 1/L$, the stabilizing effect depends on the cross section and the inductance of the connection between the upper and the lower passive coils which have to be connected antidirectional in series because otherwise they would shortcircuit the toroidal electric field.

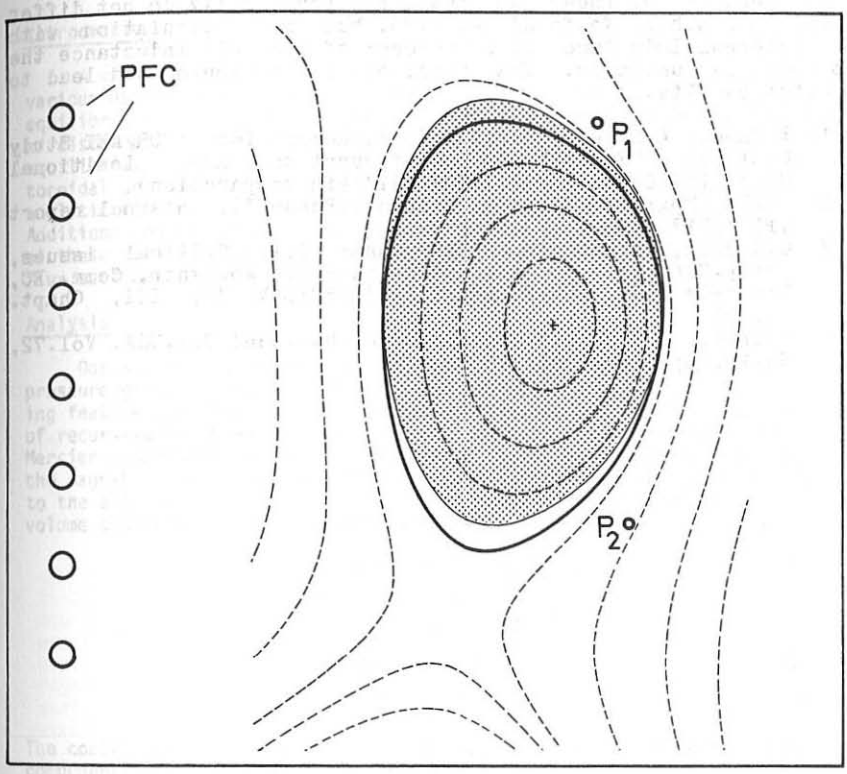

The Fig. shows the flux pattern of an INTOR configuration for an initial equilibrium state and the equilibrium position of the plasma after application of a radial magnetic field. P_1, P_2 - passive conductor elements; PFC - poloidal field coils

For an INTOR configuration described in /3/ we took two passive coils (P_1, P_2 in the Fig.) with a cross section of 0.09 m^2. Their selfinductance is L = 51μH. With this value we found α = 1.5 which means that the additional inductances have to be significantly smaller than 25μH. The induced current is $I_{P_1} = -I_{P_2} = \gamma I_P \xi_z$, with γ = 0.15 m^{-1} and I_P the total toroidal plasma current. For larger displacements ξ_z = 0.1 m some nonlinear effects give a small enhancement to α = 1.6. There was no significant difference between parabolic and flat plasma current distributions.

The ASDEX-UG configuration /2/ has a system of 2x 3 passive coils, the upper and the lower ones in parallel, respectively, with a total cross-section of 2x 0.024 m^2. At present we are not able to treat parallel connected coils, so we connected them in series or separated them into three pairs of two coils. The results of these two treatments practically do not differ from each other. We found α = 1.25, but in a calculation with an external inductance of 20 percent of the coil inductance the plasma is unstable. The parallel connection should lead to better results.

/1/ F.Casci, A.Kaleck, H.P.Zehrfeld, Report for INTOR/NET Study Contract "Equilibrium Configuration and Positional Stability Control for INTOR/NET" (in preparation)

/2/ ASDEX Upgrade Project Proposal Phase II, internal report IPP 1/217 (1983)

/3/ O.Gruber, K.Lackner, INTOR-Phase IIa, Critical issues, Europ.Contrib. to the INTOR-Phase IIa Workshop, Comm. EC, Brussels 1982, EUR-Fu-BRU/XII-132/82/EDV 30, III, Chapt. IX, 81

/4/ H.Grad, P.N.Hu,D.C.Stevens, Proc.Nat.Acad.Sci.USA, Vol.72, No.10, pp.3789-3793, 1975

FORCE-FREE MHD EQUILIBRIA IN NON-AXISYMMETRIC TOROIDAL GEOMETRY*

M. P. Bernardin and J. A. Tataronis
University of Wisconsin, Madison, Wisconsin U.S.A.

Abstract

The existence and properties of force-free MHD equilibria in three dimensional toroidal configurations are examined. Utilizing an expansion scheme in distance ρ from an arbitrary magnetic axis, the equilibrium magnetic fields are computed. In addition, a Hamiltonian formalism for the lines of force of the magnetic field is constructed to address the existence of magnetic flux surfaces.

Introduction

A variety of investigative methods have been developed to study various aspects associated with three dimensional toroidal hydromagnetic equilibria [1-5]. In this paper, we adopt an expansion technique in terms of distance ρ from a given magnetic axis [1], to study 3-D, force-free MHD equilibria. Motivated by the investigation of Alfvén wave heating in 3-D toroidal geometry [6], the primary purpose of this research is to obtain analytic representations of the equilibrium magnetic field components. Additional objectives of this research include the examination of stability of these equilibria as well as consideration of the existence of magnetic flux surfaces.

Analysis

Our analysis of force-free MHD eqilibria parallels that of the finite pressure-gradient analysis of Lortz and Nührenberg [1]. The distinguishing feature contained in the analysis of this document is the determination of recursive relations for the nth order expansion coefficients. Using a Mercier coordinate system (ρ,θ,s) where s is the arc length measured along the magnetic axis, and ρ,θ are polar coordinates in a plane perpendicular to the axis, we expand the contravariant magnetic field components and the volume continued within a flux surface, with respect to ρ.

$$B^{\rho} = a_1\rho + a_2\rho^2 + a_3\rho^3 + \cdots \tag{1}$$

$$B^{\theta} = b_1\rho + b_2\rho^2 + b_3\rho^3 + \cdots \tag{2}$$

$$B^{s} = c_0 + c_1\rho + c_2\rho^2 + \cdots \tag{3}$$

$$V = V_2\rho^2 + V_3\rho^3 + \cdots \tag{4}$$

The coefficients are functions of θ and s. The expanded magnetic field components are then substituted into the force-free hydromagnetic equilibrium equations,

$$\nabla \cdot \vec{B} = 0 \tag{5}$$

$$\vec{J} \times \vec{B} = 0 \tag{6}$$

$$\nabla \times \vec{B} = \mu_0 \vec{J} \tag{7}$$

and solved order by order. With the specification of information about the cross-sectional shape of the flux surfaces, the volume V is solved for by substituting Eq. (4) into

$$\vec{B} \cdot \nabla V = 0 \tag{8}$$

and again solving order by order.

To simplify our analysis, we have begun the expansion for B^θ with a first order term rather than a zeroth order term. The price paid for the additional simplification is further restrictions on the shape of the equilibrium flux surfaces. For example, a well known result of the finite pressure-gradient analysis is [1],

$$j/c_0 = \text{const.} \tag{9}$$

where j is the current density on axis. The selection of $b_0 = 0$ specifies the constant in Eq. (9). The primary consequence of neglecting the zeroth order term is the constraint

$$c_0(s)\ \tau'(s) = 0 \tag{10}$$

where c_0 is the magnetic field along the magnetic axis and τ is the torsion of the magnetic axis. With $c_0(s) \neq 0$, the resulting constant torsion constraint, $\tau'(s) = 0$, is easily satisfied for tokamaks and standard stellarators, which have $\tau = 0$. To examine toroidal equilibria with spatial axes, it becomes necessary to address the question of existence of closed, constant torsion curves, say on a torus. There are indications that these curves may exist [7], but further study is needed. Additional aspects of this question will be addressed in a later publication. We have previously analyzed and reported the results of satisfying Eq. (10) with $c_0 = 0$ [8,9]. In this report, we state the results of satisfying Eq. (10) with $\tau = \text{const.}$

As a preliminary step, we give the prescription of solving for the expansion coefficients. Substituting Eqs. (1)-(3) into Eqs. (5)-(7), a set of three coupled PDE's are obtained for the coefficients c_{n+1}, a_n and b_{n-1}. Denoting partial differentiation with respect to θ and s by subscript θ and prime respectively, these equations read,

$$(n+1)\ a_n + b_{n-1,\theta} = R_{1n} \tag{11}$$

$$(n+1)\ c_{n+1} - a_n' + (n+3)\tau\, b_{n-1} = R_{2n} \tag{12}$$

$$c_0 c_{n+1,\theta} - 2c_0\tau\, a_n + a_1 a_{n,\theta} - (n+1)\ a_1 b_{n-1} + c_0\tau\, b_{n-1,\theta} - c_0 b_{n-1}' = R_{3n} \tag{13}$$

In Eqs. (11)-(13), the quantities R_{1n}, R_{2n} and R_{3n} are functions of lower order coefficients. Solving Eqs. (11) and (12) for a_n and c_{n+1} in terms of b_{n-1}, and substituting into Eq. (13), the following third order PDE is obtained for b_{n-1}.

$$c_0[b_{n-1,\theta\theta}' + (n+1)^2 b_{n-1}'] - \frac{n+1}{2}\, c_0'[b_{n-1,\theta\theta} + (n+1)^2 b_{n-1}] =$$

$$c_0 R'_{1n,\theta} - 2c_0\tau(n+1)R_{1n} + a_1(n+1)R_{1n,\theta} + c_0(n+1)R_{2n,\theta} - (n+1)^2 R_{3n} \quad (14)$$

Since the RHS of Eq. (14) is known, the (single-valued) solution of Eq. (14) is

$$b_{n-1}(\theta,s) = \beta_{n+1,c}\cos(n+1)\theta + \beta_{n+1,s}\sin(n+1)\theta + \beta_{n-1,c}\cos(n-1)\theta + \\ + \beta_{n-1,s}\sin(n-1)\theta + \cdots + \begin{cases} \beta_{1c}\cos\theta + \beta_{1s}\sin\theta & (n \text{ odd}) \\ \beta_{10} & (n \text{ even}) \end{cases} \quad (15)$$

The coefficients β_i, are functions only of s. $\beta_{n+1,c}$ and $\beta_{n+1,s}$ are specified by solving for the V_{n+2} volume coefficient in Eq. (8).

Specific results for the lower order coefficients are as follows:

$$b_1 = \beta_{3c}\cos 3\theta + \beta_{3s}\sin 3\theta - \frac{3}{2}c_0\tau k\cos\theta + (\frac{5}{16}c_0' k + \frac{1}{8}c_0 k')\sin\theta$$

$$a_1 = -\frac{c_0'}{2}$$

$$a_2 = \beta_{3c}\sin 3\theta - \beta_{3s}\cos 3\theta - (\frac{15}{16}c_0' k + \frac{3}{8}c_0 k')\cos\theta - \frac{1}{2}c_0 k\tau\sin\theta$$

$$c_0 = c_0(s) \quad c_1 = 2c_0 k\cos\theta \quad c_2 = \frac{3}{2}c_0 k^2\cos 2\theta + \frac{3}{2}c_0 k^2 - c_0\tau^2 - \frac{c_0''}{4}$$

$$c_3 = -\frac{1}{3}(\beta'_{3s} + 5\tau b_{3c} - 3c_0 k^3)\cos 3\theta + \frac{1}{3}(b'_{3c} - 5\tau\beta_{3s})\sin 3\theta - \\ \frac{1}{16}(24c_0 k\tau^2 - 48c_0 k^3 + 13c_0' k + 7c_0 k' + 2c_0 k'')\cos\theta - \\ \frac{\tau}{16}(11c_0' k + 6c_0 k')\sin\theta$$

Through the recursive relations, Eqs. (11), (12) and (15), we have formally established the analytical representation of the equilibrium magnetic fields. We now address the question of existence of magnetic surfaces.

Magnetic Surfaces

With the expansions we have incorporated, it can be stated that magnetic surfaces will exist to all orders [10]. However, without a definitive statement on the convergence of the series for the volume V, the implied magnetic surfaces must be regarded as asymptotic. To establish the rigorous existence of magnetic surfaces, it must be shown that the expansion series converge. To this end, we cast the equations for the lines of force for the magnetic field into a Hamiltonian form [11]. The existence of magnetic surfaces is now coupled with the identification of an invariance associated with the Hamiltonian. Beginning with Eq. (5), the field line equations in terms of the contravariant components of the magnetic field are the following,

$$\frac{d\rho}{B^\rho} = \frac{d\theta}{B^\theta} = \frac{ds}{B^s}$$

while the associated Hamiltonian form of the system is given by

$$\frac{dp}{ds} = -\frac{\partial H}{\partial q} \quad \frac{dq}{ds} = \frac{\partial H}{\partial p} \quad \frac{dH}{ds} = \frac{\partial H}{\partial s}$$

The Hamiltonian, H, is a function of a generalized coordinate q, conjugate momentum p, and a time-like coordinate s. In this case, we choose $q = \theta$, while the momentum, p, and the Hamiltonian, H, are respectively

$$p = \int d\rho\sqrt{g}\, B^s \qquad H = \int d\rho\sqrt{g}\, B^\theta + \delta(\theta,s) \tag{16}$$

where $\delta(\theta,s)$ satisfies the following equation,

$$-\frac{\partial}{\partial\theta}\,\delta(\theta,s) = \frac{\partial}{\partial\theta}\int d\rho\sqrt{g}\, B^\theta + \frac{\partial}{\partial s}\int d\rho\sqrt{g}\, B^s + \sqrt{g}\, B^\rho$$

Substituting into Eq. (16) the expansions for B^ρ, B^θ and B^s given above, we find the following expanded forms of p and H:

$$p = \frac{c_0}{2}\rho^2 + \frac{c_0 k\cos\theta}{3}\rho^3 + \cdots + \frac{c_{n-2}-c_{n-3}k\cos\theta}{n}\rho^n + \cdots$$

$$H = V_0(s) + \frac{b_1}{3}\rho^3 + \cdots + \frac{b_{n-2}-b_{n-3}k\cos\theta}{n}\rho^n + \cdots$$

$V_0(s)$ may be dependent on the choice of the gauge. The predictin of an invariant and hence the existence of magnetic surfaces can be accomplished by invoking repeated canonical transformations, a process similar to a method of accelerated convergence [12]. Further details will be presented at the conference.

* This work is supported by NSF Contract No. ECS-8110038.

References

[1] Lortz, D., Nührenberg, J., Z. Naturforsch. 31a (1976) 1277.
[2] Greene, J.M., Johnson, J.L., Phys. Fluids 4 (1961) 875.
[3] Bauer, F., Betancourt, O., Garabedian, P., J. Comp. Phys. 35 (1980) 341.
[4] Boozer, A.H., Bull. Am. Phys. Soc. II, 27 (1982) 941.
[5] Hirshman, S.P., Whitson, J.C., Sherwood Theory Conference (1983) 3A3.
[6] Bernardin, M.P., Tataronis, J.A., to be published in Phys. Fluids.
[7] Lortz, D., Nührenberg, J., Z. Naturforsh. 34a (1979] 171.
[8] Bernardin, M.P., Tataronis, J.A., Sherwood Theory Conference (1983) 1R5.
[9] Bernardin, M.P., Tataronis, J.A., University of Wisconsin-Madison Physics Dept. Report PPL 902 (1983).
[10] Greene, J.M., Johnson, J.L., Advances in Theoretical Physics 1 (1965) 211.
[11] Lichtenberg, A.J., Lieberman, M.A., Regular and Stochastic Motion (Springer-Verlag, New York), (1983).
[12] Bogoljubov, N.N., Mitropoliskii, Ju.A., Samoilenko. A.M., Methods of Accelerated Convergence in Nonlinear Mechanics (Hindustan, Delhi, India), (1976).

CONDITION FOR THE STABILITY OF DISSIPATIVE MODES IN A STELLARATOR.

L.M.Kovrizhnykh, S.V.Shchepetov
Institute of General Physics of the USSR Academy of Sciences, Moscow, USSR

In Ref. 1 a system of averaged MHD equations was derived which make it possible to study plasma dynamics in a stellarator using wellknown methods proposed earlier to study plasmas in tokamaks. It should be noted, however, that although using a formalism of averaged equations simplifies the problem (reducing it to the axisymmetric case), but the use of a complete system of averaged MHD equations encounters essential mathematical limitations. For this reason we are going to present later on a simplified system of MHD equations designed with a set of small parameters. As a main parameter we employ $\Delta_p = |B_\perp| / B_T$: the ratio of the transverse components of the magnetic field towards the longitudinal magnetic field. Taking the approach of Ref. 2,3 in deriving a similar system of equations for a tokamak, we obtain a system of equations describing plasma dynamics in a stellarator within the accuracy up to Δ_p^2, and incorporating the first order in the toroidal effects:

$$\frac{dW}{dt} = \hat{B}^{-2} \mathrm{div} \Big\{ \Big([\vec{\nabla}_\perp \Psi \times \vec{B}_T] + (B_T h)^{-1} \vec{\nabla}_\perp \frac{\partial \mathcal{H}}{\partial z} \Big) \mathcal{L} \Psi^3 + h^{-1} B_T \vec{\nabla}_\perp \partial \Psi / \partial z + [\vec{\nabla} p \times \vec{B}_T] / \hat{B}^2 - [\hat{\rho} \vec{v} v^2 \times B_T] / 2 \Big\} ; \quad (1)$$

$$\frac{d\Psi}{dt} = - \frac{d\Phi}{dz} / (h B_T) + E_s / B_T + \mathcal{L} \Psi^3 / \sigma_\parallel ; \quad (2)$$

$$\mathcal{L}(U + \Phi) + \hat{k} \cdot \mathcal{L} U + \vec{\nabla}_\perp U \cdot \vec{\nabla}_\perp \hat{k} = 0 ; \quad (3)$$

$$W = \hat{B}^{-2} \, \mathrm{div} \hat{\rho} \nabla_\perp U \quad (4)$$

$$\mathrm{div} B_T^2 \vec{\nabla}_\perp (\hat{k} + \hat{\rho} v^2 / 2) = \mathrm{div} \{ (B_T^2 W \vec{\nabla}_\perp U) - \vec{\nabla}_\perp p + B_T^2 \Psi^* \vec{\nabla}_\perp \mathcal{L} \Psi^3 - (\mathcal{L} \Psi^3) B_T^2 \vec{\nabla}_\perp \Psi^3 \} ; \quad (5)$$

$$\hat{\rho} \frac{d v_s}{dt} = - \frac{\partial p / \partial z}{h B_T^2} + \vec{e}_s \cdot [\vec{\nabla}_\perp \hat{K} \times \vec{\nabla}_\perp \Psi] + \vec{\nabla}_\perp \Big(\frac{\partial \Psi^3}{\partial z} \Big) \cdot \frac{1}{h} \vec{\nabla}_\perp \Psi ; \quad (6)$$

$$\hat{k} = - \Delta \mathcal{H} / B_T^2 \quad (7)$$

$$\frac{d\hat{\rho}}{dt} = 0 \qquad (8) \qquad \frac{dp\hat{B}^{-2\gamma_0}}{dt} = 0 \qquad (9)$$

where: $\Psi = \Psi^J + \Psi^*$ is the poloidal flux; Ψ^J - is the poloidal flux, produced by the currents, flowing through the plasma, Ψ^* - is the effective field flux, $\vec{B}^* = \vec{B}^*_s + [\vec{\nabla}\Psi^* \times \vec{B}_T]$ - is the effective magnetic describing the averaged contribution of the magnetic-field helical components; $\vec{B}^*_s = -\vec{e}_s \langle (\vec{\nabla}\Phi^M) \rangle B_T^{-1}$; Φ^M is the potential of a helical magnetic field (angular brackets represent averaging with respect to s); Φ - is the electic-field potential, $\mathcal{X}$ - is the function describing transverse components of the magnetic field vector potential $\vec{A}_p = \Psi \vec{B}_T + [\vec{\nabla}\mathcal{X} \times \vec{B}_T] B_T^{-2}$; $E = E_s \vec{e}_s - \nabla\Phi - \partial A_p/\partial t$; $\vec{B} = (B_T + B^*_s)\vec{e}_s + \mathrm{rot}\ \vec{A}_p$; $B_T = B_0/h$ and $E_s = E_0/h$ are longitudinal components of the vacuum magnetic and electric fields; $\hat{k}$- is the function describing the change in a longitudunal field due to finite pressure and current; $\vec{v} = v_s \vec{e}_s + v_\perp$; $\vec{v}_\perp = [\nabla_\perp U \times B_T]/\hat{B}^2$; $\hat{B}^2 = B_T(B_T + B^*_s)$ $\hat{\rho} = \rho/\hat{B}^2$; $L = B_T^{-2} \mathrm{div}\, B_T^2 \vec{\nabla}_\perp$; $\vec{\nabla} = \vec{\nabla}_\perp + \vec{e}_s \frac{1}{R_0 h} \partial/\partial s$; $\frac{d}{dt} = \frac{\partial}{\partial t} + \vec{v}_\perp \vec{\nabla}_\perp$
We used above a quasitoroidal coordinate system in which the arc element is: $(dl)^2 = (dr)^2 + (r\,d\vartheta)^2 + (R_0 h\,ds)^2$; $z = R_0 s$; $h = 1 + (1/R_0) r \cos\vartheta$. Other symbols traditional.

Using the system of Eqs. (1) - (9) and the results of Refs. 4 and 5 we obtain the condition for the stability of resistive flute modes :

$$D_R = D_0(\hat{W} - D_2)/(t')^2 > 0 ; \qquad (10)$$

$$\hat{W} = (\sqrt{g}/g_{33})^{(0)} (p'/\Phi_0'^2)(t^2 g_{22}^{(0)\prime} + g_{33}^{(0)\prime} - [B^*_s g_{33}/B_T]^{(0)\prime}); \qquad (11)$$

$$D_0 = [(g_{33}/\sqrt{g}) g^{11}]^{(0)}; \qquad (12)$$

$$D_2 = (p'/t\Phi_0')^2 [g_{33}(\widetilde{\sqrt{g}})^2/\sqrt{g}\ g^{11}]^{(0)} \qquad (13)$$

where: g_{ik} are metric coefficients of the coordinate system $x^i = \{a, \vartheta, s\}$ with the straightened lines of force of the average magnetic field, t - is the rotational transform, Φ_0 - is the toroidal flux of the effective magnetic field, prime corresponds to differenciation over a, index (0) represents averaging over the poloidal azimuth ϑ , tilde represents the

the term varying along ϑ , $g^{ik} = g_{ik}^{-1}$. Metric coefficients expressed in terms of plasma parameters (i.e. displacement, ellipticity) are given in Ref.6. The term $\sim B_S^*$ is a measure of the magnetic hump of a straight system, $\hat{W}$ is a measure of the resulting magnetic well (hump) of the system, D_2 represents destabilizing ballooning effects. The expression for D_R is rather awkward so here we'll give only some estimations and and results of numerical calculations. We must note that for systems with positive shear ($\iota'/\iota > 0$) the criterion is necessary and sufficient condition for stability of dissipative modes with large wave numbers (stability condition for so-called ballooning modes is less stringent). Condition (10) is more stringent than Mercier criterion as dissipative modes are not stabilized by shear. Analysis of the condition (10) show that, in contrast with the situation in tokamaks, in stellarators there is no plasma selfstabilization at the edge of a system (for case of rotational transform due to current $\iota^J = 0$ and $\iota^{*\prime}/\iota > 0$, where ι^* - is stellarator rotational transform). For example, for L-2 stellarator in the Lebedev Institute ($\iota^J = 0$, $\iota^* = 0.2 + 0.7\,a^2/a_c^2$, $\delta = a_0/R_0 = 0{,}115$; $N/n_0 = 7$ - are the ratio of the numbers of helical winding periods in φ to number of periods in ϑ) at zero ohmic heating current, at $\beta = 2p/B^2 = 5\%$ the condition (10) is satisfied only at $a/a_c < 0.45$, where a_c - is the radius of plasma boundary. Stability conditions are degraded by the presence of the ohmic heating current. For example, for the L-2 stellarator parameters a magnetic well at the center disappears at $\beta = 1\%$, $\iota^J(0) > 0.5$ when current density and pressure profiles are parabolic. For shearless syatems ($\iota^{*\prime} = 0$) it is easy to find a current at which a magnetic well disappears at the axis of a system. When a helical field is produced by conductors carrying a current installed according to the law $\varphi + C_1 z_0/R_0 \cdot \sin\varphi + N\zeta/n_0 = \text{const}$ (z_0 - is the radius of winding), a magnetic well disappears at $\iota^J(0) = (12 + 12C_1 - 4N\iota^*/n_0)/(4N/n_0)$.

In the case of $D_R > 0$, finite pressure and toroidal effects may improve the condition for stability low-wave-number tearing modes. Using the results of Ref.5 we obtain stability condition for tearing modes:

$$\Delta' < \Delta_c \quad ; \quad \Delta_c > 0$$

$$\Delta_c = 1.5 \left(\frac{a^3 \iota^{*\prime} m}{a_0 R_0 (1 + 2\iota^{-2})^{1/2}} \right)^{1/3} \left(\frac{\tau_s}{\tau_A} \right)^{1/3} D_R^{5/6} \qquad (14)$$

where Δ' is the difference of logarithmic derivaties of an excited magnetic flux on the rational magnetic surface, m - is the poloidal wave number, $\tau_s = a_0^2/\chi$ is the scale skin time, $\tau_A = a_0\sqrt{\rho}/B_\varphi$ is the scale alfven time; when $\beta \to 0$ $\Delta_c \to 0$. For shearless systems ($\iota^{*\prime} = 0$) tearing mode stabilization takes place as well as in tokamaks. For example, in the magnetic confinement system with the following parameters $n_e = 10^{14}\,cm^{-3}$, $T_e = 1\,kev$, $\iota^* = 0.25$, $\delta = 1/20$, $\beta_p = 3\,\kappa g s_2$, $C_1 = 0$ m = 3 mode is stable at a current density $j \sim j_c(1 - a^2/a_c^2)^2$. For the systems with large

magnetic shear $\hat{\iota}^{*\prime}(a_0)a_0/\hat{\iota}^{*}(a_0)<1$ (for example L-2), the finite pressure effects cannot stabilize current driven tearing modes as the resonance surfaces occure in the region $D_R<0$ where resistive ballooning modes are unstable.

/1/ Kovrizhnykh, L.M., Shchepetov, S.V.: Fizika Plazmy 6 (1980) 976, Sov. J. Plasma Phys. 6 (1980) 533.
/2/ Edery, D., Pellat, R., Soule, J.L. : Rep EUR-CEA-FC-1109 (1981)
/3/ Schmalz, R.F. : Phys. Lett. 82A (1981) 14.
/4/ Mikhajlovsky, A.B. : Neustoichivosti Plazmy v magnitnykh lovushkakh (Plasma Instabilities in Magnetic Traps) Atomizdat, Moscow (1978) 3.
/5/ Glasser, A.H., Greene, J.M., and Johnson, J.L. : Phys. Fluids 18 (1975) 875.
/6/ Kovrizhnykh, L.M., Shchepetov, S.V. : Nucl. Fusion 23, N°6 (1983).

IDEAL MHD STABILITY OF A TOKAMAK IN THE HIGH-BETA TOKAMAK ORDERING

J. Rem, R.M.O. Galvão*, J.P. Goedbloed, and P.H. Sakanaka**
Association Euratom-FOM, FOM-Instituut voor Plasmafysica "Rijnhuizen", Nieuwegein, The Netherlands.
*) Laboratório de Estudos Avançados, Centro Técnico Aerospacial, São José dos Campos, São Paulo 12200, Brazil.
**) Instituto de Fisica "Gleb Wataghin", Universidade Estadual de Campinas, Campinas, São Paulo 13100, Brazil.

A numerical program, HBT /1/, has been employed to study equilibrium, low-n global stability, and high-n ballooning stability of a large number of high-beta tokamak configurations with circular cross-section. The highest value of $\langle\beta/\varepsilon\rangle = 0.077$ was obtained in an equilibrium with $q_a/q_0 \sim 2$ and a value of the safety factor on the magnetic axis q_0 close to unity.

The equilibrium is determined by prescribing in the Grad-Shafranov equation the profiles for the pressure and the toroidal magnetic field. These profiles are introduced in the following way:

$$\tfrac{1}{2}(\alpha^2/\varepsilon^2 B_0^2)\,\frac{d}{d\psi}\,(R^2B_\phi^2/R_0^2 - B_0^2 + 2p) = -A\Gamma(\psi)\ ,$$
$$\alpha^2/\varepsilon B_0^2\,\frac{dp}{d\psi} = -\tfrac{1}{2}\,AB\Pi(\psi)\ , \qquad (1)$$

where $\varepsilon = a/R_0$, R_0 is the major radius, a is the minor radius, B_0 is the vacuum magnetic field at R_0, B_ϕ is the toroidal magnetic field, $\psi = \phi/\phi_a$ a dimensionless flux, ϕ is the poloidal flux, ϕ_a the value of ϕ at a, $\alpha = a^2B_0/\phi_a$ is a dimensionless parameter that provides the scaling discussed in Ref. /2/, and the functions $\Gamma(\psi)$ and $\Pi(\psi)$ are normalized profile functions, i.e. $\Gamma(0) = \Pi(0) = 1$; furthermore, no surface currents will appear, so that $\Gamma(1) = \Pi(1) = 0$.

The definitions of $\langle\beta\rangle$, β_p, q^*, the average beta, the poloidal beta and the safety factor related to the current /1/ for a circular cross-section reduce to:

$$\langle\beta\rangle = 2\mu_0\langle p\rangle/B_0^2;\ \beta_p = 8\pi^2a^2\langle p\rangle/\mu_0 I_p^2;\ q^* = 2\pi a^2B_0/\mu_0R_0I_p\ , \qquad (2)$$

where $\langle\ \rangle$ stands for averaging over the plasma cross-section and I_p represents the toroidal current. Clearly, these quantities are related in the following way:

$$\varepsilon\beta_p = \langle\beta/\varepsilon\rangle\, q^{*2}\ . \qquad (3)$$

In the high-beta tokamak ordering, the equilibrium is not only independent of ε but also independent of q^*. For given functional dependences of $\Gamma(\psi)$ and $\Pi(\psi)$ the equilibrium is determined by the shift of the magnetic axis, or $\varepsilon\beta_p$, only.

In the stability analysis, the high-beta tokamak ordering leads to the introduction of a stream function for the plasma displacement in the plane of the cross-section. This function is expanded in special radial polynomials and harmonics in the poloidal angle, so that the potential energy is reduced to a quadratic form in these expansion coefficients, with matrix elements that are double integrals over equilibrium and expansion functions. The

growthrate of the most unstable mode thus corresponds to the lowest eigenvalue of this quadratic form . The growthrate depends on the equilibrium ($\varepsilon\beta_p$) and nq* where n stands for the toroidal mode number. Therefore, the stability results will be presented in an $\varepsilon\beta_p$ versus nq* diagram; in the following we shall consider only the most unstable modes: n=1.

A stability study of the configurations $\Gamma(\psi) = (1-\psi)^{\nu_\gamma}$, $\Pi(\psi) = (1-\psi)^{\nu_\pi}$, $\nu_\gamma, \nu_\pi > 1$, shows the well-known stability of a plasma with respect to external modes: a peaked current is more stable. However, for reasonable values of the current, i.e. q* = 2-3, such configurations always lead to values of q_0 smaller than unity. Since the ordering has led to the neglect of terms this stability limit for localized modes near the magnetic axis is not recovered here. Therefore we must impose this condition as an additional requirement. This led to a study of more general configurations:

$$\Gamma(\psi) = \left(1+a_\gamma\psi+b_\gamma\psi^2+c_\gamma\psi^3+d_\gamma\psi^4\right)^{\nu_\gamma} \text{ and } \Pi(\psi) = \left(1+a_\pi\psi+b_\pi\psi^2+c_\pi\psi^3+d_\pi\psi^4\right)^{\nu_\pi} , \qquad (4)$$

with values of ν_γ and ν_π smaller than unity. The additional freedom would seem to make the problem of finding a "good" configuration more difficult. Fortunately, there is one limit of our model that has been thoroughly investigated, namely at $\varepsilon\beta_p = 0$ the equilibrium corresponds to that of a straight cylinder /3,4,5/. In such a plasma, modes can be distinguished by their poloidal mode number and the stability depends on the behaviour of the current near the surface. A constant current is unstable for all values of nq* and only the integer values of nq* are marginally stable points. With a radially decreasing current density and no current on the plasma surface, stable regions develop above these marginal points. The m=2 mode is stable in a region above nq* = 1, but retains its other marginal point at nq* = 2. Likewise there develops a stable region for the m=3 mode above nq* = 2. With increasing values of m the stable regions are larger. All these stable regions depend on the current gradient near the surface and on the position of a wall outside the plasma. A smaller gradient and a wall nearby lead to larger stable regions. Based on such considerations the configuration parameters in (4) were restricted to the conditions:

$$1 + a_\gamma + b_\gamma + c_\gamma + d_\gamma = 0 , \quad a_\gamma + 2b_\gamma + 3c_\gamma + 4d_\gamma = 0 , \qquad (5)$$

and similarly for a_π, etc. The results of a variety of different configurations show that they can roughly be divided in two classes, one stable at high values of $\varepsilon\beta_p$ near nq* = 3 and another class with a stable region near nq* = 2. The first class was disregarded because all configurations had currents that reversed on the inside of the cross-section. Out of the second class we selected one and optimized this further by varying ν_γ and ν_π.

The configuration that led to the highest value of $\langle\beta/\varepsilon\rangle$ has the following parameters:

$$\Gamma(\psi) = \Pi(\psi) = \left(1-\psi+2\psi^2-5\psi^3+3\psi^4\right)^{\frac{1}{2}} = (1-\psi)(1+\psi+3\psi^2)^{\frac{1}{2}} . \qquad (6)$$

The stability of this configuration with respect to external modes (no wall) is depicted in Fig. 1. The regions of stability at $\varepsilon\beta_p = 0$ are clearly visible on the low current side of integer values of nq*. These stability properties have been verified with a cylindrical code where the growthrate of a mode is determined by solving the differential equation for the radial perturbation directly with an ODE routine. Although near all marginal points (A, B and C) the modes are clearly surface modes /6/ the behaviour of δW in

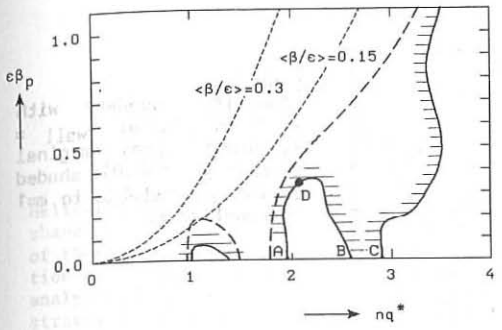

Fig. 1.
Stability boundaries without a wall: s_{wall} = 100; drawn lines: marginal stability (σ^2=0.0), shaded side indicates unstable region; dashed lines: σ-stability σ^2 = 0.1.

the neighbourhood of these points differs. One might think that the code cannot resolve these modes and that the positions of A, B and C are inaccurate. This is only true for the points A and C, because here δW depends very weakly on nq* and its behaviour with m ($\delta W \propto 1/m$) explains the larger deviation of C from nq*=3. While one can argue that these modes are not relevant because they are strongly localized near the surface, this argument cannot be employed at $\varepsilon\beta_p \neq 0$. Even at small values of $\varepsilon\beta_p$ the perturbation is global /6/. Of the three stable regions the one near nq*=2 is the most interesting; the region near nq*=1 involves nq_0 smaller than unity and the region at high $\varepsilon\beta_p$, near nq*=3, has reversed currents. The optimum value of $\langle\beta/\varepsilon\rangle$ is reached in the point D: $\langle\beta/\varepsilon\rangle$ = 0.077; close to the curve $\langle\beta/\varepsilon\rangle$ = 0.1. In this point, $q_a \sim 2$ and q_0 is close to unity, and the dominant perturbation is that of an m=2 mode.

The various modes that determine the stability boundary become apparent when the position of the wall is varied. With the wall on the plasma the unstable region shrinks to a narrow strip on the low nq*-side of the q_0=1 curve, showing the presence of the m=1 internal mode (Fig. 2); the lower stability boundary in $\varepsilon\beta_p$ agrees very well with the stability limit obtained from the ballooning code. The unstable region does not extend to $\varepsilon\beta_p$ = 0, because in this limit the plasma is stable to internal modes. In the same figure we plotted the curves where q_a = 2 and 3, and q_0 = 2. Modes related to these quantities appear (Fig. 3) when the wall is moved away to s_{wall} = 1.25 (wall at a radius of 1.25 a). Here we see that the internal m=1,2 modes interact with the kink modes m=1, 2 and 3. The m=1 external kink is unstable in region I, while in II the internal m=1 interacts with the m=2 kink mode and in region III the internal m=2 interacts with the m=3 kink mode. All these regions are connected when the wall is far away (Fig. 1). Observe that the unstable regions are always on the low nq*-side of the q_a or q_0=m curves, indicating that the rational surface is just in the vacuum region or in the plasma near the magnetic axis.

The above analysis explains why, without a stabilizing wall, an optimum was found by varying the current gradient at the plasma boundary. A decrease of this gradient leads to an improved stability to the external modes, but must be accompanied by a motion of the q_0=1 and 2 curves to higher values of nq*, i.e. a decreased stability of the internal modes. The interaction of the internal m=1 and the external m=2 explains why in this optimum $q_a \sim 2$ and q_0 is somewhat above unity /7/.

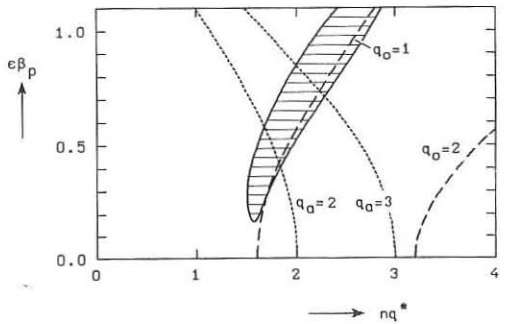

Fig. 2.
Stability boundary with wall on plasma: s_{wall} = 1; drawn lines: marginal stability (σ^2=0.0); shaded region is unstable to m=1 internal mode.

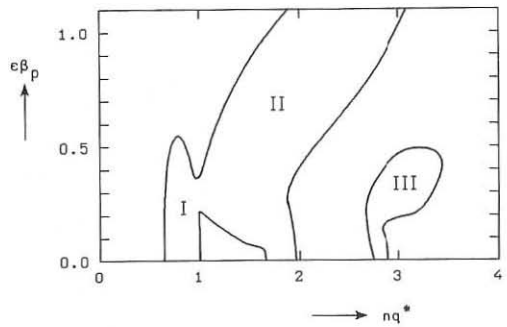

Fig. 3.
Stability boundaries with wall near plasma: s_{wall} = 1.25; drawn lines: marginal stability (σ^2=0.0); regions I, II and III are unstable.

This work was performed under the Euratom-FOM association agreement. It was financially supported by the "Stichting voor Fundamenteel Onderzoek der Materie" (FOM), the "Nederlandse Organisatie voor Zuiver-Wetenschappelijk Onderzoek" (ZWO), EURATOM, the "Conselho Nacional de Desenvolvimento Centifico e Technológico", "Comissão Nacional de Energia Nuclear (Brazil)", and "Financiadora de Estudos Projetos".

References

/1/ Galvão, R.M.O., Goedbloed, J.P., Rem, J., Sakanaka, P.H., Schep, T.J., and Venema, M., Proc. 9th Int. Conf. on Plasma Phys. and Contr. Nucl. Fusion Res., Baltimore, 1982, IAEA-CN-41/P-1-1.
/2/ Bateman, G. and Peng, Y.-K.M., Phys. Rev. Lett. 39 (1977) 829.
/3/ Shafranov, V.D., Sov. Phys. - Tech. Phys. 15 (1970) 175.
/4/ Wesson, J.A., Nucl. Fusion 18 (1978) 87.
/5/ Freidberg, J.P., Rev. Mod. Phys. 54 (1982) 801.
/6/ Kerner, W., Gautier, P., Lackner, K., Schneider, W., Gruber, R., and Troyon, F., Nucl. Fusion 21 (1981) 1383.
/7/ Saurenmann, H., Gruber, R., Semenzato, S., and Troyon, F., INTOR Phase IIa, European Contributions to the 5th Workshop, Vol. I, EUR-FU-BRU/XII-132/82/EDV20, IAEA-Vienna.

EVALUATION OF MERCIER'S CRITERION IN 3D HELIAC EQUILIBRIA

R. Großmann, F. Herrnegger, J. Nührenberg
Max-Planck-Institut für Plasmaphysik
EURATOM Association, D-8046 Garching

Helically symmetric equilibria with strong $\ell = 1$ helical curvature and bean-shaped cross-section have attracted attention for a long time /1/ because of their conjectured good finite-β MHD stability properties. This expectation was verified stepwise with increasing credibility of the theoretical analyses /2, 3, 4/ to the point that $<\beta>$ values of up to 0.3 were demonstrated as completely ideal MHD stable, i.e. stable to high-n ballooning as well as low-n internal and external modes /5/. The revived interest in toroidal versions of these equilibria /6/ (HELIAC) has prompted 3D finite-β computational studies /7, 8/ which verified the good gross equilibrium properties as were expected on the basis of the standard estimate $\beta_e \approx \iota^2/A$ and the large rotational transform (twist) per field period of $\iota_p \sim 0.3$. In this paper, we continue the stability analyses /2, 3/ of HELIAC equilibria on the basis of the JMC (currents J and Mercier Criterion) code for the evaluation of 3D computational equilibria with respect to Mercier's necessary stability criterion /9/. First results concerning tests and the W VII-AS stellarator /10/ have already been obtained with JMC /11/. We recall /4, 5/ that in the helically symmetric case of the type of equilibria considered here Mercier's criterion turned out to be sufficient. This stresses the interest of the results described here, although the sufficiency of Mercier's criterion in toroidal stellarators /12/ has not yet been proved.

The JMC code, which is to be described in detail elsewhere, is constructed as a diagnostic package applicable to the results obtained with a 3D energy minimizing equilibrium code which uses flux surfaces as one of the independent variables. Currently, the published version of the BBG code /13/ is being used and the only output needed concerns the geometry of the flux surfaces. The linear problems as i) $\vec{j} \cdot \nabla s = 0$, where $\vec{j}$ is the current density and s the flux label, ii) the currents I and J and the one-dimensional part of the equilibrium equation $p'V' = I'F_T' + J'F_P'$ (F_T, F_P toroidal and poloidal fluxes, which are input functions for the BBG code, V volume, $' = d/ds$), iii) the equation for $X = j_{\shortparallel}/B$ are solved by the JMC code itself in a way which is appropriate for the evaluation of Mercier's criterion. It is written in the following form:

$$K_2^2 - K_1 K_3 > 0 \text{ for Mercier stability,}$$

$$K_2 = \frac{1}{2}\left(F_P'F_T'' - F_T'F_P''\right) + \int XB^2\sqrt{g}'\,|\nabla s|^{-2}\,dudv\ ,$$

$$K_1 = I'F_T'' + J'F_P'' - V''p' + p'^2\int B^{-2}\sqrt{g}'\,dudv + \int X^2B^2\,|\nabla s|^{-2}\sqrt{g}'\,dudv\ ,$$

$$K_3 = \int B^2\sqrt{g}'\,|\nabla s|^{-2}\,dudv\ .$$

Here, s, u, v are the independent variables and $\sqrt{g}'$ the Jacobian in the BBG code /13/.

The following type of helically symmetric and toroidal HELIAC equilibria is

investigated. The plasma boundary is given by

$$r = \Sigma \Delta_{\ell m} \cos\, 2\pi[(\ell - 1)u - mv]$$

$$z = \Sigma \delta_{\ell m} \sin\, 2\pi[(\ell - 1)u - mv]$$

$\Delta_{20} = 1$, $\Delta_{11} = 0.96$, $\Delta_{22} = -0.24$ or -0.29, $\Delta_{31} = 0.38$, $\Delta_{33} = 0.11$, $\Delta_{44} = -0.04$

$\delta_{20} = 1$, $\delta_{11} = -0.96$, $\delta_{22} = 0.24$ or 0.29, $\delta_{31} = 0.38$, $\delta_{33} = -0.11$, $\delta_{44} = 0.04$

$\Delta_{\ell m} = \delta_{\ell m} = 0$ for all other indices.

Here, $\Delta_{22} = -0.24$ for the "nonresonant" case (where $0.274 \leq \iota_p \leq 0.314$) and $\Delta_{22} = -0.29$ for the resonant case (where $0.32 \leq \iota_p \leq 0.36$). Thus, the resonance $\iota_p = 1/3$ is considered in the second case. The ι_p interval indicated gives the range occurring between the magnetic axis and the boundary. Figure 1 indicates the geometry of the nonresonant case; the boundary in the resonant case differs only slightly. The only difference between the helically symmetric and the toroidal case is that the major torus radius R_T is chosen in such a way that an infinite ($R_T = \infty$) or finite ($R_T < \infty$) number N of field periods may be considered. The total twist is $\iota = N\iota_p$; the aspect ratio of a period is $A_p \approx 2.5$, and the toroidal aspect ratio is $A = NA_p$. In the range of β values considered the equilibria are net current free in good approximation, $AdJ/dI \lesssim 0.1$.

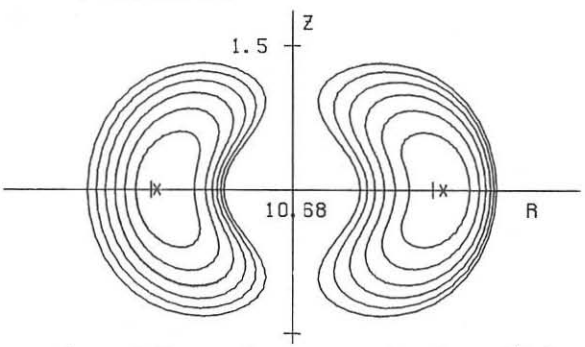

Fig.1: Cross-sections of flux surfaces at v = 0 and v = 1/2 for the nonresonant case with 4 periods and $\langle\beta\rangle = 0.075$.

First, an equilibrium with $\langle\beta\rangle = 0.075$ and approximately parabolic (in the distance from the magnetic axis) pressure profile is considered. This case is stable if helically symmetric. Considering N = 13, 10, 6, and 4, we find decreasing stability, as is shown in Fig.2 for s = 1/2, with a stability boundary at $N \approx 7$. Discussion of the various stabilizing and destabilizing terms in the criterion shows that the contributions of the first and second terms in K_1 as well as the influence of K_2 are negligible, so that the stability behaviour is governed by the last three terms of K_1. Instability comes about by an increase of the fifth term, which contains the parallel current density. Unstable behaviour occurs first at the plasma boundary in keeping with the fact that the pressure gradient is strongest there for the profile chosen.

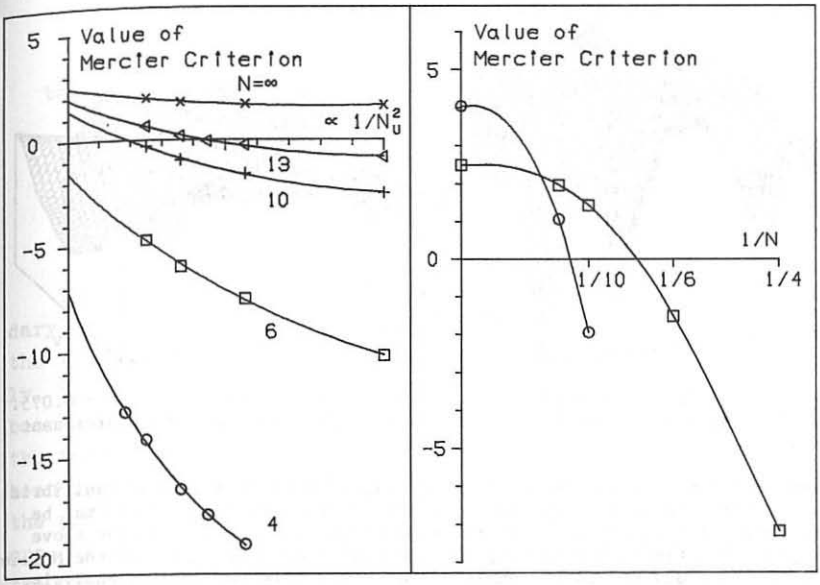

Fig.2: The left part of the figure shows the extrapolations of the values of the Mercier criterion at s = 1/2 to zero mesh size for the nonresonant case with $\langle\beta\rangle$ = 0.075 and N periods. The finest mesh used is 29/56/56, the coarsest 13/24/24. The right-hand part of the figure shows the extrapolated values for $\langle\beta\rangle$ = 0.075 (□) and 0.13 (○) as functions of 1/N.

The above result cannot, however, be considered to yield a reliable stability boundary for the following reasons. Considering N = 4 and the resonant case, the code result shows a large parallel current density with the 1/3-resonance structure (see Fig.3). Accordingly, Mercier's criterion is formally strongly violated. We do not stress the credibility of this result; more refined methods of investigating the actual structure which may occur at a low-order resonance already exist /14, 15/. Rather, we would advocate the conclusion that avoiding low-order resonances is advisable. In the nonresonant case (see Fig.3), some resonance structure is still visible in accordance with the choice of the twist ι = 0.294, which avoids the resonances 1/4 and 1/3. The main Fourier component of the current density here is the m = 1, n = 0 component which is driven by the torus effect. This component (which has the structure of the original PS current) likewise occurs in an axisymmetric torus. It here brings about the Mercier unstable behaviour (see Fig.2). On the other hand, the extrapolation to zero mesh size is difficult, because in the cases considered here the extrapolation yields a value which is approximately one order of magnitude smaller than the sum of the absolute values of the three constituents.

If the interpretation of the above results as Mercier instability at low N is correct, the unstable behaviour should be more obvious for a higher β value. Considering $\langle\beta\rangle$ = 0.13, we indeed find a stability boundary of N≈12 at s = 1/2. Figure 2 shows the extrapolated results for $\langle\beta\rangle$ = 0.075 and 0.13.

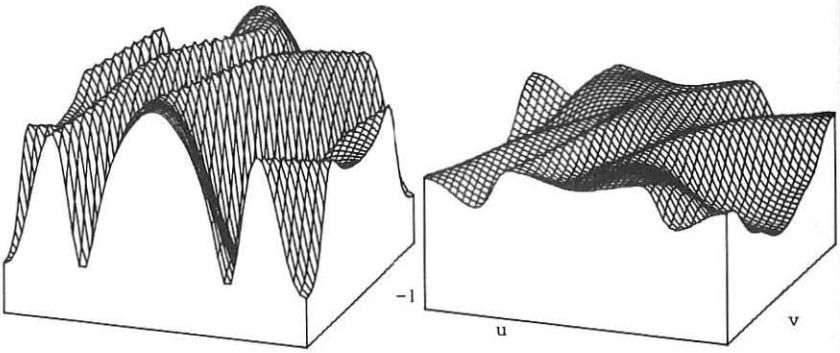

Fig.3: $X = j_{\parallel}/B$ as a function of u and v at $s = 1/2$ and $N = 4$, $\langle\beta\rangle = 0.075$. The left-hand part shows the resonant, the right-hand part the nonresonant case.

Apart from the general comment that "strongly" three-dimensional equilibria (i.e. equilibria with large twist per period and only few periods) may be considered with reserve, there are two obvious conclusions from the above results: i) optimization may improve the stability behaviour, ii) the Mercier instability study has to be complemented by low node number mode analysis.

References

/ 1/ Furth, H.-P., Killeen, J., Rosenbluth, M.N., Coppi, B., in Plasma Phys. and Contr.Nucl.Fusion Res.1965 (IAEA, Vienna, 1966) Vol.I.p.103.
/ 2/ Lortz, D., Nührenberg, J., in Plasma Phys.and Contr.Nucl.Fusion Res.1978 (IAEA, Vienna, 1979) Vol.II, p.309.
/ 3/ Nührenberg, J., Proc.Intern.Conf.on Plasma Physics, Nagoya 1980, paper 10b-I-03.
/ 4/ Gruber, R., Kerner, W., Merkel, P., Nührenberg, J., Schneider, W., Troyon, F., Comp.Phys.Comm.24 (1981) 389
/ 5/ Merkel, P., Nührenberg, J., Gruber, R., Troyon, F., to be published in Nucl.Fus.1983.
/ 6/ Yoshikawa, S., Princeton University Plasma Physics Lab.Annual Rep.1981.
/ 7/ Herrnegger, F., MPI f.Plasmaphysik Annual Report 1982.
/ 8/ Bauer, F., Betancourt, O., Chu, T.K., Proc.Sherwood Meeting, Santa Fe (1982) paper 3C28.
/ 9/ Mercier, C., in Plasma Phys.and Contr.Nucl.Fusion Res.1961, Nucl.Fus. 1962 Suppl.2, IAEA, Vienna (1962) 801.
/10/ Broßmann, U., et al., in Plasma Phys.and Contr.Nucl.Fusion Res.1982, IAEA-CN-41/Q5.
/11/ Großmann, R., Herrnegger, F., Nührenberg, J., Proc.Sherwood Meeting, Arlington (1983) paper 1S21.
/12/ Shafranov, V.-D., Phys.Fluids 26 (1983) 357.
/13/ Bauer, F., Betancourt, O., Garabedian, P., A Computational Method in Plasma Physics, New York, Springer Verlag, 1978.
/14/ Betancourt, O., Garabedian, P., Comm.on Pure and Appl.Math.35 (1982)365.
/15/ Betancourt, O., Garabedian, P., Proc.Sherwood Meeting, Arlington (1983) paper 2S1.

Critical plasma pressure provided by the ballooning modes of helical instability in tokamak

O.P.Pogutse, E.I.Yurchenko

I.V.Kurchatov Institute of Atomic Energy,
Moscow, USSR

The ballooning modes of helical instability with free boundary, i.e. the large-scaled modes of helical instability within the torus were first found analytically in /1/ and, independently, by numerical methods in /2-4/. The studies in /1,2/ have been done for a model homogeneous current distribution across the toroidal plasma column. In /3,4/, the calculations have been done for the arbitrary current density distributions across the plasma column for both free plasma boundary and the fixed one. As in the numerical calculations /3,4/ and later in /7/, the critical β dependence on the current was the same as that derived analytically, $\beta_c \sim J^2$, all seemed to be clear in this problem.

Recently, the calculations of stability for the toroidal plasma column with inhomogeneous current distribution across it were done again /8/, but, in difference from all the previous calculations, another dependence of critical β on the current was found, $\beta_c \sim J$.

In the the present paper, we give an explanation of the contradiction arisen, as we show analytically that at the inhomogeneous current density, the ballooning modes of helical instability, in difference from the case of homogeneous current, give the linear dependence of β on the current.

Let us consider the model which allows to solve analytically the problem of plasma stability to the ballooning modes of helical instability. Assume that the plasma column of circular cross-section with a radius, a, through which a current J passes, is a torus with a major radius R located in vacuum with a strong magnetic field, B_0 i.e. $B_J << B_0$ (B_J is the magnetic field produced by the current). In this case, it is con-

venient to use the energy principle /1/, /9/.

Let's assume that the current distribution is slightly inhomogeneous: $j = j_0[1 - \nu(r)]$, where $\nu(r) << 1$. This allows to use the theory perturbation with respect to a small parameter of the current inhomogeneity, $\nu(r)$, and with respect to a small toroidicity ($\varepsilon = r/R$). In other words, we consider a cylindrical plasma column, $L = 2\pi R$ long, with homogeneous current density across it, j_0, as a zero approximation. Then, we bend it into the torus and produce an inhomogeneous current density.

Let's include the trial function - a combination of eigenfunctions from the cylindrical problem - into the energy principle.

The solvability condition for a set of equations derived leads to a following dispersion equation:

$$\begin{vmatrix} \tilde{\gamma}^2 + 2(m - nq)[m - 1 - nq + \Delta_m] & \varepsilon(\beta_j + 1) \\ \varepsilon(\beta_j + 1)\frac{m}{m+1} & \tilde{\gamma}^2 + 2(m - 1 - nq)[m - nq + \Delta_{m+1}] \end{vmatrix} = 0 \quad (1)$$

Here

$$\tilde{\gamma}^2 = \gamma^2 a^2 / C_{\theta a}^2, \quad C_\theta^2 = B_j^2 / 4\pi\rho, \quad q = \alpha B_0 / R B_j$$

$$\Delta_m = 2m \int_0^a \nu(r)(r^{2m-1}/a^{2m})\,dr$$

One derives an expression for the increment of M^{th}-mode from the equation (1) in the cylindrical approximation ($\varepsilon \to 0$). From this expression, it follows that a current drop results in the emergence of the ranges in nq, where the plasma is stable ($\tilde{\gamma}^2 < 0$). The widths of these stability "slits" are determined not only by a shape of the current drop. At $\varepsilon \neq 0$, the widths of the stability "slits" also depend on the plasma pressure. At a small width of the "slit" for the M^{th} mode, one can derive an approximate value of increment from the equation (1):

$$\tilde{\gamma}^2 = -nq\gamma_m + \varepsilon(\beta_j + 1)(m/m+1)^{1/2} \quad (2)$$

where, $\gamma_m = 2\int \nu(r)(r^{2m+1}/a^{2m})\,dr$ is the numerical coefficient.

From the expression (2), one can see that an increase in q, in the tokamaks with inhomogeneous current, i.e. a decrease in the current, $J \sim 1/q$, stabilizes the plasma, an increase in pressure destabilizes it. The critical pressure, with increase of which the plasma becomes unstable with respect to the ballooning modes of the helical instability with free boundary, is easely found from the expression (2):

$$\beta_c = \frac{\varepsilon}{q}\left(n\nu_m^* - \frac{\varepsilon}{q}\right) \qquad (3)$$

where, $\nu_m^* = \nu_m\left(m+1/m\right)^{1/2}$

In the modern tokamaks $\varepsilon/q \sim 10^{-1}$. Therefore, at $n\nu_m^* > \varepsilon/q$, it follows from (3) that $\beta_c \sim J$. The relation (3) is obtained at $\nu << 1$, but one can hope that it is true up to $\nu \leq 1$.

This result explains the contradiction appeared in the numerical calculations /3,4/ and in /12/. Indeed, as the critical β is determined by the ballooning modes of a flute-like instability, the dependence $\beta_c \sim J^2$ should arise, but in the case, when the ballooning modes of the helical instability with a free boundary are driven, the critical β is found to be directly proportional to J. Which ballooning modes - large-scaled or small-scaled - are more dangerous, i.e. responsible for β_c ? The answer to this question depends mainly on the current density and pressure distribution profiles across the plasma column, on the cross-section configuration of the magnetic surfaces and on the disposition of the conducting case or on the feedback response /8/. It is evident that this answer can be obtained for the real conditions only in the numerical calculations, but the analysis given above shows that the dependence, $\beta_c \sim J^{\alpha}$, where $1 \leq \alpha \leq 2$, arisen in the calculations does not contradict the theory of ballooning modes.

The authors wish to express their gratitude to academician B.B.Kadomtsev for helpful discussion.

References

1. Pogutse D.P., Yurchenko E.I., PPPL-trans. 127, 1977, ORNL-trans. 4410, 1977, Nucl.Fus. 18, 1629, 1978.
2. Berger O. et al. Plasma Phys. Contr. Nucl. Fus. Res. Berchtesgaden, VII, 411, 1977.
3. Todd A.M.M. et al. Phys. Rev. Lett. 38, 826, 1977.
4. Bateman G., Peug Y.-K., Ibid. 38, 829, 1977.
5. Шафранов В.Д. ЖТФ, 1970, 40, 241.
6. Погуце О.П., Юрченко Э.И. Письма в ЖЭТФ, 1978, 28, 344.
7. Todd A.M.M. et al. PPPL-1470, 1978.
8. Sauremann H. et al. Intor Phase II^{A} Europ. Contr. 6th Workshop-Meeting, ch.IV, 1.2. 1982.
9. Погуце О.П., Юрченко Э.И., В кн."Вопросы теории плазмы", Вып.II, Под ред. М.А.Леонтовича и Б.Б.Кадомцева, М., Энергоиздат, 56, 1982.

RADIAL STRUCTURE OF RESISTIVE BALLOONING MODES

O.P.Pogutse, N.V.Chudin
I.V.Kurchatov Institute of Atomic Energy,
Moscow, USSR

A linear theory of ballooning modes /1-4/ is a problem which requires to solve the partial differential equations with oscillating coefficients, the precise analytical solution of which is unknown. Therefore, the instability of ballooning modes first was studied by numerical methods. A numerical approach allows to consider the ballooning modes with low numbers well, but it does not make their physical nature clear. Therefore, a great attention was paid recently to the analytical studies. A considerable progress has been reached by this approach in the understanding of the nature of ballooning modes. The success in the analytical study is explained by creation of a mathematical method which works well for the ballooning modes with high numbers. These modes often possess, as it has been shown, of the greatest growth rate. At the first stage, the analytical stability problem is reduced to the finding of a local growth rate in the ballooning modes from the ordinary differential equation in terms of "angular" variables in the Fourier space. At the second stage, at the next order of magnitude for the parameter 1/nq, an equation for the radial structure of instability arises and the problem of localizing the oscillations along the radius is solved. This problem has been considered in some papers for ideal ballooning modes. But the study of radial structure for resistive instabilities has not been carried out yet.

In the present paper, a problem of radial structure for the ballooning instability with the use of variational method is formulated anew. The variational method is applied below for studying the radial structure of resistive thresholdless instability in the ballooning modes. It is sufficient to consider one equation for a disturbed potential of the electric field /4/ for description of this instability:

$$\gamma^2 \operatorname{div}\frac{\nabla_\perp \varphi}{c_A^2} - \frac{\partial\left(\frac{4\pi p'}{\sqrt{g}B_0^\zeta}\frac{\partial\varphi}{\partial\theta}, 1/B_0^\zeta\right)}{\partial(a,\theta)} + \frac{4\pi\gamma}{c^2}(B\nabla)\frac{\sigma}{B^2}(B\nabla)\varphi = 0 \qquad (1)$$

This equation is written in a system of coordinates with straight field lines. A functional can be put into correspondence with this equation for low-scaled perturbations with $n \gg 1$:

$$W = \frac{1}{2}\int dv\left\{\frac{\gamma^2 g^{33}}{c_A^2 g}\left[g_{11}\left(\frac{\partial\varphi}{\partial\theta}\right)^2 + g_{22}\left(\frac{\partial\varphi}{\partial a}\right)^2 - 2g_{12}\frac{\partial\varphi}{\partial a}\frac{\partial\varphi}{\partial\theta}\right] - \right.$$
$$\left. - \frac{4\pi p'}{gB_0^\zeta}\frac{\partial\varphi}{\partial\theta}\frac{\partial(\varphi, 1/B_0^\zeta)}{\partial(a,\theta)} + \frac{4\pi\sigma}{c^2}\frac{\gamma}{B^2}(B\nabla\varphi)^2\right\} \qquad (2)$$

Using the transformation /5/

$$\varphi = \sum_{n,m} \exp\left[in\zeta - im\theta\right]\int_{-\infty}^{\infty} dy F(a,y)\exp\left[i(m-nq)y\right], \qquad (3)$$

in the limit, $nq \to \infty$, one derives from (2) a functional:

$$W_o = \frac{1}{2}\int_o^{a_o}\int_{-\infty}^{\infty} \frac{dady}{aR}\, n^2\left\{\left[\gamma_o^2\tau_\theta^2(1+t^2) - \alpha(\cos y + t\sin y)\right]F^2 + \frac{\gamma_o\tau_s}{n^2q^2}\left(\frac{\partial F}{\partial y}\right)^2\right\}, \quad (4)$$

where $\alpha = -8\pi p' Rq^2/B_o^2$, $t = sy$, $s = aq'/q$, is the shear, $\tau_s = 4\pi\sigma a^2/c^2$ is the skin time, $\tau_\theta = Rq/c_A$ is the Alfven time. The Euler equation for this functional determines a local growth rate of the thresholdless resistive instability:

$$\frac{\gamma_o\tau_s}{n^2q^2}\frac{\partial^2 F_o}{\partial y^2} - \left[\gamma_o^2\tau_\theta^2(1+t^2) - \alpha(\cos y + t\sin y)\right]F_o = 0 \quad (5)$$

An approximate analytical expression for the growth rate $\gamma = (\alpha^2/2N)^{1/3}/\tau_\theta$, ($N = \tau_s/\tau_\theta/n^2q^2$ was derived in /4/ by the averaging method. It is evident that the solutions of the type $F = A(a)F_o(a,y)$ also satisfy the equation (5). Substitute such a trial function into the initial functional (2), considering $A(a)$ to be much localized than F_o. Then, the terms of the order of n^2 again give us a functional W_o, the terms of the next order of n give us a functional:

$$W_1 = \frac{1}{2}\int_o^{a_o}\frac{da}{aR}\, n\left\{c_1\left[\gamma - \gamma_o(a)\right]A^2 + \frac{c_2}{n^2}\left(\frac{\partial A}{\partial a}\right)^2\right\}, \quad (6)$$

where, $c_1 = \tau_\theta\int_{-\infty}^{\infty} dy\left[2\gamma_o\tau_\theta(1+t^2)F_o^2 + N\left(\frac{\partial F}{\partial y}\right)^2\right]$,

$$c_2 = (\gamma\tau_\theta a/q)^2\int_{-\infty}^{\infty} F_o^2\, dy.$$

Varying the expression (6) with respect to A, one obtains an equation for an amplitude of the envelope, which characterizes the radial structure of perturbations:

$$\frac{c_2}{n^2}\frac{\partial^2 A}{\partial a^2} - c_1 n\left[\gamma - \gamma_o(a)\right]A = 0 \quad (7)$$

As the coefficients c_1 and c_2 are positive, a shape of the potential and, as a sequence, the possibility of localizing perturbations are determined by a local growth rate with an opposite sign $/-\gamma_o(a)/$. If this expression has a local minimum, one will obtain a potential of the oscillator with a characteristic localization width; $\Delta x \sim 1/\sqrt{n}$, near it. In this case, a real growth rate γ is found to be less than the local one by $1/n$.

For the thresholdless resistive instability, determining the radial dependence of a local growth rate, an eigenvalue problem is solved numerically for (5) in order to precise an approximate analytical expression obtained by the averaging method. The averaging method works well, when a rather high number of oscillations, $\Delta y/2\pi \gg 1$, takes place within a characteristic scale for the average part of the function, $\Delta y = (N/\gamma\tau_\theta)^{1/4}/\sqrt{s}$. This condition can restrict its application at the plasma column periphery, where there is a bad conductivity and rather large shear.

Calculations were carried out for the current density with square parabolic distribution and $q(1) = 2.5$. The plasma density and its temperature are also considered to be distributed by a parabolic law ($n(0) = 5.x10^{13}\ cm^{-3}$, $T(0) = 1keV$). At the longitudinal magnetic field, $B_o = 20$ kG, it corresponds to the experimental conditions with $\beta(0) = 1\%$. The local growth rate of the thresholdless resistive instability for the toroidal harmonics

with n=50, 100, 200 vs. radius, as a result of calculation, is shown in Fig.1. The behaviour of the eigenfunction $F_o(y)$ (solid line), corresponding to the maximal local growth rate ($r/a_o=0.5$), is shown in Fig.2 as an illustration for n=100. The dashed line in this figure shows the shape of a potential U (y) from the equation (5). As one can see in Fig.1, the local growth rate has no maximum within the plasma column, it rises monotonically towards its edge. Therefore, one can conclude that the thresholdless resistive modes cannot be localized in the plasma core, they tend to shift towards the plasma edge. A problem of the instability existence near the plasma edge needs additional considerations with the impurity and other near-wall effects. The fact that the thresholdless resistive ballooning modes tend to shift towards the plasma edge seems to explain the absence, in the experiment, of noticeable macroscopic effects related to the ballooning modes up to the pressure threshold determined by ideal ballooning modes, for which the possibility of localizing within the plasma column has been previously proved.

References

/1/ Connor J.W., Hastie R.J., Taylor J.B. Phys. Rev. Lett., 1978, v.40, p.396.

/2/ Lee Y.C., Van Dam J.W. Proc. of the Finite Beta Theory Workshop, Varenna, 1977, p.93.

/3/ Pogutse O.P., Yurchenko E.I. Pis'ma v JETF, 1978, v.28, p.344.

/4/ Pogutse O.P., Yurchenko E.I. Voprosy teorii plasmy, vol.11, Moskow, Energoizdat, 1982, p.56.

/5/ Connor J.W., Hastie R.J., Taylor J.B. Proc. Roy. Soc. A., 1979, v.365, p.1.

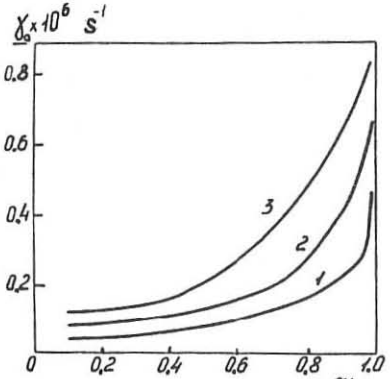

Fig.1

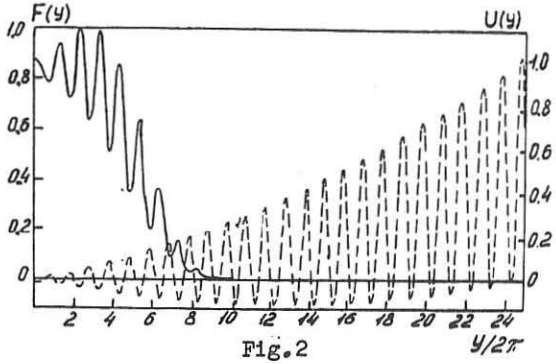

Fig.2

On Tearing Modes in a Resistive Medium

Philip Rosenau
Faculty of Mechanical Engineering
Technion - Israel Institute of Technology
Haifa, Israel

ABSTRACT

The theory of tearing modes in a cylindrical symmetry is reexamined. The resistive medium is embedded with the simplest Ohm's law. By considering β, the ratio of thermal to magnetic pressure, as a parameter with respect to which the sought after eigenvalues were scaled, a very simple description was obtained. Many of the classical results were obtained in a more simple way. Among the new results are: (1) the possibility of the existence of a tearing mode on a resistive time scale and which is hardly affected by drift effects, (2) for modes of an almost marginal growth rate inertia does not play an important role, slab and cylindrical modes are fundamentally different and finite-β effects play a crucial role.

Preliminary Abstract (4-page paper not received in time).

BIFURCATION THEORY FOR TEARING MODES

E.K. Maschke and B. Saramito*

ASSOCIATION EURATOM-CEA SUR LA FUSION
Département de Recherches sur la Fusion Contrôlée
Centre d'Etudes Nucléaires
Boîte Postale n° 6. 92260 FONTENAY-AUX-ROSES (FRANCE)

Abstract. A plane plasma model including resistivity and viscosity is shown to possess stationary tearing solutions that bifurcate from equilibrium at a critical magnetic Reynolds number.

1. INTRODUCTION

Magnetically confined plasmas are often in weakly turbulent, stationary or quasiperiodic states. Such states are appropriately described in the framework of bifurcation theory by studying the asymptotic solutions of the nonlinear equations describing the system. The tearing instability has been investigated earlier in terms of bifurcating equilibria [1,2]. Here we study the bifurcation of stationary solutions, for which first results were given in a preceding paper [3].

2. THE MODEL

2.1. Equations for stream functions.

We consider a plane plasma slab of thickness d in the x direction and periodic in the y and z directions. Assuming constant density ρ_o, we write the MHD equations including resistivity η and perpendicular viscosity ν in dimensionless form.

$$\left.\begin{aligned} \left(\frac{\partial}{\partial t} + \vec{V}.\nabla\right)\vec{V} &= -\nabla P + S^2(\vec{B}.\nabla)\vec{B} + \mathcal{P}_R \Delta \vec{V} \\ \frac{\partial \vec{B}}{\partial t} &= \nabla \times (\vec{V} \times \vec{B}) + \Delta \vec{B} \quad , \qquad \nabla.\vec{B} = 0 \end{aligned}\right\} \quad (1)$$

Here time is normalized with respect to the resistive time scale $\tau_R = 4\pi\, d^2/\eta$, lengths are expressed in units of d, velocity in units of $V_R = d/\tau_R$, and B in units of a characteristic field strength B_o. The equations contain two dimensionless parameters : The magnetic Reynolds number $S = \tau_R/\tau_H$ where $\tau_H = dB_o^{-1}(4\pi\,\rho_o)^{1/2}$ and the "resistive Prandtl number" $\mathcal{P}_R = \nu/\eta$.

We limit our investigation to (nonlinear) solutions having a given helical symmetry, thereby avoiding the problem of destruction of magnetic surfaces. Thus, we assume that all physical quantities depend at most on two variables x and $(k_y y + k_z z)/(k_y^2 + k_z^2)^{1/2}$. In order to simplify we put $k_z = 0$ so that the variables are x, y, and we write k instead k_y.

The magnetic field may be expressed in the form

$$\vec{B} = B_z(x,y)\,\vec{e}_z + \vec{e}_z \times \nabla\psi(x,y) \quad (2)$$

* Chargé de Recherche au C.N.R.S.

As the x and y components of eqs. (1) do not contain B_z and V_z, it is sufficient to consider the two-dimensional problem corresponding to the x and y directions only.

With the boundary conditions, which will be specified below, eqs. (1) admit an equilibrium solution that is independent of y. We put

$$\left.\begin{aligned} \vec{B} &= \vec{B}_{eq}(x) + \vec{b}(x,y) \quad , \qquad \psi = \psi_{eq}(x) + \tilde{\psi}(x,y) \\ \vec{V} &= \vec{V}_{eq}(x) + \vec{v}(x,y) \quad , \qquad \nabla . \vec{v} = 0 \end{aligned}\right\} \tag{3}$$

and we assume that the equilibrium diffusion is compensated by an appropriate mass source : $\nabla . V_{eq} = S_m(x)$. Due to the helical symmetry the divergence-free vector $\vec{v}$ may be written in terms of a stream function :

$$\vec{v} = v_z \vec{e}_z + \vec{e}_z \times \nabla \phi(x,y) \tag{4}$$

Eqs. (1) now reduce to two scalar equations for $\tilde{\psi}$ and ϕ.

2.2. Equilibrium

We consider equilibrium solutions such that

$$B_{eq,x} = 0 \quad , \qquad V_{eq,y} = V_{eq,z} = 0 \tag{5}$$

We are free to choose the form of $B_{eq,y}(x)$. Eqs. (1) then determine $P_{eq}(x)$ and $V_{eq}(x)$, hence $S_m(x)$. In the following we study the particular equilibrium given by

$$B_{eq,y}(x) = \tanh(\alpha x) \tag{6}$$

2.3. Boundary conditions

We require

$$\left.\begin{aligned} v_x &= 0 \quad , \quad \partial v_y/\partial x = 0 \\ b_x &= 0 \quad , \quad \partial b_y/\partial x - V_{eq}(x) b_y = 0 \end{aligned}\right\} \quad \text{for } x = \pm \tfrac{1}{2} \tag{7}$$

We also require periodicity in y with period L_y, and the flux conservation relations

$$\int_{-1/2}^{+1/2} b_y(x,0)\, dx = 0 \quad , \qquad \int_{-1/2}^{+1/2} v_y(x,0)\, dx = 0 \quad . \tag{8}$$

3. BIFURCATION OF A STATIONARY SOLUTION

3.1. Choice of bifurcation parameter.

Our problem contains three dimensionless parameters, S, P_R, and α. The parameter P_R, which is the ratio of two physical constants, will be considered as a given fixed quantity. Then two different points of view are possible : (1) We choose fixed boundary conditions, thereby fixing α, and consider S as the bifurcation parameter. Or, (2) we choose a fixed value of S and vary α, thereby changing the ratio of the distance of the walls, d, to the equilibrium scale length. The first point of view was chosen in our previous work [3] and will again be adopted here. The second point of view has been adopted in earlier work [1,2].

3.2. Bifurcation of a stationary solution for $S > S_c > 0$.

On the basis of certain reasonable assumptions about the values of the physical parameters we have proved that if S is below some finite critical value S_c, the equilibrium solution which satisfies eqs. (5) is stable. The proof uses a priori bounds on the solutions of the problem, for which the presence of the two dissipative terms is essential. This mathematical result justifies the search for the smallest strictly positive value of S at which the equilibrium becomes unstable and where a bifurcation may occur.

By linearizing eqs. (1) about the equilibrium (5), (6), assuming the time and space dependence of the perturbations in the form $\exp(\gamma t + iky)$ and investigating for fixed k the resulting eigenvalue problem for γ, we find numerically that $\mathrm{Im}\,\gamma = 0$ for all values of S. From this we conclude that the loss of stability of the equilibrium is connected with the bifurcation of a new stationary solution. Solving the linearized equations with $\gamma = 0$ we obtain for each k a bifurcation point S(k), as shown in Fig. 1. We note that this figure has been calculated by putting formally $V_{eq} = 0$ in the equations for Ψ and ϕ. This approximation, which corresponds in time dependent problems to neglecting variations on the time scale of resistive diffusion, is not essential as far as the qualitative results are concerned. Results obtained with $V_{eq} \neq 0$ will be published elsewhere.

The smallest S(k) compatible with the boundary conditions in the y direction is the critical value S_c at which the equilibrium becomes unstable and a new solution bifurcates.

Assuming, as indicated by our numerical results, that the eigenvalue S_c is simple, we can apply known theorems on bifurcation [4] and prove that a parabolic branch of stationary solutions behaves as $(S-S_c)^{1/2}$.

The bifurcating branch has been calculated numerically for increasing values of S (at present up to S = 2000). It shows the familiar features of a tearing mode : There are magnetic islands centered about the rational surface where $B_{eq_y} = 0$ (Fig. 2a), and the velocity field forms a set of convective cells (Fig. 2b).

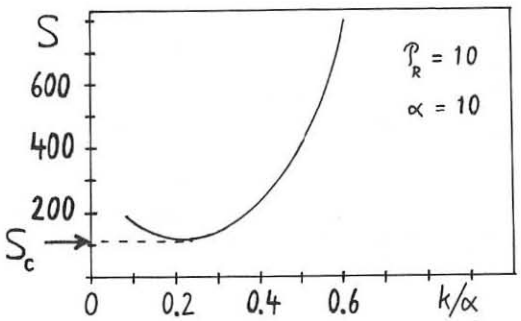

Fig. 1 - Value of S for marginal stability of the mode k.

REFERENCES

[1] REBUT, P.H., Plasma Physics 4 (1962) 159

[2] RUTHERFORD, P.H., H.P. FURTH, M.N. ROSENBLUTH, Proceedings IV. Internat. Conf. Plasma Physics and Contr. Nucl. Fusion Research, Madison, I.A.E.A. Vienna (1971)

[3] MASCHKE, E.K. and B. SARAMITO, Invited paper 1982 Internat. Conf. Plasma Physics, Göteborg, published in Physica Scripta T2:2 (1982), 410

[4] CRANDALL, M.G. and P.H. RABINOVITZ, J. Funct. Anal. 8 (1971) 321.

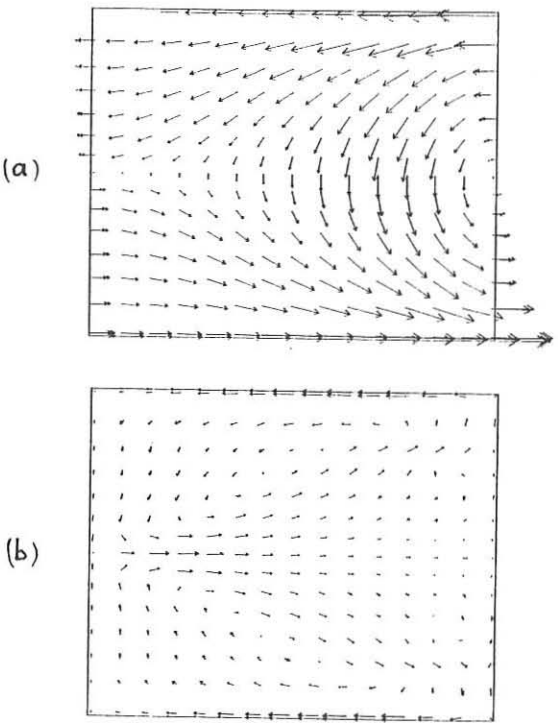

Fig. 2 - Half period of (a) magnetic field and (b) velocity field, for $S = 1000$, $\alpha = 10$, $P_R = 10$, $k = 2.5$

Non-linear evolution of helical modes in a tokamak with low q

Yu.N.Dnestrovskij

I.V.Kurchatov Institute of Atomic Energy

D.P.Kostomarov, A.M.Popov, E.A.Shagirov

M.V.Lomonosov State University

Moscow, USSR

The nonlinear stabilization of a kink instability in plasma with finite conductivity is studied. We are interested here in the evolution of a mode with $m/n = 2$. A free plasma boundary is simulated by a large difference between the plasma and vacuum resistivities $\eta_p \ll \eta_v$ (usually, $\delta = \eta_p/\eta_v \sim 10^{-4} \div 10^{-5}$). The behaviour of plasma and its cold "coat" (vacuum) are described by a joint reduced set of MHD-equations /1/ with dissipative terms:

$$\frac{\partial \omega}{\partial t} + I(\omega, u) = S^2 I(j, \psi)$$
$$\frac{\partial \psi}{\partial t} + I(\psi, u) = \eta(\psi) j - E_0 \qquad (1)$$
$$\Delta u = \omega \,, \quad j = \Delta\psi - 2\frac{h}{m} \,, \quad I(\omega, u) = [\vec{\nabla}\omega, \vec{\nabla}u]_z$$

A helical symmetry is introduced, i.e. all the functions are considered to be dependent on two space variables $f(r, \theta = \varphi - \alpha z)$, where $\alpha = \frac{m}{n R_0}$, R_0 is the major plasma radius. In (1) ψ and u are the functions of the helical fluxes of magnetic and velocity fields, respectively; ω and j are the longitudinal components of velocity vortex and current density, respectively; E_0 is the constant electric field. The boundary conditions on the conducting wall with radius r_w are: $\psi(r_w, \theta, t) = u(r_w, \theta, t) = 0$.

A set (1) is written in the dimensionless alfvèn units, $S = \tau_R/\tau_{H_p} = 10^6$, $\tau_R = a^2\mu_0/\eta$, $\tau_{H_p} = R_0(\mu_0\rho_0)^{1/2}/B_z$

The initial conditions are set as an axially-symmetric equilibrium state perturbed by the eigenfunction of a linearized problem. We have considered two types of current profiles $j_0(r)$. The first one corresponds to a monotonically decreasing distri-

bution $$j_0 = \begin{cases} \frac{2}{q_0} - 4\left(\frac{1}{q_0} - \frac{1}{q_a}\right)\left(\frac{r}{a}\right)^2, & 0 \le \frac{r}{a} \le 1 \\ j_1 = \text{const}, & 1 \le \frac{r}{a} \le \frac{r_w}{a} \end{cases} \qquad (2)$$

Here, $q_0 = q(0)$, $q_a = q(a)$, $j_1 << 2/q_0$. The second type corresponds to a non-monotonous distribution. In our model the resistivity η is a function of helical flux ψ in the process of nonlinear evolution: $\eta = \eta_p(\psi)$ in plasma, $\eta = \eta_v = \text{const}$ in vacuum. A value $\psi = \psi_p$ corresponds to the plasma boundary and separates the cold region from the hot one. The uniqueness of such a determination is lost at a time when ψ_p coincides with a value of ψ on the "vacuum" separatrix, where $\nabla\psi = 0$. In that case, we have considered two models of resistivity transition: model of "vacuum heating" and that of"plasma cooling". In the model of "heating", we set $\eta = \eta_p$ along the joint field line formed after reconnection. In the model of "cooling", we set $\eta = \eta_v$ along that line.

A 2-D code REMP with good dispersion and diffusion properties, which allows to simulate the motion of the plasma boundary with the peaked current expulsions, was developed. The calculations by the linear code LIREK have been done to find the regions of linear instability and the increment values. A change of the parameter δ from $\delta = 10^{-5}$ to $\delta \sim 1$ allows to follow the transition from the external mode to the internal tearing instability.

In the nonlinear evolution of the external mode $m = 2$, the cross-section of the plasma column becomes close to an elliptic one with semiaxes a and b. The dependence of the ratio a/b on time, t/τ_{H_p} at different $q_{r_0} = 0{,}93$, 1.0, 1.2, 1.8 and at $q_{r_a} = 1.85$, $r_w/a = 1.5$ is shown in Fig.1a. One can see that the non-linear stabilization exists at $q_0 < 1$ /2/. In Fig.1 (b,c) a plasma cross-section is shown at $t = 40\tau_{H_p}$ in the absence of non-linear stabilization ($q_0 = 1.2 > 1$) in the model of "heating"(b) and in that of "cooling" (c). Note that the localized near-surface currents, emerging in the plasma motion, are located at the internal side of the plasma boundary, in the hot zone, and

they don't damp for hundreds of the alfvén units.

In Fig.2 on the plane of the parameters q_a/q_o and q_a, the area above the trace L corresponds to a linear instability of the mode $m/n = 2/1$ for a current profile (2) and $r_w/a = 1.5$. In the shaded zone below the straight line $q_o = 1$, there is a non-linear stabilization. The point marked "0" corresponds to calculations /2/.

For a non-monotonous current, the condition of non-linear stabilization $q_o < 1$ changes by $q_{min} < 1$: e.g. in the case $q_o = 1.2$, $q_a = 1.85$, $q_{min} = 0.85$, $r_w/a = 1.5$, a stabilized value $a/b = 1.2$.

References

1. Kadomtsev B.B., Pogutse O.P., JETP, 65, (1973) 575.
2. White R.B., Monticello D.A., Rosenbluth M.N., Strauss H.R., Kadomtsev B.B., Plasma Phys. and Contr.Nucl.Fusion Res., IAEA, Vienna, 1975, 1, p.495.
3. Zakharov L.E., Fizika Plazmy, 7 (1980) 18.

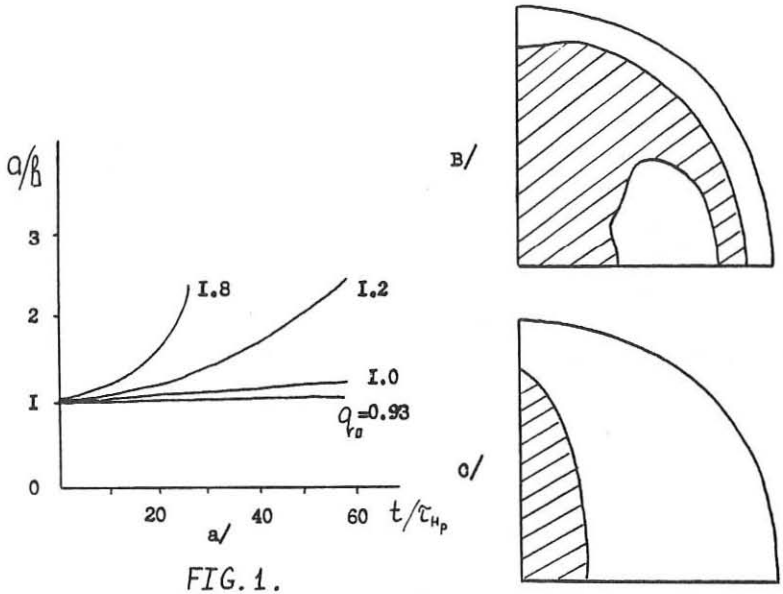
a/b
3
2
I
0
I.8
I.2
I.0
q_{ra}=0.93
20
40
60
a/
t/τ_{H_p}
B/
c/

FIG. 1.

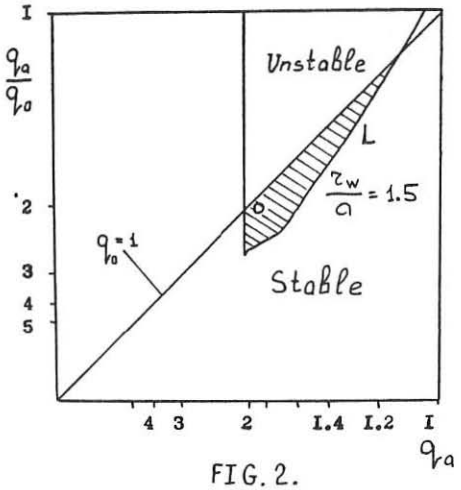
I
$\frac{q_a}{q_a}$
Unstable
L
$\frac{\tau_w}{a}$ = 1.5
q_a = 1
Stable
·2
3
4
5
4 3
2
I.4 I.2
I
q_a

FIG. 2.

DIAMAGNETIC DESTABILIZATION OF MAGNETIC ISLANDS IN THE NON LINEAR REGIME

A. SAMAIN
ASSOCIATION EURATOM CEA SUR LA FUSION
CEN FAR - B.P. N° 6 - 92260 FONTENAY AUX ROSES, FRANCE

ABSTRACT: The non linear behaviour of small amplitude tearing modes is found to be strongly influenced by electron diamagnetism when one takes account of the friction forces experienced by electrons and ions from the microturbulence.

One major issue for understanding turbulence in toroidal configurations is to determine whether this turbulence contains drift tearing perturbations. It has been shown that such perturbations may be linearly unstable in the presence of a thermal gradient. /1,2,3/. However a collisional regime is necessary ($\omega < \nu_{ee}$), to insure proper differential response of cold and hot electrons to the electromagnetic perturbation. The drift tearing instability problem may be posed also in non linear regimes, where the island width δ is large enough, so that at least electrons reach thermodynamical equilibrium over each perturbed magnetic surface. The density n and temperature T of electrons (charge $+e$), and the electric potential U (in the frame of reference rotating around the major axis where the island structure is at rest) are then related by

$$\mathcal{L}og(n) + \frac{eU}{T} = h(\psi) \quad ; \quad T = T(\psi) \qquad (1)$$

where ψ labels each perturbed magnetic surface. In such situations it is generally understood that the island growth rate γ takes the Rutherford's value $\gamma = \Delta' \eta c^2 / 4\pi\delta$. /4,5/. Indeed, near the islands, the effects of inertia, finite ion Larmor radius and viscosity are typically small. If one assumes local ambipolar diffusion of ions and electrons, the transverse current reduces to the divergenceless diamagnetic contribution. The charge continuity equation then imposes a constant parallel current over each perturbed magnetic surface, leading to the Rutherford's scheme. On the other hand the mode exchanges momentum with ions through viscosity effects only. Momentum balance then implies that the islands follow the plasma mass motion at some distance from the islands. /5,6/.

In this paper we question the local ambipolarity of particle diffusion near the islands. Rather than to collisions, this diffusion (and also the electron heat transport) is due to momentum exchange P_e or P_i in the transverse direction between the ion (i) or electron (e) assemblies and the microturbulent modes. The radial diffusion fluxes $\phi_{e,i}$ of electrons or ions (charge $-e$) are given by $\phi_{e,i} = P_{e,i} / (+,-) eB$. We suppose that the azimuthal wave numbers (ℓ, m) for the tearing mode in the poloidal (θ) and toroidal (φ) directions are small compared to those for the turbulent modes. For large island widths δ, the latter adjust locally to the density and temperature gradients within the island structure.

The equilibrium and ambipolarity equations $P_e + P_i = o$, $e\phi_e - e\phi_i = o$ should then be verified at each point. The situation is different for small δ ,for example smaller than the radial extension of the turbulent modes. Such δ should be largely compatible with electron equilibrium (1). The turbulent modes then integrate out the density and temperature gradients over a radial width $> \delta$,and the turbulent spectrum $S(\Omega, K)$ in frequency Ω and wave number K is not severely modified by the presence of the islands. One must note here that the quasilinear turbulent friction forces $P_{e,i}$ are proportional to the difference between the phase velocities Ω / K_θ and the macroscopic velocities V_θ along θ of each assembly (e) or (i)/7,8/. With $S(\Omega, K)$ unperturbed, the variations of $P_{e,i}$ and $\phi_{e,i}$ then simply reflect those of V_θ ,i.e., the variations of the diamagnetic velocities,proportional to $\partial n / n \partial r$ and $(\mathcal{E}/T - 3/2)\, \partial T / T \partial r$ (at energy $\mathcal{E}$),and of the electric drift velocity $V_{E\theta}$,proportional to $\partial U / \partial r$. We have

$$\phi_{e,i} = A_{e,i} - n\, D_{e,i} \left(\frac{\partial n}{n \partial r} + (+,-) e \frac{\partial U}{T \partial r} + \alpha_{e,i} \frac{\partial T}{T \partial r} \right) \qquad (2)$$

where the constants $A_{e,i}$, $D_{e,i}$ and $\alpha_{e,i}$ have the same value as in the absence of the islands. A similar equation is also valid for the flux of electron energy $\phi_{\mathcal{E}e}$. Such equations should apply even for non linear interaction between turbulence and particles. However the Eq (2) somewhat simplifies the situation for ions: the ion coupling coefficients could significantly depend on $V_{E\theta}$, introducing a further dependance of P_i and ϕ_i on $\partial U / \partial r$ .It must be noticed that the coefficient α_e reflects the relative weight of hot and cold electrons in resonance with the turbulence. To simplify we neglect the thermal gradient $\partial T / \partial r$ for ions.

Clearly,the Eqs (2) for electrons and ions do not imply the local ambipolarity constraint $e\phi_e - e\phi_i = o$ near the islands. The arguments given above leading to Rutherford's growth rate and rotation of the islands at the mass velocity are in principle no longer valid. In fact the empirical values of the diffusion coefficient $D_e \sim D_i \sim (1\text{-}5) 10^3$ cm^2/s imply a dependance on $\partial U / \partial r$ of the transverse current $I_\perp$ through the term $e\phi_e - e\phi_i$,which is generally much stronger than that introduced by the inertia, ion finite Larmor radius and viscosity effects.These effects may therefore be neglected. The calculations,given in detail in/9/, are obviously simplified by this situation. Another simplification results from the special structure of the fluxes ϕ_e and $\phi_{\mathcal{E}e}$ given by (2), which depend on $\partial(\log n + eU/T)/\partial r$ and $\partial T / \partial r$ only: for a given magnetic perturbation, expressing that ϕ_e and $\phi_{\mathcal{E}e}$ have a constant integrated value over the perturbed magnetic surfaces ψ then directly produces the functions $h(\psi)$ and $T(\psi)$ which appear in (1),independantly of the value of the potential U. These functions havethe usual elliptic structure,with coefficients proportional to $\omega - \omega_n^*$ and ω_T^* ,respectively,imposed by matching with conditions prevailing at some distance from the islands: here ω_n^* , $\omega_T^* = (\ell/r)(c/eB)\, T(\partial n / n \partial r\,,\, \partial T / T \partial r)$ are the usual unperturbed electron diamagnetic frequencies,while ω is the frequency of the tearing mode ($\propto \exp i(\ell\theta + m\varphi - \omega t)$) in the frame of

reference rotating around the major axis where the unperturbed radial electric field cancels. One may note that if the ions are at rest in the laboratory frame because of the effect of viscosity or ripples of the toroidal field, the mode frequency ω in this frame must be corrected by the ion diamagnetic frequency $-\omega^*_n$, so that $\omega' = \omega + \omega^*_n$.

If the island width δ is not large so that the ions do not reach thermodynamical equilibrium over each surface ψ, the parallel current density $I_{//}$ near the islands is carried by electrons. The local electron continuity equation

$$\nabla_{//} I_{//} + div(n e V_E) + \frac{\partial}{\partial r}(e\phi_e) = 0 \; ; \; V_E = -\frac{c}{B^2}\nabla U \times B$$

where V_E is the electric drift velocity, then produces the value of $I_{//}$ as the sum $\bar{I}(\psi) + I_{dia} + I_{diff}$ of a function $\bar{I}(\psi)$ constant over each surface ψ and of two currents I_{dia} and I_{diff}, proportional to $div(ne V_E)$ and $\partial e\phi_e/\partial r$, respectively. The average value $\bar{I}(\psi)$ of $I_{//}$ is in fact the Rutherford's inductive current proportional to the growth rate γ. The current I_{diff} is proportional to $(\omega - \omega^*_n - \alpha_e \omega^*_T)$ and is always in quadrature with the tearing parallel potential vector δA. It is responsible for momentum exchange between the mode and the electron assembly. The current I_{dia} is only present when U is not a function of ψ. In fact only the calculation of this current necessitates the calculation of U through the continuity equation for ions, reduced to $div(n V_E) + \partial\phi_i/\partial r = 0$. For small island widths δ such that $\omega < D_i/\delta^2$, this equation reduces to $\partial\phi_i/\partial r = 0$. It then produces a value of I_{dia} in phase with δA. This current is relatively important and may sustain through the Ampere law the tearing perturbation for large values of ℓ, m : the corresponding values of $\Delta' = -|2\ell/r|$ may be typically $\sim \beta_\theta/\delta$, where β_θ is the poloidal β. In fact the values of ℓ, m are limited by the conditions:

$$|\omega| < D/\delta^2 \text{ and } k^*_{//}\,\delta V_{thi} < D/\delta^2 < MIN\left(k^*_{//}\,\delta V_{the}, \frac{(k^*_{//}\,\delta V_{the})^2}{\nu_{ce}}\right)$$

$$(k^*_{//} = |R^{-1}\ell\,\partial q/q^2\partial r|; \; D_i \sim D_e \sim D) \qquad (3)$$

the second expressing that ions and electrons (thermal velocities V_{thi} and V_{the}) do not and do reach thermodynamical equilibrium over each surface ψ. In the considered case the mode exchanges momentum with the electron assembly only. Momentum balance then implies that $I_{diff} = 0$, i.e., $\omega = \omega^*_n + \alpha_e \omega^*_T$. The regime is similar to the linear collisional drift tearing instability in the sense that instability needs a thermal gradient and a proper differential response of hot and cold electrons to the perturbation: instability requires indeed that the coefficient α_e which appears in Eq. (2) for electrons is positive.

For larger values of δ, for which (3) is no longer verified, the potential U tends to be a function of ψ. The value of I_{dia} appears only at first order in D_i/δ^2 and is in quadrature with δA. In fact I_{dia} then reflects momentum exchange

of the mode with the ion assembly. In that case the island growth rate takes the Rutherford's value. However momentum balance for the mode requires cancellation of the out of phase current $I_{diff} + I_{dia}$. This imposes a mode frequency ω which is reminiscent of both electron and ion diamagnetism

$$\omega = \left(D_e \left(\omega^*_n + \alpha_e \omega^*_T \right) + D_i \left(- \omega^*_n \right) \right) \Big/ \left(D_e + D_i \right) \quad (4)$$

This regime continues as long as the turbulent modes integrate the plasma gradients over the island structure. It is only when the width δ is large enough so that these modes adjust locally to the gradients that the island rotation is determined by viscosity effects and follows the ion mass motion. One then should have : $\omega = - \omega^*_n$.

In connection with the above considerations, a crucial point is of course to check if the microturbulence is or is not affected by small magnetic islands. This could be done experimentally by measuring the level of correlation between the Mirnov signals associated with rotating predisruptive islands $q = 2$ and the microwave or I.R. light power scattered near these islands. On the other hand the above theory predicts the diamagnetic rotation (4) of such islands as long as the turbulent modes are not perturbed. This could be checked by discussing the island amplitude at which the mode rotation is effectively slowed down. For proper (> 0) α_e, the theory also predicts diamagnetic destabilization of negative Δ' tearing modes at the level specified by (3). For very low ℓ, m modes, island widths in the range of millimeters are found possible. These modes could perhaps be detected as a low level M H D noise during non disruptive phases of Tokamak or Stellarator discharges.

/1/ R.D.Hazeltine, D.Debrott and T.S.Wang, Phys. Fluids 18, 1778 (1975)
/2/ S.M.Mahajan, R.D.Hazeltine, H.R.Strauss and D.W.Ross, Phys. Fluids 22, 2147 (1979)
/3/ J.F.Drake, N.J.Gladd, C.S.Liu and C.L.Chang Phys.Rev.Letters 44, 994 (1980)
/4/ P.H.Rutherford, Phys.Fluids 16, 1903 (1973)
/5/ D.Biskamp, Nuclear Fusion 19, 777 (1979)
/6/ P.H.Rebut and A.Samain, in Controlled Fusion and Plasma Physics (Proc. 5th Eur. Conf., Grenoble, 1972, Vol.I, p.29, Vol.II, p.232)
/7/ W.Horton, Phys.Fluids 19, 711 (1976)
/8/ F.Koechlin and A.Samain, Nuclear Fusion 18, 1509 (1978)
/9/ A.Samain, Rapport EUR-CEA 1977 (1983), submitted for publication in Plasma Physics.

CURRENT-CONVECTIVE TURBULENCE AND ANOMALOUS DIFFUSION IN TOKAMAKS

A.V.Nedospasov

Institute of High Temperatures, USSR Academy of Sciences

The up-to-date tokamaks contain a certain number of impurity ions with respect to their charge and mass. The impurities may significantly affect hot plasma properties so as a relatively small number of trapped particles may alter the transfer processes. Thus the development of current-convective instability as it was shown in /1/ may turbulize plasma containg impurities and the anomalous diffusivity at a plasma column periphery may significantly exceed it's neoclassical value.

The statements of the work /1/ proved correct after the paper was sent to the press when the two new experimental facts became known:

1) The sharp increase of the plasma lifetime in currentless modes in Stellarator W-VII /2/ confirms the connection between diffusion across the magnetic field and longitudinal current in the tokamaks.

2) The turbulent diffusion was directly observed in the near-wall region in Caltech tokamak /3,4/. The density and azimuthal electrical field fluctuation levels measured in /3/ agree with the current-convective turbulence picture.

The assumption of a steady-state distribution of the impurities across the plasma column being reached under dynamical balance of the neoclassical inward collisive diffusion and outward turbulent diffusion makes it possible to find relation between the radial impurity profile and density temperature distribution of the basic plasma. Equilibrium equation for the impurity ions with charge Z and mass $m_I \gg m_H$ is:

$$\frac{D_T}{Z n_I}\,\frac{dn_I}{dz} = F\left[C_{11}\frac{dn}{dz} + (C_{11}+C_{12})\frac{n}{T}\frac{dT}{dz}\right]T \qquad (1)$$

where D_T is turbulent diffusivity, C_{11} and C_{12} are the known constants /5/, $F = \frac{4\sqrt{2\pi}}{3}\cdot e^2 c^2 \sqrt{m_H}\,\lambda\, T^{-3/2} B_T^{-2}$, m_H is mass of the basic plasma ion, index I is related to the impurity ions.

The extimate $\frac{D_T a}{Z F n_{(o)} T_{(o)}}\cdot\frac{d\ln n_I}{dz} \sim 1$ is taken from (1). If $D_T \gg Z\,Fn(o)T(o) \approx Z\,\frac{\rho_i^2}{\tau_i}$ then $\frac{d\ln n_I}{dz} \ll \frac{d\ln n}{dz} \sim a^{-1}$ i.e. the impurity is distributed rather uniformly along the minor radius. This distribution indicates the growth of the effective plasma ions charge Z_{eff} from the centre to the periphery of the plasma column and relative occurance of electroconductivity gradient.

Max-Planck-Institut für Plasmaphysik
8046 Garching bei München

In it's turn this is the condition, discussed for the first time in /6/, for sustaining the current-convective turbulence on the impurities. The turbulent cells with small sizes across, strongly stretched along the magnetic field characterize this process. The time required to equalize density pulsations in basic plasma due to the longitudinal movement in these cells is higher than the radial drift time under the azimuthal electrical field fluctuations. Moreover, the turbulent diffusivities of basic plasma and the impurities are nearly equal, and the outward plasma flux may be substantially higher than neoclassical one.

The hypothesis being discussed in this presentation may explain the nature of density fluctuations observed in many tokamaks with relatively low frequences /7/. This hypothesis leads to relation between the fluctuations level and density gradients for plasma and that for the impurities. This relation was discovered in PLT with pulsed gas puffing /8/. In particular, the fluctuations amplitude was falling in the centre where the density gradient was lower while it was growing at the periphery where the gradient was higher. The experiment allowing to measure the fluctuations level when solid hydrogen tablets are injected into plasma might surve as a best verification of this fact.

In /9/ the current turbulence (rippling mode) in nearwall region of the tokamaks is discussed and it is shown that the turbulent transfer may be significant even in the ideally pure plasma. We think that the presence in this region of the impurities would substantially enhance turbulence.

The plasma lifetime as a function of Z_{eff} value was observed in tokamaks T-10 and Alcator.

Finally we would like to note that the nearwall turbulence most likely plays a positive role /10,11/.

REFERENCES

/1/ A.V.Nedospasov: Pis'ma v JTF 8, N 17, 1045 (1982).

/2/ G.Cattanei et al.: 9-th Intern.Conf. on Plasma Physics and Controlled Nucl. Fusion Res., L5, Baltimore, (1982).

/3/ S.Zweden, P.C.Liower and R.W.Gould, Journ. of Nucl.Mat. 111-112, 39 (1982).

/4/ S.Zweden et al.: Preprint of California, Institute of Technology, (1983).

/5/ P.H.Rutberford et al.: Proc. of the Intern.Symp. on Plasma Wall Intern., p.173, Julich, (1976).

/6/ V.G.Petrov: Fizika plazmy, 3, 562 (1977).

/7/ J.Hugill, Nucl. Fusion, 23, 331 (1983).

/8/ J.D.Strachan et al.: Nucl. Fusion 22, p.1145 (1982).

/9/ J.D.Callen et al. 9-th Intern. Conf. on Plasma Physics and

Contr. Nucl. Fusion Res. D-2-2, Baltimore (1982).

10. A.V.Nedospasov: Proc. 7-th Europ.Conf. on Contr. Fusion and Plasma Phys., Laussanne, 1, p.129 (1975).

11. A.V.Nedospasov, M.Z.Tokar: Journ. of Nucl. Mat. 93-94, p.248 (1980).

ON THE SOLUTION OF THE EQUATION OF PLASMA EQUILIBRIUM IN A TOROIDAL CONFIGURATION

E A Evangelidis
Plasma Physics Division
NUCOR - Pelindaba
Private Bag X256, Pretoria South Africa

An analytical class of solutions has been found for the Grad-Shafranov equation up to any degree of non-linearity. If θ, ω, ϕ are toroidal coordinates then it is /1/

$$\frac{\partial^2 F}{\partial\theta^2} + \frac{\partial^2 F}{\partial\omega^2} - \coth\theta\,\frac{\partial F}{\partial\theta} + \tfrac{1}{4}F =$$

$$-\frac{32\pi^2 R_0}{c\left[2(\cosh\theta-\cos\omega)\right]^{3/2}}\left\{4R_0^2 A(\psi)\,\frac{\sinh^2\theta}{\left[2(\cosh\theta-\cos\omega)\right]^2} + B(\psi)\right\} \qquad (1)$$

with the constant magnetic flux surfaces given by

$$\psi = F(\theta,\omega)\left\{2(\cosh\theta-\cos\omega)\right\}^{-\frac{1}{2}} \qquad (2)$$

Thus the solutions found are of the form

$$\psi = \sum_{K,L=-\infty}^{\infty} \phi_{L,K-L+2}\,\frac{\sinh^{K-L+2}\theta\,\sin^{L}\omega}{\left[2(\cosh\theta-\cos\omega)\right]^{K+2}} \qquad (3)$$

with the following recursion relation between the coefficients

$$(K-L+2)(K-L)\phi_{L,K-L+2} + (L+1)(L+2)\phi_{L+2,K-L} =$$

$$= -\frac{32\pi^2 R_0^2}{c}\sum_{p=0}^{\infty} 4R_0^2 C_p\cdot{}^{p}\sigma_{L,K-L-2} + e_p\cdot{}^{p}\sigma_{L,K-L} \qquad (4)$$

Since mathematical details have been given in /2/, /3/, /4/, /5/ we summarise the results only. For $c_p = e_p = 0$ it is

$$\psi = \frac{\sinh^2\theta}{\left[2(\cosh\theta-\cos\omega)\right]^3}\left\{\phi_{1,2}\sin\omega + \phi_{0,2}\,2(\cosh\theta-\cos\omega)\right\} \qquad (5)$$

For p = 0, it is (K = 0, 2, L = 0)

$$\psi = \frac{\phi_{0,2}\sinh^2\theta+\phi_{2,0}\sin^2\omega}{\left[2(\cosh\theta-\cos\omega)\right]^2} + \frac{\phi_{0,4}\sinh^4\theta+\phi_{2,2}\sin^2\omega\sinh^2\theta}{\left[2(\cosh\theta-\cos\omega)\right]^4} + \phi_{0,0} \;\ldots\; (6)$$

Special cases of expression (6) have been given by /1/, /2/, /6/, where also the Fourier analysis /1/, /2/, is given for specific boundary value problems.

For p = 1, the recursion relation becomes

$$(K-L+2)(K-L)\phi_{L,K-L+2} + (L+1)(L+2)\phi_{L+2,K-L} =$$

$$= -\frac{32\pi^2 R_0^2}{c}\cdot\left\{4R_0^2\left(C_0\cdot{}^{0}\sigma_{L,K-L-2} + C_1\cdot\phi_{L,K-L-2}\right) + \right.$$

$$\left. + e_0\cdot{}^{0}\sigma_{L,K-L} + e_1\phi_{L,K-L}\right\} \qquad (7)$$

Upon retaining the values K = 0, 2, μ, L = 2i one finds the solution first given in /7/. In a subtler way, one finds further the solutions given in /8/, /9/, /10/. Solution /11/ merits special mention since it exemplifies the peculiarity of the solution of the Grad-Shafranov equation; namely, that higher and higher terms on the r.h.s. of (1) contribute to the l.h.s. A fact which for computational purposes imposes a cut-off in the terms retained in (3). For instance in /11/ terms were retained up to sixth degree, inclusive, (cf. /4/ for a minor correction and completion), although higher degree terms can be included.

The non-linear case p = 2 has been treated under special restrictions in /2/. More general non-linear results are available but in unpublished form. Thus, we concentrate on the other important case of the magnetic force-free case. Although one could proceed from (1), the fact that Grad-Shafranov equation is valid for axisymmetric systems only, this would be too restrictive for the class of solutions (3) envisaged. Therefore, adopting Chandrasekhar's formulation /12/ and employing (3) one finds the 3-dimensional solution for the magnetic flux surface in the form

$$\psi = e^{i\lambda\phi} \sum_{\ell=0,m=\lambda} \phi_{\ell,m} \sin^{\ell}\omega \sinh^{m}\theta (\cosh\theta - \cos\omega)^{-(\ell+m)} \tag{8}$$

with the recursion relation

$$\phi_{\ell,m} = \alpha^2 \frac{\phi_{\ell-2,m} - \phi_{\ell,m-2}}{m^2 - \lambda^2 - \ell(\ell-1)}$$

Then the magnetic field with the required property - continuous along the $\underline{e}_\theta$-direction - is

$$T_{\ell,m} = \{0, \; -\lambda \sin(\lambda\phi) \sum_{\ell=0,m=\lambda} \phi_{\ell,m} \frac{\sin^{\ell}\omega \sinh^{m-1}\theta}{(\cosh\theta - \cos\omega)^{\ell+m-1}} \; ,$$

$$, \; \cos(\lambda\phi) \sum_{\ell=0,m=\lambda} \phi_{\ell,m} \frac{\sin^{\ell-1}\omega \sinh^{m-1}\theta}{(\cosh\theta - \cos\omega)^{\ell+m}} \left[\ell + m - \cos\omega(\ell\cosh\theta + m\cos\omega)\right] \}$$

References

/1/ Shafranov, V.D.: Equilibrium of a Plasma Toroid in a Magnetic Field, Sov. Phys. JETP, 37 (1960) 775-779.

/2/ Evangelidis, E.A.: Equilibrium of Space Plasma Torus, Astrophys. Space Sci. 75 (1981) 315-327.

/3/ Evangelidis, E.A.: Equilibrium of Toroidal Configurations, Astrophys. Space Sci. 77 (1981) 479-491.

/4/ Evangelidis, E.A.: Force-Free Fields in a Three Dimensional Plasma Torus, Astrophys. Space Sci. 81 (1982) 261-268.

/5/ Evangelidis, E.A.: Toroidal Solutions of the Gegenbauer Equation, Astrophys. Space Sci. 87 (1982) 117-120.

/6/ Küppers, G., Pfirsch, D., Tasso, H.: MHD-Stability of Axisymmetric Plasmas. In: Plasma Physics and Controlled Nuclear Fusion Research IAEA 2, p.529-538.

/7/ Mazzucato, E.: Exact Equilibria of Axisymmetric Magnetic Configurations, Phys. Fluids 18 (1975) 536-540.

/8/ Strauss, H.R.: Critical β for Toroidal Equilibrium, Phys. Rev. Lett. 26 (1971) 616-618.

/9/ Maschke, E.K.: Exact Solutions of the MHD Equilibrium Equation for Toroidal Plasma, Plasma Physics 15 (1973) 535-541.

/10/ Suzuki, Y.: Critical β in a Torus with Rectangular Cross Section, Nucl. Fusion 13 (1973) 369-372.

/11/ Soloviev, L.S.: The Theory of Hydromagnetic Stability of Toroidal Plasma, Sov. Phys. JETP 26 (1968) 400-407.

/12/ Chandrasekhar, S.: On Force-Free Fields, Proc. Nat. Acad. Sciences, 42 (1956) 1-5.

VARIATIONAL PRINCIPLE IN FLUX VARIABLES FOR THE TOROIDAL PLASMA EQUILIBRIUM

M.I.Mikhailov
"Energiya" Scientific Manufacturing Association
V.D.Shafranov
I.V.Kurchatov Institute of Atomic Energy,
Moscow, USSR

Possibility of applying the variational principle for approximate calculation of the 3-D plasma equilibrium is discussed.

As known, the toroidal magnetic field with nested magnetic surfaces can be represented in the form /1/

$$\vec{B} = \frac{1}{2\pi}\left(\nabla\psi \times \nabla\zeta + \nabla\Phi \times \nabla\theta + \nabla a \times \nabla\eta\right), \qquad (1)$$

where $\Phi(a)$, $\psi(a)$ are toroidal and external poloidal magnetic fluxes; θ, ζ are the angular variables; $\eta(a,\theta,\zeta)$ is the unique function of its variables. In the coordinates a, θ,ζ a vector equilibrium equation $\nabla p = \vec{j} \times \vec{B}$ is reduced to the condition $p = p(a)$ and to the equations

$$p' = \sqrt{g}\,(j^2 B^3 - j^3 B^2), \qquad (2)$$

$$j^1 = 0, \qquad (3)$$

where $\sqrt{g} = (\nabla a, \nabla\theta\cdot\nabla\zeta)^{-1} = (\mathrm{Det}\, g_{ik})^{1/2}$, $B^2 = \vec{B}\nabla\theta$, $B^3 = \vec{B}\nabla\zeta$, $\sqrt{g}j^1 = \partial B_3/\partial\theta - \partial B_2/\partial\zeta$, $\sqrt{g}j^2 = \partial B_1/\partial\zeta - \partial B_3/\partial a$, $\sqrt{g}j^3 = \partial B_2/\partial a - \partial B_1/\partial\theta$. Covariant components of the vector $\vec{B}$ entered in j^i are expressed in terms of B^2, B^3 via the metrical coefficients g_{ik}, dependent on the geometry of the system:

$$B_1 = g_{12}B^2 + g_{13}B^3,\ B_2 = g_{22}B^2 + g_{23}B^3,\ B_3 = g_{23}B^2 + g_{33}B^3 \qquad (4)$$

The eq. (3), $j^1 = 0$, is reduced to the 2-D equation for η on the magnetic surface $a = \mathrm{Const}$:

$$\hat{L}\eta = -\Phi'\left[\frac{\partial}{\partial\theta}\left(\frac{g_{33}}{\sqrt{g}}\right) - \frac{\partial}{\partial\zeta}\left(\frac{g_{23}}{\sqrt{g}}\right)\right] - \psi'\left[\frac{\partial}{\partial\zeta}\left(\frac{g_{22}}{\sqrt{g}}\right) - \frac{\partial}{\partial\theta}\left(\frac{g_{23}}{\sqrt{g}}\right)\right], \qquad (5)$$

where

$$\hat{L} = \frac{\partial}{\partial\theta}\left[\frac{g_{33}}{\sqrt{g}}\frac{\partial}{\partial\theta} - \frac{g_{23}}{\sqrt{g}}\frac{\partial}{\partial\zeta}\right] + \frac{\partial}{\partial\zeta}\left[\frac{g_{22}}{\sqrt{g}}\frac{\partial}{\partial\zeta} - \frac{g_{23}}{\sqrt{g}}\frac{\partial}{\partial\theta}\right]. \qquad (6)$$

To extract the geometrical part of η one can put, e.g., $\eta = \Phi'\eta(\vec{r},q)$. More refined representation suggested by V.V.Drozdov is

$$\eta = \eta_1\psi' + \eta_2\Phi'. \qquad (7)$$

$$\hat{L}\eta_1 = \frac{\partial}{\partial\theta}\left(\frac{g_{23}}{\sqrt{g}}\right) - \frac{\partial}{\partial\zeta}\left(\frac{g_{22}}{\sqrt{g}}\right),\quad \hat{L}\eta_2 = \frac{\partial}{\partial\zeta}\left(\frac{g_{23}}{\sqrt{g}}\right) - \frac{\partial}{\partial\theta}\left(\frac{g_{33}}{\sqrt{g}}\right) \qquad (8)$$

The equilibrium equation(2) for a "radial" distribution of the quantities expressed in terms of ψ', Φ' has the form:

$$(\Phi' + \frac{\partial\eta}{\partial\theta})\frac{\partial}{\partial\alpha}\left[\frac{g_{33}}{\sqrt{g}}(\Phi' + \frac{\partial\eta}{\partial\theta}) - \frac{g_{23}}{\sqrt{g}}(\psi' + \frac{\partial\eta}{\partial\zeta})\right] +$$

$$+ (\psi' + \frac{\partial\eta}{\partial\zeta})\frac{\partial}{\partial\alpha}\frac{g_{22}}{\sqrt{g}}(\psi' + \frac{\partial\eta}{\partial\zeta}) - \frac{g_{23}}{\sqrt{g}}(\Phi' + \frac{\partial\eta}{\partial\theta}) -$$

$$- (\Phi' + \frac{\partial\eta}{\partial\theta})\frac{\partial}{\partial\zeta}\frac{g_{13}}{\sqrt{g}}(\Phi' + \frac{\partial\eta}{\partial\theta}) - \frac{g_{12}}{\sqrt{g}}(\psi' + \frac{\partial\eta}{\partial\zeta}) -$$

$$- (\psi' + \frac{\partial\eta}{\partial\zeta})\frac{\partial}{\partial\theta}\frac{g_{12}}{\sqrt{g}}(\psi' + \frac{\partial\eta}{\partial\zeta}) - \frac{g_{13}}{\sqrt{g}}(\Phi' + \frac{\partial\eta}{\partial\theta}) = -4\pi^2\sqrt{g}p'(\alpha) \qquad (9)$$

Here ψ', Φ' can be expressed in terms of the toroidal J and the external poloidal, F, currents:

$$J = -\alpha_{22}\psi' + \alpha_{23}\Phi',$$
$$F = -\alpha_{23}\psi' + \alpha_{33}\Phi', \qquad (10)$$

where

$$\alpha_{22} = \left\langle \frac{g_{22}}{\sqrt{g}}(1 + \frac{\partial\eta_1}{\partial\zeta^1}) - \frac{g_{23}}{\sqrt{g}}\frac{\partial\eta_1}{\partial\theta}\right\rangle_\theta ; \quad \alpha_{33} = \left\langle \frac{g_{33}}{\sqrt{g}}(1 + \frac{\partial\eta_2}{\partial\theta}) - \frac{g_{23}}{\sqrt{g}}\frac{\partial\eta_2}{\partial\zeta}\right\rangle_\zeta ,$$
$$\alpha_{23} = \left\langle \frac{g_{23}}{\sqrt{g}}(1 + \frac{\partial\eta_2}{\partial\theta}) - \frac{g_{22}}{\sqrt{g}}\frac{\partial\eta_2}{\partial\zeta}\right\rangle_\theta = \left\langle -\frac{g_{33}}{\sqrt{g}}\frac{\partial\eta_1}{\partial\theta} + \frac{g_{23}}{\sqrt{g}}(1 + \frac{\partial\eta_1}{\partial\zeta})\right\rangle_\zeta \qquad (11)$$

The angular brackets here $\langle\ \rangle_\theta$, $\langle\ \rangle_\zeta$ denote an averaging over θ, ζ respectively.

Among the five physical surface quantities, J, F, ψ, Φ, p, two of them, say, $p(a)$ and $J(a)$, should be considered as prescribed ones. Others can be found from two equations (10) together with an integral equilibrium condition

$$F' = (J'\psi' - p'V')/\Phi' \qquad (12)$$

which is an average of an eq. (9).

A map of magnetic surfaces is determined by solving the eq. (9) together with the eq.(5). In the case of axial and helical symmetry as well as in the so-called stellarator approximation, the function η can be excluded from eq.(9) explicitly.In this case the system is reduced to one equation for ψ with p' and FF' in its right-hand side.

In the variational approach one can start from a functional

$$Q_1 = \int\left(\frac{B^2}{2} - p\right)d\tau \qquad (13)$$

with flux conserving constraint $q=q(\psi)$. Here $|\vec{B}|^2$ should be expressed in terms of ψ, Φ using the metrical coefficients g_{ik}. The coordinates r, z, φ or quasipolar ones ρ, θ, ζ, entered into g_{ik} and the function η should be considered as varying functions. It is easy to show that coressponding Euler equations lead to the eq.(9) and to the

eq.-s $\vec{B}\cdot\nabla p=0$, $\vec{j}\cdot\nabla p=0$ (i.e. $p=p(\psi)$, $j^1=0$).

For an approximate solution one can represent the sought - for functions in the parametrical form:

$$\rho = \sum_i \lambda_i(a) f_i(a,\theta,\zeta); \quad \eta = \sum_i \delta_i(a) h_i(a,\theta,\zeta), \tag{14}$$

where f_i, h_i are the known functions. Integrating in eq.(13) over the θ,ζ we reduce the functional to the 1-D one:

$$Q_1^* = \int \left[\frac{1}{2}(\alpha_{22}\psi'^2 - 2\alpha'_{23}\psi'\Phi' + \alpha'_{33}\Phi'^2) - p(\psi)V'\right]da \tag{15}$$

where $V = 4\pi^2\langle\sqrt{g}\rangle_{\theta,\zeta}$.

Varying ψ we obtain the eq. (12), varying λ_i, δ_i, we get a set of equations

$$\left[\frac{\psi'^2}{2}\frac{\partial}{\partial\lambda'_i}(\alpha_{22}+2\alpha_{23}q+\alpha_{33}q^2)\right]' - \frac{\psi'^2}{2}\frac{\partial}{\partial\lambda_i}(\alpha_{22}+2\alpha_{23}q+\alpha_{33}q^2) = p'\frac{\partial V'}{\partial\lambda'_i};$$

$$\langle h_i \hat{L}\eta_1\rangle = \left\langle h_i \frac{\partial}{\partial\theta}\left(\frac{g_{33}}{\sqrt{g}}\right)\right\rangle - \left\langle h_i \frac{\partial}{\partial\zeta}\left(\frac{g_{23}}{\sqrt{g}}\right)\right\rangle; \quad \langle h_i \hat{L}\eta_2\rangle = \left\langle h_i \frac{\partial}{\partial\zeta}\left(\frac{g_{33}}{\sqrt{g}}\right)\right\rangle - \left\langle h_i \frac{\partial}{\partial\theta}\left(\frac{g_{23}}{\sqrt{g}}\right)\right\rangle \tag{16}$$

The total volume $V=\int V'(a,\lambda_i)da$ is not changed, thus the condition $\frac{\partial}{\partial a}(\partial V'/\partial\lambda') = \partial V/\partial\lambda$ is taken into account.

The 1-st of eq. (16) have been obtained earlier in the paper /2/. In that work, however, the coefficients α_{ik} were associated with the straight-field-line coordinates which are unknown. Here we directly indicate the way for calculations of α_{ik} in the preset coordinate system.

Note that in two-dimensional systems the coefficients α_{ik} are expressed in terms of g_{ik} and, consequently, in terms of λ_i and λ'_i. In this case, the problem is reduced to the solving of a rather simple set of 1-D differential equations /3/. The same is true for ordinary stellarators when an usual ordering is used. As an example, we give a brief derivation of the equation for the shift Δ in ordinary stellarator. According to the ref. /4/, the vacuum straight-field-line flux coordinate system ρ_v, θ_v, ζ (its metrics is easely determined) and flux systems for $\nabla p\neq 0$, a,θ,ζ are related by means of 2-D transformation

$$\rho_v\cos\theta_v = a\cos\theta + \Delta(a), \qquad \rho_v\sin\theta_v = a\sin\theta \tag{17}$$

One can show that in this case

$$\alpha_{22} \approx \frac{a}{R}\left(1 + \frac{1}{2}\Delta'^2\right), \qquad \alpha_{33} \approx \frac{R}{a}\left(1+\frac{\Delta}{R} + \frac{\alpha\Delta'}{2R}\right),$$

$$V' \approx 4\pi^2\left(aR+a\Delta+\frac{a^2\Delta'}{2}\right), \quad \alpha_{23} \approx \frac{1}{2\pi R}\int_0^{2\pi}\mu_0(\rho_v)\,(a+\Delta\cos\theta)d\theta. \tag{18}$$

Here $\mu_0(\rho_v)$ is a vacuum rotational transform. Substituting this into eq. (16), one obtains the well-known Greene-Johnson-Weimer equation for the shift Δ :

$$(a^3\mu^2\Delta')' + \mu(\mu'_0 a^3)'\Delta = 2p'a^2R/B_0^2 \tag{19}$$

As for the general case of 3-D systems, the α_{ik} are not expressed explicitly in terms of g_{ik} but include the solution for η as well. The final set of the 1-D equations appears

to be more complicated in this case.

References

/1/ Zakharov L.E., Shafranov V.D. In: "Voprosy theorii plasmy" v.11. Editors M.A.Leontovich and B.B.Kadomtsev, Moscow, Energoizdat, 1982, p.118-235.

/2/ Bateman G. Nuclear Fusion, 13, 227 (1973).

/3/ Khait V.D. Fizika plasmy, 6, 871 (1980).

/4/ Mikhailov M.I., Pustovitov V.D., Shafranov V.D. Pis'ma v JETF, 35, 152 (1982).

Z-PINCH EQUILIBRIA IN AN EXTERNAL MAGNETIC MULTIPOLE FIELD

C. Wahlberg, A.K. Arora*, R. Ring
Institute of Technology, Box 534, S-751 21 Uppsala, Sweden
* Department of Physics, University of Rajasthan, Jaipur-302004, India

Abstract
A perturbation method by means of which approximate equilibria for Extrap type of configurations can be obtained rather easily is developed.

1. Introduction

The Extrap scheme of magnetic confinement is one of several high-β "alternative" concepts that have been proposed recently /1/. From a theoretical point of view the somewhat complicated geometry of the configuration (a z-pinch immersed in a transverse magnetic multipole field) offers some difficulties and already the equilibrium problem has to be treated numerically in general. Thus, with a view to providing a technique by means of which at least approximate equilibria can be found without too much numerical effort, a perturbation expansion with the small parameter $\varepsilon = (R_P/R_C)^N$ is employed here (R_P is the plasma radius, R_C the distance from the axis of symmetry to the external conductors and N is the number of external conductors).

2. Integral equation formulation of the plasma equilibrium problem

The momentum balance of a plasma with scalar pressure is for straight geometry ($\partial/\partial z \equiv 0$) and z-directed current density $j\hat{z}$ equivalent to the requirement $j = j(\Psi)$, Ψ being the flux function. The difficulty of the equilibrium problem is then to find current and field distributions which are consistent with Ampères law as well, i.e.

$$\nabla^2\Psi = -\mu_o j(\Psi) \qquad (1)$$

The external magnetic field of the Extrap configuration (generalized to N conducting rods with currents I_C) can be written

$$\Psi_C = \sum_{n=1}^{\infty} \frac{\mu_o I_C}{2\pi n} \left(\frac{r}{R_P} \right)^{nN} \varepsilon^n \cos nN\theta \qquad (2)$$

(The polar coordinates are chosen such that one conductor is located on the surface $\theta = 0$). To zero order in ε we choose an ordinary θ-independent z-pinch equilibrium with some arbitrary current profile $j(r)$. Furthermore, we initially consider the plasma to be composed of a large, but finite number of concentric shells with radii $r = r_{o,\ell}$, $\ell = 1,2,\ldots, L$ and surface currents

$K_{o,\ell}$. To higher orders we can write the perturbed positions and surface currents of the shells in the form

$$r_\ell(\theta) = r_{o,\ell} + \sum_{n=1}^{\infty} r_{n,\ell} \cos nN\theta, \qquad K_\ell(\theta) = K_{o,\ell} + \sum_{n=1}^{\infty} K_{n,\ell} \cos nN\theta \qquad (3)$$

respectively, with $r_{n,\ell}$ and $K_{n,\ell}$ $O(\varepsilon^n)$, θ-independent quantities. It is easy to show that consistency of the quantities $r_{n,\ell}$ and $K_{n,\ell}$ with respect to the condition $j = j(\Psi)$ requires in first order that $K_{o,\ell} = j_\ell \Delta r_o$, $K_{1,\ell}/K_{o,\ell} = \Delta r_{1,\ell}/\Delta r_o$ where $\Delta r_o = r_{o,\ell} - r_{o,\ell-1}$ and $\Delta r_{1,\ell} = r_{1,\ell} - r_{1,\ell-1}$. Then, to achieve consistency with respect to Ampères law (1) as well, we explicitely calculate the magnetic field from the shells $\ell = 1,2,\ldots, m-1, m+1,\ldots, L$ and from the external conductors, in the region between shell m-1 and shell m+1, and impose the condition that $r_{1,m}$ is of such magnitude that the magnetic field is tangent to $r_m(\theta)$. The details of this calculation can be found in Ref. /2/. After passing to the continuous limit this yields the following integral equation for the first order deviation $r_1(r)$:

$$\int_o^r d\xi j(\xi)\left[\xi \frac{dr_1}{d\xi} + (N+1)r_1\right]\left(\frac{\xi}{r}\right)^N + \int_r^{R_P} d\xi j(\xi)\left[\xi \frac{dr_1}{d\xi} - (N-1)r_1\right]\left(\frac{r}{\xi}\right)^N - \frac{2Nr_1}{r}\int_o^r d\xi j(\xi)\xi = -\frac{NI_C}{\pi}\left(\frac{r}{R_C}\right)^N \qquad (4)$$

3. First order equilibria

A "rule of thumb" for the behaviour of the deviation $r_1(r)$ is readily obtained from equation (4) by considering the case $N \gg 1$, i.e.

$$\frac{r_1}{R_P} \simeq \varepsilon \frac{I_C}{I_p(r)}\left(\frac{r}{R_P}\right)^{N+1}, \text{ where } I_p(r) = \int_o^r d\xi j(\xi) 2\pi\xi \qquad (5)$$

We notice that the important quantity is the integrated current $I_p(r)$; thus, current profiles where $j(r)$ increases towards the plasma boundary should give a relatively large deviation in the central region as compared to r_1 corresponding to a current density which has the opposite behaviour. This feature of the solutions to equation (4) has been observed in all the cases that we have studied. In Fig. 1a we show a few solutions to eq. (4) corresponding to $N = 4$ and $j(r)$ proportional to 1. $(1+r^2)$, 2. const, 3. $(1-r^2)$ and 4. $(1-r^2)^2$ (r=normalized plasma radius. The quantity shown is normalized according to $r_1 \to r_1 R_P \varepsilon I_C/I_P$). For the "skin"-current profile

$$j(r) = A_\mu r^\mu \qquad (6)$$

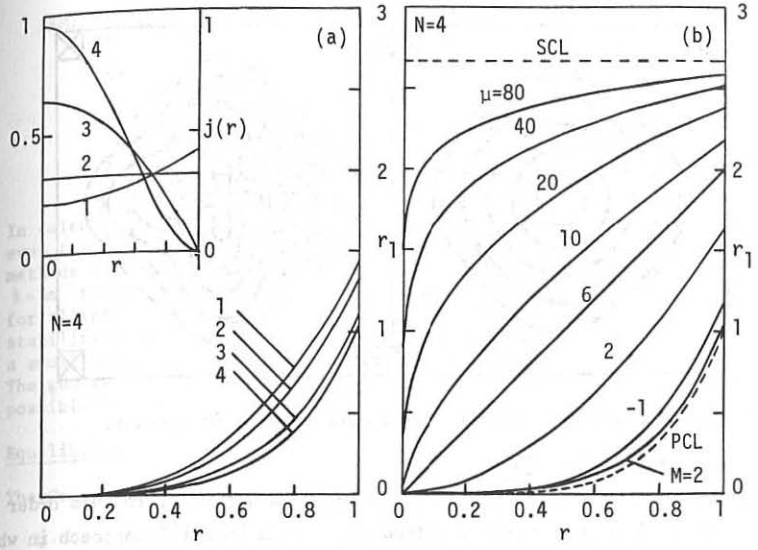

Fig. 1a) First order deviation r_1 as a function of plasma radius for the current profiles shown. b) A series of deviations r_1 corresponding to various values of μ for the skin current model (6).

the solution to eq. (4) is given by

$$\frac{r_1}{R_P} = \varepsilon \frac{I_C}{I_P} B_\nu \left(\frac{r}{R_P} \right)^\nu \qquad (7)$$

where $\nu = \sigma-\mu-1$, $\sigma = [N^2 + (\mu+1)^2 - 1]^{1/2}$ and $B_\nu = 2N(N-\sigma)/[(\mu+2)(\sigma-N-\mu)]$. In Fig. 1b we show a series of deviations (7) corresponding to various values of μ. Also shown is r_1 corresponding to the "peaked" current profile $(1-r)^M$ with M = 2. The largest possible deviation (= 2N/(N-1) over the entire plasma) occurs in the limit $\mu \to \infty$, and is in the figure referred to as the surface current limit (SCL). The smallest possible deviation occurs when the current is concentrated to the axis, and from the solution (7) we obtain the peaked current limit (PCL)$=r^{N+1}$ as $\mu \to -2$. Fig. 2 illustrates the character of the magnetic surfaces for current profiles close to the two extreme cases PCL and SCL above; in Fig. 2a the current is "peaked"(M=2 case above) whereas Fig. 2b corresponds to the skin current (6) with μ=80 (N=4, $I_P=-I_C$, $R_P/R_C=0.5$ in both figures).

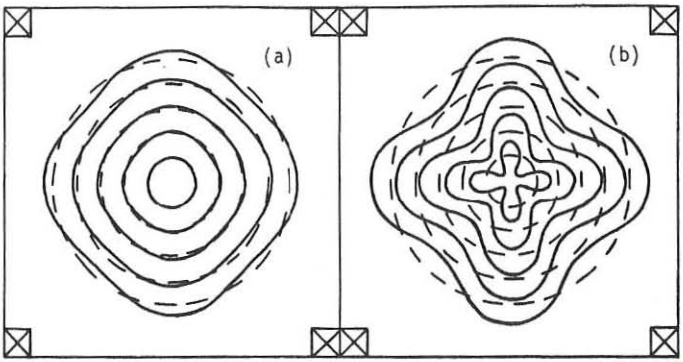

Fig. 2. Extrap equilibria for a) peaked current b) skin current.

4. Second order equilibria

In Ref. /2/ the analysis is performed to second order in ε. To this order the problem is most conveniently solved by using a "hybrid" approach in which a conventional expansion of Ampères law (1) is supplemented with a boundary condition provided by the second order integral equation. A simple case is the constant current density $j=j_o$, in which case we find

$$\Psi = -\frac{1}{4}\mu_o j_o r^2 + \frac{\mu_o I_C}{2\pi}\left[\frac{N}{N-1}\varepsilon\left(\frac{r}{R_p}\right)^N \cos N\theta + \frac{N}{2N-1}\varepsilon^2\left(\frac{r}{R_p}\right)^{2N}\cos 2N\theta\right] \quad (8)$$

Acknowledgements

Helpful discussions with Dr. J. Brynolf and Prof. E.T. Karlson are gratefully acknowledged.

References

/1/ Lehnert, B.: The Extrap Concept. In: Unconventional Approaches to Fusion. Brunelli, B. and Leotta, G.G. (Ed.). Plenum Press, New York 1982, p. 135-155.

/2/ Wahlberg, C., Arora, A.K. and Ring, R.: Uppsala Univ. Rep. 8335 R, Uppsala 1983.

SEMIANALYTIC CALCULATION OF EQUILIBRIUM AND AXISYMMETRIC STABILITY OF FINITE ASPECT RATIO TOKAMAKS WITH ELLIPTIC CROSS-SECTION

R. Grauer, E. Rebhan
Institut für Theoretische Physik II
Universität Düsseldorf
D-4000 Düsseldorf, FRG

In calculating equilibrium and stability of finite aspect ratio tokamaks, even for circular and elliptical plasma cross-sections intricate numerical methods are necessary which require a fast and large computer. Only for $A = \infty$ these calculations can be carried out analytically. In this paper, for elliptical cross-sections the problem of equilibrium and axisymmetric stability of finite aspect ratio was prepared analytically so fas that only a small amount of numerical calculation on a small computer was necessary. The generalisation of the method to more complicated cross-sections appears possible by using conformal mappings.

Equilibrium

The Grad-Shafranov equation

$$\nabla\cdot(\nabla\psi/R^2) = -p'(\psi) - \Delta\Delta'(\psi)/R^2 \qquad (1)$$

was solved for constant $p'(\psi) = p_1$ and $\Delta\Delta'(\psi) = q_1$ by an expansion with respect to the inverse aspect ratio $\varepsilon = 1/A$

$$\psi = \sum_{n\geq 0} \psi^{(n)} \varepsilon^n \qquad (2)$$

If in the poloidal planes elliptical coordinates are introduced, for $\psi^{(n)}$ the simple ansatz

$$\psi^{(n)} = \begin{cases} \sum_{i,k=0}^{\frac{n+2}{2}} a_{ik}^{(n)} \cosh 2iu \cos 2kv & n \text{ even} \\ \sum_{i,k=0}^{\frac{n+1}{2}} a_{ik}^{(n)} \sinh(2i+1)u \cos(2k+1)v & n \text{ odd} \end{cases} \qquad (3)$$

lead to a solution. This is due to the fact that to lowest order in ε the problem can be solved exactly in these coordinates. Inserting (2) into (1), a simple recurrence schema is obtained for the calculation of the coefficients $a_{ik}^{(n)}$. Satisfaction of the boundary condition

$$\psi = 0$$

on the elliptical plasma surface $\partial\Omega_{pl}$ becomes especially simple in elliptical coordinates.

As a typical result of the calculations Fig. 1 shows the poloidal shift of the magnetic axis s_M as a function of ε for different values of

$$\beta_{pol} = \left[1 + \frac{g_1}{p_1 R_0^2} \right]^{-1} . \qquad (4)$$

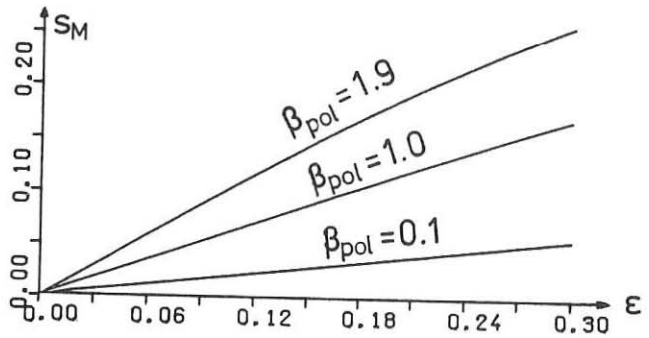

Fig. 1: Poloidal shift of the magnetic axis

Stability

Linear stability of the equilibria was only considered for prolate elliptical cross-sections. For these, antisymmetric perturbations

$$\xi_\psi(R,z) = -\xi_\psi(R,-z) \qquad (5)$$

are the most dangerous ones (Ref. /1/). For these, by minimalisations the energy variation $\delta^2 W$ can be reduced to (Ref. /2/)

$$\delta^2 W = \delta W_{pl} + \delta W_v$$

$$\delta W_{pl} = \frac{1}{2} \oint_{\Omega_p} d\tau \left(\frac{\nabla X}{R} \right)^2 - \frac{1}{2} \oint_{\partial\Omega_{pv}} \left(p_1' + \frac{g_1}{R^2} \right) \frac{X^2}{R B_\chi} \, dF$$

$$\delta W_v = \frac{1}{2} \oint_{\Omega_v} d\tau \left(\frac{\nabla \phi}{R} \right)^2 \qquad (6)$$

where $X = R B_\chi \xi_\psi$, $R B_\chi = |\nabla\psi|$ and where ϕ is a poloidal flux function for $\delta \underline{B} = \nabla\theta \times \nabla\phi + \iota \nabla\theta$. It can be shown that $\iota = 0$, while X and ϕ must satisfy the boundary value problems

$$\nabla\cdot(\nabla X/R^2)=0 \quad \text{in } \Omega_P \,, \quad \nabla\cdot(\nabla\phi/R^2)=0 \quad \text{in } \Omega_V \tag{7}$$

$$\underline{n}\times\nabla\theta\cdot\nabla(X+\phi)=0 \quad \text{on } \partial\Omega_{PV} \,, \quad \underline{n}\times\nabla\theta\cdot\nabla\phi=0 \quad \text{on } \partial\Omega_{VL} \tag{8}$$

Taking the symmetry condition (5) into account for X and ϕ the ansatz

$$X=\sum_{n\geq 0} X^{(n)}\varepsilon^n \qquad \phi=\sum_{n\geq 0}\phi^{(n)}\varepsilon^n$$

$$X^{(n)}=\sum_{k\geq 1} X_k^{(n)}(u)\sin kv \qquad \phi^{(n)}=\sum_{k\geq 1}\phi_k^{(n)}(u)\sin kv \tag{9}$$

$$X_k^{(n)}=\sum_{i\geq 0} a_{ik}^{(n)}\sinh iu+b_{ik}^{(n)}\cosh iu \qquad \phi_k^{(n)}=\sum_{i\geq 0}\tilde{a}_{ik}^{(n)}e^{iu}+\tilde{b}_{ik}^{(n)}e^{-iu}$$

is possible. Again, inserting (9) into the equations (7) and boundary conditions (8), for the coefficients $a_{ik}^{(n)}, b_{ik}^{(n)}, \tilde{a}_{ik}^{(n)}, \tilde{b}_{ik}^{(n)}$ simple recurrence schemes are obtained which can easily be evaluated numerically. The solutions X, ϕ thus obtained are introduced in (6) which by partial integration can be brought into the form

$$\delta^2 W=\pi\sum_{k,\ell\geq 1} W_{k\ell}\, X_k(u_0)\, X_\ell(u_0) \tag{10}$$

where $u=u_0$ on $\partial\Omega_{PV}$. For determing stability, the matrix $W_{k\ell}$ was truncated and her lowest eigenvalue was calculated.

As a typical stability result Fig. 2 and 3 show the critical elongation

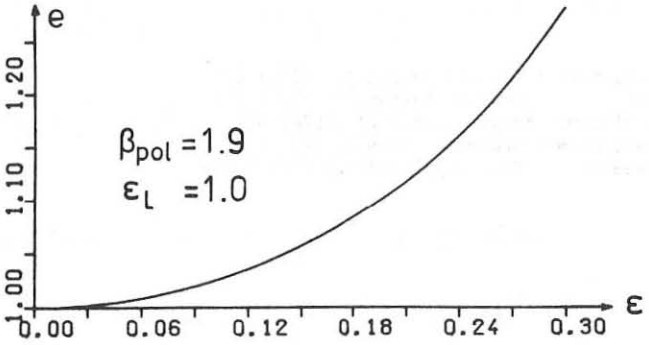

Fig. 2: Critical elongation $e=e(\varepsilon)$ for given β_{pol}

of the plasma cross-section as a function of ε (β_{pol} fixed) and β_{pol} (ε fixed) resp., ε_L being the inverse aspect ratio of a stabilizing elliptical wall of infinite conductivity surrounding the plasma in the vacuum region. The stability results agree rather well with these of Ref. /3/ (surface current model) and Ref. /2/ (same profiles $p(\psi)$, $\Delta(\psi)$ as here, but Soloveev equilibria (Ref. /4/) with almost elliptical cross-sections surrounded by a rectangular stabilizing wall).

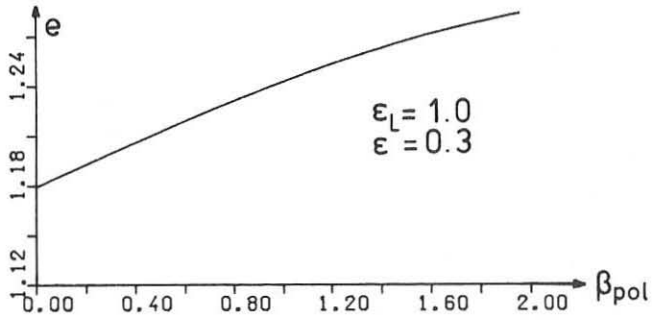

Fig. 3: Critical elongation $e = e(\beta_{pol})$ for given ε

/1/ Rebhan, Salat: Nuclear Fusion 16 (1976) 805
/2/ Jukes: Nuclear Fusion 16 (1970) 131
Chu, Miller: Phys. Fluids 21 (1978) 817
/3/ Rebhan, Salat: Nuclear Fusion 17 (1977) 251
/4/ Soloveev: Sov. Phys.-JETP 26 (1968) 400

CALCULATION OF GROWTH RATES FROM THE MARGINAL MODE

K.A. Kratzsch, E. Rebhan
Institut für Theoretische Physik
Universität Düsseldorf
D-4 Düsseldorf, FRG

Using the concept of a driving parameter, the eigenvalue problem of linear ideal MHD stability theory is solved by means of a perturbation expansion. To lowest order, approximations for the plasma oscillation frequencies or growth rates resp. are obtained just from the marginal mode /1/. The quality of approximations is demonstrated in specific applications.

1. General Theory

It is assumed that the MHD equilibria under consideration depend on a driving parameter λ such that the plasma goes from stable to unstable when λ exceeds a critical value λ_0. Examples for driving parameters are the inverse safety factor $1/q$ in tokamaks, β, geometry factors, the distance of a stabilizing wall etc. The equilibrium quantities $p_0, \underline{B}_0, \underline{B}^v_0$ (pressure, magnetic field in the plasma and in the vacuum), the perturbations $\underline{\xi}, \underline{A}$ (plasma displacement and vector potential of $\underline{B}^v - \underline{B}^v_0$) and the oscillation frequency ω are expanded with respect to

$$\tau = (\lambda - \lambda_0)/\lambda_0 \tag{1}$$

e.g.

$$\begin{aligned} p_0 &= p_{00}(\underline{r}) + p_{01}(\underline{r})\tau + \cdots \\ \underline{\xi} &= \underline{\xi}_0(\underline{r}) + \underline{\xi}_1(\underline{r})\tau + \cdots \\ \omega^2 &= \omega_1^2\tau + \omega_2^2\tau^2 + \cdots \end{aligned} \tag{2}$$

The expansions are inserted in the linear eigenvalue problem which, for external modes and without external wall, is

$$-\rho_0\omega^2\underline{\xi} = \underline{F}_0(\underline{\xi}, \underline{\lambda}), \quad \nabla\times\nabla\times\underline{A} = 0, \quad \nabla\cdot\underline{A} = 0 \tag{3}$$

$$\left.\begin{aligned} -\underline{\xi}\cdot\nabla p_0 - \tfrac{5}{3}p_0\nabla\cdot\underline{\xi} + \underline{B}_0\cdot[\nabla\times(\underline{\xi}\times\underline{B}_0)] &= \underline{B}^v_0\cdot(\nabla\times\underline{A}) \\ \underline{n}\times\underline{A} &= -\underline{n}\cdot\underline{\xi}\,\underline{B}^v_0 \end{aligned}\right\} \text{on } S_0 \tag{4}$$

$\underline{F}_0$ being the linear MHD operator and S_0 the plasma surface.

For $\underline{\xi}_m$ and $\underline{A}_m$, the following equations are obtained:

$$-\varrho_0 \sum_{\kappa=1}^{m} \omega_\kappa^2 \underline{\xi}_{m-\kappa} = \sum_{\kappa=0}^{m} \underline{F}_{0\kappa}(\underline{\xi}_{m-\kappa}) \tag{5}$$

$$\underline{F}_{0\kappa}(\underline{\xi}) = \sum_{\varepsilon=0}^{\kappa} \{ [\nabla \times \nabla \times (\underline{\xi} \times \underline{B}_{0\varepsilon})] \times \underline{B}_{0\kappa-\varepsilon} + (\nabla \times \underline{B}_{0\varepsilon}) \times [\nabla \times (\underline{\xi} \times \underline{B}_{0\kappa-\varepsilon})] \}$$
$$+ \nabla (\underline{\xi} \cdot \nabla p_{0\kappa} + \tfrac{5}{3} p_{0\kappa} \nabla \cdot \underline{\xi})$$

$$\nabla \times \nabla \times \underline{A}_m = 0 \quad , \qquad \nabla \cdot \underline{A}_m = 0 \tag{6}$$

$$\sum_{\kappa=0}^{m} \{ -(\underline{\xi}_{m-\kappa} \cdot \nabla p_{0\kappa} + \tfrac{5}{3} p_{0\kappa} \nabla \cdot \underline{\xi}_{m-\kappa}) + \sum_{\varepsilon=0}^{\kappa} \underline{B}_{0\kappa-\varepsilon} \cdot [\nabla \times (\underline{\xi}_{m-\kappa} \times \underline{B}_{0\varepsilon})] \}$$
$$= \sum_{\kappa=0}^{m} \sum_{\varepsilon=0}^{\kappa} \underline{B}_{0\kappa}^{v} \cdot (\nabla \times \underline{A}_{m-\kappa}) \tag{7}$$
$$\underline{n} \times \underline{A}_m = -\sum_{\kappa=0}^{m} \underline{n} \cdot \underline{\xi}_{m-\kappa} \underline{B}_{0\kappa}^{v}$$

The condition

$$-\sum_{\kappa=1}^{m} \omega_\kappa^2 \int_{Pl} \varrho_0 \underline{\xi}_0 \cdot \underline{\xi}_{m-\kappa} \, d\tau = \sum_{\kappa=0}^{m} \int_{Pl} \underline{\xi}_0 \cdot \underline{F}_{0\kappa}(\underline{\xi}_{m-\kappa}) \, d\tau \tag{8}$$

must be satisfied in order that (5) is integrable. For internal modes, $\underline{F}_{00}$ is selfadjoint and $\int_{Pl} \underline{\xi}_0 \cdot \underline{F}_{00}(\underline{\xi}_m) \, d\tau = 0$. For external modes, using the boundary conditions (7), $\underline{\xi}_m$ can be eliminated from (8) yielding

$$\sum_{\kappa=1}^{m} \omega_\kappa^2 \int_{Pl} \varrho_0 \underline{\xi}_0 \cdot \underline{\xi}_{m-\kappa} \, d\tau = 2 \sum_{\kappa=1}^{m} W_\kappa^{Pl}(\underline{\xi}_0, \underline{\xi}_{m-\kappa}) + \sum_{\kappa=0}^{m} \int_{S_0} \{ \underline{n} \cdot \underline{\xi}_0 [\underline{B}_{0\kappa}^{v} \cdot \nabla \times \underline{A}_{m-\kappa}$$
$$- (\underline{n} \cdot \underline{\xi}_{m-\kappa}) \underline{n} \cdot \nabla (p_{0\kappa} + \tfrac{1}{2} \sum_{\varepsilon=0}^{\kappa} (\underline{B}_{0\varepsilon} \cdot \underline{B}_{0\kappa-\varepsilon} - \underline{B}_{0\varepsilon}^{v} \cdot \underline{B}_{0\kappa-\varepsilon}^{v}))] \} \, d\sigma \tag{9}$$
$$+ \int_{S_0} [\underline{B}_{00}^{v} \cdot (\nabla \times \underline{A}_0)] [\underline{n} \times \underline{A}_m + \sum_{\kappa=1}^{m} (\underline{n} \cdot \underline{\xi}_{m-\kappa}) \underline{B}_{0\kappa}^{v}] \cdot \underline{B}_{00}^{v} / (B_{00}^{v})^2 \, d\sigma$$

$$W_\kappa^{Pl}(\underline{\xi}, \underline{\eta}) = \tfrac{1}{2} \int_{Pl} \{ (\underline{\eta} \cdot \nabla p_{0\kappa} + \tfrac{5}{3} p_{0\kappa} \nabla \cdot \underline{\eta}) \nabla \cdot \underline{\xi}$$
$$+ \sum_{\varepsilon=0}^{\kappa} [(\nabla \times \underline{B}_{0\varepsilon}) \cdot [\underline{\xi} \times \nabla \times (\underline{\eta} \times \underline{B}_{0\kappa-\varepsilon})] + [\nabla \times (\underline{\eta} \times \underline{B}_{0\varepsilon})] \cdot [\nabla \times (\underline{\xi} \times \underline{B}_{0\kappa-\varepsilon})] \} \, d\tau$$

If the marginal mode $\underline{\xi}_0$, $\underline{A}_0$ is known, ω_1^2 follows directly from (9). Generally, it is easier to determine the marginal mode than other eigenmodes, since it can be obtained from the energy principle by minimizations disregarding the first of the boundary conditions (7). If, in addition, $\underline{\xi}_1$ and $\underline{A}_1$ are determinated from (5)-(7), ω_2^2 follows from (9), and similarly ω_3^2, ω_4^2 ... can be determined order for order.

2. Applications

2.1 m = 1 mode in a z-pinch with circular cross-section and constant j_z, B_z

In this case, the inverse of the safety factor

$$q = k r_0 B_z / B_\varphi(r_0) \qquad (10)$$

is used as driving parameter, for $k r_0 = 2.5$ the plasma being stable if $q > q_0 \approx 0.75$ and unstable if $q < q_0$. Fig. 1 shows the (normalized) square of the oscillation frequency. The dotted curve $\Omega^2(q)$ was obtained from the exact theory /2/. The curve $\Omega_1^2(q)$ shows the lowest order approximation and the curve $\Omega_2^2(q)$, which almost exactly coincides with the exact result, is the second order approximation.

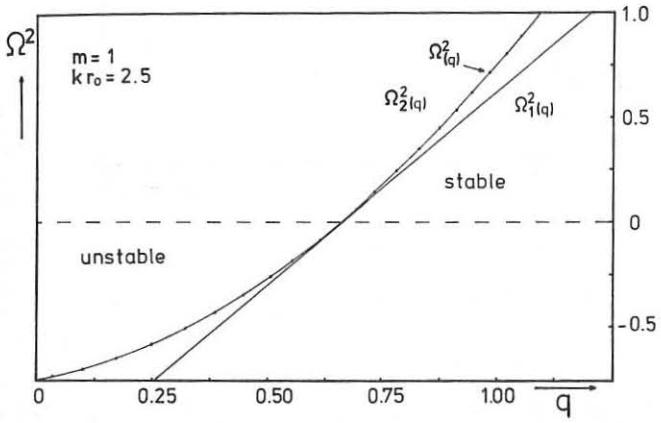

Fig. 1: m = 1 kink mode in a z-pinch

2.2 m = 1, k = 0 mode in a z-pinch

In the configuration of Sect. 2.1, also the m = 1, k = 0 mode was considered. The plasma is just marginally stable if a circular, infinitely conducting wall is placed at infinity. It becomes stable if this wall is pushed to a finite distance d from the plasma. d was used as driving parameter. The general theory of Sect. 1 must be modified in this case to include the stabilizing wall with position depending on λ. In addition, it must be taken into account that the exact eigenvalue problem for stable oscillatory modes is singular, the position of the singularity depending on λ.

Fig. 2 shows the exact solution and the second order approximation, $\Omega_2^2(\tau^2)$, Ω_1^2 being zero. Especially in this example, the amount of calculation required to obtain the lowest significant order of the perturbation method is almost negligible as compared to that for obtaining the exact solution.

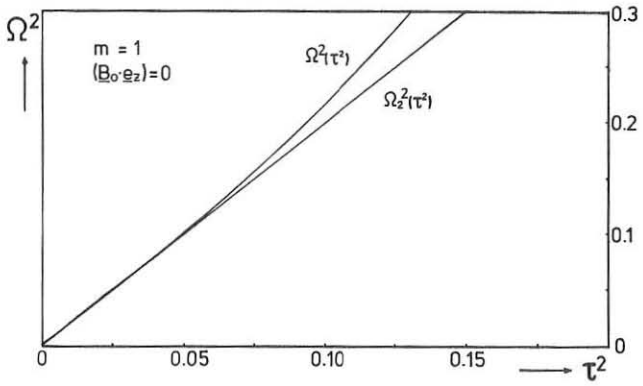

Fig. 2: k = 0, m = 1 mode in a z-pinch

/1/ E. Rebhan: Nonlinear evolution of internal MHD modes near the boundary of marginal stability, Z. Naturforsch. 37a (1982) 816

E. Rebhan: Nonlinear evolution of external MHD modes near the boundary of marginal stability, submitted to Z. Naturforsch.

/2/ R.J. Tayler: The influence of an axial magnetic-field on the stability of a constricted gas discharge, Proc. Roy. Soc. (London) B 70 (1957) 1049

APPLICATION OF THE STELLARATOR EXPANSION TO EQUILIBRIUM AND STABILITY STUDIES OF THREE-DIMENSIONAL TOROIDAL CONFIGURATIONS[a]

G. Rewoldt, J. L. Johnson,[b], G. Anania,[c], M. S. Chance, J. Manickam, and R. C. Grimm
Plasma Physics Laboratory, Princeton University
P.O. Box 451, Princeton, New Jersey 08544, U.S.A.

ABSTRACT
The stellarator expansion utilizes a small inverse aspect ratio to reduce the stellarator equilibrium and stability problems to two-dimensional ones. Application of this model to the ATF-1 stellarator indicates that free boundary instabilities may occur at experimentally observable values of β.

A large aspect ratio assumption with the multipolar field magnitude ordered as the square root of the inverse aspect ratio reduces the lowest order equilibrium and stability problems to two-dimensional ones similar to those of tokamaks. Numerical implementation of this model has been achieved. /1,2/ The code can be used to study low-n free boundary modes /2/ as well as to evaluate the Mercier criterion and to investigate localized ballooning modes. /3/ Comparison has been made with another equilibrium code that incorporates this expansion. The equilibrium properties that are obtained, including rotational transform, average magnetic well, and axis shift, are in good agreement. /4/ Comparison of the results obtained from the expansion model with those from three-dimensional codes shows that, even when using large expansion parameters, much better agreement is obtained than should be expected. /5/

The code has been used to investigate equilibrium and stability results for several existing and proposed stellarators including Wendelstein VII-A, Heliotron-E, and some modular stellarator configurations. /2/ In all these cases, instabilities set in at fairly low values of $\langle\beta\rangle$, with the perturbations having an interchange or ballooning character, centered on or near rational magnetic surfaces which lie in regions of unfavorable average magnetic curvature.

We have also applied the code to study the behavior of the ATF-1 device, an $\ell = 2$ torsatron which will be built at the Oak Ridge National Laboratory. /6/ The basic design criterion for this machine was to have vacuum fields with moderate shear and no low order rational surfaces in regions of unfavorable curvature. For this work we used exact vacuum fields, introducing a straightforward averaging over the toroidal coordinate to obtain the input parameters. Previous studies /2/ showed that with a pressure distribution such that $p \propto \Psi^2$ and a centering vertical field $B_v/B_o \sim 0.02$, the system is stable for $\langle\beta\rangle = 2.5\%$ ($\beta(0) = 6.5\%$), even for free boundary modes. Instabilities can be found with less peaked pressure profiles.

For $\langle\beta\rangle = 2.6\%$ ($\beta(0) = 7.5\%$) with $p \propto \Psi^2$ and the same centering vertical field, the lowest-order (averaged over the toroidal coordinate) magnetic surfaces are given in Fig. 1. The most important equilibrium properties are the rotational transform χ and the rate of change of volume with toroidal flux $V'(\Phi)$, which determines the nature of the average magnetic curvature. These are given in Fig. 2. It should be noted that an $\chi = 0.5$ rational surface exists in a region of unfavorable average magnetic curvature, where $dV'(\Phi)/d\Psi > 0$. In the earlier $\langle\beta\rangle = 2.5\%$ case,

this surface was further inside, in a region of favorable average curvature. Figures 3 and 4 show the Fourier components of the stream function η, such that $\xi^{(o)} = \nabla\phi \times \nabla\eta \exp i(m\theta - n\phi)$, and the displacement vector $\xi^{(o)}$ for the n = 1 mode. Evaluation of the Mercier criterion and use of the ballooning mode formalism shows that no high-n localized instabilities can occur at this value of $\langle\beta\rangle$. The n = 1 mode can be stabilized by placing a conducting shell at b/a ~ 1.6 outside the plasma. To stabilize the n = 2 and n = 3 modes, b/a ~ 1.5 is necessary.

It is difficult to determine from these figures just what is responsible for the instability. A cursory look at the flow diagram indicates that the mode has a strong ballooning character, centered around the outer χ = 0.5 magnetic surface. More careful study of the stream function shows that the behavior is much more complicated, with several large Fourier components existing throughout the plasma. The m = 2 component is largest at the inner χ = 0.5 surface where the average curvature is stabilizing, but it has a pronounced knee at the outer one. The m = 0 and 1 components of the perturbed magnetic field extend well into the vacuum region. Since the criterion for stability of localized modes is satisfied, it is clear that the standard picture, that plasma expansion is the dominant driving mechanism as in an interchange mode, is inadequate. Indeed, removal of the $J_{\parallel} \times \xi^{(o)} \cdot \mathcal{Q}_{\perp}$ term nearly stabilizes the mode. This supports an interpretation that the Pfirsch-Schlüter terms directly affect stability properties as well as modify the equilibrium conditions.

Since these theoretical results are strongly dependent on the exact shape of the equilibrium parameters, this study indicates that experimental study of β-limits in ATF-1 will be interesting. It should not be expected that this mode will limit the pressure that can be sustained in the device. A small change in the shape of the pressure distribution, especially near a low-n rational surface, could strongly modify the shape of the Pfirsch-Schluter current and thus change the equilibrium characteristics and the stability properties. Comparison of theoretical models with experimental results should clarify the mechanisms involved in stellarator confinement. Since a net toroidal current is not needed in these systems to provide a rotational transform, the results may illuminate the analogous problems in tokamaks.

We appreciate the cooperation of the ORNL MHD group, particularly J. A. Holmes, who gave us the vacuum fields for this work.

[a]Work supported by U.S. DoE Contract # DE-AC02-76-CHO-3073.
[b]On loan from Westinghouse Research & Development Center.
[c]At Booz Allen and Hamilton, Management Consultants.

/1/ G. Anania, J. L. Johnson and K. E. Weimer, Phys. Fluids (in press).
/2/ G. Anania and J. L. Johnson, Phys. Fluids (in press).
/3/ J. L. Johnson, G. Rewoldt, and M. S. Chance, Sherwood Theory Meeting, (Arlington, March, 1983), paper 2S15.
/4/ G. Rewoldt, J. L. Johnson, and J. A. Holmes, Sherwood Theory Meeting, (Arlington, March, 1983), paper 1P18.
/5/ J. A. Holmes, et al., Bull. Am. Phys. Soc. 27 (1982) 1020.
/6/ J. F. Lyon, et al., Bull. Am. Phys. Soc. 27 (1982) 1021.

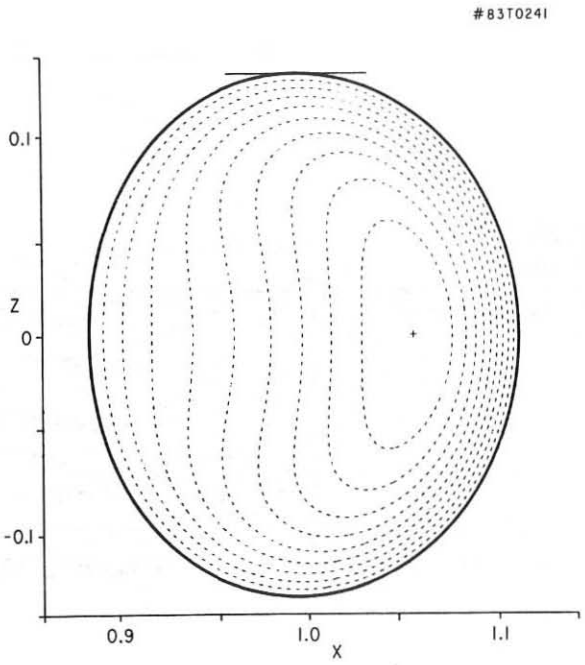

Fig. 1.
Averaged magnetic surfaces in ATF-1 with $p \propto \Psi^2$, $\langle\beta\rangle = 2.6\%$, $B_v/B_o = 0.02$.

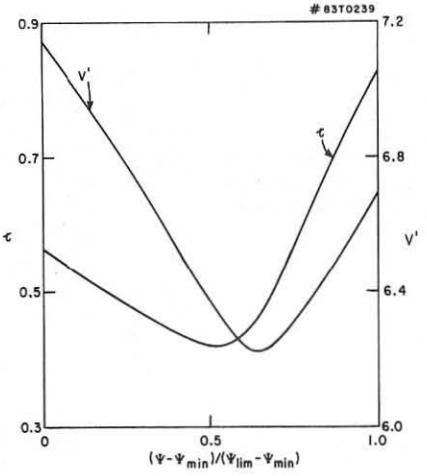

Fig. 2.
ι and V'(Φ) in the configuration of Fig. 1.

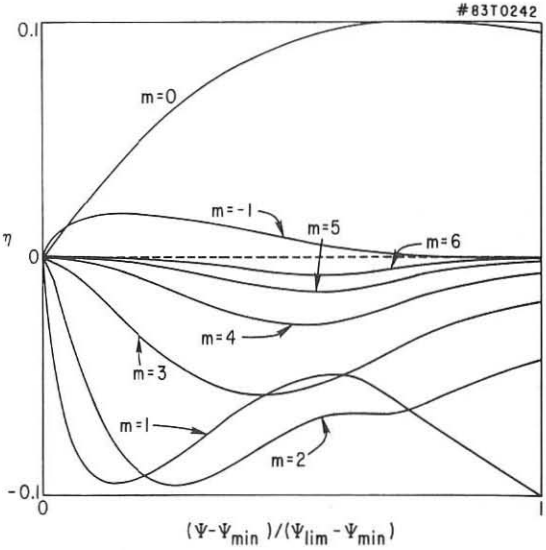

Fig. 3.
Stream function $\eta_m(\Psi)$ for the free boundary, n = 1 mode for configuration of Fig. 1.

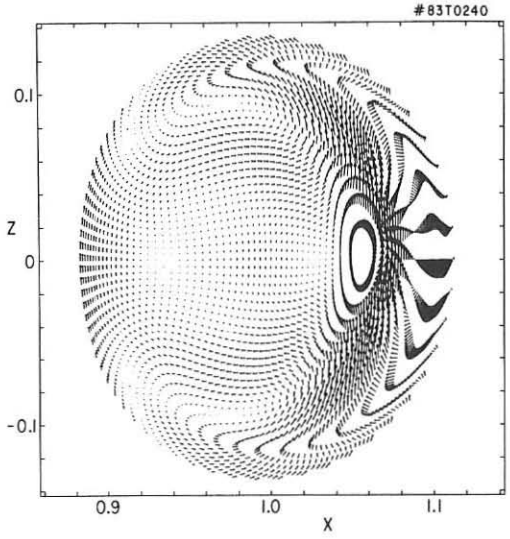

Fig. 4.
Displacement associated with Fig. 3. The length of the arrow denotes the magnitude of the vector.

Beta Limit for Ballooning Instabilities in EBT*

T. Kammash and K. Nguyen
University of Michigan
Ann Arbor, Mich. 48109

Abstract

Most of the estimates of the core beta (ratio of plasma to magnetic field pressures) limits in the Elmo Bumpy Torus (EBT) plasma confinement device have been based on stability of the interchange modes in which variations along the magnetic field are ignored. In this paper we investigate the macroscopic stability of EBT plasma in a slab model taking into account variations of the field curvature along the magnetic field. We solve an eigenvalue problem which reveals that the upper bound on the core beta, β_c, is dictated by the interacting ballooning mode which becomes unstable when $\beta_c \geq \lambda_p / R_{MP}$ where λ_p is the density gradient scale length and R_{MP} is the radius of curvature at the midplane. It is also shown that increasing the hot-electron ring length and the vacuum mirror ratio enhance β_c although in the latter case it may be done at the expense of reducing the stability of the background plasma.

Analysis and Results

The EBT device has been viewed by many as a potentially attractive fusion reactor because of several unique plasma confinement properties. Among these is its ability to support a relatively large plasma beta due to the stabilizing effect of the hot electron ring. Estimates of the beta values have been based primarily on the stability of the interchange modes which are driven by bad magnetic field curvature. A more realistic assessment must of course be based on the stability of the ballooning modes which take into account variations of the field curvature along itself. In this analysis we take that into account and address the ballooning stability problem using a quasi-kinetic approach in which we include the interaction of the hot electrons with the background plasma as well as the finite Larmor radius effects of the plasma ions. The geometry we consider is that of an equivalent bumpy cylinder with $\hat{z}$ taken along the axis of the cylinder. The equilibrium force equation is given by

$$\frac{\underset{\sim}{J} \times \underset{\sim}{B}}{c} = \nabla \cdot \underline{\underline{P}} + \underset{\sim}{F} \qquad (1)$$

where $\underset{\sim}{J}$ is the current density, $\underset{\sim}{B}$ is the magnetic field, c is the speed of light, $\underline{\underline{P}}$ is the pressure tensor prescribed by the Chew-Goldberger-Low (CGL) form, and $\underset{\sim}{F}$ is a general force. Expressing the perturbed fields by the vector and scalar potentials $\underset{\sim}{A}$ and φ, and assuming that such quantities are of

the form

$$\varphi = \varphi(z) \exp i\left[\frac{m}{r}\theta - \omega t\right] \tag{2}$$

with m being the azimuthal mode number, and ω being the frequency the ballooning equation can be shown to be put in the form

$$B\,\underline{b}\cdot\nabla\left(\frac{\tau}{r^2 B}\,\underline{b}\cdot\nabla\varphi\right) + \frac{1}{r^2 V_A^2}\,\omega(\omega - \omega_{*i})\,\varphi + \mu_0\,\frac{\omega}{mcB}\,\frac{(P_\parallel' + P_\perp')}{r R_c} = 0 \tag{3}$$

In this equation $\underline{b}$ is a unit vector along the field, V_A is the Alfvin speed, R_c is the radius of curvature, ω_{*i} is the diamagnetic frequency and τ is given by

$$\tau = 1 + \mu_0\,\frac{(P_\perp - P_\parallel)}{B^2} \tag{4}$$

It should be noted that when the first term in Eq. (3) is ignored the equation reduces to that of the familiar interchange mode[1]. If we further assume that the field variations are only along z, and introduce the various betas the ballooning equation can be written as

$$\frac{d}{dz}\left(\frac{\tau B_z}{r^2 B^2}\,\frac{d\varphi}{dz}\right) + \left\{\frac{1}{V_A^2}\,\omega(\omega - \omega_{*i}) + \frac{\beta_c}{2 r_p R_c}\left(2 + \frac{\beta_h(1-\beta_c)}{\beta_c(1+\beta_h) - 2 r_p \tau / R_c}\right)\right\}\frac{\varphi}{r^2 B_z} = 0 \tag{5}$$

where β_c and β_h denote the core and hot electron betas respectively, and r_p represents the density gradient scale length. The variation of the radius of curvature with z is obtained using the vacuum fields of a standard mirror with a mirror ratio M and a distance L between the mirrors. In solving the eigenvalue problem the vanishing of the potential and its derivatives at the mirror throats as well as at the points where the compression term due to the hot electrons had a pole, were used as boundary conditions. With "l" denoting the length of the hot electron ring the results of the analysis show that $\beta_h \gtrsim 0.21$ and $\beta_c \simeq 11\%$ when $M = 2$ and $l/L = 0.3$ for geometric parameters commensurate with present day EBT experiments. The results further indicate a significant stabilization as reflected in the drop of the β_h value from 0.21 to about 0.11 when l/L was increased from 0.3 to 0.5 indicating the stabilizing effects of longer rings. This is expected since longer rings imply that the wells dug by the hot electrons extend further into the throats of the mirror. By increasing the mirror ratio from 2 to 3 the analysis further shows a substantial improvement in β_c from 11% to about 17%

resulting from the stabilization of the interacting ballooning mode, but this enhancement is accompanied by an increase in the critical β_h value from 0.21 to about 0.45 reflecting a loss of stabilization for the background plasma interchange mode. In addition, we have demonstrated analytically using an energy principle for an EBT plasma with a rigid electron ring that the critical β_h value is the same as that obtained by others[2] employing numerical techniques.

References

*Work supported by U.S. DOE

1. J. W. Van Dam and Y. C. Lee, Proc. Workshop on EBT Ring Physics, Oak Ridge, CONF-7911228, Dec. 1979, p. 471

2. D. B. Nelson and C. L. Hedrick, Nuc. Fusion 19, 283 (1979)

SHEAR ALFVÉN WAVES AND BALLOONING MODES IN TOKAMAKS*

C. Z. Cheng, L. Chen, M. S. Chance, G. Rewoldt, and W. M. Tang
Plasma Physics Laboratory, Princeton University
P.O. Box 451, Princeton, New Jersey 08544, U.S.A.

ABSTRACT — For high n modes we show the breakup of the high n ideal shear Alfven continuous spectrum by toroidal coupling effects. Including resistivity the continuum disappears and a total of four branches of eigenmodes exists in the resistive MHD model. They are (1) shear Alfven-Landau modes, (2) resistive entropy modes, (3) periodic shear Alfven waves, and (4) resistive ballooning modes. Kinetic effects are also taken into account to study ballooning stability by employing a reduced kinetic model. Results from the reduced code are compared with those from a more comprehensive, but much slower code.

In the absence of the ion sound effects, the ideal MHD equations for the shear Alfven waves in an infinite sheared slab reduce to

$$\left[\frac{d}{dx}\left(\Omega^2 - k_y^2x^2\right)\frac{d}{dx} - k_y^2\left(\Omega^2 - k_y^2x^2\right)\right]\Phi(x) = 0 \quad , \tag{1}$$

where $\Omega = \omega/\omega_A$, $\omega_A = v_A/L_s$, L_s is the magnetic shear scale length. This type of equation has been extensively studied by Barston /1/ via normal mode analysis and by Sedlacek /2/ by employing a Laplace transform technique to solve the corresponding initial value problem of Eq. (1). Especially, Sedlacek showed that the Green's function has branch point singularities at $\Omega^2 = k_y^2x^2$, which gives rise to the continuous spectrum. In addition, he found discrete singularities on the analytic continuation of the Green's function into the lower half of the complex ω-plane across the branch cuts. In our case, we refer to these discrete, exponentially decaying eigenmodes as shear Alfven-Landau modes.

In an axisymmetric toroidal plasma, the magnetic field is nonuniform over a magnetic surface. This nonuniformity can cause coupling of neighboring poloidal harmonics and results in the breakup of the continuous spectrum into small segments of continuous spectra with the gaps located in the immediate vicinity of rational surfaces. /3/ In terms of high-n ballooning representation, the resistive MHD equations for a large aspect ratio, low β toroidal plasma reduce to

$$\phi'' + Q\phi = 0 \quad , \tag{2}$$

where

$$Q = \Omega^2 K(\theta)(1 + 2\varepsilon_o \cos\theta) + \alpha_p f(\theta)/G(\theta)$$
$$- [1 - i\nu g(\theta)(1 - 3s^2\theta^2)/\Omega]/g^2(\theta)K^2(\theta) \quad ,$$

$\phi = \Phi G^{1/2}$, Φ is the electrostatic potential, $G(\theta) = g(\theta)/K(\theta)$, $K(\theta) = 1 + i\nu g(\theta)/\Omega$, $g(\theta) = 1 + s^2\theta^2$, $\nu = \eta/\omega_A$, $\varepsilon_o = r/R$, $\alpha_p = -2q^2Rp'/B^2$, $f(\theta) = \cos\theta + s\theta\sin\theta$, $s = rq'/q$, $p' = dp/dr$, q is the safety factor, p is the plasma pressure, and η is the plasma resistivity. When $\nu=\varepsilon_o=\alpha_p=0$, Eq. (2) is essentially the Fourier transform of Eq. (1) with $s\theta = k_x/k_y$ and it gives the continuous spectrum for all real θ with $\phi \sim \exp(i\Omega\theta)$ for large θ due to the causality condition. By analytic continuation of θ into the complex plane, we can solve for the discrete shear Alfvén-Landau modes by

the WKB method with the knowledge of the turning points θ_T defined by $Q(\theta_T) = 0$. For shear Alfven-Landau modes the eigenvalues are given by

$$\Omega^2 = 1 - i\ \mathrm{sgn}(\Omega_r)\ \sqrt{2}\ (2N + 1) \quad , \tag{3}$$

where $\mathrm{sgn}(\Omega_r)$ is the sign of Ω_r, and N = 0, 1, 2, ... The eigenfunction ϕ is unbounded for large real θ.

With small but finite resistivity ($\nu << 1$), the eigenvalues of the shear Alfven-Landau modes are little affected and ϕ becomes bounded along real θ. For $\nu >> 1$, Ω_i depends linearly on ν. This can be calculated by the WKB method. In the limits $\nu >> 1$, $\nu\theta^2/\Omega < 1$, $\theta^2 < 1$, we have $Q \simeq \Omega(\Omega + i\nu) + i\nu\Omega\theta^2$. The eigenvalues for $\nu >> N$ (N = 0, 1, 2, ...) are then given by

$$\Omega \simeq -i\nu \pm (1 + 2N) \quad . \tag{4}$$

The numerical solutions of Ω vs. ν for the shear Alfven-Landau modes are shown in Fig. 1 for s = 1, $\varepsilon_o = \alpha_p = 0$.

Also shown in Fig. 1 are the numerical eigenvalues of the resistive entropy modes vs. ν. This mode (with $\Omega \sim \nu^{1/3}$) has been extensively studied. /4/ For $\alpha_p = 0$, s = 1, $\nu << 1$, $\Omega \sim \nu^{1/3}$, Q has two turning points: $\theta_1 = \Omega^{-1/2}$, $\theta_2 \simeq (i\Omega/\nu)[1 - (3i\nu/\Omega^3)^{1/3}]$. The WKB quantization condition gives the eigenvalues

$$\Omega \simeq e^{-i\pi/6}\ \nu^{1/3}[2(N + 1/2)^2\pi^2]^{1/3} \quad . \tag{5}$$

For $\varepsilon_o \neq 0$, $\nu = \alpha_p = 0$, and large θ where $g \sim \theta^2$, Eq. (2) is essentially the Mathieu equation and it admits an infinite set of real eigenvalues Ω (periodic shear Alfven modes) with the lowest eigenvalues given by

$$\Omega^2 \simeq 1/[4(1 \pm \varepsilon_o)] \quad . \tag{6}$$

These eigenvalues define the gaps between the continuous spectra segments. In addition to the Mathieu type solutions, Eq. (2) also admits a marginally stable mode ($\Omega \simeq \pm 0.5$) inside the gap defined by Eq. (6) because of the contribution from $1/g^2$. These periodic shear Alfven modes have also been confirmed numerically as well as analytically.

The effect of resistivity on the periodic shear Alfven waves can be evaluated by employing a two scale analysis. Let

$$\phi = A_s(\theta)\ \sin\hat{\Omega}_o\theta + A_c(\theta)\ \cos\hat{\Omega}_o\theta \tag{7}$$

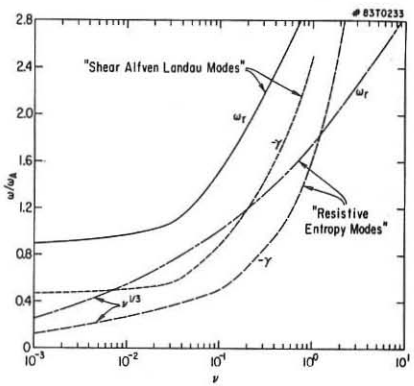

Fig. 1. Eigenfrequencies versus resistivity ν for both the shear Alfven-Landau modes and the resistive entropy modes for s = 1, $\varepsilon_o = \alpha_p = 0$.

where $A_s(\theta)$ and $A_c(\theta)$ have slow θ variations due to resistivity. $\Omega_o = \pm m/2$ ($m = 1, 2, \ldots$) are the eigenvalues of the periodic shear Alfven waves in the limit $\varepsilon_o = 0$ and we will show the case with $\Omega_o = 1/2$. Averaging over fast θ variation, assuming $A'' < A$, A', and taking the limits $\nu \ll 1$, $\nu\theta^2/\Omega < 1$, $\nu\theta^4 \sim 1$, Eq. (2) becomes

$$A'' + \left[\frac{\Omega^2(1\pm\varepsilon_o)(1+i\nu s^2\theta^2/\Omega)-1/4}{1+1/[\Omega^2(1\mp\varepsilon_o)-1/4]} \right] A = 0 \quad . \tag{8}$$

The eigenvalues, $\Omega = \Omega_o + \delta$ with $\delta \ll \Omega_o$, are given by

$$\Omega_{o\pm}^2 = 1/[4(1 \pm \varepsilon_o)] \quad ,$$

and

$$\delta_\pm = -[N + (1/2)]s \left\{ \frac{-i\nu[\Omega_{o\pm}^2(1\mp\varepsilon_o)+3/4]}{\Omega_o(1\pm\varepsilon_o)[\Omega_{o\pm}^2(1\mp\varepsilon_o)-1/4]} \right\}^{1/2} \quad , \tag{9}$$

where $N = 1, 2, \ldots$. From numerical solutions of Eq. (2), Fig. 2 shows the periodic shear Alfven eigenfrequencies in the complex ω-plane for $\nu = 10^{-6}$, $\varepsilon_o = 0$, 2, $\alpha_p = 0$, $s = 1$. In Fig. 3 the $\nu^{0.47}$ scaling of the damping rates for modes approaching the end points of the continuum gap is close to the $\nu^{1/2}$ theoretical estimate. Also shown in Fig. 3 is the $\nu^{0.96}$ scaling for modes approaching the marginal periodic shear Alfven wave inside the continuum gap because the zeroth order solution exists and a regular perturbation in ν will hold.

When the curvature effects are taken into account ($\alpha_p \neq 0$), the ideal MHD model would predict unstable ballooning modes for $\beta > \beta_c$. With resistivity, the ballooning modes are also unstable for $\beta_c > \beta > 0$ and the growth rates are proportional to $\nu^{1/3}$. These results may be modified for different equilibria. If kinetic effects such as FLR, wave-particle resonances, trapped particles and collisions are properly taken into account, the ballooning mode stability properties can also be quite different. The numerical results from (a) the ideal MHD model, (b) a

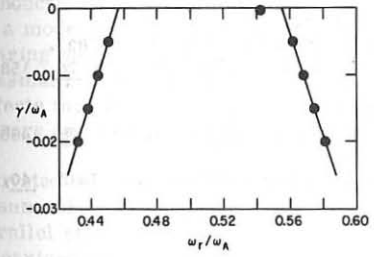

Fig. 2. Eigenfrequencies for the periodic shear Alfven modes in the complex ω-plane for $\nu = 10^{-6}$, $\varepsilon_o = 0.2$, $\alpha_p = 0$, $s = 1$.

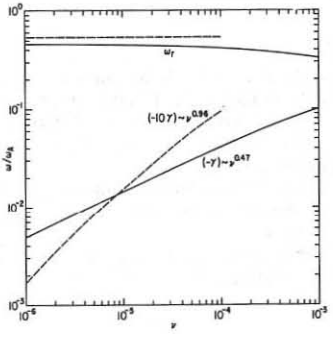

Fig. 3. Eigenfrequencies versus resistivity ν for the periodic shear Alfven waves for $\varepsilon_o = 0.2$, $\alpha_p = 0$, $s = 1$.

reduced model /5/ including most of the important kinetic effects, and (c) a fully kinetic /6/ but much slower code are compared for an analytic model equilibrium. /7/ The frequency regime considered is ω_{bi}, $\omega_{ti} < \omega < \omega_{be}$, ω_{te}. Figure 4 shows (a) the growth rates and (b) the real frequencies for a representative set of PDX L-mode operational parameters. In many cases it is found that the growth rates can be significantly smaller than the ideal MHD estimates. On the other hand, kinetic ballooning instabilities can persist over a wider range of β values than that predicted by ideal MHD. These residual type modes can be driven, for example, by wave-particle magnetic drift resonances.

*Work supported by U.S. Department of Energy Contract No. DE-AC02-76-CHO-3073.

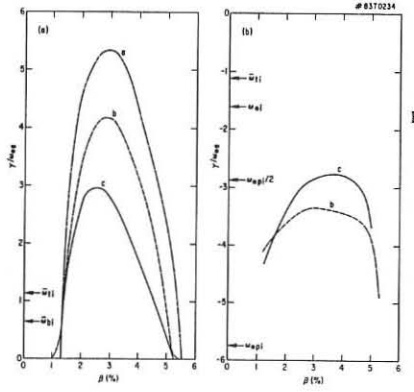

Fig. 4. Eigenfrequencies versus β from (a) an ideal model, (b) a reduced kinetic model, and (c) a fully kinetic model for the set of PDX L-mode parameters $T_e/T_i = 0.619$, $\varepsilon_n = 0.1511$, $\varepsilon_o = 0.1516$, $k_\theta \rho_s = 0.1696$, $q = 1.408$, $s = 0.9051$, $\eta_e = 2.107$ and $\eta_i = 2.563$.

REFERENCES

/1/ E. M. Barston, Ann. Phys. (N.Y.) 29, 282 (1964).
/2/ Z. Sedlacek, J. Plasma Phys. 5, 239 (1971).
/3/ C. E. Kieras and J. A. Tataronis, J. Plasma Phys. 28, 395 (1982).
/4/ J. W. Connor, W. M. Tang, and J. B. Taylor, Phys. Fluids 26, 158 (1983).
/5/ C. Z. Cheng, Nucl. Fusion 22, 773 (1982).
/6/ G. Rewoldt, W. M. Tang, and M. S. Chance, Phys. Fluids 25, 480 (1982).
/7/ J. W. Connor, R. J. Hastie, and J. B. Taylor, Phys. Rev. Lett. 40, 396 (1980).

RESISTIVE BALLOONING MODES IN A HIGH TEMPERATURE PLASMA

A. K. Sundaram, A. Sen and P. K. Kaw
Plasma Physics Programme
Physical Research Laboratory
Ahmedabad 380009, INDIA

ABSTRACT : We examine the linear stability of resistive ballooning modes in a high temperature Tokamak plasma, taking account of the effect of temperature gradients and finite parallel electron thermal conductivity. The analysis is based on the Braginskii fluid equations and is carried out in the ballooning mode formalism.

Recently, it has been suggested that the observed anomalous electron heat transport in neutral-beam heated Tokamak discharges may be related to the excitation of resistive ballooning modes /1/. Physically the modes are excited because the stabilizing effects associated with bending of field lines are weakened by resistive dissipation of parallel current perturbations. The modes can grow as rapidly as a fractional power of resistivity because the perturbations get large in the vicinity of mode rational surfaces. Early work on resistive ballooning modes has been done in the incompressible resistive MHD approximation. In a recent paper, Strauss /2/ has carried out a detailed calculation on resistive ballooning modes and has emphasised the important role played by interchange effects and parallel ion motion and associated compressional effects. It has also been demonstrated that in the ballooning mode formalism, the resistive ballooning modes are closely related to classical tearing modes modified by finite β effects. In fact, the two modes correspond respectively to the even and odd-ϕ parity ('twisting' and 'tearing' parities) solutions of the same set of equations. In this calculation, Strauss /2/ does not include the drift effects (important for moderate R_L) arising from $\nabla_{\parallel} p_e$ terms in the parallel Ohm's law. In classical tearing mode theory it has been shown by Drake et al. /3/ that introduction of $\nabla_{\parallel} p_e$ terms (with finite ∇T_e) and parallel electron thermal conductivity effects generates large parallel currents in the neighborhood of a mode rational surface and completely change the character of the tearing mode. These results are particularly relevant to high temperature plasmas. It is therefore of considerable interest to examine how these effects modify the stability properties of resistive ballooning modes. This papers aims at an investigation of this question.

Our starting equations are the Braginskii two fluid equations /4/. We assume that $T_i = 0$ and that the only finite transport coefficients are the parallel electron thermal conductivity, $\chi_{\parallel}$ and resistivity, η. The linearised equation of motion for the plasma is identical to that of Strauss /2/. The pressure perturbation $\tilde{p}$ due to the electron fluid is given by

$$\tilde{p} = n_0 \tilde{T}_e + \tilde{n} T_e$$

where the quasi-neutral density perturbation $\tilde{n}$ is governed by the ion

continuity eqn.

$$\frac{\partial \tilde{n}}{\partial t} = -n_0(\hat{b}\cdot\nabla)\tilde{v}_{\parallel} + \frac{c\nabla\tilde{\phi}\times\hat{b}}{B_0}\cdot\nabla n_0, \quad \hat{b} = \vec{B}_0/|\vec{B}_0| \qquad (1)$$

and the electron temperature perturbation $\tilde{T}_e$ is governed by

$$n_0\left(\frac{\partial}{\partial t} + c\frac{\hat{b}\times\nabla\phi}{B_0}\cdot\nabla\right)\tilde{T}_e + \frac{2}{3}T_e n_0\nabla_{\parallel}\tilde{v}_{\parallel e} = -\frac{2}{3}\nabla_{\parallel}\left[-\chi_{\parallel}\nabla_{\parallel}\tilde{T}_e + 0.71\, n_0 T_e \tilde{u}_{\parallel}\right] \qquad (2)$$

All symbols have the same meaning as in Strauss /2/ except that we replace his U by $-\phi$ and note that $\tilde{v}_{\parallel e} = -j_{\parallel}/en_0 + v_{\parallel}$

Note that the difference from Strauss /2/ arises in replacing his equation of state by a more complicated set above and also incorporating additional terms in the parallel Ohm's law, viz.,

$$-i\omega\tilde{A}_{\parallel} = -\hat{b}\cdot\nabla\tilde{\phi} + \eta\nabla^2\tilde{A}_{\parallel} + \hat{b}\cdot\nabla\tilde{p}/en_0 + 0.71(\hat{b}\cdot\nabla)\tilde{T}_e/e + \nabla p_0\times\nabla\tilde{A}_{\parallel}\cdot\hat{b}/en_0B_0 + 0.71\,\nabla T_e\times\nabla\tilde{A}_{\parallel}\cdot\hat{b}/eB_0 \qquad (3)$$

Assuming circular flux surfaces near the magnetic axis and introducing the ballooning representation

$$\tilde{F}(x,\theta,\zeta) = \sum_{l=-\infty}^{+\infty} F(\theta+2\pi l)\exp\left[in q' x(\theta+2\pi l) + in(q_0\theta - \zeta)\right]$$

where $x = r - r_{mn}$ is the rational surface, $q(r_{mn}) = q_0 = m/n$ $q(r) = rB_0/RB_\theta$, $q' = dq/dr$, r, θ are the polar flux coordinates, ζ is the toroidal angle, the relevant equations take the approximate form

$$\left(\frac{\omega s}{\omega_A}\right)^2(1+s^2\theta^2)\phi = \frac{d}{d\theta}(1+s^2\theta^2)\psi + i\sigma s\psi + D(T_e+N) \qquad (4)$$

$$-\psi\left[1 - \frac{\omega_*}{\omega} - 1.71\frac{\omega_{*T}}{\omega} + iv_R(1+s^2\theta^2)\right] = \left[\frac{d\phi}{d\theta} + \frac{\omega_*}{\omega}(1+\eta_T)\left\{\frac{dN}{d\theta} + 1.71\frac{dT_e}{d\theta}\right\}\right] \qquad (5)$$

$$\frac{iv_D}{\omega}\frac{d^2T_e}{d\theta^2} - T_e = \frac{\eta_T - 0.67}{1+\eta_T}\phi + \frac{iv_D}{\omega}\frac{\eta_T}{1+\eta_T}\frac{d\psi}{d\theta} - 0.67N \qquad (6)$$

$$N = -\frac{\phi}{1+\eta_T} - \left(\frac{\omega_s}{s\omega}\right)^2\left[\frac{d^2}{d\theta^2}(T_e+N) - \frac{d\psi}{d\theta}\right] \qquad (7)$$

with $\nu_R = \eta c^2 k_\perp^2/4\pi$, $\nu_D = 1.07 v_{the}^2/\nu_e q^2 R^2$, $\omega_* = -(CT_e/eB_0)(k_\perp n'/n)$, $S = \frac{rq'}{q}$, $\eta_T = d\ln T/d\ln n$, $\omega_S = Sc_S/qR$, $\omega_A = Sc_A/qR$, $\sigma = J_0' qR / k_\perp S B_0$ and the ballooning and interchange driving term

$$D = \alpha(\cos\theta + S\theta\sin\theta) - \alpha^2/2 - 2\alpha\epsilon S, \quad \epsilon = r/R$$

$$\alpha = -2p_0' q^2 R / B_0^2$$

Eqs. (4) - (7) can be solved by the method of averaging. When $\omega >> \omega_S/S$ incompressible MHD is a reasonable approximation and we get coupled set of differential equations between $\bar{T}_e$ and $\bar{\Phi}$. When $\omega_S/S \gtrsim \omega \gtrsim \omega_S$, we get a modified Strauss approximation giving a coupled set involving $\bar{\Phi}, \bar{N}, \bar{T}_e$ & $\bar{\Psi}$. For arbitrary $\chi_{||}$, the various equations are intricately coupled. Using the tearing mode calculations of Drake et al. /3/ as a guide, it would appear that d^4/dz^4 and higher derivative terms (corresponding to x^4 etc. in usual spatial variable) are crucial and that the approximation of large or small $\nu_D\, d^2/dz^2$ is not uniformly valid all over z space. A detailed investigation of these equations for arbitrary ν_D is in progress. Here we report some results for the cases when ν_D is assumed small or large such that the problem can be reduced to a second order eqn. and can be solved by variational method. The resulting dispersion relations are tabulated in Table 1. These results are only to be treated as a qualitative guide to a more exact investigation of the problem.

This work was supported by Department of Science and Technology, Government of India.

TABLE - 1

DISPERSION RELATIONS

Incompressible limit ($\omega >> \omega_S/S$) :

$$\omega^2(\omega - \omega_* - 1.71\,\omega_{*T}) = -\frac{i\alpha^2}{2S^2}\nu_R\omega_A^2 \quad (\nu_D \to 0)$$

$$\omega^2(\omega - \omega_* - i\nu_R)(\omega - \omega_* - 1.71\,\omega_{*T}) = -\frac{i\nu_R\alpha^2}{2S^2}\omega_A^2 \quad (\nu_D \to \infty)$$

Compressible limit ($\omega_S/S \gtrsim \omega \gtrsim \omega_S$) :

$$\omega^2\{(\omega - \omega_*) - 1.71\,\omega_{*T}\} = -i\nu_R\omega_A^2 \quad (\nu_D \to 0,\ \omega >> \omega_S)$$

$$\omega^2(\omega - \omega_*) = -i\nu_R\omega_A^2 \quad (\nu_D \to \infty,\ \omega >> \omega_S)$$

References :

1. B. A. Carreras, P. H. Diamond, M. Murakami, J. L. Dunlap, J. D. Bell, H. R. Hicks, J. A. Holmes, E. A. Lazarus, V. K. Pare, P. Similon, C. E. Thomas and R. M. Wieland., Phys. Rev. Lett. 50, 503 (1983)

2. H. R. Strauss, Phys. Fluids 24, 2004, 1981.

3. J. F. Drake, T. M. Antonsen, A. B. Hassam and N. T. Gladd., IAEA-CN-41/P-2-3, Ninth Int. Conf. on Plasma Physics and Controlled Nuclear Fusion Research, Baltimore, USA, September, 1982.

4. S. I. Braginskii, in Reviews of Plasma Physics, (Ed). M. A. Leontovich, Consultant's Bureau, New York, Vol. 1, p. 205.

RESISTIVE MAGNETOHYDRODYNAMIC SPECTRUM FOR TOROIDAL PLASMAS

R.G. Storer

School of Physical Sciences
The Flinders University of South Australia
Bedford Park, South Australia
5042

The resistive MHD spectrum for an incompressible toroidal plasma has been found using a numerical procedure. The results are checked by comparison with the corresponding complex eigenfrequencies found using an exact solution of a cylindrical MHD plasma with constant current. The results obtained show that there can be considerable damping of some of the stable eignemodes even for quite small resistivities.

The method used starts from the linearized incompressible resistive MHD equations expressed in terms of vector potentials of both the magnetic field and the velocity field. These are written in a coordinate system in which one of the coordinate surfaces coincides with the surfaces of constant flux of the MHD equilibrium. The equations are fourier analysed in both the poloidal and toroidal direction and expressed in finite difference representation in the flux coordinate. The complex eigenfrequencies are then found by means of a procedure which uses the properties of Cauchy integrals in a search on the complex plane. The eigenfunctions can then be found by means of a block-diagonal matrix inversion routine.

Preliminary Abstract (4-page paper not received in time).

QUASI-LINEAR EVOLUTION OF TEARING MODES

M. TAGGER, M. FREY, R. PELLAT *

ASSOCIATION EURATOM-CEA SUR LA FUSION
Département de Recherches sur la Fusion Contrôlée
Centre d'Etudes Nucléaires
Boîte Postale n°6. 92260 FONTENAY-AUX-ROSES (FRANCE)

It has been shown by Rutherford [1] that when the width of a magnetic island, due to a high-m ($m \geq 2$) tearing mode, exceeds that of the resistive layer, non-linear $\vec{j} \times \vec{B}$ forces result in a regime of algebraic growth. This result has been extended to a model with anomalous electron viscosity, due to braided magnetic field lines [2,3] .

This however does not explain the saturation of the instability, observed both in experiments [4] and in numerical simulations [5,6] . Saturation was found in a semi-analytical calculation by White et al [5] . It is obtained when the slope-jump Δ' of the "outer" solution, measured at the separatrix of the magnetic island, vanishes. But their matching of the "inner" and "outer" solutions at the separatrix leads them to neglect, outside of the island, Rutherford's current and some important resistive effects, as will be seen. We address this problem in a more systematic manner, using standard singular perturbation techniques [7] . Such techniques have already been used to regularize Rutherford's solution, which was singular at the separatrix [8] .

We start from the equations of resistive MHD :

$$\frac{\partial \Psi}{\partial t} - \vec{B} \cdot \vec{\nabla} u = \eta \left(j_z - j_0(x) \right) \qquad (1)$$

Where $j_z = j_z(\Psi)$ (neglecting plasma inertia), Ψ and u are the stream functions of the magnetic field and velocity :

$$\vec{B} = B_z \vec{e}_z + \vec{e}_z \times \vec{\nabla} \Psi$$

$$\vec{v} = \vec{e}_z \times \vec{\nabla} u$$

Equilibrium is defined by $j = j_0(x) = \frac{\partial^2 \Psi_0}{\partial x^2}$, $B_0 = \frac{\partial \Psi_0}{\partial x}$, and $\Psi = \Psi_0(x) \approx B_y' \frac{x^2}{2}$

in the island region. It has been shown [1] that the harmonics of the mode can be neglected if they are sufficiently damped. Then writing :

$$\Psi = \Psi_0 - \tilde{\Psi}$$

$$\tilde{\Psi} = \Psi_1(x,t) \cos ky + \delta\Psi_0(x,t)$$

where $\delta\Psi_0$ is the quasi-linear perturbation of the equilibrium flux, we write eq. (1) as :

* Ecole Polytechnique, Palaiseau, France.

$$\frac{\partial^2 \tilde{\Psi}}{\partial z^2} = \Delta \tilde{\Psi} = \frac{\left\langle \frac{1}{\eta}\frac{\partial \Psi}{\partial t} \Big/ \frac{\partial \Psi}{\partial x} \right\rangle}{\left\langle 1 \Big/ \frac{\partial \Psi}{\partial x} \right\rangle} + \left[j_0(x) - \frac{\left\langle j_0 \Big/ \frac{\partial \Psi}{\partial x} \right\rangle}{\left\langle 1/\partial\Psi/\partial x \right\rangle} \right] \qquad (2)$$

where the brackets mean the average at constant Ψ . In the island region ($x \sim x_T = 2\,(\Psi_1/B'_y)^{1/2}$) we solve eq. (2) order by order in $\varepsilon = \Delta' x_T \sim \frac{\tau_R^i}{\tau_c}$, where $\frac{1}{\tau_c} \sim \frac{\partial}{\partial t} \sim \eta \frac{\Delta'}{x_T}$, and $\tau_R^i = \frac{x_T^2}{\eta}$ is the resistive time through the island. As pointed out by Drake et al [9] the "constant - Ψ" approximation is just the calculation to lowest order in ε. Here we write :

$$\tilde{\Psi} = \Psi_i(t)\left[1 + \Delta' s\, x + \varepsilon\, h_0(x) + \varepsilon^2 h_1(x)\right] \cos ky + \varepsilon\, \delta\Psi_0(t)\left[1 + g_0(x) + \varepsilon\, g_1(x)\right]$$

s is an integration constant which implies an asymmetry of the island, due to that of the outer solution. h and g, integrals of Rutherford's current, are even functions vanishing at x = 0. We find :

$$\varepsilon \frac{\partial^2}{\partial x^2}\left[\Psi_i h_0 \cos ky + g_0\, \delta\Psi_0\right] = \frac{1}{\eta}\frac{\partial \Psi_i}{\partial t} \frac{\left\langle \cos ky / x^* \right\rangle}{\left\langle 1/x^* \right\rangle} \qquad (3a)$$

$$\varepsilon^2 \frac{\partial^2}{\partial x^2}\left[\Psi_i h_1 \cos ky + g_1\, \delta\Psi_0\right] = \frac{\varepsilon}{\eta} \frac{\left\langle \frac{\partial}{\partial t}\left(\Psi_i h_0 \cos ky + g_0\, \delta\Psi_0\right)/x^* \right\rangle}{\left\langle 1/x^* \right\rangle}$$

$$+ \frac{\varepsilon}{\eta}\frac{\partial \Psi_i}{\partial t} \frac{1}{\langle 1/x^* \rangle^2}\left\{ \left\langle \frac{M}{x^*} \right\rangle \left\langle \frac{\cos ky}{x^*} \right\rangle - \left\langle \frac{M \cos ky}{x^*} \right\rangle \left\langle \frac{1}{x^*} \right\rangle \right\} \qquad (3b)$$

where $$x^{*2} = \frac{2}{B'_y}\left[\Psi + \Psi_i(t) \cos ky + \varepsilon\, \delta\Psi_0(t)\right]$$

$$M = \left[\left(h_0 - x^* h_0'\right)\Psi_i \cos ky + \left(g_0 - x^* g_0'\right)\delta\Psi_0\right] \Big/ B'_y x^{*2}$$

and the primes denote derivatives with respect to x. Eq. (3a) is that solved by Rutherford. Detailed solutions will be given in a separate publication [10] . Expanding them for $\tilde{X} = \frac{x}{x_T} >> 1$ (where they will be matched to the outer solutions), we obtain :

$$\Psi_i\left(\varepsilon h_0 + \varepsilon^2 h_1\right) = \varepsilon\, a_0 + \left(\varepsilon\, a_1 + \varepsilon^2 a_2\right) x_T |\tilde{X}| \qquad (4a)$$

$$\varepsilon\, g_0\, \delta\Psi_0 = \varepsilon\, a_3\, Ln\,|\tilde{X}| \qquad (4b)$$

Where the a_n' s depend on $\frac{\partial \Psi i}{\partial t}$ and on integrals calculated numerically.

In the outer region, we solve Eq. (2) by expansion in $\frac{\tilde{\Psi}}{\Psi} << 1$, with $\tilde{\Psi} = \Psi_e(x,t) \cos ky + \delta\Psi_0(x,t)$, to obtain :

$$\Delta\left(\Psi_e \cos ky\right) = \left[\frac{j_0'}{B_0} + \frac{j_0'}{B_0^2}\delta\Psi_0' - \frac{1}{B_0}\frac{1}{\eta}\frac{\partial}{\partial t}\delta\Psi_0'\right]\Psi_e \cos ky \qquad (5a)$$

$$\left(\frac{\partial^2}{\partial x^2} - \frac{1}{\eta}\frac{\partial}{\partial t}\right)\delta\psi_o = -\frac{\partial}{\partial x}\left(\frac{\psi_e^2 j_o'}{2B_o^2}\right) + \frac{1}{\eta}\frac{\partial}{\partial t}\frac{\partial}{\partial x}\left(\frac{\psi_e^2}{4B_o}\right) \qquad (5b)$$

Far from the island ($X = \Delta' x > 1$) Eq. (5b) gives the usual ideal-MHD result $\delta\psi_o = -\frac{\partial}{\partial x}(\psi_e^2/4B_o)$[5] but this easily shown to contribute only to order $(\varepsilon^2 x_T/a)$ (where a is the plasma radius) to the slope-jump. For $x \sim \frac{x_T}{\varepsilon^{1/2}}$ (which is the resistive depth on a time τ_c) we find :

$$\frac{1}{\eta}\frac{\partial}{\partial t}\delta\psi_o' = -\frac{1}{\eta^2}\left[\frac{\partial^2}{\partial t^2}\frac{\partial^2}{\partial x^2}\frac{\psi_e^2}{4B_o}\right]\cdot\frac{x^3}{2\eta^2 t^2}\cdot\frac{1}{2i\pi}\int_{\alpha-i\infty}^{\alpha+i\infty} dp\,\frac{e^{pt}}{p^{5/2}}\,H(x\sqrt{p})$$

$$H(z) = e^{-z}E_i(z) + e^{z}E_1(z) - \frac{2}{z}$$

which matches for small x to Eq. (4b) and for large x to the ideal solution. Substituting this result into Eq. (5a) we get :

$$\psi_e(x,t) = \psi_{eL} + \delta\psi_e$$

$$\delta\psi_e = -\frac{\psi_{eL}}{4B_y'^2}\left[\frac{1}{\eta^2}\frac{\partial^2}{\partial t^2}\psi_{eL}^2\right]\cdot\frac{1}{\Delta'\eta^2 t^2}\cdot\frac{1}{2i\pi}\int_{\alpha-i\infty}^{\alpha+i\infty} dp\,\frac{e^{pt}}{p^{5/2}}\int_{x\sqrt{p}}^{\infty} dz\,\frac{H(z)}{z} \qquad (6)$$

where ψ_{eL} is the linear solution. For $x \sim x_t << \frac{x_T}{\varepsilon^{1/2}}$ we obtain :

$$\psi_e = \psi_e(t)\left[1 + b_\pm X + j_o' B_y'^{-1}\left(\Delta' b_\pm \frac{X^2}{2} + \frac{X}{\Delta'}\,Ln|X|\right) + \varepsilon^{3/2}\,\alpha\,|X|\right]$$

where $X = \Delta' x$, $b_+ - b_- = 1$ (giving the linear slope-jump), the terms in the parenthesis are of order $(a\Delta')^{-1}$ and can be neglected (they match to a small term in the linear inner solution) and :

$$\varepsilon^{3/2}\alpha = \frac{-1.9}{\Delta' B_y'^2 \psi_e'^{1/2}}\left(\frac{1}{\eta}\frac{\partial\psi_e}{\partial t}\right)^{5/2}$$

The ordering in $\varepsilon^{3/2}$ comes from the resistive diffusion on a scale length $x_T\,\varepsilon^{-1/2}$. Matching the inner and outer solutions gives

$$\psi_i = \psi_e - \varepsilon\,a_o \quad , \quad s = \frac{b_+ + b_-}{2}\,\frac{\psi_e}{\psi_i} \quad , \quad \varepsilon = \Delta' x_T = 2\Delta'(\psi_i/B_y')^{1/2}$$

$$\frac{1}{\eta}\frac{\partial\psi_e}{\partial t} = .61\,\Delta'(B_y'\psi_e)^{1/2}\left[1 - .16\varepsilon - .40\varepsilon^{3/2}\right] \qquad (7)$$

To lowest order we recover Rutherford's result. To the following orders, although we are limited to small ε, we see that saturation can occur for $\varepsilon = \Delta' x_T \sim 1$ (which is indeed the order of magnitude observed in numerical simulations), due to the quasi-linear evolution of the flux (or current) profile. We notice that at saturation, $\delta\psi_o$ would keep diffusing, from the level reached during the growth of the mode, on a scale length $x_T\varepsilon^{-1/2} \sim x_T\left(\frac{t}{\tau_c}\right)^{1/2}$. The "outer" slope jump would then be altered only to order x_T/a. The slow evolution of

$\delta\Psi_o$ after saturation has been observed in numerical simulations [5]

Work is in progress to study a similar effect, due to the diffusion of the heat generated by Rutherford's current.

The authors are happy to aknowledge many stimulating discussions with Drs. Bussac, Edery, Somon and Soulé.

REFERENCES :

/1/ : P.H. RUTHERFORD, Phys. fluids 16, 1903 (1973).
/2/ : P.K. KAW, E.J. VALEO, P.H. RUTHERFORD, Phys. Rev. Lett. 43, 1398 (1979).
/3/ : R.G. KLEVA, Phys. fluids 25, 330 (1982)
/4/ : TFR Group, Nuclear Fusion 17, 1983 (1977)
/5/ : R.B. WHITE, D.A. MONTICELLO, M.N. ROSENBLUTH and B.V. WADDEL, Phys. Fluids 20, 800 (1977)
/6/ : D. BISKAMP, H. WELTER, in "Plasma PHysics and Controlled Nuclear Fusion Research", IAEA, Vienna, 1977 p. 579
/7/ : M. VAN DYKE, Perturbation Methods in Fluid Mechanics, Academic Press, New York, 1964.
/8/ : D. EDERY, M. FREY, J.P. SOMON, M. TAGGER, J.L. SOULE, R. PELLAT, M.N. BUSSAC, Phys. Fluids 26 (5), 1165 (1983)
/9/ : J.F. DRAKE, P.L. PRITCHETT, Y.C. LEE, Bull. Am. Phys. Soc. 23, 866 (1978)
/10/ : M. TAGGER, M. FREY, R. PELLAT, Submitted to Journal de Physique.

PLASMA PRESSURE DROPS PRODUCED BY THE BALLOONING MODES

V.M.Gribkov, B.B.Kadomtsev, O.P.Pogutse
I.V.Kurchatov Institute of Atomic Energy,
Moscow, USSR

In the recent experiments on high-pressure plasma production in tokamaks by the injection of neutrals /1/, /2/, a high MHD-activity has been observed. In a more pronounced form it occured on PDX /2/, where all diagnostics registered a series of oscillatory bursts (Fig.1). These series of bursts seem to be related to low-order ballooning modes /2/-/4/, and its non-linear nature is worth of more detailed theoretical analysis.

A set of equations to explain an explosive nature of the instability is suggested in this paper.

The first equation, which describes an increase of the energy of oscillations, W is expressed as:

$$\frac{dW}{dt} = 2\gamma(\beta - \beta^*)\, W - \frac{1}{\tau_W} W \qquad (1)$$

The first term is responsible for the drive of oscillations with a growth rate, γ, when the plasma pressure, β, exceeds some critical value, β^*. Plasma is considered to include a cold (main) component, β_c, and a hot one, β_h, from a beam of neutrals, the contribution of which into the total pressure is characterized by a factor σ : $\beta=\beta_c+\sigma\beta_h$ ($0\leqslant\sigma\leqslant1$). Both γ and β^* can be determined from the theory of ballooning modes, /3/, /5/. When $\beta<\beta^*$, the growth rate, $\gamma=0$, and the second term of the equation (1) describe a damping of oscillations with a characteristic time, τ_W. This is a known damping of the Alfvén waves in an inhomogeneous plasma due to a spread in the wave packet /6/ and $\tau_W \sim 10\psi/c_\theta$, where $c_\theta = B_\theta/(4\pi\rho)^{1/2}$ is the Alfvén velocity with respect to the current field.

The second equation relates to the pressure of the main plasma component:

$$\frac{dB_c}{dt} = \frac{1}{\tau_t}\beta_h - \frac{1}{\tau_E}\beta_c - \frac{1}{\tau_c} W\beta_c \qquad (2)$$

The first term describes heating of the cold component due to thermalization of the hot one, β_h. At the moderate energies of neutrals of the beam, the characteristic time of thermalization, $\tau_t \sim 0.01$ s /2/. The second term in (2) describes ordinary energy losses of the main component (τ_E is the thermal confinement time). $\tau_E \sim 20$ ms in the experiments /2/. The last term in the right-hand side of the equation (2) takes the energy release of the main component due to the instability into account.

The third equation is written for a hot component produced by the injection source with the power, P (note that all the values are normalized to the energy of magnetic field, therefore, W and β are dimensionless, and P is expressed in 1/s):

$$\frac{d\beta_h}{dt} = P - \frac{1}{\tau_t}\beta_h - \frac{1}{\tau_h} W\beta_h \qquad (3)$$

The second term of the equation (3) takes the cooling of hot component, due to the beam thermalization, into account; the last term describes a release of fast particles, experimentally observed, which is considered to be rising with an increase of the energy.

The parameters P, τ_E, τ_t in the equations (1)-(3) are well known. β^* and γ are known with the less accuracy. τ_c and τ_h, which describe the energy release, are the most uncertain parameters. A study of the equations show that there is a rather narrow range of τ_c and τ_h, within which the result of integration of the set (1)-(3) describes an experimental situation.

A study of the set, (1)-(3), is natural to start from a linear stage. It is found that there is a critical power of injection, over which the instability arises. It is convenient to introduce the following designations: density of the equilibrium energy of oscillations*)

$$W_o = \frac{\tau_h}{\tau_t}\left[\frac{\tau_E P}{\beta^*} / \left(1+\frac{1}{2\beta^*\gamma\tau_E}\right) - 1\right] \qquad (4)$$

and the critical energy of oscillations, $W_{cr} = \tau_h/\gamma\tau_t^2$. When $W_o < W_{cr}$, all the three roots of a characteristic equation for a linearized set give the damping solutions; when $W_o = W_{cr}$ two neutral oscillations at the frequency $\omega_{1,2} = \pm(1/\tau_E\tau_t)^{1/2}$ emerge, the third root, $\omega_3 = -i/\tau_t$, gives a damping solution again. When $W_o > W_{cr}$**) , the real roots $\omega_{1,2}$ shift towards the complex region so that they acquire a positive imaginary part corresponding to the drive of oscillations. If the magnitude of the damping root, ω_3, is considerably greater than that of the driving ones, one will be able to expand the equations (1)-(3) in terms of an inverse value of that ratio. As a result, one obtains two equations, which describe a self-excited oscillator, instead of three ones. In this approximation, there are comparatively-smooth periodic non-linear oscillations near the equilibrium energy, W_o (4). The situation will be changed if the parameters of the set are such that all the three roots are of the same order of magnitude. Then, one is forced to use all the three equations. The energy of oscillations vs.time, in the time range of 5 τ_E, obtained as a result of a numerical integration of the set (1)-(3), is shown in Fig.2a. At the chosen values of the parameters, the period and the duration of expulsions satisfactory coincides with the experiment. A proximity of the critical power of injection, $P_{theor} \sim 2.5$ MW (see**), at which the instability evolves, to the experimental value, $P_{exp} \sim 3$ MW, and the fluctuations in the pressure of hot component, $\beta_h \sim$ 40-60% (see Fig.2 b),serve as additional arguments in favor of the model suggested.

Thus, one can think that the suggested simple model describes the main qualitative features of the bursts of non-linear oscillations and of the hot-particles-pressure drops observed in PDX.

References

/1/ Leonov V.M., et al., 8-th Intern.Conf. on Plasma Phys. and Control Nucl. Fusion Res., Brussels, 1980, IAEA-CN-38/N-2.

/2/ Johnson D. et al., 9-th Intern.Conf. on Plasma Phys. and Control Nucl. Fusion Res., Baltimore, USA, 1982, p.A-1.

/3/ Pogutse P.O., Yurchenko E.I. Voprosy teorii plasmy, v.11, Moskow, Energoizdat,1982.

/4/ Todd A.M., Mahickam J., Okabayshi M. et al., Nucl.Fusion, 1979, v.19, p.743.

/5/ Holmes J.A. et al., Phys.Fluids, 1982, v.25, p.800.

/6/ Tataronis J.A., J.Plasma Phys., 1975, v.13, p.87.

*) For simplicity we assume that $\tau_c \to \infty$.

**)The condition $W_o > W_{cr}$ is practically reduced to $\tau_E P \gg \beta^*$.

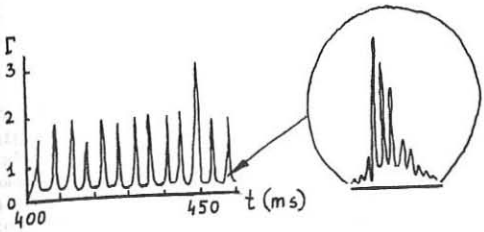

Fig.1 Flux of fast neutrals obtained in PDX /2/.

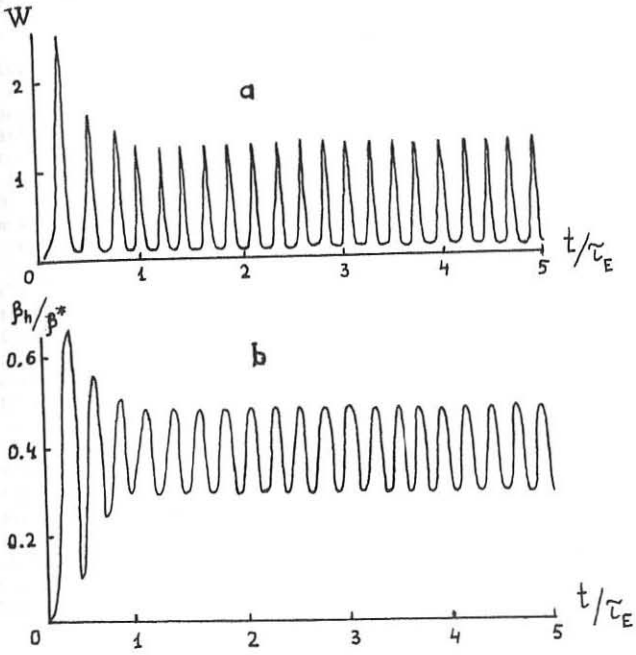

Fif.2 Results of a numerical solution for a set (1)-(3)
a) change in energy of oscillations, W
b) pressure fluctuations in the hot plasma component, β_h/β^* .

MAGNETIC FLUCTUATIONS IN HIGH β_p TOKAMAK PLASMAS*

J. K. Lee, M. S. Chu, F. J. Helton, and W. Park**
GA Technologies Inc., San Diego, California, U.S.A.

ABSTRACT: The magnetic fluctuations resulting from the nonlinear evolutions of high β_p long parallel wavelength resistive MHD modes are studied for tokamak plasmas with a free boundary. Large amplitude fluctuations cause increased magnetic field stochasticity with increasing $\varepsilon\beta_p$. These fluctuations, when coupled to an anomalous energy loss mechanism, may lead to β_p-saturation in total input power. Modeling of the H-mode with a line tied plasma to the divertor plate shows substantial stabilization of edge instabilities. Calculations for recent high β noncircular discharges in DIII compare well with experimental observations.

Large amplitude magnetic fluctuations have been observed to be characteristic of tokamaks with high plasma pressure or with low safety factor at the limiter q_ℓ. These fluctuations have been associated[1] with a limitation in particle and energy confinement of the discharges. Plasma evolutions in tokamaks with high β_p have been simulated using the resistive MHD model by Carreras et al.[2] with fixed boundary plasmas. For free boundary plasmas, the ideal MHD β_p limit has been studied[3] using the linear stability code GATO. To account for the free energy from the large toroidal current in tokamaks, a realistic modeling of the edge region is necessary. To describe the nonlinear evolution of MHD modes, a resistive MHD model is necessary. For such an edge region a free boundary external kink mode has been found to be the dominant mode. This high β_p external kink mode couples with various resistive internal modes through finite pressure and toroidal effects. Magnetic field line stochasticity results from the nonlinear interaction among these modes. The anomalous transport from this stochastic field can be shown to cause the experimentally observed phenomenon similar to β_p-saturation in neutral beam heated discharges.

For the calculations from equilibrium to nonlinear evolution, the resistive MHD code HIB[4] is used. The initial high β_p equilibria are computed using $q(r) = q_0[1 + x^{2\lambda}(Q^\lambda - 1)]^{1/\lambda}$ and $p(r) = p_0(1 - x^2)^\nu$ where $x = r/a$, $Q = q_\ell/q_0$. The vacuum region in a $\leq r \leq r_w$ is modeled as a highly resistive, current-free, pressureless plasma with a finite density. The vacuum region not only introduces the external kink mode, but also provides substantial destabilization of the internal tearing modes, notably those whose singular surfaces are close to the plasma-vacuum boundary.[5]

The linear eigenfunction shows richness in harmonic content due to geometric coupling, which increases with increasing $\varepsilon\beta_p$. The typical dependence of the linear growth rate on $\varepsilon\beta_p$ at various q_ℓ is shown in Fig. 1(a). A high growth rate ($\gamma_L \gtrsim 10^{-2}\ \omega_A$) regime occurs when the β_p value exceeds the threshold β_{pc}. The results shown are for $\nu = 4$, $\lambda = 4$, and $\eta_p \equiv 1/(\tau_r\omega_A) = 10^{-6}$. The q-value at the plasma center has been fixed at $q_0 = 1.05$ to focus on $m>1$ modes in the outer plasma region rather than in the inner region. γ_L has also been found to depend on η_p and on the viscosity μ. This dependence

*Work supported by U.S. Department of Energy, Contract DE-AT02-76ET51011.
**Permanent Address: Princeton Plasma Physics Laboratory, Princeton, New Jersey, U.S.A.

becomes weaker as β_p increases, showing the ideal MHD character of the mode, and has compared favorably with the GATO code.[3] β_{pc} also has been found to depend strongly on ν, but only weakly on λ. The effect of ν on γ_L is summarized in Fig. 1(b). Also shown as the dashed curve are the experimental β_p-values for the onset of high magnetic fluctuations in PDX.[6] Since the details of the experimental profiles are not known, we could postulate that in the low q_ℓ discharges with $q_\ell \simeq 2$, the plasma is likely to have a broader pressure profile than the higher q discharges, for example, with $q_\ell \simeq 4$.

In the nonlinear regime, modes with n = 0, 1, 2, 3 and m from -2 to 15 are followed in time. The amplitude of the magnetic perturbations at the quasi-saturation is characterized by $\tilde{B}$, the ratio of the maximum perturbed magnetic field to the equilibrium poloidal field at r = a. When $\tilde{B}$ increases, magnetic island sizes increase, and the magnetic field shows increased stochasticity, especially near the plasma outer region. This stochasticity could be recognized both by the appearance of broken magnetic surfaces in the field line plot and also by positive Lyapunov number calculated in the outer portion of the plasma. The magnetic field line is nonstochastic when $\tilde{B}$ is small (e.g., $\tilde{B} \lesssim 10^{-2}$). In Fig. 2(a), the value of $\tilde{B}$ at various values of $\varepsilon\beta_p$ and q_ℓ is summarized. The high β_p regime, corresponding to large linear growth rates in Fig. 1(a), shows large nonlinear magnetic fluctuation amplitudes together with a strong dependence on $\varepsilon\beta_p$.

Since transport was neglected in the simulation, we may assume at steady state, input power P balances the anomalous loss to give $P = 1/r\ \partial/\partial r(rQ_r)$, where $Q_r \propto \tilde{B}^g\ n_e(\partial T_e/\partial r)$. Various theoretical analyses[1] give $g \gtrsim 1$ in a stochastic magnetic field. From Fig. 2(a), we found $\tilde{B} \propto \beta_p^f$. This can be combined with the power balance condition to yield, at steady state, $\beta_p \propto P^d$, where $d = 1/(fg + 1)$. Since d is much less than 1 in the stochastic region, the β_p-increase is small as P is increased. This near-saturation of β_p with respect to P is a general feature in a wide range of the scaling parameters f or g. The dependence of β_p on P for various q_ℓ-values is plotted in Fig. 2(b) with $\varepsilon = 1/3$. In the low β_p regime below β_{pc}, the dependence is linear for the nonstochastic region, indicated as a dashed line. In the high β_p regime, the β_p-dependence on P is very weak, indicated as solid curves for various q_ℓ-cases. These characteristics could be correlated with observations in the PDX discharges.[6] The low q_ℓ discharges (with $B_T = 0.7$ T) in PDX, marked as triangles, show phenomenon similar to β_p-saturation in P, while the high q_ℓ discharges (with $B_T = 1.5$ T) marked as daggers, do not. The latter may be due to the higher transition value of β_{pc} as obtained in our calculations.

The effects of a mantle region on these high β_p modes have been examined by assuming the existence of a warm plasma region just outside the separatrix in an expanded boundary discharge such as H-mode operation. These effects are stabilizing and the line tying effect of grounding the electrostatic potential contributes to further stabilization. The stabilizing effect becomes particularly substantial as the maximum pressure gradient region falls closer to the plasma edge.

Comparison with experiments for recent high β discharges in DIII show good agreement for both H-mode and L-mode types. For example, the predicted poloidal dependence of eleven Mirnov probes amplitudes agrees well with experiment for an H-mode discharge. Also, the predicted scaling of Mirnov amplitudes with β_p agrees qualitatively with experiment; e.g., $B \propto \beta_p^5$. The

dominant mode has n = 1 and m = 0, 1, 2, 3, 4 with very small magnetic islands (~1%).

In conclusion, numerical simulations have been performed for high β_p, low q_ℓ tokamaks with a free boundary. The high β_p regime is characterized by external kink modes with large linear growth rates and high magnetic fluctuations. The parametric dependence of these fluctuations has been combined with an anomalous transport model to show a feature similar to β_p-saturation with respect to input power for circular tokamaks. The onset of the β_p-saturation should be able to be shifted to a higher β_p-value when a broader pressure profile is employed. The stabilizing effects of a mantle, line tied to a divertor plate, could be substantial in an H-mode type situation. Comparison with experiment is reasonably good for some recent high β discharges in DIII.

We acknowledge helpful discussions with Drs. L. C. Bernard, R. Izzo, E. J. Strait, R. D. Stambaugh, D. A. Monticello, and R. B. White.

REFERENCES

/1/ Boozer, A.H., and White, R.B.: Particle Diffusion in Tokamaks with Partially Destroyed Magnetic Surfaces, Phys. Rev. Lett. 49 (1982) 786-789; Rechester, A.B., and Rosenbluth, M.N.: Electron Heat Transport in a Tokamak with Destroyed Magnetic Surfaces, Phys. Rev. Lett. 40 (1978) 38-41; Yamagishi, T., Hinton, F.L., Bhadra, D.K., and Miller, R.L.: Electron Thermal Conductivity in an Ergodic Magnetic Limiter, Nucl. Fusion 23 (1983) 189-194.

/2/ Carreras, B.A., Diamond, P.N., Murakami, M., Dunlap, J.L., Bell, J.D., Hicks, H.R., Holmes, J.A., Lazarus, E.A., Paré, V.K., Similon, P., Thomas, C.E., and Wieland, R.M.: Transport Effects Induced by Resistive Ballooning Modes and Comparison with High-β_p ISX-B Tokamak Confinement, Phys. Rev. Lett. 50 (1983) 503-506.

/3/ Bernard, L.C., Helton, F.J., Moore, R.W., and Todd, T.N.: MHD Beta Limit Scaling Laws and Comparison with Doublet III Data, GA Technologies Report GA-A16981 (1983).

/4/ Park, W., Monticello, E., and White, R.B.: Nonlinear Ballooning Modes, Bull. Am. Phys. Soc. 23 (1978) 779; Strauss, H.R., Park, W., Monticello, D.A., White, R.B., Jardin, S.C., Chance, M.S., Todd, A.M.M., and Glasser, A.H.: Stability of High-Beta Tokamaks to Ballooning Modes, Nucl. Fusion 20 (1980) 638-642.

/5/ Lee, J.K., Chu, M.S., and Helton, F.J.: Tearing Modes in a General Cross-Section Force-Free Cylindrical Tokamak, Phys. Fluids 26 (1983) 766-774.

/6/ Johnson, D., et al.: High Beam Experiments with Neutral-Beam Injection on PDX, IAEA, Baltimore, Maryland, U.S.A. (1982) Vol. 1, 9-25; McGuire, K., et al.: Studies of High-Beta MHD Modes and Fast-Ion Losses in PDX, Phys. Rev. Lett. 50 (1983) 891-895.

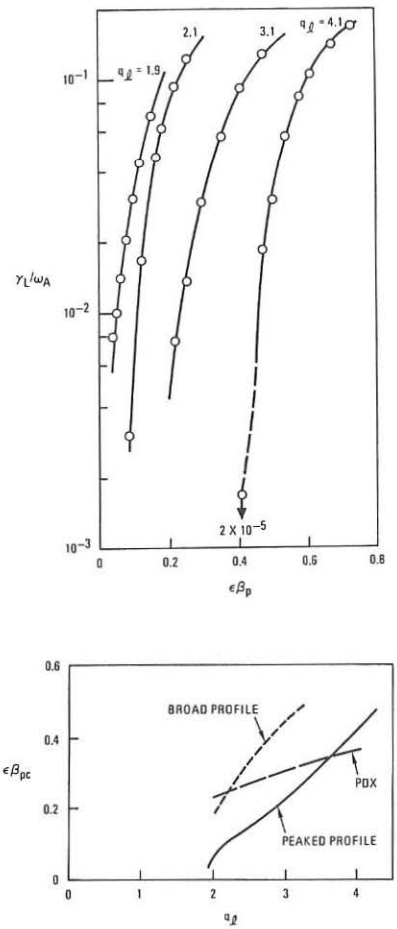

Fig. 1. Dependence of linear growth rates on $\epsilon\beta_p$ and threshold β_p-value β_{pc} for onset of a strong instability. The dashed curve is the experimental β_p-values for onset of high magnetic fluctuations in PDX.

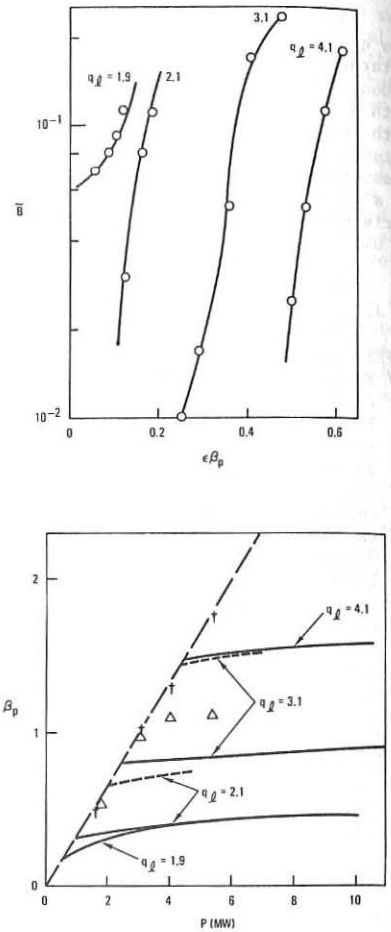

Fig. 2. Dependence of nonlinear magnetic fluctuation amplitudes on $\epsilon\beta_p$ and scaling of β_p with respect to total power P. Triangular symbols indicate low q_ℓ discharges in PDX; daggers indicate high q_ℓ discharges.

11th European Conference on Controlled Fusion and Plasma Physics,
Aachen (FRG), 5 - 9 Septemeber 1983.

COLLISIONAL AND KINETIC EFFECTS ON ELECTROMAGNETIC MODES IN TOROIDAL GEOMETRY

L. Klieb, T.J. Schep, and M. Venema
Instituut voor Plasmafysica "Rijnhuizen", Nieuwegein, The Netherlands.

F. Pegoraro
Scuola Normale Superiore, Pisa, Italy,

Electromagnetic modes with low frequencies are studied in the framework of the ballooning representation which employs an extended poloidal variable in the range $(-\infty,\infty)$. Collisional fluid equations are used to obtain the density, parallel current and temperature fluctuations of the electrons, whereas the perturbed ion density is obtained from the Vlasov equation. The perturbed parallel ion current is omitted so that the coupling to electrostatic drift and to ion sound waves is not included. The effect of the parallel equilibrium current is neglected, so that the modes can be distinguished as even and odd. If temperature fluctuations are neglected or if they are taken to be adiabatic, the modes are described by a second arder differential equation in the poloidal variable which contains collisions and finite ion gyro-radius corrections. This equation is solved analytically by the method of asymptotic matching. Alfvén, microtearing and collisional tearing modes are obtained. For relatively large ion gyro-radii the former two modes can be obtained as limiting cases of a common dispersion relation. A detailed comparison with the usual representation will be made.

Numerically, the mode equation is solved by a shooting code and by WKB techniques. The latter method provides a deeper physical understanding of the phenomena. Toroidicity can strongly affect these modes. In particular, the asymptotic behaviour along the field lines, now governed by a Mathieu euqation, may change drastically. Results will be presented for a collisional as well as for a collisionless plasma.

Preliminary Abstract (4-page paper not received in time).

DRIFT MODES IN TOROIDAL GEOMETRY

T.J. Schep and M. Venema
Association Euratom-FOM, FOM-Instituut voor Plasmafysica "Rijnhuizen", Nieuwegein, The Netherlands

In a plane slab geometry, universal drift modes are damped due to the convection of energy away from the region where the parallel wave number is small. When toroidal effects are taken into account, in particular ion magnetic curvature drifts, the anti-well structure of the potential is changed and local wells appear /1/. If the toroidicity is strong enough, i.e., if the ratio ε_n of the density scale length $L_n = |n^{-1}dn/dr|^{-1}$ to the radius of curvature R exceeds a critical value, such wells give rise to a branch of quasi-bounded eigenmodes which are quasi-marginally stable /1/. By taking into account inverse Landau damping in the plane slab form /2/, or the inverse damping of circulating particles alone /3/, this branch becomes unstable. In the present work the collisionless responses of trapped and circulating electrons are fully retained and their effect on the stability of the toroidal branch of the drift eigenmodes is investigated. When the ratio of the thermal ion gyroradius to the perpendicular wavelength, $k_\perp \rho_i$, of the mode is increased the real part of the frequency decreases. Then, the approximation that the frequency is large compared to the magnetic drift frequency of a thermal ion is not valid anymore and ion magnetic drift resonances have to be taken into account /4,5/. The toroidal branch is unstable due to these resonances and is further destabilized by the inverse Landau damping. The lowest odd mode remains marginally stable when the inverse Landau damping is included and higher-n modes are stable. A WKB code /6/ has been applied and the resulting approximate eigenvalues are compared with the exact ones. An explanation for the dependence of the slab-like branch on ε_n is obtained from the location of the turning points and the associated structure of the Stokes lines.

We consider electrostatic perturbations of an axisymmetric toroidal geometry with concentric, circular cross-sections. The perturbed electric potential can be written in the form $\tilde{\phi} = \phi(r,\theta)\exp[-i\omega t + i\ell(\zeta - q\theta)]$. In the case of high toroidal mode numbers ℓ, the two-dimensional problem in (r,θ) can be converted into one in the single extended poloidal variable $\hat{\theta} = \theta + 2\pi m$, m being an integer, on the domain $(-\infty,+\infty)$ /7/. In this ballooning representation, the eigenmode equation for the perturbed potential $\hat{\phi}(\hat{\theta})$ of a symmetrical mode is

$$-2\xi^6 H \frac{d^2}{d\hat{\theta}^2}\hat{\phi} + \frac{\Omega^2\tau^2\hat{b}q^2}{\varepsilon_n^2}\left[\frac{1 + 1/\tau}{1 + 1/\Omega\tau}\frac{1}{\Gamma_o} + \xi Z(\xi)\right] + \frac{\Omega^2\tau\hat{b}q^2}{\varepsilon_n^2}\frac{1}{\Gamma_o}\frac{\hat{N}(\hat{\theta})}{1 + 1/\Omega\tau} = 0 , \qquad (1)$$

where $\Omega = \omega/\omega_*$, $\omega_* = k_\perp T_e/(\Omega_i m_i L_n)$, $k_\perp = \ell q/r$, $\Omega_i = eB/m_i c$, $\tau = T_e/T_i$, $\hat{s} = rq'/q$, $\Gamma_o = I_o(b)\exp(-b)$, I_o being the modified Bessel function, $b = \hat{b}(1 + \hat{s}^2\hat{\theta}^2)$, $\hat{b} = \frac{1}{2} k_\perp^2\rho_i^2$, $\xi^2 = -\Omega\tau/[4\varepsilon_n(\cos\hat{\theta} + \hat{s}\,\hat{\theta}\sin\hat{\theta})]$, $\mathrm{Im}(\xi) > 0$, $Z(\xi)$ being the plasma dispersion function, and $H = 1/\pi^{\frac{1}{2}} \int_{-\infty}^{\infty} \exp(-y^2)y^2/(y^2 - \xi^2)^3]\,dy = \frac{1}{2}\,\partial^2/\partial(\xi^2)^2\,[\xi Z(\xi)]$. Here, we have made the approximation $v_\perp^2 \simeq 2v_\parallel^2$ in the ion magnetic drift frequency: $\omega_{Di} \simeq 4v_\parallel^2\,\varepsilon_n\omega_*(\cos\hat{\theta} + \hat{s}\,\hat{\theta}\sin\hat{\theta})/(\tau v_{thi}^2)$. The ion contribution to Eq. (1) is derived for mode frequencies which are large com-

pared to the transit frequency of a thermal ion. The function $\hat{N}$ represents the non-adiabatic parts of the responses of trapped and circulating electrons. For localized modes it is given by /8/,

$$\hat{N}(\hat{\theta}) = -\frac{(\hat{b}\tau)^{\frac{1}{2}} q}{(2\pi)^{\frac{1}{2}}\varepsilon_n}\left(\frac{m_e}{m_i}\right)^{\frac{1}{2}}(1-\Omega)\int_{-\pi}^{\pi} d\theta'[K^+(\theta,\theta')\hat{\phi}(\theta'+2\pi m)+K^-(\theta,\theta')\hat{\phi}(-\theta'+2\pi m)]. \tag{2}$$

The kernels $K^{\pm}$ are integrals over the velocity spaces of trapped and circulating electrons. Neglecting magnetic drift resonances, they are given by

$$K^+ = \int_0^{\Lambda b\ell} d\Lambda \frac{B/B_o}{L(\theta)L(\theta')} A_c(a|\beta|) + \int_{\Lambda b\ell}^{\bar{\Lambda}} d\Lambda \frac{B/B_o}{L(\theta)L(\theta')} A_T(a|\beta|,a), \tag{3}$$

$$K^- = \int_{\Lambda b\ell}^{\bar{\Lambda}} d\Lambda \frac{B/B_o}{L(\theta)L(\theta')} A_T(a|\beta+\tfrac{1}{2}|,a). \tag{4}$$

Here, $\Lambda b\ell$ is the value of Λ at the boundary between trapped and circulating particles, $\bar{\Lambda} = B_o/B(\bar{\theta})$ is the value for which the particle's turning point at θ_o coincides with $\bar{\theta} = \max(|\theta|, |\theta'|)$, B_o is a reference value of the magnetic field, $L(\theta) = (1-\Lambda B(\theta)/B_o)^{\frac{1}{2}}$, and

$$a = 4\Omega\omega_* q R/v_{the}\int_0^{\theta_o} d\theta/L(\theta), \quad \alpha\beta = \Omega\omega_* q R/v_{the}\int_{\theta'}^{\theta} d\alpha/L(\alpha). \tag{5}$$

A_c and A_T contain summations over the resonant denominators related to all the harmonics of the bounce and transit frequencies and are weighted by the Maxwellian distribution function. When the mode frequency is below the bounce frequency of a deeply trapped, thermal electron they can be analytically approximated by relatively simple functions which are valid up to second order in a and $a\beta$. A_c and A_T and their approximations are given in /8/. In the numerical calculations we use the approximate expressions. It has been checked that there is a good agreement with calculations using the exact expressions, which contain the integrals over the energy.

Equation (1) has been solved numerically by a shooting code. The shooting axis is rotated in the complex $\hat{\theta}$-plane such that it connects remote regions where the WKB solution is subdominant. The non-adiabatic response $\hat{N}$ has been treated iteratively. The usual boundary condition of outgoing wave energy at large $\hat{\theta}$ has been adapted. In the absence of dissipation and for sufficiently large values of ε_n the toroidicity-induced mode has small damping rates of $O(10^{-4})$. Here, the ion drift resonances have been neglected. In Fig. 1a the eigenfrequency Ω is plotted versus $\hat{b}$ for $\tau = \hat{s} = q = 1$, $\varepsilon = \varepsilon_n = 0.1$ and $m_i/m_e = 1836$ for the cases with and without $\hat{N}$. In Fig. 1b the eigenfunction with $\hat{N}$ is plotted for $\hat{b} = .025$. It is seen that the collisionless dissipation destabilizes the mode, leading to positive growth rates, and causes a decrease in $\mathrm{Re}(\Omega)$. The real part of the frequency slowly decreases with increasing $\hat{b}$ but the imaginary part of the frequency increases drastically with increasing $\hat{b}$. This is in agreement with the results of /3,4/. In Fig. 2a the eigenfrequency Ω and in Fig. 2b the eigenfunction ($\hat{b} = .025$, $\hat{N} \neq 0$) are plotted for the same set of parameters, but now with the ion drift resonances retained, for the cases with and without $\hat{N}$. It is seen that the mode is already unstable when $\hat{N} = 0$ and is further destabilized when the inverse Landau damping is included. The mode can be followed for larger $\hat{b}$ and $\mathrm{Im}(\Omega)$ has a maximum near $\hat{b} = .02$. We do not expect that higher-n modes become unstable by the introduction of $\hat{N}$. This has been checked for the lowest odd mode which gets slightly larger damping rates. We will now discuss discuss a mode which, for $\hat{s} = 1$, can coexist with the mode

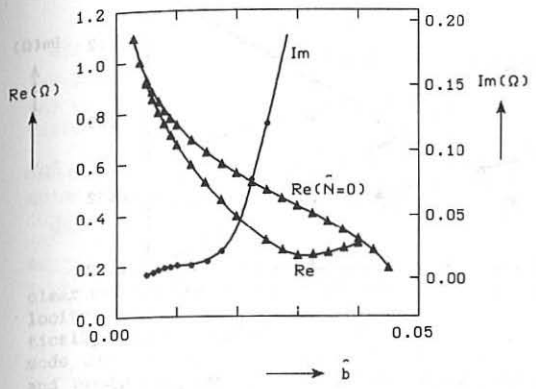

Fig. 1a.

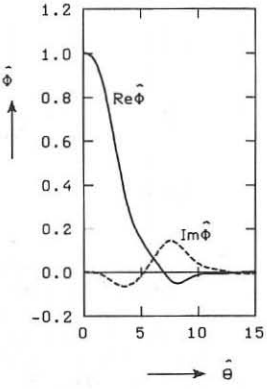

Fig. 1b.

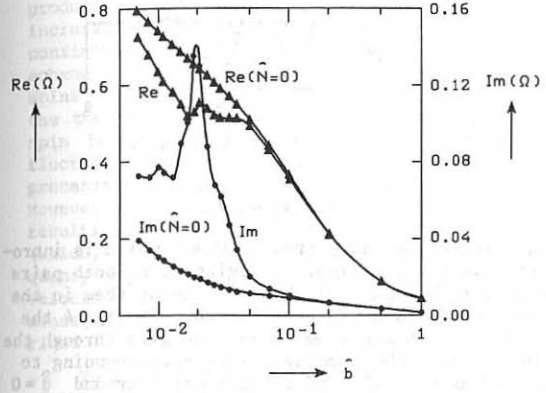

Fig. 2a.

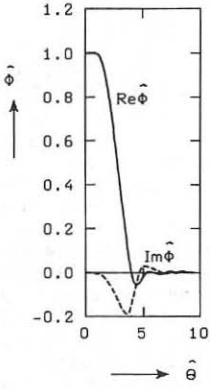

Fig. 2b.

discussed above for small values of ε_n. For these values of ε_n this mode can be labelled by the WKB method /6/ as an n = 0 mode. The slab mode, present without toroidicity, continuously changes into this mode, which can thus be called a slab-like mode. The connection between the n = 0 slab-like mode and the higher harmonics of the toroidicity-induced mode is shown in Fig. 3, where $\hat{\Omega}$, together with its WKB approximations is plotted versus ε_n for $\hat{b} = .1$, $\hat{s} = q = \tau = 1$. For $\varepsilon_n \lesssim .055$ the n = 0 WKB approximation is very good. A fifth order equation in $\hat{\Omega}$ has been derived by expanding the potential around $\hat{\theta} = 0$, which gives a Weber equation for $\hat{\Phi}$. Its solution closely follows the n = 0 WKB approximation. For $\varepsilon_n \gtrsim .06$ the mode is well described by the n = 8 WKB approximation. This change in n-number of the mode is connected with the fact that the mode is determined for $\varepsilon_n \lesssim .055$ by a pair of turning points close to $\hat{\theta} = 0$

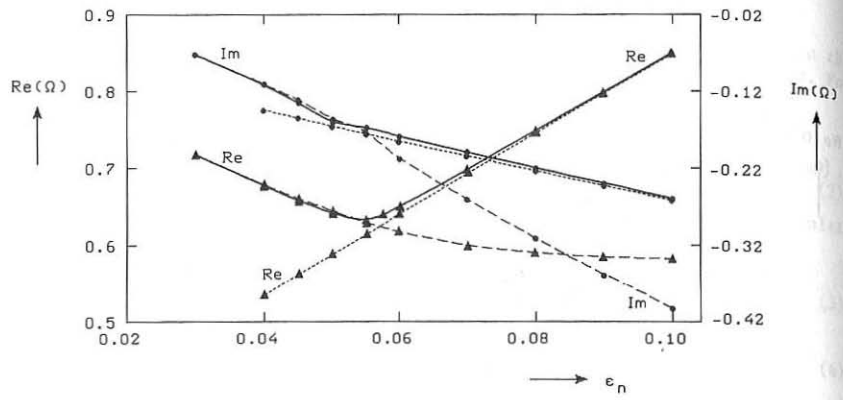

Fig. 3, ---: WKB, n = 0 .....: WKB, n = 8.

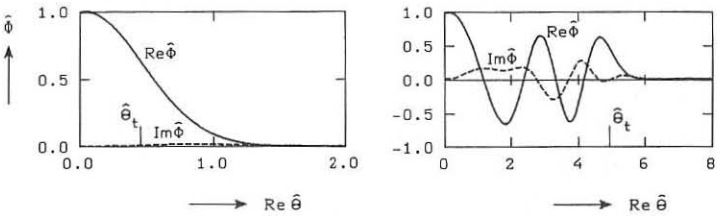

Fig. 4: $\epsilon_n = .04$ $\epsilon_n = .08$.

and for $\epsilon_n \gtrsim .06$ by a pair that is farther away from $\hat{\theta} = 0$ and which is introduced by the ion magnetic drift. In the intermediate region of ϵ_n both pairs of turning points are important for the mode and choosing one of them in the WKB integral condition will not lead to a good approximation. In Fig. 4 the eigenfunctions for $\epsilon_n = .04$ and $\epsilon_n = .08$ are shown along an axis through the relevant turning point. The position of the turning points corresponding to the n = 0 and n = 8 modes shows why an expansion of the potential around $\hat{\theta} = 0$ will not yield an approximation to the frequency for the n = 8 mode.

Acknowledgement: This work was supported by FOM, ZWO and EURATOM.

References:

/1/ Chen, L. and Cheng, C.Z., Phys. Fluids 23 (1980) 2242.
/2/ Cheng, C.Z. and Chen, L., Phys. Fluids 23 (1980) 1770.
/3/ Hesketh, K.W., Nucl. Fusion 20 (1980) 1013.
/4/ Hesketh, K.W., Nucl. Fusion 21 (1981) 275.
/5/ Cheng, C.Z. and Tsang, K.T., Nucl. Fusion 21 (1981) 643.
/6/ White, R.B., J. Comput. Phys. 31 (1979) 409.
/7/ Pegoraro, F. and Schep, T.J., in Proc. 7th Intern. Conf. on Plasma Phys. and Contr. Nucl. Fusion Res., IAEA, Vienna 1978, Vol. I, p. 507.
/8/ Schep, T.J., Braams, B.J., and Pegoraro, F., Phys. Fluids 25 (1982) 1871.

ELECTROMAGNETIC ION CYCLOTRON MODES IN A PLASMA WITH POLARIZED NUCLEAR SPINS

B. Coppi, F.Pegoraro and J. Ramos
Scuola Normale Superiore 56100 Pisa ITALY
Massachusetts Institute of Technology 02139
Cambridge, Mass. U.S.A.

We present an instability (1) that can be excited in a thermonuclear burning plasma with spin polarized nuclei by the anisotropy in velocity space of the fusion reaction products. In the case of a magnetically confined deuterium-tritium plasma, the frequency of the excited mode can coincide with that of the deuteron spin precession frequency and produce a spin depolarization rate considerably faster than the fusion reaction rate.

Recently (2) new interest has been expressed in the possibility of producing thermonuclear plasmas with polarized nuclear spins so as to increase the fusion reaction rate and/or improve the (single particle) confinement of the charged reaction products. The validity of this scheme rests on the expectation that the depolarization rate of the spins will be relatively slow, despite the very large difference between the thermal energy of the plasma and the energy splitting between the spin levels. This expectation holds provided the level of magnetic fluctuations in the plasma, in the frequency range close to the spin precession frequency, is not greatly enhanced above its thermal level. However in a multispecies plasma electromagnetic modes with frequencies resulting from combinations of the fusing nuclei cyclotron frequencies (which, in the case of a D-T plasma, are close to the precession frequency of the deuteron) can be driven unstable by the anisotropy in velocity space of the fusion reaction products, which is a direct consequence of the fact that the spins of the fusing nuclei are polarized.

To illustrate this point we neglect at first the spatial variations of the equilibrium magnetic field and, referring to a D-T plasma, look for electromagnetic fluctuations with frequencies that can resonate both with the deuteron spin precession frequency $\Omega_D^P = 0.8574\,\Omega_D$ (Ω_D = deuteron cyclotron frequency) and with the α-particles produced by the D-T fusion reactions. Since $\Omega_\alpha = \Omega_D$, the latter condition can be written as $\omega - \Omega_\alpha \simeq k_\parallel \langle v_\alpha \rangle$, where $\langle v_\alpha \rangle^2 \equiv 2\langle \varepsilon_\alpha \rangle / m_\alpha$ and $\langle \varepsilon_\alpha \rangle$ is a representative energy of the α particle slowing-down distribution that is considered in the range 3.5 MeV to about 0.7 MeV (see Ref. 3). In order to produce a significant growth rate we shall also require that $k_\perp \langle v_\alpha \rangle / \Omega_\alpha \sim 1$. Here $k_\parallel$ and $k_\perp$ are the parallel and perpendicular mode numbers of the fluctuations. In addition, in order to avoid an appreciable Landau damping by the (Maxwellian) electron distribution we shall consider $\omega^2 \gg v_{the}^2 \left| \tilde{E}_\parallel / \tilde{\phi} \right|^2$ where $\tilde{E} = -\nabla\tilde{\phi} - (\partial \tilde{A}/\partial t)/c$, $\nabla \cdot \tilde{A} = 0$ and $\tilde{\phi}$ and $\tilde{A}$ are the fluctuation potentials. Since the α-particle concentration n_α

/n_e (n_e = electron density) is small, and given the requirements on the mode wave-lengths and frequencies that we have indicated earlier, we can derive the dispersion relation for the real part of the frequency by the cold plasma approximation for both the electrons and the fuel nuclei. The relevant equations are $\tilde{n}_e = \tilde{n}_D + \tilde{n}_T$, $\tilde{\underline{J}} = (c/4\pi)k^2 \tilde{\underline{A}}$, $\tilde{\underline{J}} = e\,(\tilde{\underline{u}}_D n_D + \tilde{\underline{u}}_T n_T - \tilde{\underline{u}}_e n_e)$, $\omega \tilde{n} = \underline{k}\cdot\tilde{\underline{u}}$ for each species, $-i\omega m_i \tilde{\underline{u}}_i = e\,(\tilde{\underline{E}} + \tilde{\underline{u}}_i \times \underline{B}/c)$ where $i = D,T$, $\tilde{u}_{i\parallel} = 0$, $\tilde{\underline{E}} + \tilde{\underline{u}}_e \times \underline{B}/c = 0$, and $-i\omega m_e \tilde{u}_{e\parallel} = -e\tilde{E}_{\parallel}$. Here $\tilde{\underline{J}}$ is the perturbed current density and $\tilde{\underline{u}}$ is the perturbed average velocity of the different species. In addition we consider $k^2 d_e^2 \ll 1$ where $d_e = c/\omega_{pe}$, and notice that $|k_\perp/k_\parallel|^2 = |\Omega_D/(\omega-\Omega_D)|^2 \gg 1$.

A systematic expansion in all the small parameters that we have indicated yields the following dispersion relation:

$$\omega^2(\omega^2-\bar{\bar{\Omega}}^2) = k_\perp^2 \bar{v}_A^2(\omega^2-\Omega_h^2) \qquad (1)$$

where $\Omega_h \equiv (\Omega_D \Omega_T \bar{\bar{\Omega}}/\bar{\Omega})^{1/2}$ is the relevant ion hybrid frequency, $\bar{\Omega} \equiv \alpha_D\Omega_D + \alpha_T\Omega_T$ and $\bar{\bar{\Omega}} \equiv \alpha_T\Omega_D + \alpha_D\Omega_T$ are weighted averages of the two ion cyclotron frequencies, and $\alpha_D \equiv n_D/n_e$, $\alpha_T \equiv n_T/n_e$ are the concentrations of deuterium and tritium ($\alpha_D+\alpha_T=1, \alpha_D\neq 0, \alpha_T\neq 0$). The dispersion relation (1) has a cut-off at $\omega^2 = \bar{\bar{\Omega}}^2$, a resonance at $\omega^2 = \Omega_h^2$ and consists of two branches corresponding to two "MHD" waves: $\omega^2 \simeq k_\perp^2 \bar{v}_A^2$ for $\omega^2 \gg \Omega_{D,T}^2$, and $\omega^2 \simeq k_\perp^2 \bar{\bar{v}}_A^2$ for $\omega^2 \ll \Omega_{D,T}^2$ where $\bar{v}_A \equiv d_e(\Omega_e\bar{\Omega})^{1/2}$ and $\bar{\bar{v}}_A \equiv \bar{v}_A\Omega_h/\bar{\bar{\Omega}}$. In the special interesting case where $\alpha_D = \alpha_T = 1/2$, we have $\bar{\Omega} = \bar{\bar{\Omega}} = (5/6)\Omega_D$ and $\Omega_h = (\Omega_D\Omega_T)^{1/2} = (2/3)^{1/2}\Omega_D$. In this case, a frequency exactly equal to Ω_D^p can be obtained from the upper branch for finite values of $k_\perp \bar{d}_i \equiv k_\perp \bar{v}_A/\bar{\Omega}$. If we think of a realistic magnetic confinement configuration in which a mode with frequency ω around $\bar{\bar{\Omega}}$ is excited, it is clear that the magnetic field inhomogeneity will make the mode frequency equal Ω_D^p and Ω_h in relatively close regions of space. It is clear however that the spatial dependence of the relevant modes and the consequence of this on their time evolution is an important question that deserves a separate analysis (4).

A relevant factor for the problem under consideration is the polarization of the fluctuating fields in the plane perpendicular to the equilibrium magnetic field. In the cold plasma limit considered thus far and for nearly perpendicular propagation ($k_\perp^2/k_\parallel^2 \gg 1$) along the x direction, we obtain:

$$\frac{\tilde{B}_\parallel}{B} = \frac{\tilde{n}_e}{n_e}, \quad \frac{\tilde{B}_x}{B} = -\frac{k_\parallel}{k_\perp}\frac{\tilde{B}_\parallel}{B}, \quad \frac{\tilde{B}_y}{B} = -i\lambda(\omega)\frac{k_\parallel}{k_\perp}\frac{\tilde{B}_\parallel}{B} \qquad (2)$$

where

$$\lambda(\omega) = \frac{\tilde{B}_y}{i\tilde{B}_x} = \frac{i\tilde{E}_x}{\tilde{E}_y} = \frac{\omega\left[\alpha_D(\Omega_T^2-\omega^2)+\alpha_T(\Omega_D^2-\omega^2)\right]}{\alpha_D\Omega_D(\Omega_T^2-\omega^2)+\alpha_T\Omega_T(\Omega_D^2-\omega^2)} \quad . \qquad (3)$$

Notice that $\lambda(\Omega_D) = \lambda(\Omega_T) = 1$, $\lambda(\Omega_h) = \infty$ and $\lambda(\bar{\bar{\Omega}}) = -1$. Hence the fluctuating perpendicular electromagnetic fields have right-circular, linear, and left-circular polarization, at the deuterium or tritium cyclotron frequencies, the resonance frequency, and the cutoff frequency respectively. At the deuteron spin precession frequency and for $\alpha_D = \alpha_T = 1/2$, $\lambda(\Omega_D^P) \simeq 0.2$. Near this frequency λ is a rapidly varying function of ω due to the proximity of the pole of $\lambda(\omega)$ at Ω_h.

In order to evaluate the mode growth rate γ, we recall that the angular distribution of the emitted α particles, when both the deuteron and triton spin are oriented in the same direction along the magnetic field lines, is proportional to $\sin^2\theta = v_\perp^2/v^2$. Here $\varepsilon = mv^2/2$ is the particle kinetic energy and $v^2 = v_\perp^2 + v_\parallel^2$. Since the collisional slowing down does not change the particle pitch angle we consider the α-particle distribution to be of the form $f_\alpha = (v_\perp^2/v^2) f_\alpha^o(v^2)$ where $f_\alpha^o(v^2)$ is isotropic and has the characteristic dependence $f_\alpha^o \propto 1/v^3$ in the range $0.7\ \text{MeV} \lesssim \varepsilon_\alpha \lesssim 3.5\ \text{MeV}$ following the arguments given in Ref.3. The evaluation of γ is obtained by adding the contribution of the perturbed α-particle distribution to both the positive charge density and to the electrical current density. Given our choice of mode frequency and wave-number range, the α- particle contribution to the growth rate is dominated by the $\omega = k_\parallel v_\parallel + \Omega_\alpha$ resonance and is given by

$$\gamma = 2\pi^2\left\{\sum_{i=D,T} \frac{\alpha_i\Omega_i[\Omega_i-\omega\lambda(\omega)]^2}{(\Omega_i^2-\omega^2)^2}\right\}^{-1} \frac{\Omega_\alpha^3}{k_\perp^2|k_\parallel|n_e} \times \qquad (4)$$

$$\times \int_0^\infty dv_\perp^2 \left[\lambda(\omega)J_1 - \frac{v_\perp k_\perp}{\Omega_\alpha}J_1'\right]^2 \left[\frac{\partial f_\alpha}{\partial v_\perp^2} + \left(\frac{\Omega_\alpha}{\omega}-1\right)\left(\frac{\partial f_\alpha}{\partial v_\perp^2} - \frac{\partial f_\alpha}{\partial v_\parallel^2}\right)\right]_{v_\parallel = v_{\parallel 1}}$$

where J_1 is the Bessel function of argument $v_\perp k_\perp/\Omega_\alpha$ and $v_{\parallel 1} = (\omega-\Omega_\alpha)/k_\parallel$. It is clear that, for $\omega \simeq \Omega_D^P$, the anisotropic features of the α-particle distribution function result in a positive contribution to γ. In order to establish an instability condition we choose $k_\parallel$ in such a way that $m_\alpha v_{\parallel 1} \geq (2-4\Omega_\alpha/5\omega) \times 3.5$ MeV. A direct differentiation of the α- particle distribution function shows now that the integrand in Eq.(4) is positive definite except for the contribution of the sharp drop of f_α as ε_α exceeds 3.5 MeV. This negative contribution is localized near $\varepsilon_\alpha = 3.5$ MeV and may be overcome by bringing this point close to a zero of the multiplying function $[\lambda(\omega)J_1 - (k_\perp v_\perp/\Omega_\alpha)J_1']^2$.

We now turn to the question of estimating the deuteron depolariza-

tion rate as a result of its interaction with the fluctuating magnetic field. As consistent with the previously derived dispersion relation, we assume the plasma to be infinite and homogeneous so that the interaction takes place over a long time. Since the transverse wavelength of the considered perturbation is much greater than the ion gyroradius the spin does not feel its spatial variation. In addition the relevant longitudinal Doppler shift can be neglected. Then the transition probability per precession period is given by

$$w = 2\pi^2 \Omega_D^p \left|\frac{\tilde{B}_\perp}{B}\right|^2 \frac{[1-\lambda(\Omega_D^p)]^2}{1+\lambda(\Omega_D^p)^2} \delta(\Omega_D^p-\omega) \quad . \tag{5}$$

In order to give a numerical estimate for the relevant rate of depolarization a further assumption has to be made on the nature of the spectrum of the excited fluctuations. We may consider for example a narrow spectrum of frequencies of width $\Delta\omega$ around the spin resonance. If we normalize the fluctuation level to a value of the order $|\tilde{B}/B| \simeq |\tilde{n}_e/n_e| \simeq 10^{-2}$ we find the transition probability per unit time $\nu_{dep} = w\,\Omega_D^p/2\pi$ to be:

$$\nu_{dep} \simeq 4\times10^3 \left(\frac{\Omega_D^p}{10\Delta\omega}\right) \left|\frac{10^3\tilde{B}_\perp}{B}\right|^2 \left(\frac{B}{5\times10^4\,\text{gauss}}\right)^2 \text{ s}^{-1} \tag{6}$$

A similar estimate is obtained under the assumption of a broad spectrum by counting the number of the relevant standing waves and by normalizing the fluctuation level one order smaller. These estimates indicate that the rate of spin depolarization can be significantly faster than that of fusion reaction and would lead us to conclude that after thermonuclear burn begins the deuterium spins are rapidly depolarized.

/1/ Coppi, B., Pegoraro, F., and Ramos, J.: Massachusetts Institute of Technology Report PTP-83/5, Submitted to Physical Review Letters

/2/ Kulsrud, R.M., Furth, H.P., Valeo, E. and Goldhaber, M.: Phys.Rev. Letters 49, 1248 (1982)

/3/ Pfirsch, D.: in Physics of Plasmas Close to Thermonuclear Conditions, Eds. B. Coppi et al., Vol.I, p.237 (Publ.Commision of the European Communities, Directorate General, Brussels, Belgium, 1981)

/4/ Coppi, B., Pegoraro, F., and Ramos, J.: Invited Paper 2C-2 at the 1983 Sherwood Theory Meeting, (Washington, DC, 1983) Abstract Proceedings published by Laboratory for Plasma and Fusion Energy Studies, University of Maryland (College Park, MD, 1983).

Drift Wave Spectra, Energy Fluxes and Impurity Transport in Tokamak Plasmas

Günter Hasselberg and Andrê Rogister

Institut für Plasmaphysik der Kernforschungsanlage Jülich GmbH,
5170 Jülich, Association EURATOM/KFA, FRG

A. Compton and induced scattering by ions (nonlinear ion Landau "damping") are the dominant stabilization mechanisms of drift instabilities whenever they have a radiation structure. The conditions for efficient nonlinear interactions are such that coupling effectively occurs between waves of nearby frequencies $[w - w' \sim (k_\parallel - k'_\parallel)\, c_i \ll w, w'$ where $k_\parallel$ is the parallel mode number and c_i the ion thermal velocity] and therefore - in view of the linear dispersion relation - with poloidal mode numbers $k'_\theta \cong k_\theta$ and $k'_\theta \cong k_\theta^\dagger$ where $w(k_\theta^\dagger) = w(k_\theta)$. There results that the integral wave kinetic equation of weak turbulence theory can be converted into a nonlocal partial differential equation connecting the spectra at k_θ and $k_\theta^\dagger$ /1/:

$$\left[y \frac{\partial}{\partial y} \bar{f} + \frac{2-y}{1-y} \bar{f} + (2-y)^2 \frac{\partial}{\partial y} \bar{f}^\dagger + \frac{2-y}{1-y} \bar{f}^\dagger \right] f = sf \qquad (1)$$

where $\bar{f}^\dagger \equiv \bar{f}(y^\dagger)$, $y \equiv k_\theta^2 a_s^2$ (a_s is the ion-sound Larmor radius) and we assume $T_i/T_e \ll 1$ so that $y^\dagger = y^{-1}$. The normalization is defined by

$$/\tilde{n}/^2 = \frac{1}{9\pi} \frac{1}{k_{rc}^4 a_i^4} \frac{a_s^2}{/L_s L_N/} \int_0^\infty \frac{dy}{y^{3/2}} \bar{f} \qquad (2)$$

where $\tilde{n}$ is the density fluctuation level; L_s, respectively L_N, are the shear, respectively the density, lengths; k_{rc} is the cut-off radial mode number according to linear eigenmode theory. The source term s involves the linear growth rate, including shear stabilization.

The nonlinear character of Eq. (1) stems from the requirement of a positive defined spectral function f(y). Its nonlocal character appears to be the key in resolving many puzzling experimental results. These are analysed in Sections B-D.

B. Although Eq. (1) can be integrated analytically /1/ we prefer to discuss the numerical results. It is found that energy cascades, owing to close interaction (the first two terms of Eq. (1)) towards longer wavelengths if $k_\theta a_s < 1$ and towards shorter wavelengths if $k_\theta a_s > 1$. The reversed cascading direction occurs because the group velocity $\partial w / \partial k_\theta$ changes sign where $k_\theta a_s = 1$ ($y = y^\dagger$). Without the distant interaction (the last two terms of Eq. (1)) the short wavelength spectrum would remain practically empty. As $k_\theta a_s$ approaches a given value, $\cong 0.62$, corresponding to a regular singular point of the second order equation that one can derive from (1), the nonlocal character of the wave equation starts to play a significant role with energy being transferred from the long towards the correspondingly short wavelengths ($k_\theta k_\theta^\dagger a_s^2 \cong 1$). Cascading of course goes on both branches. Ultimately the long wavelength spectrum returns to thermal noise owing to shear stabilization whereas the short wavelength branch adopts a form according to Kolmogoroff's inertial subrange theory /2/ $[\partial / \partial k_\theta (|E_{\vec{k}}|^2 w \partial \varepsilon / \partial w) \cong 0]$.

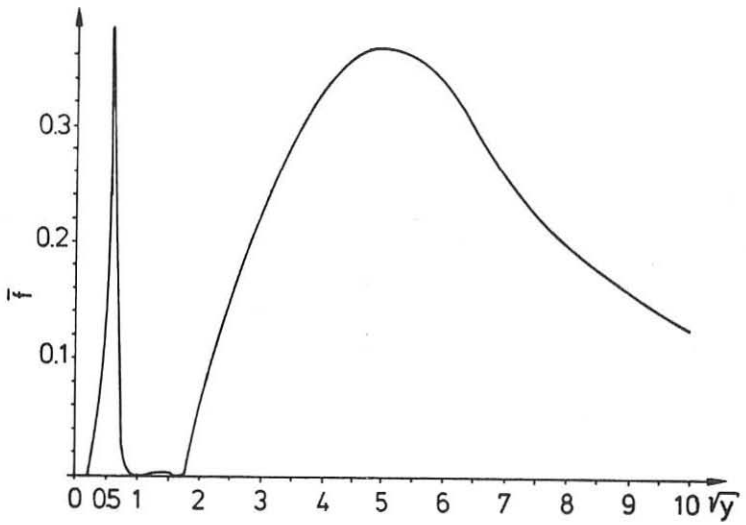

Fig. 1: Fluctuation Spectrum of the polodial electric field at the normalized radius $\varrho = 0.5$ of the moderate density TFR discharge

It is remarkable that the value of the mode number where energy transfer sets in (Fig. 1) and where the theoretical long wavelength spectrum is largest corresponds well to the observed maximum $k_\theta a_i \cong 0.5$ /3/. Experimental observations of drift turbulence on the Macrotor Tokamak /4/ further show that the spectral index at high k_θ's is $n \cong 4$ when $T_i \ll T_e$: the Kolmogoroff spectral index in comparison is n = 3.5.

C. The short wavelength branch of the fluctuation spectrum predicted by theory, but out of reach of present detection systems, is found to yield the dominant contribution (> 90 %) to the turbulent heat transfer which can be characterized by the equivalent electron heat conduction coefficient

$$K_e = \frac{2o}{9\pi} \frac{(T_i/T_e)^{1/2}}{k_{rc}^5 \, a_i^5} \quad \nu^* \sim 1 \quad \frac{a_e^2 c_e}{|L_s|} \quad \int_o^\infty \frac{dy}{y} \, (1+y) \quad \bar{f} \qquad (3)$$

where $c_e = (T_e/m_e)^{1/2}$ and $a_e = c_e/\Omega_e$ are the electron thermal velocity and Larmor radius; ν^* is the standard collisionality parameter. This result permits to resolve the apparent paradox between the following experimental results: (a) drift wave transport estimated from the measured spectra (i.e. the long wavelength branch) is insufficient to explain the anomalous fluxes obtained from the power balance equation; (b) the plasma profiles are always found to be close to marginal stability with respect to the dissipative trapped electron mode /5/ which implies a contrario that the latter should easily drive the required anomalous losses. Point (b) more precisely sug-

gests that the turbulent transport is a very rapidly increasing function of the linear growth rate, so rapid indeed as to prevent strongly unstable situations to develop. We have checked that the theory reproduces this behaviour by multiplying by 1.5 the destabilizing electron term calculated with the parameters of a moderate density TFR (Tokamak Fontenay-aux-Roses) discharge /6/. Surprisingly the heat flux increased by a factor ~ 10.

The rapid increase of the fluxes, which warrants the marginal stability of the profiles, is also the theoretical basis for the phenomenology of sawtooth relaxation proposed elsewhere /7/.

It can further be demonstrated that the particle confinement time increases with base ion atomic mass as $\tau_i \sim m_i^{5/8}$ which agrees reasonably well with the Huggill-Shefield scaling law /8/.

D. Recent experiments with injected non recyclable high Z impurities /9, 10/ have demonstrated that their transport properties are much more favourable than the neoclassical theory predicts /11/. We have thus developed a specific transport calculation to obtain the following equivalent diffusion coefficient /12/

$$(D_I)_d \simeq \frac{1}{50\pi} \frac{T_e/T_i}{k_{rc}^2 a_i^2} \frac{a_s^2 c_s}{L_s} \frac{(-L_N)}{L_s} \int_0^\infty \frac{dy}{y} K(y, y^+) \bar{f} \bar{f}^+ \qquad (4)$$

where the kernel K is symmetric in y and y^+ and L_N is the base ion density scale length. This result, valid in lowest order of the 1/Z expansion (Z is the charge of the impurity) shows that the diffusion occurs mainly through the resonant scattering of the particles with the modes of wave number k_θ and k_θ^+ : thus distant interactions are here also essential.

Numerical estimates show that $(D_I)_d \sim 2 \cdot 10^3$ cm^2/sec in TFR discharges, i.e. about ten times the neoclassical value. This result agrees well with experimental data. It is noted that $(D_I)_d$ is independent from the ratio Z/m_I. It can further be convincingly shown on the basis of Eq. (4) that the impurity confinement time increases with base ion mass as $\tau_I \sim m_i^s$, $5/8 < s < 17/8$. Both predictions are qualitatively verified by the experiments.

During the abrupt decay of the sawteeth - according to our calculations - the anomalous impurity fluxes should increase even more dramatically than the heat fluxes which, however, must then sweep across the plasma all the power accumulated in the core during the slow rise. This prediction is consistent with the observed but not understood cleaning action of the sawteeth, and, in agreement with experimental observations /9/, opposes the previous conjecture that impurity transport ought to approach the neoclassical limit at high densities to lead to accumulation at the center of the discharge.

In contrast to the diffusive impurity transport, the frictional flux, which is proportional to the base ion density gradient and is usually directed inwards, plays a marginally subdominant role in view of the larger corresponding neoclassical value. We shall not discuss it further.

E. To conclude, we should briefly explain the procedure that we followed in analysing the discharges. We considered two plasmas from TFR /6/, one

at moderate density ($N(r=o) = 0.75 \times 10^{14}$ cm^{-3}), the other at high density ($N_o = 1.2 \times 10^{14}$ cm^{-3}). The destabilizing trapped electron term was normalized to yield the proper transport rate. The fitting parameters, respectively $\mu = 1$ and $\mu = 2$ are within the "error bars" of the theoretical and experimental approximations or simplifications. The spectra were then uniquely determined and the turbulence levels and impurity fluxes were calculated at different radii. In each case, all theoretical predictions agreed simultaneously well with experiment.

We note also that the theory of nonlinear saturation sketched in B supposes that the waves have a radiating structure à la Pearlstein and Berk. We have verified that the criteria for this hypothesis to be valid were verified for the profiles considered.

References

/1/ Rogister, A., and Hasselberg, G., Phys. Rev. Lett. 48(1982)249-252 and Phys. Fluids, to appear (June 1983)

/2/ see Lin, C.C., and Reid, W.H.: Handbuch der Physik, 2nd edition, J. Springer, Berlin, (1964)438

/3/ Mazzucato, E., Phys. Rev. Lett. 48(1982) 1828-1830; TFR Group in Controlled Fusion and Plasma Physics. (Proc. 8th Eur. Conf. Prague, 1977) Institute of Plasma Physics, Prague, Vol I (1978)2

/4/ Semet, A., Mase, A., Peebles, W.A., Luhmann, N.C., and Zweben, S: Phys. Rev. Lett. 45(1980) 445-448

/5/ Manheimer, W.M., and Antonsen, T.M.: Phys. Fluids 22 (1979) 957-970

/6/ Equipe TFR: in Plasma Physics and Controlled Nuclear Fusion Research (Proc. 8th Int. Conf. Brussels, 1980) IAEA, Vienna, Vol I (1981) 425-437

/7/ Rogister, A., Hasselberg, G., and Waelbroeck, F.: paper , this conference, and Report KFA-JÜL-1829, submitted to Phys. Rev. Lett (1983); Hasselberg, G., and Rogister, A.: Report KFA-JÜL-1830, submitted to Nucl. Fus. (1983)

/8/ Hugill, J., and Sheffield, J.: Nucl. Fus. 18(1978) 15-22

/9/ Marmar, E.S., Rice, J.E., Allen, S.L.: Phys. Rev. Lett. 45 (1980) 2025-2028; Marmar, E.S., Rice, J.E., Terry, J.L., Seguin, F.H.: Nucl. Fus. 22(1982)1567-1575; Seguin, F.H., Petrasso, R., Marmar, E.S.: MIT Report PFC/JA-82-25 (1982) unpublished

/10/ TFR Group: Phys. Lett. 87A (1982) 169-174

/11/ Rutherford, P.H.: Phys. Fluids 17 (1974) 1782-1784

/12/ Rogister, A., and Hasselberg, G.: Report KFA-JÜL-1846, submitted to Nucl. Fus. (1983)

THE EFFECT OF TEMPERATURE GRADIENTS ON THE CURVATURE DRIVEN TRAPPED ELECTRON MODE

P. Andersson
Institute for Electromagnetic Field Theory and EURATOM-FUSION Research
Chalmers University of Technology
S-412 96 Göteborg, Sweden

The trapped particle modes are among the most dangerous ones in tokamaks and multi mirror machines. The curvature driven trapped electron mode (ref. 1), can become purely growing for a particular modenumber causing large anomalous transport. The growth rate of this mode can be of the order of the MHD ballooning mode.

Using the low β representation we have

$$\bar{E} = - \nabla\phi - \nabla_{\perp}\Phi \tag{1}$$

From the parallel equation of motion we obtain the circulating electron response

$$\frac{\delta n_{ec}}{n_o} = \frac{e}{T_e}\left(\phi + \frac{\alpha\omega_{*e}}{\omega}\Phi\right) \tag{2}$$

when ω_{*e} is the electron diamagnetic drift frequency and $\alpha = 1 + \partial \ln T_e/\partial \ln n$.

The trapped electron response is obtained from the electron equation of continuity, where the parallel motion is averaged to zero

$$\frac{\delta n_{et}}{n_{et}} = \frac{\omega_{*e} + \vec{k}\cdot\vec{v}_g}{\omega + \vec{k}\cdot\vec{v}_g}\,\frac{e}{T_e}(\phi + \Phi) \tag{3}$$

where $\vec{v}_g = 2\frac{T_e}{m_i\Omega_{ci}}(\hat{e}_{\parallel} \times \vec{k})$, $\hat{e}_{\parallel} = \frac{\vec{B}_o}{B_o}$ and $\vec{k} = (\hat{e}_{\parallel}\cdot\nabla)\hat{e}_{\parallel}$

The ion response can be written (ref. 2)

$$\frac{\delta n_i}{n_o} = \frac{\beta\omega_{*e}\Lambda + x\vec{k}\cdot\vec{v}_g - \frac{T_e}{T_i}(1-\Lambda)\omega}{\omega - \gamma x\vec{k}\cdot\vec{v}_g} \tag{4}$$

where

$$\Lambda = e^{-s}I_o(s), \quad \beta = 1 - \frac{\partial \ln T_i}{\partial \ln n}\cdot s\left(1 - \frac{J_1(s)}{J_o(s)}\right)$$

$x = 1 - \frac{1}{2}s\left(1 - \frac{I_1(s)}{I_o(s)}\right)$ $\quad s = k_{\perp}^2\rho_i^2$ $\quad \rho_i$ is the ion larmor radius and γ relates pressure and density perturbations ($\gamma \gtrsim 1$).

The parallel current is obtained from Maxwell's equations

$$j_{\parallel} = en_o k_{\perp}^2 \rho^2 \frac{k_{\parallel} v_A^2}{\omega} \frac{e\phi}{T_e} \tag{5}$$

where $\rho = \rho_i \cdot T_e/T_i$

Neglecting the parallel ion motion we can obtain a relation between ϕ and ϕ using the equation of continuity for the total electron density. The low frequency approximation $\nabla \cdot j_{\parallel} = 0$ then gives the dispersion relation

$$\left[\tau\omega(1-\Lambda) + \omega_{*e}(1-\beta\Lambda) + k_y v_g \frac{1}{\omega} k_y^2 \rho_i^2 \left(1 - \frac{I_1}{I_o}\right)\right]$$

$$\cdot (\omega + k_y v_g) \frac{\omega - \alpha\omega_*}{\omega - \omega_{*e}} - k_y^2 \rho^2 k_{\parallel}^2 v_A^2 \left[1 - \frac{xk_y v_g (1+\gamma/\tau)}{\omega - \omega_{*e}}\right] \tag{6}$$

$$+ k_y^2 \rho^2 DX \frac{\omega - \alpha\omega_{*e}}{\omega - \omega_{*e}} \left(1 + \frac{k_y v_g}{\omega_{*e}}\right)$$

$$= k_y^2 \rho^2 k_{\parallel}^2 v_A^2 \frac{\tau\omega(1-\Lambda) + \omega_{*e}(1-\beta\Lambda) + k_y v_g \frac{1}{2} k_y^2 \rho_i^2 (1 - \frac{I_1}{I_o}) + fk_y^2\rho^2 \frac{DX}{\omega_{*e}} \frac{(\omega_{*e} + k_y v_g)}{(\omega + k_y v_g)}}{(1-f)(\omega - \omega_{*e})}$$

where $D = -\omega_{*e} k_y v_g (1+\gamma/\tau)/k_y^2\rho^2$, $\tau = \frac{T_e}{T_i}$ and f is the fraction of trapped electrons.

We have also used the slab notations $\vec{k} \cdot \vec{v}_g \to k_y v_g \qquad k_{\perp} \to k_y$

For small ω ($\frac{1-f}{f} \frac{\tau\Delta(1-\Lambda)\omega^4}{(1+\gamma/\tau)^2 \varepsilon^2 \omega_{*e}^4} \ll 1$) we can dropp ω^4 and ω^3 terms in 6 and obtain

$$\omega\left[\omega - \omega_{*e} \frac{1+\varepsilon-\delta-\Gamma[L(k_y^2\rho_i^2) - \varepsilon\tau(1-\Lambda)] - \Delta\left[X(1-\varepsilon(1-\frac{1}{\alpha})) - \xi[L(k_y^2\rho_i^2)(1+\frac{\varepsilon}{2}) - \varepsilon\tau\alpha(1-\Lambda)]\right]}{(1-\Lambda)\Gamma + \frac{1}{\tau} - \Delta[X(1-\varepsilon) - \xi[L(k_y^2\rho_i^2)(1+\frac{\alpha}{2\varepsilon}) - (1-\Lambda)(\alpha\tau - \frac{\tau\varepsilon}{2})]]}\right]$$

$$= -k_y^2\rho^2 \kappa_g \frac{(1+\gamma/\tau)(\Gamma-1)(1-\varepsilon) - \Gamma L(k_y^2\rho_i^2) + 1 - \delta + \Delta\left[\frac{\xi}{2}\alpha\tau L(k_y^2\rho_i^2) - X\alpha(1-\varepsilon)\right]}{(1-\Lambda)\Gamma + \frac{1}{\tau} - \Delta[X(1-\varepsilon) - \xi[L(k_y^2\rho_i^2)(1+\frac{\alpha}{2\varepsilon}) - (1-\Lambda)(\alpha\tau - \frac{\tau\varepsilon}{2})]]} \tag{7}$$

where $L(k_y^2\rho_i^2) = 1 - \beta\Lambda - \frac{\varepsilon}{2} k_y^2\rho_i^2 \left(1 - \frac{I_1}{I_c}\right)$, $\delta = X\varepsilon(1 + \gamma/\tau)$, $\xi = \frac{2}{\gamma+\tau}$

$$\kappa g = \xi D/2 = \frac{1}{\tau}\varepsilon\omega_{*e}^2/k_y^2\rho^2 \quad , \quad \Gamma = \frac{1}{1-f} \quad \text{and} \quad \varepsilon = -\frac{k_y v_g}{\omega_{*e}}$$

From (6) and (7) it is clear that the effect of the electron temperature gradient vanishes if $\Delta \to 0$ (electrostatic case) while the effect of the ion temperature gradient vanishes if $k_y^2\rho^2 \to \infty$.

Neglecting ε terms the condition for pure growth is

$$1 - \beta\Lambda = -\frac{1-\Delta}{\Gamma-\Delta} \tag{8}$$

showing that the ion temperature gradient decreases the mode number for pure growth since $1 - \beta\Lambda < 1 - \Lambda$.

For $k_y^2\rho^2 << 1$ we have, still neglecting ε terms and assuming $J = \gamma = 1$

$$\omega(\omega - \omega_{*e}) = -k_y^2\rho^2\kappa g \left[2 + \frac{(2\Gamma - 1) + (2 - \alpha)\Delta}{1 - \Delta}\right] = 0 \tag{9}$$

The destabilizing electromagnetic effect in this region is then reduced by the electron temperature gradient.

For $k_y^2\rho^2 >> 1$ we have

$$\omega(\omega + \omega_{*e} \frac{\Gamma - 1}{\Gamma+1+\Delta\alpha(\frac{1}{\varepsilon} - 1)}) = -k_y^2\rho^2\kappa g \frac{\Gamma - 1 - \frac{\alpha\Delta}{2}}{\Gamma + 1 + \Delta\alpha(\frac{1}{\varepsilon} - 1)} \tag{10}$$

The electron temperature gradient is here found to enhance the electromagnetic effect which is mostly stabilizing. The effect of inhomogeneous curvature was studied in ref. 3 in the absence of temperature gradients and found to show a small increase in the electromagnetic character of the mode.

References:

/1/ Coppi, B., and Rewoldt, G.: Phys. Rev. Lett. 33 (1974) 1329.

/2/ Pegaro, F., and Shep, T.J.: Phys. Fluids 24 (1981) 478.

/3/ Andersson, P., and Weiland, J.: Phys. Rev. A. 27 (1983) 1556.

Ripple-induced Radial Diffusion of Fast Ions in Tokamaks

H. Hamnén, A. Bondeson, D. Anderson, M. Lisak and W.G.F. Core*

Institute for Electromagnetic Field Theory

Chalmers University of Technology

S-412 96 Göteborg, Sweden

*JET Joint Undertaking

Abingdon, Oxfordshire, England

Inherent in the tokamak devices is a small component of toroidal field ripple, due to the finite number of toroidal field coils. This ripple component could have a considerable effect on bulk plasma transport processes and fast ion behaviour. In particular, fast ions, such as alpha particles and fast injected ions, could become trapped in ripple wells, thereby drifting vertically out of the containment region. This process becomes unimportant when $\alpha \equiv \varepsilon |\sin\theta| / Nq\delta$ exceeds unity. However, another important process still persists, [1], namely the ripple component causes a small variation in the location of the trapped particles' bounce points. Connected with this is a small variation in radial position, corresponding to a diffusive process, where the appropriate diffusion coefficient has been calculated in ref [1]. We analyze the Fokker-Planck equation, including this radial diffusion. Assuming that the ripple strength is given by $\delta(r) \sim r^{\lambda}$, we show that λ must be larger than 5 to avoid excessive losses of α-particles. Thus, this process could pose relatively stringent design constraints on the toroidal field coils.

References

[1] R.J. Goldston, H.H. Towner, J. Plasma Phys., 26 (Oct. 1981), 283.

Preliminary Abstract (4-page paper not received in time).

A NONLINEAR GYROKINETIC EQUATION

OBTAINED BY INTEGRATION ALONG UNPERTURBED ORBITS

Jan Weiland
Institute for Electromagnetic Field Theory and
EURATOM-FUSION Research
Chalmers University of Technology
S-412 96 Göteborg, Sweden

Abstract

A nonlinear gyrokinetic equation for low β plasmas has been derived using the simple method of integration along unperturbed orbits. The result is applied to large mode number flute modes and previous results are recovered for the drift and first order Larmor radius terms.

Introduction

The problem of describing low frequency perturbations in inhomogeneous magnetized plasmas has recently attracted much attention. A major problem is the complicated unperturbed orbit in inhomogeneous magnetic fields, making an integration along unperturbed orbits complicated. To deal with such situations a gyrokinetic approach has been developed for modes with $\omega \ll \Omega_{ci}$. This method requires, however, a transformation to the guiding centre phase space which involves extensive tensor formalism /1,2/. In the present work we make use of the integration along unperturbed orbits to derive a nonlinear gyrokinetic equation without performing the full orbit integration. This method provides a substantial simplification of previous derivations.

Analytic Formulation

In Fourier space we may obtain the perturbed distribution function by an integration along unperturbed orbits as

$$f_{k,\omega} = f^{(1)}_{k,\omega} + f^{(2)}_{k,\omega}$$

where

$$f^{(1)}_{k,\omega} = -\frac{q}{m}\int_0^\infty \left[\vec{E}_{k,\omega} + \frac{1}{c}(\vec{v} \times \vec{B}_{k,\omega})\right]\cdot \frac{\partial f_o}{\partial \vec{v}}\, e^{-i\alpha(\tau)} d\tau \qquad (1a)$$

$$f^{(2)}_{k,\omega} = -\frac{q}{m}\int_0^\infty \sum_{k',\omega'} \left[\vec{E}_{k'\omega'} + \frac{1}{c}(\vec{v} \times \vec{B}_{k'\omega'})\right]\cdot \frac{\partial f_{k-k',\omega-\omega'}}{\partial \vec{v}}\, e^{-i\alpha(\tau)} d\tau \qquad (1b)$$

and

$$\alpha(\tau) = \int_0^\tau \left[\vec{k}\cdot\vec{v}(\tau) - \omega\right] dt = \frac{k_\perp v_\perp}{\Omega_c}\left[\sin(\Omega_c\tau + \varphi - \theta) - \sin(\varphi - \theta)\right] - \int_{t'}^{t} \tilde{\omega}(t'')dt''$$

where

$$\tilde{\omega}(t) = \omega - k_{\parallel} v_{\parallel} - \vec{k} \cdot \vec{v}_c(\tau)$$

and $\tau = t - t'$ where t' is the time along the orbit.

Here φ is an arbitrary phase angle of the gyrovelocity, θ is the angle in the perpendicular plane of $\vec{k}_{\perp}$ and $\vec{v}_c$ is the curvature drift which due to its inhomogeneity is time dependent along the orbit. The remaining notations are standard.

We will here assume a locally Maxwellian distribution where

$$\frac{\partial f_o}{\partial \vec{v}} = - \left(\frac{\vec{\kappa}}{\Omega_c} + \frac{m}{T} \vec{v} \right) f_o \tag{2}$$

and $\vec{\kappa} = - \nabla f_o / f_o$

We will also use the low β field representations

$$\vec{E}_{k,\omega} = - i\vec{k}\phi_{k,\omega} + i \frac{\omega}{c} A_{k,\omega} \hat{e}_{\parallel} \quad , \quad \vec{B}_{k,\omega} = i(\vec{k} \times \hat{e}_{\parallel}) A_{k,\omega} \tag{3}$$

Introducing now $\omega_* = - \vec{k} \cdot \frac{\vec{\kappa} T}{m \Omega_c}$ we find

$$\left[\vec{E}_{k,\omega} + \frac{1}{c} (\vec{v} \times \vec{B}_{k,\omega}) \right] \cdot \frac{\partial f_o}{\partial \vec{v}} = i \frac{m}{T} f_o \left[(\vec{v} \cdot \vec{k} + k_{\parallel} v_{\parallel} - \omega) \phi + (\omega - \omega_*) \left(\phi - \frac{v_{\parallel}}{c} A_{\parallel} \right) \right] \tag{4}$$

Here the first part gives a total derivative when inserted into (1a) and can be integrated immediately. The second term gives, for time independent $v_{\parallel}$, an integral of only the exponential factor. We will here evaluate this term by dividing the integration into steps of gyroperiods.

$$\int_o^{\infty} e^{-i\alpha(\tau)} d\tau = \sum_j \Delta\tau \frac{1}{\Delta\tau} \int_{\tau_j}^{\tau_j + \Delta\tau} e^{-i\alpha(\tau)} d\tau = \sum_j \Delta\tau \langle e^{-i\alpha(\tau_j)} \rangle \approx \int_o^{\infty} \langle e^{-i\alpha(\tau_j)} \rangle d\tau \tag{5}$$

Here $\Delta\tau = \frac{2\pi}{\Omega_c}$, $\langle\ \rangle$ means gyroaverage and the last equality is valid if $\tilde{\omega} << \Omega_{ci}$. Expanding $e^{-i\alpha(\tau)}$ in Besselfunctions we find

$$\langle e^{-i\alpha(\tau)} \rangle = e^{iL_k} J_o(\xi_k) e^{i \int_t^{t} \tilde{\omega}(t'') dt''} \tag{6}$$

where $L_k = (\vec{v} \times \hat{e}_{\parallel}) \cdot \vec{k} / \Omega_c$ and $\xi_k = \frac{k_{\perp} v_{\perp}}{\Omega_c}$.

After inserting (4), (5) and (6) in (1b) we now change the integration variable to t', i.e.

$$\int_o^{\infty} d\tau \rightarrow \int_{-\infty}^{t} dt'$$

and differentiate with respect to t. We then obtain the usual linear gyrokinetic equation which we, for future use formulate as

$$f^{(1)}_{k,\omega} = -\frac{q f_o}{T} H_{k,\omega} \; ; \quad H_{k,\omega} = \phi_{k,\omega} + \Gamma_{k,\omega} e^{iLk} \tag{7}$$

$$\Gamma_{k,\omega} = \frac{\omega_* - \omega}{\tilde{\omega}} (\phi_{k,\omega} - \frac{v_\parallel}{c} A_{k,\omega}) J_o(\xi_k)$$

In order to obtain an explicit solution from (1b) we have to substitute (7) in the nonlinear term. As it turns out, averages of the form $\langle \vec{k}_i \cdot \vec{v}(\tau) e^{i\vec{k}_j \cdot \vec{v}(\tau)} \rangle$ are a factor Ω_c/ω larger when $\vec{k}_i$ and $\vec{k}_j$ are not parallel and $\langle e^{i\vec{k} \cdot \vec{v}(\tau)} \rangle$ is comparable to the case where $\vec{k}_i$ and $\vec{k}_j$ are parallel. Then including only the leading order terms we obtain in analogy with (5)

$$f^{(2)}_{k,\omega} \simeq \left(\frac{q}{T}\right)^2 f_o \sum_{k'} \int_o^\infty \left\{ G(\xi_k) \phi_{k',\omega'} \phi_{k-k',\omega-\omega'} - \frac{T}{m v_\perp} (\phi_{k',\omega'} - \frac{v_\parallel}{c} A_{k',\omega'}) i\Gamma_{k-k',\omega-\omega'} \right.$$
$$\left. (R(\xi') + Q(\xi')) \right\} d\tau \tag{8a}$$

where

$$G(\xi) = \langle i\vec{k}' \cdot \vec{v}_\perp e^{-i\alpha_k(\tau)} \rangle \tag{8b}$$

$$R(\xi') = \langle i\vec{k}' \cdot \vec{v}_\perp \frac{\partial L_{k-k'}}{\partial v_\perp} e^{-i\theta(\tau)} \rangle \tag{8c}$$

and $$Q(\xi') = \langle i\vec{k}' \cdot (\hat{e}_\parallel \times \hat{v}_\perp) \frac{\partial L_{k-k'}}{\partial \varphi} e^{-i\theta(\tau)} \rangle \tag{8d}$$

where $\theta(\tau) = \alpha_k(\tau) - L_{k-k'}(\tau)$. The averages are here only evaluated for the gyropart of $v_\perp$ and the calculations are straightforward after using expansions in exponential functions and Besselfunctions. The results are

$$G(\xi) = \frac{v_\perp}{k_\perp} (\vec{k} \times \vec{k}') \cdot \hat{e}_\parallel e^{iL_k} \frac{\partial}{\partial \xi} J_o(\xi_k) \, e^{i \int_{t'}^{t} \tilde{\omega}(t'')dt''}$$

$$R(\xi_{k'}) + Q(\xi_{k'}) = i \frac{v_\perp}{\Omega_c} (\vec{k} \times \vec{k}) \cdot \hat{e}_\parallel \, e^{iL_k} J_o(\xi_{k'}) \, e^{i \int_{t'}^{t} \tilde{\omega}(t'')dt''}$$

We now change the integration variable to t' as in the linear case and differentiate with respect to t. We then observe that the first "adiabatic response" term in (8a) cancels upon summation over $\vec{k}'$. We then obtain the nonlinear part of the gyrokinetic equation

$$(\omega - k_\parallel v_\parallel - \vec{v}_c \cdot \vec{k}) f^{(2)}_{k,\omega} = \frac{q^2 f_o}{mT\Omega_c} \sum_{\substack{k'+k''=k \\ \omega'+\omega''=\omega}} (\vec{k}' \times \vec{k}'') \cdot \hat{e}_\parallel J_o(\xi_{k'}) e^{iL_k} (\phi_{k',\omega'} -$$

$$- \frac{v_\parallel}{c} A_{k',\omega'}) (\phi_{k'',\omega''} - \frac{v_\parallel}{c} A_{k'',\omega''}) \frac{\omega''_* - \omega''}{\tilde{\omega}''} J_o(\xi_{k''}) \tag{9}$$

In (9) as in the expression for $f^{(1)}_{k,\omega}$ we may make the transformation $i\vec{k} \to \nabla$ and use the gyrokinetic equation as an eigenvalue equation. In the WKB limit when the space variation is quasiharmonic we may use (9) to derive coupling-factors for nonlinear interactions. For the low frequency perturbations considered here, dispersion relations can usually be obtained by using quasi-neutrality. For this purpose we add the linear and nonlinear density responses obtainable by integrating (7) and (9) over velocity. Particularly simple results are obtainable if we can expand the Besselfunctions. In particular we obtain to lowest order in Larmor radius if $\omega >> k_\parallel v_t$ and we drop nonlinear curvature effects

$$\frac{\delta n^{(2)}_{k,\omega}}{n} = \frac{q^2}{mT\Omega_c\omega} \sum_{\substack{k'+k''=k \\ \omega'+\omega''=\omega}} (\vec{k}' \times \vec{k}'')\cdot\hat{e}_\parallel \left[\frac{\omega''_*}{\omega''} (1 - \tfrac{1}{2}k''^2_\perp\rho^2) + \tfrac{1}{2}k''^2_\perp\rho^2 - \right.$$

$$\left. - \tfrac{1}{2}k'^2_\perp\rho^2(1 - \frac{\omega''_*}{\omega''}) \right]\phi_{k'\omega'}\phi_{k''\omega''} \qquad (10)$$

In (10) the first two terms are proportional to the linear density perturbation. These terms will cancel in a dispersion relation if linear quasineutrality is used in the nonlinear terms. The last term in (10) is the nonlinear polarisation drift. It can be obtained from $n_0\nabla\cdot\vec{v}_p$ in a fluid description by substituting the $\vec{E} \times \vec{B}$ and perturbed diamagnetic drifts into the convective part of the operator $\frac{d}{dt}$ in the polarisation drift and using the linear density response in the diamagnetic drift. We may then recover the coupling factors for ballooning modes obtained in /3/.

References

/1/ Frieman,E.A., and Chen, Liu: Phys. Fluids 25 (1983) 502.

/2/ Dubin, D.H.E., Krommes, J.A., Oberman, C., and Lee, W.W.: Princeton University preprint PPPL-1969(1983).

/3/ Weiland, J., and Mondt, J.P.: Phys. Rev. Lett. 48 (1982) 23.

A NEW PSEUDO-CLASSICAL TRANSPORT THEORY FOR TOKAMAK PLASMAS

Lucio De Meio and Aldo Nocentini
Istituto di Meccanica dell'Università
Trieste, Italy.

The neoclassical transport theory of tokamak plasmas /1/, being theoretically well founded, has been widely studied in the past to get precise predictions on tokamaks' behaviour. Unfortunately, these predictions are clearly contradicted by the experimental results. This is attributed to turbulence, and to the "anomalous transport" it yields. On the other hand, being the problem of non-linear waves in toroidal geometry extremely difficult to solve, anomalous transport theory has not been developed so far to allow the derivation of a well defined set of transport coefficients. The consequence of this situation is that presently, for practical purposes, the expressions of the transport coefficients are conjectured from the results of the experiments and not inferred from a theory, what is clearly unsatisfactory.

A possible compromise to get out of this situation is to assume that the whole effect of turbulence consists in the modification of some parameters of the collisional theory, and to re-derive consistently the fluxes remaining in the framework of neoclassical theory. The fluxes obtained by this method have then well determined expressions, in which a relatively small number of coefficients appear, which have to be determined by comparison with the experimental results. The so called "pseudo-classical" transport model /2,3/, in which the whole effect of turbulence is assumed to consist in the enhancement, by an anomaly factor, of the classical transport coefficients, is an example of this kind of approach. Adopting it, in this paper we develop what could be called a "pseudo-neoclassical" transport model. More precisely, we develop the neoclassical transport theory assuming that the electron-electron collision frequency is anomalous,

$$\nu_e^{an} = A\,\nu_e \quad , \tag{1}$$

that the electron-ion and the ion-ion collision frequencies are classical, and that the thermal force too remains classical. This is equivalent to assume that turbulence affects only the electrons, increasing the frequency of their mutual collisions, but not influencing the thermal force. To restrict the effect of turbulence to the electron species is clearly suggested by the experimental results, which are in good agreement with the predictions of neoclassical theory as far as the ion heat flux and the electric resistivity are concerned, but exhibit an electron heat flux much larger, by orders of magnitude, than the neoclassical one. We do not discuss here which kind of waves could yield this effect.

In Eq.(1) ν_e is the classical electron-electron collision frequency for 90° scattering and $A>1$ is an enhancement factor which can depend on the value of the equilibrium quantities (density, temperature, etc.), and will be chosen in such a way that the radial heat flux of the electrons is consistent with the experimental value. We anticipate here that this implies $A>100$. As a consequence of this choice the electrons turn out to be in the Pfirsch-Schlüter regime in practically the whole parameter region of existing tokamaks, hence we develop here only the Pfirsch-Schlüter (as far as the electrons are concerned) regime. Moreover we restrict to magnetic surfaces

with circular, concentric cross sections, in the large aspect ratio limit.

The collision dominated regime for the electrons (which does not coincide anymore, even in a two species plasma, with the collision dominated regime for the ions) is defined by

$$\eta_e^{an} = A\,\eta_e = A\,r\nu_e B / r_{Le} B_p \Omega_e > 1 \quad , \tag{2}$$

where r is the small radius of the magnetic surface under consideration, B and B_p, respectively, the total and the poloidal magnetic field, r_{Le} and $\Omega_e = eB/m_e c$, respectively, the Larmor radius and the gyrofrequency of electrons (c is the speed of light, e the elementary charge). Hence for $A>1$ the transition between the weakly collisional and the collision dominated regimes occurs at much lower classical collisionalities. The thermal coupling between ions and electrons is negligible if

$$s_{an}^2 = 3\mu\{\chi_{i,\parallel}^{-1} + (\chi_{e,\parallel}^{an})^{-1}\}\, NB^2 r^2 / B_p^2 \tau_e < 1 \quad , \tag{3}$$

were $\mu = m_e/m_i$ is the mass ratio, N is the electron number density,

$$\tau_i = \frac{3\sqrt{m_i}\,T_i^{2/3}}{4\sqrt{\pi}\Lambda e^4 N} \quad , \qquad \tau_e = \frac{3\sqrt{m_e}\,T_e^{3/2}}{4\sqrt{2\pi}\Lambda e^4 N} \quad , \tag{4}$$

$$\chi_{i,\parallel} = 3.9 N T_i \tau_i / m_i \quad , \qquad \chi_{e,\parallel}^{an} = A^{-1}\, 5.51\, N T_e \tau_e / m_e \quad , \tag{5}$$

are the classical collision times and the parallel heat conductivities, for ions and electrons respectively, and T the temperature. The Pfirsch-Schlüter regime is defined by the two inequalities (2) and (3), which separate it from the plateau and from the highly collisional regime, respec-

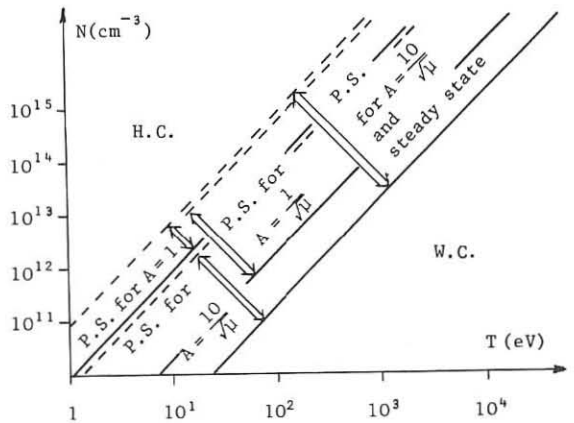

Fig.1.: The Pfirsch-Schlüter region of the Frascati tokamak (safety factor at the wall 3, major radius 83 cm) for different values of A.

tively (see Fig.1). We see that, in comparison with the classical case A=1, it covers, for $A \gg 1$, a much larger region of the N,T parameter space of a tokamak plasma.

The derivation of the expressions of the heat and particle fluxes across the magnetic surfaces proceeds, in the presence of the anomaly factor A, as in the classical case. The important difference is now that the parallel and perpendicular electron heat conductivities are anomalous, the first one being smaller than the classical one by a factor of the order of 1/A (see Eq.5), the second one being larger than the classical one by a factor of the order of A :

$$\chi_{e,\perp}^{an} = A\sqrt{2}\, NT_e/m_e\Omega_e^2\tau_e \quad . \tag{6}$$

Hence the poloidal dependent part of the electron temperature is larger, with respect to the classical case, by the factor A, and the same happens for the toroidal contribution and the temperature gradient part of the cylindrical contribution to the radial electron heat flux averaged over the magnetic surface. Without going through the details of the derivation, we write here the relevant results:

$$\frac{\partial T_e}{\partial \vartheta} = -5\,\frac{cNT_e}{e\chi_{e,\parallel}^{an}}\,\frac{r^2 B_T}{RB_p^2}\cos\vartheta\left\{\frac{dT_e}{dr} - 0.28\,\frac{dP}{Ndr}\right\} \quad , \tag{7}$$

$$\bar{q}_e = \bar{q}_e^{cyl} + \bar{q}_e^{tor} \quad , \tag{8}$$

$$\bar{q}_e^{cyl} = -\chi_{e,\perp}^{an}\,\frac{dT_e}{dr} + \frac{3}{2}\,\frac{cNT_e}{eB}\,\frac{1}{\Omega_e\tau_e}\,\frac{dP}{Ndr} \quad , \tag{9}$$

$$\bar{q}_e^{tor} = -\frac{25}{2}\,\frac{q^2}{\chi_{e,\parallel}^{an}}\left(\frac{cNT_e}{eB}\right)^2\left\{\frac{dT_e}{dr} - 0.28\,\frac{dP}{Ndr}\right\} \quad , \tag{10}$$

$$\bar{\Gamma} = -\frac{c^2}{B}\,N\left\{\eta_\perp\left(\frac{dP}{dr} - \frac{3}{2}\,N\,\frac{dT_e}{dr}\right) + 2q^2\left[\eta_\parallel^{an}\,\frac{dP}{Ndr} + \right.\right.$$
$$\left.\left. - 0.71\,\frac{5NT_e}{2e^2\chi_{e,\parallel}^{an}}\left(\frac{dT_e}{dr} - 0.28\,\frac{dP}{Ndr}\right)\right]\right\} \quad , \tag{11}$$

where $P = N(T_e+T_i)$ is the total pressure, R the major radius of the torus, B_T the toroidal magnetic field, the bar denotes averages over the magnetic surfaces, $q = rB_T/RB_p$ is the safety factor, Γ the particle flux across the magnetic surface, $\eta_\perp$ and $\eta_\parallel^{an}$ the electric resistivities. Notice that the presence of an anomalous e-e collision frequency does not affect $\eta_\perp$, while $\eta_\parallel^{an} \cong \eta_i$ because for $A \gg 1$ the electron distribution function tends to remain locally maxwellian also in the presence of a parallel electric field.

From Eq.s(8-11) we see that the electron heat flux and the particle flux are enhanced, with respect to the classical case, by the same factor A, which should now be determined by requiring for the electron heat flux a value in agreement with the experimental findings. Doing this, we cannot ignore that the tokamak discharges are actually steady states with respect to the elec-

tron energy confinement time, and hence, in the framework of our theory, with respect to the particle confinement time too. Hence, in the absence of particle sources, we have to impose $\bar{\Gamma} = 0$, from which, at lowest order in $1/A$,

$$0.28\, dP/Ndr = dT_e/dr \quad , \qquad \text{i.e.:} \qquad N/T^{0.76} = \text{constant} \quad . \tag{12}$$

This theory leads then to a "universal" relation, Eq.(12), between the density and temperature profiles in tokamaks operating in steady state conditions (we have to stress that the particular value 0.76 depends on our assumption that the thermal force is not modified by turbulence). In these conditions the poloidal dependence of the electron temperature and the toroidal contribution to the electron heat flux across a magnetic surface are reduced, with respect to the non-equilibrium case, by a factor $1/A$. The first consequence of this is that, for steady states, the Pfirsch-Schlüter regime is no more limited, on the high-density-low-temperature side, by the condition (3), but by the condition (see Fig.1)

$$3\mu NB^2 r^2/\tau_e B_p^2 \chi_{i,\parallel} < 1 \quad . \tag{13}$$

The second consequence is that (for $A > q^2$) the electron heat flux is dominated by the cylindrical contribution, $q_e = q_e^{cyl}$ (the term proportional to the electron temperature gradient being the only one which survives). The anomalous factor A is then determined by the condition that the value of $-\chi_e^{an}\, dT_e/dr$ is equal to the experimental value found for the electron heat flux. In order to get an idea of the value so obtained for A, let us notice that for $A = q^2\mu^{-1/2}$ the electron heat flux is equal to the ion heat flux (in the Pfirsch-Schlüter regime). Hence typical values for A should range from a few hundredths to some thousandths.

In conclusion, the pseudo-neoclassical tokamak transport theory presented here implies: (i) that in the steady states observed in tokamaks the temperature and density profiles should be related by Eq.(12); (ii) that the ion heat transport (which is not influenced by e-e collisions, nor by the shape of the electron distribution function) should be neoclassical; (iii) that no Ware effect nor bootstrap current should be present (because electrons are in the Pfirsch-Schlüter regime); (iv) that the parallel electric resistivity should be equal to the perpendicular one, i.e. it should have twice its classical value. Moreover, if by some external means (for instance gas puffing) a deviation from a steady state is induced, the characteristic time to go back to a steady state should be shorter than the electron energy confinement time (measured in the steady state) by a factor $1/q^2$. In fact in such a case, as long as Eq.(12) is not fullfilled, the large terms in the toroidal contribution to the electron heat flux and in the particle flux do not cancel anymore, hence $\bar{q}_e^{tor}$, which is typically q^2 times larger than $\bar{q}_e^{cyl}$, dominates, and the value of the electron energy confinement time drops by a factor $1/q^2$ with respect to its steady state value, and the particle confinement time drops to the same value.

/1/ Hinton, F.L., Hazeltine, R.D.: Theory of plasma transport in toroidal confinement systems, Rev. Mod. Phys. 48 (1976) 239-308.
/2/ Artsimovich, L.A.: Tokamak devices, Nucl. Fus. 12 (1972) 215-252.
/3/ Yoshikawa, S.: Possibility that anomalous plasma diffusion depends on geometric factor, Phys. Rev. Lett. 25 (1970) 353-356.

A NOVEL TEST-PARTICLE APPROACH TO ANOMALOUS TRANSPORT IN TOKAMAKS

A Thyagaraja and F A Haas
Culham Laboratory, Abingdon, Oxon OX14 3DB, UK
(Euratom/UKAEA Fusion Association)

Abstract

In this paper a new derivation of test particle diffusivity in tokamaks is given. The role of collisions and the periodicity of the device is taken into account and shown to be important.

1. INTRODUCTION

Electron energy transport in tokamaks is known to be anomalous. Many authors following Callen /1/ and Rechester and Rosenbluth /2/ have discussed this anomaly in terms of test particle diffusion caused by 'ergodic' field lines. In this approach one splits the total tokamak magnetic field into a 'mean' part which defines nested surfaces (on which mean temperature and density are uniform) and a small-amplitude 'fluctuating' part. The latter is taken as given by a quasi-static ensemble with well-defined correlation functions that are in principle determined by experiment. The motion of test electrons are then considered by treating them rather like beads on a wire. The field fluctuations are then supposed to lead to a quasi-linear expression for the test particle diffusivity which is interpreted as a thermal diffusivity in this picture. The purpose of the present paper is to present a new derivation of test particle diffusion in tokamaks showing the importance of the role of collisions and the periodicity of the tokamak geometry.

2. ASYMPTOTIC SURFACE CONSTRUCTION

Consider a periodic cylinder model of a tokamak with periodicity length $2\pi R$ and minor radius a. The unperturbed magnetic field is given by $B_{oz}(r)$ and $B_{o\theta}(r)$ such that $q(r) = rB_{oz}/RB_{o\theta}$ is typically monotonic increasing in r, varying from $q(o) \gtrsim 1$ to $q(a) \simeq 3$. The radial field fluctuation must be of the form

$$\frac{\Delta B_r}{B_{oz}} = \varepsilon \sum_{|m|=1}^{\infty} \sum_{|n|=1}^{\infty} b_{mn}(r) \cos\left(m\theta + \frac{nz}{R} + \phi_{mn}\right) \qquad (1)$$

where ε is typically $< O(10^{-3})$. The amplitudes $b_{mn}(r)$ and ϕ_{mn} are assumed to be sufficiently smooth in r and could be slowly varying functions of t. It is assumed on physical grounds that either the series (1) is effectively finite or that b_{mn} dies off exponentially with $|m|$ and $|n|$. The equations of motion for test-particles are not the full Newtonian ones but take the 'kinematic' forms

$$\frac{d\vec{r}}{dt} = V_{\parallel} \frac{\vec{B}}{|\vec{B}|} \qquad (2)$$

where $V_{\parallel}$ is constant between collisions. We take $\langle V_{\parallel} \rangle = 0$ and

$\langle V_{\parallel}^2 \rangle = V_{the}^2 = (T_e/m_e)$. The average here is for a given test particle and is a time mean. It is also equivalent to an ensemble average over many test particles. The particle is also assumed to 'jump' through a distance of the order of a Larmor radius to a nearby field line at every collision.

A function $S(r,\theta,z)$ is an exact invariant of (2) (assuming the fluctuation is 'quasi-static' on the time scales τ_e, qR/V_{the}) if and only if

$$(\vec{B}_o + \Delta\vec{B})\cdot\nabla S = 0 \tag{3}$$

If $\Delta\vec{B} \equiv 0$, clearly $S \equiv S_o(r)$ is a solution of (3) for an arbitrary function S_o. It is easy to show that we can write $S = S_o(r) + \varepsilon S_1 + \varepsilon^2 S_2 + \ldots$ and satisfy (3) to any finite order in ε, provided $S_o(r)$ is suitably chosen to 'kill off' the resonant denominators that arise in calculating S_1.

For example, consider S_o defined by

$$\frac{dS_o}{dr}(r,\varepsilon) = \exp\left[-\varepsilon^{\frac{1}{2}}\left\{\sum_{|m|=1}^{\infty}\sum_{|n|=1}^{\infty}\frac{m^2}{(m+nq)^2}|b_{mn}(r)|\right\}\right] \tag{4}$$

It is easy to show (Ref. /3/) that for the given assumptions (4) defines a monotonic increasing $S_o(r,\varepsilon)$ which reduces to r as $\varepsilon \to 0$ and which is infinitely differentiable in r provided $q(r)$ and $|b_{mn}(r)|$ are such functions. We then have

$$S_1 = -qR\left[\sum_{|m|=1}^{\infty}\sum_{|n|=1}^{\infty}\left(\frac{b_{mn}(r)}{m+nq(r)}\right)\sin(m\theta + \frac{nz}{R} + \phi_{mn})\right]\frac{dS_o}{dr} \tag{5}$$

It is easy to show that $S_o + \varepsilon S_1$ is a uniformly valid asymptotic invariant of (2) to $O(\varepsilon^2)$ almost everywhere. Even in the immediate vicinity of the low order resonances the error is at most $O(\varepsilon^{3/2})$. The series can be continued to any finite order but it is not known if it ultimately diverges for non zero values of ε.

The importance of asymptotic (as opposed to exact) invariants like $S_o + \varepsilon S_1$ arises from the fact that a given test particle does not stay on a specific field line for times longer than a collision time τ_e. Since τ_e is typically (PLT : $n \sim 5 \times 10^{13}$ cm^{-3}, $T_{oe} \sim 1$ keV, $R \sim 150$ cms, $a \sim 30$ cms, $q \sim 2.0$, $\varepsilon < 10^{-3}$) is 6×10^{-6} sec and is much smaller than a confinement time - ~ 30 ms, the exact invariants along field lines (whether or not they exist!) are irrelevant as is the 'ultimate' ergodicity of a field line. Since $S_o + \varepsilon S_1$ is certainly a good constant for $t \ll qR/V_{the}\varepsilon$, we can estimate the test particle diffusion from such functions.

3. TEST PARTICLE DIFFUSION

From what we have said it follows that $\tau_e \simeq 6 \times 10^{-6}$s $\ll qR/V_{the}\varepsilon \simeq 3 \times 10^{-4}$s. Thus in a given 'time-step' τ_e, $\langle(\Delta r)^2\rangle$ can be estimated (details will be published elsewhere) to be

$$\langle(\Delta r)^2\rangle = \varepsilon^2 q^2 R^2 \sum_m \sum_n \langle b_{mn}^2(r)\rangle \frac{\left\{\sin^2\left(\frac{V_{the}\tau_e}{qR}(m+nq)\right)\right\}}{(m+nq)^2} + O\left(\frac{V_{the}^2\tau_e^2}{q^2R^2}\varepsilon^4\right) \quad (6)$$

The ensemble average $\langle b_{mn}^2(r)\rangle$ is the Fourier coefficient of the correlation function

$$\left\langle \frac{\Delta Br}{B}(r,\theta',z') \frac{\Delta Br}{B}(r,\theta'+\theta,z'+z)\right\rangle.$$

The associated test particle diffusivity is then

$$D_\perp = \frac{\varepsilon^2 q^2 R^2}{\tau_e} \sum_m \sum_n \frac{\langle b_{mn}^2(r)\rangle}{(m+nq)^2} \sin^2\left\{\frac{V_{the}}{qr}(m+nq)\tau_e\right\} \quad (7)$$

Clearly $D_\perp$ is independent of the choice of S_o as it should be. It could also be directly derived from the Langevin equation (2) taking explicit account of collisions and the statistics of the random 'parameters' $V_{\shortparallel}$ and $\Delta\vec{B}$. The formula is valid in a periodic system and takes due account of the time scales τ_e and qR/V_{the}. At high collisionality, $\tau_e \gg qR/V_{the}$ and $D_\perp$ reduces to the Callen form,

$$D_\perp = \varepsilon^2 v_{the}^2 \tau_e \sum_m \sum_n \langle b_{mn}^2(r)\rangle$$

$$= \chi_{\shortparallel}\ \text{(Braginskii)}\ \left\langle\left(\frac{\Delta Br}{B}\right)^2\right\rangle. \quad (8)$$

If $qR/V_{the} \ll \tau_e \ll \frac{qR}{V_{the}\varepsilon}$,

$$D_\perp \simeq \varepsilon^2 \chi_{\shortparallel}\ \text{(Braginskii)} \sum_m \sum_n \langle b_{mn}^2(r)\rangle \delta_{m,-nq} \quad (9)$$

which can also be written as

$$D_\perp \simeq \varepsilon^2 \pi R V_{the} \sum_m \sum_n \langle b_{mn}^2(r)\rangle \delta\left(\frac{m+nq}{q}\right) \quad (10)$$

Equation (9) is identical with the Rechester-Rosenbluth /2/ expression if the sum over n is replaced by an integral. This replacement is only valid in an infinite system. In general (9) is the correct form in tokamaks.

4. DISCUSSION

It is easy to see that $D_\perp$ given by (9) only leads to a flattening of the temperature profile at the resonant points. Equation (7) does appear to be capable of predicting the correct order of $\chi_{\perp e}^{obs}$ given typical fluctuation

levels. In particular (7) implies that an upper limit to test particle diffusion is given by the simple expression

$$D_{\perp max} = \frac{\varepsilon^2 q^2 R^2}{\tau_e} \sum_m \sum_n \frac{\langle b^2_{mn}(r) \rangle}{(m + nq)^2} \qquad (11).$$

Although singular at the resonant points, $D_{\perp max}(r)$ does lead to smooth $T_{oe}(r)$ profiles. It does not need to invoke any topological properties of the field lines and yet reduces in suitable limits to formulae which supposedly depend crucially on such properties. In the absence of collisions, the successive 'steps' of a random walk are completely correlated. In this case, even if the field line 'looks' ergodic it is difficult to see how a non-zero diffusivity arises except possibly at resonant points. Furthermore, the equations (2) are reversible and hence could not be expected to yield physical diffusion in a periodic (as opposed to an infinite) system. Equations (7) and (11) obviate the need to consider such philosophic questions and furthermore make quite specific and testable experimental predictions.

REFERENCES

/1/ Callen, J. D. Phys. Rev. Lett. 39 (1977) 1540-1542.

/2/ Rechester, A. B., and Rosenbluth, M. N. Phys. Rev. Lett. 40 (1978) 38-40.

/3/ Arnold, V., and Avez, A. Ergodic Problems of Classical Mechanics, Benjamin Inc., New York 1968.

Simulation of convective electron transport in T-10 tokamak

A.V.Gurevich, Ya.S.Dimant
Lebedev Institute of Physics

Yu.N.Dnestrovskij
I.V.Kurchatov Institute of Atomic Energy

D.P.Kostomarov, A.P.Smirnov
M.V.Lomonosov State University
Moscow, USSR

1. Three classical factors, at least, distort the electron distribution function in tokamaks:

1) constant longitudinal electric field,
2) pulsed electric field arising at MHD-mixing,
3) drift of electrons trapped in the ripples of the magnetic field.

A kinetic equation for the electron distribution function, $f(t, \mathcal{E}, s, \rho)$ is represented as /1-2/:

$$\frac{\partial f}{\partial t} + \frac{\partial I_{\mathcal{E}}}{\partial \mathcal{E}} + \frac{\partial I_s}{\partial s} + \frac{1}{\rho}\frac{\partial}{\partial \rho}\left(\rho I_\rho\right) = 0 \qquad (1)$$

where, $\mathcal{E}$ is the electron energy, s is the dimensionless magnetic moment of electron, ρ is the coordinate of the magnetic surface. A simultaneous effect of the factors (1) - (3) on the electron distribution function in T-10 is analyzed by the numerical integration of the equation (1) in this paper.

2. Let's estimate the characteristic values of the main parameters which have the effect on deviation of the f-function from the maxwellian one. An effect of the longitudinal electric field is described by a parameter $\gamma = E/E_{cr}$, where $E_{cr} = 4\pi e^3 n e n \Lambda / T_e$. For T-10, $n = 2\text{-}5 \cdot 10^{13}\ cm^{-3}$, $T_e = 1\text{-}1.3\ keV$ the loop voltage, $U = 1{,}5 - 2$ V, $\gamma \sim 0.005 - 0.02$.

The pulsed electric field emerges at a time of mixing, and its duration is $\tau_p \sim 100\ \mu s$. A model of mixing suggested by B.B.Kadomtsev /3/ for a change in the poloidal flux, $\delta\psi$, in the core gives $\frac{1}{c}\delta\psi = U_p \tau_p \lesssim 3\text{-}4 \cdot 10^{-3}$ Vs, $U_p \lesssim 40$ V $\sim (20\text{-}30)\,U$. The 2-d MHD calculations of mixing /4

show that $E_{\parallel}$ is localized close to the resonance surface, $\rho \sim \rho_s$ in this case, $U_p \gtrsim (3\text{-}4)U$.

The ripple in T-10 is great: $\Delta = (B_{max} - B_{min})/B_o \sim 0.1$ at the radius ρ = 35 cm.

Calculations were carried out for the plasma parameters corresponding to the experiments /5/: $T_e(o)$ = 1 keV, $n(o) = 2.5 \cdot 10^{13}\ cm^{-3}$, $B_o = 1.5\ T$. The maxwellian functions were preset as initial distributions. The equations (1) was integrated with respect to time. An intensity of radiation from the unit volume, I, and a flux along a vertical chord, I_ν were calculated by the f-function:

$$I(\varepsilon, \rho, \chi) = \frac{1}{\varepsilon} \int_{\varepsilon}^{\infty} d\varepsilon \int_{s=o}^{s=1+x/R} f\, d\left(\sqrt{1 - \frac{s}{1+x/R}}\right), \quad I_\nu = \int_o^{\sqrt{a^2-x^2}} 2I\, dz, \quad x = R + \rho\cos\vartheta$$

The spectra εI_ν at U_p =0 for X=0;8 and ± 16 cm, at U =1.5V(γ = 0.015) are given in Fig.1. The dashed trace shows the experimental spectra for X=0 and 8 cm related to the calculated ones at ε =5 keV. One can see that the distortion of the experimental spectra is more pronounced than that of the calculated ones. For a chord X=16 cm, the main distortion is introduced into the spectrum by a drift of supertrapped electrons.

Let's consider the effect of a pulsed field. Choose the function $U_p = \lambda U \Pi(t; t_o, t_o + \tau_p) \Pi(\rho; \rho_1, \rho_2)$ where $\Pi(x; x_1, x_2)$ is the Heaviside function. In Fig.2, the spectra, εI_ν at different times are shown at λ=10, t_o =1 ms, τ_p = = 0,1 ms, ρ_1 = 0, ρ_2 = 0,4 a for the chords X=0 and X=16 cm. The distortion of spectra reaches the region $\rho > \rho_2$ with a delay. A turn of longitudinally-accelerated electrons by pitch angles occurs due to collisions in the region, $\rho < \rho_2$,first. Then, the "tails" of the distribution function at the periphery are enhanced due to the drift in the ripples.

One should make an averaging on saw-tooth oscillation period τ_z for the comparison of the calculated spectra with the measured ones. The energy spectra $\varepsilon \overline{I}_\nu = \varepsilon/\tau_z \int_{t_o}^{t_o+\tau_z} I_\nu\, dt$ for the chords x=0;8 and 16 cm and for the parameters corresponding to Fig.2 are given in Fig.3. Here, the dashed trace shows the experimental spectra /5/. The effective electron temperature

profiles, T_{eff} calculated for different parts of the spectra at λ =0 and at λ =10 are given in Fig.4. The solid traces correspond to the experimental profiles. The dash-dotted traces in Figs.3,4 are the results of calculations for the case, when the pulsed electric field is localized close to the resonance surface, ρ_s =0.35 a(λ =23, ρ_1 =0.3a, ρ_2 =0.4a). In this case, the spectra along the chords, X=0 and X=8 cm, and the effective temperatures are in a reasonable agreement with the experiment.

References

1. A.V.Gurevich, Ya.S.Dimant, Nucl.Fusion, 21 (1981) 159.
2. A.V.Gurevich, Ya.S.Dimant, Yu.N.Dnestrovskij, K.A.Razumova, Pis'ma v JETP, 26, N 11 (1977) 733.
3. B.B.Kadomtsev, Fizika Plazmy, 1 (1975) 710.
4. A.F.Danilov, Yu.N.Dnestrovskij, D.P.Kostomarov, A.M.Popov, Fizika Plazmy, 2 (1976) 167.
5. N.D.Vinogradova, Yu.V.Esipchuk, P.E.Kovrov, K.A.Razumova et al., Plasma Phys. and Contr. Nucl.Fusion Res., 1978, Vienna, 1 (1979) 257.

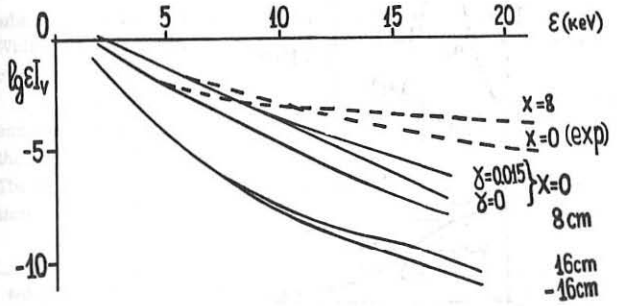

Fig.1. λ=0

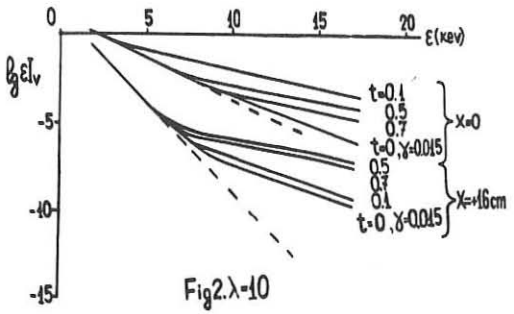

Fig 2. λ=10

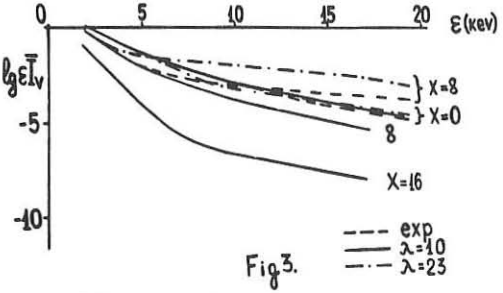

Fig 3.

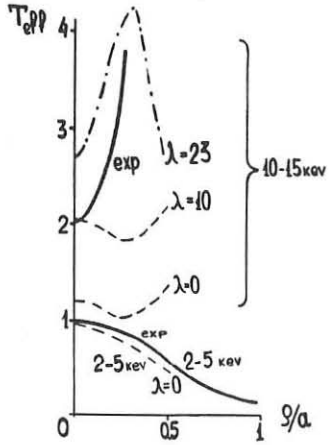

Fig 4.

ANOMALOUS PINCHING AND PARTICLE BALANCE IN TOKAMAK

Yu.N.Dnestrovskij, S.V.Neudatchin, G.V.Pereverzev,
A.R.Polevoj
I.V.Kurchatov Institute of Atomic Energy,
Moscow, USSR

I. The time of particle confinement, τ_p, in tokamak is known to be anomalous /1-3/. At the same time, determination of the particle transport coefficients, until now, according to the experimental data, is characterized by a great uncertainty. First, the particle transport is provided by a few differently - directed processes; second, the sources of particles are very skinned. The mutual compensation of differently - directed fluxes in the particle transport equation:

$$\frac{\partial n}{\partial t} = \frac{1}{r}\frac{\partial}{\partial r} r \left(D \frac{\partial n}{\partial r} + n v_p\right) + nN < \sigma_{ion} v_e > \qquad (1)$$

is extremely great at the steady-state of the discharge. Therefore, for determining the partial values of the pinching flux $\Gamma_p = - n v_p$ and those of the diffusion flux, $\Gamma_D = - D \frac{\partial n}{\partial r}$ one needs to study different non-stationary processes.

Simulation of the stationary density distribution and that of three non-stationary processes: MHD-mixing by the internal mode m=1, density drop at ECRH and at the pulsed gas puffing are done in this paper. The results obtained on T-1O /4/, T-11 /5/, TM-4/6/, Tuman-3 /7/, PLT /3/, FT /8/, Alcator-A /9/ and on Alcator-C /10/ are analyzed. It is shown that the diffusion coefficient D and the pinch velocity v_p are determined by the formulas

$$D = \frac{\mathcal{Ae}}{n(r)} \approx \frac{\chi_e}{2 \div 3}, \qquad v_p = \alpha_p \left(\frac{r}{R}\right)^2 c \frac{E_{\parallel}}{B_p}, \qquad (2)$$

where χ_e is the electron thermal conductivity coefficient, $\mathcal{Ae}$ = const (r), α_p = 50 - 70. Within the core ($r < 0.2a$), the relationship (2) gives the pinch velocity close to the neoclassical one, v_p^{neo}.

2. In the stationary case, the source of particles is practically absent in the core, and the particle balance equation, $\Gamma_D + \Gamma_p = 0$, allows to bind the ratio $\alpha_p / \mathcal{Ae}$ with the parameter γ which characterizes a peak of the density profile, $n(r)=n(o)\,(1 - \gamma(r/a)^2)$. The results are given in Table I. The last two columns follow from the additional assumption, $\mathcal{Ae} = n\chi_e/(2 \div 3)$

Table I

tokamak	U (v)	B(T)	q (0)	$n_e(0)$ 10^{13} cm^{-3}	γ	$10^{17} \frac{\alpha_p}{\mathcal{Ae}}$	$10^{-17}\mathcal{Ae}$	α_p
T - 10	1.5	3	1	5.5	1.3	150	0.4	60
TM-4	2.7	1.5	1.2	2.5	1.15	80	1.0	80
FT	1.9	7	1	76	1.75	20	2.4	50
PLT	1.5	2.5	1	2.6	1.2	90	0.8	70

3. In the process of saw-tooth oscillations, the density gradient within the mixing zone is usually low and $\Gamma_D \ll \Gamma_p$. As a result, the equation (1) includes only one uncertain parameter, α_p, which can be found from the measured amplitude of density oscillations.

Table 2

tokamak	U (v)	B (T)	$n(o)$ (10^{13})	τ_E (ms)	n/n (%)	α_p	v_p r=0.2a cm/s	v_p^{neo}
T - 10	2.2	1.5	2.2	3.5	6	56	35	40
TM-4	3	2	4.5	0.6	11	70	140	140
Tuman-3								
(I)	25	0.25	1.6	0.7	36	50	1000	600
(II)	2	0.4	1.8	0.8	23	50	500	350

If the mixing zone is great, $\Gamma_D \sim \Gamma_p$ and one will need to use (1). The density distributions along radius before and after mixing in the regime I are given in Fig.1 for the tokamak Tuman-3. The results of calculation are shown with a dashed trace ($\alpha_p = 50$, $æ = 1.5 \cdot 10^{17} cm^{-1} s^{-1}$).

4. The density drop at ECRH was observed on ISX-B, T-10, TM-4, JET-2. In our model, it follows from a decrease in the pinch velocity, v_p, with a decrease in $E_{//}$. The solid traces in Fig.2 show the experimental profiles, n(r), for T-10. The calculated profiles are shown with the dashed traces. A good agreement is also obtained on TM-4.

5. During the gas puffing at the moments of time, when density profile is flat, one can find α_p knowing $\frac{\partial n(r=o)}{\partial t}$. The results of calculations are given in Table 3.

Table 3

tokamak	$n(o)$ ($10^{13} cm^{-3}$)	$\frac{\partial n(o)}{\partial t}$ ($10^{13} cm^{-3} s^{-1}$)	U (v)	B(T)	q(o)	α_p
T - 10	2	12.5	2.2	1.5	1	60
T- 11	3	200	1.5	0.85	1	63
PLT	4	27	1.5	2.5	1	65
FT	32	320	2	8	1	64
Alcator-A	50	2000	2.2	8	1.5	75
Alcator-C	20	400	2.7	8	1	70

The experimental and calculated traces (dashed line) of the profiles n(r) at the gas puffing in PLT are given in Fig.3. The values $v_p(r)$ (2) and v_p^{PLT} (r), which is an extremely overestimated pinch velocity accepted in the calculations /3/, are also given. The results of calculations for Alcator-A at $\alpha_p = 70$, $æ = 3.10^{17} cm^{-1} s^{-1}$ are given in Fig.4. The experimental data are labelled with crosses. In the main volume of plasma, the source is small and the build-up is determined by pinching.

References

/1/ Dnestrovskij Yu.N., Lysenko S.E., Neudatchin S.V. et al., X Eur.Conf. on Contr. Fusion and Plasma Phys., Moscow, 1981, v.1, B-15.

/2/ Coppi B., Sharky N., Nucl.Fusion, 1981, 21, 1363.

/3/ Strachan J.D., Bretz N., Mazzucato E. at l. Nucl.Fusion, 1982, 22, 1145.

/4/ Alikaev V.V., X Eur.Conf.on Contr.Nucl.Fus. and Plasma Phys., Moscow, 1981,2, 11.

/5/ Vlasenkov V.S., Leonov V.M., Lohr J. et al. Plasma Phys. and Contr.Nucl. Fusion Res., IAEA, Vienna, 1979, v.1, 211.

/6/ Bugarja V.I., Gorshkov A.V., Grashin S.A. et al. Preprint N 3630/7 I.V.Kurchatov Institute of Atomic Energy, 1982.

/7/ Golant V.E., Evtushenko T.P., Lebedev S.V. et al. Fizika Plazmy 1982, 8, 1167.

/8/ Alladio F., Bardotti G., Bartiromo R., et al. X Eur.Conf. on Contr. Fusion and Plasma Phys., Moscow, 1981, 1, A-2.

/9/ Apgar E., Coppi B., Gondhalekar A. et al. Plasma Phys. and Contr.Nucl. Fus.Res., IAEA, Vienna, 1977, v.1, 247.

/10/Fairfax S., Gondhalekar A., Granetz R., et al. Plasma Phys. and Contr.Nucl.Fus.Res., IAEA, Vienna, 1981, v.1, 439.

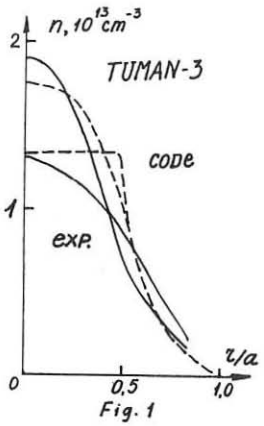

Fig. 1

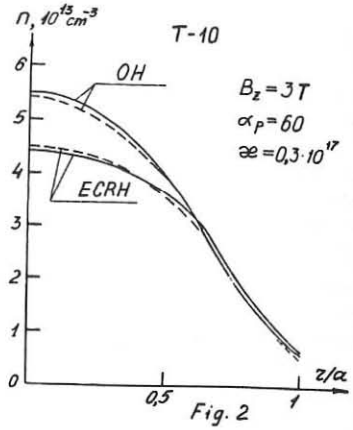

Fig. 2

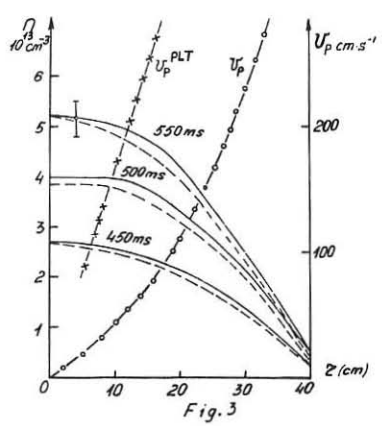

Fig. 3

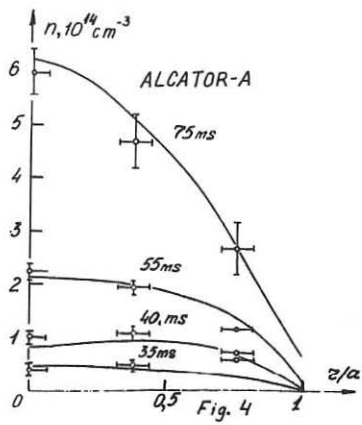

Fig. 4

Generalized ripple-banana transport in tokamak

P.N.Yushmanov

I.V.Kurchatov Institute of Atomic Energy
Moscow, USSR

A magnetic field in real tokamaks has no axial symmetry because of a discreteness of the magnetic system. Under these conditions, the losses due to axial asymmetry (ripple) in the toroidal magnetic field are added to the known neoclassical transport /1/. If the ripple, $\delta = (B_{max} - B_{min})/(B_{max} + B_{min})$, does not exceed 0.5%, a considerable part of these losses is produced by the banana particles trapped at the exterior torus outline. In the paper presented, the known results on the theory of ripple transport for the banana particles are summarized, new regimes are studied and a generalized expression for a flux, which describes each regime independently and smooth transition from one regime into another, is given.

In an ideal axially-symmetric tokamak, the banana orbits of particles are being precessed around the main axis of the torus, shifting around the toroidal angle

$$\Delta\varphi = \frac{2\sqrt{2}\,q^2 K}{v\,\varepsilon^{3/2}}\left[-v_E + 2v_d\left(\frac{E}{K} - \frac{1}{2} + 2\frac{r}{q}\frac{dq}{dr}\left(\frac{E}{K} - \cos\frac{\vartheta_0}{2}\right)\right)\right] \quad (1)$$

for the full turn period τ_b /1/,

where $E = E\left(\sin\frac{\vartheta_0}{2}\right)$, $K = K\left(\sin\frac{\vartheta_0}{2}\right)$

are the complete elliptic integrals; $v_E = c\,E_r/B$ and $v_d = v_{one}^2/2\omega_B R$ are the electrical drift velocity and the diamagnetic velocity respectively, ϑ_0 is the poloidal angle at the reflection point of a banana trajectory. These particles after each reflection acquire a radial displacement, d, due to noncompensated toroidal drift within the rippled magnetic field. For a not very high ripple, $\delta \lesssim \varepsilon/Nq$ d is determined by the relationship /2/:

$$d = \frac{\delta(\vartheta_0)}{\omega_B}\left(\frac{q}{\varepsilon}\right)^{3/2}\left(\frac{\pi N}{\sin\vartheta_0}\right)^{1/2} v \sin\left[N\varphi \pm \left(Nq\vartheta_0 - \frac{\pi}{4}\right)\right] = d_0 \sin F, \quad (2)$$

where, N is the number of the toroidal field coils, $\varepsilon = r/R$ is the ratio of a minor radius to the major radius of the torus, $q = d\varphi/d\vartheta$ is the safety factor. A total displacement of a particle after a few consecutive reflections is a sum of displacements (2). The quantity $\Delta r = \sum d = d_0 \sum \sin F$ is noticeably dependent on a change in the displacement phase $F = N\varphi \pm (Nq\vartheta_0 - \pi/4)$. An increment in F for a time between reflections τ_b, is determined by different processes dependent on $\Delta\varphi$ and on d. This corresponds to different transport regimes. In this case, classification of the ripple transport regimes for the banana particles and the processes in their nature are similar to the transport within the tandem mirror machines /3/.

At a relatively low energy of particles (for the installations with reactor parameters $w \lesssim 10$ keV), the phase F is changed mainly due to collisions. Under these conditions, a ripple-plateau regime is realized /2/. With an increase in the energy of particles, the role of collisions becomes insignificant and a toroidal precession becomes dominant. If $\Delta\varphi \lesssim 1/N$, the banana-drift transport regime will be realized /4/; if $\Delta\varphi > 1/N$, the resonance transport regime will take place /5/. When $w \gtrsim 1$ MeV, a change in phase due to the radial displacement of the orbit, d_0, becomes the most important. In this case, a stochastic transport can emerge /6/. But, these regimes taken separately don't reproduce the whole process: at a change in the parameters, the ranges of energy, in which this or that regime is true, shift respective to each other and overlap each other. As a result, a intermediate regime is realized in a wide range of parameters, where a joint effect of collisions, toroidal precession and radial displacement of the banana orbits is important.

All these effects are taken into account when a drift kinetic equation is used to describe the ripple transport for the banana particles:

$$\frac{v_\parallel}{qR}\frac{\partial f}{\partial \vartheta} + \left(\vec{v}_\varepsilon + \vec{v}_d + \vec{v}_\delta\right)\frac{\partial f}{\partial \vec{r}} - St(f) = -\vec{v}_\delta \frac{\partial F_0}{\partial \vec{r}}, \qquad (3)$$

where, F_0 is the unperturbed distribution function, f is the ripple addition, $v_\delta = \delta(\vartheta \mp \vartheta_0)\, d v_\parallel / qR$ is the velocity of a drift provided by the ripple. Presence of the δ-function in the expression for v_δ illustrates the fact that the displacement due to the ripples occurs only close to the reflection points. Solution to the equation (3) is easy to obtain, when a characteristic width of the distribution function is greater than the characteristic width of inhomogeneity in the right-hand side of the equation (3), $\Delta\vartheta \gtrsim 1/Nq$. In this case, the collision operator can be written in the τ-approximation

$$St(f) = -\frac{2\nu v_\parallel^2 N^2 q^2}{\varepsilon^2 v^2 \sin^2\vartheta_0} f = -\frac{f}{\tau_{eff}} \qquad (4)$$

The equation (3) with the collision operator (4) is solved by integration over the trajectories and results in the following expression for particle and heat fluxes

$$\begin{bmatrix} n v_r \\ Q \end{bmatrix} = \frac{\pi N q^2}{2\omega_0^2 m^3 R \varepsilon^3} \int \frac{\partial F_0}{\partial r} \delta^2(v_0) \begin{bmatrix} 1 \\ w \end{bmatrix} I w^2 d\vartheta_0\, dw, \qquad (5)$$

where

$$I = \frac{1 - e^{-4\Gamma}}{(1 - e^{-2\Gamma})^2 + 4e^{-2\Gamma}(\sin^2 N\Delta\varphi + 0.46\alpha^2)} + \frac{1}{1 + \exp(6.9 - 5.5\alpha)},$$

$$\Gamma = \frac{8\sqrt{2}\,\nu(v) N^2 q^3 R}{\varepsilon^{3/2} v \sin^2\vartheta_0}\left(E - \cos\frac{\vartheta_0}{2} K\right), \quad \alpha = N d_0\left(\vartheta_0 \frac{dq}{dr} + \frac{q}{r} ctg\vartheta_0\right).$$

The expression (5) describes all the ripple transport regimes for the banana particles known previously as limiting cases: a ripple-plateau regime, when $\Gamma \gg 1$ (I=1), a banana-drift regime ($I = \Gamma/(\Gamma^2 + N^2\Delta\varphi^2)$) when $\alpha \ll \Gamma \ll 1$, $N\Delta\varphi \ll 1$ a stochastic regime (I= 1), when $\alpha \gg 1$. An advantage of the expression (5), besides its versatility, is that the intermediate regimes($\Gamma \sim 1$, $N\Delta\varphi \sim 1$, $\alpha \gtrsim \Gamma$) can be described with it.

A dependence of the ripple-banana heat conductivity coefficient, χ^{RB}, on the temperature, obtained from (5) in assumption that F_0 is the maxwellian function, is given in the figure as an illustration. The solid traces show the

function $\chi^{RB}(T)$ at $E_r = 0$. A shaded region shows possible changes in χ^{RB} vs. the radial electric field in a range $|E_r| \lesssim \frac{8T}{eR}$. It has been assumed in calculations that $W_T = W_P$, where $W_T = m\omega_B^2 r^3 / 16 N^2 q^4 R$, $W_P = (8T^{3/2}\nu(T) m^{1/2} q^3 R^{5/2} / r^{3/2})^{4/2}$. A dashed trace in the figure shows the dependence of a ripple-plateau heat conductivity coefficient, χ^{RP} on temperature /2/:

$$\chi^{RP} = 3\sqrt{\frac{\pi}{2}}\left(\frac{T}{m}\right)^{3/2} n \frac{N}{R} \frac{q^2}{\omega_B^2 \varepsilon^2} \frac{1}{2\pi} \int_0^{2\pi} \delta^2(\vartheta)\, d\vartheta,$$

for comparison. It allows to link the relative units of the graph with the real values of heat conductivity.

Some words should be said about the validity of the assumption $\Delta\vartheta \gtrsim 1/Nq$ used in derivation of the equation (5). The detailed analysis, which has been omitted in this paper, shows that this assumption is true, when $\delta \gtrsim \varepsilon/(Nq)^{3/2}$. When this inequality is violated, α in the expression (5) should be substituted by $\alpha/(1+\sqrt{\varepsilon/\delta(Nq)^{3/2}})$.

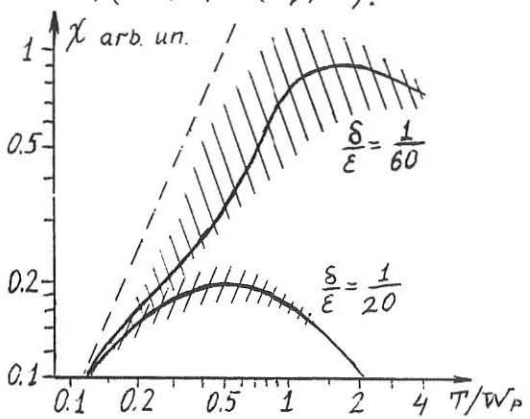

References

1 A.A.Galeev, R.Z.Sagdeev, Voprosy teorii plazmy 7 (1973) 205.
2 A.H.Boozer, Phys. Fluids.23 (1980) 2283.
3 D.D.Ryutov, G.V.Stupakov, Pis'ma ZhETF 26 (1977) 186.
4 P.N.Yushmanov, Nucl. Fusion 22 (1982) 1199.
5 P.N.Yushmanov, Dokl. Akad. Nauk SSSR 266 (1982) 1123.
6 R.J.Goldston, R.B.White, A.H.Boozer, Phys. Rev. Letters 47 (1981) 647.

high energy ion confinement in tokamaks with local divertor

P.N.Yushmanov
I.V.Kurchatov Institute of Atomic Energy
Moscow, USSR

A local toroidal divertor, in difference from the poloidal one, produces a strong perturbation of the toroidal magnetic field. This perturbation results in the strong violation of the axial symmetry of the system and consecutively in the additional losses of particles and heat. These losses can also be named the ripple ones, similar to the losses provided by periodic perturbations of the toroidal field.

A preliminary study of the ripple losses in tokamaks with local divertor can be carried out using the known results fmom the ripple transport theory for the installations with periodic perturbations of the toroidal field. The ripple losses in such installations are produced by two groups of particles: first, by banana particles trapped at the exterior torus outline, second, by the particles trapped within the local traps in the regions of decreased toroidal field. The flux of banana particles is found to be proportional to δ^2 [1] , where $\delta = (B_{max} - B_{min})/(B_{max} + B_{min})$ is the ripple depth. A radial flux of locally-trapped particles rises much faster as $\delta^{3/2}$ [2] - and at $\delta \geq 1\%$ exceeds the flux of banana particles. Therefore, in the installations with local divertor, where magnetic field perturbations are great, one can expect the dominance of losses provided by the locally-trapped particles.

Besides these two groups of particles discussed, a contribution into the ripple transport within the installations with local divertor can be done by untrapped particles. It is due to the fact that a strong localized perturbation in the toroidal field can result in a destruction of magnetic surfaces [3] . In this paper, the magnetic surfaces are assumed to be undistructed in the plasma column bulk and therefore the ripple losses produced by untrapped particles are small.

Let's consider the losses of particles captured in local mirrors within the regions of decreased toroidal magnetic field. A typical picture of the contour lines of magnetic mirror depth $\Delta(R, z)$ ($\Delta = 1 - B_{min}/B_{max}$, where B_{min} and B_{max} are the local values of B_{min} and B_{max} along the field line) produced by a local divertor is given in Fig.1. The depth, Δ, rapidly rises at the approach to the external edge of the chamber and slowly decays with a distance from the horizontal plane of symmetry. At such a dependence of $\Delta(R, z)$, the locally-trapped particles of high energies can drift to the wall of the chamber directly from the plasma column core. Therefore, the toroidal field perturbation produced by a local divertor is much dangerous than the perturbation produced by a magnetic system discreteness.

One can use a kinetic equation averaged over fast oscillations between the magnetic mirrors for a qualitative analysis of the losses of locally-trapped high energy particles [2]:

$$v_d \frac{\partial f}{\partial z} = \frac{\nu(w)}{\partial \mathcal{J}_\parallel / \partial \chi} \frac{\partial}{\partial \chi}\left(\mathcal{J}_\parallel \frac{\partial f}{\partial \chi}\right), \qquad (1)$$

where $\mathcal{J}_\parallel = \oint v_\parallel dl$ is the longitudinal adiabatic invariant, $\chi = 1 - \mu B_{min}/w$, $v_d = w/m\omega_B R$ is the drift velocity, μ is the magnetic moment, w is the energy of particles. The left-hand side of the equation describes the motion along the drift trajectories which are straight vertical lines for high-energy particles. The right-hand side of the equation (1) describes a change in the distribution function due to collisions. In this case, the operator of collisions includes only the terms describing the angular scattering. An area where the locally-trapped particles present is the strip, $0 < \chi < \Delta$. On the right boundary, $\chi = \Delta$, the distribution of locally-trapped particles continuosly makes a transition into the banana particle distribution $f(\chi, z)_{\chi=\Delta} = f_0(z)$, which is considered to be preset. No additional conditions for the left boundary are needed because $\mathcal{J}_\parallel|_{\chi=0} = 0$.

A flux Γ integrated over the field line (i.e. over all the trapped particles) is determintd by an equality [2]

$$\vec{\Gamma} = 2\pi\Sigma\sigma \int dl \int \frac{dw}{m^2} \int \frac{f\,\vec{v}_d B}{|v_{||}|} d\mu = \frac{2\pi}{m} \int_0^\infty dw \int_0^\Delta \frac{\partial \vartheta_{||}}{\partial \chi} f\,\vec{v}_d\, d\chi$$

Using the equation (1), this relationship can be rearranged as

$$\Gamma = \frac{2\pi}{m} \int dw \int \nu \left[\vartheta_{||} \frac{\partial f}{\partial \chi}\right]\Big|_{\chi=\Delta} dz = \int G(w)\sqrt{w}\, dw, \qquad (2)$$

where, $G(w)$ is the flux of particles with the energy w. From (2), one can see that it is sufficient only to know $\partial f/\partial \chi$ on the right boundary, $\chi = \Delta$ for determining the flux of locally-trapped particles. It can be found, when one does not solve the equation (1) completely.

Let's consider first the simpliest case $\Delta(z) = const$, corresponding to the vertical lines of a level $\Delta(R, z)$. In this case, using the results from [4], one has

$$\frac{\partial f}{\partial \chi}\Big|_{\chi=\Delta} = \frac{1}{\Delta} \int \frac{\partial f_0}{\partial \gamma} M\left(\int_\gamma^z \frac{\nu(t)\,dt}{\Delta\, v_d} \right) d\gamma, \qquad 3$$

where $M(x) = \sum_1^\infty EXP\left(-z_k^2 x/4\right)$, z_k is the k^{th} zero of the Bessel's function, J_0. The relationships (2), (3) give an analytical expression for the flux of locally-trapped ions, which can be used for determining the quantity, $G(w)$ in the whole range of energies.

The flux G calculated in this way, later designated as G_{con} (i.e. at $\Delta = const$), will be a reference for comparison with the calculated fluxes with real profiles, $\Delta(R, z)$. We don't study the behaviour of G_{con} in detail. Let's consider only a qualitative dependence of G_{con} on energy. At the comparatively low energies, $(\nu(w)\, z \gg \Delta\, v_d)$, the function $M(x)$ can be considered as δ-function that leads to the known result [5], $G_{con} \sim v_d^2/\nu \sim w^{7/2}$. At the limit of high energies, $(\nu(w)\, z \ll \Delta\, v_d)$, the argument of the function M is small, and it can be substituted by the approximate quantity $M(x) \approx 1/\sqrt{\pi x}$. After substituting such $M(x)$ into the relationships (3) and (2), one obtains $G_{con} \sim \sqrt{\nu}\, v_d \sim w^{-1/4}$. From this estimation, one

can see that at high energies (at thermonuclear parameters $w \gtrsim 30$keV), the losses of locally-trapped particles are stabilized and even slightly decrease.

At $\Delta(z) \neq const$, the derivative $\partial f / \partial \chi$ on the boundary, $\chi = \Delta$, will be found, if one reduces the equation (1) to the integral equation

$$\int_0^\tau EXP\left(-\frac{\Delta(t)+\Delta(\tau)}{t-\tau}\right) I_0\left(\frac{2\sqrt{\Delta(t)\Delta(\tau)}}{t-\tau}\right) \frac{\Delta(\tau)}{t-\tau} \left.\frac{\partial f}{\partial \chi}\right|_{\chi=\Delta} d\tau =$$

$$= \frac{f_0}{2} + \int_0^t EXP\left(-\frac{\Delta(t)+\Delta(\tau)}{t-\tau}\right)\left[-\frac{1}{t-\tau}\frac{d\Delta}{d\tau} I_0 + \frac{\Delta(\tau)}{(t-\tau)^2}\left(\sqrt{\frac{\Delta(t)}{\Delta(\tau)}} I_1 - I_0\right)\right] f_0(\tau)\, d\tau, \qquad (4)$$

where I_0, I_1 are the McDonald functions, $\tau = \int \nu v_d^{-1} dz$. The equation (4) is solved with the computer. A dependence of G/G_{con} on energy for typical distributions, Δ, corresponding to Fig.1 is shown in Fig.2. When $w > w_a$ (w_a is found from the condition $\nu(w_a)\, z = v_d(w_a)\, \Delta$), the ratio G/G_{con} starts to decrease rapidly. Taking into account that the quantity G_{con} slightly decreases with a rise in w in this range of parameters, one can make a conclusion about satisfactory confinement of locally-trapped high energy particles in tokamaks with local divertor. A decrease in Δ along the drift trajectories is the most important factor for the confinement of particles. This mechanism is effective when Δ_E at the upper end of the trajectory is 2-3 times less than Δ_S on the horizontal plane of symmetry.

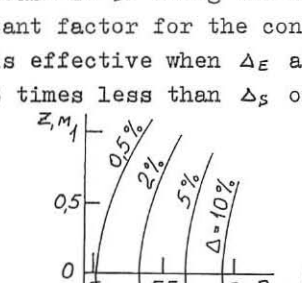

Рис.1

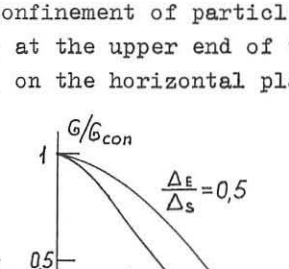

Рис.2

References

1 P.N.Yushmanov, Dokl. Akad. Nauk USSR 266 (1982) 1123.
2 P.N.Yushmanov, Nuclear Fusion 22 (1982) 315.
3 R.N.Fowler, D.K.Lee, P.W.Gaffney, J.A.Rome, ORNL/TM-6293 1978.
4 A.V.Gurevich, Ya.S.Dimant, Nuclear Fusion 18 (1978) 629.
5 T.E.Stringer, Nuclear Fusion 12 (1972) 689.

IS MOTION OF CHARGED PARTICLE IN MIRROR OF TRUE MARKOVIAN NATURE?

Avinash

Physical Research Laboratory

Navrangpura, Ahmedabad 380 009

India

Abstract

Standard mapping of Chirikov arises in a number of dynamical processes, one of it being the motion of charged particles in the adiabatic trap. One characteristic of this mapping is that even in the so-called stochastic limit and large number of iterations there is always some finite correlation between the initial and final states [1]. This is reflected in the fact that when diffusion coefficient is calculated from this map, it diverges as $t \longrightarrow \infty$ [2]. To remove this divergence, then extra stochasticity has to be introduced by hand [3]. All this has led to the widespread belief that dynamical phenomenon governed by the standard map are not truely stochastic by themselves. True stochasticity here would mean the Markovian stochasticity. In this paper with the help of the ensemble view point introduced by Varma [4], we have shown that atleast one phenomenon governed by the standard map i.e. the motion of charged particle in the mirror trap is a true Markovian process. In the ensemble view point the probability density $F(x,t)$ (x is the co-ordinate along the field line) is expressed as

$$F(x,t) = \sum_{n=-\infty}^{\infty} |\psi_n(x,t)|^2$$

where $\psi_n(x,t)$ is the wave function in the n^{th} ensemble mode. Each of the $\psi_n(x,t)$ obey an one-dimensional (along x) Schrodinger-like equation where the role of $\hbar$ is played by μ_0/n, μ_0 being the initial value of the magnetic moment. From this we obtain temporal transformation

equation for the joint probability function $f(x, p_x, t)$ (p_x is the momentum conjugate to x) of the form

$$f(x_1, p_{x_1}, t) = \iint K[x_1, p_{x_1} | x_0, p_{x_0}, t_1 - t_0] f(x_0, p_{x_0}, t_0)$$

Then we have shown that as long as the jumps in μ , whenever the particle crosses the mid-plane, are finite K obeys Chapman Kolmogorov's equation thereby indicating the Markovian nature of the process. If the jumps in μ i.e. $\Delta\mu \to 0$ the $K \longrightarrow \delta(x_1 - x_0)\,\delta(p_{x_1} - p_{x_0})$ which signifies the deterministic character. This agrees with the conclusion of the symbolic dynamics [5] wherein many dynamical systems a discrete chain is Markovian while a continuous chain is deterministic.

References

1 B.V. Chirikov, Phys. Reports 52 (1979) 263.

2 J.R. Cary, J.D. Meiss, A. Bhattacharjee, Phys. Rev. A, 23 2744 (1981).

3 A.B. Rechester, M.N. Rosenbluth and R.B. White, Phys. Rev. A23 2664 (1981).

4 R.K. Varma, Phys. Rev. Lett. 261 (1971), 417.

5 V.M. Alekseev, M.V. Yakobson, Physics Reports 75 (1981) 287.

Preliminary Abstract (4-page paper not received in time).

COULOMB SCATTERING BETWEEN MAXWELLIAN PLASMA AND MONOENERGETICAL BEAM

J.M. Riedler, M. Heindler, Institut für Theoretische Physik, Techn. Univ. Graz, Petersgasse 16, Graz, Austria
G.H. Miley, 214 Nuclear Engineering Laboratory, 103 S. Goodwin Avenue, Urbana, Illinois 61801, USA

INTRODUCTION

Recent publications on advanced fuels have shown that an energy multiplication factor Q>1 may not be feasible for fusion plasmas in thermal equilibrium /1/. This rises the interest in an analysis of the non-Maxwellian tail caused by an injected beam which may enhance the fuel reactivity and hence the power density.

We have developed an analytical method to calculate the non-Maxwellian peak of the velocity distribution due to injection. As a first approach, one species of fuel ions is considered. The use of toroidal coordinates in velocity space enabled us to apply expansion techniques yielding a first order Fokker Planck equation.

The convergence problems appearing in previous publications /2/ do not occur here because we choose the evaluation point exactly at the support of the source beam.

This theory can also be applied to beam injection in tokamaks. The advantage of analytical calculations versus numerical computation is that trends can be interpreted from formulae rather than from point results.

DEFINITION OF THE PROBLEM, ASSUMPTIONS

We assume (i) quasi stationarity, (ii) one species of particles, (iii) homogeneous, infinitely extended background plasma (temperature T, density n), (iv) trapped beam particles are monoenergetical and move perpendicular to the magnetical field lines; the ionisation density is taken to be constant in configuration space. Therefore the source is:

$$S(\underline{v}) = (S_o/4\pi v_o^2)\ \delta(v-v_o)\ \delta(\cos\theta),\quad \theta=\sphericalangle(\underline{v}_o,\underline{B}) \tag{1}$$

We are interested in the shape of the distribution function in the neighbourhood of the injection circle defined by

$$v = v_o \quad \text{and} \quad \theta = \pi/2 \tag{2}$$

MATHEMATICAL FORMULATION

The equation describing the scattering process owing to weak classical Coulomb collisions is the Fokker-Planck-equation:

$$L\{f\} = 0 = 4\pi f^2 + (1/2)(\partial^2 f/\partial v_i \partial v_i)\cdot(\partial^2 g/\partial v_i \partial v_i) + \Gamma S(\underline{v}), \tag{3}$$

where the Liouville operator L{f} has been set equal to zero, according to the assumptions given above. $S(\underline{v})$ is the source originating from a monoenergetical beam, eq.(1), and the loss region is usually taken into account by boundary conditions /3,4/.

A common way to find the velocity distribution is to expand it in a series of Legendre polynomials. This has been done by Cordey /2/, but "the series expansion converges slowly for velocities in the region of v_o and the series has to be evaluated numerically". Our alternate approach is to transform the Fokker Planck scattering operator into natural toroidal coordinates

$$v_r = v_o/(\sqrt{v_o^2+u^2} - u\cos(\omega))$$
$$v_z = v_o u \sin(\omega)/(\sqrt{v_o^2+u^2} - u\cos(\omega)) \qquad (4)$$

in such a manner that the injection circle, eq.(2), is enclosed by the torus surface for any u>0 (Fig.1). This will allow us to expand the Fokker Planck scattering term (3) in powers of (u/v_o) around the injection circle (2).

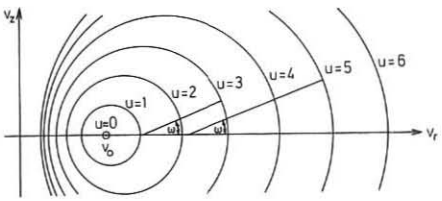

Fig.1, Natural toroidal coordinates

Starting from eq.(3) the steps that have to be performed are:
- o linearization of eq.(3) (f_M = Maxwellian background):

$$f(\underline{v}) = f_M(v) + \delta f(\underline{v}) \;;\; g(\underline{v}) = g_M(\underline{v}) + \delta g(\underline{v}) \qquad (5)$$

- o transformation into natural toroidal coordinates (see 4)
- o the resulting equation is expanded in powers of u and truncated after the first nonvanishing coefficient of u

The result is the following equation, with $\xi = u/v_o$

$$-(S_o/2\pi^2\Gamma)\,\delta'(\xi) = \{(-3/2)g'+(1/2)(1+\cos 2\omega)v_o g''\}\,\delta f_{\xi\xi} + \qquad (6)$$
$$\{2\sin 2\omega\cdot g' - \sin 2\omega\cdot v_o g''\}(1/\xi)\delta f_{\xi\omega} + \{g'+(1-\cos 2\omega)v_o g''/2\}(1/\xi^2)\delta f_{\omega\omega}$$
$$\{2g'+(1-\cos 2\omega)v_o g''/2\}(1/\xi)\delta f_{\xi} + \{-\sin 2\omega\cdot g' - \sin 2\omega\cdot v_o g''\}(1/\xi^2)\delta f_{\omega}$$

which is Eulerian in respect to u.

ANALYTICAL SOLUTION

Fourier transformation of the angular part leads to an infinite system of coupled differential equations; we find for n=0:

$$-(S_o/\pi^2\Gamma)\delta'(\xi) = (-3a+b)\delta f_o''+1/2b\delta f_2''+(4a+b)(1/\xi)\delta f_o'+$$

$$(-4a+3/2b)(1/\xi)\delta f_2' + (2a+4b)(1/\xi^2)\delta f_2 \qquad (7)$$

with $a = g'(v_o)$ and $b = v_o g''(v_o)$. For n = 1,2,3 ... we get only homogeneous equations. According to the theory of complex functions we expect a general solution of the form

$$\delta f_n(\xi) = A_n \xi^{\alpha n} \log(\xi) + B_n \xi^{\beta n} \qquad (8)$$

To obtain the first derivative of the delta function we use the pseudofunction Pf as defined by L.Schwartz /6/, chapter 2; it can be shown that

$$-Pf(x^{-2}) - \delta'(x) = d/dx\ Pf(x^{-1}) = d^2/dx^2\ Pf(\log(x)) \qquad (9)$$

In eq.(9) the representation by a second derivative was chosen in view of eq.(7) which is of second order in ξ. This suggests

$$\delta f_o(\xi) = A \log(\xi) \qquad (10)$$

By use of eq. (9) we can determine the constant A in ansatz (10) by comparison of the coefficients in eq. (7):

$$A = -S_o/\{\pi^2\Gamma(3g'(v_o) - v_o g''(v_o)\} . \qquad (11)$$

The functions δf_n, n>0, eq.(8), turn out to be constants: B_{2n} are defined by a recursion formula and B_{2n+1} are zero. As a result for δf we find in the limit $\xi \to 0$:

$$\delta f(\xi,\omega) \simeq \sum_{k=0}^{\infty} \delta f_k(\xi) \cos(k\omega) = A \log(\xi) + \sum_{k=1}^{\infty} B_{2k} \cos(2k\omega) \qquad (12)$$

where A is given by eq.(11) and the infinite sum is a periodic function of ω, $V(\omega)$. Transforming the variables ξ,ω into cylindrical coordinate and adding the Maxwellian f_M to δf we get the overall distribution function ($v^2 = v_r^2 + v_z^2$):

$$f(v_r,v_z)\ d^3\underline{v} = (\delta f + f_M)\ v_r dv_r dv_z d\phi =$$

$$= \{Q_o/(4\pi^2 e^4/m^2 \ln\Lambda\ n\ F(mv_o^2/2kT))(\ln 1/\xi + V(\omega))\theta(1-\xi) \qquad (13)$$

$$+ n\ (mv_o^2/2\pi kT)^{3/2} \exp(-mv^2/2kT)\}(v_r/v_o)d(v_r/v_o)d(v_z/v_o)d\phi$$

where $F(x) = 3-(7/2x)\cdot\Phi(x)+3x\cdot\Phi'(x)$; $\Phi(x)$ = error function,

$$\xi = (1/v_r v_o)\sqrt{\{(v_r+v_o)^2+v_z^2\}\{(v_r-v_o)^2+v_z^2\}}$$

The Heaviside step function is added in eq.(13) because our formalism is valid only for small ξ, say $\xi \ll 1$. Regarding the $\delta f \ll f_M$-assumption we have shown that for S_o-values satisfying

$$S_o \tau_{90°}/n \ < \ 0.05\ (2kT/mv_o^2)^{3/2}, \qquad (14)$$

the density of the non-Maxwellian part is less than 10% of the total. Results for typical fusion plasmas are shown in Fig.2.

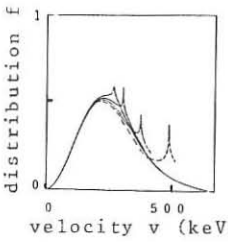

Fig.2: Distribution function $f(v,\theta=\pi/2)$ of a 100 keV deuterium plasma at density $10^{14}cm^{-3}$ distorted by a D-beam of $10^{13}cm^{-3}$ sec^{-1} at injection energies 150, 200, 300 and 500 keV

CONCLUSION

For a deutrium plasma at a temperature kT=100 keV and a density $n=10^{14}$ particles per cm^3 the density of the non-Maxwellian part is less than 10% of the total even if the power density of the beam (energy per injected deuteron = 150 keV) is equal to the fusion power density of the plasma. Therefore our formalism is applicable to fusion plasmas.

From our one-species model the results show that the non-Maxwellian peak is relatively large if

a) the charge/mass ratio is low
b) the injection energy is high compared to the average energy of the background.

Quantitative results can be easily obtained from numerical evaluation of eq.(13). Also the mathematical method developed here allows a straightforward extension to several particle species and the explicit inclusion of a loss cone.

REFERENCES

/1/ Dawson,J.M.: Advanced Fusion Reactors
Fusion Vol.1, Part B (1981), p.453

/2/ Cordey,J G.,Houghton,M.J.:Problems Associated with the Injection of a High-Energy Neutral Beam into a Plasma, Nuclear Fusion 13(1973)215

/3/ Pastukhov,V.I.: Collisional Losses of Electrons in a Plasma with Positive Potential, Nuclear Fusion 13(1974)215

/4/ Futch,A.H.,Holdren,J.P.,Killeen,J.,Mirin,A.A.: Multi Species Fokker Planck Calculations, Plasma Physics 14(1971)211

/5/ Schwartz,L.: Theorie des distributions. Hermann, Paris 1966

Transport Codes

A12 - A21

B15 - B23

SOME EFFECTS OF FINITE PLASMA PRESSURE IN THE ADVANCED STELLARATOR WENDELSTEIN VII-AS

R. Chodura, J. Kisslinger, W. Lotz, F. Rau, H. Wobig

Max-Planck-Institut für Plasmaphysik, EURATOM-Association,
D-8046 Garching, FRG

ABSTRACT: Modifications of the W VII-AS vacuum fields by a finite plasma pressure are studied numerically. For the parameter range investigated critical or deleterious effects are absent.

INTRODUCTION .

Experiments in the forthcoming "Advanced Stellarator" WENDELSTEIN VII-AS aim at attaining the long mean-free-path regime at substantial densities. Among the essential properties of W VII-AS are the reduction of the PFIRSCH-SCHLÜTER currents and of the collisional diffusion. Therefore the question arises whether these properties are maintained also in the finite - β - equilibrium. In this paper we study modifications of the magnetic topology of W VII-AS by a finite plasma pressure, as well as associated effects on its confinement. This is done using three numerical codes:

- the CHODURA-SCHLÜTER code /1/ which calculates magnetic field and pressure distributions in a fixed spatial grid,
- the GOURDON field tracing code /2/, yielding also essential magnetic field properties,
- the LOTZ code /3/, from which a particle diffusion coefficient is obtained by MONTE-CARLO technique.

SHAFRANOV SHIFT .

The SHAFRANOV shift is evaluated for the standard configuration /4/ of W VII-AS, and for a superimposed vertical field. In the CHODURA-SCHLÜTER code a radial pressure distribution $p(x) \sim \beta(o) \cdot f(x)$ is used, with peak value $\beta(o)$, and an initial radial profile $f(x)$ being characterized by an integer NEXP = 4 or 2 (steep or flat profile, resp.). The fixed spatial grid is centered at R = 206 cm, the average major radius of the W VII-AS vacuum magnetic axis. The grid is of rectangular cross section and comprises 22 or 36 points in each of the three dimensions, (toroidal = one field period). The coarse grid (22) allows a useful aspect ratio of $A \approx 16$. The initial vacuum field is from the actual W VII-AS coil geometry. The accuracy of this grid is sufficient to study the shift Δ of the magnetic axis, see Fig. 1, left part, normalized by the minor plasma radius a = 0.2 m. At $\beta(o) = 5.3$ %, $\Delta/a = 0.36$ and 0.23 are obtained at the toroidal positions 0 and 1/2 field periods (▷ and ○ ,resp.). A flat pressure distribution yields a slightly lower shift. A superimposed vertical field $B_z/B_t = 1$ % introduces an inward (negative) shift of the vacuum configuration. This shift is balanced by $\beta(o) = 3.3$ %, (lower curve); at $\beta(o) = 9$ % the average shift $\Delta/a \approx 0.2$. At elevated β-values both curves tend towards a saturation. The SHAFRANOV shift in W VII-AS is reduced by a factor of $\approx$ two compared with a conventional $\ell = 2$ stellarator.

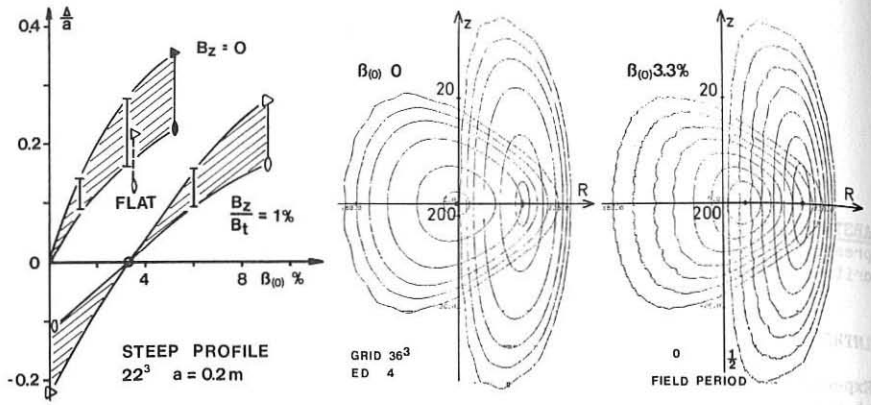

Fig.1 SHAFRANOV shift in W VII-AS for the "standard configuration" as well as for B_z / B_t = 1 % (grid 22), and magnetic surfaces at β (o) = 0 and 3.3 % (grid 36) .

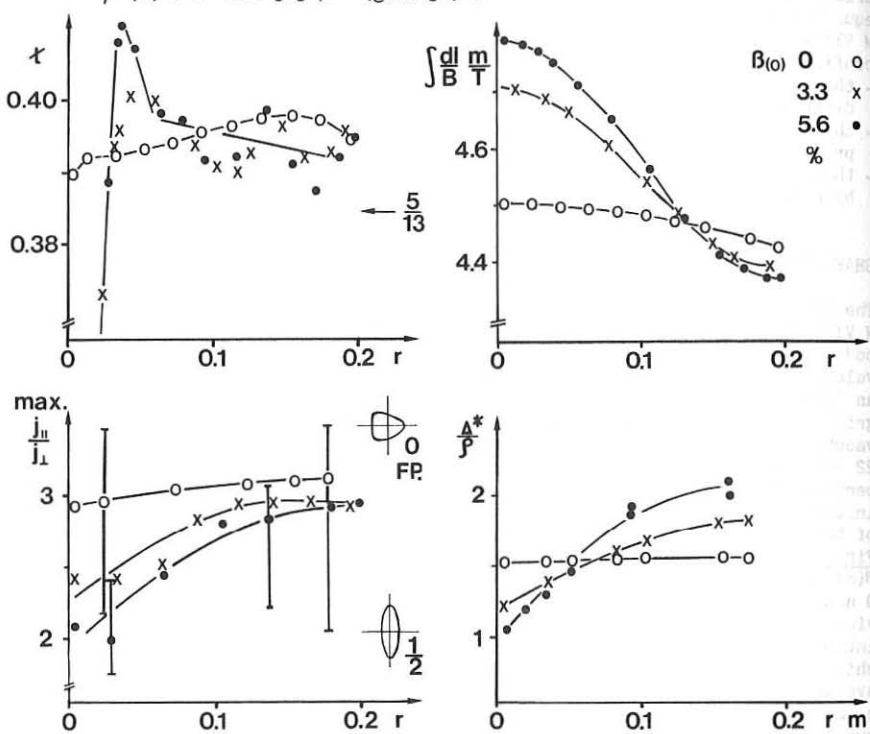

Fig.2 Radial profiles for various properties of the W VII-AS topology, at β(o) = 0 , 3.3 , and 5.6 % .

MAGNETIC SURFACES AND THEIR PROPERTIES .

Magnetic surfaces (Fig.1, right part) and their properties are obtained at a fine grid with 36 points. The full aspect ratio $A \approx 10$ of W VII-AS is attained by first computing a set of DOMMASCHK-potentials /5/ using an appropriate magnetic surface of the original W VII-AS configuration. Thus the influence of large fields close to the W VII-AS coils is avoided, by virtue of the smoother behaviour of the DOMMASCHK fields. At $\beta(o) = 3.3$ % the SHAFRANOV shift thus obtained is $\approx$ 15 % less than the value of Fig.1, and the magnetic surfaces are "reasonably" smooth.

For $\beta(o) = 0$, 3.3 and 5.6 %, Fig.2 shows properties of the magnetic surfaces as radial profiles. Increasingly with $\beta(o)$, and close to the magnetic axis, the rotational transform ("twist") ι is found to be reduced, as compared to the vacuum field. This drop appears to be compensated by an associated outer overshoot. At $r > 0.1$ m the values agree within 2 % of ι. The rational 5/13 is avoided at the edge. The influence of the grid structure on the scatter of the curves is unknown. The profiles of $\int dl/B$ are smooth and show a substantial deepening of the magnetic well, for $r < 0.1$ m. Within this range some reduction is seen, of the maximum values of $j_{\parallel} / j_{\perp}$ (parallel and perpendicular diamagnetic current density, resp.), as well as of Δ^* / ρ (Δ^*= average offset of drift surfaces for passing particles with LARMOR-radius ρ).

DIFFUSION COEFFICIENT .

Fig.3 shows the particle diffusion coefficient obtained by the LOTZ code in the absence of an electric field. The guiding center motion of 64 particles, starting at random from the magnetic surface with aspect ratio $A = 50$, is followed numerically. The energy is constant. For $0.3 < \lambda \iota / R < 300$ small-angle collisions are simulated by random changes of the velocity direction. At constant collision length λ , the diffusion coefficient $DIF1 \sim \langle x^2 \rangle / T$ is evaluated from the average offset $\sqrt{\langle x^2 \rangle}$ of the particles, attained after the total time T of the chosen number of collisions. For $\beta(o) = 0$ and 5.5 % the results coincide for $\lambda \iota / R < 30$. The values are reduced by identical factors in comparison to D_{P1} and D_{PS}, the plateau and PFIRSCH-SCHLÜTER coefficients, see also /6/, for vacuum fields. A diffusion coefficient at finite $\beta(o)$ and a low aspect ratio remains to be evaluated.

SUMMARY AND CONCLUSION .

As expected, a finite plasma pressure with a steep profile at $\beta(o) \lesssim 5$ % modifies the vacuum magnetic fields of W VII-AS only in the vicinity of the magnetic axis. There the magnetic well is deepened, and the maxima of $j_{\parallel} / j_{\perp}$ are favourably reduced. On the other hand, the particle diffusion coefficient appears to be less influenced. So far, it remains open, whether its slight increase at large values of $\lambda \iota / R$ is due to some numerical effects or is caused by the plasma pressure. For $\beta(o) \approx 3$ %, as expected in the experiments in W VII-AS, no essential change of the optimized properties due to a finite plasma pressure is found in the present study.

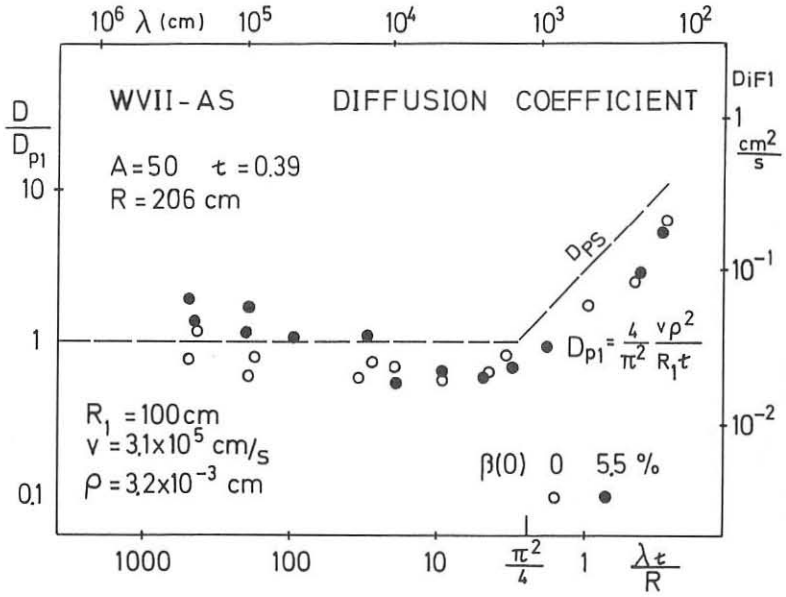

Fig.3 Diffusion coefficient normalized to the plateau value for β (o) = 0 and 5.5 % , at an aspect ratio of A = 50 in W VII-AS .

REFERENCES .

/1/ R. Chodura, W. Dommaschk, W. Lotz, J. Nührenberg, and A. Schlüter, Proc. 8th Conf. Pl. Phys. and Contr. Nucl. Fus., Brussels 1980, paper BB-2(A)

/2/ C. Gourdon et al., Fontenay Report EUR-CEA-FC 449, 1968

/3/ W. Lotz and J. Nührenberg, Proc. Annu. Meeting Theor. Aspects of Contr. Fusion, Austin, 1981, paper 3B41

/4/ J. Kisslinger, F. Rau, and H. Wobig, Proc. 12th SOFT, Jülich 1982, Vol. II, 1051

/5/ W. Dommaschk, Z. Naturforsch. 36a, 251 (1981)

/6/ U. Brossmann, W. Dommaschk, F. Herrnegger, G. Grieger, J. Kisslinger, W. Lotz, J. Nührenberg, F. Rau, H. Renner, H. Ringler, J. Sapper, A. Schlüter, H. Wobig, Proc. 9th Conf. Pl. Phys. and Contr. Nucl. Fus., Baltimore 1982, paper Q5

TWO-DIMENSIONAL COMPUTER MODELLING OF JET AS A SPECIFIC EXAMPLE OF D-SHAPED TOKAMAK PLASMAS

A. Nicolai and D. Reiter

Institut für Plasmaphysik der Kernforschungsanlage Jülich GmbH, Association EURATOM-KFA, P.O.Box 1913, D-5170 Jülich, FRG

1. INTRODUCTION

The axisymmetry of the Tokamak plasma allows a two-dimensional description which is based on a 1d-transport code and a semifree boundary equilibrium solver. The modules for additional heating and for defining the plasma aperture are coupled with the plasma module via the loss and sink terms and with the equilibrium module via the flux surface geometry.

Advancing the plasma parameters and the effective poloidal field with respect to a fixed flux surface geometry, and updating the plasma equilibrium with the q-profile and the pressure-profile, both obtained from the plasma module, leads to a selfconsistent description of Tokamak discharges.

2. EQUILIBRIUM

The poloidal and the toroidal components of the plasma current interact with the poloidal and toroidal field maintained by the plasma current itself and by the outer coils. This interaction provides the plasma equilibrium /1,2/ the time evolution of which emanates from the "q diffusion" /3,4/ and the time dependence of the plasma pressure.

The magnetostatic equations can be combined to a partial differential equation, the Grad-Shafranov equation ("PDE") /2/ for the spatial dependence of the poloidal flux function in two dimensions.

A consequence of the PDE is the ordinary differential equation ("ODE") /1,2/ for the flux profile $\Psi(V)$. The solution method iterates between the PDE determining the geometry and the ODE providing the flux profile.

The time evolution of the poloidal flux function with respect to a fixed flux surface geometry, is described by a one dimensional diffusion equation, the coefficients of which depend on the toroidal flux function and the flux surface geometry /3/.

In order to center the plasma and to maintain its shape, the currents in the poloidal field coils have to be controlled during the plasma's evolution. An arbitrary plasma shape can in principle only be achieved by dense coil fence rather than by discrete coils /5/. The fence's current density, which yields the coil currents approximately,can be computed from the condition that the flux function vanishes at the plasma boundary /5/.

3. PLASMA ENERGETICS AND CHARGED PARTICLE INVENTORY

The time evolution of the electron and ion temperatures depends essentially on the power and the distribution of the energy sources, as Ohmic, neutral injection or high frequency heating, and on the energy losses effected by conduction, convection, line radiation, brems-radiation, charge exchange, ionization and recombination. The particle source and loss mechanisms which determine the particle inventory, are the diffusion perpendicular to the magnetic field, the inward flow, the recycling and the deposition by neutral injection. Accounting for the processes mentioned above and for a time

independent flux surface geometry one arrives at transport equations /3/ for the particle densities and the electron and ion temperatures $T_{e,i}$ of multispecies plasma, including protons, deutons, tritons, α-particles, a light impurity species (e.g. oxygen) and a heavy impurity species (e.g. iron).

The particle flux densities and energy flux densities in these equations account for diffusion, an inward flow /7/, conduction and convection. Neoclassical fluxes are neglected throughout. A simple empirical model is chosen /3/ for the transport coefficients.

The radiative cooling rates are obtained from the tables of Jensen et al. /8/. The evolution of the flux surface geometry implies an adiabatic transformation of the plasma parameters after each updating of the equilibria data.

4. NEUTRAL PARTICLES

In this approach the source terms due to the neutral gas influx are computed by means of the SPUDNUT code /8/ using a hydrogen plasma with an average atomic mass as background and assuming 100 % recycling. At selected time points, however, the neutral gas parameters (density and kinetic temperature) are computed by the two-dimensional Monte-Carlo code NAURORA /9/ resorting to effective variance reduction techniques and a superposition of the track-length- and collision estimator. Comparison of the source terms obtained by NAURORA and those by SPUDNUT shows agreement thus justifying the combination of SPUDNUT and NAURORA.

RESULTS

The calculations are based on JET data /10/: initial mean deuton density $n_D = 2.2 \times 10^{13}/cm^3$, initial mean triton density $n_T = 2.2 \times 10^{13}/cm^3$, plasma current $I_p = 4.80$ MA, toroidal field $B_t = 30$ kG, ICRH power $p_I = 20$ MW, beam power $p_b = 17.25$ MW, beam energy $E_b = 160$ keV, effective minor radius $a = 1.65$ m, major radius $R_o = 2.98$ m, ellipticity $\varepsilon = 1.77$ and D-shapeness $d = 1.68$.

The ICRH and beam turn on times are $t_I = 1$ sec and $t_b = 0$, respectively.

The beam geometry is determined by the beam divergence $d = 0.7°$, the horizontal focal length $f_H = 10$ m, vertical focal length $f_V = 14$ m, the beam line length $b_L = 7.91$ m, bucket width $W = 0.18$ m, bucket hight $H = 0.45$ m, pivot radius $r_p = 1.71$ m, beam tangency radius $R_t = 1.33$ m.

Neglecting impurities, a maximum ion and electron temperature $T_i(o) = 19$ keV, $T_e(o) = 16$ keV and a maximum Shafranov shift $d_s = 46$ cm are obtained at the end of the discharge ($t = 5$ sec).

Accounting for 2 % oxygen and for iron due to charge exchange sputtering the corresponding values are $T_i(0) = 11$ keV (Fig. 1), $T_e(0) = 9.8$ keV, and $d_s = 23$ cm, thus showing the importance of clean plasma conditions. The two-dimensional distribution of the toroidal current density (Fig. 2) has its maximum value $j_{max} = 0.11$ kA/cm² at $R = 3.6$ m, where the pressure gradient has its maximum in absolute value. The time evolution of the coil currents (Fig. 3)

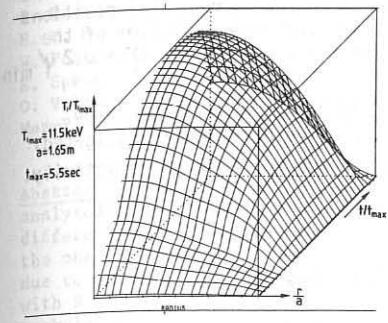

Fig. 1

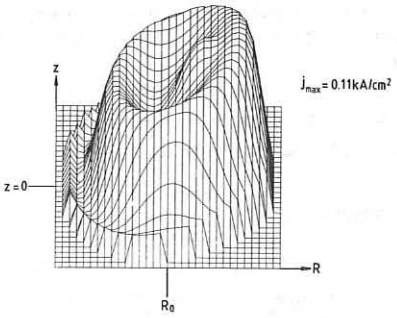

Fig. 2

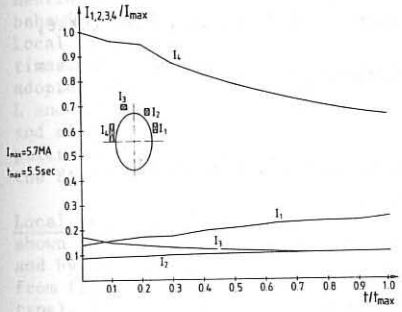

Fig. 3

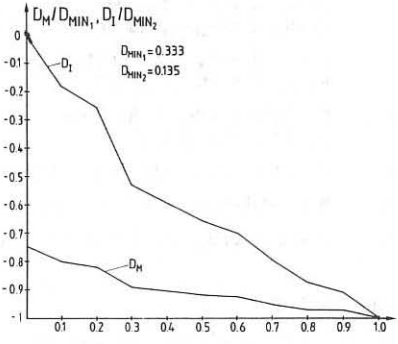

Fig. 4

is characterized by increase of the current I_1 in the outermost coil and a decrease of the current I_4 in the innermost coil due to the rising pressure. The coil fence, which the calculations are based on, is assumed to have the distance d = 1 m from the plasma edge. This reproduces the radial positions of the coils only roughly /11/. Fig. 4 displays the time evolution of the stability quantities D_M and D_I calculated for the flux surface $\psi = 0.2\,\psi_{min}$ /3/.

The stability criteria advanced by Mercier and Glasser require $D_M < 0$ $D_I < 0$; this is fulfilled during the 5 sec pulse duration investigated, except at $t \simeq 0$ where D_I is slightly positive due to the high resistivity.

REFERENCES

/1/ F.L. Hinton, R.D. Hazeltine, Rev. Mod. Phys. 48, 239 (1976)

/2/ H. Grad, P.N. Hu, C. Stevens
Proc. Nat. Acad. Sci. USA, Vol 72, 3789 (1975)

/3/ J.T. Hogan, Nucl. Fus. 19 (1979) 753

/4/ V.O. Shafranov, G.V. Pereversev,L.E. Zakharov,
3rd Int. Conf. Plasma Theory (Kiev) Trieste 1977

/5/ A. Nicolai, Fusion Technology (1982),
Proc. 12th Symposium, 1221

/6/ W. Engelhardt, K. Behringer and G. Fussmann,
Verhandlungen der Deutschen Physikalischen Gesellschaft,
Frühjahrstagung Hamburg (1981) Vortrag p. 3

/7/ R.V. Jensen, D.E. Post, H.H. Grasberger, C.B. Tarter, W.A. Lokke,
Nucl. Fusion 17 (1977) 1187

/8/ K. Audenaerde, G.A. Emmert, M. Gordinier,
UWFDM - 259 (1978)

/9/ J. Nucl. Mat. 111/112 (1982) 434

/10/ M.L. Watkins, T.E. Stringer, Private communication (1981)

/11/ The JET project, EUR-JET-R5 (1975) 41

FIGURE CAPTIONS

Fig. 1 Time evolution of the ion temperature

Fig. 2 Distribution of the toroidal current density

Fig. 3 Time evolution of the coil currents

Fig. 4 Time evolution of the Mercier- and Glasser-quantity

TRANSPORT MODELLING OF NEUTRAL BEAM HEATED L AND H DISCHARGES IN ASDEX

G. Becker and K. Behringer, K. Bernhardi, A. Eberhagen, G. Fußmann, O. Gehre, J. Gernhardt, G. v. Gierke, E. Glock, G. Haas, F. Karger, M. Keilhacker, S. Kissel[x], O. Klüber, M. Kornherr, K. Lackner, G. Lisitano, G.G. Lister, H.-M. Mayer, K. McCormick, D. Meisel, E.R. Müller, H. Murmann, H. Niedermeyer, W. Poschenrieder, H. Rapp, F. Schneider, G. Siller, P. Smeulders, F. Söldner, E. Speth, A. Stäbler, K. Steinmetz, K.-H. Steuer, Z. Szymanski[xx], G. Venus O. Vollmer, F. Wagner
Max-Planck-Institut für Plasmaphysik, EURATOM-Association, D-8046 Garching

Abstract. Local transport of divertor plasmas in the L and H regimes is analyzed by a prediction code. In the L regime two types of discharges with different local confinement are distinguished and studied. It is found that the observed decrease of the τ_E with increasing neutral injection power is due to an enhancement of the electron heat diffusivity. In L discharges with $\beta_p << 1$ there are indications that transport results from drift-wave turbulence, while for $\beta_p \gtrsim 1$ pressure-driven modes could be involved. With I_p = 300 and 380 kA transport in the H phase is characterized by flat $\chi_e \simeq 2$ to 3 x 10^4 $cm^2 s^{-1}$, D = 0.2 χ_e and neoclassical χ_i. The observed improvement of τ_E and τ_p compared with the L phase is due to a reduction of χ_e and D by a factor of two in the whole plasma. The diffusivities χ_e and D in L and H discharges do not depend on density and decrease with increasing plasma current.

Introduction. As in divertor discharges in ASDEX very clean plasmas have been achieved with ohmic (OH) and neutral injection (NI) heating /1/, they are particularly suitable for studying particle and energy transport. With neutral-beam injection two types of discharges with different confinement behaviour denoted as L (low β_p) and H (high β_p) have been found in ASDEX /2/. Local transport analysis is preferable to the study of global confinement times, since it is more selective with respect to the type of theory to be adopted. Thus, our main objectives are to investigate local transport in the L and H regimes and to find the scaling laws of the diffusion coefficient D and of the thermal diffusivities of electrons and ions χ_e and χ_i. The computer simulations are carried out with modified versions (BALDI09R) /3/ of the BALDUR prediction transport code.

Local transport in L discharges. Extensive studies of L discharges have shown that larger χ_e values are obtained by reducing the plasma current (I_p) and by increasing the beam power (P_{NI}). Local transport is found to change from flat $\chi_e(r)$ and D = 0.2 χ_e (LI type) to steep $\chi_e(r)$ and flat D(r) (LII type), if χ_e is raised above a value of about 5 x 10^4 $cm^2 s^{-1}$.

---

[x] On leave from Massachusetts Institute of Technology, Cambridge, USA

[xx] On leave from Institute of Fundamental Technological Research, Warsaw, Poland

The results obtained in an earlier work /3/ (LI type) have been confirmed by a series of L discharges with I_p = 380 kA, B_t = 1.9 T and $\bar{n}_e$ = 2.7 x 10^{13} cm^{-3}, in which P_{NI} was scanned. Hydrogen is injected tangentially into a deuterium target with co-beam power P_{NI} between 0.3 and 2.5 MW. Compared with OH plasmas there is a change in scaling, which suggests that a different transport mechanism is present with NI /3/. The enhanced diffusivities with NI appear and disappear with time delays relative to the beginning and end of NI and are found to be correlated with $\eta_e = d \ln T_e / d \ln n_e$, which is an important parameter for collisionless drift instabilities.

In both the ohmic and L phases the velocity of the anomalous inward flux $v_{in} = 245\ r/r_w\ cms^{-1}$ /3/ with wall radius r_w = 49 cm and without Ware pinch is consistent with the experimental data. Good agreement with measured $n_e(r)$, $T_e(r)$, $T_i(o,t)$, τ_E and $\beta_p(t)$ is reached, if flat $\chi_e(r)$, $D = 0.2\ \chi_e$ and 1 to 3 times neoclassical χ_i values are applied. The increase of the homogeneous χ_e in the range $r_{q=1} < r < 0.9a$ with P_{NI} is shown in Fig. 1. The circles result from simulations, while the crosses are $\chi_e(a)$ values derived from the experimental variation of τ_E with P_{NI} by assuming $\tau_E(a) \sim 1/\chi_e(a)$. Obviously, the observed decrease of τ_E with increasing P_{NI} is due to enhanced electron heat diffusivities.
Even at the smallest absorbed beam power (P_b=0.3 MW < P_{OH}=0.4 MW) the scaling for OH plasmas is no longer applicable. Here, β_p (= 0.3) is not raised by NI but the quantity η_e has changed indicating that for $\beta_p \ll 1$ the turbulent state responsible for the enhanced χ_e and D is not due to pressure-driven modes but rather due to drift instabilities.
Scanning P_{NI} at 300 kA can raise χ_e above 5 x 10^4 cm^2s^{-1} and results in a transition to the LII regime with steep $\chi_e(r)$ (see Fig. 2). A practically time independent χ_e profile of this shape yields the measured peaked $T_e(r,t)$ (see Fig. 3). Agreement with measured $n(r)$, $T_i(o)$, τ_E and β_p is obtained for flat D(r) that are no longer coupled to χ_e. Such a situation is indicative of transport in stochastic magnetic fields /4/. According to this model electron thermal transport is enhanced by conduction $\parallel B$ in braided magnetic fields, while mass transport remains unchanged, since it is limited by ambipolar potentials. In the collisionless case of ASDEX $D/\chi_e = v_s/v_{Te} \simeq 0.02$ results, where v_s is the ion sound speed and v_{Te} the thermal velocity of the electrons.
The transition to the LII regime coincides with $(\beta_p)_{tot}$ (sum of thermal and beam contributions) becoming larger than unity. According to theory pressure-driven modes could be involved, which are capable of producing the B_r-fluctuations necessary for magnetic braiding. For $\beta_p \gtrsim 1$ resistive ballooning instabilities with high wave numbers m and n are expected to be dominant. These modes occur, if the ratio S of resistive and Alfvén time scales amounts to typically 10^5 to 10^6. As the high central T_e values reached in ASDEX correspond to $S \approx 10^8$, ideal pressure-driven modes are more likely.

Local transport in H discharges. The H phase is always found to develop from an L discharge and to return to an L phase after turning off neutral-beam injection. Modelling typical H discharges in double-null divertor configuration with I_p = 380 kA and P_{NI} = 2.5 MW yields flat χ_e = 4.7 x 10^4 cm^2s^{-1} and $D = 0.2\ \chi_e$ during the L phase and flat χ_e = 2 x 10^4 cm^2s^{-1} and $D = 0.2\ \chi_e$ during the H phase. The ion heat diffusivity is again approximately neoclassical. It is found that the improvement of energy and particle confinement in the H regime is due to a clear reduction of χ_e and D over the whole plasma cross-section.
Scans of $\bar{n}_e$ in the H regime show that τ_E and the diffusivities are indepen-

dent of density as in L discharges. In the H regime $\tau_E \sim I_p$ is observed as in both L regimes. These results prove that in H discharges the transport scaling of OH plasmas in not recovered.
In simulations of H discharges with 300 kA and 2.5 MW flat $\chi_e = 3 \times 10^4$ $cm^2 s^{-1}$ and $D = 0.2\ \chi_e$ have to be applied in the H phase, while the χ_e profile is steep during the L phase. Here, the reduced χ_e values in the H phase should correspond to smaller fluctuation levels, which seem to be insufficient for magnetic braiding.
These conclusions are confirmed by discharges with $I_p = 200$ kA for which the electron heat diffusivity exceeds 5×10^4 $cm^2 s^{-1}$ both in the L and in the H regime. Here, the corresponding higher fluctuation level leads to steep χ_e profiles even during the H phase. The improvement of τ_E in the H phase can be explained again by the reduction of the electron thermal diffusivity in the whole plasma.

Conclusions. In the L regime two types of discharges LI and LII with different local confinement can be distinguished. The decrease of τ_E observed with higher P_{NI} is explained by increased electron heat diffusivities. In the L regime there are indications that for $\beta_p \ll 1$ drift-wave turbulence is present, while for $\beta_p \gtrsim 1$ pressure-driven modes could be involved. With $I_p = 300$ and 380 kA transport in the H phase is characterized by flat $\chi_e \simeq 2$ to 3×10^4 $cm^2 s^{-1}$, $D = 0.2\ \chi_e$ and neoclassical χ_i. Compared with L discharges χ_e and D are reduced by a factor of about two in the whole plasma. In both the H and L regime χ_e and D decrease with increasing I_p, but are independent of n_e. These parallels in scaling should reflect the influence of the saturated microturbulent state.

References.

/1/ Keilhacker, M., Becker, G., Behringer, K., Campbell, D., Eberhagen, A., et al., Proc. 9th Int. Conf. on Plasma Physics and Contr. Nucl. Fus. Research, Baltimore 1982, paper IAEA-CN-41/R-2.
/2/ Wagner, F., Becker, G., Behringer, K., Campbell, D., Eberhagen, A., et al., ibid., paper IAEA-CN-41/A3.
/3/ Becker, G., ASDEX Team, Neutral Injection Team, Nuclear Fusion 22 (1982) 1589.
/4/ Rechester, A.B., Rosenbluth, M.N., Phys. Rev. Lett. 40 (1978) 38.

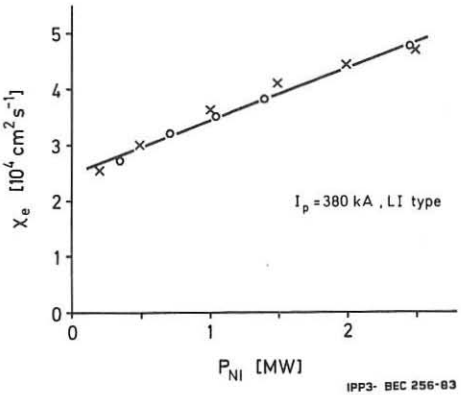

Fig. 1: Electron thermal diffusivity from simulations (circles) vs. neutral injection power. For comparison $\chi_e(a)$ (crosses) derived from τ_E scaling are shown.

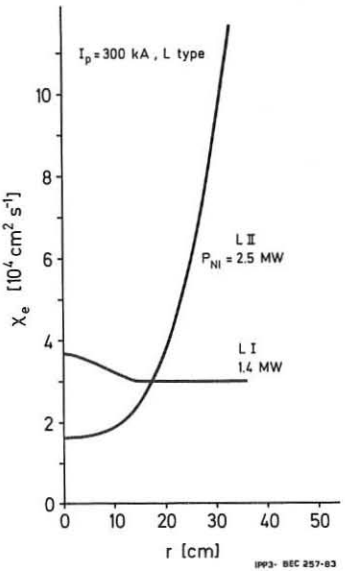

Fig. 2: Different local transport behaviour in the LI (P_{NI} = 1.4 MW) and LII regime (2.5 MW) shown by $\chi_e(r)$.

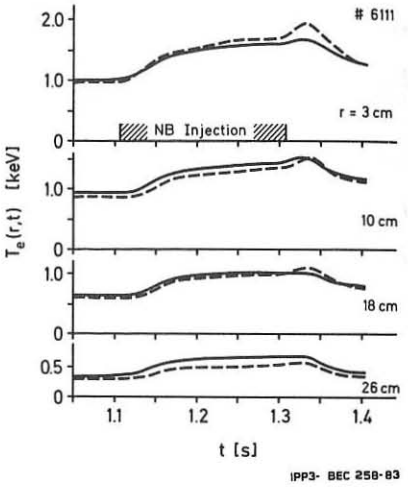

Fig. 3: $T_e(r,t)$ in an LII discharge with 300 kA and 2.5 MW computed with $\chi_e(r)$ from Fig. 2 (solid curves) compared with ECE measurements (dashed curves).

Tokamak transport calculations for JET with different limiter materials.

M. L. Watkins and A.E.P.M. Abels-van Maanen*
JET Joint Undertaking, Abingdon, Oxfordshire, OX14 3EA, England.

INTRODUCTION

Adequate impurity control has been achieved in short pulse tokamak experiments using suitable limiter or divertor configurations. The aims of JET will require effective impurity control with long pulses.

We assess the choice of nickel, graphite and beryllium for the limiter in JET and the effectiveness of additional impurity control using a specified influx of neon to cool the edge plasma. The limiter materials are distinguished with respect to their ability, or otherwise, to allow plasmas with high central temperatures and low limiter erosion.

Plasma transport calculations similar to those reported in /1-3/ are used to make this assessment for JET with the full planned heating power. As pointed out in /1/ there are many uncertainties in the models used for these calculations (particularly for the edge plasma) and no model describes tokamak plasmas in sufficient detail. In the present paper we concentrate on the effect of changes in the particle transport and the effect of neon as a control gas to illustrate important features of the assessment.

MODEL ASSUMPTIONS

A particular 1-D model for transport transverse to the magnetic field is augmented by a phenomenological model for the parallel transport in the shadow of the limiter. The dominant terms in the equations for electron density, n_e, impurity density, n_z, and electron and ion pressures (p_e and p_i) are:

$$\frac{\partial n_e}{\partial t} + \frac{1}{r}\frac{\partial r\Gamma_e}{\partial r} = S_n^o + S_n^z - \frac{n_e}{\tau_{||}} \qquad \Gamma_e = -D_e\frac{\partial n_e}{\partial r}$$

$$\frac{\partial n_z}{\partial t} + \frac{1}{r}\frac{\partial r\Gamma_z}{\partial r} = S_z^z - \frac{n_z}{\tau_z} \qquad \Gamma_z = -D_z\frac{\partial n_z}{\partial r}$$

$$\frac{3}{2}\frac{\partial p_e}{\partial t} + \frac{1}{r}\frac{\partial}{\partial r}r\left(\frac{3}{2}kT_e\Gamma_e - n\chi_e\frac{\partial kT_e}{\partial r}\right) = S_e^o - S_e^z - \frac{2n_ekT_e\gamma}{\tau_{||}}$$

$$\frac{3}{2}\frac{\partial p_i}{\partial t} + \frac{1}{r}\frac{\partial}{\partial r}r\left[kT_i\left(\frac{3}{2}\Gamma_e + y\,\Gamma_i\right) - n\,\chi_i\frac{\partial kT_i}{\partial r}\right] = S_i^o - \frac{2n_ekT_i}{\tau_{||}}$$

INTOR values are taken for D_e and χ_e. D_z is a multiple of D_e. Neoclassical values are taken for the ion heat transport terms χ_i, $y\Gamma_i$. Transport in the scrape-off layer is characterised by the parallel confinement time, $\tau_{||} = L/V$ (where L is the effective connection length taken to be πRq and V is the effective flow speed /4/) for electrons and for hydrogenic ions and $\tau_z = \tau_{||}$ or ∞ for impurities. Plasma ions are recycled at the limiter and wall as neutrals, giving rise to the terms S_n^o, S_e^o and S_i^o. Impurities are produced at

the limiter by sputtering by charged particles and at the nickel wall by charged particles and charge-exchanged neutrals, giving rise to the terms S^Z (electron stripping), S^Z_e (coronal radiation) and S^Z_Z (impurity production) /1/.

Additional inward anomalous transport is modelled with the following particle fluxes for the electrons and ions:

$$\Gamma_e = - D_e \left(\frac{\partial n_e}{\partial r} + \frac{2r}{a^2} n_e \right) \qquad \Gamma_z = - D_z \left(\frac{\partial n_z}{\partial r} + \frac{2r}{a^2} n_z \right)$$

APPLICATION

The present application is to a circular cross-section plasma with the same volume as JET (effective limiter radius, 1.62m; wall radius, 1.72m; major radius, 2.96m). The heating sources correspond to the full planned power for JET and comprise the sum of (a) ohmic heating with a current of 4.8MA at a field of 3.45T, (b) injection of neutral deuterium at a power level of 10MW at an energy of 160kV (17.25MW including the fractional energy components) (c) a uniform ion heating profile of about $0.1 MWm^{-3}$ to represent some form of radio frequency heating at an effective level of 15MW within the limiter radius, and (d) alpha particle heating by plasma-plasma and beam-plasma interactions assuming a 50:50 mixture of deuterium and tritium.

RESULTS

A particularly pessimistic assumption used previously /1/ for the impurity transport ($D_Z = \tau_Z = \infty$) illustrates the benefits of forming a cool plasma mantle (CPM) of acceptable width: nickel limiters result in the formation of too wide a CPM (see Table, cases A) before the edge temperature and hence the impurity sputtering become sufficiently low. Almost all the input power is radiated. With the radiating layer at 0.95m the central temperature and global energy confinement time are low. Beryllium limiters lead to a narrow CPM in which the density is high and the temperature is low. The sputtering of both beryllium and nickel is limited to tolerable levels. Sputtering of wall material by hot charge-exchanged neutrals is important in establishing these conditions with ~90% of the input power radiated, predominantly by nickel. The performance is similar with graphite, although the high radiating efficiency of carbon at low temperatures tends to overcool the edge plasma. There is little ionisation of the recycled flux in the edge and the width of the CPM increases to compensate.

Substantial improvement in performance with nickel limiters is achieved by a specified influx of neon to cool the edge plasma (case B). The necessary concentration of control gas is acceptably low (~1%).

Calculations for a nickel limiter /1/ with $D_Z = D_e$ and $\tau_Z = \tau_{||}$ indicate that edge accumulation of impurities occurs. The total impurity content and the width of the CPM is reduced and the overall performance improves. We now find that with each limiter material examined a similar central temperature and global energy confinement time is achieved (cases C). The edge conditions and the global power balance are, however, dependent on the limiter material. With nickel limiters the edge temperature is low, but the impurity concentration is sufficiently high to radiate almost all the input power. With beryllium limiters the edge temperature is sufficiently high for parallel thermal transport to the limiters to be the dominant loss channel. With graphite limiters, most of the input power is finally radiated, with carbon radiation accounting for ~85% of the total.

Control of the erosion of nickel limiters is demonstrated using a specified influx of neon. This control is achieved, however, at the expense of reduced plasma performance since a wider CPM forms (case D).

With additional inward transport that leads to more peaked density profiles, the behaviour is dominated by the low edge density which provides little shielding of the wall from hot charge-exchanged neutrals. Again there is little dependence on the choice of limiter material (case E).

SUMMARY

The calculations indicate the benefits of forming an edge radiating layer of sufficient width. Otherwise the sputtered influx of impurities can lead to an unacceptably high impurity concentration or severe limiter erosion. Acceptable conditions can be achieved in general with a controlled influx of low Z material and sometimes with a combination of a low Z limiter and nickel wall.

The dependence of performance on limiter material is most pronounced for a transport model with rapid cross-field transport and good impurity confinement. Nickel limiters lead to small aperture plasmas with low central temperatures and global energy confinement times. The performance improves using a controlled influx of neon or by replacing the nickel limiters by beryllium or graphite.

There is little dependence on the limiter material for models that lead to a large recirculation of impurities in the edge, or for models that lead to insufficient ionisation in the edge plasma, since there is then little protection of the wall from hot charge-exchanged neutrals. The limiter erosion can be reduced by using a controlled influx of neon.

ACKNOWLEDGEMENT

The work by one of the authors (A-vM) was performed under the Euratom-FOM Association Agreement with financial support from ZWO and Euratom.

REFERENCES

/1/ Watkins, M.L., Cordey, J.G., Abels-van Maanen, A.E.P.M., Roberts, J.E.C., and Stubberfield, P.M.: 9th Int. Conf. on Plasma Physics and Controlled Nuclear Fusion Research, IAEA-CN-41/D-2-1, Baltimore (1982).

/2/ Neuhauser, J., Lackner, K., and Wunderlich, R.: Int. Conf. on Plasma Physics, 12BI:1, Gothenburg (1982).

/3/ Gibson, A., Dietz, K.J., Abels-van Maanen, A.E.P.M., and Watkins, M.L.: Proc. IAEA Tech. Com. Mtg. on Divertors and Impurity Control, III.R2, Garching (1981).
Also, Watkins, M.L., Abels-van Maanen, A.E.P.M., and Gibson, A.:III.C1.
Also, Lackner, K., and Neuhauser, J.: II.R2 and III.C2.

/4/ Ogden, J.M., Post, D.E., Jensen, R.V., and Seidl, F.G.P.:Report PPPL-1608, Princeton Plasma Physics Lab., U.S.A. (1980).

* On attachment from FOM-Instituut voor Plasmafysica, Nieuwegein, The Netherlands. Present affiliation: Math. Inst. of the Univ. of Oxford, U.K.

Results after 3s of additional heating

Limiter Material	Nickel						Beryllium						Graphite					
Transport Model	$\hat{T}_i$ (keV)	$\bar{\tau}_E$ (s)	r_{CPM} (m)	T_i^{lim} (eV)	n_e^{lim} ($10^{19}m^{-3}$)	P_{RAD} (MW)	$\hat{T}_i$ (keV)	$\bar{\tau}_E$ (s)	r_{CPM} (m)	T_i^{lim} (eV)	n_e^{lim} ($10^{19}m^{-3}$)	P_{RAD} (MW)	$\hat{T}_i$ (keV)	$\bar{\tau}_E$ (s)	r_{CPM} (m)	T_i^{lim} (eV)	n_e^{lim} ($10^{19}m^{-3}$)	P_{RAD} (MW)
$D_z = \tau_z = \infty$ (A)	8.6	0.18	0.95	9.8	5.2	38.5	9.0	0.71	1.55	11.6	6.9	28.8	11.8	0.76	1.49	2.6	1.1	30.5
+ Neon Influx (B)	12.1	0.53	1.34	8.8	5.8	31.7												
$D_z = D_e$ $\tau_z = \tau_{\|\|}$ (C)	17.0	1.0	1.59	15.6	5.1	27.1	16.7	1.56	1.63	98.0	5.0	5.6	15.6	1.24	1.62	49.0	5.1	23.4
+ Neon Influx (D)	12.8	0.73	1.48	2.7	2.9	30.7												
$D_z = D_e$ $\tau_z = \tau_{\|\|}$ (E) + Inward	8.8	0.75	1.59	19.4	2.3	31.0	8.7	0.59	1.56	38.8	0.7	32.9	8.5	0.57	1.56	40.0	0.7	29.6

NUMERICAL CALCULATIONS OF PLASMA PARAMETERS FOR A STEADY-STATE ALFVEN-WAVE TOKAMAK

V.P.Sidorov, V.P.Minenko, K.G.Komoshvilli (Vekua Institute of Physics and Technology, Sukhumi, USSR); A.P.Favorsky, M.V.Dmitrieva, V.F.Tishkin (Keldysh Institute of Applied Mathematics, Moscow, USSR).

Experimental and theoretical research for recent years have demonstrated the possibility of noninductive current generation in toroidal systems using the traveling RF waves /1/, wich can be based upon absorption of the Alfven wave ($\omega = k_{\parallel} c_A$) power by plasma electrones. While calculating steady-state tokamak parameters, absorption of monochromatic Alfven wave energy and momentum with Landau damping and Coulomb collisions have been taken into account. In such a case, absorbed, parallel to the magnetic field momentum component excites the current drive, while the binormal one generates a radial plasma drift capable of compensating diffusive expasion. In order to outline the plasma parameters redistribution transient process, a system of equations for heat, particles and poloidal field with external supplies of energy, momentum and particles is solved. The heat balance equations include losses due to heat conductivity, cyclotron radiation and bremsstrahlung. Heat is supplied by Ohmic heating, Alfven wave power absorption and thermonuclear burning. The ion heat conductivity was assumed to be neoclassical, while for electrons, Alcator scaling was used. In order to compensate diffusion losses, two varieties of fuel pellets injection have been proposed. The initial discharge is provided by an inductive current and on exhausting volt-seconds at a sufficiently hot phase ($T_{e,i}$=2 keV) Alfven wave absorption is initiated /2/. The inductive current becomes entirely replaced by the current drive during the skin time ($\sim 2 \cdot 10^3$ s for INTOR device). Based on previous calculations /3/, the RF power absorption profile was taken as $Q(x,t) = Q_o[1-\exp(-t/\tau)]\exp[-\gamma(x/x_*-1)^2]$, where $x_*=r_*/a$ is the Alfven resonance location, γ =3 and τ is the absorption "switch-on" time. The power amplitude Q_o is determined by current constancy condition

$$\frac{e^2}{m_e}\int_0^1 \frac{n(x,t)E e^{-t/\tau}}{\nu_{ei}(x,t)}\,xdx - \frac{ek_z}{m_e\omega}\int_0^1 \frac{Q(x,t)}{\nu_{ei}(x,t)}\,xdx = \frac{I_p}{\pi a^2}\,, \qquad (1)$$

where E is the inductive-generated eddy electric field and I_p is the plasma total current. The resonance point is defined as the maximum, over the $0 \leq x \leq 1$ range, root of equation

$$\omega = \omega_*(x,t) \equiv \frac{N}{R}\cdot\left(1 + \frac{H}{Nq(x,t)}\right)\cdot c_A(x,t), \qquad (2)$$

where ω, M, N are the frequency and the RF wave numbers; R is the torus major radius, q being the safety factor.

Calculations have been carried out for INTOR parameters in "hard" (τ =1-5 ms) and "soft" (τ =5 s) modes of the power initiation. Due to the "hard" case, electron and ion temperatures encrease rapidly, while the current grows slowly forming dips at either side of the resonance region (Fig.1). Such a delay in current growth is due to the E.M.F. The current drive is sustained by an external source, whereas the induced countercurrent is decayed diffusing in both directions from x_*. For the "soft" case, the dips on the current curve are smaller. With the axial fuel injection, the density profile becomes sharp and the resonance region displaces to the plasma center. As for the volume injection, it results in a steady density profile (Fig.2). For $M/N<0$ (M=-3, N=4; the diamagnetic wave rotation) any variation in the current profile sets near resonance conditions (Fig.3) over the considerable part of the radius. The resonance curve plateau formation is due to two competing mechanisms. Namely, the local RF power absorption leads to the poloidal field change so that the value of $k_\parallel = \vec{k}\cdot\vec{h}$ is diminished to the right of the resonant point, while to the left it is encreased. On the other hand, changes in the poloidal magnetic flux cause the field diffusion its time scale in a hot plasma being large enough. As a result, the resonant point displacements of relaxation oscillations type occur, their dynamics being shown in Fig.4. The relaxation oscillations allow supply the RF power into a plasma volume comparable to the total one. For $M/N>0$, there are no relaxation oscillations, the resonant point being displaced towards the boundary. Fig.2

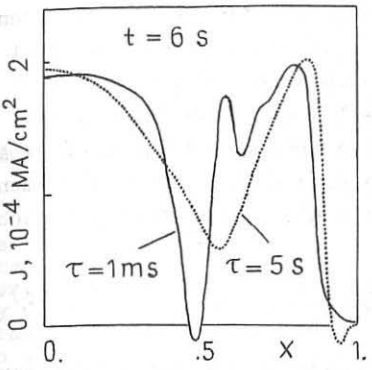

FIG.1

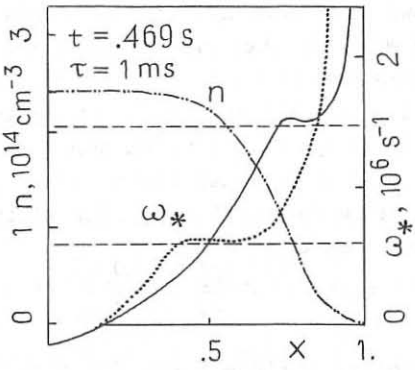

FIG.2

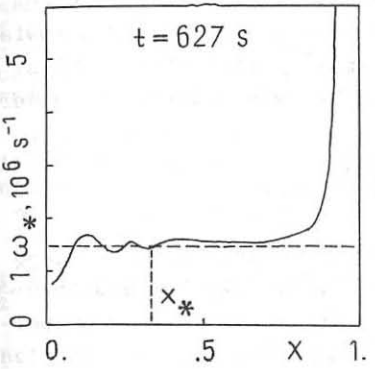

FIG.3

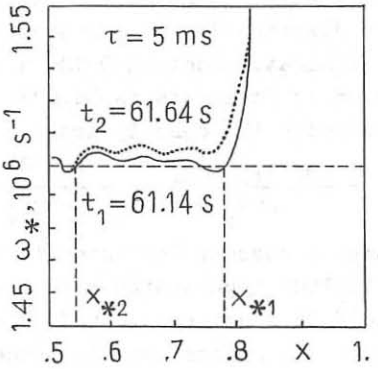

FIG.4

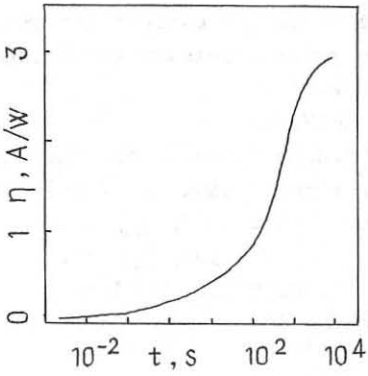

FIG.5

shows the resonance plateau appearance for two various frequences with the same values of M amd N. Efficiency η of current generation depends in time upon the temperature due to its growth as thermonuclear burning result, and amounts to 3 A/W level (Fig.5). Diffusion compensation process is revealed as a drift in a toroidal field under the Alfven wave binormal momentum component influence. The steady-state radial flux for such a case amounts to

$$\langle nv_r \rangle = -D \frac{dn}{dr} - \frac{cMQ_o B_z}{eB^2 r \omega} \left(1 - \frac{r}{R} \frac{NB_\varphi}{MB_z}\right). \qquad (3)$$

Selecting various M and N one may preassign the drift term sense and value and, thereby, control the radial plasma flux. The necessary energy consumption estimation for the $\langle nv_r \rangle = 0$ case gives a distribution n(r) approaching to a rectangular-stepwise one, the Alcator scaling $D = 10^{17} n^{-1}$ $cm^2 s^{-1}$ being chosen. This allows us to integrate in Eq.(3) and to relate the total power absorbed with the density drop:

$$W = \frac{4\pi^2 R r_*^2 eB^2 D_*}{cMB_z} \left(1 - \frac{r_*}{R} \frac{NB_\varphi^*}{MB_z^*}\right)^{-1} \omega \cdot \Delta n. \qquad (4)$$

The power necessary for establishing the steady state $\langle nv_r \rangle = 0$ in an IGNITOR type system with $\omega = 10^6$ s^{-1}, M=2, N=3 and $\Delta n = 6 \cdot 10^{14}$ cm^{-3} does not exceed 5MW. The total power W is in proportion with the plasma volume, hence, for the INTOR type devices W amounts to 100-200 MW. Thus, the monochromatic Alfven wave absorption is capable of providing the steady-state operation in tokamaks. In such a case, the current generation efficiency is order of 1 A/W, the power necessary for balancing the diffusion being defined by Ex.(4).

REFERENCIES

/1/ R.A.Demirkhanov, Yu.S.Khodyrev. Nucl. Fusion. 1962, Supplement, p.1, 259; R,Klima. Plasma Phys. 1973, 15, 10; N.T.Fish. Phys. Rev, Lett. 1978, 41, 837; R.A.Demirkhanov, A.G.Kirov. Pis'ma v ZhETF. 1981, 33, 31.

/2/ M.V.Dmitrieva, K.G.Komoshvilli. Keldysh IAM-195, 1982.

/3/ O.S.Boordo, V.V.Gorin. 10th Europ. Conf. Contr. Fusion and Plasma Phys. 1981, v.1, H-10; D.W.Ross, G.L.Chen. Phys. Fluids. 1982, 25, 646.

NEOCLASSICAL EQUILIBRIUM OF PLASMA DURING ION HEATING IN STELLARATOR

N.T.Besedin, O.S.Pavlichenko, V.N.Pyatov,
A.S.Slavny, O.M.Shvets
Institute of Physics &Technology,Ukr.Acad.Sci.,Kharkov,USSR

ABSTRACT. The evolution of plasma parameters during HF-ion heating in "Uragan-2" stellarator is studied by means of 1D transport model. It is shown that under the experimental conditions plasma evolves to a stationary state characterized by a sharply peaked ion temperature and hollow electron density profiles. The neoclassical thermodiffusion is shown to play a major role in the setting in of such equilibrium.

INTRODUCTION. In experiments on a high temperature plasma in stellarators there are many indications of the neoclassical behaviour of plasma transport/1-3/. The multiplication factor of neoclassical heat conductivity was 1 for ions /1-3/and not exceeding 6 for electrons /3/. These results give a basis for modelling plasma parameters evolution in stellarators and were used to study HF plasma heating in "Uragan-2" stellarator.

MODEL. Plasma evolution was described by means of 1D diffusion model of energy and particle balance for electrons and ions:

$$\frac{\partial n}{\partial t} = -\frac{1}{r}\cdot\frac{\partial}{\partial r}\left(r\cdot\langle n\cdot v\rangle_r\right) + S_{ion} - S_r - \nabla_\parallel \Gamma_\parallel \ ,$$

$$\frac{3}{2}\frac{\partial (n\cdot T_i)}{\partial t} = -\frac{1}{r}\cdot\frac{\partial}{\partial r}\left(r\cdot q_i\right) + P_i - P_{ie} - P_{cx} - \nabla_\parallel q_{i\parallel} \ , \qquad (1)$$

$$\frac{3}{2}\cdot\frac{\partial (n\cdot T_e)}{\partial t} = -\frac{1}{r}\cdot\frac{\partial}{\partial r}\left(r\cdot q_e\right) + P_{ie} - P_{ion} - P_{ex} - P_{rad} - \nabla_\parallel q_{e\parallel},$$

In these equations S_{ion} and S_r account for ionization and recombination of hydrogen; P_{ie} and P_{cx} - for the ion energy losses due to collisions with electrons and charge exchange process; $P_{ex,ion}$ and P_{rad}- for the electron energy losses due to excitation and ionization of hydrogen and impurity radiation; P_i- for the ion heating source. Radial particle, $\langle n\cdot v\rangle$, and energy, $q_{i,e}$, fluxes were described by the neoclassical theory /4-6/; for the electron neat flux q_e we introduced an anomaly factor A. On plasma border we supposed existence of a scrape-off layer with thickness Δ and longitudinal losses of particles $\nabla_\parallel \Gamma_\parallel$ and energy $\nabla_\parallel q_\parallel$ /7/.

N-Neutral hydrogen behaviour was described by equation /8/;

$$v_r\cdot\frac{\partial f_n(r,v)}{\partial r} + \left[\alpha_i(r)+\alpha_{cx}(r)\right]\cdot n(r)\cdot f_n(r,v) = \qquad (2)$$
$$= \alpha_{cx}(r)\cdot f_i(r,v)\cdot N(r) + \alpha_r\cdot f_i(r,v)\cdot n(r) \ ,$$

where $f_{n,i}(v)$- velocity distribution functions for atoms and ions, $(v^2 = v_r^2 + v_\varphi^2 + v_z^2)$, N- neutral hydrogen density, $\alpha_{i,r,cx}$, are the rate coefficients for ionization, recombination and charge exchange reactions of hydrogen.

The impurities, (C,Fe)$_{ox}$, were described by the "average ion" model and taken into account at radiation losses P_{rad} and collision frequencies $\nu_{e,i}$ calculations.

The equations (1,2) were solved for boundary conditions at the chamber wall ($n(a)=2\cdot10^{11}cm^{-3}$; $T_{i,e}(a)=2eV$) and parabolic initial density and temperature profiles;

$$n(r)|_{t=0}=[n(0)-n(a)]\cdot[1-(r/a)^3]+n(a),\quad n(0)=5\cdot10^{11}cm^{-3}$$

$$T_{i,e}(r)|_{t=0}=[T_{i,e}(0)-T_{i,e}(a)]\cdot[1-(r/a)^3]+T_{i,e}(a);\quad T_{i,e}(0)=5eV.$$

For neutral hydrogen, we fixed a boundary temperature at 2 eV and time behaviour of hydrogen density $N(a)$was chosen to provide a necessary time behaviour of line averaged electron density $\bar{n}$ (t). We supposed that the ion heating term P_i doesn't depend on radius.

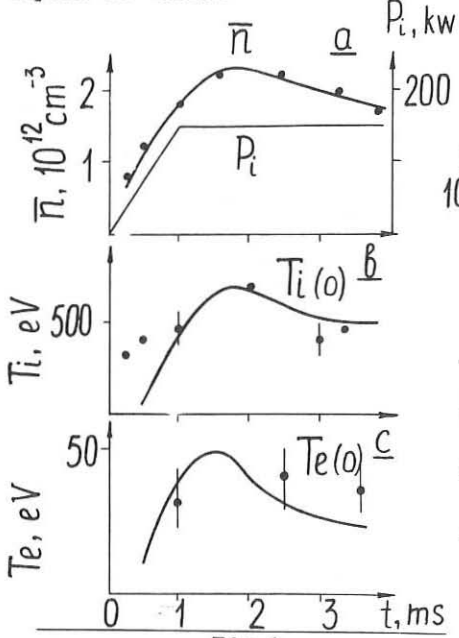

Fig.1

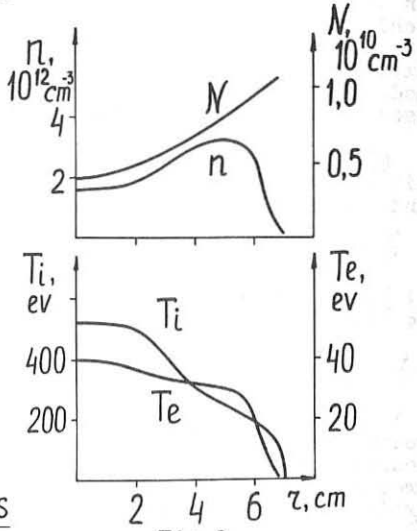

Fig.2

COMPARISION OF EXPERIMENT AND MODEL RESULTS. Fig.1 presents results of the experiment on HF ion heating in "Uragan-2" stellarator (points),i.e.line averaged electron density (8 mm interferometer), ion temperature (charge exchange analysis), electron temperature (carbon lines time hystory). The absorbed HF power in this experiment was 150±30 kW. The solid lines in Fig.1 show the numerical results computed for time behaviour of P_i and $\bar{n}$ shown in Fig.1a and $n_{Fe}=2\cdot10^{10}cm^{-3}$, A=1. One can see that the adopted model gives a realistic description of

time behaviour of T_i and T_e . The computed profiles of plasma parameters are shown in Fig.2 (for t=2,5 msec). The distinct feature of model behaviour was existence of hollow electron density profiles (for $t \geq 2{,}0$ msec).

A parametric study revealed that this phenomena was most pronounced at the electron density $n=1.10^{13}$cm (Fig.3). An increase of the absorbed HF power resulted in enhanced ion temperature peaking and deeper well on the electron density profile.

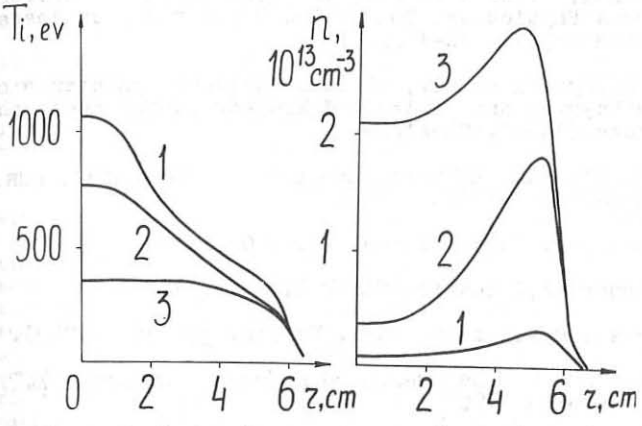

Fig.3. The radial ion temperature and electron density profiles computed for different values of electron density ($1-\bar{n}=2\cdot10^{12}cm^{-3}$; $2-\bar{n}=1\cdot10^{13}cm^{-3}$; $3-\bar{n}=2{,}2\cdot10^{13}cm^{-3}$; $P_i=300$кW)

An analysis of particle flux radial distribution showed that this flux was outward directed all along the plasma radius despite the skin distribution of electron density (Fig.4). This apparent contradiction was resolved by separately examining the diffusion $\Gamma_{\nabla n}$ and thermodiffusion $\Gamma_{\nabla T}$ parts of the neoclassical partical flux /4-6/. Comparision of these fluxes showed (Fig.4) that the outward directed thermodiffusion flux $\Gamma_{\nabla T}$ predominates and defines the total flux Γ_z direction.

DISCUSSION.The computer simulation of ion heating in stellarator showed that the theory-predicted thermodiffusion can under certain conditions influence electron density profiles. In the case when plasma power balance is defined by absorption of external power by ions, rapid ion heating takes place near the discharge axis at the density build-up phase. Rising thermodiffusion hinders density increase on the discharge axis and results in establishing of the stationary state characterized by peaked ion temperature and hollow electron density profiles. Homogeneous energy deposition supposition has a weak effect on our conclusions: the effect even strenghtens at peaked energy deposition profile. The effect doesn't depend on supposition of which plasma component-electrons or ions-absords energy and

heats.

Thus, the stationary hollow electron density profile should be one of the attributes of the neoclassical equilibrium of plasma in stellarator when a particle balance is maintained by gas influx.

REFERENCES.

1. A.G.Diky, S.S.Kalinichenko et al., Plasma Physics, 18 587 (1976).

2. G.Gattanei, D.Dorst et al., IX International Conference on Plasma Physics and Controlled Nuclear Fusion Research, Baltimore (1982), CN-41/L-5.

3. K.Uo, A.Iiyoshi et al., IX International Conference on Plasma Physics and Controlled Nuclear Fusion Research, Baltimore (1982), CN-41/L-3.

4. А.А.Галеев, Р.З. Сагдеев, Вопросы теории плазмы, вып.7 М., Атомиздат (1973), с.205.

5. T,E.Stringer, Phys. Fluids, 13, 810 (1970).

6. J.W.Connor, R,J.Hastie, CLM-P 341 (1973).

7. A.T.Mense, G.A.Emmert, Nucl. Fusion, 19, 361 (1979).

8. Н.Т.Беседин, Н.Б.Марущенко, В.Н.Пятов, препринт ХФТИ 81-38, Харьков (1981).

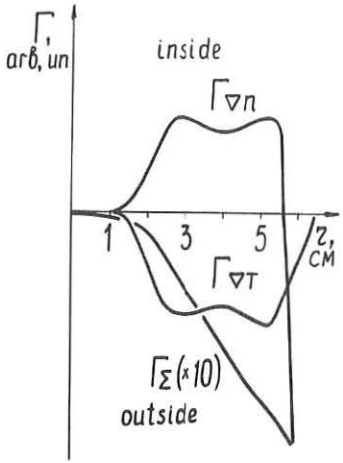

Fig.4.

A 2-D Model for the Calculation of Neutral Transport in Tokamaks with Non-Circular Magnetic Surfaces

W G F Core

JET Joint Undertaking. Abingdon
Oxfordshire, OX14 3EA, England

Abstract

An efficient procedure for the determination of the 2-D distribution of neutral particles in present tokamak systems is given. In the case of the JET plasma, where the neutral particle production is dominated by plasma-limiter interactions, results are in good agreement with Monte-Carlo calculations. For a 1000 particle Monte-Carlo simulation, and a good initial guess, a reduction in computing time to 10% is obtained.

For an effective use of transport simulation codes in the prediction of tokamak performance it is essential that an efficient procedure for the calculation of the distribution of neutral particles within the plasma volume be available. While Monte-Carlo methods provide an accurate description of the neutral particle behaviour they are far too costly for use in the transport code environment. The application of semi-analytic techniques to the problem [1,2] has produced a number of efficient procedures for deployment in 1-D transport codes or for use as fast diagnostic tools. In this work a formulation is given for the efficient determination of the 2-D distribution in present tokamak containment systems. The consideration is restricting to systems in which:-

(i) The influx of primary neutral particles into the plasma is dominated by localised sources on or near the plasma edge.
(ii) The region of the vessel wall in the proximity of the sources can be approximated by a cylindrical developement.
(iii) The important atomic interaction processes of charge exchange and ionisation by electron impact, are taken to be independant of neutral particle energy.

In accordance with (i) -(iii), the Boltzmann equation describing the transport of neutral particles in an inhomogenous cylinder of radius a, is

$$\cos\phi\frac{\partial f}{\partial r} - \frac{\sin\phi}{r}\frac{\partial f}{\partial\phi} + \frac{\lambda}{v_\perp}f = \frac{\beta}{v_\perp}f_i\int_0^{2\pi}d\phi\int_0^{\infty}v_\perp dv_\perp f + \frac{S}{v_\perp} \qquad \ldots(1)$$

with boundary condition,

$$\underline{f} = h\int_{-\pi/2}^{\pi/2}\cos\phi\, d\phi\int_0^{\infty}v_\perp^2 dv_\perp f_+ \qquad \ldots(2)$$

where $f = \int dv_\parallel f(r,\theta,v_\parallel,v_\perp,\phi)$, is the neutral particle distribution function, $v_\parallel, v_\perp$ are the components of velocity along and perpendicular to the axis of the cylinder, $\lambda = n(\langle\sigma v\rangle_{cx} + \langle\sigma v\rangle_{ii})$ is the sum of the rate coefficient [3], $n = n(r,\theta)$ is the plasma electron/ion density, $\beta = \beta(r,\theta) = \langle\sigma v\rangle_{cx}$ is the velocity-cross section product for charge exchange reactions,

$f_i = f_i(r,\theta) = n(r,\theta)/\pi T(r,\theta)\ exp(-V_1^2/T(r,\theta))$ is the plasma ion distribution function, $S = S(r,\theta,V_1)$ is the distribution of primary neutral particle sources within the plasma volume, and $h = h(a,\theta,V_1) = \pi^{-1/2} T_w^{-3/2} exp(-V_1^2/T_w)$, is the function describing the neutral particles emitted from the wall, at temperature T_w.

For the case of particular interest, where the production of primary neutrals is dominated by plasma-limiter surface interactions, integral equations for the neutral flux to the wall and density within the plasma volume are readily obtained. Introducing into Eq.(1) the trajectory invariant $\rho = r\sin\phi$, setting $S = \delta(V-V_0)\,\delta(\theta)\,\delta(r-a)/2\pi V_0^2 r$ (a primary particle source located in the median plane, at the plasma edge, and emitting neutrals isotropically with velocity V_0), using Eq.(2), and integrating over particle trajectories gives the following coupled equations for the flux $\Gamma_+(\theta)$ and density $N(r,\theta)$,

$$\Gamma_+(\theta) = \frac{\cos\phi}{2\pi} K_{i_2}\left\{\frac{\lambda_a' + \lambda_a''}{V_0}\right\} + \int_{-\pi/2}^{\pi/2} \cos\phi\, d\phi\, \Gamma_+(\theta'') V_2\left\{\sqrt{\frac{2}{T_w}}\left(\lambda_a' + \lambda_a''\right)\right\}$$

$$+ \frac{\beta}{2\pi}\int_{-\pi/2}^{\pi/2} \cos\phi\, d\phi \int_{\rho}^{a} \frac{\eta\, d\eta}{\sqrt{\eta^2-\rho^2}}\left[n V_{i_1}\left\{\sqrt{\frac{2}{T}}\left(\lambda_a' - \lambda_\eta''\right)\right\} N(r,\theta') \right.$$

$$\left. + n V_{i_1}\left\{\sqrt{\frac{2}{T}}\left(\lambda_a'' + \lambda_\eta'\right)\right\} N(r,\theta'')\right], \qquad \ldots(3)$$

where $\theta + 2\phi'' - \phi''/|\phi''|\pi = 0$, and

$$N(r,\theta) = \frac{1}{2\pi}\left[K_{i_1}\left\{\frac{\lambda_a' - \lambda_r'}{V_0}\right\}\left\{1 - \frac{r\cos\phi}{\sqrt{r^2-\rho^2}}\right\}^{-1}_{\phi=\phi'} + K_{i_1}\left\{\frac{\lambda_a'' + \lambda_r'}{V_0}\right\}\left\{1 + \frac{r\cos\phi}{\sqrt{r^2+\rho^2}}\right\}^{-1}_{\phi=\phi''}\right]$$

$$+ \frac{1}{\sqrt{4\pi T_w}}\int_{-\pi/2}^{\pi/2} d\phi \left[\Gamma_+(\theta') V_{i_1}\left\{\sqrt{\frac{2}{T_w}}\left(\lambda_a' - \lambda_r'\right)\right\} + \Gamma_+(\theta'') V_{i_1}\left\{\sqrt{\frac{2}{T_w}}\left(\lambda_a'' + \lambda_r''\right)\right\}\right]$$

$$+ \frac{\beta}{\sqrt{2\pi}}\int_{-\pi/2}^{\pi/2} d\phi \int_{\rho}^{a} \frac{\eta\, d\eta}{\sqrt{\eta^2-\rho^2}}\left[\frac{n}{\sqrt{T}} V_0\left\{\sqrt{\frac{2}{T}}\left(\lambda_\eta' - \lambda_r'\right)\right\} N(r,\theta') \right.$$

$$\left. + \frac{n}{\sqrt{T}} V_0\left\{\sqrt{\frac{2}{T}}\left(\lambda_\eta'' + \lambda_r'\right)\right\} N(r,\theta'')\right], \qquad \ldots(4)$$

where $\theta+\phi'-\sin^{-1}(\rho/a)=0$, $\theta+\phi''-\phi''/|\phi''|\pi+\sin^{-1}(\rho/a)=0$, $K_{i_n}\sim\sqrt{2/\pi}\exp(-\tau)/\sqrt{\tau+n}$, $V_n(\tau)\sim\sqrt{2\pi/3}\exp(-3\tau^{2/3}/2)\tau^{-h/3}$, $\lambda_r=\int_\rho^r \frac{\eta\,d\eta}{\sqrt{\eta^2-\rho^2}}\lambda(\eta,\theta^s)$, $\theta'=\theta+\phi-\sin^{-1}(\rho/\eta)$, $\theta''=\theta+\phi-\phi/|\phi|\pi+\sin^{-1}(\rho/\eta)$, and $N(r,\theta)=\int_{-\pi/2}^{\pi/2}d\phi\int_0^\infty v_\perp\,dv_\perp f$.

To complete the model a description of the mapping of the plasma onto the cylinder is required. The prescribed variations in plasma density and temperature are mapped onto the cylinder using a shaped magnetic flux representation of the form [4],

$$\left.\begin{aligned} R &= \alpha + \beta(\xi) + \gamma(\xi)\cos\eta + \Delta(\xi)\sin^2\eta \\ Z &= \kappa(\xi)\sin\eta \end{aligned}\right\}, \qquad \ldots(5)$$

and

$$\left.\begin{aligned} R &= R_c + r\cos\theta \\ Z &= r\sin\theta \end{aligned}\right\},$$

where $\alpha, \beta, \gamma, \Delta, \kappa$ are constants which specify the plasma shape, density and temperature. Inversion of Eq(5) leads directly to a quadratic equation for ξ^2. The plasma density $n(\xi^2)$, and temperature $T(\xi^2)$ profiles, which take the usual form of $(1-\xi^p)^q$, where p,q are profile constants, are then readily calculated. Regions of the cross-section external to the actual plasma are filled with pseudo plasma of arbitrary large density, with temperature of the wall, and where ionization by electron impact is forbidden, Fig.1.

The numerical solution of Eqn.(3) and (4) is a standard procedure. By approximating the integrals by finite summations, the integral equations are converted to matrix form, and the solution then follows directly through numerical interation.

The results of a comparison with Monte-Carlo simulation of the JET situation is shown in Fig.2. Further applications of the method to the JET plasma will be presented.

ACKNOWLEDGEMENTS
The author wishes to thank Dr. Reiter, KFA Jülech for the Monte-Carlo results.

REFERENCES

(1) K H Burrell, Journal of Computational Physics 27, 88 - 102, (1978)
(2) S Tamor, Journal of Computational Physics, 40, 104 - 119 (1981)
(3) R L Freeman, E M Jones, "Atomic Collision Processes in Plasma Physics Experiments 2", Culham Laboratory Report CLM - R 137
(4) T E Stringer, Private Communications.

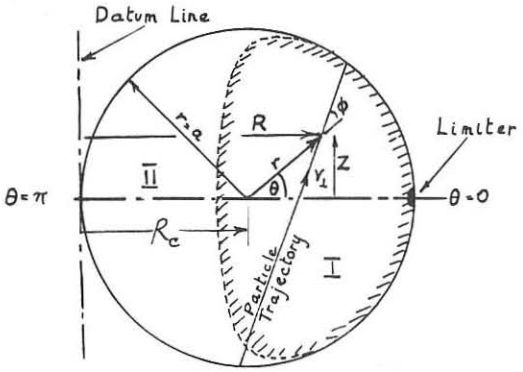

Fig. 1 : The shadow of the plasma on the circle and coordinate system is shown. Region I is the actual plasma. Region II is the pseudo plasma region where the interacting processes are restricted to charge exchange and the electron/ion density is sufficiently great that neutral particles penetrating this region are reflected back into Region I with an energy corresponding to the temperature of the wall.

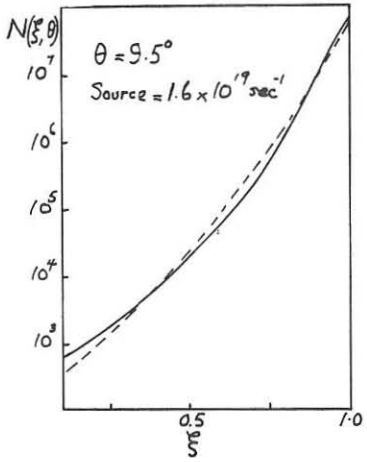

Fig. 2 : A comparison with a 1000 particle Monte Carlo simulation is shown. The neutral particle profiles along the radius $\theta = 9.5^{\circ}$ when the primary neutrals entering the system are from a point source located at $\theta = 0$, $\xi = 1$ are shown. The broken line is the model calculation.

MODELLING OF TOKAMAK DISCHARGES BASED ON TRANSPORT PROCESSES ALONG OBLIQUE MAGNETIC FIELD LINES

A. Nicolai and G.H. Wolf

Institut für Plasmaphysik, Kernforschungsanlage Jülich GmbH, Association EURATOM-KFA, P.O.B. 1913, D-5170 Jülich, FRG

1. INTRODUCTION

Electron energy confinement in Tokamaks is significantly lower than predicted by neoclassical theory. Attempts to explain this behaviour /e.g. 1-4/ include island formation and the development of regions with field line ergodization. In particular, resistive MHD activities cause major magnetic islands in the vicinity of rational flux surfaces /5/, and, at higher β_p, pressure driven modes may evoke numerous small islands /6/. Their common feature is an erosion of the system of nested toroidal flux surfaces in certain plasma regions or perhaps even in the total plasma volume. This results in an enhancement of the effective radial transport caused by transport parallel to magnetic field lines being inclined against the toroidal direction.

In the present paper an attempt is made to account for these effects in the frame of a transport code by introducing a time-averaged angle $\varepsilon(r) = \langle |B_r/B| \rangle$ of field line inclination in the radial direction throughout the whole plasma volume to describe the deterioration from ideal toroidal confinement. (B is the total magnetic field strength, B_r is the radial field component and $\langle \ldots \rangle$ denotes the average over an otherwise unperturbed flux surface.) The angle $\varepsilon(r)$ replaces those anomaly-factors which are generally used in codes to simulate the observed electron "cross-field" transport. Values around 10^{-4} - coinciding roughly with results from the "magnetic flutter" model /1,7/ - lead to a suggestive agreement of the computed parameters with experimental results for both, ohmically heated plasmas and powerful additional heating.

The chosen procedure is an extension of a previous model developed /8-10/ for the description of deliberately ergodized boundary layers which are predicted to act as a magnetic limiter; there the required value of $\varepsilon(a)$ is of the order 10^{-3}, i.e. one order of magnitude beyond that suited to model the confinement features of the bulk plasma.

2. MAGNETIC FIELD STRUCTURE

In this first approach, the following crude assumptions are used to model the field structure applicable for a one-dimensional simulation code:

i) B_r is independent of time, plasma pressure and other parameters.

ii) The island structure/ergodization does not cause major disruptions or otherwise influence the dynamics of the discharge.

iii) The inclination angle $\varepsilon(r)$ varies with radius like

$$\varepsilon(r) = \varepsilon(a) \left(\frac{r}{a}\right)^2 \qquad (1)$$

$\varepsilon(r)$ be the average over the torus surface at the radius r.

Inconsistencies of this field structure with respect to Maxwell's equations are neglected.

3. TRANSPORT MODEL

Transport parallel to $\vec{B}$ is described by (subsonic) ion sound flow and by parallel heat conduction. Accordingly, the following particle and energy flux densities $\Gamma_{\parallel}$, $Q_{e_{\parallel}}$ and $Q_{i_{\parallel}}$ are taken /10/:

$$\begin{aligned} \Gamma_{\parallel} &= -M n_i v_s \, \mathrm{sign}(dp/dl_{\parallel}) \\ Q_{e_{\parallel}} &= -n_e \chi_{e_{\parallel}} \left(\partial T_e / \partial l_{\parallel} \right) + \tfrac{3}{2} k T_e \Gamma_{\parallel} \\ Q_{i_{\parallel}} &= -n_i \chi_{i_{\parallel}} \left(\partial T_i / \partial l_{\parallel} \right) + \tfrac{3}{2} k T_i \Gamma_{\parallel} \end{aligned} \qquad (2)$$

For simplicity reasons, impurities are not included here.

$l_{\parallel}$ is the coordinate along $\vec{B}$.

v_s is the local ion sound speed. M(r) is the Mach number profile accounting roughly for the momentum transfer to the plasma from recycling processes and viscosity. In this approach M = 0.3 is assumed throughout as suggested from divertor experiments /13/, though only for the boundary region.

Since the choice of M accounts for the hydrodynamics of the flow, the pressure gradient parallel to $\vec{B}$ enters only through its sign. N_e, n_i, T_e, T_i, are the electron density, ion density, electron and ion temperature, respectively, k is the Boltzmann's constant. The parallel electron and ion heat diffusivities $\chi_{e_{\parallel}}$ and $\chi_{i_{\parallel}}$ are taken from /11/. The simplified magnetic field structure yields

$$d/dl_{\parallel} = \varepsilon \, d/dr. \qquad (3)$$

Hence the effective radial particle, electron and ion energy flux densities can be derived from eq. (2). These parallel flux densities are superimposed upon those radial flux densities which result from neoclassical cross-field transport /10/. However, instead of a neoclassical inward flow, the phenomenological inward flow term proposed by Engelhardt et al. /13/ is used according to its successful fit to measured n_e-profiles.

Since our model is not suited to describe the dynamics of internal disruptions, the region of sawteeth activity is only globally treated by applying an averaging process, i.e. only there an anomalous cross-field heat diffusivity equal to the Bohm value is applied whenever $q(r) < 1$ in order to stabilize q(r) around unity.

To introduce additional plasma heating a simple bell shaped deposition profile is taken with half of the total heating power acting on the electrons, the other half acting on the ions; starting from this, energy transfer between the two species and also the usual energy losses like radiation, charge exchange etc. are included.

RESULTS

The simulation code with the described features has been applied to TEXTOR parameters:

R_0 = 1.75 m, a = 0.5 m, B_T = 2 T and, for q = 3, I_p = 476 kA. The volume-averaged electron density $\bar{n}$ has been varied between 2 and $6 \cdot 10^{13}/cm^3$, though experimentally $\bar{n}$ is confined yet to the lower value.

Fig. 1 shows, for $\varepsilon(a) = 10^{-4}$, the dependence of the energy confinement times applied upon a) the electron energy and b) the total energy. They are normalized to their values at $\bar{n} = 2 \cdot 10^{13}/cm^3$ and compared with an Alcator-

type scaling law, i.e. $\tau_{el} \sim \bar{n}$. The indexing is done as follows: "Ω" stands for ohmic heating, "H" for additional heating with a power of P_H = 4.5 MW. "el" stands for the electron energy and "t" for the total energy, "sc" denotes the Alcator-scaling law. As to be expected, the curves for τ_{el_H} and τ_{el_Ω} lie very close to τ_{sc} since conduction is dominant in that case and $\chi_{el_\parallel}$ is proportional to $1/n_e$. By contrast, τ_{t_H} is somewhat reduced due to the specific contribution of the loss channels for the ion energy growing with n_i.

Fig. 2 shows, for $\varepsilon(a) = 10^{-4}$, the degradation of confinement time with increasing heating power due to the $T_e^{5/2}$ dependence of the parallel electron heat conductivity. This result reveals a coincidence with heating experiments in Tokamaks like e.g. in ASDEX (l-regime) /14/.

Fig. 3 displays for both, $\varepsilon(a) = 0.5 \cdot 10^{-4}$ and $\varepsilon(a) = 10^{-4}$ the peak ion temperature heating power per particle $P/\bar{n}$. The electron density $\bar{n}$ is in the range between $2 \cdot 10^{13}$ and $6 \cdot 10^{13}/cm^3$, the additional heating power between 1.12 and 4.5 MW.

Again, the computed trends agree with experimental results on PLT and TFR /15,16/ for both, the linear dependence of T_i on $P/\bar{n}$ and, roughly, also for the absolute values of T_i.

REFERENCES

/1/ M.N. Rosenbluth and P. Rutherford in FUSION Vol. 1, Part A, Page 109 ff, Academic Press 1981

/2/ H.P. Furth ibid. Page 216 ff

/3/ B.B. Kadomtsev, Nucl. Fusion 23, 106 (1983)

/4/ P.H. Diamond et al., Nucl. Fusion Suppl. I, 259, Vienna (1983)

/5/ S. v. Goeler, Proc. EPS Conf. on Contr. Fusion and Plasma Physics II, 71, Lausanne (1975)

/6/ B.A. Carreras et al., 9th Int. Conf. on Plasma Physics and Contr. Nucl. Fusion, Baltimore, IAEA-CN-41/P-4 (1982)

/7/ A.B. Rechester and M.N. Rosenbluth, Phys. Rev. Lett. 40, 38-41 (1978)

/8/ G.H. Wolf, KFA-Report Jül-1666, ISSN 0366-0885 (1980)

/9/ W. Feneberg and G.H. Wolf, Nucl. Fusion 21, 669 (1981)

/10/ A. Nicolai and D. Reiter, J. of Nucl. Mat. 111/112, 428 (1982)

/11/ S.I. Braginski, Reviews of Plasma Physics (Consultants Bureau, New York, 1965) Vol. I, p. 183

/12/ S.J. Fielding and A.J. Wootton, Phys. Scripta 23, 97 (1981)

/13/ W. Engelhardt et al., Verhandlungen der Deutschen Physikalischen Gesellschaft 4/1981, ISSN 0420-0195, 875 (1981)

/14/ F. Wagner et al., 9th Int. Conf. on Plasma Physics and Contr. Nucl. Fusion, Baltimore, IAEA-CN-41/A-3 (1982)

/15/ W. Stodiek et al., Nucl. Fusion Suppl. I, 9, Vienna (1981)

/16/ Equipe TFR, Heating in Toroidal Plasmas, Proc. 3. Varenna Grenoble Int. Symp., EUR 7979 EN, Vol. I, 225 (1982)

FIGURE CAPTIONS

Fig. 1 Energy confinement times τ versus mean plasma density: for ohmic heating (Ω) only and for additional heating of 4.5 MW

Fig. 2 Degradation of the electron energy confinement time τ_{el} with increasing additional heating power P for three values of the mean plasma density

Fig. 3 Peak ion temperature T_i versus additional heating power per particle for two values of ε (a)

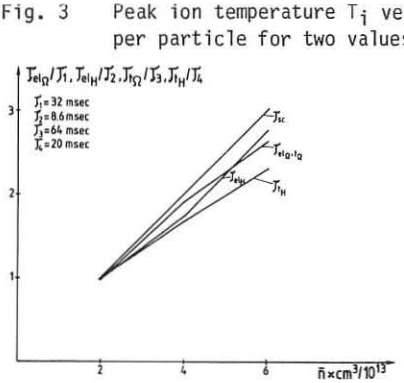

Fig. 1

Fig. 2

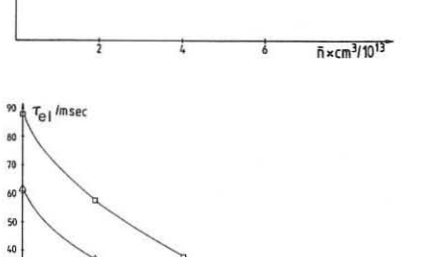

n_e = ○ $2 \cdot 10^{13}/cm^3$ △ $4 \cdot 10^{13}/cm^3$ □ $6 \cdot 10^{13}/cm^3$

Fig. 3

Neutral Beam Injection Studies for W VII AS using the 3-D Computer Code FAFNER

G.G.Lister, F.P.Penningsfeld, W.Ott, and E.Speth
Max-Planck-Institut für Plasmaphysik, EURATOM Association
D-8046 Garching, Federal Republic of Germany

ABSTRACT

Results of 3-D numerical computations predicting deposition profiles, shine through and fast ion orbit losses for neutral injection experiments in the W VII-AS stellarator are presented. For 40 keV H injection into D plasma, total power losses are restricted to $\sim$ 10 % over a wide range of plasma parameters and significant heating ($\sim$ 2 W/cc for 1.5 MW injected power) is predicted.

1. INTRODUCTION

Following the success of neutral beam heating experiments in sustaining currentfree plasmas in the W VII-A stellarator /1/, a new experiment, W VII-AS /2/, is planned in which the helical windings will be replaced by modular coils. Suitable modification of these coils at the neutral beam entry ports will permit the beams to be injected tangentially to the magnetic field. Losses due to shine through or trapping in local magnetic field ripples are thus minimised.

The total injected power projected for the first phase of W VII-AS is 1.5 MW, which will be obtained using 4 periplasmatron sources /3/ of the type currently used on ASDEX. This power may be doubled if the full beamlines with 8 sources were used.

Results presented in this paper are for plasma parameters extrapolated from W VII-A results /4/. We discuss the effects of plasma density and injection energy on the expected heating efficiency and show power deposition profiles for typical cases.

2. THE NEUTRAL BEAM-PLASMA SYSTEM

W VII-AS will be a stellarator of major radius 200 cm, effective minor radius 22 cm, toroidal magnetic field 3 T and external iota of between 0.25 and 0.6 (normal operating value 0.4). The neutral beam system and the target plasma are illustrated in Fig. 1. L_1, L_2, L_1', L_2', each represent a pair of vertically stacked sources, placed equidistant from the mid plane of the torus, and directed at an angle $\pm$ 2.86° to the horizontal. Sources L and L' are oppositely directed, to prevent toroidal plasma rotation and to cancel beam driven currents. It was found that the optimum radius of tangency for sources L_1, L_1' is R_1 = 191 cm, which restricts that for the set L_2, L_2' to R_2 = 164 cm.

Cross sections of the target plasma in different azimuthal planes ϕ are also illustrated in Fig.1, onto which have been superposed neutral particle contours from the two sources L_1 in these planes. In the region where the beams enter the plasma, the lines of equal magnetic flux are relatively close together, and hence fast ion deposition in the plasma is highly sensitive to the choice of density profiles.

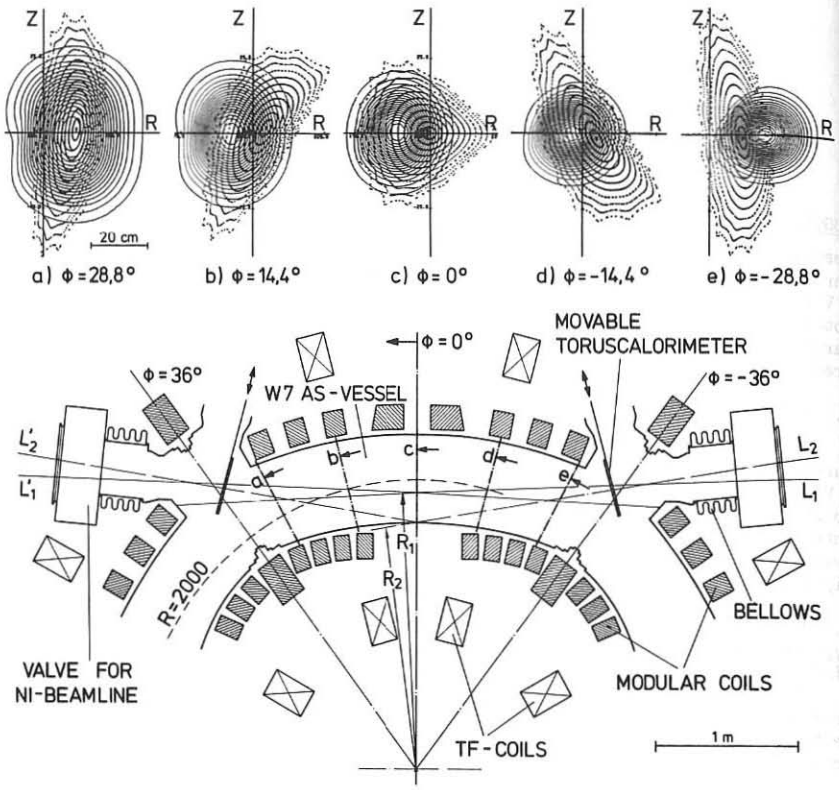

Fig. 1: W VII-AS injection geometry and cross sections of beam and plasma

3. NUMERICAL METHODS AND PLASMA PROFILES

Standard Monte Carlo methods have been used to model the trapping of neutral particles and the subsequent interaction of the resulting fast ions with the plasma /5/. A new code, FAFNER /6/ has been constructed to include the 3-dimensional plasma and a more detailed description of the beamline, necessary in view of the comparable dimensions of the plasma and beam cross sections. The magnetic field configuration is modelled by a set of coefficients supplied by Dommaschk /7/.

The plasma density and temperature profiles are given as a function of the flux function s, defined as the distance from the plasma axis along the line z=0 (torus mid plane) in the Ø=0 plane, where the plasma is approximately triangular. Each point in the plasma will thus have a defined density and temperature by a suitable coordinate transformation into the Ø=0 plane. Profiles used to obtain results presented in this paper are:

$n_e = n_e(0)/(1+(s/b)^6)$ b = 12 cm

$T_e = T_e(0)\cdot(1-(s/a)^2)$ a = 22 cm.

The absolute values for $n_e(0)$ and $T_e(0)$ were obtained from transport simulations /4/.

4. RESULTS AND CONCLUSIONS

Results of computations are shown in Figs. 2-5. In Fig. 2 computed fractional orbit losses, shine through losses (a and b) and heating power fractions to ions p_i and electrons p_e versus central electron density n(0) are plotted.

A comparison is made between inner (L_1) and outer (L_2) sources of shine through losses for different densities. Clearly, losses in the low density ECRH generated plasma ($n_e(0) = 4x10^{13}$ cm^{-3}) using the inner sources would prove acceptable. We also show expected losses, and the fraction of power given to plasma ions and electrons from sources L_1 and L_1'. As expected, there is a slight increase in orbit losses for higher densities, due to the higher fraction of fast ions born near the plasma edge, but this is partially compensated by the reduction in shine through losses, resulting generally in a power loss of $\simeq$ 10 %. The plasma electrons receive an increased share of the available power for higher density, due to the lower T_e with increasing density /4/.

Figure 3 shows power deposition profiles (to ions and electrons) versus effective radius, for a high density, $n_e(0) = 2x10^{14}$ cm^{-3} plasma. The ions in the central plasma receive $\lesssim$ 1 W/cc power and the electrons $\lesssim$ 1 W/cc, assuming a total injected power of 1.5 MW.

Figures 4 and 5 illustrate the effect of varying the injection energy over a range of 20 to 50 keV. For high density plasmas differences between 40 and 50 keV injection are not statistically significant. However, 30 keV injection would result in a markedly poorer performance. Deposition profiles, illustrated in Fig. 4, show a marked central hollow, and orbit losses increase from 5 % to 12 %, due to the reduced penetration of the beam for lower energies. Increase of E_o/E_c (E_o is injection energy, E_c is "critical energy"), however, results in a lower fraction of power delivered directly to the ions (Fig. 5).

REFERENCES

/1/ W VII A-Team, NI-Team, 9th Conf.Plasma Phys.Contr.Nucl.Fusion Res., Baltimore, 1982, paper IAEA-CN-41/L5

/2/ Broßmann,U., Dommaschk,W., Herrnegger,F., Grieger,G., Kißlinger,J., Lotz,W., Nührenberg,H., Rau,F., Renner,H., Ringler,H., Sapper,J., Schlüter,A., Wobig,H.; ibid; Paper IAEA-CN-41/Q5

/3/ Bonnal,J.F., Bracco,G., Bussac,J.P., Druaux,J., Oberson,R., Romain,R. Proc. 8th Symp. Engin.Probl.Fus.Res., San Francisco, 1979, Vol.II, 1056

/4/ Wobig,H., to be published

/5/ Goldston,R., McCune,D.C., Towner,H.H., Davis,S.L., Hawryluk,R.J., and Schmidt,G.L., J.Comp.Phys. 43, 1981, 65

/6/ Lister,G.G., to be published

/7/ Dommaschk,W., 1978, IPP-Report 0/38.

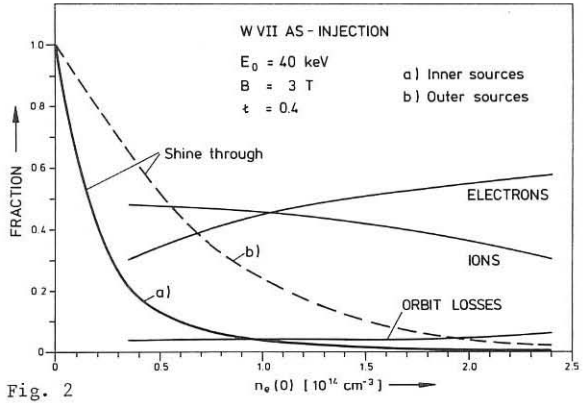

Fig. 2

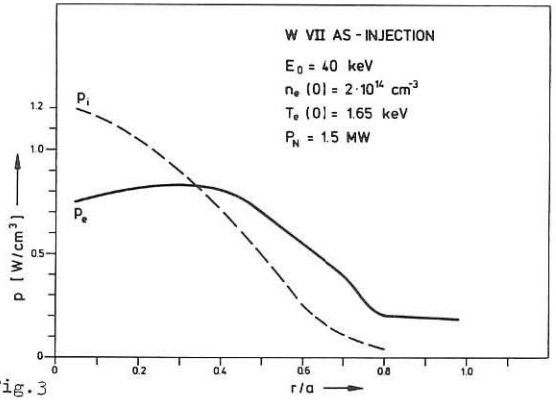

Fig.3

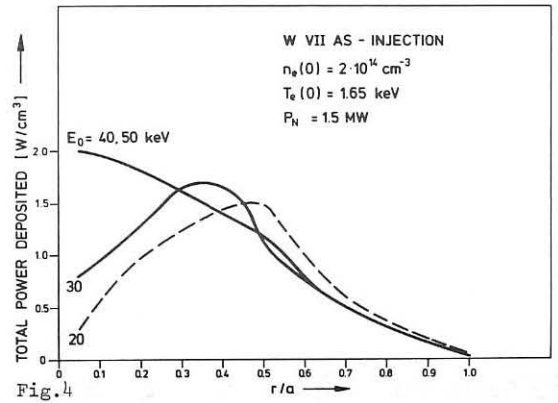

Fig.4

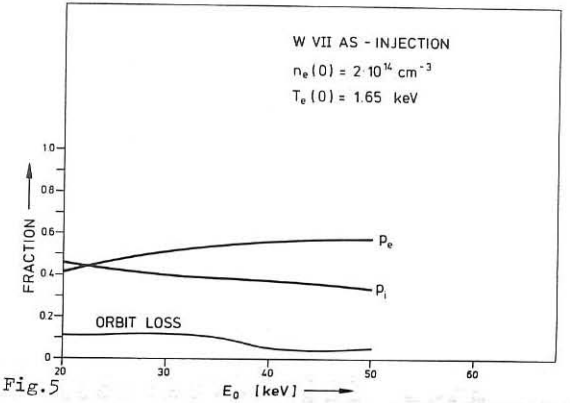

Fig.5

Is Additional Edge Transport Beneficial?

M L Watkins, D F Duchs and P Noll
JET Joint Undertaking, Abingdon, Oxfordshire, Ox14 3EA, England.

INTRODUCTION

An obvious need in experimental fusion plasma research is the control of plasma-wall interactions. Besides the use of limiters and divertors, schemes have been proposed /1-5/ which rely on the formation of ergodic magnetic regions for the control of the plasma transport in the boundary layer. Particular attention has been focussed on the broadening of the scrape-off layer thickness by additional transport so as to distribute more evenly the heat load on the limiters and walls and on the effect of the additional transport on the impurity behaviour.

We report parameter studies on the performance of JET plasmas obtained by artificially varying both the magnitude of additional transport coefficients and the width of the boundary layer. We use the one-dimensional transport model, ICARUS. Hydrogenic and impurity particle transport and electron and ion thermal transport is artificially enhanced between radius, r_1, and the wall. This region includes the limiter shadow. The enhanced transport affects the impurity concentration, f_z, and the plasma size, a (defined by $T_e(a)=50eV$). As a result the plasma performance, indicated by the central ion temperature, $\hat{T}_i$, and the global energy confinement time τ_E, also changes. We find that with additional transport inboard of the limiter radius the plasma parameters generally deteriorate. However, even relatively small additional transport in the limiter shadow can improve the overall plasma performance.

MODEL ASSUMPTIONS

A particular 1-D model for transport transverse to the magnetic field is augmented by a phenomenological model for the parallel transport in the shadow of the limiter. The dominant terms in the equations for electron density, n_e, impurity density, n_z, and electron and ion pressures (p_e and p_i) are:

$$\frac{\partial n_e}{\partial t} + \frac{1}{r}\frac{\partial r\Gamma_e}{\partial r} = S_n^o + S_n^z - \frac{n_e}{\tau_{||}} \qquad \Gamma_e = -D_e\frac{\partial n_e}{\partial r}$$

$$\frac{\partial n_z}{\partial t} + \frac{1}{r}\frac{\partial r\Gamma_z}{\partial r} = S_z^z - \frac{n_z}{\tau_z} \qquad \Gamma_z = -D_z\frac{\partial n_z}{\partial r}$$

$$\frac{3}{2}\frac{\partial p_e}{\partial t} + \frac{1}{r}\frac{\partial}{\partial r}r\left(\frac{3}{2}kT_e\Gamma_e - n\chi_e\frac{\partial kT_e}{\partial r}\right) = S_e^o - S_e^z - \frac{2n_ekT_e\gamma}{\tau_{||}}$$

$$\frac{3}{2}\frac{\partial p_i}{\partial t} + \frac{1}{r}\frac{\partial}{\partial r}r\left[kT_i\left(\frac{3}{2}\Gamma_e + y\,\Gamma_i\right) - n\chi_i\frac{\partial kT_i}{\partial r}\right] = S_i^o - \frac{2n_ekT_i}{\tau_{||}}$$

To the reference INTOR values for the electron transport coefficients χ_e and D_e, impurity diffusion coefficient, D_z, and the neoclassical values for the ion transport coefficients, χ_i, and Γ_i are added additional contributions χ_{Add}, defined as:

$$\chi_e^{tot} = \chi_e + \chi_{Add} \qquad \chi_i^{tot} = \chi_i + \chi_{Add}$$

$$D_e^{tot} = D_e + g\,\chi_{Add} \qquad D_z^{tot} = D_z + g\,\chi_{Add}$$

Transport in the scrape-off layer is characterised by the parallel confinement time, $\tau_{//}$=L/V (where L is the effective connection length taken to be πRq and V is the effective flow speed /6/) for electrons and hydrogenic ions, and $\tau_z=\tau_{//}$ or ∞ for impurity ions. Plasma ions are recycled at the limiter and wall as neutrals, giving rise to the terms S°_n, S°_e and S°_i. Impurities are produced at the limiter by sputtering by charged particles and at the wall by both charged particles and charge-exchanged neutrals, giving rise to the terms S^Z_n (electron stripping), S^Z_e (coronal radiation) and S^Z_Z (impurity production) /7/.

APPLICATION

The present application is to a circular cross-section plasma with the same volume as JET (effective limiter radius, 1.62m; wall radius, 1.72m; major radius, 2.96m). The heating sources correspond to the full planned power for JET and comprise the sum of (a) ohmic heating with a current of 4.8MA at a field of 3.45T, (b) injection of neutral deuterium at a power level of 10MW at an energy of 160kV (17.25MW including the fractional energy components) (c) a uniform ion heating profile of about 0.1MWm^{-3} to represent some form of radio frequency heating at an effective level of 15MW within the limiter radius, and (d) alpha particle heating by plasma-plasma and beam-plasma interactions assuming a 50:50 mixture of deuterium and tritium.

RESULTS

We first keep the additional thermal transport constant at a level χ_{Add}=10m^{2}s^{-1} (INTOR value of $\chi_e \sim 1$m^{2}s^{-1} in the edge plasma) and vary the radial extent defined by r_1 in the range 1.42m $\leq r_1 \leq$ 1.62m (Figure 1). All sputtered impurities remain in the discharge ($\tau_z = \infty$) and there is no additional particle transport (g=0). As the extent of the region increases, the impurity content increases and leads to smaller plasmas with lower central temperatures and global energy confinement times. With additional transport only in the shadow of the limiter there is some improvement over the equivalent case without any additional transport as indicated on the right hand side of Figure 1.

We now examine the effect of increasing the magnitude of the additional transport from 0 to 40m^{2}s^{-1} with the ergodic region confined to the shadow of the limiter (r_1=1.62m). There is a steady improvement in the performance (Figure 2) which is most noticeable in the global energy confinement time which is almost a factor of two higher than for the equivalent case without any additional transport (indicated on the left hand side of Figure 2). The heat transport to the wall increases and to the limiter decreases.

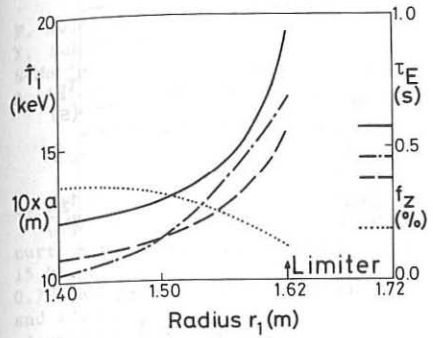

Figure 1. Variation of $\hat{T}_i$ (—•—), τ_E (——), a(- -) and f_z (...) with r_1 for $\chi_{Add}=10m^2s^{-1}$, $\tau_z=\infty$, g=0. Values for r_1=1.72m are indicated on right hand side of figure.

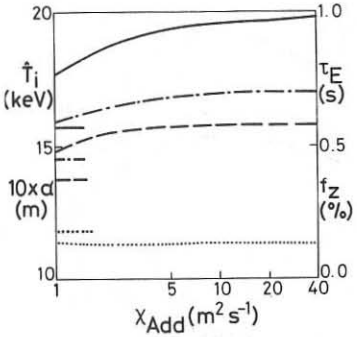

Figure 2. Variation of $\hat{T}_i$ (—•—), τ_E (——), a(- -) and f_z (...) with χ_{Add} for r_1=1.62m, $\tau_z=\infty$, g=0. Values for χ_{Add}=0 are indicated on left hand side of figure.

The more evenly spread heat load on the limiter leads to lower sputtering and lower impurity concentration. The size, a, of hot plasma increases. Radiation remains the dominant energy loss.

The reduction in the edge temperature leads to less ionisation of the recycled flux in the scrape-off layer and lower edge densities. The introduction of additional particle transport (g=1/4) aggravates the reduction of the edge density. For low values of the additional transport, the effect of additional particle transport is not significant (compare Figures 2 and 3). When the additional transport exceeds $10m^2s^{-1}$, the edge density is so low that sputtering of wall material by charge-exchanged neutrals becomes the dominant impurity source. The performance then deteriorates rapidly as the transport is increased further. At a level of $40m^2s^{-1}$, the density at the limiter tip is $7.6\times10^{18}\ m^{-3}$, the impurity concentration is 0.2%, the effective plasma size is 1.3m and the global energy confinement time is 0.48s.

We find it necessary to rely on effective pumping of the impurities, as suggested in /4/ or as illustrated by setting $\tau_z=\tau_{//}$ (Figure 4, to be compared with Figure 3). As found in /7/ the sensitivity to changes in the edge behaviour is reduced considerably, and the degradation of performance with increasing additional transport is substantially lower even though the edge density is low.

In summary, using the present definition of plasma performance the sensitivity of the results to the additional transport is rather small; variation of up to 40 in the magnitude of the additional transport leads to changes of about 2.

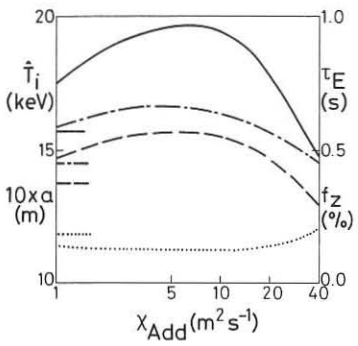

Figure 3. Variation of $\hat{T}_i$ (—•—), τ_E (——), a(- -) and f_z (...) with χ_{Add} for r_l=1.62m, $\tau_z^z=\infty$, g=1/4. Values for χ_{Add}=0 are indicated on left hand side of figure.

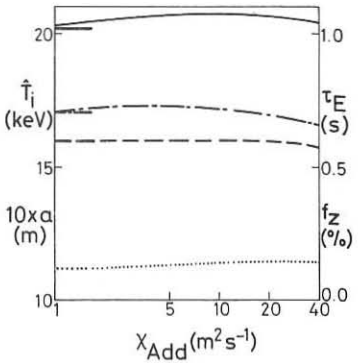

Figure 4. Variation of $\hat{T}_i$ (—•—), τ_E (——), a(- -) and f_z (...) with χ_{Add} for r_l=1.62m, $\tau_z^z=\tau_{//}$, g=1/4. Values for χ_{Add}=0 are indicated on left hand side of figure.

REFERENCES

/1/ Feneberg, W.: in Contr. Fusion and Plasma Physics (Proc. 8th European Conf. 1977) 1, (1977)3.

/2/ Engelhardt, W. and Feneberg, W.: J. Nucl. Mat. 76/77 (1978)518.

/3/ Feneberg, W. and Wolf, G.H.: Nucl. Fus. 21 (1981)669.

/4/ Samain, A., Grosman, A. and Feneberg, W.: J. Nucl. Mat. 111/112 (1982)408.

/5/ Nicolai, A. and Reiter, D.: J. Nucl. Mat. 111/112 (1982)428.

/6/ Ogden, J.M., Post, D.E., Jensen, R.V., and Seidl, F.G.P.: Report PPPL-1608, Princeton Plasma Physics Lab., U.S.A. (1980).

/7/ Watkins, M.L., Cordey, J.G., Abels-van Maanen, A.E.P.M., Roberts, J.E.C., and Stubberfield, P.M.: 9th Int. Conf. on Plasma Physics and Controlled Nuclear Fusion Research, IAEA-CN-41/D-2-1, Baltimore (1982).

ION AND ELECTRON ENERGY BALANCE ANALYSIS OF NEUTRAL-BEAM-HEATED HELIOTRON E PLASMAS

F. Sano, T. Obiki, K. Hanatani, H. Zushi, S. Sudo, A. Sasaki, S. Besshou, Y. Nakashima, M. Sato, T. Mutoh, H. Kaneko, T. Mizuuchi, K. Kondo, S.Morimoto, M. Nakasuga, I. Ohtake, M. Iima, N. Nishino, O. Motojima, A. Iiyoshi, and K. Uo

Plasma Physics Laboratory, Kyoto University
Gokasho, Uji, Kyoto 611, Japan

1. INTRODUCTION

Neutral beam injection of up to 1.7 MW beam power into low ohmic-current plasmas of the Heliotron E device (R=2.2 m, a=0.2 m, B=1.8 T, $I_{OH} \lesssim$ 15 kA, $\bar{n}_e$=2.1 x 10^{13} cm^{-3}) has created plasmas with $T_i(0) \approx 0.95$ keV, $T_e(0) \approx$ 0.70 keV, and $\beta(0) \approx 1.0\%$. In this paper, a description is given of the ion and electron energy balances for those neutral beam heated Heliotron E plasmas with special reference to the evaluation of the energy transport coefficients during injection. The experimental ion and electron thermal diffusivities, χ_i and χ_e, have been examined using the numerical ion and electron temperature profile analysis codes which respectively employ the neoclassical ion thermal conductivity and the INTOR-scaling electron thermal coductivity as the reference conductivities. It is found, from the measured and calculated ion temperature profiles, that the ion heating during injection can be explained in terms of the classical beam power deposition and usual neoclassical thermal conduction processes. An attempt of obtaining the gross behavior of χ_e has also revealed that the calculated upper limit of χ_e during injection is below or of the same order of the INTOR-scaling value.

2. EXPERIMENTAL ANALYSIS

An important problem relevant to the ion and electron energy balance of a neutral beam heated plasma is the mechanism of power deposition by injected beam ions (fast ions), which is usually assumed to be classical in tokamaks. Therefore, in tokamaks, neutral beam heated plasmas have, at least in principle, an advantage of the reasonably accurate prediction of the input power deposition profile by means of the Monte-Carlo code. As the consequence, such neutral beam heated plasmas facilitates the determination of the experimental energy transport coefficients and the comparisons of those coefficients with theoretical values. On the other hand, as for stellarators, there is scant information about whether or not the same explanation applies to stellarator plasmas. In WVII-A/1,2/, it is reported that the energy balance analysis of neutral beam heated plasmas arouses some puzzling questions about classical assumptions: the experimental energy balance of the plasma requires higher ion heating than that predicted classically. Therefore, what is required now for us is a detailed energy balance analysis of our neutral beam heated plasmas with a view to determining whether or not a classical explanation of power deposition can be applied to Heliotron E plasmas.

Typical time behavior of plasma current I_{OH}, loop voltage V_L, line-averaged electron density $\bar{n}_e$, central electron temperature $T_e(0)$, and central ion temperature $T_i(0)$ for the NBI heating experiments in Heliotron E is shown in Fig. 2 of ref. 3 under conditions where about 1.7 MW beam power is injected into a low ohmic-current target plasma. The hydrogen gas puffing is turned off just before injection in this case. The gradual

density decrease during injection is considered to be a so-called "density clamping". This phenomenon may be explained as being due to a decrease in particle recycling caused by the hardening of charge-exchange neutral flux incident on the wall, but the detailed study remains as a future work in connection with particle transport and particle confinement.

The ion and electron energy balances have been studied at ~ 70 ms after injection at which time the ion temperature reaches the maximum; the corrected, measured central ion temperature $T_i(0)$ is around 0.95 keV. The slight variations of density and temperatures around this time make little contribution to the energy balance calculations, so that the quasi-steady approximation is utilized. We will here consider the following form of neoclassical ion thermal diffusivity for stellarator plasmas as a matter of practical convenience:

$$\chi_i^{NC} = (1.0 + C_i \cdot \varepsilon_h^{\frac{3}{2}} / \nu) \cdot \chi_i^{HH} \qquad (1)$$

where C_i (~ 3.5) can be given as the constant in the first approximation; ε_h is the helical field ripple; ν is the normalized ion collision frequency; χ_i^{HH} is the neoclassical ion thermal diffusivity of a tokamak /4/. The 1-D T_i-profile analysis code provides the numerical ion temperature profile as shown in Fig.1-(b) under conditions where (i) the anomaly factor with regard to χ_i^{NC} is 1.0 and (ii) the constant C_i is 3.5 or 0.0; the experimentally determined profile is also shown in Fig. 1-(a). In this case, the profile for C_i = 0.0 is found to provide a better agreement with the experiment within error limits. A relatively large difference between the profiles of C_i = 0.0 and C_i = 3.5 is caused by the different estimations of χ_i in the localized-particle regime which dominates nearly a-half-of-plasma-radius region in this case. This result implies that the tokamak-like scaling χ_i^{HH} offers a more reasonable explanation even in the localized-particle regime although the conclusive evidence including the effect of a radial electric field is not yet obtained.

On the other hand, based upon the ion temperature profile calculated assuming C_i = 0.0, we have studied the electron energy balance for the same plasma. Under the condition of the net radiative loss Prad(r) = 0, the diffusivity χ_e is inferred to be of the same order of the INTOR-scaling value. When we take some account of the net radiative loss Prad (r) = Prad*(r) speculated from the bolometer measurements, the gross trend of the conductivity $k_e = n_e \cdot \chi_e$ is that k_e increases with increasing electron temperature T_e. The result of the 1-D T_e-profile analysis code in this case is shown in Fig. 2, and the diagram of $n \cdot \chi_e$ versus T_e is shown in Fig.3. Although the precise dependence of χ_e on T_e is difficult to determine because of experimental uncertainties (e.g., net radiative loss), its linear dependence on $1/n_e$ is likely to be justified.

Figure 4 shows the ion and electron energy flows from the core within r = a/2. In this injection case, the total absorbed beam power is about 0.81 MW, and about 27 percent (~ 0.22 MW) of the absorbed power is lost to the wall by fast-ion charge exchange while the rest is deposited to the ions and electrons. About 0.39 MW beam power is deposited inside r = a/2 to the ions (~ 0.16 MW) and to the electrons (~ 0.23 MW), which shows that the electron heating is still larger than the ion heating. The calculation results also indicate that the dominant power loss of the electrons is through thermal conduction and that the radiative and particle diffusion losses are small. The small particle diffusion loss reflects the small neutral particle density in this injection case where the gas puffing is turned off during injection. The dominant power loss of the ions is caused by the electron-ion coupling, which reflects the higher temperature of the

ions than that of the electrons in the core: this loss value reaches about a half of the input beam power to the ions. The plasma energy loss from the core via the ions is about 0.09 MW while that via the electrons is about 0.33 MW; the latter is found to be dominant. In conclusion, this energy flow diagram indicates that the global plasma energy confinement time at r = a/2 ($\sim$ 10 ms) is limited by the large electron thermal conduction loss.

3. FUTURE WORK

It should be noted here that the energy transport behavior during injection is strongly dependent on the confinement properties of the applied target plasma. For instance, we have some indications of obtaining very low $n_e \cdot \tau_e$ values when the current-less, electron cyclotron resonance heated plasma is utilized as a target plasma/5,6/. The relevant studies are now in progress by using a 53 GHz electron cyclotron resonance heated target plasma. The presented results are obtained using ohmically heated target plasmas, but the analyzed data as a whole suggest that the classical explanation of beam power deposition is sufficient to be applied to the neutral beam heating in Heliotron E plasmas.

References

/1/ WVII-A Team and NI Group, Proc. 8th Int. Conf. Plasma Phys. Cont. Nucl. Fusion Res., Brussels, IAEA-CN-38/H-2-1 and H-2-2 (1980).

/2/ WVII-A Team and NI Group, Proc. 9th Int. Conf. Plasma Phys. Cont. Nucl. Fusion Res., Baltimore, IAEA-CN-41/L-5 (1982).

/3/ K. Uo et al., in this conference.

/4/ R.D.Hazeltine and F.L.Hinton, Phys. Fluids, 16 (1973) 1883.

/5/ K. Uo et al., Proc. 9th Int. Conf. Plasma Phys. Cont. Nucl. Fusion Res., Baltimore IAEA-CN-41/L-3 (1982).

/6/ K. Uo et al, Nucl. Intrum. Meth. 207 (1983) 151.

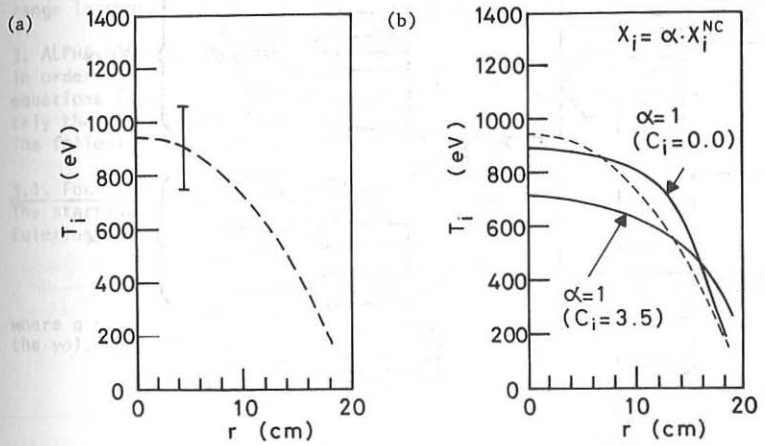

Fig. 1 Ion temperature profiles in NBI heating experiments: (a) measured ion temperature profile corrected with a numerical model taking into account the neutral density profile; (b) calculated ion temperature profiles of α=1, and C_i=0.0 or C_i=3.5. The dotted and full curves, respectively, show the experimental and numerical profiles.

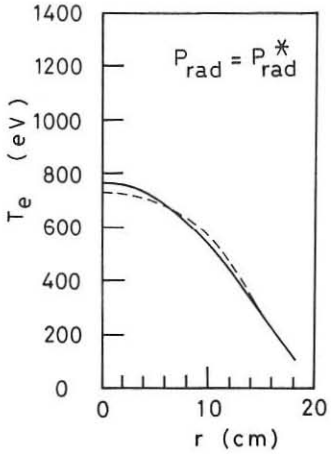

Fig. 2 Numerical electron temperature profile at $P_{rad}(r) = P^*_{rad}(r)$. The dotted curve is the experimental profile by Thomson scattering.

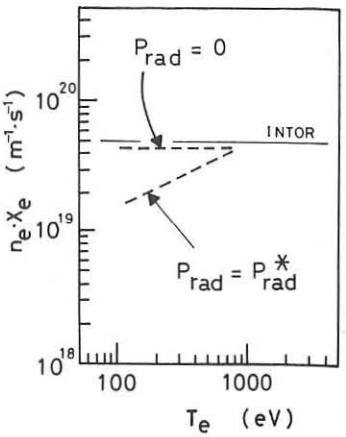

Fig. 3 Diagram of $n_e \cdot \chi_e$ versus T_e for $P_{rad}(r) = 0$ and $P_{rad}(r) = P^*_{rad}(r)$.

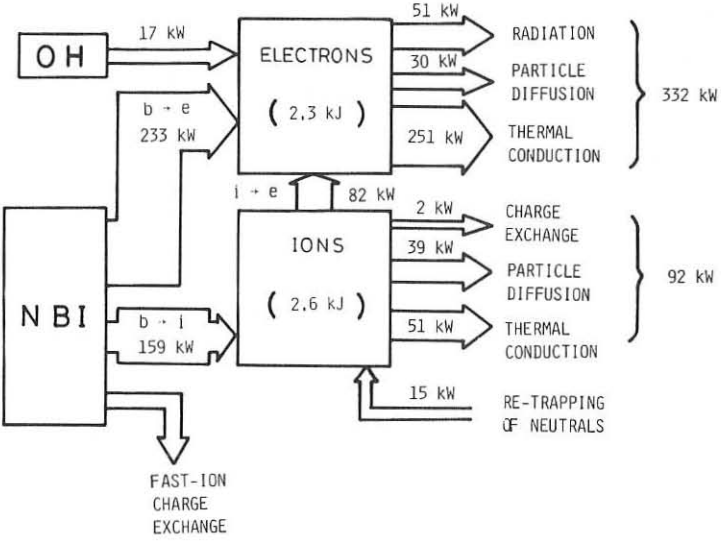

Fig. 4 Ion and electron energy flows from the hot plasma core within r = a/2.

"ANALYSIS OF CHARGED-PARTICLE ENERGY DEPOSITION FOR ICF CALCULATIONS WITH THE NORCLA CODE"

G. Velarde, J.M. Aragonés, R. Arroyo, J.A. Gago, J.J. Honrubia, F.M. Fanegas, J.M. Martínez-Val, E. Minguez, J.L. Ocaña, J.J. Peña, J.M. Perlado, J.M. Santolaya, J.F. Serrano

Departamento de Energía Nuclear
E.T.S.I. Industriales (U.P.M.)
P°de la Castellana, 80. Madrid (6)

1. THE "NORCLA" CODE

NORCLA is a computing modular system to carry out the thermohydrodynamic and nuclear evolution of ICF targets. Its original features are described in ref.1 (Velarde et al). It has been used to analyze the physics and performance of both solid and single-shell ICF microballs (2,3). In order to broaden the range of application and to improve its accuracy, some new modules have been developed in relation to the charged-particle phenomenology in inertial confinement fusion.

2. ION BEAM-TARGET INTERACTION

A computing module (called STOP) has been written to calculate the driver ion energy deposition in the outer shells of the targets. It also takes into account the momentum transfer from the ions to the stopping material (3).
The energy and momentum deposition is carried out at every mesh interval each time step, accounting for the actual conditions of density, temperature and ionization, that have been perturbed by the ions which have interacted formerly with the target. In figure 1, the radial profiles of the dE/dx values are plotted for an DT-Al-Pb target, at three different times. The driver ion range is shorthened by the increase of temperature and ionization degree.

3. ALPHA-PARTICLE TRANSPORT METHODS

In order to evaluate properly the source terms of the ion and electron energy equations (a 2T model is used in NORCLA), it is necesary to carry out accurately the transport and energy deposition of the fusion-born alpha-particles. The following two methods were envisaged to deal with this problem.

3.1. Fokker-Planck via Finite Element Method

The starting point of this method was the Fokker-Planck equation in modified Eulerian coordinates

$$\frac{1}{qV}\,\partial_t(V\Psi)+\vec{\Omega}.\nabla\Psi = \frac{\partial(M\Psi)}{\partial E}+\tau\Psi+Q \qquad (1)$$

where q stands for the relative speed to the medium ($\vec{v}=\vec{q}+\vec{u}$) and V stands for the volume of the lagrangian interval. The operators are defined as follows

$$\partial_t = \frac{\partial}{\partial t}+\vec{u}.\nabla \qquad (2)$$

$$M = S+D \qquad (3)$$

$$S = \sum_b N_b U_b \qquad \text{(stopping power)} \qquad (4)$$

$$D = m(\mu\ddot{r}+\mu^2 q(\frac{\partial\dot{r}}{\partial r}-\frac{\dot{r}}{r})+q\frac{\dot{r}}{r}) \qquad (5)$$

(mesh drag speeding-up or slowing-down)

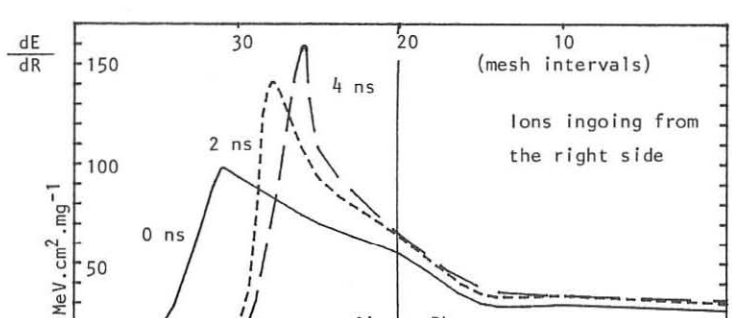

FIG. 1. Time evolution of driver-ion energy deposition

$$\tau = T\frac{\partial}{\partial\mu}(1-\mu^2)\frac{\partial}{\partial\mu} + \frac{\partial}{\partial\mu}(1-\mu^2)G \qquad (6)$$

$$T = \sum_b A_b U_b / 4E \qquad \text{(continous deflection)} \qquad (7)$$

$$G = \frac{m}{2E}\left(\ddot{r}+\mu q\left(\frac{\partial \dot{r}}{\partial r} - \frac{\dot{r}}{r}\right)\right) \qquad (8)$$

(mesh drag angular redistribution)

It is worth noting that the drag effects produced by the moving radii have been included, which is an unusual feature on the methods to treat the alpha-particle transport. The weak formulation of the aforementioned equation has logically been used to establish the finite element algorithm. It holds

$$\left\langle \frac{1}{qV}\partial_t(V\Psi),\xi\right\rangle - \langle\Psi,\vec{\Omega}\nabla\xi\rangle + \left\langle M\Psi\frac{\partial\xi}{\partial E}\right\rangle +$$

$$+\int dE\int_{\varepsilon}\int_{\partial R^+} d\vec{s}.\vec{\Omega}\xi\Psi + \int_R dV\int_{\partial\varepsilon^+} dE\xi M\Psi =$$

$$= \int_{\varepsilon} dE \int_{\partial R^-} d\vec{s}.\vec{\Omega}\xi\Psi + \int_R dV \int_{\partial\varepsilon^-} dE\xi M\Psi + \langle\tau\Psi,\xi\rangle + \langle Q,\xi\rangle \qquad (9)$$

where R stands for the spacial domain, E for the energy domain, ∂R^+ and ∂R^- for the outgoing and ingoing spatial boundaries, and $\partial\varepsilon^+$ and $\partial\varepsilon^-$ for the lower and upper energy boundaries. A discontinuous representation of the angular flux has been selected, hence reducing the general problem to a set of local equations, weighted via the Galerkin procedure.
This method has been used to analyze some ICF targets evolutions (3) and to obtain figures 2, 3 and 4.

3.2. Partial range expansion of anisotropic scattering

The coexistence of small-angle and large-angle collisions in the same problem has lead to develop a computing method, expanding the differential transfer cross sections as a sum of series of Legendre polynomials defined only over partial angular ranges. This allows the resolution of the multigroup set of equations over each discrete direction with a standard discrete ordinates procedure, or to arrive to a coupled multi-P_n system of equations.

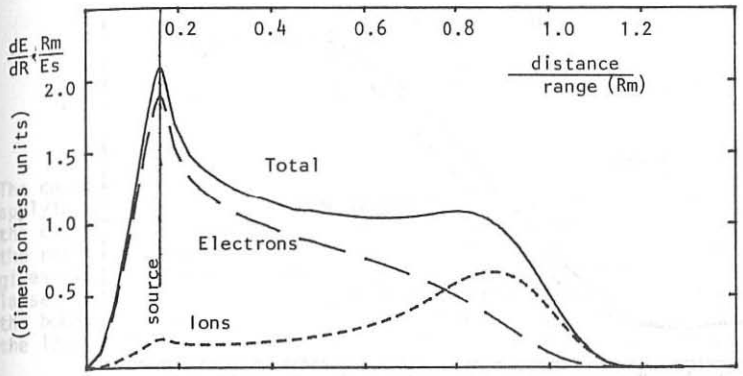

FIG.2. Alpha-particle energy deposition in DT (10 kev)

3.3. Validation of the methods

The methods were validated before being used in ICF calculations. In figures 2 and 3, the energy deposition to ions and electrons in a DT overdense plasma at 10 kev are plotted. In figure 2, a monochromatic spectrum has been used. In figure 3, a distributed spectrum (4) was assumed, what enhances the straggling effect.

4. IMPORTANCE OF CHARGED-PARTICLE TRANSPORT IN ICF CALCULATIONS

In figure 4 it is shown the effect of treating the fusion-born alpha-particles assuming local energy deposition (α-local) and transport calculated energy deposition (α-transport). The ρR parameter has been chosen to characterize this effect. It is seen that delay of 5 picoseconds it is found out, due to the time required for the alpha-particle to deposit their energy. However, the maximum value of ρR is the same in both cases. Our analysis has lead to the conclusion that alpha-particle transport is not too critical in ICF target studies, if a clear burn propagation is produced. However, in

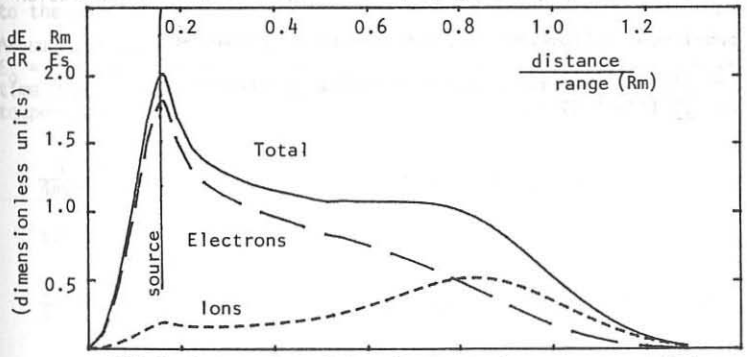

FIG.3. Energy deposition in DT. Real spectrum at 10 kev

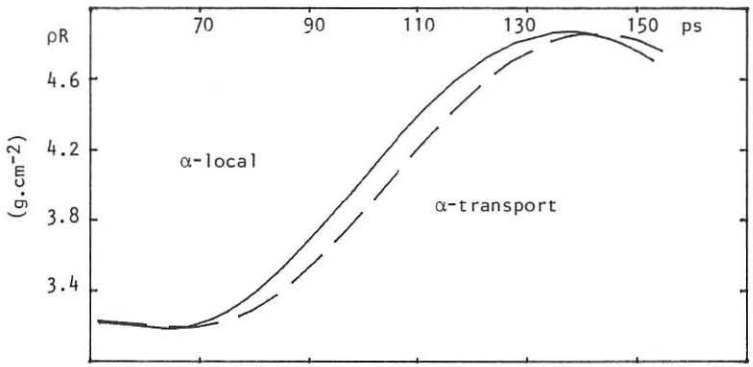

FIG.4. ρR evolution after ignition in an ICF target

those cases in which the ignition conditions are hardly achieved, a detailed alpha-particle transport and energy deposition ought to be done, because the aforementioned delay can play a major role in feedbacking or in quenching the fusion burst.

REFERENCES

(1) Velarde, G.,Ahnert, C., Aragones, J.M., Gómez-Alonso, M., Leira, G., Luqui, R., Martínez-Val, J.M., and Perlado, M.
"Analysis of laser-fission-fusion system"
Atomkernenergie/Kerntechnik, 35 (1980) 40-53

(2) Velarde, G., Ahnert, C., Aragones, J.M., Leira, G., Luqui, R. and Martínez-Val, J.M.
"Coupled nuclear-thermohydrodynamic analysis of laser-fusion-fission microspheres"
Atomkernenergie/Kerntechnik, 36 (1980) 213-217

(3) Velarde, G., Aragones, J.M., Arroyo, R., Gago, J.A., Honrubia, J.J., Martínez Fanegas, F., Martínez-Val, J.M., Minguez, E., Ocaña, J.L., Peña, J.J., Perlado, M., Santolaya, J.M., Serrano, J.F.
"Analysis of the physics and performance of inertial confinement fusion systems"
To be published in Atomkernenergie/Kerntechnik, Volume 40

(4) Liskien, H.
"The particle spectrum to be expected from a DT plasma"
Sci. Eng. 71 (1979) 57-58

Plasma Circuit Instability and Current Disruption

E. Minardi
Associazione EUR-CNR, Via Bassini 15, MIlano, Italy

Abstract

The coupled system of the Ohm-Maxwell and transport equations is solved applying a 1-D code to a one-fluid plasma in a cylindrical Tokamak. In the case of a current channel sourrounded by a large and cold plasma region, the resistive decoupling between poloidal and toroidal magnetic surfaces gives rise to an unstable dissipative mode. The current shrinks and collapses on the axis with a time scale which depends on the resistivity at the boundary. The profiles are controlled by the parameter $n\,q\,RU/B_z$ (U is the loop voltage) and a very steep gradient is developed at high density.

While in a Tokamak the toroidal magnetic surfaces ϕ are essentially determined by the given external field, the poloidal surfaces ψ change in time as a consequence of the current diffusion. Two classes of solutions exist depending whether a surface ϕ = const or ψ = const is taken as a boundary surface on which the temperature T is given. The former class constitutes the ordinary case of the resistive dissipation. The latter class represents a new case in which, through the motion of the boundary poloidal surface T = const, a functional dependence of the temperature and of the Spitzer resistivity on the current is introduced. This gives rise to a new unstable dissipative mode related to a situation similar to the instability of an electric circuit with a current-dependent resistance.

The plasma-circuit instability above is applied to the description of the current quenching in the last phase of the major disruption. It is assumed that as a consequence of the previous phases of the disruptive process the plasma is globally in a resistive equilibrium characterized by a central current profile decreasing outwards up to r = a and sourrounded by a large and cold boundary region up to the wall at r = b, in which the current and temperature profiles are flat. The flatteness of the temperature represents the consequence of a strong increase of the radial thermal conductivity in the boundary region possibly resulting from instability processes related to the existence of magnetoactive resonant surfaces.

Assuming a constant density $\bar{n}$ and starting from a zero order equilibrium $E_o = \eta(T_o) j_{zo}$, the problem can be reduced to the following equations for the time dependent part χ_1 of the helical fluxe χ ($\chi \equiv -mA_z - nrA_\theta/R$) and for the temperature T:

$$\frac{1}{4\pi m r}\frac{\partial}{\partial r} r \frac{\partial}{\partial r}\chi_1 = E_o\left[\frac{1}{\eta(T)} - \frac{1}{\eta(T_o)} + \frac{1}{mn(T)}\frac{\partial \chi_1}{\partial t}\right] \quad (0 \le r \le b) \tag{1}$$

$$\chi(r,t) = \chi(\rho,0) \tag{2}$$

$$\frac{3}{2}\bar{n}\left[\left(\frac{\partial T}{\partial t}\right)_\chi + \frac{\partial T}{\partial \chi}\frac{\partial \chi}{\partial t}\right] - \frac{\bar{n}\chi_e}{V'(\rho)}\frac{\partial}{\partial \rho}\left[V'(\rho)\left(\frac{d\rho}{dr}\right)^2 \frac{\partial T}{\partial \rho}\right] = \eta j_z^2 \quad (0 \le \rho \le a) \tag{3}$$

$$\frac{3}{2}\bar{n}\left(\frac{\partial T}{\partial t}\right)_r - \frac{\bar{n}\chi_e}{r}\frac{\partial}{\partial r}\left(r\frac{\partial T}{\partial r}\right) = \eta j_z^2 \qquad 0 \le r \le r_m(t) \qquad (4)$$

with the boundary conditions

$$\left(\frac{\partial \chi_1}{\partial r}\right)_o = \left(\frac{\partial T}{\partial r}\right)_o = 0\ , \quad \chi_1(b) = 0\ , \quad T(\rho) = \text{const for } a \le \rho \le b$$

When a positive root r_m of $\chi(r_m,t) = \chi(0,0)$ exists, it represents a lower bound in r-space of the mapping (2) of the segment $0 \le \rho \le a$ into the r-space. This means that new magnetic surfaces were born during the time $t > 0$ in the segment $0 \le r \le r_m(t)$, whose temperature cannot be determined by (3), which describes only the evolution of the temperature on magnetic surfaces which already existed at $t = 0$. For $0 \le r \le r_m(t)$ one has then to solve (4) in r-space and match the solutions continuously through $r_m(t)$.

The plasma-circuit instability arises for any initial strong perturbation which decreases the temperature when the boundary region is sufficiently large and cold. The calculations were performed taking initially $\chi_1 \sim a_o \cdot \cos(\pi r/2b)$ with $a_o \approx 15\%$.

Fig.1 shows the marginal curve for a parabolic current profile in the Γ-(b/a) space, where $\eta_o/\eta_b = 1-\Gamma$ is the center-boundary resistivity ratio. The instability takes the form of a progressive cooling of the central current channel starting from the edge.

As shown in fig. 2 , for a sufficiently low temperature at the boundary the process takes the form of a collapse of the current towards the axis. The duration of the current quenching is of the order of the dissipation time at the boundary $\tau_b = 4\pi a^2/\eta_b$. Inspection of the figures shows that the evolution of the profiles depends on the parameter $c \equiv \tau_o/6\tau_E \sim \tau_b/\tau_E$ where $\tau_o = 4\pi a^2/\eta_o$ and τ_E is the confinement time. If $\tau_E \sim \tau_b$ the heat would remain confined in the central region during τ_b, unless the temperature gradient becomes very steep. As shown by the figures this is indeed the case when c approaches 1. Noting that

$$\tau_o = \frac{4\pi a^2 j_o}{E_o} = \frac{4\pi a^2 B_z}{\eta_o U}$$

where $U = 2\pi R E_o$, $q_o = B_z/2\pi R j_o$, and taking $\tau_E \sim 10^{-20}\bar{n}a^2R(s)$ one has that the condition $c < 10$ gives

$$\frac{\bar{n}q(a)R}{B_z} > \frac{4\cdot 10^{19}}{U} \quad (m^{-2}T^{-1}) \qquad (U \text{ in Volt})$$

We find here a connection with the Hugill-Murakami limit. At high density the system evolves towards very steep current profiles and becomes bound to MHD instabilities.

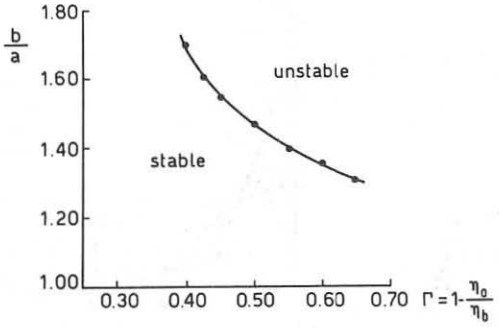

Fig . 1

Fig. 1 - Marginal Stability Curve in the Γ - (b/a) space.

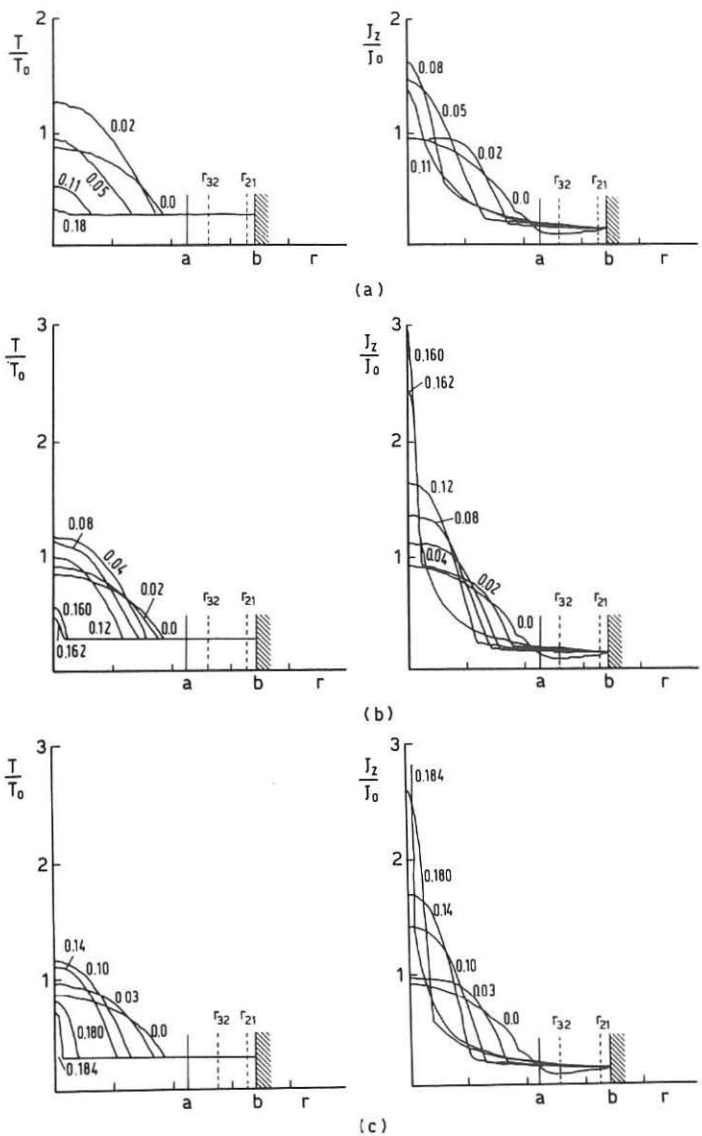

Fig. 2 - Time evolution of the temperature and current profiles for $\Gamma = 0.85$, $b/a = 1.50$, $nq_0/m = 0.35$, $a_0 = 0.15$.
The location of the m, n resonant surface is indicated by r_{mn}. The labelling parameter is τ/τ_{0S}. a) c = 20 b) c = 2.5 c) c = 1.

NUMERICAL SIMULATIONS OF THE OXYGEN IMPURITY TRANSPORT AT THE PLASMA PERIPHERY IN A TOKAMAK

M. Tendler, Royal Institute of Technology, Stockholm, Sweden;
and
J. Neuhauser and R. Wunderlich, Max-Planck-Institut für Plasmaphysik, EURATOM Association, D-8046 Garching, Germany.

INTRODUCTION

The behaviour of oxygen, which is one of the most frequently encountered impurity species in tokamaks, is particularly complicated due to the intensive cross charge exchange processes between oxygen and hydrogen. The other complications arise due to the fact that oxygen is desorbed from the metallic surfaces as hydrogenic or metallic compounds, undergoing a sophisticated multistep evolution before arriving at the neutral atomic state.

Here, we aim at studying the influence of these effects, using the numerical algorithm, which allows a fast solution of both the steady-state and the time-dependent one-dimensional finite rate diffusion equation /1/. The auxiliary calculations, accounting for the cross charge exchange and the sub-routine, describing the low energy chemical kinetics are incorporated in the code.

RESULTS AND DISCUSSIONS

The cross charge exchange processes affect both oxygen neutrals and the singly ionized oxygen ions, if their mean free paths for charge exchange are of the same order as the ionization mean free path.

For oxygen atoms, injected with an initial energy much less than the plasma temperature, the cross charge exchange processes dominate over the ionization by the electron impact, producing fast oxygen neutrals with an average energy of the order of the plasma temperature and at the same time retarding their directed motion by randomizing their volecity distribution. Some part of the oxygen neutrals (roughly one half for low temperatures) returns to the wall reducing the flux of the injected impurities. The other part, moving into the plasma, penetrates much deeper due to the increased velocity reaching the region with the higher temperature, where the ionization to the second ionization state by electron impact increases drastically and the amount of the neutral hydrogen decreases.

The charge exchange processes with hydrogen affect not only the oxygen neutrals but also the diffusion of the singly ionized oxygen ions. They diffuse much faster as a result of the multiple charge exchange collisions and thus undergo greater recycling. It implies an increase of the effective diffusion coefficient of the singly ionized oxygen ions as described in /2/.

To demonstrate some of the typical examples of the 1-D multispecies, non-corona impurity transport code, some steady radial density profiles for oxygen are given in Figs. 1 and 2 for temperature and density profiles similar to those of an ohmically heated ASDEX plasma.

The effect of the cross charge exchange plays an important role if the neutral hydrogen flux exceeds the value 10^{17} $cm^{-2}sec^{-1}$ for the plasma tempera-

ture at the wall equal to 10 eV, scaling slower than the penetration depth of oxygen neutrals for a given flux density, due to the increased albedo of the plasma. The enhancement factor for the total impurity content is 5 - 6 for the hydrogen flux changing from 10^{17} to 10^{19} $cm^{-2}sec^{-1}$. (Fig.4). Though the latter flux might appear excessive compared with the typical value averaged over the flux surfaces, due to the significant poloidal and toroidal asymmetries observed in the outer regions of the tokamak plasma, this value, corresponding to $n_H \leq n_e$, can locally become of the right order of magnitude. This is certainly true for the regions with the large content of the neutral hydrogen, such as the area in the close vicinity of the limiter's top /4/ or the gas inlet.

Significant modifications appear also in the distribution of the oxygen ions over the ionization states. The low ionization states are usually located at the periphery and therefore strongly influenced by the cross charge exchange processes. Owing to the enhanced diffusion, the amount of impurities in the low ionization states (O II - O V) decreases, their profiles get flatter at the much lower level. It might be one of the reasons for the observational difficulties of these ions /3/. On the other hand, the relative amount of the higher ionization states increases, leading to the growing radiative efficiency. The other important implication of the effect occurs if the decay length is much larger than the mean free path for charge exchange. It might lead to increased oxygen recycling at the first wall instead of, as usual, taking place at the limiter. The effect gets less important with the decreasing value of the decay length in the scrape-off, owing to the rapid loss of the O II at the limiter. For obvious reasons the total amount of impurities gets smaller by one order of magnitude if the decay length is less than the width of the limiter and the penetration depth of the impurity neutrals. (Fig.4).

As far as molecules are concerned, the drastically increased penetration depth of the oxygen impurities is the result of the low energy chemical processes occuring to the oxygen molecular compounds, released from the wall. For the case of ASDEX it reaches the values up to 5 - 10 cm. The profile of the total number of impurity ions is shown in Fig. 3.
Important consequences arise from the combination of these effects with charge exchange: the penetration depth of the atomic impurities increases further and much less (roughly one fourth) of the oxygen atoms produced from the molecular compounds return to the wall. The total number of impurities scales even stronger than the penetration depth of oxygen atoms for a given inflow of impurities.

ACKNOWLEDGEMENTS

The authors wish to thank Prof. B. Lehnert and Dr. K. Lackner for discussions.

REFERENCES

/1/ K. Lackner et al., Z. Naturforsch. 37a, 931, 1982

/2/ M. Tendler, Pl. Phys. July 1983

/3/ TFR Group, Nucl. Fus. 22, 1173, 1982

/4/ S. Allen et al., Nucl. Fus. 21, 251, 1981.

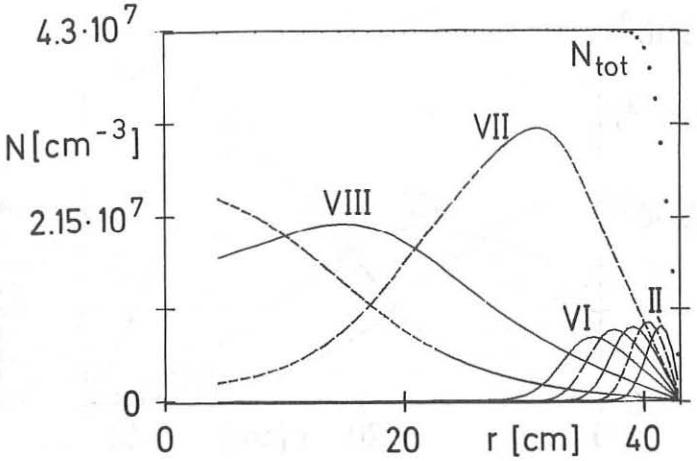

Fig. 1: Profiles of oxygen ionization states for hydrogen and oxygen fluxes $\Gamma_H = 0$, or $\Gamma_o = 10^{11}$ cm^{-2}sec^{-1}, respectively. Dashed and solid lines are used for even and odd ionization states respectively. The dotted line gives the total density of the oxygen ions. The scrape-off layer is switched off.

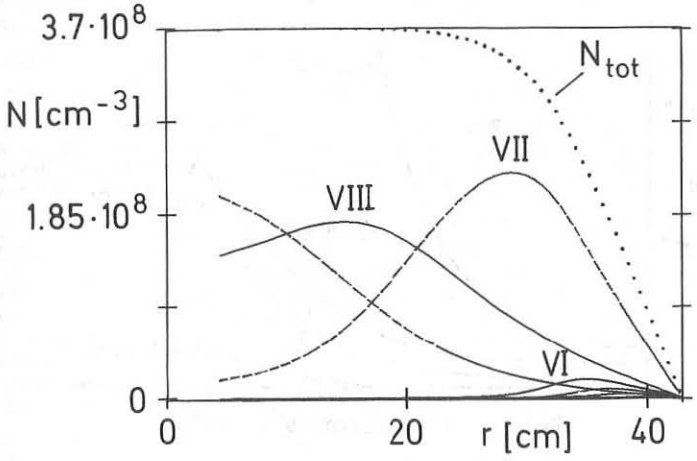

Fig. 2: Profiles of oxygen ionization states for the hydrogen flux $\Gamma_H = 10^{19}$ cm^{-2}sec^{-1}. Otherwise, notations and conditions are the same as for Fig. 1.

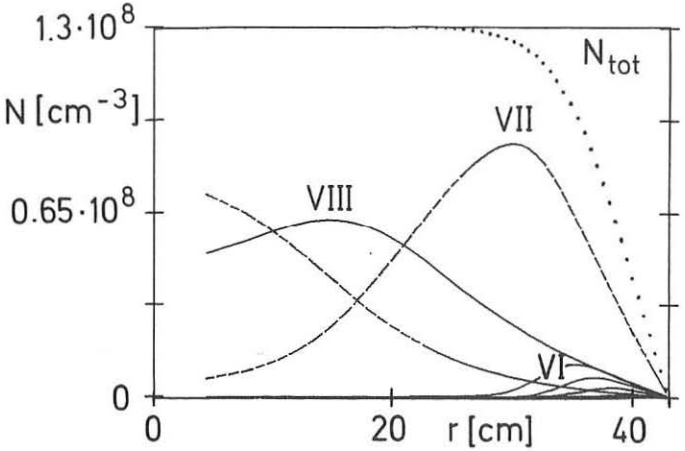

Fig. 3: Profiles of oxygen ionization states for the density of the oxygen molecules $N_{MOL} = 10^7$ cm^{-3} and an energy 0.03 eV at the wall. The oxygen atomic flux $\Gamma_o = 0$. Otherwise, the same as for Figs. 1 and 2.

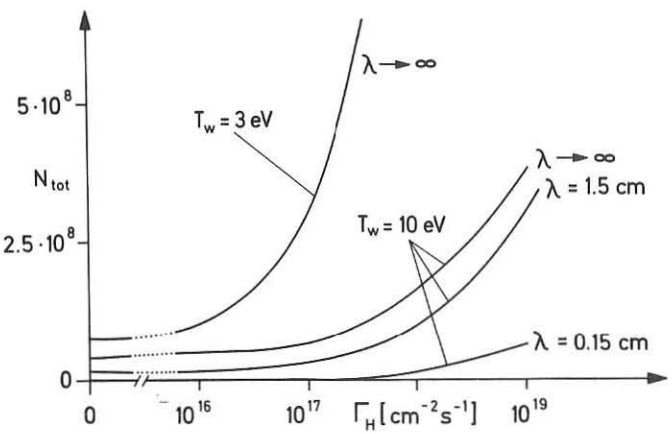

Fig. 4: Maximum total oxygen ion density as functions of hydrogen flux for different plasma decay lengths λ and wall temperatures T_W. For $T_W = 10$ eV, the drastic increase occurs when the hydrogen flux changes from $\Gamma_H = 10^{17}$ to $\Gamma_H = 10^{19}$ cm^{-2} sec^{-1}.

EXTRAP in the quasi-stationary regime

M. Tendler

Royal Institute of Technology, Stockholm, Sweden

ABSTRACT

It has been shown that the pinch radius time evolution is determined by the energy balance. The physical reason for it is the unique relation between the plasma temperature and the total current, derived from the Bennet's condition. The quasi-stationary value of the pinch radius is shown to be the function of the energy losses. For the parameters of the experiments, studied to date, the latter is found when the pinch radius coincides with the separatrix. The underlying effect is the strong enhancement of the radial energy flux due to the magnetic field nulls at the separatrix.

1. INTRODUCTION

The Z-pinch immersed in a multipole magnetic field (EXTRAP) [1] has some peculiar physical properties, making it very much different from both the closed and open magnetic field confinement schemes. There is no toroidal magnetic field, and the field lines have no rotational transform. The total magnetic field, which includes both the field generated by the plasma current and the external multipole field is zero at four X-points, defining a separatrix, and at the 0-point on the axis (see Fig.1).

In our previous publication on this subject, it has been shown that the crucial parameter in EXTRAP, essential for the establishment of the certain equilibrium, is the ratio between the plasma diffusion time $T_p=r_p^2B^2c^2\sigma/p$ and the flux diffusion time $\tau_s=4r_s^2\pi\sigma/c^2$. For a plasma with $\beta\sim1$ this ratio is very close to 1. However, in EXTRAP the existence of the magnetic field nulls on the separatrix might lead to the excessive mass flow there, thus redistributing the magnetic field within the pinch by the plasma motion and generating surface currents on the time scale of the experiment (see Fig.5 in [2]). Another type of equilibrium arises if the flux diffusion time is much shorter than the plasma diffusion time. The plasma and current density, the electron temperature and the magnetic field radial profiles have been obtained in [2] for this case under the assumption of both a strong and weak electron-ion energy exchange (see Figs. 3 and 4 in [2]). All these considerations should be, of course, reconciled with the equilibrium, employed for the stability analysis. It has been anticipated in [3] that the stable equilibrium can be achieved only if the plasma is limited by the separatrix.

Here, we aim to show that the equilibrium exists at all only if the pinch boundary coincides with the separatrix irregardless of the stability considerations. The physical effect, which implies the positioning of the pinch radius at the separatrix is the drastically enhanced radial energy transport due to magnetic field nulls and further transition of the field geometry transport. Our estimates show that if the pinch radius is located well inside the separatrix, the energy balance for given plasma parameters

implies the continuous growth of the pinch until the plasma hits the separatrix. This effect is shown to be dominant even when a substantial part of the energy is lost to the electrodes by convection, via bremsstrahlung or linear radiation. Here, the mass accretion effects have been neglected.

2. TIME-DEPENDENT ENERGY BALANCE.

For a channel with total particle density n, radius R, and total current I, the condition for a balance between magnetic field and plasma pressure is given by the Bennet formula:

$$4c^2NT = I^2 \tag{2.1}$$

where $N = \int_0^R 2\,rn(r)dr$, $T = T_e = T_i = \frac{1}{N}\int_0^R Tn2\pi rdr$ - the average temperature and I - the total current.

The energy balance equation for a plasma with $T_e = T_i = T$ reads:

$$3n\frac{dT}{dt} + p\nabla\cdot V - \nabla q = Q$$

The first term in equation (3.2) gives the change in internal energy, the second corresponds to the expansion work, q is the heat flow and Q is the energy gain. Assuming the second type of equilibrium and integrating equation (2.2) over the cross-section of the pinch, we get

$$3N\frac{dT}{dt} + 4NT\frac{1}{R}\frac{dR}{dt} = \frac{I^2}{\pi R^2\sigma} + Q_{aux} - Q_L \tag{2.3}$$

and Q_L is the total loss of energy from the pinch. So, the evolution of the pinch radius in time is determined by the energy balance and not by the force balance of the $\underline{E}$ x B and diamagnetic drifts at the boundary. The physical reason for it is the fixed relation between the plasma temperature and the total current, established by equation (2.1). So, the combination of the compression work with the ohmic heating provided for a certain value of the temperature for a given current in a pinch with the small energy sink. Microscopically this compression or expansion is governed by the change of the electric field in the plasma.

At the early time the energy losses are unimportant so using equation (2.1), we get from (2.3):

$$\frac{3}{2}I^2R^2\frac{dI}{dt} + IR\frac{dR}{dt} = 2.55\,\frac{c^5N^{3/2}}{\pi\sigma_o} \tag{2.4}$$

Equation (2.4) is important for the start up process in EXTRAP. Due to the small value of the current rise in the EXTRAP experiment, the plasma builds up radially outward. It implies that the second term at the l.h.s. of equation (2.4) dominates. Thus, the development of the EXTRAP discharge is different from the conventional Z-pinch, where the discharge starts at the wall due to the significantly larger current rate-of-rise time employed.

At the later stages of the discharge, the energy losses become important and govern the time dependence of the pinch radius.

At first, we consider the case, when the pinch plasma has expanded up to the separatrix and assume the energy losses are limited by the electron heat conduction flow, parallel to the magnetic field lines. The electron heat flow along the field lines is given by:

$$q_{\parallel,e} = K_{\parallel} \frac{dT}{d\ell} = 1.94\ 10^{20}\ \frac{T^{7/2}(ev)}{L} \qquad (2.5)$$

where L(in cm) is the length along the field lines from the boundary of the pinch to the wall.Using (2.5) in (2.3) as the energy sink, we get for ΔR (the radial distance between the plasma boundary and the separatrix:

$$\Delta R \cong 3.53 \cdot 10^{-76}\ \frac{LN^5}{R_s^3\ I^8(KA)} \qquad (2.6)$$

Using the experimental parameters given in [4] we get $\Delta R \cong 0.02$ mm. The time dependence of the pinch radius is given in Fig.2. A remarkable feature of eq. (2.6) is the extremely strong dependence on the total current. Further, we assume that the energy losses occur at the electrodes, and the sink is given by [5]:

$$q_L = \frac{5}{2} \frac{JT}{eA} \qquad (2.7)$$

where A is the length of the pinch.

Substituting (2.7) into (2.3) we solve eq. (2.3)(see Fig.2) and get for the quasi-stationary value of the plasma radius:

$$R = 3.74\ 10^{-19}\ \frac{A^{1/2}N^{5/4}}{I^2(KA)} \qquad (2.8)$$

For experimental parameters of EXTRAP it gives R 100 mm, being much larger than the radial distance to the rods. It implies that these losses are negligible for the case of EXTRAP. Bremsstrahlung or other types of radiation losses give even smaller contribution.

Acknowledgements.

The author wishes to thank Prof. B. Lehnert and Drs. M. Bureš, A. Kuthy and J. Drake for numerous discussions on the subject.

References

[1] Lehnert, B., Physica Scripta 10 (1974)139.

[2] Tendler, M., Nucl.Instr.Meth. 207(1983)233.

[3] Hellsten, T., Nucl.Fus.22 (1982)565.

[4] Drake, J. TRITA-PFU-83-04 and Pl.Phys. to be published.

[5] Lehnert. B., Zeit.f.Naturfor. 37a (1982)769.

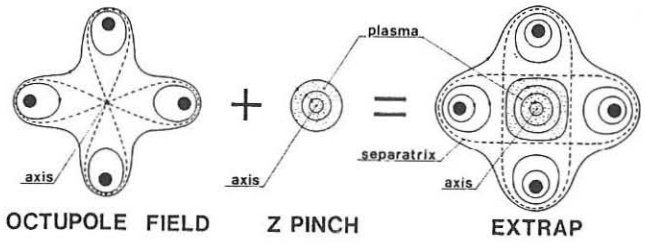

Fig.1. Schematic representation of the cross-section of an Extrap Z-pinch. In a linear device, the axis is the Z-axis of a cylindrical coordinate system. In a toroidal device the axis is the minor axis of a toroidal coordinate system.

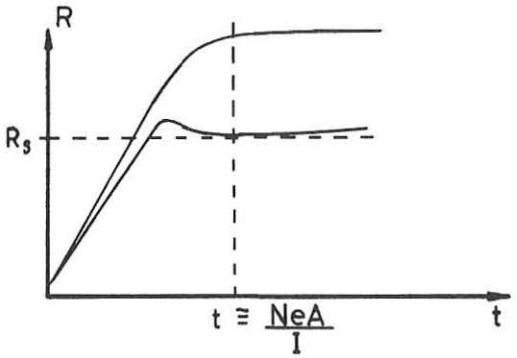

Fig.2. The pinch radius as a function of time. The lower curve corresponds to the case when the energy losses occur at the separatrix due to electron heat conduction flow. The upper curve describes the case, when the energy is lost to the electrodes.

An Implicit "Quasineutral" Plasma Simulation Method which includes Sheath and Vacuum Regions

E.L. Lindman*, G. Rickard and M.G. Haines
Blackett Laboratory, Imperial College
Prince Consort Road, London SW7 2BZ, U.K.

INTRODUCTION

In plasma simulation codes designed to study the low frequency behaviour of plasmas efficiently, the high frequency modes (eg: lightwaves, plasma oscillations, electron cyclotron motion, etc.) must be removed from the algorithm. One may use an approximate set of equations from which these effects have been removed /1-4/ or a time-differencing method which converts the high frequency modes to damped modes /5-8/ oscillating at a frequency determined by the time step. In either case, these approximations (the Darwin model, quasineutrality, massless electron fluid, etc.) lead to equations for the fields which are elliptic instead of hyperbolic. Thus the fields cannot be stepped forward in time as in electromagnetic simulations using the full set of Maxwell's equation. Instead the fields and the sources must be found, implicitly, at each time step. The two techniques currently used for this purpose are the "direct implicit" method /1,5,6/ and the "implicit moment" method /2,3,7,8/.

In the "implicit moment" method the moments which appear in the continuity and momentum equations are accumulated on the mesh from the particle data available at the current time level. These data are then used to step ρ and $\underline{J}$ forward to the new time level using moment equations with no further reference to the particle data. The fields at the new time level are then computed and used to step the particles forward in time to this time level. A correction using the new particle data could now be applied but is usually not worth the expense in additional computer time required /7/. Thus, in this method, the sources at the new time level are expanded about the particle data at the old time level. On the other hand it seems reasonable that stepping the particles foward using the old values of the fields would lead to particle positions and velocities, and hence sources, closer to their final values at the new time level. An expansion about these data might then be more accurate and/or converge faster than the expansion about the data at the old time level. Such an expansion is used in the direct implicit method.

In the "direct implicit"method the particle data at the current time level is extrapolated forward to an optimum intermediate time using an extrapolated value of the fields. From the equations of motion, corrections to these positions and velocities are obtained as a function of the unknown fields. By summing over the particle data we can obtain expressions for the corrected sources as a function of the unknown fields. The moments which appear in these equations are accumulated on the mesh and these equations are then solved for the new fields with no further reference to the particle data. When both the positions and velocities of the particle are adjusted in solving for the fields an unwieldy set of

*On leave from the Los Alamos National Laboratory, NM 87545, U.S.A.

equations is obtained, particularly in 2 or 3 dimensions /5,6/. In contrast, when the positions are not adjusted and the conservation of canonical momenta can be used to determine the velocities, very simple equations are obtained /1/. The extension to the case where the positions are not adjusted and the canonical momenta are not conserved is included in the method presented below along with elements of the "implicit moment" method.

DERIVATION OF LOW FREQUENCY EQUATIONS

We are interested in following the details of the ion dynamics in regions where the finite-larmor-radius expansion breaks down such as on the axis of a Z-pinch. The ions are therefore treated as particles using the usual particle-in-cell methods for depositing Ni and Ni$\underline{U}$i on the mesh and interpolating the fields to move the particles. For the electrons on the other hand we wish to include only the low frequency part of the motion, and, hence, eliminate plasma oscillations and cyclotron motion in addition to lightwaves. Several approximations to the electron fluid equations and to Maxwell's equations are generally required to do this.

The assumption of quasi neutrality is usually made to eliminate plasma oscillations. This approximation, however, is unnecessarily restrictive and eliminates the possibility of including vacuum regions and sheaths in the problem. Attempts to patch such regions into the problem after the physical link to them has been removed from the equations is unsatisfactory /3,4/. The removal of lightwaves from the problem is usually accomplished by removing $\partial\underline{E}/\partial t$ from Maxwell's equations. This approximation is a low frequency approximation which can also be used to remove plasma oscillations from the problem without using quasineutrality.

Using the appropriate Maxwell's, and assuming $\partial\underline{E}/\partial t = 0$, we define Ne and Ne$\underline{U}$e as follows.

$$Ne = Ni - \nabla\cdot E/(4\pi e) \tag{1}$$

$$Ne\underline{U}e = Ni\underline{U}i - C\nabla\times B/(4\pi e) \tag{2}$$

If we substitute these into the electron continuity equation and use the fact that Ni and Ni$\underline{U}$i satisfy an ion continuity equation, we obtain $\partial\ (\nabla\cdot E)/\partial t = 0$. which is consistent with the original assumption. Combining the appropriate Maxwell's equations, we have

$$-C^2\nabla\times\nabla\times E = 4\pi e\,\frac{\partial}{\partial t}\,(Ni\underline{U}i - Ne\underline{U}e). \tag{3}$$

And from the momentum equations for ions and electrons, we have

$$\frac{\partial}{\partial t}\,(NjUj) = \frac{ej}{mj}\,(Nj\underline{E} + \frac{Nj\underline{U}j}{C}\times\underline{B}) - \nabla\cdot(Nj\underline{U}j\underline{U}j + \underline{\underline{P}}\,j/mj). \tag{4}$$

Because we have introduced an ion fluid equation, we have used the "implicit moment" method here. Combining Eqs (3) and (4) we obtain an implicit equation for $\underline{E}$.

$$-\nabla\times\nabla\times\underline{E} = \underline{j}(\underline{E}) \tag{5}$$

$$\underline{j}(\underline{E}) = -\frac{4\Pi}{2} \sum_j \frac{e_j^2}{m_j} (n_j\underline{E} + \frac{n_j\underline{U}_j}{C} \wedge B) - e_j\nabla\cdot(N_j\underline{U}_j\underline{U}_j + \underline{P}_j/m_j) \qquad (6)$$

Equation (5) must be handled with some care. In particular, the divergence of the left-hand-side is easily seen to be zero while that of the right-hand-side is in general not zero. For mathematical consistency we must require that the divergence of the right-hand-side be zero also. This gives us an additional equation to solve:

$$\nabla\cdot\underline{j}(\underline{E}) = 0 \qquad (7)$$

If we write $\underline{E}$ as the sum of a transverse and longitudinal part: $\underline{E} = \underline{E}_T - \nabla Q$, we may regard Eq.(5) as the equation for $\underline{E}_T$ and Eq.(7) as the equation for Q. Furthermore the left-hand-side of Eq.(5) involves only $\underline{E}_T$ allowing us to use the well-known vector identity to convert $\nabla\wedge\nabla\wedge$ to the vector Laplacian which is far more convenient to deal with numerically:

$$\nabla^2\underline{E}_T = \underline{j}(\underline{E}) \qquad (8)$$

Equations (7) and (8) are a complicated set of nonlinear equations which contain several physical effects. In high density regions they reduce to the quasineutral equations. At the boundary of the plasma Debye sheaths, electromagnetic sheaths and magnetic insulation phenomena can be obtained. And, of course, outside these sheath regions the correct equations for the vacuum fields arise. Equation (7), in particular contains a term of the form $\nabla\cdot(\nabla^2 Q)\nabla Q$. The mathmatical properties of the solutions of such an equation are not well-known and questions of existence and uniqueness are not easily brushed aside.

In problems such as the simulation of a Z-pinch, the details of the solution in the sheath and vacuum are not of interest. A sufficiently accurate link between the vacuum fields and those within the plasma are all that is required. In such applications the Debye sheath is irrelevant and may be removed from the problem by setting the electron temperature equal to zero. The electromagnetic skin depth on the other hand must be included and may be too small for the mesh. In such cases artificially enhancing its size to a cell size will probably give an adequate approximation. Other approximations such as replacing the electron density in a vacuum region by a constant such that c/ω_{pe} is large compared to the radius of the computational region are also being explored.

The low frequency set of equations then consists of Eqs. (1), (2), (7), (8) and Faraday's law for the B field, Eq.(9).

$$\partial\underline{B}/\partial t = -C\nabla\wedge\underline{E}_T \qquad (9)$$

TIME INTEGRATION METHOD

The procedure for stepping these equations forward in time is as follows. We start at a particular time level with values for the ion positions and velocities, $\underline{X}^j$, $\underline{V}^{j-\frac{1}{2}}$ and the fields, $\underline{E}^j$, $\underline{B}^j$ and step the ions forward using Nielson's method /2/.

$$\underline{V}^* = \underline{V}^{j-\frac{1}{2}} + \tfrac{1}{2}\,\Delta t\,\frac{e}{M}\left(\underline{E}^j + \frac{1}{C}\underline{V}^{j-\frac{1}{2}} \wedge B^j\right) \qquad (10)$$

$$\underline{v}^{j+\frac{1}{2}} = + \underline{v}^{j-\frac{1}{2}} + \Delta t \frac{e}{M} (\underline{E}^j + \frac{1}{C} \underline{V}^* \wedge \underline{B}^j) \quad (11)$$

$$\underline{X}^{j+1} = \underline{X}^j + \Delta t \, \underline{v}^{j+\frac{1}{2}} \quad (12)$$

At this point we can deposit on the mesh the ion density at j+1, but because the ion velocity is a half-step behind we cannot deposit the ion current density. To overcome this difficulty a predictor corrector method will be used which is similar to the "direct implicit" method. First, the best prediction for the velocity at j + 1 is obtained using the fields at j with the positions at j+1.

$$\underline{V}^* = \underline{v}^{j+\frac{1}{2}} + \tfrac{1}{2} \Delta t \frac{e}{M} (\underline{E}^j(\underline{X}^{j+1}) + \frac{1}{C} \underline{V}^{j+\frac{1}{2}} \wedge \underline{B}^j (\underline{X}^{j+1})) \quad (13)$$

The ion moments Ni, NiUi*, etc are then deposited on the mesh. The fields are then stepped forward in a manner similar to that used for the particles.

$$\underline{B}^* = \underline{B}^j - \Delta t \; C \; \nabla \wedge \underline{E}^j \quad (14)$$

$$\nabla \cdot \underline{\dot{J}}(\underline{E}^*, \underline{B}^*, \; Ni \; \underline{Ui}^*, \ldots) = 0 \quad (15)$$

$$\nabla^2 \underline{E}_T{}^* = \underline{\dot{J}} \; (\underline{E}^*, B^*, NiUi^*, \ldots) \quad (16)$$

$$\underline{B}^{j+1} = \underline{B}^j - \tfrac{1}{2} \Delta t \; \nabla \wedge (\underline{E}^* + \underline{E}^j) \quad (17)$$

The "direct implicit" correction step then follows.

$$\underline{Ui}^{j+1} = \underline{Ui}^* + \tfrac{1}{2} \tilde{\Delta} t \frac{e}{m} \; (\underline{E}^* - \underline{E}^j) + \frac{1}{C} \underline{Ui}^* \wedge (\underline{B}^{j+1} - \underline{B}^j) \quad (18)$$

$$\nabla \cdot \dot{J} \; (\underline{E}^{j+1}, \underline{B}^{j+1}, \; Ni\underline{Ui}^{j+1} \ldots) = 0 \quad (19)$$

$$\nabla^2 \underline{E}_T^{j+1} = \dot{J} \; (\underline{E}^{j+1}, \underline{B}^{j+1}, \; Ni\underline{Ui}^{j+1} \ldots) \quad (20)$$

This correction step may not be required in all cases. Although a second pass through the particle table is not necessary to carry it out, it is still computationally expensive because of the numerical work involved in solving equations (19) and (20).

CONCLUSION

We have constructed an algorithm which reduces to quasineutrality in high density plasma regions but also contains the physics necessary to describe sheath and vacuum regions. To do this a low frequency approximation was used in place of the usual quasineutrality approximation. A time differencing of these equations has also been presented which uses features of both the "direct implicit" method and the "implicit moment" method.

REFERENCES

/1/ Dickman, D. O., Morse, R. L., and Nielson, C. W.: Numerical Simulation of Axi symmetric, Collisionless Finite-Beta Plasma, Phys.Fluids 12 (1969) 1708.

Material in excess of 4 pages.

A MODEL FOR THE MAGNETIC FIELD STRENGTH ALONG A STELLARATOR FIELD LINE AND ITS APPLICATION TO PARTICLE ORBIT CALCULATIONS

W.N.G. Hitchon and H.E. Mynick
University of Wisconsin Torsatron/Stellarator Laboratory
Madison, Wisconsin, 53706 (USA)

I INTRODUCTION

In any toroidal system which lacks symmetry in the toroidal direction, confinement of single particles cannot be guaranteed. A potentially significant consequence of the loss of an invariant of the motion, namely, the toroidal component of the canonical angular momentum, is that toroidally-trapped alpha particles may undergo stochastic orbits if the magnetic field "ripple" exceeds a rather low value, [1, 2, 3]. Such particles may then be relatively rapidly lost from the plasma.

The study of stochastic orbits is facilitated by the generation of a plot such as Fig. 1, of the successive intersections of particles with some plane. On such a plot, regions of stochastic behavior will in general be evident, some bounded on both sides by invariant surfaces and some extending to the edge of the plasma from the outer invariant surface (which may not exist, in which case all the orbits are stochastic and all the particles in question will be lost). The calculation of the intersections by direct integration of the equations of motion will in general require considerable computational effort. For a rippled tokamak, the simplicity of the magnetic field allows analytic expressions for the field to be used to make guiding-centre following calculations feasible [3]. An analytic map which simulates the orbits [1, 2] is much faster although generally somewhat pessimistic by comparison in that it tends to overestimate the extent of the stochasticity.

For stellarators, the complexity of the fields makes it appear unlikely that a useful analytic map could easily be developed. Direct integration of guiding-centre equations in fields generated by "real" coils for many orbits and for large distances would be prohibitively time-consuming. The flux-coordinate guiding-centre equations of Boozer, et al. [4] may, on the other hand, be integrated very rapidly. The difficulty with this technique is obtaining a good representation of the field in flux coordinates. In this paper, we use an analytic representation of stellarator-type fields in flux coordinates to study alpha particle behaviour in various stellarator reactor geometries.

II MODEL FIELD

As has been pointed out previously [5, 6], the stellarator field given by $\underline{B} = \nabla V$, where

$$V = B_0 R_0 \phi + b_\ell a \rho^\ell \cos(\ell\theta + p\phi) + \ldots \qquad (1)$$

has magnitude

$$B(\bar{\rho},\bar{\theta},\phi) \simeq B_0(1 + \varepsilon\bar{\rho}\cos\bar{\theta} + \varepsilon\bar{\rho}\delta\{\sin(m\bar{\theta} + p\phi) - h\bar{\rho}\sin(\ell\bar{\theta} + p\phi)\}) \quad (2)$$

$m \equiv \ell - 1$, when expressed in the "flux coordinates" $\bar{\rho}$, $\bar{\theta}$, which characterise a field line. $\bar{\rho}$, $\bar{\theta}$ are defined by

$$\rho = \bar{\rho}(1 + \delta\sin(\ell\bar{\theta} + p\phi))$$
$$\theta = \bar{\theta} + \delta\cos(\ell\bar{\theta} + p\phi) \quad (3)$$

$\rho_0 = \bar{\rho}$ and $\theta_0 = \bar{\theta} - \iota\phi$ are the coordinates of the field line at the plane $\phi = 0$. ι is the rotational transform. The major and minor radii are R and a: (r, θ, ϕ) are a set of local quasi-cylindrical coordinates.

$\varepsilon \equiv a/R$ and $\rho \equiv r/a$. $\delta \equiv \frac{b_\ell}{\varepsilon B_0}\frac{\ell}{p}\rho_0^{\ell-2} \ll 1$.

The parameter $h \equiv \varepsilon p^2/\ell$ determines whether the extra terms in (2) which vary as $\sin(m\bar{\theta} + p\phi)$ are significant or not. Typically, if $h \lesssim 1$ (which is the case in most stellarators) it will be crucial to allow for them whereas for $h \gg 1$ (which is the case in Torsatrons/Heliotrons) it would appear to be less vital. However, it has been found [7] that the results of Monte Carlo calculations for Heliotron-E (where $h \simeq 12$) were significantly altered by the $\sin(m\bar{\theta} + p\phi)$ term.

III ORBIT CALCULATIONS

In modular stellarator reactor configurations (see Ref. [8]), localised alpha particles (trapped in the helical ripple) will tend to be lost from the plasma as they undergo uncompensated nearly vertical drifts. In addition, a large population of toroidally trapped alphas exists whose orbits exhibit two interesting features: i) the majority of the particles undergo stochastic orbits which appear, however, to be bounded in radius and ii) despite their evidently sampling a substantial region of physical space, they rarely become trapped in the helical ripple, since for p = 3-4 the ripple wells are shallow and occupy a small fraction of the length of a field line.

In some torsatron-type reactors, the helical ripple is much larger than the toroidal modulation of the field. As a result, many localised particles and very few toroidally trapped particles exist. The former group tends to have drift surfaces close to magnetic surfaces, instead of drifting vertically. Thus, on the time scale on which a particle makes a poloidal transit, they are confined. For ATF-1 parameters however, the toroidal ripple is comparable with the (large) helical ripple. Many alphas are localised, and these drift straight to the wall. In the central region, toroidally trapped alphas exist, but in contrast to the stellarator case these become localised (and are lost) very rapidly because p = 12 and helical wells are to be found everywhere.

Figure 1 shows alternate (outer) intersections of toroidally trapped particles, all launched with the same E, μ (representing 3.5 MeV alpha particles) with the midplane of the torus in a modular stellarator coafiguration with ℓ=2, p=3, $\varepsilon=\frac{1}{9}$, ι=0.48 as discussed in [8]. A band of stochastic behavior is bounded on the outside by the inner one of a pair

FIGURE 1

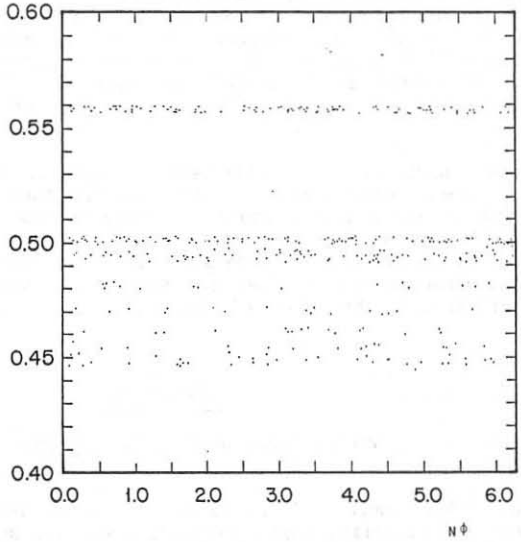

FIGURE 2

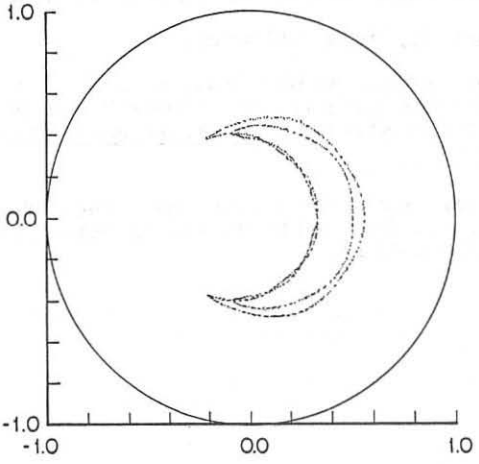

of 'lines' each generated by the same orbit, shown in Fig. 2. Although this particle in this orbit apparently retraces almost exactly the same path in the course of hundreds of banana orbits, its mid-plane intersections show stochasticity, on close inspection. However, the existence of orbits such as this explains why other orbits do not necessarily lead to helical trapping and loss of toroidally trapped alphas.

Thermal particles are observed to exhibit the same sort of behavior: they undergo banana orbits whilst toroidally trapped, and although their orbits become stochastic they do not tend to trap in the helical wells unless launched into an orbit which is close to being marginally trapped. This suggests that the various 'banana-drift' diffusion mechanisms which have been studied in tokamak geometry could also be important in this class of stellarators.

REFERENCES

[1] Goldston, R.J., White, R.B., Boozer, A.H., Phys. Rev. Lett. 47 (1981) 647.

[2] White, R.B., Boozer, A.H., Goldston, R.J., Hay, R., Albert, J., Karney, C.F.F., Plas. Phys. and Cont. Nuc. Fus. Res. (Proc. 9th Intl. conf. Baltimore, 1982) IAEA-CN-41/T-3.

[3] Hitchon, W.N.G., Hastie, R.J., Nuc. Fusion 23 (1983) 533.

[4] Boozer, A.H., Kuo-Petravic, G., Phys. Fluids 24 (1981) 851.

[5] Hitchon, W.N.G., Nuc. Fusion 22 (1982) 1661.

[6] Hitchon, W.N.G., McLenithan, K.D., Mynick, H.E., (to be published).

[7] Wakatani, M., (to be published).

[8] Hitchon, W.N.G., Johnson, P.C., Watson, C.J.H., "Parameter and Cost Optimisations for a Modular Stellarator Reactor", Culham Report CLM-P682, (to be published in Journal of Fusion Energy).

This work was supported by the U.D. Department of Energy under contract No. DE-AC02-78-ET53082 and by the National Science Foundation under grant No. ECS-82-06027.

JET SIMULATION

M.F.Turner
UKAEA Culham Laboratory,
Abingdon, Oxon,OX14 3DB, UK.
(Euratom/UKAEA Fusion Association)

J.A.Wesson
JET Joint Undertaking
Culham Laboratory
Abingdon,Oxon,OX14 3DB,UK

Abstract. A 3-D computer code (MASCOT) has been designed to simulate the MHD behaviour of tight aspect ratio tokamaks of non-circular cross-section. The initial application of the code is to JET. First calculations have followed the electromagnetic diffusion of the equilibrium up to 20 seconds. In preliminary non-linear studies the growth of an m=2 tearing mode has been followed up to saturation.

Introduction. The tight aspect ratio and D-shaped cross-section of the JET tokamak precludes the application of the commonly used approximations for large aspect ratio and circular cross-section. A 3-D MHD simulation code, MASCOT, has therefore been devised, which makes no geometrical approximations.

The initial objective is to study the non-linear behaviour of JET on the resistive time scale. To this end special techniques are used to avoid fast hydromagnetic waves.

The model includes energy transport and the facility for additional heating and radiation losses. Rapid transport around field lines is also included.

The Model. The general problem presents a substantial computational task and it is necessary therefore that the model should be made as simple as possible whilst still including the necessary physics.

We have the usual Ohms Law and Maxwell Equations

$$\frac{\partial \underline{B}}{\partial t} = -\nabla \times \underline{E} \quad (1), \qquad \underline{E} = \eta \underline{j} - \underline{v} \times \underline{B} \quad (2), \qquad \underline{j} = \frac{1}{\mu_o} \nabla \times \underline{B} \quad (3).$$

A fundamental objective of the code is to follow the growth of the non-linear tearing modes on a resistive time scale. Such development can be modelled by following a sequence of non-axisymmetric equilibria. A reasonable representation of the resistivity is important in such equilibria as this will affect the distribution of current density. An energy equation is therefore included to provide evaluation of the electron temperature from which the resistivity is determined. At present we have a one fluid model.

$$\frac{3}{2}\frac{\partial p}{\partial t} = Q - \nabla \cdot \underline{q} - L \qquad (4)$$

The cross-field energy-transport is computed from $q = K\nabla T$ where K is an empirically determined conductivity. Q is the heating, including ohmic heating (ηj^2) and any additional heating, L is the heat loss. A constant density is assumed.

To complete the basic model a method has been devised for evaluating the resistive flow velocities which avoids the problem of fast hydromagnetic waves. The following equation is solved

$$\frac{\partial \underline{v}}{\partial t} = c_1(\underline{j} \times \underline{B} - \nabla p) + c_2 \nabla^2 \underline{v} - c_3 \underline{v} \qquad (5)$$

Here c_1 can be seen as the reciprical of an effective inertia whilst c_2 and c_3 are damping coefficients. c_1 is arranged to be as small as possible consistent with maintaining the proper resistive flows. Essentially a high effective inertia is simulated. The reasoning is that the resistive diffusion will not be affected by the effectively large inertia if it is kept below a critical value. The sequence of developing equilibria can still therefore be accurately modelled. The procedure can be considered as a numerical technique for relaxing to equilibria. This feature allows the computations to be carried out on the resistive time scale thus keeping computational times within practicable limits. However, phenomena related to the very short inertial timescale can be studied over a short period by increasing c_1 and reducing the timestep.

Further to the basic model, rapid parallel heat flow is simulated by a technique of equalising the temperature around field lines.

Boundary conditions at present assume a conducting wall at the plasma edge,the normal component of $\underline{B}$ being put to zero. The toroidal electric field at the boundary is automatically adjusted to maintain a specified total current. Flows are allowed to continue across the boundary. The temperature is given a small pedestal value at the boundary to avoid the problem of the resistivity becoming very large because of its $T^{-3/2}$ dependence.

Numerical Method. The equations are solved on a 2-D rectangular mesh in the minor cross-section using a 2 step Lax-Wendroff scheme. The third dimension is computed using a full spectral method which involves expansion into Fourier modes around the toroidal direction.

Preliminary Results. The early development work on the code is discussed elsewhere.[1]

In a test calculation the completed axisymmetric version of the code (MASCOT2) has modelled the evolution in JET of the plasma from a cold Solovev equilibrium with flat current profile to an ohmically heated equilibrium with peaked current profile. Fig.1 shows the evolution of this current profile.

The full 3D version (MASCOT3) is now operating with an n = 1 mode only in the toroidal direction. The initial run with MASCOT3 has been the simulation in JET of the development of an m = 2 tearing mode island. This island is depicted in Fig.2. For this case B_ϕ = 1T and the total current is 2MA with ohmic heating only. The values of q_0 and q_{edge} are 1 and 4 respectively.

Further Studies. The next stage in the development of MASCOT3 will be the setting up of a vacuum region around the plasma to allow magnetic fluctuations at the plasma surface.

With the facilities available for simulating additional heating, radiation losses and for introducing higher n-modes a whole range of phenomena are open to investigation including m=1 kink instability, disruptions and the anomalous current penetration due to high-m tearing modes.

Acknowledgements. We wish to thank A.Sykes and J.W.Connor for helpful and stimulating discussions.

Reference.

Turner, M.F., and Wesson J.A. Computer Physics Comm. 24(1981) 343-354.

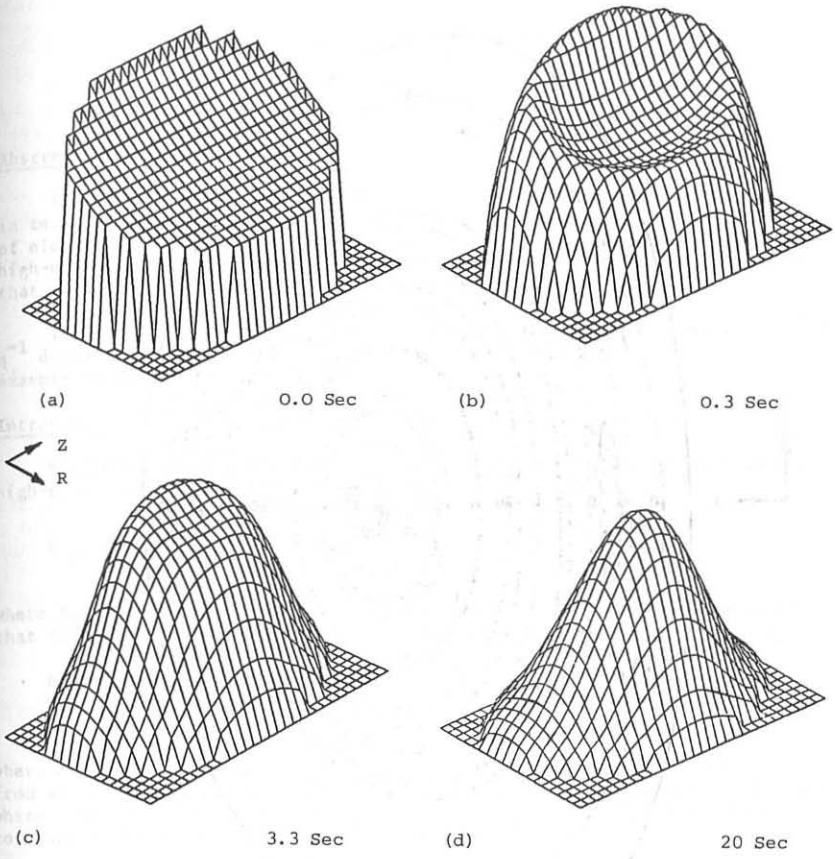

Fig.1.

Evolution of current in JET from a cold Solovev equilibrium with flat current profile(a) to an ohmically heated equilibrium with a peaked current profile (d). Total current is 2MA and B_ϕ = 1T. Note that the scale differs for each subpicture. Peak values of current density, (j) for each case are given below along with values for q and β.

Picture	(a)	(b)	(c)	(d)
Maximum j(Ma/m^2)	0.36	0.40	0.46	0.63
q_0	3.07	2.8	1.4	0.94
q_{edge}	3.70	3.5	3.8	3.98
$<\beta>$	0.09%	0.45%	0.53%	0.57%
β_J	0.02	0.10	0.12	0.12

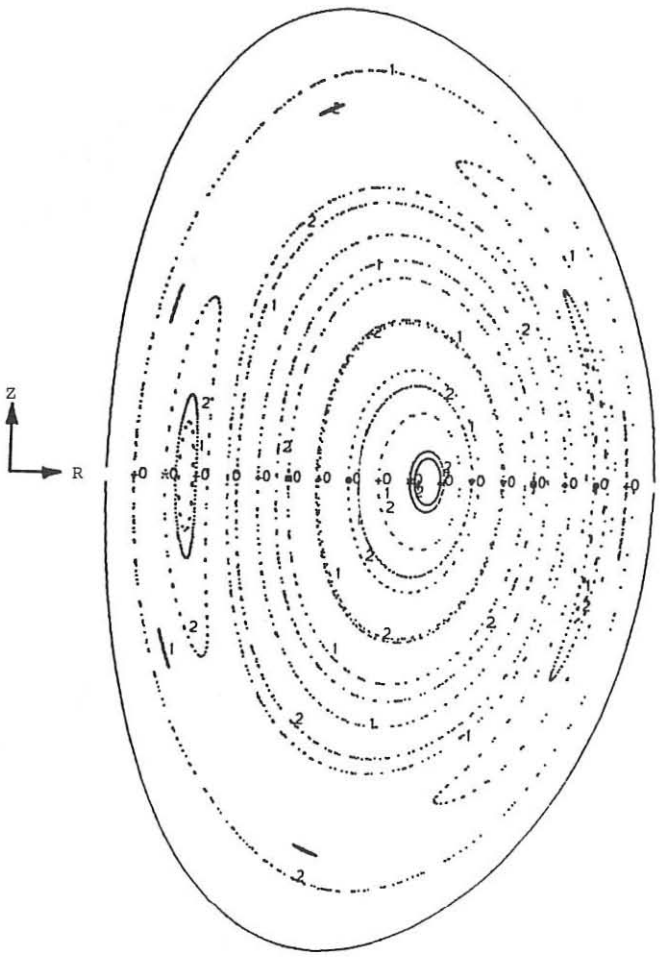

Fig.2.

Example of m=2 tearing mode islands in JET.
Total current = 2MA. Toroidal field = 1T.
$q_0 = 1$ $q_{edge} = 4$ $\langle\beta\rangle = 0.6\%$ $\beta_J = 0.13$
Ohmically heated plasma with no radiation losses.

BETA LIMITS IN TOKAMAKS DUE TO HIGH-N BALLOONING MODES

A. Sykes, M. F. Turner, S. Patel
UKAEA Culham Laboratory, Abingdon, Oxon, OX14 3DB, UK.
(Euratom/UKAEA Fusion Association)

Abstract

By adopting a modified definition q_J of the edge safety factor (defined in terms of current/area), we find that for a general Tokamak configuration of elongation E and aspect ratio A, the maximum β for marginal stability to high-n ideal ballooning modes is well represented by $\beta = 22E/Aq_J$, provided that sufficient triangularity is used to ensure Mercier stability.

This simple expression is compared with other published results, and its q^{-1} dependence (rather than the theoretical q^{-2}) explained. The particular example of JET is considered.

Introduction

By fitting functional forms to results obtained from 2D transport and high-n ballooning stability codes, Tuda et al (1) derived

$$\beta_{opt} = 7.8\ E^{1 + 0.14(q_s - 1)}\ q_s^{-0.54}\ (A - 1)^{-0.76}$$

where β_{opt} is an optimised value, i.e. the configuration has been evolved so that (almost?) all the plasma is at marginal stability to high-n modes.

Bernard et al (2) have derived

$$\beta_{max} = 27\ E^{1.2}\ (1 + 1.5\delta)\ q_s^{-1.1} A^{-1.3}$$

where δ is the triangularity, and βmax represents the maximum β obtainable from a certain family of profiles, and so is not at marginal stability everywhere. In both the above results, $\beta = 2\mu_o \langle p \rangle / B_o^2$ where B_o is the vacuum toroidal field at the geometric centre R_o.

Inspired by the differences between the two results; seeing that neither obeys the theoretical q^{-2} scaling; and wishing to compare with previous published results, we have undertaken our own series of optimisation calculations.

Optimisation method

We use the same procedure as Sykes & Turner (3). Equilibria are obtained by solving the Grad-Shafranov equation with the pressure and toroidal field terms p' and ff' being determined by spline fit to 11 nodal values. The $q(\psi)$ profile is determined by the initial choice of p'and ff' and is kept constant.

The procedure is as follows:- stability to high-n modes is found by solving the ballooning equation (5) around each flux surface. We increase

p_i' if the ith surface is stable, and decrease if unstable, adjusting ff' to maintain the original q-profile. The Grad-Shafranov equation is then re-solved. In this way we eventually converge to an equilibrium having the prescribed q-profile but being at marginal stability to high-n modes almost everywhere - since we insist on zero edge current (and hence $p' = 0$) we have positive stability there.

Most of the results given in the next section are produced by optimising to q profiles of the form given by $p' = \psi^{\alpha}$. However other forms have been used, in particular Gaussian profiles as used in (2) and polynomial functions as used in (1), with surprisingly little difference.

Note that this optimisation technique determines the appropriate value of β_J, which typically varies from 0.5 at high total current to 1.5 at low current. The optimised value is independent of the initial value.

Results

Fig. 1 gives results of the optimisations for circular plasmas at aspect ratios 4.5:1 and 3:1. In each case $q_o = 1.05$, and the total current is varied by altering α. β is shown plotted against $1/q_J$, where $q_J = 2B_o/(R_o J/\text{area})$. This re-definition of q_J (which coincides with q_s for large aspect ratio cylinders) was suggested to us by the strong dependance of the usual q_s on the proximity of separatrices and shaping of the inner plasma edge, whereas we expect ballooning modes to be more influenced by behaviour at the outside edge.

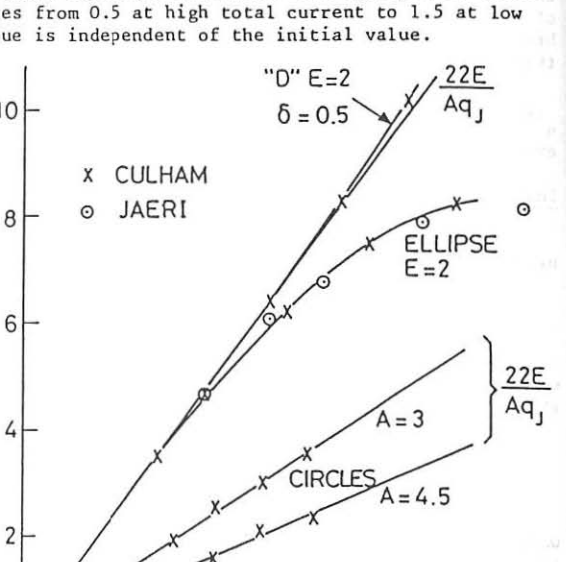

Fig. 1.

From these two optimised, marginally stable cases we derive the empirical formula

$$\beta_{opt} = \frac{22E}{Aq_J}, \text{ where } q_J = \frac{2B_o}{R_o J/\text{area}} \qquad [1]$$

After deriving this formula, it has come to our notice that Rutherford has given (6) a very similar expression as a "crude fit to a sequence of low q ideal MHD stability calculations". We are here demonstrating a more general application.

For an elliptical plasma of elongation E=2 at aspect ratio 3:1 we find

that at low current results are also well fitted by [1], but at higher curren the central flux surfaces become very elongated and the Mercier criterion is violated: this is evidenced in Fig. 1 by an ejection of pressure from the inner plasma, as we insist q_o = 1.05. Use of a strong D component (δ=0.5) satisfies the Mercier criterion and the formula continues to hold even for high current (Fig. (1)).

In Fig. 2 we replot the results of Sykes & Turner (3), which used an early model of the JET plasma shape having δ=0.168. We see a degradation from the linear case at high current. However we now repeat the work using the present JET plasma design shape having more triangularity (δ=0.24) and find that this is sufficient to avoid Mercier instability at the design current. The optimum β_J is also shown; note that this exceeds unity at the JET design current.

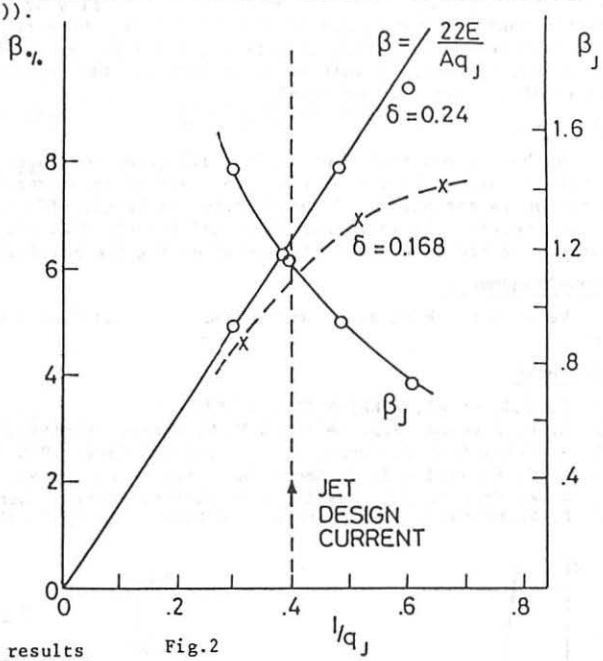

Fig.2

Comparison with other results

Since other results are usually quoted in terms of q_s we show in Fig. 3 the ratio of q_s/q_J at different aspect ratios for circles; 2:1 ellipses; and 1.8:1 D's of triangularity 0.5. Using these approximate relationships we can re-plot the results of Tuda et al (1) and Bernard et al (2) on β vs $1/q_J$ plots, finding that the βmax of Bernard et al lies below our βopt, as expecte whereas the βopt of Tuda et al has very similar values to our results, showin evidence of Mercier violation at higher currents (Fig. 1).

Good agreement is also obtained when comparing with the results given in (4). Bernard & Moore also included surface kink stability, and found that th optimum plasma shape had a strong D component, with q_s>3 being necessary for kink stability. After conversion to q_J using Fig. 3, our formula exceeds th β values given in (4) by 10% in each of the 4 cases - as we might expect due to our fuller optimisation.

Theoretical scaling

The theoretical result $\beta \sim 1/(Aq^2)$ might lead us to expect that halving the total current would quarter the β. In practice, however, we are moving from a $1 < q < 2$ equilibrium (say) to a $1 < q < 4$ equilibrium, which has more shear; and the compatibility of our linear global relationship with the theoretical quadratic one can be seen as follows. From the definition of β

and integrating by parts, we obtain

$$\beta = \frac{1}{R}\int r^2\alpha/q^2 dr, \text{ where } \alpha = -2Rq^2p'/B_o^2 \quad \text{(From (5))}.$$

Fig. 4 shows the results obtained by evaluating this expression using two simple approximations to the marginal stability s/α curve (Fig. 1 of (5); firstly taking α = 0.5; and secondly s = 1.7α, where shear s = rq'/q. In each case we use a typical q-profile $q = 1 + (q_s - 1)^3$. Each case yields an approximately linear result as q_s is varied. The result predicted by formula [1] is also shown (dashed line).

Conclusion

We have shown that βopt = 22E/(Aq_J) gives good agreement to computationa results of high-n limits over a wide range of parameters, provided the Mercie criterion is satisfied. Triangularity has little effect at low currents, but at high currents it increases shear and has the dual effect of raising q_s to improve surface kink stability and of easing the Mercier criterion.

Acknowledgements

We wish to thank J. A. Wesson and T. N. Todd for many helpful discussions.

References

(1) T. Tuda et al, JAERI-M 82-104 1982
(2) L. C. Bernard, F.J. Helton & R. W. Moore, submitted to Nuclear Fusion.
(3) A. Sykes & M. F. Turner et al Innsbruck Conf. 1978 IAEA-CN-37/K-S
(4) L. C. Bernard & R. W. Moore Phys. Rev. Lett. 46 No. 19 p1286 1981.
(5) J. W. Connor, R.J. Hastie, J.B. Taylor, Phys.Rev.Lett.40,No.6,p396,1978.
(6) P. Rutherford, U.S. contrib'n to INTOR. FED-INTOR 82-1 Atlanta Ga (1982)

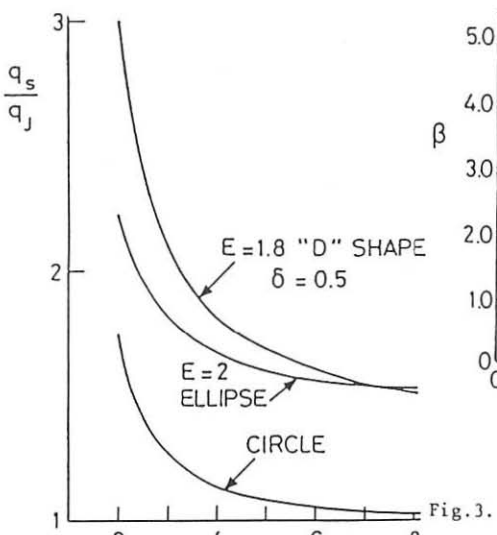

Fig.3.

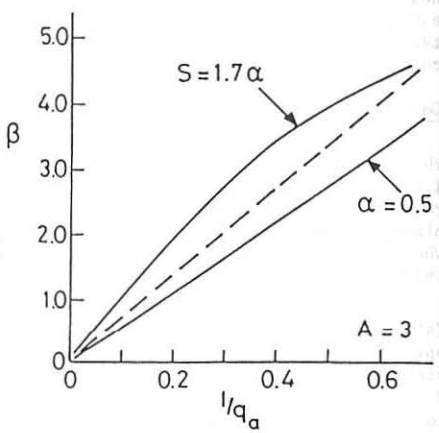

Fig.4.

Plasma-Wall Interaction, Divertors

O05

O06

O21

A32 - A42

B32 - B40

C25 - C36

BOLOMETER MEASUREMENTS OF THE ENERGY LOSSES IN THE GRAPHITE WALL TOKAMAK

E.J.Dobrokhotov, M.M.Dremin, Yu.D.Pavlov, D.P.Petrov,
A.M.Solntsev, A.M.Stefanovskij, A.L.Terebkov, A.F.Shcherbak
I.V.Kurchatov Institute of Atomic Energy,
Moscow, USSR

The studies of discharges within a graphite liner have been completed on the TM-G tokamak. The main goal of experiments was to find out the level of plasma contamination by the carbon ions resulting from a graphite sputtering and to study the effect of impurities on the discharge and plasma parameters. The sputtering coefficients for graphite, impurity transport within plasma, total radiation losses (charge-exchange included) and Z_{eff} of plasma were measured in accordance with the program.

Parameters of the studied regimes are given in Table I. All the measurements were done at the temperature of the graphite walls, $T_g = 350°C$, that was necessary for a hydrogen removal from the graphite walls after each discharge /1/.

A ratio P_r/P_{OH} is given in Fig.1a for a discharge with the plasma current of 40 kA at different average plasma densities. An average specific power released on the graphite wall is also given in the same Figure. It is obtained from the assumption of uniform (in poloidal and toroidal directions) energy deposition on the walls. The real local power of energy deposition can be 2-3 times higher. The dependence of the ratio P_r for other regimes is similar to the given one. The only difference is that the greater plasma density corresponds to the greater discharge current (see Fig.1 b) at the same ratio P_r/P_{OH}. The absolute radiation energy losses are determined only by the plasma density and do not practically depend on a plasma current. This property is more pronounced in Fig.2, where the total power of radiation losses is shown as a function of an average plasma density.

Measurements of C-II (4267 Å) line radiation intensity have shown that the influx of carbon atoms into plasma rises proportionally to the plasma density. Therefore, at high densities the main fraction of radiation losses is associated with the line radiation of carbon ions. The bolometric measurements, made when the graphite wall was irradiated by the pulsed laser beam and also when cold hydrogen was puffed into the plasma, show that the main part of radiation losses is produced by carbon ions with a low ionization state. The total radiation power is larger than the level determined from the corona equilibrium model by a factor of a few tens.

The rate of impurity spread within the plasma column was determined by measuring of a delay between the laser pulse and the additional line luminosity for the ions with different charge and intensity of soft X-rays. The delay was found to be 0.4 - 0.5 ms for the CV-line (2271 Å) and 1.4 - 1.6 ms for the intensity of SXR from the central region of the plasma column. As the region on intense luminosity of the CV line is localized at $r > 5$ - 6 cm, the rate of the "impurity wave" spread is approximately 10^4 cm/s at the plasma periphery and a little less near its axis. The confinement time for highly-ionized ions near the axis (determined from a decay of additional soft-X-ray intensity) is 1.5 - 2 ms, that corresponds to the diffusion coefficient, $(1 - 3) \cdot 10^3 cm^2$/sec. As it is known /2,3/, fast diffusion (or penetration) of the carbon ions towards the plasma column axis results in a steep rise of line radiation intensity and that of radiation losses from plasma, that

seems to have place in the TM-G plasma. The charge exchange between carbon ions and hydrogen atoms does not yield an appreciable contribution to the radiation losses.

The measurements of Z_{eff} were carried out in two regimes. In the first case (J_p = = 40 kA, n_e = 3 - 3.5 . 10^{13} cm^{-3}), the measurements were made at the impurity injection by a laser. The amplitude and time characteristics of additional pulses in the CV-line intensity and in the soft X-ray radiation were registered. From the C^{+4}- ion concentration (determined by the absolute intensity of the 2271 Å - line) from the decay of an additional pulse of this line (approximately equal to the ionization time for C^{+4}) and from the soft X-ray intensity decay (equal to the life time of highly-ionized ions of carbon), one can calculate an average concentration of the ions of carbon near the axis of the plasma column: $\langle n^{+5+6} \cdot v^{+5+6} \rangle \tau_p^{+5+6} \sim \langle n^{+4} v^{+4} \rangle \tau_i^{+4}$. The ratios of the quasi-constant pulse intensity to that of additional pulse in the soft X-rays and in the CV line give an opportunity of determining the factor of soft X-ray excess related to the bremsstrahlung and recombination of the ions of carbon. In accordance with these measurements, concentration of the ions of carbon near the axis equals to 10^{-2} of the plasma electron density and, hence, Z_{eff} (0) ~ 1.2 - 1.3.

In the second case (J_p = 60 kA, n_e = 6.7 . 10^{13} cm^{-3}), the bremsstrahlung radiation intensity from plasma in the visible range was found to correspond to Z_{eff} ~ 1.5 that seems to result from an increase of average charge of the carbon ions (due to a rise in the electron temperature), from an insignificant increase in the carbon flux from the walls (due to an increase in the plasma current) and from a possible weak rise in the life-time of carbon ions in plasma with a density increase.

Conclusion

In difference from the majority of tokamaks, the impurity influx into the TM-G plasma from the walls appreciably rises with an average plasma density rise that is explained by the characteristic property of the graphite sputtering. Some increase in this influx is also observed with a plasma current rise (or with a rise in the power of ohmic heating). In the discharges with the same currents, the correlation between the energy flux to the wall and the influx of impurities is absent. The impurity flux and the life time of impurities in plasma are such that Z_{eff} is found to be in a range Z_{eff} = 1 - 2 in all the regimes studied and the radiation losses are about 30 - 40%. All these results are obtained within the chamber of graphite at the temperature 350°C after long outgassing of graphite. Thus, the graphite as the material for the chamber walls in the research tokamak is not a barrier for obtaining the discharges with low q and Z_{eff}, low level of radiation losses and with rather high time of energy confinement in plasma.

References

/1/ E.J.Dobrokhotov et al. JAEA, Baltimore, USA, 1982, R-6.
/2/ D.E.Roberts. Nucl. Fus., v.21 (1981), 215.
/3/ R.J.Hawryluk et al. Nucl. Fus., v.19 (1979), 607.

Plasma and discharge parameters

Table I.

J_p кА	20	40	60	80
$\overline{j_p}$, А/см^2	105	210	315	420
q	3	3($q_{min} \leq 2$)	3	3
B_T, Т	0,8	1,6	2,4	3,2
$\overline{n_e}\cdot 10^{13}$ см$^{-3}$	1 ÷ 4,5	1,5 ÷ 8	2 ÷ 9,5	(2,5÷10–13)
V_o, V	1,7÷2,6	1,4÷2,7	1,2÷2,4	1,7÷2,2,
$\overline{W_v}$, Вт/см^3	0,9	1,4	2,7	3
$\overline{W_s}$, Вт/см^2	3,2	5,1	9,5	11
P_r/P_{OH}, %	7 ÷ 32	5 ÷ 35	5 ÷ 38	6 ÷ 40
$\tau_{\varepsilon max}$, мс	0,9	1,9	3,5	
Z_{eff}		1,2÷1,4	1,5	

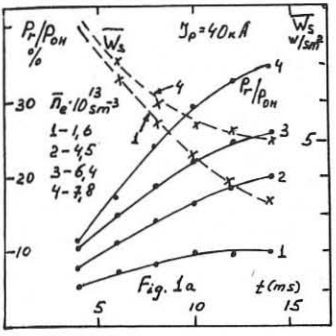

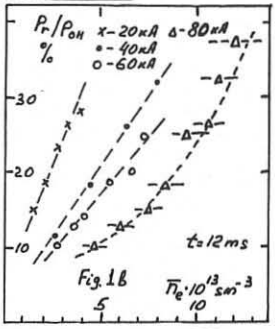

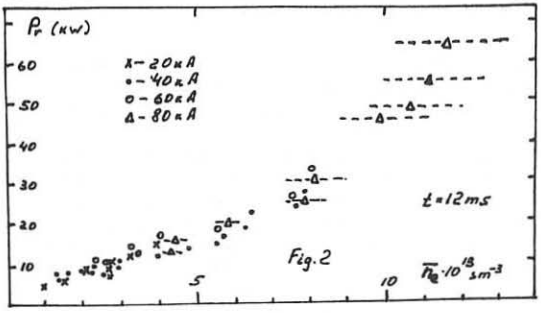

IMPURITY RETAINMENT IN THE DIVERTOR OF ASDEX

G. Fussmann, K. Behringer, K. Bernhardi, G. Haas, W. Poschenrieder, B. Richter, Z. Szymanski[+] and A. Eberhagen, O. Gehre, J. Gernhardt, G. v. Gierke, E. Glock, F. Karger, M. Keilhacker, S. Kissel[++], O. Klüber, M. Kornherr, G.G. Lister, G. Lisitano, H.-M. Mayer, K. McCormick, D. Meisel, E.R. Müller, H. Murmann, H. Niedermeyer, H. Rapp, B. Scherzer, F. Schneider, G. Siller, P. Smeulders, F. Söldner, E. Speth, A. Stäbler, P. Staib, G. Staudenmaier, K. Steinmetz, K.-H. Steuer, E. Taglauer, O. Vollmer, G. Venus, F. Wagner
Max-Planck-Institut für Plasmaphysik, EURATOM-Association, D-8046 Garching

Abstract. The retainment and exhaust capability of the ASDEX divertor for neon and argon is studied and compared with limiter discharges. No significant influence of the scrape-off plasma on the divertor impurity outfluxes is observed. The fluxes, however, show a strong top-bottom asymmetry reversing with the direction of the toroidal field.

Introduction. An important characteristic of a divertor is its efficiency for retaining impurities. In this respect, impurities with high probability for readsorption, e.g. metal vapour or highly active gases are to be distinguished from gases with low adsorption, e.g. rare gases. In case of the latter kind - on which we are concentrating in here - the divertor retainment efficiency is characterized by a divertor containment time τ_D. In terms of this quantity the flux out of the divertor is given by $\phi_D = N_D/\tau_D$, where N_D is the number of particles in the divertor. Under stationary conditions (without external pumping) this flux is balanced by a corresponding flux of ions $\phi_p = N_p/\tau_p$ leaving the plasma, with τ_p being the particle confinement time in the plasma. The exhaust efficiency of the divertor, defined as the ratio of number of particles in the divertor and the plasma, is thus given by $N_D/N_p = \tau_D/\tau_p$. Whereas τ_p is known to be of the order 5-20 ms for light and medium impurities in ASDEX /1/, no experimental information existed until recently on τ_D. From Monte Carlo code calculations /2/ as well as 1D scrape-off modelling /3/ a very high retainment efficiency was expected (at least for the ohmic case where thermal forces are negligibly small) because of the high streaming velocity of the background plasma towards the neutralizer plates.

In case that impurities are not ionized in the divertor throat the divertor confinement is determined purely by geometry; the corresponding vacuum time constant $\tau_{D,vac}$ should impose a lower limit on τ_D.

Retainment of gaseous impurities. The retainment of gaseous impurities is studied by injecting short puffs ($\Delta t \sim 6$ ms) of neon or argon either into the plasma chamber, or the upper or lower divertor chambers. In addition single and double null configurations are realized. The number of injected atoms is typically 5×10^{17}, i.e. approximately 1 % of the plasma particles. Most of the experiments were performed in ohmic discharges with narrow divertor slits ($d_s = 3.5$ cm) but in some cases neutral injection heating has been applied during and after the gas puff. The impurity density in the plasma is obtained

[+] On leave from Institute of Fundamental Technological Research, Warsaw, Poland
[++] On leave from Massachusetts Institute of Technology, Cambridge, USA

from absolute spectroscopy measurements whereas the partial pressures in the divertor- and plasma-chambers are measured by means of mass spectrometers.

It is found that in any of the nine possible combinations of gas inlet and divertor configuration a quasi-stationary state is reached after a few 100ms. During this phase only 3 % of the injected particles (neon) are found in the plasma. Consistent with this approximately 100 % of the particles are detected initially in the divertor chambers. The volume outside of the plasma in the plasma chamber is observed to be effectively "pumped" by the plasma. In the single null configurations the concentration in the plasma is typically twice as large as in the double null case. An assessment of particle balance during and after the discharge shows a deficiency of about 20 % of the initially injected particles, which is obviously due to implantation of high energy ions ($T_i \gtrsim 20$ eV) in the neutralizer plates.

From transport calculations as well as experiments under limiter conditions we get a particle confinement time of ~10 ms for neon. Multiplying this value with the measured ratio of N_D/N_p a divertor confinement time of τ_D = 150-300 ms is obtained which is close to the vacuum time constant $\tau_{D,\,vac}(Ne)$ = 150 ms in contrast to expectations.

A more direct measurement of τ_D is possible in the double null configuration by puffing gas into the top chamber and measuring the pressure built up in the bottom chamber, or vice versa. Furthermore, a direct comparison with $\tau_{D,vac}$ is possible by shifting the plasma to the single null configuration and puffing into the non-activated divertor chamber. From such measurements the agreement between τ_D and $\tau_{D,vac}$ can be proved in case of neon for various plasma parameters (I_p = 300 - 380 kA, $n_e = 1.8 - 4 \times 10^{13}$ cm^{-3}) during the ohmic phase. The same measurements are also performed for argon (the ionization energy of which is markedly reduced compared to neon; 21.6 eV and 15.8 eV), where in addition the influence of neutral injection is investigated. Results are presented in Fig. 1 where normalized partial pressure signals are plotted as a function of time after gas puffing (t = 0.8 s; time constant of mass-spectrometer 160 ms, curve 1). Also in this case the rise times do not differ by more than a factor of two. However, with neutral injection (P_{NI} = 1.6 MW, Δt = 0.4 s, curve 2) τ_D is found to be even smaller than $\tau_{D,vac}$ (curve 3).

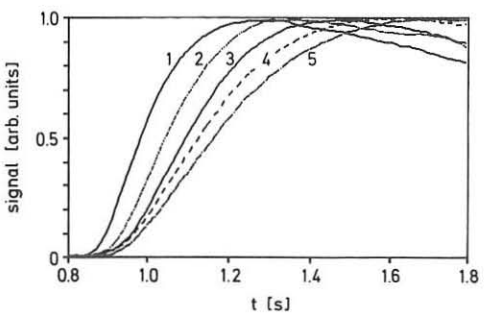

Fig. 1:
Normalized signals of Ar-pressure increase in bottom divertor in case of Ar-injection into plasma chamber (1) or top divertor (2-5) for various scenarios: single null (3), double null with N.I. (2), OH-phase (4), OH-phase with divertor slits enlarged (5)

After widening the divertor throats preliminary results show an increase in τ_D (curve 5), quite opposed to assumptions. Furthermore a significant dependence on plasma density (τ_D increasing with n_e) now requires more investigations.

The small influence of the plasma scrape-off on the impurity outflux of the divertor is difficult to explain. Thus, according to Langmuir probe measurements close to the neutralizer plates /4/, lower limits of the electron temperature and density within the divertor slits are estimated to $T_e \sim 20$ eV, yielding ionization lengths of 1.7 cm and 0.2 cm for neon and argon, respectively, so that in particular in case of Ar the divertor throats should be opaque for neutrals.

The exhaust efficiency of the divertor is also checked by comparison with limiter discharges. For this purpose equal amounts of neon are puffed into the plasma chamber using first a carbon mushroom limiter (without separatrix) and thereafter realising the double null configuration. The spectroscopic traces of NeX and Ne VIII-lines are shown in Fig. 2 for the two cases. Both signals yield an intensity ratio of ~4.5. Since the plasma parameters differ only slightly in the two discharges (divertor: $n_e = 1.9 \times 10^{13}$ cm^{-3}, $T_{eo} = 1.20$keV; limiter; $n_e = 2.1 \times 10^{13}$ cm^{-3}, $T_{eo} = 1.25$ keV) this ratio reflects directly the ratio of the impurities. Although this comparison demonstrates the divertor exhaust, the effect is much less than expected. Obviously, also in the limiter case only a fraction of ~15 % of the injected particles are found in the plasma. The majority is supposedly implanted into the limiter within a time interval ~10 ms (Fig. 2) since the recycling rate in a limiter discharge is much higher than in a divertor discharge; thereafter a recycling equilibrium is established. This assumption is supported by the observation of a successive increase of neon from shot to shot.

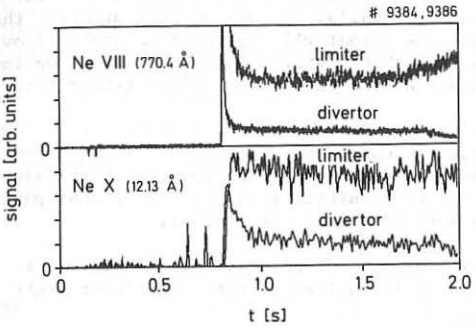

Fig.2:
Ne VIII- and Ne X-line intensities versus time for a limiter and a divertor discharge (equal neon puffs at t = 0.8 - 0.804 s into plasma chamber).

Up-down asymmetries in particle fluxes. When comparing the partial pressures in the upper and lower divertor chambers with a simple dynamic divertor model it becomes obvious that there is an asymmetry in the impurity fluxes leaving the plasma. The up-down ratios in the partial pressures are typically 1.5 in case of neon but rise up to ~5 for argon. Moreover, it is observed that the asymmetry changes sign when reversing the direction of the toroidal magnetic field. An example is shown in Fig. 3 where Ar is puffed into the plasma chamber. Neutral injection (N.I.) is applied in both cases, too, but seems to have no influence (Fig. 3). A vertical displacement of the plasma column, which could cause the asymmetry, can be excluded within an accuracy of $|\Delta Z| \leq 0.2$ cm from magnetic position measurements as well as n_e-interferometer measurements at $Z = \pm a/2$ (minor plasma radius a = 40 cm).

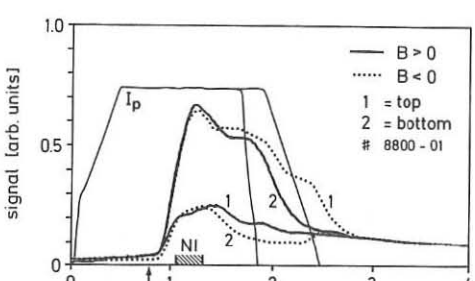

Fig. 3:
Ar-pressure signals from top and bottom divertor demonstrating inversion of top-bottom asymmetry when changing sign of toroidal magnetic field. Ar-puff at t=0.8s. The plasma currents (300 kA) are also shown as a function of time.

Summary. The retainment capability of the divertor is quantitatively associated with the molecular flow conductance of the narrow divertor throats. Accordingly, no pronounced reduction of impurity recycling by the counter-streaming plasma can be proved, though, ionization of neutrals within the divertor throats is most likely. With divertor throats widened up, however, preliminary results show a marked improvement in retainment with increasing electron density.

A possible explanation for such unexpected small influence of the scrape-off plasma may be due to cross diffusion of low Z-ions in the divertor throat and subsequent neutralization at the throat walls. Because of this process, the flow of particles penetrating into the throat will approach molecular flow conditions especially with decreasing throat width. This suggests an optimum width for divertor throats and also the use of aperture slits rather than long ducts.

The exhaust capability of the divertor could be demonstrated by injection of neon into similar limiter and divertor discharges. In comparing both cases, however, attention must be paid to the possibility that a significant portion of the injected particles may be implanted into the limiter.

A strong asymmetry, which changes sign with TF-polarity, is found in the impurity fluxes into the divertor. It is indicated that this effect might originate from high ionic charges.

References

/1/ Behringer, K. et al., "Production and Transport of Impurities in the ASDEX Tokamak Plasma", this conference.
/2/ Schneider, W., Heifetz, D., Lackner, K., Neuhauser, J., Post, D. and K.G. Rauh, "Modelling of the ASDEX Scrape-off and Divertor", Symposium on Energy Removal and Particle Control in Toroidal Fusion Devices, July 1983, Princeton.
/3/ Neuhauser, J., Schneider, W., Wunderlich, R. and K. Lackner "Modelling of Impurity Flow in the Tokamak Scrape-off Layer, IPP 1/216 (April 1983).
/4/ Shimomura,Y., et al., Nucl. Fus. 23/7 (1983).

PLASMA FLOW IN A DIVERTOR WITH STRONG RECYCLING

A.V.Nedospasov, M.Z.Tokar'

Institute of High Temperatures of the USSR Academy of Sciences, Moscow, USSR

Neutral particles, born during neutralization of charged particles on collector plates, strongly influence on a tokamak divertor plasma. Ionization of atoms by electrons and charge-exchange of them with ions result in that plasma flux on the plates substantially exceeds that across separatrix. Additionally the neutrals, passing the plasma layer without ionization and entering a pumped volume, have some probability to return back into the plasma. Repeated participation of the neutral particles, before their pumping out, in acts of interaction with charged particles constitutes entiry of strong recycling.

Recently it has been shown theoretically /1/ and experimentally /2/ that with strong recycling the plasma flow velocity along magnetic field far from the plates may be small in comparison with the ion sound that $V_s = \sqrt{2T/m_i}$, to which the plasma is accelerated immediately near the plate.

In present paper it's shown, that the plasma flow in the divertor may have a highly intricate pattern.Thus near the surface beween the plasma and a gas in the pumped volume it's possible the existence of the plasma flow from the divertor back to the main part of scrape-off zone.

Geometry under consideration is represented in Fig.1. With small angles between the plate plane and the magnetic field the neutral particle behaviour in the plasma is described by one-dimensional kynetic equation:

$$v_x \frac{\partial f_a}{\partial x} = -(k_i + k_{ex}) n f_a + k_{ex} n_a f_i \qquad (1)$$

where f_a, f_i are the velocity distribution functions, n_a, n - are the densities of the atoms and ions, respectively; k_i k_{ex} are the ionization and charge-exchange constants. To simplify calculation we assume that the neutral component is presented only by the charge-exchanged atoms with the plasma temperature. It's naturally because the path length of the neutrals, entering the plasma from the plates and the pumped chamber, is smaller than that of charge-exchanged atoms. Thus one may consider the plasma layer boundaries as a single source of the neutral with the plasma temperature. The ion distribution function is treated as two-velocity one: $f_i = \frac{n}{2}[\delta(v_x - v_i) + \delta(v_x + v_i)]$, where $v_i = \sqrt{\frac{2T}{\pi m_i}}$.

The boundary conditions for Eq.(1) are following. It's assumed

a full recycling at the plates, that is the atom influx in the plasma equals the ion flux on the plate. At the plasma-gas boundary ($x = \delta$) we define a recycling efficiency, which equals the probability w for the neutrals, entering the pumped chamber, return back to the plasma. w value may be evaluated as follows. The plasma steady state is supportered by volume pumping of molecules, born during surface and volume recombination of the atoms. The probability for molecule to hit the plasma equals ratio of chaotic flux $n_m V_m S_e/4$ through the surface AB to it's sum with the outflux into pumps - $n_m \dot{V}$. Here n_m, v_m are the density and mean velocity of molecules, S_e is AB surface area. If ξ is probability of molecule transformation in charge-exchanged atom (through dissociation and charge-exchange of Franck-Condon atoms) one may obtain for w : $w = 1/(1 + \frac{4\dot{V}}{V_m \cdot S_e \xi})$.

The plasma is treated as quasineutral and isothermal. With reasonable dimensions of the divertor and the plasma transport coefficients we may neglect transports of the charged particles and heat by the plasma across the magnetic field and take into account only longitudinal those. In this case equations of hydrodynamics have a form:

$$\sin\psi \frac{\partial n V_\parallel}{\partial y} = K_i n n_0 \qquad (2)$$

$$\sin\psi \frac{\partial (n V_\parallel^2 + n V_s^2)}{\partial y} = K_i n n_0 V_\parallel \qquad (3)$$

$$\sin\psi \frac{\partial q_\parallel}{\partial y} = -K n n_0 \left(I - \frac{3}{2} T\right) \qquad (4)$$

where $q_\parallel = 5n V_\parallel T - \varkappa_\parallel \sin\psi \frac{\partial T}{\partial y}$, ψ is pitch angle between y=0 plane and the magnetic field, I is ionization "price" of atoms with accounting of excitation.

The integral fluxes of particles and heat into the divertor are defined:

$$2\pi R \cdot \sin\psi \int_0^{\delta} \frac{q_\parallel}{n V_\parallel}\Big|_{y=0} dx = \frac{Q_0}{J_0} \qquad (5)$$

It's adopted at the plate that $V_\parallel = V_s$, $q_\parallel = \gamma\, n V_\parallel T$. The solution of Eqs.(2),(3), obtained in Ref./1/, has shown, that the plasma density is weakly changed in the divertor along the magnetic field. It's also just for the plasma temperature, which is smoothed by electron heat conduction. Therefore at first approximation during solving of Eqs.(1),(2),(4) it's assumed that the plasma parameters are invariable in the divertor. Eq.(1) has an analytic solution within framework os formulated approximations. Introduction of expression, obtained for the neutral density n_a, in Eq.(2) and it's integration with using of Eq.(5) give the profile of the plasma velocity $V_\parallel$ at

$y = 0$;

$$V_{\parallel} = \frac{J_0 \sigma}{2\pi R}\left[\frac{e^{-\alpha s}}{1-e^{-\alpha}} + \frac{2W}{1-W}\frac{\beta}{1+\sqrt{\beta}}\, e^{-\alpha/2}\, sh\left\{\alpha\left(\frac{1}{2}-s\right)\right\}\right] \qquad (6)$$

where $\beta = \frac{K_i}{K_i + K_{ex}}$, $\sigma = \sqrt{\beta}\,(K_i + K_{ex})$, $\alpha = \sigma n \delta$, $s = x/\delta$.

The plasma temperature and "optical" thickness, characterizing the divertor plasma state, are determined by the heat and particle balances, obtained with integration in Eq.(5) /3/.

As example let's consider a tokamak-reactor of INTOR scale: $R = 5{,}5$ m, $\Psi = 10°$, $\dot{V} = 2\cdot10^5$ l/S, $J_0 = 2\cdot10^{22} S^{-1}$, $Q_0 = 50$ MW, $S_e = 20$ m^2, $\gamma = 8$, $\xi = 0{,}7$. Numerical analysis gives the divertor operation regime with plasma parameters: $\alpha = 4$, $T = 25$ eV. The profile of longitudinal velocity is represented in Fig.2. In the main part of the plasma layer $V_{\parallel}$ is much less than V_s, excepting narrow regions near the plate and the plasma-gas boundary, whose dimensions are order of the neutral path length. There is layer with the plasma flow from the divertor near the plasma-gas boundary. Ionization of neutrals, coming from the pumped volume, is reason of such a layer formation. Resulting rise of presure gradient forces the plasma to flow both to the plate and out of the divertor chamber. In this case the plasma leaves the scrape-off layer in the region of the neutral path length wide far from the plasma-gas surface. The atoms, born during the plasma neutralization on the plate, diffuse into the pumped chamber near the plate, participating in processes of ionization and charge-exchange.

REFERENCES

/1/ Nedospasov, A.V., Tokar, M.Z.: in Controlled Fusion and Plasma Physics (Proc. 10th Europ. Conf. Moscow, 1981), Vol.1, Moscow (1981) G-10.

/2/ Post D.E., Heifetz J., Petravic M.: Models for Poloidal Divertors (Rep. Plasma Phys. Lab. Princeton Univ.) PPPL-1913, 1982 (July).

/3/ Nedospasov, A.V., Tokar, M.Z.: The role of recycling in a tokamak-reactor divertor (Soviet-Americal Workshop on High temperature Plasma-Wall Ie teraction) Princeton, 1982 (August).

Fig.1. Divertor geometry under consideration.

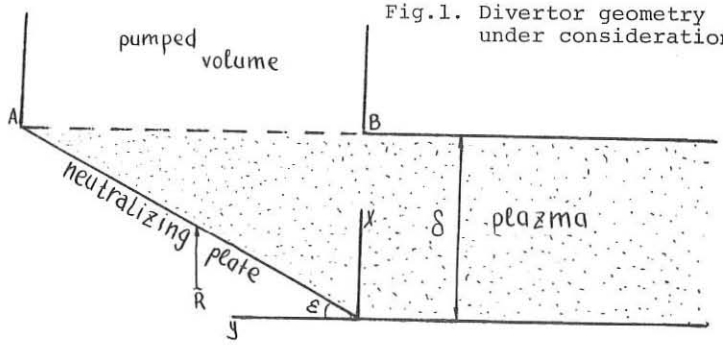

Fig.1. Divertor geometry under consideration.

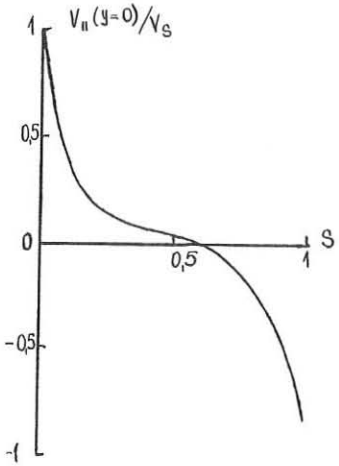

Fig.2. Profile of longitudinal velocity of plasma at the divertor throat (y=o).

Experiments on plasmainduced arcs

H. Krüger, K. Rödiger, V. Schulz, A. Stampa
Universität Essen - GHS, 4300 Essen 1, Germany F.R.

A. Introduction

One possible configuration, which results, when a hot plasma gets into contact with a metallic wall is the unipolar arc. This discharge phenomenon arises in the plasma-wall region without the application of an external voltage, the necessary emf. being supplied by the sheath mechanism. For the conception of future fusion devices it is of great interest to know the conditions for which unipolar arcs can arise spontaneously. At present such criteria are not known. The existing models /1-3/ explain the main features of the mechanism but do not say anything about the initiation process. The model of Robson and Thonemann leads to necessary conditions for the sustainment of an arc.

The experimental results are frequently not conclusive as in general the exact state of the plasma and the wall is not sufficiently well known. Simulation experiments by Höthker et al. /4/ performed at a small high frequency discharge indicated that the necessary conditions of Robson and Thonemann may also be sufficient for the prediction of arcing. Since such a behaviour would have severe consequences for a future fusion reactor, it is important to clarify, whether the results are significant for a tokamak. In the present paper we therefore report on experiments similar to those performed by Höthker but with somewhat improved plasma conditions. We especially took care to reduce gradients and to avoid erratic voltages. Additionally we obtained information on the current distribution in the surrounding of a cathode spot.

B. Experiment

A schematic diagram of the apparatus is shown in fig. 1. The plasma is produced in a pulsed high frequency discharge and heated by combined ohmic and fast wave heating. It expands thermically along a magnetic guiding field (B = 50 mT) into a vacuum tank. In order to have a sufficiently high temperature and density outside the discharge-section the power of the high frequency pulse is rather high (2 MW). The plasma-wall experiments are performed in the guiding section. Here the electron temperature, measured by Thomson scattering is 5 - 25 eV, typically 15 eV, and the electron density decreases from $10^{14}cm^{-3}$ in the discharge section to $10^{13}cm^{-3}$ at the end of the guiding section. Aside from a short heating phase the plasma parameters stay constant during the discharge (1 ms).

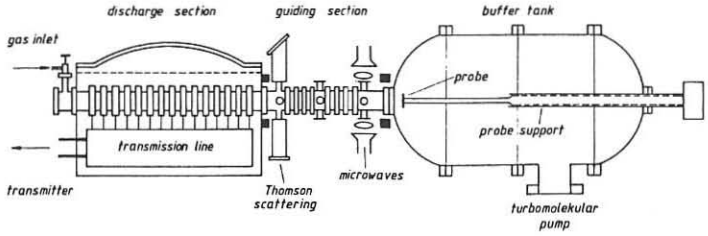

Fig. 1: Schematic diagram of the plasma source.

Wall probes were smoothed, polished and finally cleaned chemically. They were introduced into the plasma by isolated supports. The probes were provided with a small auxiliary electrode connected with the main probe via a resistance. The voltage across the resistance was measured using optical signal transmission. Two types of probes were applied: high resistance probes ($R > 20\,\Omega$) for the electrical registration of arc events and low resistance probes ($R = 0.2\,\Omega$) for current measurements. The arc ignition could be locally predetermined

by choosing a suitable electrode material or by attaching a microcontamination to the wall. The arcs were most easily ignited on stainless steel or cadmium, while it was difficult to obtain arcing on clean copper surfaces. The arc current was measured with the cathode spot moving on the auxiliary electrode, while the current distribution was obtained igniting the spot on the main probe in some distance from the small electrode and applying a magnetic field parallel to the wall. The spot then performes a rectilinear motion in the negative jxB direction ("retrograde") and the auxiliary electrode picks up a signal proportional to the current distribution. All probes were investigated optically, in some cases by electron microscopy, after an arc event had occurred.

C. Results

Arcing was produced without the application of an external voltage. All arcs which led to an electrical signal could also be detected by their erosion tracks. A single arc burning on a wall probe of stainless steel in a magnetic field parallel to the surface caused a straight erosion trace 0.3 - 1 mm broad and 5 - 20 mm long. In some cases the trace split into two or three branches. By comparing the length of the trace and the duration of the electrical signal (typically 150 µs) a mean velocity of $3 - 30 \cdot 10^3$ cm/s was obtained. This velocity is quite well in the range reported from observations at vacuum arcs. The motion followed always the -jxB direction. The trace consisted typically of 4000 circular craters with diameters of 2 - 6 µm and a mean distance of 45 µm. The surface around the large craters was covered by a small-scale erosion, which consisted of craters 0.1 - 0.3 µm in diameter, and irregular structures of melting relicts. This type of erosion was rather dense at the starting point of the arc, whereas at the end of the trace it was faint. The erosion structure seems to be identical to that one reported for arcing in tokamaks /5/, if one considers that large craters (30 - 50 µm) are not to be expected, since they are typical for extremely clear surfaces.

The experiments with low resistance probes show that the arc is formed by current loops, which close in a narrow region around the spot. This is the most direct proof that the observed arcs are unipolar. The arc current is 5 - 40 A, typically 11 A and has a constant density over the wall at least up to a distance of 1.5 cm from the cathode spot. Arcing could be completely prohibited by plasma cleaning of the wall. From this observation it is clear that also for unipolar arcs the ignition conditions are essential for their prediction.

References

/1/ A.E. ROBSON and P.C. THONEMANN
Proc. Phys. Sic. 73 (1959) 508

/2/ E. HANTZSCHE
Beitr. Plasmaphys. 20 (1980) 329

/3/ G. ECKER, K.-U. RIEMANN and CH. WIECKERT
Beitr. Plasmaphys. 22 (1982) 463

/4/ K. HÖTHKER, W. BIEGER, H. HARTWIG, E. HINTZ and K. KOITZLIK
J. Nucl. Materials 94/95 (1980)

/5/ J.D. DATLOV, A.E. GUILE, B. JÜTTNER
Beitr. Plasmaphys. 21 (1981) 135

INVESTIGATION OF ELECTRIC ARCS IN THE DIVERTOR OF THE TOKAMAK EXPERIMENT ASDEX

K. Ertl, R. Behrisch, ASDEX-Team and PWW-Team
Max-Planck-Institut für Plasmaphysik, EURATOM Association,
D-8046 Garching b. München, FRG

B. Jüttner
Akademie der Wissenschaften der DDR, Zentralinstitut
für Elektronenphysik, 1086 Berlin, GDR

1. INTRODUCTION

Traces of unipolar arcs have been frequently found at wall probes and the limiters of tokamaks /1-3/, where the most intense contact between plasma and surfaces occurs. With divertor devices the plasma-wall interaction is highest at the divertor plates and a theoretical study for INTOR resulted in predictions of considerable surface erosion in the divertor chamber by arcing /4/. In order to test this assumption, and to study the properties of arcs in dependence on plasma conditions, arcing probes and Langmuir probes have been exposed simultaneously in front of the divertor plates of ASDEX.

2. EXPERIMENTAL

The probes were rectangular plates of Ta, Mo and graphite with a surface area of 1.5 cm^2 mounted on shielded holders (Fig. 1). They were arranged to a couple - one of them being the arcing probe (AP), the other the Langmuir probe (LP) - which was positioned within the upper divertor chamber by means of a drive mechanism. The probe surfaces were adjusted parallel to the outer divertor plate, at a distance of about 2 cm.

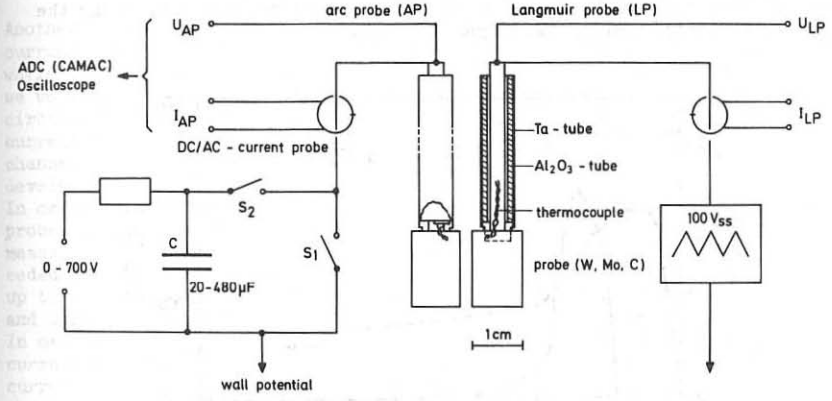

Fig. 1: Schematic of the experimental setup

A sawtooth voltage V_{LP} with adjustable frequency and a peak-to-peak amplitude of 100 V was applied to the Langmuir probe. The arcing probe was at liner potential (switch 1 closed) or it was biased with a voltage U_{AP} from the capacitor C (20 µF) by closing the electronic switch S_2 at a preselected time during the tokamak discharge (switch S_1 open). The voltages were measured by potential leads, the currents by DC/AC-current probes (Hall sensors and Rogowski-coils). The evaluation of U_{LP} and I_{LP} yielded density and temperature of the plasma near the probes, the oscillograms of U_{AP} and I_{AP} gave information about the electrical characteristics of the arcs.

3. RESULTS AND DISCUSSION

In contrast to the experience with limiter tokamaks /5, 6/, unipolar arcs did not occur in the start-up phase of the divertor tokamak ASDEX. Also in the later stages of the discharge arcs were absent unless there were disruptions or instabilities in connection with neutral beam heating. Arcs were frequently observed at the end of such tokamak pulses where the plasma density sharply decreased.
The absence of arcs during the start up phase and the stable plateau can be understood by the ignition as well as the existence conditions for arcs. During the exposure to the plasma the probes were strongly heated resulting in a relatively clean surface. Such surfaces have shown low ignition probabilities /7/. After an ignition the plasma parameters were not favourable for sustaining the arc, as demonstrated below.
The burning voltage of an arc could be deduced by using a biased probe. Figure 2 shows current and voltage for such a probe. The arc starts about 50 µs after application of the bias voltage of 200 V. After extinction of the arc the voltage supplied by the capacitor is still of the order of 100 V representing the burning voltage at this moment. This burning voltage is much higher than for arcs without a magnetic field being of the order of 15 to 20 V. This high voltage can be explained by the voltage drop along the arc column constricted by the magnetic field.

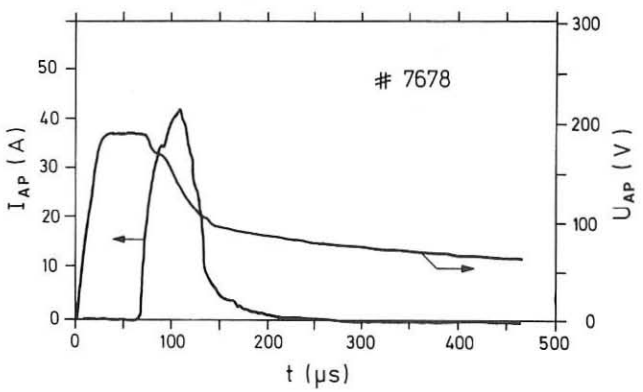

Fig. 2: Oscillogram of current and voltage of an arc with a biased probe

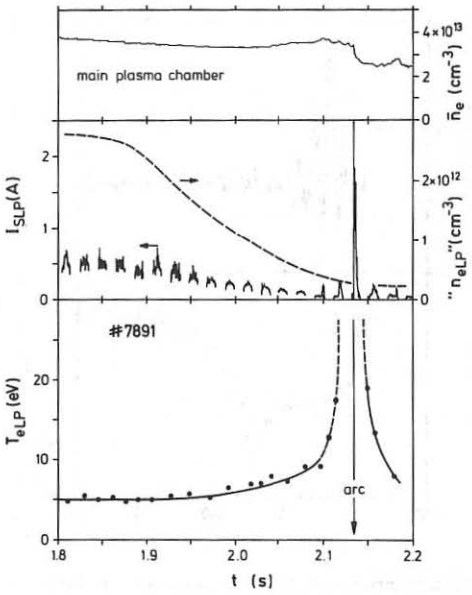

Fig.3: Plasma density in the main chamber (top), ion saturation current extracted from the Langmuir characteristic and deduced plasma density (middle part), electron temperature (bottom) during a unipolar arc at the arcing probe.

Another interesting observation shown in Fig. 2 is the temporal behaviour of current and voltage: They are out of phase, the current is still increasing while the voltage decreases. In order to explain this by a self-inductance, we would need a value of about 20 µH, which cannot be due to the outer circuit. This means that with 100 V the plasma system does not allow current rates in excess of 5×10^6 A/s. It is also possible that the arc channel (which must be rather long) needs considerable time for its development.

In order to determine the burning conditions of a spontaneous arc with the probe at wall potential the electron temperature and plasma density were measured during the arc with the Langmuir probe (Fig. 3). The arc is preceded by an increase of the electron temperature from values around 7 eV up to more than 20 eV. This could provide the necessary voltage for igniting and sustaining the arc.

In many cases the arcs were preceded by a diffuse discharge with limited current (maximum about 5 A). This discharge increases the ion saturation current at the Langmuir probe as demonstrated in Fig.4: About 25 µs before the start of the arc current the ion current at the Langmuir probe shows a sudden increase. With biased probes we found many pre-discharges that did not result in an arc. In these cases the surface was diffusely eroded, without many craters. From the involved area we get a current density of about 10^8 A/m^2, whereas the arcs showed 10^{11} - 10^{12} A/m^2. These features correspond to a transient glow discharge.

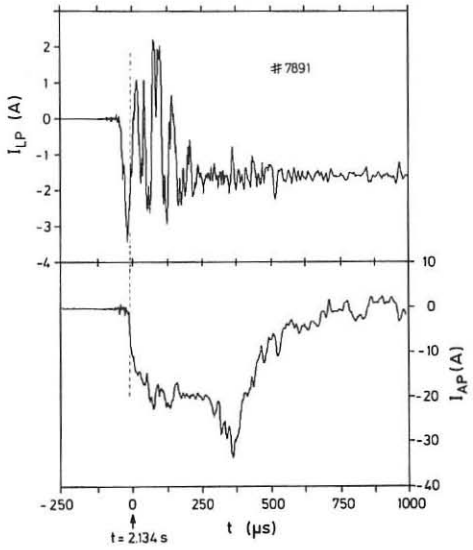

Fig.4: Ion saturation current at the Langmuir probe (top) and arc current at the arc probe (bottom), indicating a pre-discharge prior to the arc

4. CONCLUSIONS

The existence of plasma sustained arcs was found to require a higher potential difference between plasma and surface than concluded from simulation experiments without magnetic field /8/. A further restriction for the unipolar arcs is the limitation of the current rise rate, because the arc spot processes need a quick response. Therefore unipolar arcs are rare events for the normal plasma parameters in the ASDEX divertor chamber with electron temperatures around 10 eV /9/.
More frequent are diffuse discharges with currents and current densities below those of the normal vacuum arcs. They may be more important for the surface erosion.

5. REFERENCES

/1/ Staib,P., Staudenmaier,G., J.Nucl.Mater. 63, 1976, 37
/2/ McCracken,G.M., Goodall,D.H.J., Nucl.Fusion 18, 1978, 537
/3/ Hildebrand,D., Laux,M., Lingertat,J., Pech,P., Reiner,H.-D., Strusny,H., Wolff,H., Beiträge Plasmaphysik 20, 1980, 313
/4/ Nedospasov,A.V., Petrov,V.G., Teplofizika Vysokh.Temp.20, 1982, 201
/5/ McCracken,G.M., J.Nucl.Mater. 93/94, 1980, 3
/6/ Mioduszewski,P., Clausing,R.E., Heatherly,L., J.Nucl.Mater.91,1980,297
/7/ Jakubka,K., Jüttner,B., J.Nucl.Mater.102, 1981, 259
/8/ Höthker,K., Bieger,W.B., Hartwig,H., Hintz,E., Koitzlik,K., J.Nucl.Mater. 93/94, 1980, 785
/9/ Shimomura,Y., Keilhacker,M., Lackner,K., Murmann,M., Siller,G., IPP Report III/80, December 1982.

SIMULATION OF ASDEX DIVERTOR ACTION USING A REALISTIC NEUTRAL GAS MODEL

D. Heifetz*), K. Lackner, K.G. Rauh, W. Schneider
Max-Planck-Institut für Plasmaphysik, EURATOM Association,
D-8046 Garching, Germany.

Simulations of the plasma flow and the energy transport in the scrape-off layer of the ASDEX tokamak have been previously carried out using the one-dimensional, 2-fluid code SOLID /1/ to describe the parameter variation along the magnetic field lines. These calculations showed the existence of strong gradients in density and temperature between the midplane and the target plate vicinity, and three different regimes of divertor recycling also identifyable in experiments. The quantitative validity of these calculations was limited, however, by the use of a strongly simplified neutral gas model. For the present calculations the elaborate Monte-Carlo model DEGAS /2/ for two-dimensional dynamics of neutral molecules and atoms in the divertor chamber has been combined with the above fluid description of the plasma, where DEGAS now provides for all significant atomic reactions as well as for a realistic 2-dimensional divertor geometry (Fig.1).

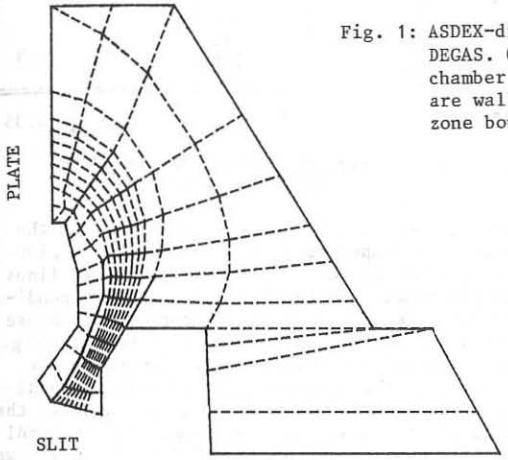

Fig. 1: ASDEX-divertor geometry used in DEGAS. Only the outer divertor chamber is modelled. Solid lines are walls, dashed lines are plasma zone boundaries.

The scrape-off plasma and the neutrals in the divertor chamber are strongly interdependent. A coherent description therefore requires the simultaneous treatment of the plasma flow and heat-conduction along the magnetic field lines onto the divertor plates and the atomic processes arising from the neutral molecules and atoms in contact with the plasma and the walls. In a preliminary version the fluid code and the Monte-Carlo code are not yet directly coupled, but are run one after the other. First the plasma profiles, i.e. the plasma density and temperatures, together with the reaction and energy transfer rates along the field lines are computed by SOLID with a simplified neutral gas model prescribing the spatial neutral particle distribution.

*)Plasma Physics Lab., Princeton University, Princeton, N.J. 08544, USA

Then the plasma parameters are transferred to DEGAS to calculate improved neutral particle profiles and atomic reaction data. By iterating this procedure, we get already qualitatively consistent solutions. A particular example is discussed below in detail:

For a given particle- and energy flux of $.1 \times 10^{22}$ 1/s and .75 MW into one divertor chamber the results of the fluid calculation are shown in Fig. 2 (n_e and T_e, T_i along the field lines within the divertor chamber, corresponding to the distance s from midplane of 10 to 15 m). The thickness of the scrape-off region was assumed to be 2 cm; for the confinement time of the neutrals in the divertor chamber 20 msec was taken. The electron density in the vicinity of the target plates is about a factor of two higher than at the divertor entrance and outside the divertor. The temperatures decrease from T_e = 45 eV, T_i = 70 eV at midplane to T_e = 40 eV, T_i = 45 eV at the divertor throat and finally to T_e = 25 eV, T_i = 10 eV near the target plates.

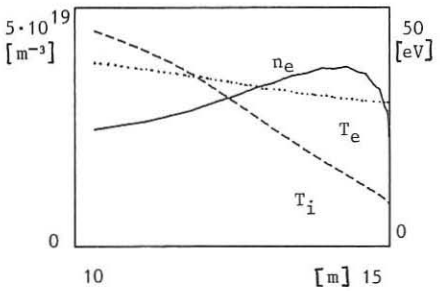

Fig. 2: Plasma profiles // B

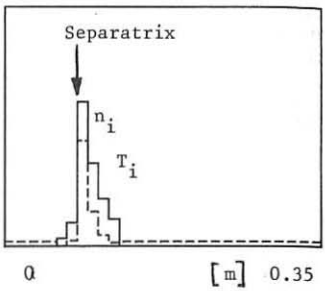

Fig. 3: Plasma profiles ⊥ B (same units as Fig. 2)

The 2-D Monte-Carlo neutral particle code DEGAS requires as input from the fluid model the plasma density and the temperatures in the divertor region and the recycling flux onto the divertor plate. Parallel to the field lines the plasma profiles can be directly taken from the SOLID results. Perpendicular to the field lines, where SOLID assumes a constant profile, we choose an asymmetric exponentially decreasing density and temperature profile (Fig.3) in accordance with experimental findings /3/ (outward decay length of the density in front of the plate: 3 cm, of the temperature: 1.5 cm). Perpendicular to the magnetic field the distance x is measured from the inner to the outer divertor wall; the profiles are taken at $s \approx 13$ m. Equal line integral densities were assumed for normalization. Gettering at the divertor walls was adjusted in order to obtain a neutral gas confinement time of 20 ms.

The neutral hydrogen densities parallel to the field lines calculated by DEGAS agree reasonably well in absolute size and shape with the profiles used in SOLID (Fig.4 ; DEGAS: solid curve, SOLID: dotted curve). The DEGAS results especially show three distinguishable regions of behaviour: in a region immediately in front of the divertor plate a part of the neutral flux originating from the plate is quickly ionized and the density decreases rapidly. Then in a plateau region the density is fairly constant. The neutrals in this region primarily arise from the dissociation of molecular hydrogen, which has a nearly constant density outside the plasma channel. Inside the divertor slits the density decreases further because the slit walls shield the plasma from the influx of molecular hydrogen. The profiles perpendicular to the field lines

confirm these conclusions. In the plateau region (Fig.5) the maximum of the neutral atom density (solid line) occurs at the outward side of the scrape-off plasma where the neutral molecules are dissociated. The molecular density (dashed line) is nearly constant in regions without plasma and about an order of magnitude larger than the atomic density. Its absolute number of $5 \cdot 10^{18}$ m^{-3} is comparable to ASDEX measurements with similar plasma conditions /3/. The neutral hydrogen temperature along s calculated by DEGAS is nearly constant (Fig. 6), thus being in reasonable agreement with the constant value of 10 eV used in SOLID.

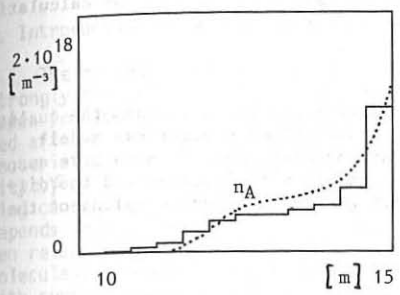

Fig. 4: Neutral atom density // B

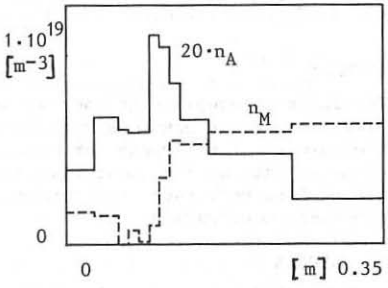

Fig. 5: Neutral densities ⊥ B

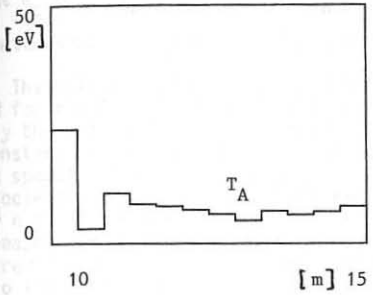

Fig. 6: Neutral atom temperature // B

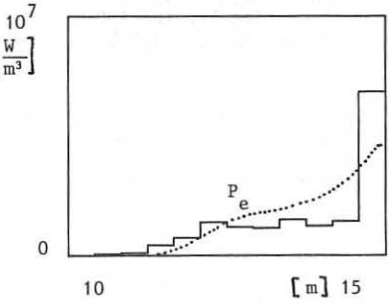

Fig. 7: Electron power loss // B

Besides the primary quantities like particle density and temperature, the dissociation-, ionization- and CX-rates together with the associated power loss densities from the electrons and ions are calculated. The agreement between the profiles along s calculated by DEGAS and the corresponding quantities used in SOLID is rather good. The total power loss density from the electrons is plotted in Fig. 7 for the two calculations (DEGAS: solid line, SOLID: dotted line). The total power loss from the electrons is .120 MW (radiative: .04 MW, ionization: .06 MW, dissociation: .03 MW). The total power loss from the ion channel (CX losses) is comparatively small: .01 MW. The comparison of this quantity was not quite as satisfactory as for the electrons. This is partly due to the fact that near the target plates the difference between the temperatures of the ions and the neutral atoms can be small and

may even change sign forming a local energy sink or source, respectively.

Starting from this example, a variation of the input particle flux, which should be a monotonic function of the averaged electron density in the bulk plasma, verified the same general features as reported in /1/.

An important quantity with respect to experimental measurements is the neutral gas divertor time constant which is defined as the ratio of the total neutral particle content in the divertor and the neutral particle outflux through the divertor slit. Considering the outer divertor chamber only, we obtain τ_{vac} = 25 msec in the absence of plasma; with plasma, the calculation yields τ_{div} = 150 msec, i.e. the plasma nearly plugs the slits.

SUMMARY

The indirect coupling of the two codes SOLID and DEGAS has shown the qualitative validity of previous results using a simplified neutral gas model. The results of the Monte-Carlo code DEGAS, however, provide much more quantitative information about the neutral particle distributions and the different loss processes. For further investigations a direct coupling of the two codes is necessary.

REFERENCES

/1/ R. Chodura et al., Plasma Phys. and Contr. Nucl. Fus. Res. 1982, IAEA 1983, Vol.1, 313

/2/ D. Heifetz et al., Journal of Computational Physics, Vol. 46(2), May 1982, p. 309

/3/ M. Keilhacker and ASDEX-team, IAEA Conf., Baltimore 1982, paper IAEA-CN-41/R-2

In Situ Measurement of the Hydrogen Recycling Constant of the TEXTOR Liner

P. Wienhold, F. Waelbroeck, J. Winter, E. Rota, T. Banno

Institut für Plasmaphysik Kernforschungsanlage Jülich GmbH, 5170 Jülich, FRG, Association EURATOM/KFA

1. Introduction

The hydrogen recycling from the tokamak walls and limiters influences strongly the particle balance during plasma discharges. Hydrogen which escapes in atomic form from the plasma and penetrates into the wall is reemitted after a certain time delay as molecules back into the vessel. The characteristic time for this release, $\tau_L = D/2\sigma k_r \alpha\varphi$, depends on the flux density $\alpha\varphi$ of the hydrogen penetrating into the wall as well as on the recycling constant $R_c = D/2\sigma k_r$. The diffusion constant D, a bulk property, depends only on the wall temperature whereas the rate constant for the hydrogen release $2\sigma k_r$ (σ = roughness, k_r = rate constant for recombination into molecules) depends on the state of the surface which can change considerably with surface conditioning. An in situ determination of R_c is therefore necessary.

In the following, the method of the determination of the recycling constant R_c of the TEXTOR liner is described and first results are presented.

2. Determination of the recycling constant of the TEXTOR liner

The method has been developed in a simulation experiment /1/ and was used for the first time in a tokamak in TEXTOR /2/. Fig. 1 shows schematically the principle of the measurement. Hydrogen molecules are let in at a constant rate E leading to a stationary gas density $n_0 = E/Sp$ (Sp = pumping speed). After the beginning of the discharge part of this hydrogen is dissociated and pumped into the liner at the flux density $\alpha\varphi$. The gas density $n_2(t)$ drops thereby abruptly and the subsurface concentration $c_0(t)$ increases progressively with time since hydrogen diffuses into the bulk. The reemission rate $v_r(t) = 2\sigma k_r c_0^2(t)$ increases, and $n_2(t)$ returns gradually to its former value n_0 (wall pumping and release effect). At later times the hydrogen flux into and out of the liner are almost equal. The liner acts as a simple "bypass" in the gas throughflow. The termination of the discharge in this situation ($\alpha\varphi = o$) is equivalent to the switch off of a "loss" term. It causes a jump of n_2 up to a higher value. The progressive release from the wall decreases c_0 and the rate v_r; $n_2(t)$ returns to the initial value n_0 (lower part of the figure).

The expected evolution of $n_2(t)$ (dashed lines), proportional to $v_r(t)$ $-\alpha\varphi$, can be simulated by use of the computer code PERI /3/ which takes into account the previous history of the liner. The fitting procedure is made taking into account the characteristic pump time τ_p of TEXTOR. This leads to a curve as indicated by the full line. We vary the quantity $D/2\sigma k_r$ until a fit between computer and experimental curves is obtained. This yields the recycling time τ_L and, if $\alpha\varphi$ is known, the recycling constant R_c; τ_L is the time after which the backflow rate of particles from the sur-

face reaches one half of the penetrating flux density; $\alpha\varphi$ is obtained from the analysis of the initial part of the curve up to the extremum.

3. Experimental results and discussion

The wall pumping and release effect in TEXTOR has been analysed during the wall conditioning phase in march 1983. Some results are presented and discussed in the following. A pressure gauge was situated laterally in one of the pump ports. An initial pressure of $\approx 2 \times 10^{-3}$ mbar was used. An RG-discharge (radiofrequency assisted glow discharge) was activated (current density $j \approx 9$ µA cm^{-2} to liner) and switched off after several minutes or hours. Typically, flux densities $\alpha\varphi \approx 10^{14}$ cm^{-2}s^{-1} and pressure changes $\Delta p \approx 5 \times 10^{-5}$ mbar have been observed. As an example fig. 2a shows the observed pressure increase Δp (thin line) after turning off an RG-discharge ($\alpha\varphi = 9.4 \times 10^{13}$ cm^{-2}s^{-1}, duration 1h). At this time (3.3.83) the liner was still contaminated with oxygen. Its temperature was T = 160 °C. Even after

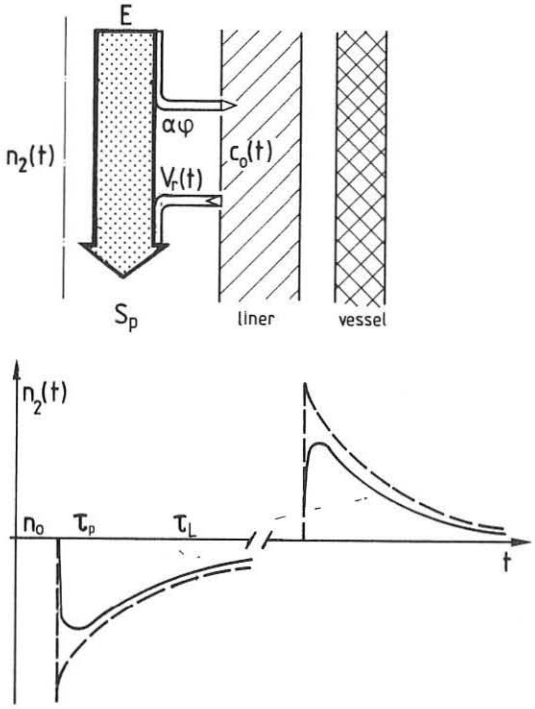

Fig. 1. Scheme of hydrogen gas flow through TEXTOR (upper part). When a discharge is switched on ($\alpha\varphi > 0$) or off ($\alpha\varphi = 0$) the molecular density $n_2(t)$ changes (bottom left and right with the characteristic time τ_L (see text)

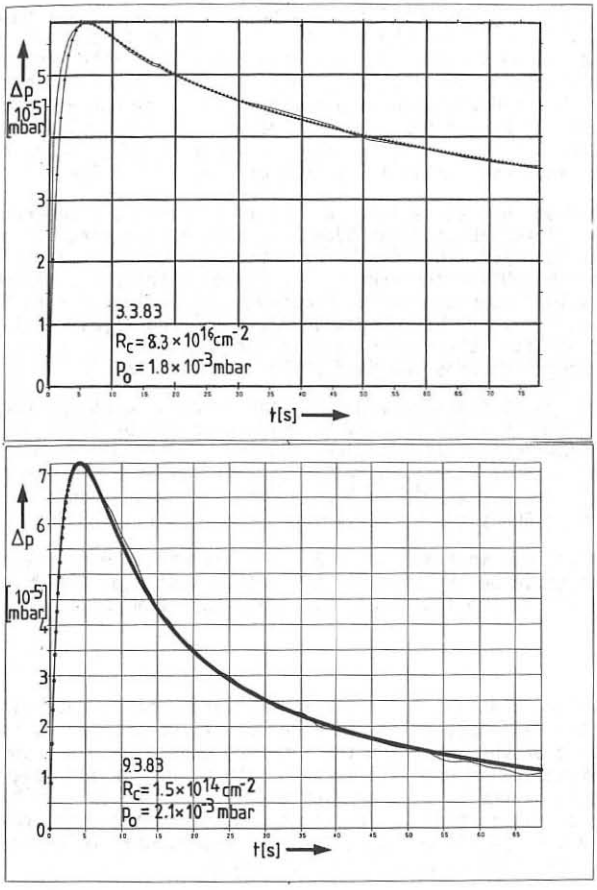

Fig. 2 Pressure increases Δ p with time (thin lines) after turning off a RG-discharge. The curves have been fitted by use of the PERI code with R_c = 8.3 x 10^{16} cm^{-2} (triangles) and 1.5 x 10^{14} cm^{-2} (circles). a) 3.3.83: after cleaning of the liner (T_L = 150 °C), carbidic carbon was deposited on its surface.

60 s Δ p has about 65 % of its maximum value 5.8 x 10^{-5} mbar. The curve has been fitted with PERI (triangles) using R_c = 8.3 x 10^{16} cm^{-2}. The uncertainty in the fit is about ± 10 % in R_c. Under such conditions the response time in a typical plasma discharge in TEXTOR ($\propto \varphi \approx$ 2 x 10^{16} $cm^{-2}s^{-1}$) would be about 8 s and therefore the time for reaching particle balance considerably longer than the duration of the discharge itself (2 - 3 s).

Baking of the liner up to 300 °C and few days RG-cleaning caused a decrease of the recycling constant by about one order of magnitude. Further

application of RG-cleaning until the 9.3.83 lowered the recycling constant to $R_c = 2.3 \times 10^{15}$ cm^{-2} (not shown here). Under these circumstances, the characteristic hydrogen recycling time would be 115 ms after the start of a plasma discharge. For the limiters, this time is further reduced according to the higher hydrogen flux impinging there. During the cleaning period the removal of oxygen has been observed by RGA and by AES of a liner sample /5/. Correlated to this, the release constant σk_r for hydrogen out of the surface increases until it is free of reducible oxides.

Starting from this state, liner and limiters have been covered with a carbidic carbon layer (about 20 at %) deposited by RG-discharge in an H_2 - CH_4 (0.85%) mixture /6/. The drastic effect of the surface change can be seen from fig. 2b: 60 s after turning off the discharge, the maximum value of $\Delta p = 7.2 \times 10^{-5}$ mbar is already reduced to 10%. In order to fit the measured curve, R_c had to be reduced to 1.5×10^{14} cm^{-2} (circles). This means that 8 ms after the beginning of a plasma discharge the release rate v_r of hydrogen reaches one half of the rate penetrating into the liner.

The following RG cleaning and decontamination brought the recycling constant back to $R_c = 1.4 \times 10^{15}$ cm^{-2}. This value can be taken as representative for a "RG-cleaned" TEXTOR liner. At the end of this conditioning phase (24.3.83) and of that of june 82, similar values have been found: $R_c = 1.2 \times 10^{15}$ and 2.0×10^{15} cm^{-2} respectively. Measurements in the laboratory on inconel 600 yield $R_c = 7.8 \times 10^{14}$ cm^{-2} at T = 150 °C.

Characteristic pump times $\tau_p = 2 - 3$ s have also been determined from the fits which could be expected for the vacuum system of TEXTOR. Its ratio of volume (17 m^3) to the installed pump speed (3 x 2 m^3/h) was of the same order.

Summary

The recycling constant R_c of the TEXTOR liner can be determined in situ by use of the wall pumping and release effect. RG-discharges used for the conditioning of the liner and the limiters generate an appropriate test plasma. Contamination of the wall surface with oxygen or its coverage with carbidic carbon changes R_c by orders of magnitude (from 10^{17} cm^{-2}) and herewith the characteristic time τ_r for the hydrogen release after the start of a tokamak discharge (from 8 s to 8 ms). A representative value for a "cleaned" TEXTOR-liner is $R_c \approx 1.5 \times 10^{15}$ cm^{-2}.

Literature

/1/ F. Waelbroeck, J. Winter, P. Wienhold, J. Nucl. Mat. 103&104(1981)471
/2/ E. Rota, Thesis, Univ. Düsseldorf, FRG
/3/ P. Wienhold, M. Profant, F. Waelbroeck, J. Winter, JÜL-1825, Jan. 1983
/4/ F. Waelbroeck, J. Winter, P. Wienhold, L. Könen, T. Banno, L. Grobusch, E. Rota, K.H. Tschersich, R.E. Clausing, TEXTOR team, IX. Int. Vacuum Congress, V. Int. Conf. on Solid Surfaces, Madrid, 26.9. - 1.10.83
/5/ R.E. Clausing, K.G. Tschersich, H.P. Fleischhauer, L. Heatherly, F. Waelbroeck, J. Winter, P. Wienhold, J. Sakamoto, S. Ishii, K. Yano, 3rd Top. Meeting on Fusion Reactor Materials, Albuquerque, Sept. 19-22, 1983, USA
/6/ J. Winter, F. Waelbroeck, P. Wienhold, G. Esser, L. Könen, T. Banno, E.Rota, paper 208, this conference
/7/ E. Rota, F. Waelbroeck, P. Wienhold, J. Winter, J. Nucl. Mat. 111& 112 (1982) 233

TWO-DIMENSIONAL CALCULATIONS OF NEAR-WALL PLASMA DYNAMICS FOR A TOKAMAK WITH A POLOIDAL DIVERTOR

Yu.L.Igitkhanov, A.S.Kukushkin, A.Yu.Pigarov,
V.I.Pistunovich
I.V.Kurchatov Institute of Atomic Energy,
Moscow, USSR

The scrape-off calculations /1/ have been shown that the distribution of parameters within the layer depends on the nature of the boundary conditions at the divertor entrance. These conditions are determined by the behaviour of the plasma within the divertor, which, in turn, was studied separately /2,3/.

In the present paper, a selfconsistent description of the scrape-off layer together with the divertor volume is developed for the first time. The geometrical model used in computations is illustrated in Fig.1. This geometry, in contrast with the previous papers, provides the natural boundary conditions: fluxes of heat and particles are preset at the separatrix, not at the divertor entrance. In this case, the problem becomes essentially a two dimensional one. Plasma entering the scrape-off diffuses towards the wall and spreads along the magnetic field lines, passing through the divertor volume and recombining at the divertor plate. Recycling of neutrals within the divertor volume increases the plasma flow towards the plate. The plasma spread along the field and the diffusion across it are described by the two-dimensional hydrodynamic equations:

$$\frac{\partial}{\partial s} n v_s = \frac{\partial}{\partial x}\left(D_\perp \frac{\partial n}{\partial x}\right) + S_o \qquad (1)$$

$$\frac{\partial}{\partial s} n\left(m v_s^2 + T_e + T_i\right) = \frac{\partial}{\partial x}\left(m v_s D_\perp \frac{\partial n}{\partial x}\right) + \frac{\partial}{\partial s}\left(mn\eta_i \frac{\partial v_s}{\partial s}\right) + P_o \qquad (2)$$

$$\frac{\partial}{\partial s}\left(\frac{5}{2} T_i + \frac{m v_s^2}{2}\right) n v_s - \chi_i^{\parallel} \frac{\partial T_i}{\partial s} = -v_s \frac{\partial n T_e}{\partial s} + \frac{\partial}{\partial x}\left(\frac{5}{2} T_i + \frac{m v_s^2}{2}\right) D_\perp \frac{\partial n}{\partial x} - \chi_i^{\perp} \frac{\partial T_i}{\partial x} + Q_{ei} + Q_{oi} \qquad (3)$$

$$\frac{\partial}{\partial s}\left(\frac{5}{2} T_e n v_s - \chi_e^{\parallel} \frac{\partial T_e}{\partial s}\right) = v_s \frac{\partial n T_e}{\partial s} + \frac{\partial}{\partial x}\left(\frac{5}{2} T_e D_\perp \frac{\partial n}{\partial x} - \chi_e^{\parallel} \frac{\partial T_e}{\partial x}\right) - Q_{ei} + Q_{oe} \qquad (4)$$

where S_o, P_o, Q_{oi}, Q_{oe} are sources and sinks due to the plasma interaction with neutral atoms; η_i is the longitudinal viscosity; Q_{ei} describes the electron-ion coupling due to Coulomb collisions. The terms $v_s \partial n T_e / \partial s$ represent the work of the electric field.

Conditions at plasma boundaries were choosen as follows:

separatrix (QD)

$$-D_\perp \frac{\partial n}{\partial x} = \Phi_s / S, \qquad m v_s D_\perp \frac{\partial n}{\partial x} = 0 \qquad (5)$$

$$-\left(\frac{5}{2} T_i + \frac{m v_s^2}{2}\right) D_\perp \frac{\partial n}{\partial x} - \chi_i^{\perp} \frac{\partial T_i}{\partial x} = W_s^i / S \qquad (6)$$

$$-\frac{5}{2} T_e D_\perp \frac{\partial n}{\partial x} - \chi_e^{\perp} \frac{\partial T_e}{\partial x} = W_s^e / S \qquad (7)$$

plate (KC)

$$\left(\frac{5}{2} T_i + \frac{m v_s^2}{2}\right) n v_s - \chi_i^{\parallel} \frac{\partial T_i}{\partial s} = f_i n v_s T_i \qquad (8)$$

$$\frac{5}{2}T_e n v_s - \chi_e^{\parallel}\frac{\partial T_e}{\partial s} = f_e n v_s T_e \qquad (9)$$

$$P_i + P_e - \eta_i \partial v_s/\partial s = 0, \quad v_s \leqslant c_s \qquad (10)$$

wall

(GK, AC) $\quad T_i = T_e = n = 0 \qquad (11)$

symmetry plane

(AQ, DG) $\quad v_s = \frac{\partial T_i}{\partial s} = \frac{\partial T_e}{\partial s} = 0$

Here Φ_s, $W_s^{i,e}$, S are the total plasma flow, the power flows through the separatrix and the separatrix area, respectively; f_i=3.5, f_e= 6. In the present paper, the neutral gas is described using a simple diffusion model. A value of the recycling coefficient, R = $= 1 - \Phi_s/\Phi_d$, is preset as a boundary condition for neutrals (Φ_d is the plasma flow towards the divertor plate). Distribution of neutrals leaving the plate is considered to be uniform across it. The set of 2-d equations together with the boundary conditions given above is solved numerically with a implicit Eulerian alternative-direction algorithm.

The calculations have been done for the ASDEX parameters /4/; 80 % of the power (W_s= 2.5 MW) deposited in the plasma enter the scrape-off. The particle flow from the main plasma, $\Phi_s = 10^{22}$ 1/s. The Bohm's coefficients were used for the transversal transport and the longitudinal one was assumed to be classical. The dependence of the peak plasma density and electron temperature near the divertor plate on both the recycling coefficient R and Φ_s are given in Figs.2,3. It is seen that with an increase in both the incoming flow and the recycling, the plasma density, n_d, rises nonlinearly, and the temperature, T_{ed}, drops down to <7 eV. At R> 90 %, considerable longitudinal gradients of plasma density and temperatures are formed, the longitudinal energy transport being provided mainly by the electron heat conduction. The steady-state regimes obtained with a dense ($n_d > 10^{14}$ cm^{-3}), cold ($T_{ed} < 10$ eV) plasma within the divertor are characterized by a subsonic plasma flow. This can be explained by a finite ion viscosity and by a momentum loss due to the collisions with neutrals.

Electron temperature, T_{ed}, vs density, n_d, near the plate at a fixed power entering the scrape-off is given in Fig.4. The solid curve is obtained in calculations with varying either the flow Φ_s or the recycling R. The experimental points from ASDEX /4/ are presented ibid. In Fig.5, the computed cross profiles of density and temperature near the divertor plate are plotted together with experimental points /4/.

The comparison between the calculations and the ASDEX results shows that the 2-d transport model developed for the scrape-off layer together with the divertor profiles has a reasonable quantitative and qualitative agreement with the experimental data.

References

/1/ Igitkhanov Yu.L., Kukushkin A.S., Pistunovich V.L., in : Plasma Phys. and Contr. Nucl. Fus. Res., 1980, v.2, p.575 IAEA, Vienna, 1981.

/2/ Igitkhanov Yu.L., in: USSR contributions to the Phase IIA of the INTOR workshop, v.1, p.VI-72, Moscow, 1982.

/3/ Petravic M., Heifetz P., Post D. et al. 9th Int.Conf. on Plasma and Contr. Nuclear Fus. Research, Baltimore, USA; 1-8 Sept; 1982, IAEA-CN-41/O-3-2.

/4/ Shimomura Y., Keilhaker M. et al. IPP III680. Dec.1982.

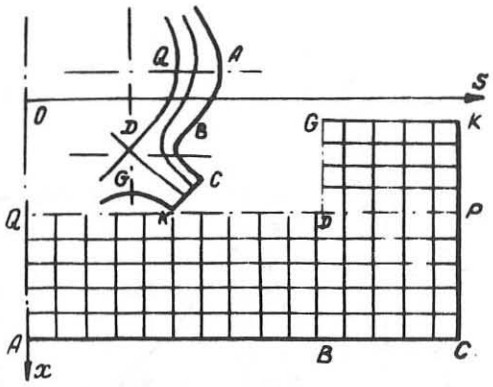

Fig.1 The geometrical model of the scrape-off layer (AQDB) and of the divertor (DGKCB). BD=4cm; AB=8m; BC=4m (along field line), KP=4cm.

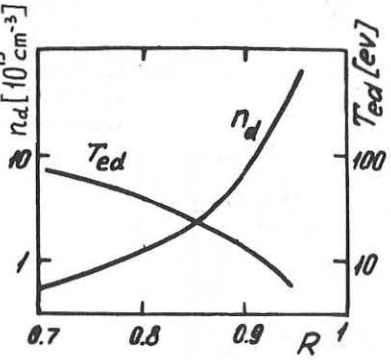

Fig.2 Peak plasma density n_d and electron temperature T_{ed} near the plate vs recycling coefficient R. W_s=2.5 MW, $\Phi_s = 10^{22} s^{-1}$.

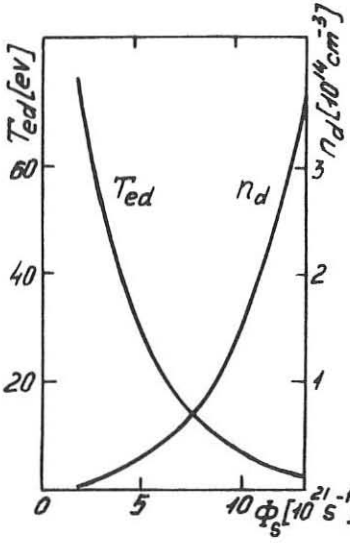

Fig.3 n_d, T_{ed} vs Φ_s.
W_s = 2,5 MW, R=93%.

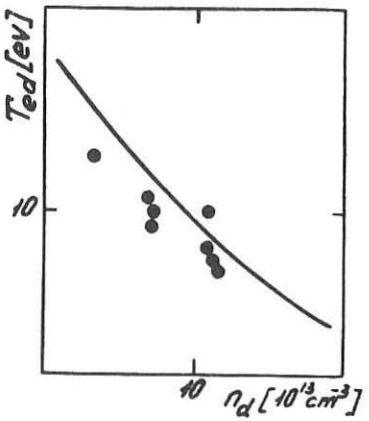

Fig.4 T_{ed} vs n_d for the fixed power W_s=2.5 MW. The black circles correspond to the ASDEX data.

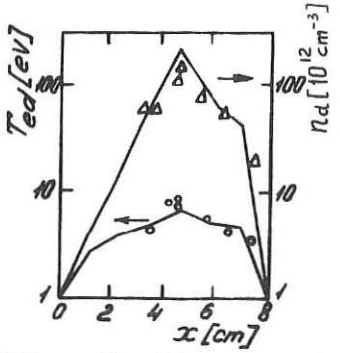

Fig.5 Cross profiles of electron temperature and plasma density near the plate. ASDEX data (see /4/, Fig.5 (1)) are plotted as circles and triangles.

THE CHARACTERISTICS OF STATIONARY PLASMA FLOW IN THE TOKAMAK SCRAPE-OFF LAYER

V.G. Petrov

Institute of High Temperatures of the USSR Academy of Sciences, Moscow, USSR

Abstract. Plasma parameters in the scrape-off layer of a toroidal limiter are calculated on the base of hydrodynamic equations. The characteristic dimension of the change in the plasma density proves to be close to the mean ion Larmor radius calculated with poloidal magnetic field.

1. The interest for the toroidal tokamak limiter is due to less tense temperature conditions. For definiteness assume that a metal limiter is placed on the inner torus equator, the toroidal electric field induced coincides in direction with the external magnetic field. The limiter height is much less than the minor tokamak radius. Toroidal corrections are not essential in the present consideration. Thus one can use rectangular Cartesian co-ordinates, the x co-ordinate is directed along the minor radius, the z co-ordinate is directed along the magnetic field, the y co-ordinate is perpendicular to ox and oz to form a right-handed co-ordinate system. The y,z co-ordinates originate in the upper lateral side of the limiter and are directed to the lower side of it across the plasma. The angle between magnetic field lines and the limiter sides is equal to a/qR (a, R are the minor and major tokamak radius, respectively, q is the safety factor). With $(a/qR)^2 \ll 1$ the width of the scrape-off layer in the y direction is practically equal to $2\pi a$. Owing to simmetry along the torus

$$\frac{\partial}{\partial z} = \frac{a}{qR}\frac{\partial}{\partial y} \tag{1}$$

The plasma in the scrape-off layer is supposed to be transparent for neutrals, the ion and electron temperatures are supposed to be equal and constant.

2. The following equations are used:

$$\frac{\partial}{\partial y}\left(nV_y + \frac{a}{qR}nV_z\right) + \frac{\partial}{\partial x}nV_x = 0 \tag{2}$$

$$\frac{\partial}{\partial y}\left(j_y + \frac{a}{qR}j_z\right) + \frac{\partial}{\partial x}j_x = 0 \tag{3}$$

$$\frac{\partial}{\partial y}\left(nV_y\bar{V} + \frac{a}{qR}nV_z\bar{V}\right) + \frac{\partial}{\partial x}\left(nV_x\bar{V}\right) = -2\frac{T}{M}\nabla n + \frac{\bar{j}\times\bar{B}}{Mc} \tag{4}$$

$$\frac{\bar{j}}{\sigma} = -\nabla\varphi + \bar{E} + \frac{\bar{V}\times\bar{B}}{c} + T\frac{\nabla n}{en} - \frac{\bar{j}\times\bar{B}}{enc} \qquad (5)$$

Here n, T are the plasma concentration and temperature, respectively, j is the current density, M is the ion mass, B is the magnetic field, σ is the plasma conductivity, φ is the electric potential, E is the toroidal electric field induced. The velocity components V_x and V_y are the drift velocities. With projecting Eq.(4) on the xy plane the left hand part of Eq.(4) can be neglected.

Introducing the expression for j_x from Eq.(4) into Eq.(3) and integrating Eqs.(2) and (3) over y one can obtain, respectively

$$-\frac{\partial}{\partial x}\left(\int_0^{2\pi a} n V_x\, dy\right) = n_+ V_+ - n_- V_- \qquad (6)$$

$$-\frac{\partial}{\partial x}\left(\int_0^{2\pi a} j_x\, dy\right) = 2\frac{cT}{B}\frac{\partial}{\partial x}(n_+ - n_-) = en_+V_+\left(1 - e^{-\frac{e\varphi_+}{T}}\right) - en_-V_-\left(1 - e^{-\frac{e\varphi_-}{T}}\right) \qquad (7)$$

Here V_-, V_+ are the ion velocity components normal to the lateral limiter surfaces at the upper and lower limiter side, respectively. $V_+ = -V_- = \frac{a}{qR}V_i$ ($V_i = \sqrt{\frac{2T}{M}}$) /1/. The quantity φ is set in such a way that with $\varphi = 0$ the electric current density through the plasma-metal surface is equal to zero.

One can also obtain from Eq.(3)

$$\frac{\int_0^{2\pi a}\left(j_y + \frac{a}{qR}j_z\right)dy}{2\pi a} = -\frac{a}{qR}en_-V_i\left(1 - e^{-\frac{e\varphi_-}{T}}\right) + 2\frac{cT}{B}\frac{\partial}{\partial x}\left(\frac{\int_0^{2\pi a} n\, dy}{2\pi a} - n_-\right) \qquad (8)$$

Expressing $\int_0^{2\pi a} j_y\, dy$, $\int_0^{2\pi a} j_z\, dy$, $\varphi_- - \varphi_+$ with the help of Eqs.(4) and (5) and the first term in the right hand part with the help of Eq.(7), introducing the designations $\frac{\partial n_+}{\partial x} = -\frac{n_+}{\ell_+}$, $\frac{\partial n_-}{\partial x} = -\frac{n_-}{\ell_-}$, $u = \frac{eB}{cT}\int_0^{2\pi a} V_x\, dy + 2\ell n\frac{n_+}{n_-}$ and the dimensionless parameters $L = \frac{qRcT}{aeBV_i}$, $A = \frac{\sigma E}{en_-V_i}$, $Q = \frac{T}{2\pi qReE}$ one can obtain

$$\frac{2L}{\ell_-} - A(1 + Qu) = \frac{1 - \frac{n_+}{n_-}e^{-u} + 2\frac{L}{\ell_-}\left(1 - \frac{\ell_- n_+}{\ell_+ n_-}\right)e^{-u}}{1 + e^{-u}} \qquad (9)$$

From the z component of Eq.(4) one can obtain that $\frac{\partial\varphi}{\partial x} > 0$ in the scrape-off layer with V_z being small in the central part of

the tokamak. The very circumstance along with the condition that the total current from the plasma to the limiter is equal to zero means that at the limiter edge the mean value of φ is negative. (The electrons hit the limiter edge in a larger number than the ions do). The electric current in the x direction originates. It reaches a maximum at that x here the mean plasma potential $\varphi = 0$.

3. The current and the characteristic dimension of the change in the plasma density at the plane x = 0 through which the current is a maximum can be evaluated from Eq.(9). To do this the estimation on the base of Eq.(6) is used

$$\int_0^{2\pi a} V_x \, dy = \frac{aV_i}{qR}\left(\frac{\ell_+ n_+ + \ell_- n_-}{n_+ + n_-}\right)$$

The ratio n_-/n_+ has been set. Calculations have been carried out for the following parameter values: B = 20 kG, a = 35 cm, R = 150 cm, q = 3, T = 20 eV, E = 3 x 10^{-3} V/cm, $\sigma = 3 \times 10^{14} c^{-1}$, $n_- = 5 \times 10^{12} cm^{-3}$. With that L = .3 cm. The dependences of ℓ_-/L and $K = \int_0^{2\pi a} j_x dy \Big/ e \int_0^{2\pi a} n V_x dy$ on n_-/n_+ are presented in Fig.1. The dependences of $e\varphi_-/T$ and $(e\varphi_- - e\varphi_+)/T$ on n_-/n_+ are presented in Fig.2. A possible value of n_-/n_+ satisfies the condition $1 < n_-/n_+ < R$. The maximum value $n_-/n_+ = R$ is likely to conform the case with the mean current density along the magnetic field being equal to σE(i.e. u = 0). In the case $n_-/n_+ = 3.7$, $\ell_- = .93$ cm, the diffusivity $D = \ell_- V_x = 1{,}3 \times 10^3$ cm^2/c $= .2 D_B$ (D_B is the Bohm diffusivity). It can be used for an estimation that the characteristic dimension of the change in the plasma concentration $\ell = \frac{3qRcT}{aeBV_i}$ and the diffusivity $D = \frac{3}{2}\frac{qR}{a^2 V_i}\left(\frac{cT}{eB}\right)^2$. For Macrotor with the magnetic field of 3 kG where the inner torus equator is served as a limiter one can obtain $\ell = 5$ cm, $D = 6 \times 10^4$ cm/c that are close to the experimental values 9 cm and 10^5 cm^2/c, respectively, /2/.

4. Slow plasma concentration drop in the scrape-off layer can be accounted for by the following. The plasma is confined in equilibrium along the minor radius by the ponderomotive force originated due to the current density component normal to the magnetic field. In the scrape-off layer the current encounters the toroidal limiter. For current closing the charge bleeding along the magnetic field or the charge leakage across the limiter is necessary. The plasma conductivity isn't high in the scrape-off layer and a significant electric potential difference should arise within the plasma. Langmuir potential drops are different at different sides of the limiter. The plasma drifts along the minor radius due to the poloidal electric field and this leads to the slow plasma concentration drop.

The limiter pattern considered does not hinder the toroidal current component and does not change the processes taking place under the Pfirsch-Schluter diffusion. The Pfirsch-Schluter diffusivity is $4(\frac{a}{R})^4$ the diffusivity obtained in the present paper. Thus neglect of the toroidal corrections is justified. The poloidal limiter case when the Pfirsch-Schluter electric potential and current distributions are modified /3/ requires a special consideration.

REFERENCES

/1/ Chodura R.:Plasma-wall transition in an oblique magnetic field, Phys.Fluids 25(1982) 1622.

/2/ Zweben S.J., Taylor R.J.: Edge plasma properties of the UCLA tokamaks. UCLA Report PGS-543 (1981).

/3/ Motley R.W.: Electrical characteristics of an ideal tokamak limiter, Nucl.Fus. 21 (1981) 1541.

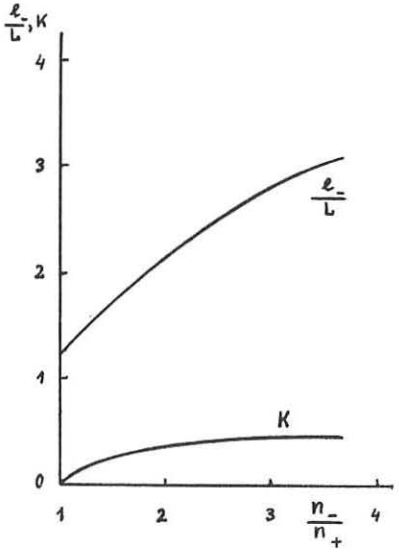

Fig.1

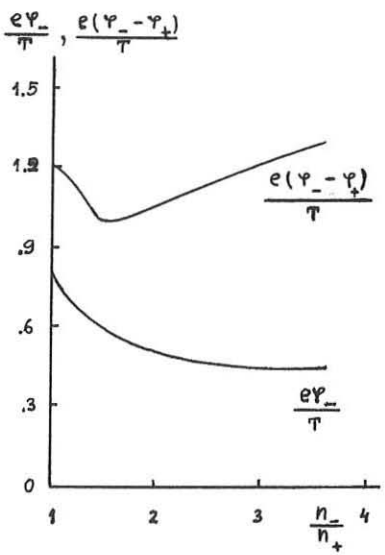

Fig.2

ARCING STUDY IN DISRUPTIVE TOKAMAK DISCHARGES

N.M.Zykova, A.O.Ikonnikov, V.N.Kabanov, A.V.Nedospasov
Institute of High Temperatures, USSR Academy of Sciences,
Moscow, USSR

The present paper is a continuation of the investigation of arcing on limiters of a small tokamak TV-1 (R = 23.5, r=4.1 cm) /1/. The arc currents and voltages between electrically isolated limiters were measured during disruptive discharges. During stable discharges the arcing between limiters was not observed. The measurements were made throughout discharges in hydrogen $q < 2.4$ with plasma density $\bar{n} \simeq 3 \cdot 10^{13} cm^{-3}$, plasma currents 7-12 kA, toroidal magnetic fields B_T = 1.2 - 1.4 T, discharge duration 6.5 - 7 mc. Stationary arc test probe used as limiter (r_p = 2.9 cm) and movable limiter were placed in horizontal ports. The arc test probe consisted of the three separate isolated parts. The plate with surfaces parallel to B_T (Fig.1) was placed between the two others plates oriented perpendicular to B_T. The azimuth angle between the limiter and the probe side facing the electron drift in vortical electric field (electron side) was 14°. Approximately 70% of the area of the probe electron side was in a shadow of a limiter. The probe and the limiter dimensions were approximately the same: along minor radius - 1 cm, height - 1.5 cm and width 0.3 cm. The material for the probe and the limiter was molybdenum. The resistance of an external circuit varied from 1 to 20 Ω . Frequency band of measuring circuit and cathode-ray recorders was down to 5 MHz.

1. The currents between separate parts of the probe (electron, ion and central) and the limiter as well as currents between opposite sides (electron and ion) of the probe were measured experimentally. Several arc pulses of different amplitudes were registered for every single discharge. The Fig.2 shows the maximum value for the currents measured separatly for every

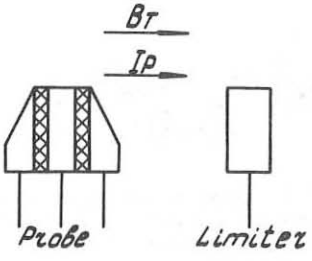

Fig.1 Diagrammatic representation of the arc test probe and the limiter.

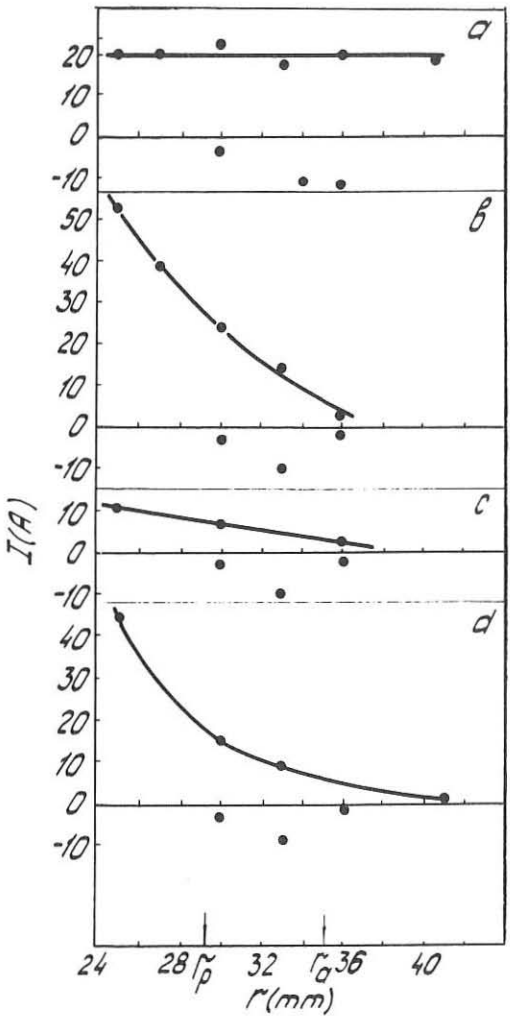

Fig. 2. The current (a) between electron and ion sides of probe, (b) between limiter and ion sides, (c) between limiter and electron side, (d) between limiter and central part of probe.

couple for various values of the minor radius of the limiter. Positive direction of the current shown in Fig. 2 coincides with that of the plasma current. The direction of the arc currents essentialy coincides with direction of plasma current but sometimes currents of opposite direction were observed (dotted in Fig. 2). The tracks of the cathode spots were registered in central part of the electron surface of the probe.

2. The connection of the electron and the ion sides of the probe with a limiter results in appearance of a simultaneous current between the "cathode" (the ion side of the probe) and the two "anodes" (limiters and probes electron sides) as well as between the second "cathode" (limiter's ion side) and anode (probe's electron side). The results for current measurements in that ramified circuit showed that current values in different parts coincide with the algebraic sum of current values measured for the twin connections (Fig. 2).

3. The average values for a velocity of the cathode spots movement and the rate of a surface erosion were evaluated according to the tracks of cathode spots. Velocity of spots in linear tracks exceeded 100 m/c on the surfaces parallel to B_T. The spots velocities on ion surfaces were 5 - 10 m/c. The erosion rate of surface evaluated from the volume of largest tracks and corresponding to largest current and arc duration was 10 mg/c. This value is several times less than a corresponding value of the erosion rate for a vacuum arc without the applied magnetic field /2/.

4. The energy released in external circuit during arc pulse was $W \simeq (1 - 5)\ 10^{-2}$ J.

5. The typical arc current pulse of positive direction had a characteristic shape: sharp increase of a current value up to I_o (during several mc) and a decrease of J(t) that can be described exponentially. It can be compared to the characteristic dependence

$$J(t) = I_o\, e^{-Rt/L}$$

with value L being of the order of $(1\text{-}3)\cdot 10^{-5}$ H. The same value of L was obtained from the equation of pulse energy

$$W = \frac{LI_o^2}{2}$$

6. The model of arc ignition on tokamak limiter was proposed in /3/. It was assumed that during the formation of a disruptive instability the plasma filaments with the current reached a limiter in order to be cut, which resulted in an overvoltage on the ion side of a limiter due to the poloidal magnetic flux stored in a filament. If it leads to arcing then the voltage

drops and the filament current I_f will subside in a skin time. With the external inductance of filament negligible in value the peak value of an overvoltage is of the order of

$$V = 2\pi\omega R \quad q \quad 10^{-9} \; I_f .$$

The value of V for tokamak TV-I estimated by this formula for $I_f = 10^2$, frequency MHD-disturbance of 10^5 Hz (which is by an order of magnitude greater than assumed in /3/ for tokamak T-4) is by an order of magnitude smaller than the value obtained between limiter sides experimentally. The obtained value of "effective inductance" (10^{-5} H) is by a factor of two greater than that assumed in /3/.

REFERENCES

/1/ Zykova N.M., Ivanov R.S., Kabanov V.N., Kurakina T.S., Nedospasov A.V.: Arcing studies in tokamak TV-1. In: X-th Europ. Conf. on Contr. Fus. and Plasma Phys., v.1, Moscow, 1981, J-4.

/2/ Kimblin C.W.: Erosion and ionisation in the cathode spot regions of vacuum arcs, J.Appl.Phys. 44(1973) 3074-3081.

/3/ Mirnov S.V.: On the possible mechanism of tokamak diaphragm erosion, Fizika plazmy 7 (1981) 687-688.

ON LONGITUDINAL TRANSPORT OF CHARGED PARTICLES TO TOKAMAK LIMITER

Fidel'man G.N., Ivanov R.S., Stotsky G.J.

Institute of High Temperatures, USSR Academy of Sciences, Moscow, USSR

Introduction.

In our recent works /1,2/ plasma transport has been shown to be non-ambipolar in the scrape-off zone of the TV-1 tokamak. The non-ambipolar plasma transport has been also observed in the experiments in a simulated magnetic divertor on the Wisconsin DC mashine /3/. The present paper aimed to determine the radial distributions of the charged particle flow to the conductive limiter and to study the "active" limiter operation when the limiter is externally biased.

Experimental Set-up and Diagnostics.

The TV-1 is a small tokamak device /4/ with a major radius of 23.5 cm and a minor radius of 4.1 cm. The apperture limiter of 3.5 cm radius was always connected electrically to the conductive wall of the vacuum vessel. The measurements of the charged particle flow distributions were performed on the ion and electron drift sides of the rail-type limiter inserted inwards through the horizontal port. The radially mavable $1 \times 3 \times 0.5$ mm^3 collector was positioned in the vicinity of the limiter surface. The limiter was connected ellectrically to the chamber wall via the measuring transformer and simultaneously to the collector via the bias voltage source and the current-measuring shunt. In 3 ms after the discharge ignition the collector was biased with the negative -150 v trapeziform pulse. The saturation ion current to the collector was supposed corresponding to the ion current to the limiter surface element of equal square. The electric current to the collector at the limiter potential was supposed to be caused by the difference of the ion and the electron currents. The average plasma density was determined by the means of the 4-mm microwave interferometer. The resonant fluorescence technique using a flashlamp dye laser enabled local measurements of the neutral hydrogen density. The analysis of the H_α line profiles was obtained by the use of the Fabry-Perot interferometer (FWHM of 0.45 A) coupled with the scanning image converter. All the experiments were performed in the single basic regime: the magnetic field was 1.4 T, plasma current was 5 kA, the discharge duration was 7 ms, the pressure of the hydrogen was 10^{-3} torr.

Results.

Non-Ambipolar transport. As it follows from the data presented on the fig.1, the resulting current to the limiter is due to the excess electrons and it is collected mostly by the narrow 2÷3 mm-wide zone behind the leading edge on the electron drift side. To preserve overall charge neutrality the limiter must conduct excess electrons from inner electron outflow regions

to outer areas of excess ion outflow (apperture limiter and the chamber walls). The neutralazing current is shorted by the external measuring circuit. Thus a direct measure of the radially separated electron and ion flow components (non-ambipolarity) is given by the current detected in this external circuit. The comparison of the total outflux of the charged particles from the plasma bulk with the non-ambipolar part of the flux to the limiter and the walls has been performed. The intensity of the non-ambipolar transport was found to be 40% of the total outflux ($10^{20}cm^{-3}s^{-1}$) of charged particles. Experimental accuracy was within the factor of 2. The total outflux was determined from the measurement of the H_α intensity which enabled the calculation of the ionization rate /5/ and from the microwave measurements of plasma density. The average electron density in this experiments was $3 \cdot 10^{13}$ cm^{-3}, while the hydrogen atom density was $(6 \div 8) \cdot 10^{9} cm^{-3}$. The additional experiments have shown that the electron impact dissociation of $H_2(H_2^+)$ molecules in the discharge scrape-off zone seemed to be the main source of neutral atoms in plasma. The effective atom temperature was about 3.5 ev and it's change during the discharge period was rather slight. The atoms of sufficiently high energy (3÷4 ev) were present at the very begining of the discharge in 0.1÷0.2ms after the current ignition. The effective hydrogen temperature has been determined from the analysis of H_α spectral line broading.

Ion and electron currents, potential drops. The results presented on fig.1 demonstrate a sharp asymmetry of the electron current distributions according to the ion and the electron drift sides of the limiter. In the zone of the preferential electron outflow the electron current exceeded 2÷3 times that of ions, while on the ion drift side the electron current is "quenched", it's magnitude being 2÷4 times reduced against the current of ions. The difference between the floating potentials of the collector and the limiter plotted on the fig.2 shows the asymmetry also of the Langmuir drops across the sheath.

At the plasma edge the difference between the potential drops on the electron and the ion drift sides of the limiter reached the value of ~80 v, that was exceeding the loop voltage by more than one order of the magnitude. The obtained current and the potential drop distributions (fig.1 and fig.2) are in a good qualitive and satisfactory quantitative agreement. Since at the plasma edge the ion current densities on both two sides of the limiter were rather close by the value (Fig.1b), while the electron current densities differed by one order of the magnitude, the difference of the potential drops between the electron and the ion sides of the limiter should reach the value of several electron temperatures.

In our experiments indeed the measured values of the electron temperature of about 20 ev satisfactory fitted the potential drop difference observed (Fig.2). Such a difference of the Langmuir drops may contribute into the asymmetry of the energy distributions of the implanted ions observed in PLT /6/ and TFR /7/ experiments on the electron and the ion drift sides of the limiter.

Active limiter operation. In 3 ms after the discharge ignition the floating at -40÷ -50 v limiter was biased by the constant voltage. The two limiters placed at different toroidal angles according to the Langmuir double probe position were alternatively used. This enabled to control the plasma parameters both in the "near" (φ = 15°) and in the "far" (φ = 165°) zones from the limiter. The abrupt decrease in the ion saturation current presented in fig.3 seems to be caused by the change of the plasma density. The results of the active limiter investigations are the following.

1) In the torroidally "far" zones the slope of plasma density profile rose when both the positive ($>$ + 50 v) and the negative ($<$ - 100 v) voltage being applied. The profile rise increased with the aplied voltage increasing. In the thin layer (30 mm $\leq r \leq$ 35 mm) the radial electric fields are found to be generated by the limiter potential. This radial electric fields may cause the change in density profile observed.

2) In the toroidally "near" zone the density profile changes were similar to those mentioned above when the negative potential being applied. At positive bias potential a tendency towards the density increase is present, as it was observed earlier /1,2/. The potential of the limiter penetrated in this case into the plasma of the "near" zone all over the radial interval of the limiter shadow.

REFERENCES

/1/ Ivanov, R.S., Nedospasov, A.V., and Fidel'man, G.N.: "Nonambipolar plasma transfer in TV-1 tokamak scrape-off-layer" in: X-th Europ.Conf. on Contr.Fus. and Plasma Phys., vol.1 (Contributed papers), j-3, Moscow, 1981

/2/ Fidel'man, G.N.: "O perenose plasmy v pristenochnoj oblasti tokamaka TV-1", Preprint IVTAN, N7-069, M., 1981.

/3/ Strawich, C.M., and Emmert, G.A.: "Nonambipolar transport in a magnetic divertor", Nucl.Fusion, 21 (1981), 1291-1300.

/4/ Bychkov, S.S., Glebko, V.E., Zykova, N.M., Ivanov, R.S., Kobanov, V.N., Kurakina, T.S., Nedospasov, A.V., Pilsky, V.I., Stotsky, G.I., Fidel'man, G.N.: "Tokamak instituta vysokih temperatur TV-1. Konstruktsija i osnovnye parametry", Preprint IVTAN, N7-071, M., 1981.

/5/ Johnson, L.C., and Hinnov, E.J.: "Ionizaition, recombination, and population of excited levels in hydrogen plasmas", Quant.Spectr.Radiate Transfer, 13(1973) 333-358.

/6/ Cohen, S.A., Dylla, H.F., Wamper, W.R., and Magel, C.W.: "Deuterium ion fluxes to probes in the PLT edge plasma", J.Nucl.Mat. 93 & 94 (1980) 109-114.

/7/ Staudenmair, G., Staib, P., and Poschenrieder, W.: "Determination of ion temperatures in the edge plasma from ion flux transmission of apertures", J.Nucl.Mat. 93 & 94 (1980) 121-126.

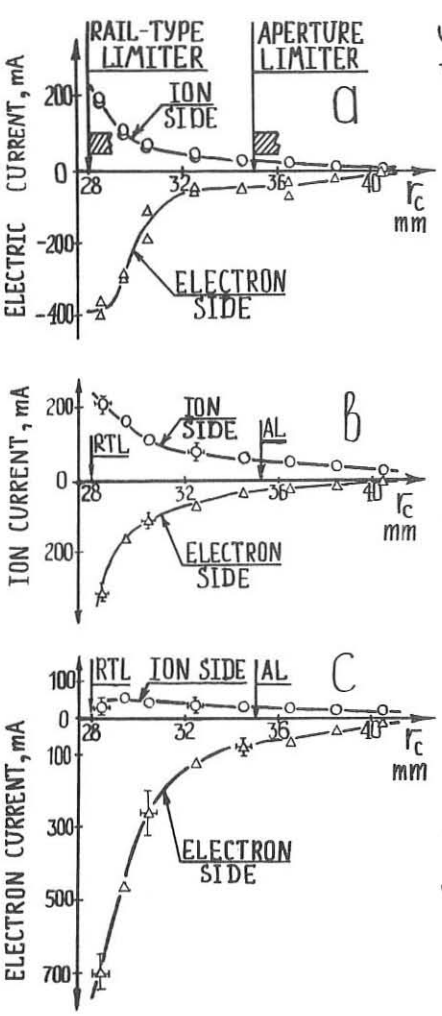

Fig.1 Radial profiles of the electric current to the collector at limiter potential (a), ion current to the collector, biased with -150 v(b), electron current to the collector at limiter potential (c)

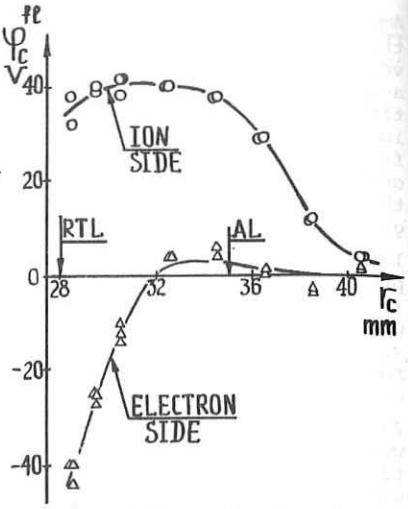

Fig.2 Profiles of collector floating potential on the ion and the electron drift sides of the limiter.

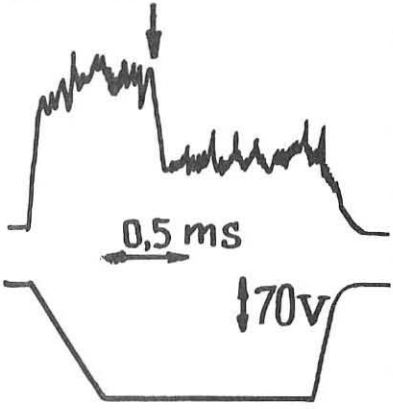

Fig.3 Oscilloscope traces of the current (the upper curve) and the voltage (the lower curve) between the probes when the limiter is biased with the -130v pulse. The arrow indicates the moment of the biased pulse starting. The radial position of the double probe is 37 mm.

Results from Infrared-Thermography on Limiters in TEXTOR

U. Samm
Institut für Plasmaphysik, Kernforschungsanlage Jülich GmbH,
Association EURATOM-KFA, FRG

In order to achieve control of plasma-wall interaction in a limiter tokamak detailed knowledge about the scrape-off layer and the thermal load is needed in particular its temporal development over time scales of several seconds. The influence of different sizes, shapes and locations of poloidal or toroidal limiter segments on the scrape-off-layer manifests itself in different thermal loads onto the limiter surface. The resulting temperature distributions can be determined by infrared-thermography /1,2,3/. To get reliable results it is appropriate to have the full information about the energy scrape-off available with a single shot.
Therefore at TEXTOR the limiters have been observed with an infrared camera together with a fast single PbSe-detector-element providing high resolution in space (two dimensions) and time.

Experimental arrangement

The limiter system of TEXTOR (Fig. 1) consists of three-main limiters movable along the minor radius within r = 45-55 cm, located in the same poloidal cross-section and covering the minor circumference by about 30 %. The limiter segments are made of stainless steel with a radius of curvature in toroidal direction of 5 cm (outer)and 1.2 cm (upper, lower).

For this paper an additional halfsphere test limiter made of stainless steel with a diameter of 13 cm is moved into the plasma from below at the toroidal position $\Theta = 90^{\circ}$ (main limiters at $\Theta = 0^{\circ}$) and is observed by two infrared detectors (Fig. 1). The thermal radiation in the wavelength intervall 0.85 - 1.2 μm is detected with a camera using a charge-coupled device (CCD) with 488 x 380 picture elements as a photosensor. This pure solid state design avoids any geometric distortion in the magnetic field, has no time lag and produces a signal linear to the light flux. The camera takes a close up view of the total limiter surface providing a spatial resolution of 0.5 mm in both dimensions and a time resolution of 20 msec. The data are stored on video tape. The dynamic range of this system is limited by the video-recorder to 1:200, thus temperature excursion up to 200° may be measured with an accuracy of typically 3°. The sensitivity of the CCD-sensor allows temperature measurements from 400 °C upwards. Therefore the test-limiter is heated up electrically to a homogeneous temperature of 400 °C, what is also useful for in-situ calibration.

The wavelength intervall of 3.0-3.4 μm is observed by the second detector, a single PbSe element of 4 x 4 mm^2 size, operated in the photoconductive mode. The signal is digitized and stored with a sampling frequency of 10 kHz. The dynamic range allows the recording of temperature excursions of more than 500° with an accuracy of typically 1°.

Both detectors are operated simultaneously and cover the full information resolved in time and space.

Energy scrape-off-layer

Fig. 2a) shows a typical infrared image of the test limiter viewed by the camera. There are two clearly separated zones of powerload along the toroidal direction with a dark (="cool") region in the middle of the limiter.

The horizontal lines of the video signal and its projection onto the side view of the limiter (Fig. 2b,e) obviously shows that there is nearly no temperature rise on top of the limiter, whereas two temperature maxima appear on those parts of the limiter surface facing the plasma flow. We conclude that the energy flux to the limiters is directed strongly along the magnetic field lines. Assuming an exponential decay of this energy flux $F(r)$ along the minor radius the heat flux into the limiter surface is $F(r) = \cos\alpha\, F_o \exp(-(r-a)/\lambda)$ with α being the angle of inclination of the limiter surface element. This gives a maximum of $F(r)$ along the toroidal direction x at (x=0 middle of limiter)

$$x_{max} = \left(\lambda\left(r_o + \lambda^2/4\right)^{1/2} - \lambda^2/2\right)^{1/2}$$

which is only a function of the energy scrape-off thickness λ (r_o=radius of limiter) and can easily be measured.

The values of λ for different limiter configurations have been determined at the test limiter with the aim to exclude the influence on the plasma boundary scrape-off of the main limiters. Therefore, beginning with all limiters at the same position r = 45 cm, the plasma column for discharges of 2.5 sec, pulse length with I_p = 340 kA, $n_e(o) \approx 3 \times 10^{13}$ cm^{-3} and $T_e(o) \approx 1.3$ keV, is shifted vertically for 0,8 sec during the flat top towards the lower limiters by 5 cm.

Then the lower main limiter and also the outer limiter is drawn back stepwise shot by shot until the test limiter takes the scrape-off energy of the first 3 cm. The resulting values for the electron-(λ_e) and ionside (λ_i) measured at t=1.4 sec are shown in table I.

Table I:

Shot	Position of limiters in cm			energy scrape off thickness (mm)	
	test	lower	outer	e	i
5180	45	45	45	5.3	9.5
5185	45	47	45	9.1	9.5
5189	45	47	47	9.7	10.3
5190	45	48	47	9.7	10.3

error $\pm$ 0.3mm

The values for λ_e and λ_i increase and become equal when the fraction of scrape-off energy taken by the test limiter is rising; this is expected when only one limiter determines the connection length for the magnetic field lines. A more detailed analysis of the scrape-off layer is obtained by computing $\Delta T(r)/\cos\alpha(r)$ at radius r, what is proportional to the energy flux density along the field line. A semilogarithmic plot of the radial profile of the energy flux density is shown in Figs. 3a, b for both sides of the limiter. The curves show the expected exponential decay, accordingly the values derived from these curves agree with the corresponding values of table I.

Absolute determination of heat flux

For the calculation of the absolute heat flux the time resolved temperature distribution is needed. Only in the case of constant heat flux to a semi-infinite uniform solid the relation between temperature rise and heat flux is very simple /4/:

$$\Delta T(t) = \frac{F_o}{k}\sqrt{\frac{\chi}{\pi}}\sqrt{t}$$

with heat conductivity χ, diffusivity K and the heat flux F_o into the surface. For our experiment these conditions are fulfilled since the curvature of the limiter is negligible compared with the depth of temperature rise and the temperature increase is proportional to $\sqrt{t}$ as is shown in Fig. 4. for a vertical plasma displacement.

A determination of the heat flux from this slope of temperature rise (Fig.5) at the point of maximum temperature is made for the different limiter positions (noted in table I). The values for Fo vary from 50 W/cm^2 - with all limiters at r=45 cm and without vertical plasma shift - up to 740 W/cm^2 - with the test limiter at r=45 cm, the main limiters withdrawn by 3 cm and with a vertical plasma shift.

From these power densities at the point of observation the energy flow along the magnetic field lines is calculated under consideration of the exponential decay. At r =45 cm the power densities vary from 300 to 3500 W/cm^2 according to the Fo values from above. This is in good agreement with the expected heat flux calculated from the estimated electron temperatures ($T_e \approx 30$eV) (confirmed by Thompson-scattering measurements), the measured electron densities ($n_e \approx 10^{12}$ cm^{-3}) at the limiter surface /5/ and with an energy transfer coefficient $\delta = 8$.

The total power load onto all limiters for standard discharges with an average power density of 300 W/cm^2 then is about 70 kW, that is 15 % of the ohmic heating power input. This result is confirmed by calorimetric measurements obtained from thermocouples implemented in all limiter segments.

Conclusions

With a CCD-camera and a fast single PbSe-detector element the surface temperature distribution of the test limiter in space and time is measured with a single shot.

- The spatial temperature distribution shows clearly the strong direction of the heat flow along the magnetic field lines.
- The radial heat flux profile decays exponentially characterized by the energy scrape-off length λ= 5-10 mm, with $\lambda_e = \lambda_i$ if the main limiters are withdrawn
- Because no fast temperature variations below 50 msec are observed, the time resolution of 20 msec of the standard TV-camera is sufficient.
- The heat flux onto the testlimiter during a vertical plasma displacement of 0.8 sec is constant.
- The absolute power densities along the magnetic field lines at r=45 cm are 300 W/cm^2 for standard discharges and 3500 W/cm^2 for plasma displacements by 5 cm towards the test limiter and the mainlimiters withdrawn.
- In standard discharges the main limiters take about 15 % of the ohmic heating power input.

I wish to thank the TEXTOR-operating team for their cooperation. The advice and the support of and discussions with E. Hintz, P. Bogen, W. Hopmann and D. Rusbüldt are gratefully acknowledged.

References

/1/ D.H.J. Goodall, Proceedings of 9th Symposium on Fusion Technology, Pergamon Press (1978) p. 523.
/2/ TFR Group, Report EUR-CEA-FC 1114 (1981)
/3/ A.E. Pontau, et.al., Proceedings of 5th International Conference on Plasma Surface Interactions in Controlled Fusion Devices, Gatlinburg (1982) page 287. North Holland Publ.
/4/ H.W. Carslaw and J.C. Jaeger, Conduction of Heat in Solids (Clarendon, Oxford, 1959)
/5/ A. Pospieszczyk et.al., Neutral particle fluxes from the TEXTOR limiter, these proceedings.

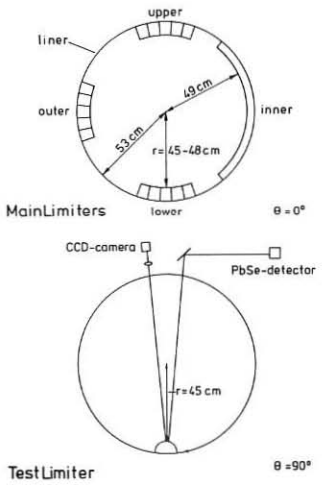

Fig.1 Arrangement of TEXTOR limiters shown in poloidal cross-sections

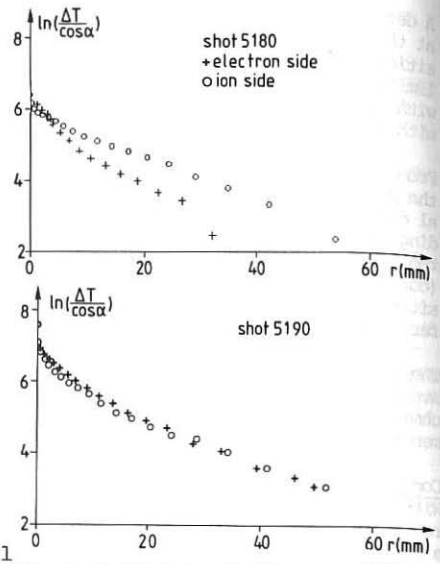

Fig.3 Radial heat flux profile

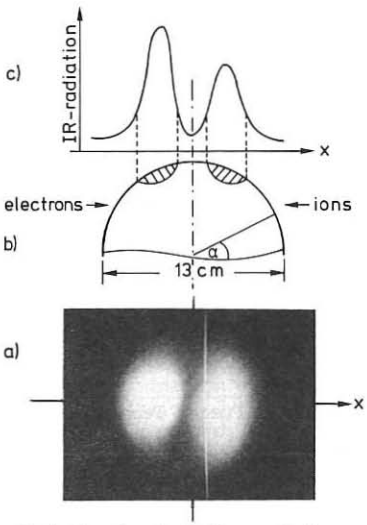

Fig.2a) Typical infrared image of the test limiter, b) side view of the test limiter, c) line scan of the IR-signal

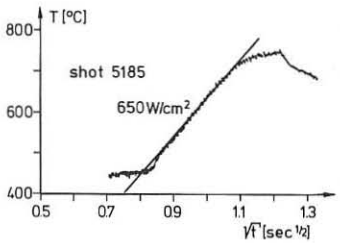

Fig.4 A constant heat flux during vertical plasma displacement

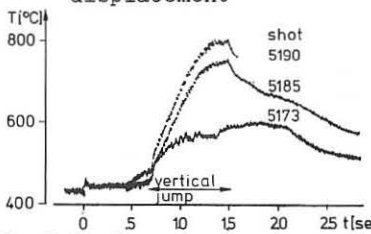

Fig.5 Surface temperature rise of the test limiter for various limiter positions

Neutral particle fluxes emitted from the TEXTOR limiter

A. Pospieszczyk, P. Bogen, U. Samm
Institut für Plasmaphysik der Kernforschungsanlage Jülich GmbH
Association EURATOM-KFA, 5170 Jülich, FRG

Introduction

In the vicinity of the TEXTOR limiter, where a plasma with $n_e \approx 10^{12}/cm^3$ and $Te \geq 10$ eV exists, the number of photons emitted from the neutral atoms is proportional to the number of ionizations and these in turn are proportional to the atom fluxes from the limiter /1/. To determine the magnitude of these fluxes and the ionization lengths of the released atoms by spectroscopic means, an experimental arrangement has been set up on TEXTOR /2/ as shown in Fig. 1. The plasma contact with the four poloidal limiter segments can be observed through a tangential port by a CCD-camera (charge coupled device) with an interference filter in front of it (high spatial information, low spectral resolution) or by a film or photomultiplier with a grating spectrometer (low spatial information, high spectral resolution).

Experimental arrangement

TEXTOR was operated with a toroidal magnetic field of 2 T, a current of 340 kA, a major radius of 175 cm and a minor radius of 50 cm. Typical peak densities were $2 \times 10^{13}/cm^3$, peak electron temperatures were about 1,3 keV. The CCD-camera system is operated in the common TV-mode (resolution 20 msec), and the results are stored on video-tape. The pure solid state design of the sensors avoids any distortion by magnetic fields, and the signal is proportional to the incident light flux. With appropriate interference filters it is then possible to observe the whole poloidal cross-section in the light of a single element. Results of this technique are shown in Fig. 2, where adjacent to the limiter a luminous layer composed of the light of chromium lines or of the H_α line is seen, the intensities of which are determined by the particle fluxes emitted from the limiter.

In order to determine the magnitude and the composition of these fluxes and in order to calibrate the camera absolutely, the emission of the layer surrounding the upper limiter was simultaneously observed with a grating spectrometer. The slit image was positioned in such a way that it pointed into the direction of the minor plasma radius with the upper end touching the limiter edge. This way of observation allowed both, to distinguish between the lines emitted by the localized plasma-limiter interaction zone and those emitted by the rest of the plasma and to make spatially resolved measurements of the neutral particle distribution in the direction perpendicular to the limiter surface.

Photographic spectra

From the photographically recorded spectra between 250 nm and 700 nm, the region around 400 nm is shown in Fig. 3. All the spectra are time integrated over an interval from 0,3 to 1,3 s for discharges of about 2 s duration so that only the plateau phase from one single shot is recorded. The length scale and the position of the limiter edge is also indicated in the figure.

Foreground lines emitted from the hot 2 m long plasma layer between limiter and window can easily be detected by their uniform intensity distribution.

They are emitted by ionized species (mainly oxygen) and by neutral hydrogen, whereas the metal atoms, which are localized in a well defined zone around the limiter, give rise to short lines of about 1-3 cm length, indicating their prenetration depth. The emission of these atoms dominates the spectra, which are composed of the neutral lines of the limiter material (Inconel 625, in particular Cr, Ni, Fe and Mo). The region around 427 nm was found to be dominated by the Cr-triplet, and these lines were used for the video recording in combination with an interference filter centered at 427 nm.

Unfortunately a photographic recording does not have a simple linear intensity response, so that bright lines easily lead to overexposure of the film. Only the faint lines give reliable information about the radial distribution of the neutrals. Therefore in order to obtain the ionization length quantitatively as well as time resolved two superior methods were used.

Ionization lengths

Firstly a rotating sector was placed in front of the entrance slit of the spectrometer, which scanned linearly over the slit, and secondly the video pictures were evaluated along a line perpendicular to the limiter. There was good agreement between the results obtained by both methods. Fig. 2 shows that the distribution in poloidal direction is rather homogeneous. In the toroidal direction the light has been integrated, so that there are no informations about the toroidal distribution of the impurity fluxes. The ionization length can be estimated from the intensity increase towards the limiter surface. The value changes with time and with discharge conditions. A typical length of about 1 cm has been found during the plateau phase. The neutral atoms released from the limiter with a velocity of v_o are ionized within an average length $l = v_o/n_e\langle\sigma_{Ion}\cdot v_e\rangle$. Assuming $T_e = 30$ eV (this is confirmed by Thomson scattering experiments) near the limiter, $v_o = 2 \times 10^5$ cm/s, and $\langle\sigma_{Ion}\cdot v_e\rangle = 2 \times 10^{-7}$ cm^3 sec^{-1} we derive an electron density at the limiter of about 1×10^{12} cm^{-3}.

The interpretation of the H_α signals in terms of hydrogen particle fluxes is more difficult, since in the emission of these particles desorption, sputtering and reflection processes are involved and since for the penetration length dissociation, ionization and charge exchange are important. Hydrogen as a molecule desorbed from the limiter was found only during the current rise phase. At later times hydrogen atoms take the more dominant part within the processes above. Thus the mean free path is determined by ionization and charge exchange and is not easy to interpret. The evaluation of the spatial profile of the H_α-intensity results into two characteristic decay lengths, at first $l_{1/e} \approx 2.5$ cm and then $l_{1/e} \approx 6.5$ cm is observed. This can be qualitatively understood by assuming that the mean velocity increases substantially with the distance from the limiter due to charge exchange - at least a factor of 2.6, but probably much faster, since the electron density also increases. It was found from H_α-line profile measurements that the energy of the hydrogen indeed rapidly reaches values of 30 eV.

Particle fluxes

The absolute intensity per cm (in poloidal direction) limiter length (toroidal direction is integrated) directly gives the number of ionizations, if we take the low density limit and neglect stepwise ionization. The simplification is probably justified at $n_e \leq 2 \times 10^{12}$/cm^3 within 30 % error. As the ratio of the ionization to excitation rate /4/ is only a slowly varying function of T_e above 10 eV for most impurities and T_e is known from Thompson scattering measurements to be around 30 eV, the flux can be derived within

a factor of two. From the measured intensity of 1.3 x 10^{14} photons/cm sec sr, we obtain a total flux from one limiter (25 cm length, T_e = 30 eV) of 1.5 x 10^{17} atoms/sec. Four limiters give a total flux of 6 x 10^{17} atoms/sec. Assuming a confinement time of 20 msec, we estimate an impurity content of 1.2 x 10^{16} Cr atoms. The total ion number is about 8 x 10^{19}; so the concentration of Cr is about 1,5 x 10^{-4}. The Cr concentration in Inconel is 20 %. Therefore, assuming for all the elements of Inconel equal sputtering rates, we obtain a metal concentration of 7 x 10^{-4} neglecting sputtering at the liner.

The hydrogen atom flux from the limiter into the plasma, derived from the H_α intensity, is about 6 x 10^{17}/sec cm (per cm limiter length in poloidal direction). This value may be compared with the ion flux to the limiter. With a mean electron density of 5 x 10^{11}/cm^3 at the limiter, a measured scrape-off layer length of 1 cm and a mean ion drift velocity of 4 x 10^6 cm/sec (30 eV), we calculate a flux of 2 x 10^{18} cm/sec. The agreement between both measurements is reasonable considering that a significant part of the neutralized hydrogen is not trapped by the plasma. The total flux emitted by the four limiter segments is about 6 x 10^{19} sec^{-1}, i.e. a factor of 100 higher than the Cr-flux.

When the plasma axis is shifted towards the upper limiter by an appropriate perpendicular magnetic field, the Cr-fluxes increase up to a factor of four (Fig. 4) whereas the Cr-fluxes from the other limiters decrease by a factor of about 3. Obviously, the total released impurity flux is about constant. The hydrogen flux increases simultaneously by the same amount indicating that the Cr-fluxes are proportional to the hydrogen (or plasma) fluxes, which are probably also proportional to the fluxes of impurity ions causing the sputtering.

Conclusions

By means of a CCD-camera a two dimensional view of the poloidal limiter cross-section in the light of a single element is recorded. This camera in combination with an intensity calibrated spectrometer allows the measurement of ionization lengths, impurity-and hydrogen fluxes in the vicinity of the limiter. The observed Cr-atom fluxes cannot be explained by H-sputtering, but probably by impurity ion sputtering. A typical electron density of about 1 x 10^{12}/cm^3 has been found at the limiter.

We want to thank the TEXTOR operating team for their assistance. The advice and support of E. Hintz is gratefully acknowledged.

References

/1/ L.C. Johnson and E. Hinnov
J. Quant. Spec. Rad. Transf. 13 (1973), 333
Equipe TFR, Nucl. Fus. 15 (1975), 1053

/2/ H. Soltwisch
First Results from the TEXTOR, these proceedings

/3/ W. Lotz, IPP 1/62 and 1/67

/4/ H. van Regemorter, Astrophys. J. 136 (1962) 906

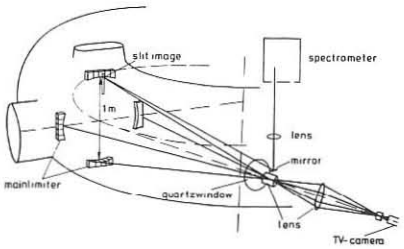

Fig.1 Experimental arrangement

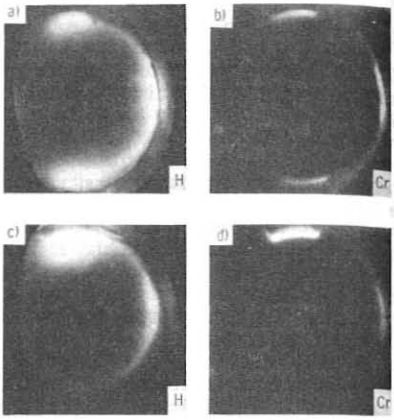

Fig.2 Photography of the limiter in the light of a Cr line and of H_α, a) and b) for a well centered discharge, c) and d) for an upwards displaced plasma

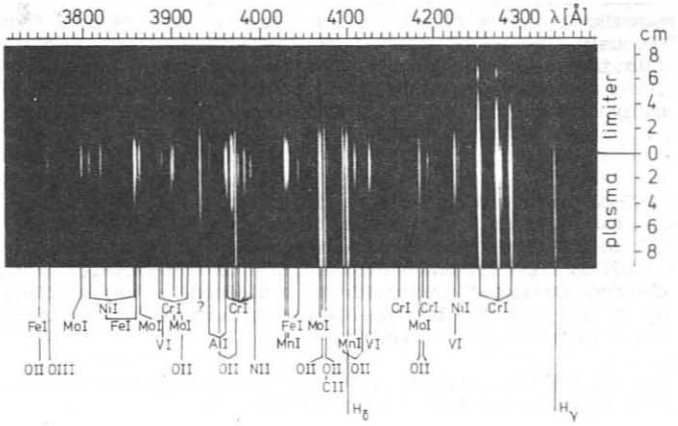

Fig.3 Spectrum of the plasma limiter interaction zone

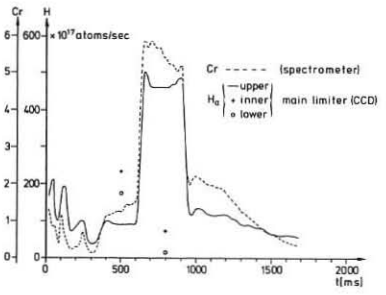

Fig.4 Chromium- and hydrogen atom fluxes from the limiters. From 600 to 959 msec the plasma is shifted upwards.

INFLUENCE OF OXYGEN COVERAGE ON THE SPUTTERING OF CHROMIUM.

G. Betz, W. Husinsky and F. Viehböck.
Institut für Allgemeine Physik, Technische Universität Wien, Karlsplatz 13, A-1040 Wien, Austria.

We have bombarded a metallic Cr target with 7 keV Kr^+ and He^+ ion beams at different oxygen background pressures. Using a quart microbalance relative sputtering yields as a function of oxygen partial pressure have been measured. By means of a Doppler-Shift-Laser-Fluorescence Spectrometer we have studied the density change of Cr atoms sputtered in the electronic ground state as a function of oxygen coverage. Furthermore the change of the velocity distribution of Cr atoms in the ground state was investigated as the oxygen background pressure was increased. The density of sputtered Cr atoms in the ground state decreased drastically by a factor more than fifty when the oxygen pressure was increased from no oxygen (the base pressure in the chamber was about $1\ 10^{-9}$ torr) to about $1\ 10^{-6}$ torr oxygen partial pressure. The total sputtering yield of Cr as obtained by the quartz microbalance, however, did not decrease by more than a factor three in this pressure regime. At the same time the maximum of the velocity distribution of sputtered atoms detected in the ground state 5 cm apart from the target shifts from about 0.9 eV to about 2 eV. This corresponds to a shift of the"surface binding energy"from 1.8 eV to 4 eV if the obtained spectra are fitted with a $v^2/(v^2+v_b^2)^3$ distribution. No difference in the velocity spectra could be found for Kr^+ and He^+ bombardment. Simultaneously with the dcrease of the intensity of sputtered ground state atoms an increase by a factor of ten in the amount of sputtered excited atoms (via light emission) and ions (current measurements) was observed, however remained a minor contribution (below 20%) to the total sputter yield. Therefore we conclude that the majority of sputtered particles are clusters.

Preliminary Abstract (4-page paper not received in time).

Radio-Frequency Divertor for Impurity Pump-Out

H. Sugai

Department of Electrical Engineering, Nagoya University
Nagoya 464, Japan

Novel active divertors using radio-frequency waves are proposed: one is based on the toroidal plasma rotation with uni-directional waves in the ion-cyclotron frequency range, and the other is based on the direct action to the impurity ions.

1. INTRODUCTION

Most of methods for impurity control such as magnetic divertor or mechanical divertor are passive in a sence that the pump-out action is not exerted directly to impurities in a hot plasma core. Recently, much attention has been given to the active impurity control which uses toroidal rotation of a plasma induced by neutral beam injection/1/. In this paper, I propose a new way of the active control, i.e., RF divertor /2,3/ where waves are launched into a plasma by external RF generator in the ion-cyclotron range of frequencies(ICRF).

In principle, RF divertor uses wave-particle interactions in a plasma. Depending on the species of resonant particles, two schemes of RF divertor are considered. When the resonant particles are impurity ions, the wave energy and/or momentum is directly deposited to the impurities, and their cross-field transport is controlled. This scheme is called the direct method, which corresponds to the right part in the flow chart shown in Fig.1. On the other hand, when the main ions are resonant, the wave energy is once given to the main ions, and they modify the impurity diffusion. This is the indirect method, which corresponds to the left part in Fig.1.

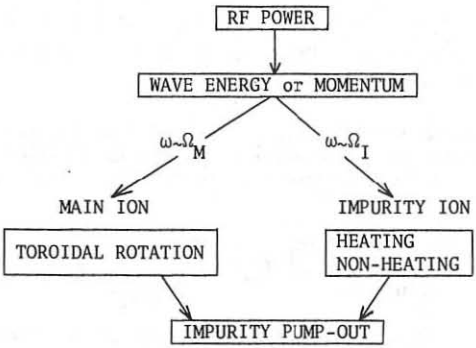

Fig.1. Two schemes of RF divertor

2. INDIRECT METHOD ——— "Rotating a plasma with Waves" ———

The use of momentum transfer due to neutral-beam injection to expel impurity ions out of a tokamak plasma has been investigated/1/. It turned out that the impurity transport can be controlled by the rapid plasma rotation induced by the tangentially injected beam. In order to rotate the plasma, I propose the use of wave momentum(energy)/3/ instead of neutral-beam injection. The underlying physical basis is common to current generation with waves/4/. Consider a steady state plasma where continuous waves are externally launched and deposit their energy to resonant particles. The crucial quantity, by which the practicality of this scheme may be assessed, is G/P_d, the amount of momentum generated per power dissipated. This quantity is obtained by replacing charge(-e) with mass(m) in the derivation of J/P_d in the current generation theory/4/ so that

$$\frac{G}{P_d} = m \frac{\hat{s}\cdot\nabla(v_z/\nu)}{\hat{s}\cdot\nabla E} \quad . \tag{1}$$

Here G is the momentum density parallel to the static magnetic field in the z direction, $\hat{s}$ is the unit vector along the displacement in the velocity space, $E=m(v_z^2+v_\perp^2)/2$ is the kinetic energy of resonant particles, ν is the effective collision frequency.

In view of G/P_d, it is straight forward to compare the momentum G_e induced in the wave-electron interaction with the momentum G_i due to the wave-ion interaction, when the same amount of RF power is dissipated. The rough estimation gives $G_e/G_i \sim (m_e/m_i)(T_e/T_i) \ll 1$. Therefore, in order to rotate the plasma efficiently, we had better adopt ions rather than electrons as the resonant particles. Suppose a plasma composed of electrons, main ions, and impurity ions. Their masses, charge states, densities, and thermal velocities are respectively denoted by m_σ, Z_σ, n_σ, and $v_{T\sigma}$ for the species σ=e, i, I. For resonant main ions with the velocity v_z in the range $v_{TI} \ll v_{Ti} \ll v_z \ll v_{Te}$, two collisional scattering rates are given from the Fokker-Planck equation; an energy loss rate $\nu_E=\nu_{oi}[1+(m_i/m_I)(n_I Z_I^2/n_i Z_i^2)]/2u^3$ and a momentum destruction rate $\nu_M=\nu_{oi}[2+(1+m_i/m_I)(n_I Z_I^2/n_i Z_i^2)]/2u^3$ where $\nu_{oi}=\omega_{pi}^4 \ln\Lambda/2\pi n_i v_{Ti}^3$, $\omega_{pi}=(n_i Z_i^2 e^2/m_i \varepsilon_0)^{1/2}$, $u=v/v_{Ti}$, and the small electron contribution has been neglected. Using these collision rates, we find

$$\nu = \nu_{oi}[5+(1+4m_i/m_I)(n_I Z_I^2/n_i Z_i^2)]/2u^3 \quad . \tag{2}$$

Since the average ion velocity $\bar{v}_{iz}$ is derived from $G_i=m_i n_i \bar{v}_{iz}$, we can estimate the RF power necessary for driving the plasma velocity up to $\bar{v}_{iz}/v_{Ti}$. In the case of deutron main-ion, the result is given by Eqs.(1) and (2) as

$$P_d = (1.0\times10^8)\frac{5+(1+8m_p/m_I)n_I Z_I^2/n_i}{2u(\delta u+3w)} T_{10}^{-1/2} n_{14}^2 \left(\frac{\bar{v}_{iz}}{v_{Ti}}\right) \quad W/m^3 \tag{3}$$

where $w=v_z/v_{Ti}$, $u=v/v_{Ti}$, m_p is the proton mass, the ion temperature T_{10} is normalized to 10 keV, and the density n_{14} is normalized to 10^{14} cm^{-3}. The resonant velocity is usually set in the range $3<w<7$. To get more simple expression we assume $w\simeq u\simeq 5$ and the trace-impurity limit $n_I Z_I^2/n_i Z_i^2 \ll 1$.

The latter assumption is valid for argon and iron in ISX-B tokamak and for tungsten in PLT. Then we have $P_d=(3.3\times10^6)(T_{10}^{-1/2})(n_{14}^2)(\bar{v}_{iz}/v_{Ti})$ W/m^3 for the energy input type(δ=0). For example, the dissipated power 330 kW/m^3 for T_{10}=1 and n_{14}=1 yields the plasma velocity $\bar{v}_{iz}/v_{Ti}$=0.1, which is comparable to or greater than the thermal velocity of heavy impurities. The neoclassical theory/1/ has shown outward transport of impurities when the velocity of toroidal rotation of the plasma exceeds the impurity thermal velocity. Thus, the cross-field transport of impurities can be controlled by the toroidal rotation induced by the acceptable RF power.

In practice, there are several possibilities to realize the wave-ion interactions. Among them, the most promising one is the ICRF heating at the second cyclotron harmonic($\omega\simeq2\Omega_M$), since the waveguide can be used as the wave launcher. The waveguide is very convenient structure for bringing the fast wave into the plasma without introducing the impurities from the launcher. In the ICRF heating, the wave-ion interaction can be regarded as the energy input type where no parallel momentum is injected. The momentum of resonant main ions is destroyed dominantly by the bulk main ions in the trace impurity limit. By the momentum conservation, the bulk main ions must drift, in the opposit direction to the resonant main ions, with the magnitude $\bar{v}_{iz}$ appeared in Eq.(3). This means that, strictly speaking, the average ion velocity vanishes if the velocity is integrated all over the distribution function of the main ion. In the impurity transport problem, however, the bulk main ions act as the dominant friction source for impurities since they are very slow and dense compared with the resonant main ions. Thus, we regard the "average" velocity $\bar{v}_{iz}$ in Eq.(3) as the "effective" rotation velocity.

In the present day tokamak experiments, the ICRF heating at the second harmonic has not been established yet. Another ICRF heating called two-ion hybrid resonance(minority ion) heating has been understood rather well. So, it is interesting to check the possibility of the plasma rotation by the minority ion heating. Suppose the minority protons introduced in the plasma containing impurities. The region of interest here is the resonant proton velocity v_z in the range v_{Ti}, $v_{Tp}\ll v_z\ll v_{Te}$, where $v_{Tp}=(T_p/m_p)^{1/2}$ is the proton thermal velocity. The similar calculations provide the RF power necessary for the rotating velocity $\bar{v}_{iz}/v_{Ti}$ as

$$P_d = (5\times10^7)\frac{(1+4\ 10^{-3}u^3)^2}{wu}T_{10}^{-1/2}n_{14}^2\left(\frac{\bar{v}_{iz}}{v_{Ti}}\right) \quad W/m^3 \qquad (4)$$

where $w=v_z/v_{Tp}$ and the temperature are assumed to be $T_e=T_i=T_p$. For example, $w\simeq u\simeq5$ yields $P_d=(4.5\times10^6)(T_{10}^{-1/2})(n_{14}^2)(\bar{v}_{iz}/v_{Ti})$ W/m^3, which is comparable to the value for the second harmonic ICRF heating.

In conclusion, the indirect method of RF divertor comprises three steps. The first is the wave energy deposit to the resonant main ions via ICRF heating. The second is the toroidal plasma rotation induced by asymmetric friction as the result of heating. The third step is to expel the impurity out of the plasma via the rapid plasma rotation. The estimation of the dissipated power supports the practicality of this scheme in a tokamak reactor.

3. DIRECT METHOD ——— "Impurity Heating and Impurity-Flux Drive" ———

In terms of collision freuency ν_I and Larmor radius ρ_I, the diffusion constant of the impurity ion is approximately expressed as $D_I \simeq \nu_I \rho_I^2$, which is a function of the impurity-ion temperature T_I. In a scrape-off layer or near the divertor plate, impurity-ion collisions with neutrals are frequent, and hence $D_I \propto T_I^{3/2}$. In a plasma core or periphery, the collisions with main ions or other impurity ions are dominant, and so $D_I \propto T_I^{-1/2}$. Also, the diffusion caused by toroidal ripple is characterized as $D_I \propto T_I^{7/2}$. Therefore, the RF impurity-ion heating diminishes the Coulomb-collision diffusion, while it enhances the neutral-collision and the ripple diffusion. Thus, the RF heating is an effective method controlling the impurity flux. Recent model experiments in TFR/5/ have demonstrated this divertor effect.

Without heating the impurity, the stationary cross-field impurity flux can be driven by the waves: the wave poloidal momentum G_{pol} is deposited to the impurity ions, and they are driven radially outward by the $\dot{G}_{pol} \times B_{tor}$ drift. This is an application of RFFC /6/ to the impurity control. Also, the wave toroidal momentum G_{tor} can be used via the $\dot{G}_{tor} \times B_{pol}$ drift of the impurity ions. The wave momentum in the radial direction never induces the radial particle flux unless the dissipation is present/7/[in Reference 2, the second order term $\langle n_0 v_2 \rangle$ was missed, which cancels out the term $\langle n_1 v_1 \rangle$].

The above direct method(impurity heating or non-heating) assumes that the wave energy(momentum) is selectively deposited to the impurity rather than the main ion. In order to realize this assumption, we adopt the wave propagating at the frequency $\omega \simeq \Omega_I$(impurity-ion cyclotron frequency). For example, the ion Bernstein wave has the large energy(momentum) around the ion-ion hybrid frequency($\sim\Omega_I$), which is dominantly absorbed by the impurity ion in the cyclotron damping process.

This work was supported by a Grant-in-Aid for Scientific Research of the Ministry of Education, Science and Culture in Japan.

/1/ Burrell, K.H., Ohkawa, T., and Wong, S.K.: Explanation of the expulsion of impurities from tokamak plasmas by neutral-beam injection, Phys. Rev. Lett. 47 (1981) 511-515.
/2/ Sugai, H.: Radio frequency control of impurity transport, Phys. Lett. 91A (1982) 73-76.
/3/ Sugai, H.: Rotating a tokamak plasma with waves for impurity control, Phys. Lett. 93A (1983) 483-486.
/4/ Fish, N.J., and Boozer, A.H.: Creating an asymmetric plasma resistivity with waves, Phys. Rev. Lett. 45 (1980) 720-722.
/5/ TFR Group: Impurity pump-out at the two-ion hybrid resonance during ICRF experiments in TFR tokamak plasmas, Nucl. Fusion 22(1982) 956-961.
/6/ Itoh, K., and Inoue, S.: Radiofrequency flux control of toroidal plasmas, Comments Plas. Phys. Con. Fusion 5 (1980) 203-212.
/7/ Nishikawa, K., private communications.

The Transport of Impurity Ions in a Scrape-off Plasma

P.J. Harbour and J.G. Morgan
Culham Laboratory, Abingdon, Oxon, OX14 3DB, UK
(Euratom/UKAEA Fusion Association)

In the vicinity of a limiter or divertor target a local maximum in plasma density can occur if there is sufficient recycling to cause local cooling and acceleration of the plasma. It has been argued, using the Boltzmann relation, $n=n_0\exp(eV/kT_e)$, that there is a maximum in the plasma potential at the position of maximum density. It has then been inferred that impurity ions formed upstream of the maximum may be prevented by the electric field from reaching the limiter or target. The basis of this argument is incorrect /1/. In this paper we use a two-fluid model for parallel flow /1,2/ and observe that the electric field, E, in the z-direction (parallel to $\underline{B}$) depends not only on the density gradient but also on longitudinal temperature gradients, particle sources, and viscosity /1/. The effect of temperature gradients can be such that in many cases there is no reversal of the electric field, even though there is a density maximum.

The transport of impurity ions in a flowing scrape-off plasma is governed by forces similar to those on the hydrogen ions. These may be appreciated by considering the ion momentum equation /3/ used by the authors /2/ to study a pure D-T plasma,

$$m_i n_i v_i dv_i/dz = -dp_i/dz + d(n_i dv_i/dz)/dz + en_i E + 0.5lm_e n_e \tau_e (v_e - v_i) + 0.7ln_e dT_e/dz, \quad (1)$$

where particle and momentum sources have been neglected. The notation is as in /2/. The force on an impurity ion may be written:

$$F = m_I v_I dv_I/dz = F_p + F_\eta + F_E + F_\mu + F_{TD}, \quad (2)$$

where F_p is the force on the ion due to the gradient in ion pressure, F_η the

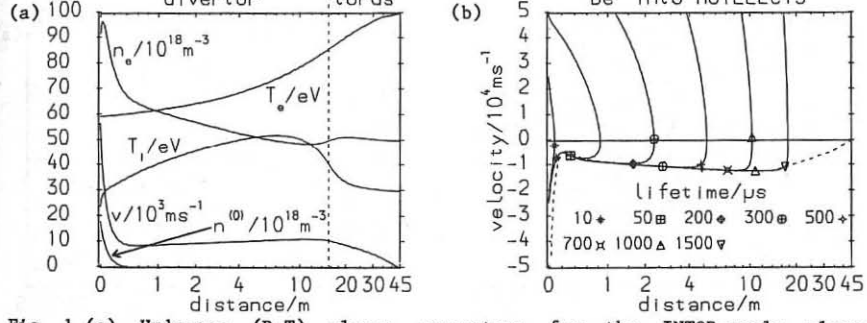

Fig. 1 (a) Hydrogen (D-T) plasma parameters for the INTOR-scale plasma "HOTELEC13" /1/. Please note the non-uniform distance scale. (b) Velocities of Be^+ ions in the same plasma (no thermal diffusion). The broken line represents the velocity at which $F_E+F_\mu=0$.

viscous force, F_E the electric force, F_μ the force due to friction between the ion and the flowing plasma, and F_{TD} the thermal diffusion force due to temperature gradients in the plasma. The terms on the right hand side of Eq.2 are analogous to those on the r.h.s. of Eq.1, but their coefficients differ both in magnitude and parametric dependence. Equation 2 is frequently simplified by neglecting the l.h.s. and also F_η and F_{TD} /4,5/ and even F_E /5/. Ohyabu /6/ has considered F_{TD} and Neuhauser et al /7/ have developed a numerical model which includes all terms except F_η. In this paper we show that every term in Eq.2 can be important if there is a high degree of recycling. We confine our attention to a scrape-off plasma described by the authors /1/, who investigated a model poloidal divertor with dimensions similar to those of the INTOR reactor. The scrape-off plasma measured 15m along the field in the divertor ($0 \leq z \leq 15$m) and 30m along the field in the torus ($15\text{m} \leq z \leq 45$m). The plasma parameters found for a pure hydrogen (D-T) plasma are shown in Fig. 1(a). The recycling coefficient for this particular run, called "HOTELEC13", was 0.90 /1/. This plasma solution was chosen because there is a region ($0.04\text{m} \leq z \leq 1\text{m}$) where the electric field points away from the target.

TRANSPORT OF LIGHT IONS

Taking Be^+ as representative, we now consider the influence of the various forces on a single test ion ($F_p \equiv 0$). Fig. 1(b) shows the variation of ion velocity with position. The method of obtaining these results will be described separately /8/. The dashed curve shows the predictions when Eq.2 is written $F_E+F_\mu=0$, other terms being ignored. The continuous curves were obtained by "launching" a Be^+ ion into the plasma from z=0 and including the effect of ion inertia. The launch velocities were chosen to allow the velocity-position phase space to be explored fully, thus representing particle sources wherever they may occur in the scrape-off layer. F_E was obtained using the electron momentum equation for E with $F_E=ZeE$. The frictional force, F_μ, was derived allowing $T_I \neq T_i$ and not relying on $|v_I - v| \ll \sqrt{[k(T_e+T_i)/m_i]}$. We only expect thermal equilibration between the test ion and the flowing plasma once momentum equilibrium has been established, and then an accurate expression for F_μ is not very important.

The velocity v_I, represented by the dashed line in Fig. 1(b), differs in several respects from the hydrogen velocity shown in Fig. 1(a), indicating the

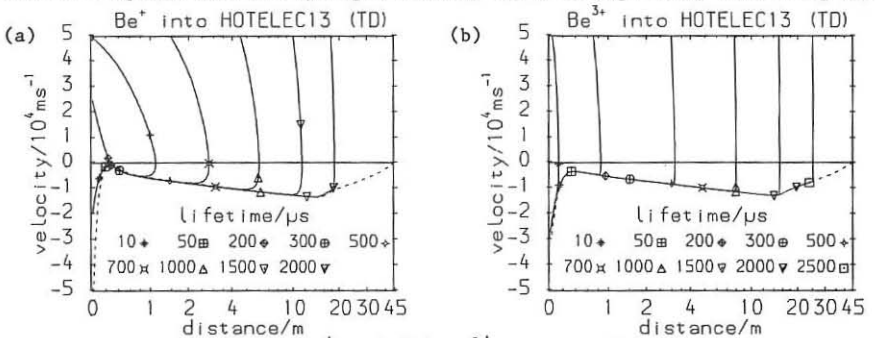

Fig. 2 Velocities of (a) Be^+ and (b) Be^{3+} ions in the plasma of Fig. 1(a) (with thermal diffusion). The broken lines represent the velocity at which $F_E+F_\mu+F_{TD}=0$.

importance of the reversed electric field for light, singly charged ions. When inertia is included the Be^+ ions take about 100μs to accelerate from rest up to the equilibrium (inertia-free) slip speed over a distance of the order of 0.5 to 1m. Evidently inertia is unimportant except within the recycling region where the scale length is 0.1m and the transit time is <100μs. As a consequence Be^+ ions are accelerated to only 24km/s at the target sheath where the hydrogen plasma speed reaches 57km/s. The energy gained by the Be^+ ion as it is driven by friction towards the target, ΔE_I, is roughly proportional to the energy of the flowing hydrogen ions and to $\ell_o Z^2/\lambda_{ii}$, provided $v_I \ll v$. Here ℓ_o is the length of the recycling region, measured in the z-direction. Although for Be^+ ΔE_I is low (~25eV in this case), it may be much larger for the more highly charged states of heavy ions.

The thermal diffusion force, F_{TD}, obtained from Chapman /9/, tends to drive impurity ions towards regions of high temperature. Fig. 2(a) shows velocities of a Be^+ test ion moving under the influence of F_E, F_μ and F_{TD}. The dashed curve (no inertia) shows that at z≈0.25m the speed of the test ion is very low, i.e. a significant slip velocity, $v-v_I$, is required to allow F_μ to cancel F_{TD} and F_E, both of which point upstream at this point. When inertia is included (solid curves) the speed is again low at z≈0.25m and it now increases to only 19km/s at the target sheath, indicating the significance of thermal diffusion.

The test ion approach is only valid if the ion under consideration is present in the plasma for periods shorter than a few times the ionisation time, τ_{ion}. For Be ions in a plasma of density $9.5\times10^{19}m^{-3}$ and T_e=60eV values of τ_{ion} (in μs) are /10/

$$Be \xrightarrow{0.01\mu s} Be^+ \xrightarrow{0.8\mu s} Be^{2+} \xrightarrow{140\mu s} Be^{3+} \xrightarrow{1100\mu s} Be^{4+}.$$

Clearly, Be^{3+} and Be^{4+} can readily be produced from particles starting from rest at z>10m. Representative velocities for more highly charged ions (Be^{3+}) are plotted in Fig. 2(b). Here the minimum speed is about 4km/s at z≈0.4m, indicating the diminishing influence of the electric field for ions of increasing Z. ($F_E \sim Z$ but all other forces $\sim Z^2$.) The inertia of Be^{3+} is evidently negligible and this ion reaches 29km/s at the target sheath. Other light ions behave similarly, i.e. they are swept into the divertor chamber by the plasma and travel smoothly to the target.

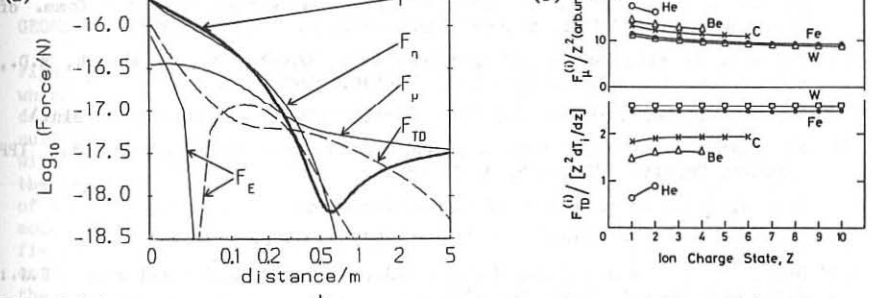

Fig. 3 (a) The forces on a W^+ ion at rest in the plasma of Fig. 1(a). Broken lines represent forces away from the target. (b) The variation with ion charge and mass of the coefficients of F_μ/Z^2 (arbitrary units) and F_{TD}.

TRANSPORT OF HEAVY IONS

As the atomic mass increases we find that at the upstream end of the recycling region (z=0.6m) there is a tendency for $|F_{TD}+F_E|$ to exceed F_μ even when $v_I=0$. Under these conditions stagnation may occur and the test ion approach would appear to break down because impurity ions would accumulate until F_p may become significant. However this might not happen for two reasons, firstly we have not included the viscous force F_η and secondly the Chapman coefficient for the thermal diffusion force is about 20-30% too high /11/. In Fig. 3(a) we show F_η, F_E, F_μ and F_{TD} (the last being the Chapman value /9/) evaluated for W^+ ions in "HOTELEC13". The viscous force was scaled from Braginskii /3/ by writing

$$F_\eta = (Z^2/n)d(n_i dv_i/dz + n_e dv_e/dz)/dz. \qquad (3)$$

It is greatest for z<0.6m. At 0.6m all the forces compete with each other and the net force F is rather small. Further upstream F increases again, mainly because of friction, and so heavy impurities are expected to be well confined within the divertor.

Fig. 3(b) shows the variation of the coefficients of F_μ and F_{TD} with charge state. The thermal diffusion force increases with ionic mass and the frictional force decreases, agreeing with our findings that for heavy ions F_{TD} may possibly cause a density increase within the divertor, but light ions flow smoothly to the target. It is worth mentioning that when the plasma temperature is lower than in "HOTELEC13" or when there is less recycling, the frictional force is relatively more important than all other forces and pressure build-up of heavy ions does not occur in any of several model plasmas we have considered.

/1/ Harbour, P.J., and Morgan, J.G.: Culham Report, CLM-R234, Dec. 1982.

/2/ Morgan, J.G., and Harbour, P.J.: Fusion Technology 1980. Pergamon 2(1981) 1187-1194.

/3/ Braginskii, S.I.: Rev. Plasma Phys. 1(1965) 205-311.

/4/ Lackner, K., Neuhauser, J., Schneider, W., and Wunderlich, R.: Impurity flow parallel to the magnetic field in the scrape-off layer. In: Section VI.5.5 of Eur. Contr. to INTOR Phase IIA Workshop, Vol. II. Comm. of Eur. Communities DGXII, Brussels Dec. 1982, p. VI-304 to 309.

/5/ Mahdavi, M. Ali, DeBoo, J.C., Hsieh, C.L., Ohyabu, N., Stambaugh, R.D., and Wesley, J.C.: Phys. Rev. Lett. 47(1981) 1602-1605.

/6/ Ohyabu, N.: Nucl. Fusion 21(1981) 519-528. (See also ref. 13 therein.)

/7/ Neuhauser, J., Schneider, W., Wunderlich, R., and Lackner, K.: IPP Garching Report, IPP 1/216, April 1983.

/8/ Morgan, J.G.: to be submitted for publication.

/9/ Chapman, S.: Proc. Phys. Soc. LXXII(1958) 353-362.

/10/ Bell, K.L., Gilbody, H.B., Hughes, J.G., Kingston, A.E., and Smith, F.J.: Culham Report, CLM-R216, Dec. 1981.

/11/ Roussel-Dupré R.: Astrophys. J. 243(1981)329-343.

NUMERICAL STUDIES OF THE TWO-DIMENSIONAL SCRAPEOFF PLASMA

B J Braams
FOM-Instituut voor Plasmaphysica "Rijnhuizen"
P.O. Box 7, 3430 AA Nieuwegein, The Netherlands
(Present address: Max Planck Institut für Plasmaphysik
D-8046 Garching bei München, F.R. Germany)

INTRODUCTION

For the operation of existing large Tokamaks and for the design of future machines an understanding (experimental, theoretical, and numerical) of the transport of particles and energy through the plasma scrapeoff layer is increasingly important. In particular the present knowledge of the profile of energy deposition on the walls and plates, of Helium pumping characteristics, and of the control of wall-produced impurities is insufficient. Most work on plasma transport to date has focussed on the region of closed flux surfaces with uniform properties and studied only the one-dimensional radial diffusion and conduction. A numerical fluid model for the edge plasma must match these transport processes, which are dominant inside the separatrix, to the flow and the thermal conduction along open field lines onto a material boundary and such a model must therefore be at least two-dimensional. It should also not neglect recycling through neutral particles and energy loss by radiation. Models which approach these aims have been presented by Emery and Windsor /1/, and by Petravic, Post, et al. /2/. The model which is the subject of this paper shares these aims.

Our system of equations describes density, two temperatures, flow, and diffusion of a plasma consisting of electrons and a single ionic species. The parallel and perpendicular thermal conductivities of electrons and ions are all finite and non-zero, and viscosity and thermal equilibration are also included. Fairly general boundary conditions are allowed. The main limitation of this work in comparison with that of ref. /2/ is the rather ad-hoc treatment of processes involving neutral particles, but on the other hand the important two-dimensional fluid dynamic aspects of the problem are included here.

GEOMETRY AND PHYSICS EQUATIONS

Figure 1 shows a projection into the poloidal plane of the sort of region which we are modelling (shaded). This drawing is for the ASDEX Upgrade design /3/, showing a double null configuration on the left and a single null on the right. The model will represent a pseudo rectangular region with the same gross parameters as the actual physical region, simplifying the geometry of the wall so that it follows a flux surface. The variation of the scrapeoff layer thickness with poloidal angle is retained in the model, as is the area change which is associated with the variation along a field line of the magnitude of the magnetic field. The region is mapped onto the x-y plane with the magnetic field lines along the x-coordinate and the radial direction along the y-coordinate.

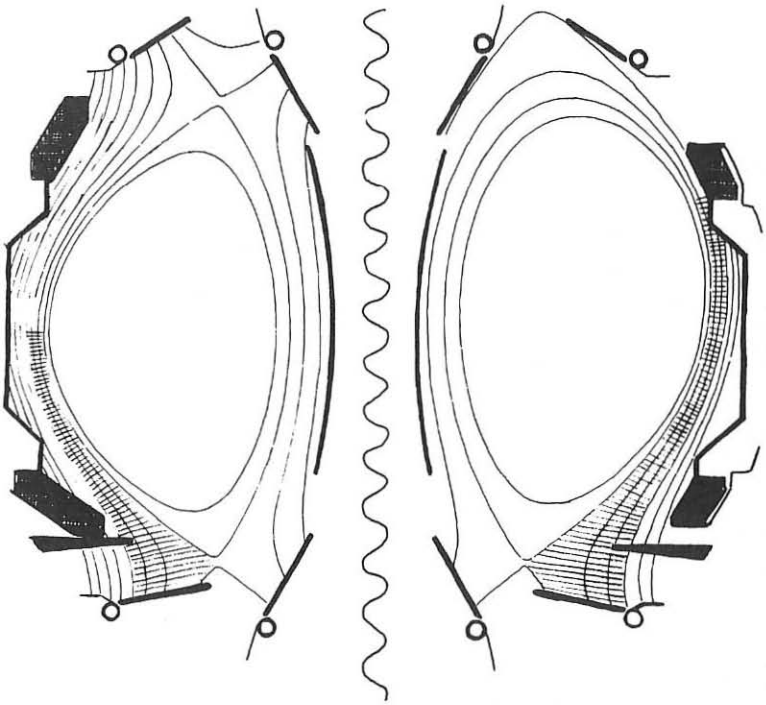

Fig. 1 ASDEX-Upgrade Edge Configurations

The plasma is specified by the variables n_i, u, v, T_e, T_i, which satisfy in rectangular geometry these equations ..

$$\frac{\delta}{\delta t}n_i + \frac{\delta}{\delta x}(n_i u) + \frac{\delta}{\delta y}(n_i v) = S_n \qquad (1)$$

$$\frac{\delta}{\delta t}(\rho u) + \frac{\delta}{\delta x}(\rho u^2 - \eta_x \cdot \frac{\delta}{\delta x}u) + \frac{\delta}{\delta y}(\rho vu - \eta_y \cdot \frac{\delta}{\delta y}u) = S_p - \frac{\delta}{\delta x}p \qquad (2)$$

$$v = \text{"some } f(x, y, n_i, T_e, T_i, \frac{\delta}{\delta y}n_i, \frac{\delta}{\delta y}T_e, \frac{\delta}{\delta y}T_i)\text{"} \qquad (3)$$

$$\frac{\delta}{\delta t}(\frac{3}{2}n_e T_e) + \frac{\delta}{\delta x}(\frac{5}{2}n_e u T_e - K_x^e \cdot \frac{\delta}{\delta x}T_e) + \frac{\delta}{\delta y}(\frac{5}{2}n_e v T_e - K_y^e \cdot \frac{\delta}{\delta y}T_e) = \\ = S_E^e - k.(T_e - T_i) \qquad (4)$$

$$\frac{\delta}{\delta t}(\frac{3}{2}n_i T_i + \frac{1}{2}\rho u^2) + \frac{\delta}{\delta x}(\frac{5}{2}n_i u T_i + \frac{1}{2}\rho u^3 - K_x^i.\frac{\delta}{\delta x}T_i) + \\ + \frac{\delta}{\delta y}(\frac{5}{2}n_i v T_i + \frac{1}{2}\rho v u^2 - K_y^i.\frac{\delta}{\delta y}T_i) = S_E^i + k.(T_e - T_i) \quad (5)$$

S_n, S_p, S_E^e, and S_E^i are volumes sources of ions, momentum, electron energy and ion energy, e.g. from ionization and radiation. On a curvilinear orthogonal grid (still with the magnetic field along the x-coordinate), the equations are modified through the introduction of scale factors h_x and h_y and the inverse Jacobian $\sqrt{g}$. ($\sqrt{g} = h_x h_y h_z$.) For any divergence substitute

$$\frac{\delta}{\delta x}J_x + \frac{\delta}{\delta y}J_y \rightarrow \frac{1}{\sqrt{g}}.\frac{\delta}{\delta x}(\sqrt{g}.J_x/h_x) + \frac{1}{\sqrt{g}}.\frac{\delta}{\delta y}(\sqrt{g}.J_y/h_y) \quad (6)$$

and for any gradient

$$(\frac{\delta}{\delta x}f, \frac{\delta}{\delta y}f) \rightarrow ((1/h_x).\frac{\delta}{\delta x}f, (1/h_y).\frac{\delta}{\delta y}f) \quad (7)$$

Diamagnetic gradients are neglected in the above set of equations, as is the Coriolis force in the momentum equation. This work has considered only steady state solutions, so (d/dt) is dropped from the equations. A more complete set of transport equations for the edge plasma is given by Singer and Langer, ref. /4/.

The boundary conditions which may be specified are either the values of the fields, or the fluxes, or relations between the two. Usually we have specified at the interface with the main plasma the value of the ion density and of the electron and ion energy fluxes; at the upstream end of the flow symmetry conditions (i.e. zero flow velocity and zero gradients along the field); at the downstream end a Mach number and the ratios between conducted and convected energy flows, and at the outer wall zero transverse diffusion and some low value for the temperatures. Either a no-slip condition or a zero transverse gradient is prescribed for the flow velocity along the wall and on the interface with the main plasma.

Recycling from the divertor plate is modelled without the use of a Monte Carlo neutral particles code by reintroducing as a localized volume source some fraction of the particles and energy which leave the computational region.

COMPUTATIONAL MODEL

The variables of the system are represented on a staggered rectangular grid. Density and electron- and ion temperatures are defined on cell centres, and the velocities on cell interfaces. The metric coefficients for the grid may be non-uniform, and are defined on all cell centres, thereby allowing to model a curvilinear region. The general approach for the discretization and solution is that of D B Spalding's school and ref. /5/. An implicit pressure correction procedure is employed for the solution of the continuity equation. With this procedure the density and two velocities are simulataneously adjusted to satisfy continuity, the adjustments being coupled through relations which are derived from the equations for the velocities. The pressure correction equation, the momentum balance equation, and the two energy equations are all of standard convection - conduction form. These equations are discretized via the

finite volume method, employing an upstream weighting technique to obtain a stable and second order accurate discretization. The values of the coefficients change gradually from those corresponding to a central difference scheme at low cell Reynolds or Péclet number to those for an upwind scheme with no conduction at high cell Re or Pé. The computational boundary conditions correspond to four insulating walls; the boundary conditions for the physical system are imposed by the choice of source terms in the outer rim of cells.

The system of equations is solved in a cyclic fashion, discretizing and relaxing each equation in turn. The strong coupling between the two temperatures is dealt with by using not Eq. (4) but the sum equation (4) + (5) to relax the electron temperature. An Incomplete L*U decomposition is used on each of the five-point equations. The convergence is monitored by following the residuals of the equations and the magnitude of the corrections. Although the discretization is fully implicit it is found neccesary to use under-relaxation or time stepping, particularly to obtain solutions with high recycling.

RESULTS

To date only exploratory runs with the code have been made. Present interest is in a geometry and boundary conditions which are relevant to the single null configuration of ASDEX Upgrade (density at interface with main plasma of $5*10^{19}$ and 0.3 MW/m^2 radial energy transport). Results under various assumptions about recycling will be reported at the conference.

Acknowledgements

I am deeply indebted to M F A Harrison and the Exhaust Physics Group (Culham) and to K Lackner and the Tokamak Theory Group (Garching) for many fruitful discussions and for their hospitality. This work was performed under the Euratom-FOM association agreement with financial support from ZWO and EURATOM.

References

/1/ Emery, M.H. and Windsor, N.K.: A Fully Two-Dimensional Equilibrium and Transport Model of the Poloidal Divertor. NRL Memorandum Report 4498, Naval Research Laboratory (1981)

/2/ Petravic, M., Post, D.E., Heifetz, D., and Schmidt, J.A.: Cool, High Density Regime for Poloidal Divertors, Phys. Rev. Lett. 48 (1982) 326-3

/3/ ASDEX Upgrade Design Team and Tokamak Theory Group: ASDEX Upgrade, Definition of a Tokamak Experiment with a Reactor-Compatible Poloidal Divertor. Reports IPP 1/197 and 1/211, Max Planck Institut fur Plasmaphysik (1982)

/4/ Singer, C.E. and Langer, W.D.: Axisymmetric Tokamak Scrapeoff Transport, Report PPPL-1920, Princeton Plasma Physics Laboratory (1982)

/5/ Patankar, S.V.: Numerical Heat Transfer and Fluid Flow. Hemisphere, New York 1980.

A Comparison of Impurity Levels in JET with Nickel, Carbon and Beryllium Limiters

S.J. Fielding and G.M. McCracken
Culham Laboratory, Abingdon, Oxon. OX14 3DB, England
(Euratom/UKAEA Fusion Association)

1. INTRODUCTION

The processes producing impurities in tokamaks are still not well understood, nor easy to predict in new machines. However, it is clear that sputtering must be minimised. A model has recently been proposed which discusses sputtering in terms of global parameters[1]. The impurity level is determined by a self-consistent energy balance between the input power, the power radiated and the power conducted out. This model has been used as the basis for comparison of three different limiter materials, nickel, carbon and beryllium. Although some plasma parameters such as particle confinement time are difficult to predict, the model allows the impurity behaviour to be readily compared under a wide range of different conditions, including varying density and additional heating. The effect of different levels of other impurities such as oxygen can also be estimated.

2. THE MODEL

The model has been described in detail previously /1/. The steady state impurity concentration due to sputtering is given by

$$\frac{n_m}{\tau_m} = \eta \left(S_p \frac{n_p}{\tau_p} + S_L \frac{n_L}{\tau_L} + S_n \frac{n_m}{\tau_m} \right) \qquad (1)$$

where S_p, S_L and S_m are the sputtering coefficients of the plasma, light impurities and impurities from the limiter, n_p, n_L, n_m are their concentrations and τ_p, τ_L and τ_m are their containment times. η is a screening coefficient determining the fraction of sputtered atoms which return to the discharge. It is assumed in the model that impurities are sputtered only by charged species at the limiters; sputtering and energy loss by charge exchange neutrals are neglected. The sputtering coefficients can be obtained from the empirical formulae proposed by Bohdansky, provided that the ion energy E is known. This is taken to be $E = 2kTe(a) + 4qkTe(a)$ where q is the charge state of the ions and Te(a) is the temperature at the plasma boundary. Te(a) can be obtained from a global power balance, where the power, P_c, transported out by particles at the plasma boundary is given by the difference between the total heating power P_H and the radiated power P_R

$$\text{i.e. } P_H - P_R = P_c = e\gamma Te(a)\ Vn_p/\tau_p \qquad (2)$$

where V is the plasma volume and γ is the factor determining the energy lost per ion-electron pair (normally in the range 5 - 10). In these calculations an average ion model /2/ has been used for calculating the power radiated, and we have assumed constant plasma and impurity density profiles and a parabolic temperature profile with an edge pedestal, Te(a). Equations (1) and (2) can then be solved self consistently to give unique values for n_m and Te(a), for a range of values of n_e, τ_p.

Results

The radiation is only weakly dependent on central temperature over the range 4 - 20 keV, and a value of 10 keV has been used for all the calculations. The confinement time τ_p is a critical parameter, whose value in JET is uncertain and we have used it as a variable parameter. It has been assumed that all ion species have the same confinement time. η has been taken to be 0.5, and the total power input to be 25 MW.

3.1 Nickel

The qualitative form of the results for nickel, fig. 1, are similar to those obtained previously for INTOR /1/. For long confinement times and low densities the impurity content builds up to near the radiation limit. For example, with $\tau = 0.1$ s and $n_e = 3 \times 10^{13}$ cm^{-3}, the metal density is approaching 1% of n_e, over 90% of the power is radiated, and edge temperature is $\sim$ 20 eV. At lower densities, the edge temperature increases and impurity self-sputtering begins to dominate.

When the density is increased or the confinement time is decreased, the edge temperature is reduced until the ion energy falls below the sputtering threshold temperature, T_c. The impurity level then falls to zero. From fig.1 it is seen that this corresponds to an edge temperature of about 8 eV. The value of density at which this happens is obtained from equation (2).

$$T_e(a) = \frac{P_H \tau_p}{e\, V n_e} < T_c \ .$$

Thus a rough scaling of the curves for different input powers and containment times can be obtained. It is clear that it is a considerable advantage to operate at as high a density as possible. Murakami scaling leads to a maximum density in JET of $\leq 10^{14}$ cm^{-3}. From fig. 1 this means that an effective containment time for plasma ions of ≤ 10 ms is required.

3.2 Carbon

The results for carbon are similar to those for nickel except that the curves are shifted to higher density, fig. 2. At low densities the edge temperature rises and the ion energy increases above the maximum in the sputtering yield curve and hence the impurity concentration decreases. The realisation of such a condition in practice is doubtful since this leads to extremely high sheath potentials and it is likely that arcing would result. For $\tau \geq 0.01$ secs, over most of the density range of interest the carbon impurity level is apparently increasing with plasma density. This is because, firstly, there is no significant amount of radiation from carbon and secondly that the ion energy at which the maximum sputtering yield occurs is lower for carbon than for nickel. Thus as the density is raised, the edge temperature decreases making the sputtering coefficient increase. However, in no case does the impurity content exceed 2%, when considering physical sputtering only. If we introduce enhanced sputtering due to chemical effects, for $\tau = 0.01$ s the carbon concentration increases to 20% over most of the density range of interest. The radiation is only high enough to effect the edge temperature for the longest containment time used (0.1 s). However, the high carbon concentration would cause significant fuel dilution of the plasma.

3.3 Beryllium

The situation for beryllium is very similar to that for physical sputtering on carbon, fig. 3. The radiation is even lower because of the lower z.

However, since in most cases the radiation from carbon is already negligible, the edge electron temperature is in fact the same for a given containment time and density over most of the range of interest. The high density cut-off is lower for beryllium than for carbon simply due to the higher energy threshold for sputtering of beryllium. As with physical sputtering on carbon the maximum impurity concentration is less than 2%. This value is determined by the numerical value of the sputtering yield in the absence of self-sputtering, as is seen from equation (1).

3.4 Effect of Oxygen

Oxygen is an ever present impurity in tokamaks and we must thus consider the effect of it on the boundary layer. Oxygen appears to recycle at the wall so that the level is relatively constant during a discharge. If we introduce a fixed level of oxygen we can calculate the steady state concentration of the wall material in the plasma, taking into account sputtering by the plasma, by oxygen and self sputtering. Results are shown in fig. 4. As the oxygen concentration is increased the wall material concentration can also increase due to the increased sputtering by the oxygen atoms. At this point the oxygen concentration is too low to effect the total radiation significantly. As the oxygen concentration increases further the radiation level increases, the edge temperature drops and the wall sputtering drops.

4. DISCUSSION AND CONCLUSION

There are two main objectives to such modelling. The first is to find out how the sputtering of a multi-component mixture behaves, in particular how the presence of light gaseous impurities (e.g. O + C) can effect the level of limiter sputtering. The second is to see how the global plasma parameters affect the impurity level, e.g. the density, the power input and the particle containment times. In order to minimise sputtering the average energy of the particles leaving the plasma i.e., $\tau_p P/n_e$, must be reduced. If the conventional plasma limits hold in JET i.e. $n_e \leq 10^{14}$ cm^{-3}, then for nickel limiters and an input power of 25 MW a containment time for particles recycled from the wall must be $\leq$ 10 ms. For carbon, considering physical sputtering, this restriction is eased considerably. A value of $\tau_p \leq 0.1$ s would be tolerable. However, since so little power is radiated inevitably more will fall on the limiters. Thus high limiter temperatures and chemical sputtering are likely to present a problem. Calculations using the appropriate sputtering yields again indicate that τ_p is $\leq$ 10 ms. For beryllium limiters the radiation is negligible even at $n_e = 10^{14}$ cm^{-3}. This means that no effective limit is put on the plasma containment time τ_p, provided that the impurity and plasma containment times are equal. We then have that the maximum impurity concentration is numerically equal to the sputtering coefficient i.e. $\sim$ 2%. The effect of sputtering by oxygen impurities has also to be considered. Considering a plasma density of 10^{14} cm^{-3} and the criteria that $P_R \leq 10$ MW then with nickel limiters the oxygen level must be less than 6×10^{11} cm^{-3}, with carbon limiters less than 1.3×10^{12}.

REFERENCES

/1/ G.M. McCracken, S.J. Fielding & H. Ohtsuka J. Nucl. Mat. 111, (1982) 396.
/2/ D.E. Post, R.V. Jensen et al At. Data Nucl. Data Tables 20, (1977), 397.
/3/ J. Bohdansky J. Nucl. Mat. 93/94 (1980) 44.

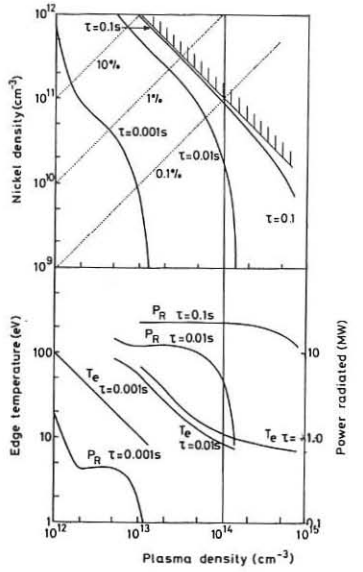

FIG. 1 Impurity level for nickel limiters

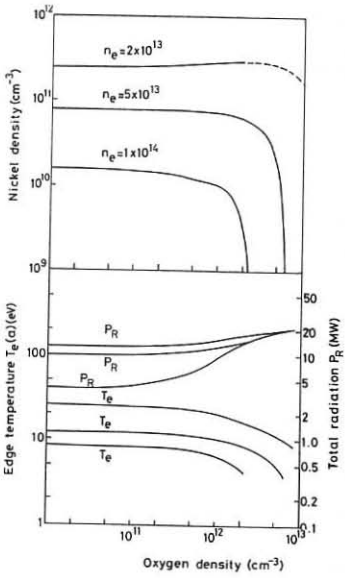

FIG. 4 Effect of oxygen

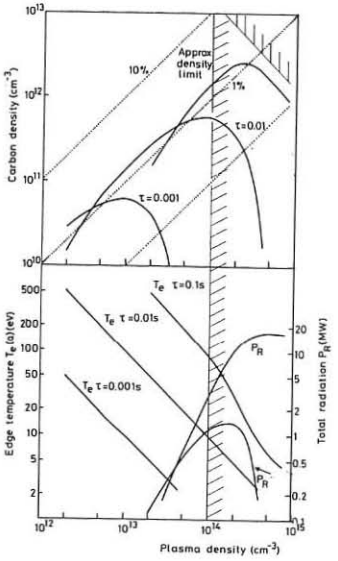

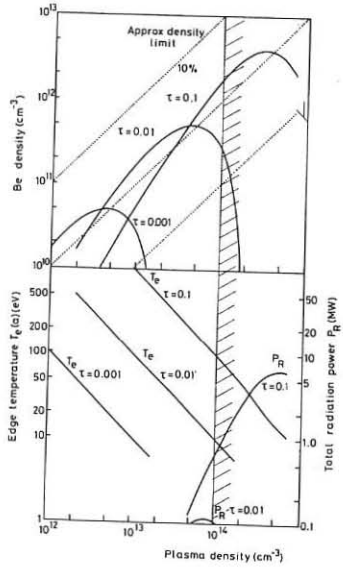

FIGS. 2,3 Impurity levels for carbon and beryllium limiters

EXHAUST OF HELIUM AND IMPURITY RELEASE IN INTOR WITH A DIVERTOR OR A PUMPED-LIMITER

M F A Harrison and E S Hotston
Culham Laboratory, Abingdon, Oxon OX14 3DB, UK
(Euratom/UKAEA Fusion Association)

1. INTRODUCTION

The single-null poloidal divertor and the toroidally symmetric pumped-limiter configurations of INTOR Phase IIA are sketched in Fig.1 and 2 respectively. The tips of the profiled limiter plate are displaced a distance X_t outboard of the separatrix in order that the local power loading $\geq 1 MW/m^2$. Sputter rates of the plasma collection surfaces and also the helium exhaust requirements are assessed here for a range of operating conditions in the main plasma. The predictions are based upon models of the boundary region /1/ whereas the main plasma is described only in terms of; (a) the uniform radial power flow $Q_\perp$ across the separatrix into the boundary and (b) the density at the separatrix. Self-sputtering by recycling ions of collector material and the behaviour of beryllium and tungsten collectors is considered.

2. PLASMA AND NEUTRAL PARTICLE TRANSPORT IN THE BOUNDARY REGION

The prescribed input of radial power flow $Q_\perp$ is balanced against the collisional transport of energy in the direction z along the open magnetic flux tubes which terminate at the plasma sheaths of the collection surfaces. Atomic losses due to the recycling of D/T, He and sputtered collector material are taken into account. The rate of energy deposition on the surface due to transport through the sheath can be expressed for fuel ions as

$$Q_t = n_t C_{s,t} A_{||,t} [(1 - R_E) (4Z + 2)kT_t + 2ZkT_t + x_i] \qquad (1)$$

where n_t and $C_{s,t}$ are the density and ion sound speed of plasma at the sheath edge, Z the ion charge state and $T_e = T_i = T_t$. $A_{||,t}$ is the effective area of the parallel flow channel. x_i is the ionisation potential of the ions. R_E is the energy reflection coefficient of the surface. Sputtering rates are determined using the assumption /3/ that the recycled impurity ions are Be^{3+} or W^{4+}.

The effective area $A_{||}$ of the parallel flow channel for a circular plasma can be expressed as $A_{||} = (2\pi\, a_s\, \Delta/q)$ where $a_s = 1.6m$ is the radius of the INTOR separatrix, Δ the scale-length of the radial profile of energy flow (assumed to be exponential) and q is the safety factor. The effective length of the channel is $L_{||} = [(\pi Rq) + L_D]$ where $R = 5.3m$ in the INTOR major radius and $L_D \approx 10m$ the length of the channel within the divertor. The INTOR plasma is elongated and it is necessary to allow for local variations in Δ with q and also for radial diffusion of plasma along the length L_D /1,2/. The power flow is assumed to be distributed equally to both the inner and outer plasma collection surfaces so that $Q_\perp = 2Q_{||} = 2[Q_t + Q_{(atomic\ losses)}]$. The effect of the temperature gradient dT/dz due to finite electron conduction is also taken into account. Plasma conditions n_t, T_t at the target are related to those at any upstream location z by

$$[n_t/n(z)] = [1 + M^2(z)]\ T(z)/[1 + M_t^2]\ T_t \qquad (2)$$

where the Mach number M is unity at the target where $z = L_{||}$; and $M(o) = 0$ where $z = 0$.

The modelling is one-dimensional in the direction z and Q_t, n and T relate to averages over the local radial extent Δ. This approximation is refined in the case of the limiter and separate flow channels are considered for the upper and lower surfaces respectively. The distribution of power is $2Q_{||}^U = Q_\perp\ \Delta[1 - \exp-(X_t/\Delta)]$ and $2Q_{||}^L = Q_\perp\ \Delta[\exp-(X_t/\Delta) - \exp-(X_w/\Delta)]$ where X_w is the spacing of the gap between the wall and the "Separatrix" and X_t is the spacing of the limiter tip.

Each plasma ion incident upon the collection surface causes the emission of either a fast backscattered atom or a detrapped, thermal energy neutral particle. These particles are assumed to have cosine distribution with respect to the surface and the average probability $\bar{P}$ for their escape from the plasma is determined on the basis of a random walk /1/. The probability F that the escaped particles pass down the ducting and are exhausted by the pumps is determined /2/ from a knowledge of the geometry of the INTOR system and the speed S of the pumps. The flow of gas that is pumped is

$$\Gamma^{(o)}_{(pump)} = N\left\{n_t\ C_{s,t}\ A_{||}\ \bar{P}/[\bar{1} - (1 - F)\bar{R}]\right\} \qquad (3)$$

where $\bar{R}$ is an average coefficient for reflection of neutral particles which re-enter the plasma /1/, N = 1 for the divertor and 2 for a double edged limiter /3/. In INTOR 2.10^{20} He atoms/s must be exhausted during steady state operation and it is also necessary to maintain a concentration $(n_{He}/n_{DT}) = 0.05$ within the scrape off region distant from the collector. The value of F determined from Eq.3 for these flows can be related to the vacuum pump speed $[S_{He}]_{5\%}$ for He gas at 300°K.

3. PREDICTED DIVERTOR PERFORMANCE

Data are presented here for the prescribed parameter /4/ $Q_\perp$ = 80MW and Δ (mid-outer-toroidal-plane) = 1.6 and 3.5 x 10^{-2}m. This density was varied from n(o) = 2.5 to an upper value 7.5 x $10^{19}m^{-3}$ which is appreciably less than the average density $\bar{n} \simeq 1.4 \times 10^{20}m^{-3}$ in INTOR.

Sputtering rates of the divertor target are indicated in Fig.3 by the effective yield Y_{eff} (target atoms/incident ion of the plasma plus its impurity content). The sputtering yield for a tungsten target when n = 5 x $10^{19}m^{-3}$ and Δ = 3.5 x 10^{-2}m is $\approx$ 2.7 x 10^{-4} and the erosion rate is negligible ($\approx$ 2mm/y at 25% availability) but reduction of Δ to 1.6 x 10^{-2}m causes an increase by a factor of about 40. However this can be more than offset if the boundary density is increased to 7.5 x $10^{19}m^{-3}$. The self-sputter yield of beryllium does not exceed unity so that the sensitivity to both Δ and n(o) is less marked. However Y_{eff} is substantial, for example 1.7 x 10^{-2} at n(o) = 5 x $10^{19}m^{-3}$ and Δ = 3.5 x 10^{-2}m and this corresponds to an erosion rate of 132 mm/y at 25% availability. However the effective erosion rate will be substantially reduced because of redeposition of sputtered material.

The speed of the vacuum pumps $[S_{He}]_{5\%} \approx$ 120 to 400m^3/s for He at 300 K and the fraction of escaped neutral particles that must be exhausted $[F_{He}]_{5\%} \approx$ 2.5 to 7 x 10^{-2} are shown in Fig.4. The exhaust speed required for beryllium

is about twice as demanding as those for tungsten because fewer energetic atoms are backscattered from a beryllium surface.

4. PREDICTED PERFORMANCE OF THE PUMPED-LIMITER

Fig.5 shows the effective sputter yield of the upper surface of a pumped-limiter when $n(o) = 5 \times 10^{19} m^{-3}$ and Δ (mid-outer-toroidal-plane) = $1.5 \times 10^{-2} m$. In this case a range of $Q_\perp$ = 10 to 80MW is considered in order to examine the effects of radiative power losses due to impurity ions inboard of the separatrix. Self-sputtering of a tungsten plate is not significant unless $2Q_{||}^U \gtrsim$ 40MW. Radiative power losses for beryllium are likely to be modest and so only conditions for $Q_\perp$ = 80MW are considered; the effective beryllium sputter yield is 1.4×10^{-1} and the erosion rate 220mm/y (25% availability). Clearly such erosion cannot be accepted unless redeposition can maintain the profile of the divertor plate.

The transport of plasma energy towards the lower collection surfaces powers the helium exhaust flow of the pumped-limiter but both the power flow and the local plasma density are uncertain; this study therefore considers conditions where $Q_{||}^L$ = 1 to 3MW and $n^L(o) = 0.5$ to $2 \times 10^{19} m^{-3}$. There is evidence /3/ that the poloidal extent of the limiter is adequate to ensure powerful localised recycling. The values of $[F_{He}]_{5\%}$ and $[S_{He}]_{5\%}$ for a tungsten limiter are shown in Fig.6 together with the isotherms of T_t. Two operating regimes are apparent and evidence of their physical difference is given by Eq.(1). When T_t > 10eV most of the kinetic energy of the plasma is deposited upon the limiter but when T_t < 10eV the energy loss is predominantly due to atomic processes. Operation in either regime depends upon the degree of localised recycling which in these conditions can be influenced significantly by the pumping speed. The results show that when $2Q_{||}^L \rightarrow$ 6MW then the exhaust speed tends to be about $100 m^3/s$ and it is insensitive to the plasma density $n^L(o)$. Pumping requirements for a beryllium limiter are about a factor two greater.

5. CONCLUSIONS

For the plasma condition considered a tungsten divertor target offers an attractive solution especially if the boundary plasma density is > $5 \times 10^{19} m^{-3}$. However self-sputtering becomes serious if radial scale length Δ for energy flow is appreciably smaller than the values assumed here. A beryllium divertor target is likely to have a much reduced lifetime.

A limiter with a high atomic number target (i.e. tungsten) is only feasible if a radiative plasma edge can be established. Radiative power losses are not essential for a beryllium limiter but its lifetime is likely to be short. Effective pumping is predicted for the limiter but only if the power flow to its lower surface is $\nmid$ 6MW.

REFERENCES

/1/ Harrison, M F A, Harbour, P J and Hotston E S: Nuclear Technology/Fusion. 3 (1983) 432-456.

/2/ Harrison, M F A and Hotston, E S: Culham Lab. Rep. CLM-R226, 1982.

/3/ Harrison, M F A and Hotston, E S: Culham Lab. Rep. CLM-R232, 1982.

/4/ International Tokamak Reactor - Phase One (Rep. Int. Tokamak Reactor Workshop Vienna 1980 and 1981) IAEA, Vienna, 1982.

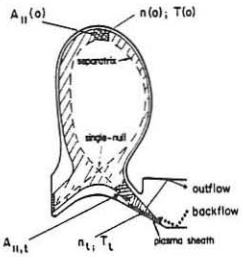

Fig.1 Single-null poloidal divertor configuration of INTOR

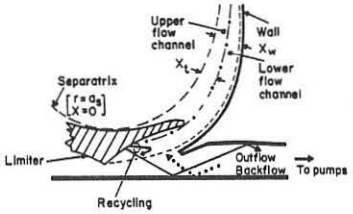

Fig.2 Pumped-limiter configuration of INTOR

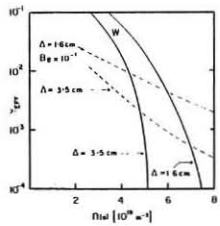

Fig.3 Effective sputter yield of tungsten and beryllium divertor targets

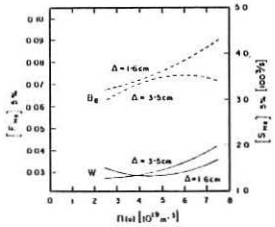

Fig.4 Requirements for divertor exhaust of He

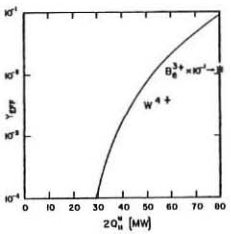

Fig.5 Effective sputter yield for limiter upper surface

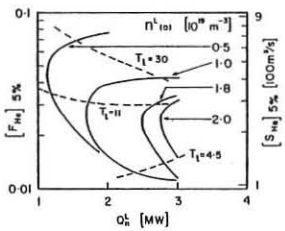

Fig.6 Helium exhaust requirements for a tungsten limiter

POLOIDAL FIELD REQUIREMENTS FOR DIVERTOR AND PUMP LIMITER DESIGN

O.Gruber, K.Lackner
Max-Planck-Institut für Plasmaphysik, EURATOM Association, D-8046 Garching, Germany

Poloidal divertors in tokamaks have proven successfull in controlling impurities at high energy flows /1/ - /3/, promise to solve with high probability the helium pumping problem of a reactor, and have recently also allowed access to a new discharge regime with improved energy confinement /4/. Their basic drawback is considered to be the increased poloidal field effort compared to a conventional limiter design.

This poloidal field effort has been quantitatively assessedby us in comparative design studies for poloidal divertor and limiter tokamak configurations for two devices (ASDEX Upgrade and INTOR) under reactor-similar geometrical restrictions. The following assumptions were made about the necessities of a tokamak reactor:

- a limiter has to be a toroidal pump limiter
- an elongated, D-shaped plasma cross-section is needed also in case of limiter configurations to achieve high ß-values
- all active poloidal field (PF)-coils are outside the toroidal field (TF)-coils.

For both devices, only configurations with target plates and pumping chambers below the bulk plasma have been considered. Calculations were carried out using different versions of the Garching equilibrium code package which applies the numerical methods described in /5/. The results are valid both for rather flat ($j \sim \psi - \psi^2$; ψ : poloidal flux function) and more peaked toroidal current densities ($j \sim \psi$).

1. ASDEX UPGRADE CONFIGURATIONS

ASDEX Upgrade /6/ is planned as a successor experiment to ASDEX, differing from the latter essentially through its higher plasma current and a reactor-similar poloidal divertor configuration. It utilizes a PF system with all coils outside the TF coils and foresees operation with double null (DN) and single null (SN) divertors and with a pump limiter (L).

The optimization criterium for the divertor configuration was to realize in a given vacuum vessel (main field volume) the largest possible plasma volume, leaving adequate space for target plates and pumping access. The PF system, on the other hand, depends critically on the required mix of quadrupole and hexapole fields to produce the D-shaped configurations: as the currents necessary increase like the second and third power with the distance coil to plasma center, respectively, even moderate hexapole moments will tend to dominate the effort in reactor-like situations.

The above criteria strongly favour SN over DN configurations: for a similar shape of the interiour flux surfaces, the volume available is more than 50 % larger in an unsymmetrically positioned SN configuration /fig. 1b/ than in a verticaly centered case with two identical divertor regions. From the magnetics point, the SN configuration can be viewed at as a DN with a superposed radial field shifting the plasma closer to one of the two stagnation points. As the distance between these two stagnation points is larger than between the ones

bounding the true DN configuration the required coil currents are also reduced as compared to the DN case.

The volume utilization of the DN configuration at given height of the stagnation points can be improved by using hexapole fields to increase its midplane diameter and, correspondingly, its triangularity $\theta = c/a$. This involves however a further dramatic increase in the required coil currents, which for ASDEX Upgrade then become a factor 2.2 larger in total ampere-turns /fig. 1a/ than those of the SN configuration at the same plasma current. DN operation is therefore only foressen at reduced parameters to study phenomena like poloidal asymmetries in the scrape-off transport. The stability of the vertical displacement mode for the SN and DN configurations shown is the same, as the smaller triangularity of the SN case is compensated by a smaller elongation.

The basic pump limiter configuration of ASDEX Upgrade has a similar shape of the interiour flux surfaces as the SN divertor case, but is vertically centered /fig. 1c/. The plasma surface is defined by

$$R = R_o + a \cdot \cos(\varphi + \theta \cdot \sin\varphi)$$

and

$$z = b \sin\varphi,$$

with $b/a = 1.6$ and $\theta = 0.1$ and is similar in shape to the top half of the SN separatrix. The total ampere-turn requirements of the PF-coils for this case are about 35 % less than those for the optimal divertor configuration. This relative small difference can be explained by the strong similarity in ths flux surface structure. Even in the limiter case stagnation points exist close to the plasma surface, defining a separatrix that would become plasma boundary if the limiter were removed. Only minor change in the external currents would then be required to connect the flux surface passing through the lower stagnation point to the old, L-case, plasma boundary in the top half to form an SN configuration.

Most of the actual difference in the PF requirements between the configurations of fig. 1b and 1c arises from the shift of the plasma centre relative to the centre of the PF coil system in the case of the divertor tokamak. This enhances somewhat the totally needed currents, but particularly produces a top-bottom asymmetry in their distribution. As a consequence of the latter, quadratic measures of the coil currents (like their magnetic energy) change stronger than $\Sigma/I_M/$.

Designing the ASDEX Upgrade PF-system we have maintained a separate, nearly stray-field free OH system with a long central solenoid. It can be shown however that during the final flat-top phase of a tokamak discharge, when OH and plasma currents are antiparallel, the stray fields produced by a short central solenoid aid the formation of a separatrix, reducing thereby the required currents in the other PF-coils. This effect has been utilized in the INTOR design studies, by subdividing the central OH coil into separately fed segments.

2. INTOR LIMITER AND DIVERTOR CONFIGURATIONS

The PF system of INTOR is additionally complicated by the distance of the PF coils which compared to the plasma dimensions is relatively larger, and the geometrical restrictions on coil location arising from maintenance and assembly requirements. Divertor configurations studied for this device in recent time have been of the SN-type, since its advantages had been pointed out in /7/.

Our PF study mainly concerned the comparative design of a SN divertor /fig. 2a/ and a pump limiter /fig. 2b/, for identical main field coils. Both plasma configurations shown have similar surface shapes in the top half (corresponding to $b/a = 1.45$, $\theta = 0.15$) where the modest values of elongation and triangula-

rity are needed to avoid in the scrape-off layer the formation of a separatrix opening up and leading to wall contact in the top half of the plasma vessel. PF coil locations and currents for the low and the high ß-case of the two configurations are shown in tables 1 and 2 of ref. /8/, where the OH contributions corresponding to the expected consumption of resistive and inductive fluxes are also included. Comparison of the usual figure of merit shows a $\Sigma/I_M/$ = 86.1 MAT for the SN divertor and of 81.6 MAT for the limiter case during the high ß-phase (I_P = 6.4 MA). These numbers are, however, inflated (and the relative differences thereby decreased) by the common OH contribution necessary to adjust the flux balance. A more reasonable comparison consists in neglecting the currents in the central core in both cases: the remaining $\Sigma/I_M/$ amounts to 51 MAT for the SN divertor and about 39 MAT for the limiter case, with a $\sim$30 % difference in this figure of merit.

3. CONCLUSIONS

The PF design calculations described above have shown that a SN divertor configuration is by far optimal compared with a DN configuration. The unexpected modest difference between the total currents required for limiter and SN divertor underlines the reactor potential of the SN configuration concerning the PF effort. The obtained, large values for $\Sigma/I_M/$ for the limiter case are of course due to the prescribed elongated, D-shaped plasma cross-sections: only about 6 MAT would be required in the INTOR case of section 2 to keep in equilibrium a circular plasma column. The contribution of the coil currents for the required additional quadrupole and hexapole moments to $\Sigma/I_M/$ dominate in a situation like INTOR or ASDEX Upgrade, while in a situation like JET with very close PF coils their contribution is swamped by the dipole field balancing the hoop force.

Table 1

PF coil locations and currents for ASDEX Upgrade ($ß_p$ = 2.2) per MA plasma current

Coil		1o	1u	2o	2u	3o	3u
position	R[m]	1.6	1.6	3.05	3.05	3.55	3.55
	Z[m]	2.34	-2.34	1.66	-1.66	0.60	-0.60
currents	[MA]						
DN		3.6	3.6	-2.28	-2.28	0.3	0.3
SN		0.85	2.50	-0.31	-1.08	-0.45	-0.35
L		1.0	1.0	-0.12	-0.12	-0.65	-0.65

REFERENCES

/1/ M.Keilhacker et al., Plasma Physics and Controlled Nuclear Fusion Research (Proc. 9th Int. Conf. Baltimore, 1982) Vol. 2 IAEA, Vienna (1982)
/2/ D.Johnson et al., ibid, Vol. 1, p. 9
/3/ M.Nagami , D.Overskei et al., ibid, Vol. 1, p. 27
/4/ F.Wagner et al., Phys. Rev. Letters, 49 (1982) 1408
/5/ K.Lackner, Comp. Phys. Commun. 12, (1976) 33
/6/ ASDEX Upgrade Project Proposal Phase II, internal report IPP 1/217 (1983)
/7/ INTOR, Japanese Contributions to the 3rd Meeting of the INTOR Workshop 16-28 June 1980, IAEA, Vienna
/8/ O.Gruber, K.Lackner, INTOR-Phase IIa, Critical issues, Europ. Contrib. to the INTOR-Phase IIa Workshop, Comm. EC, Brussels 1982, EUR-FU-BRU/XII-132/82/EDV 30, III, Chapt. IX, 81

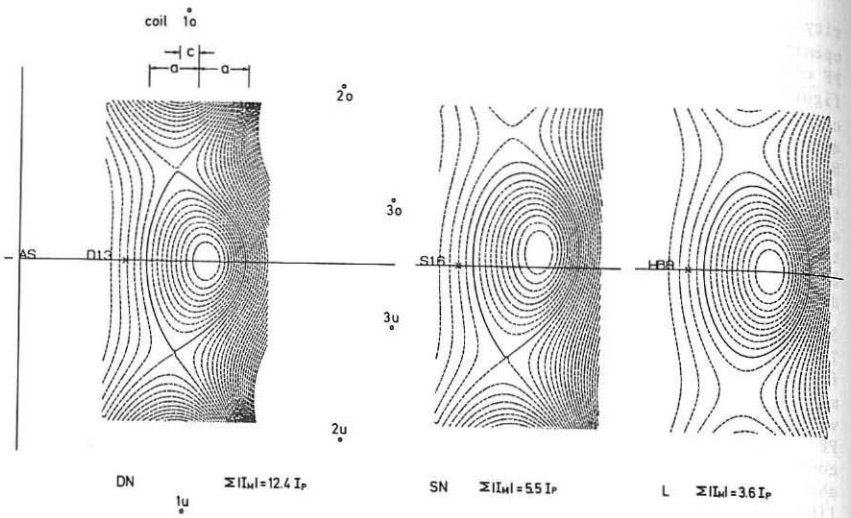

Fig.1a-c: DN, SN and Pump Limiter Configuration for ASDEX Upgrade (β_p = 2.2). The multipole currents are given in table 1 (R_p = 1.65 m, a = 0.5 m)

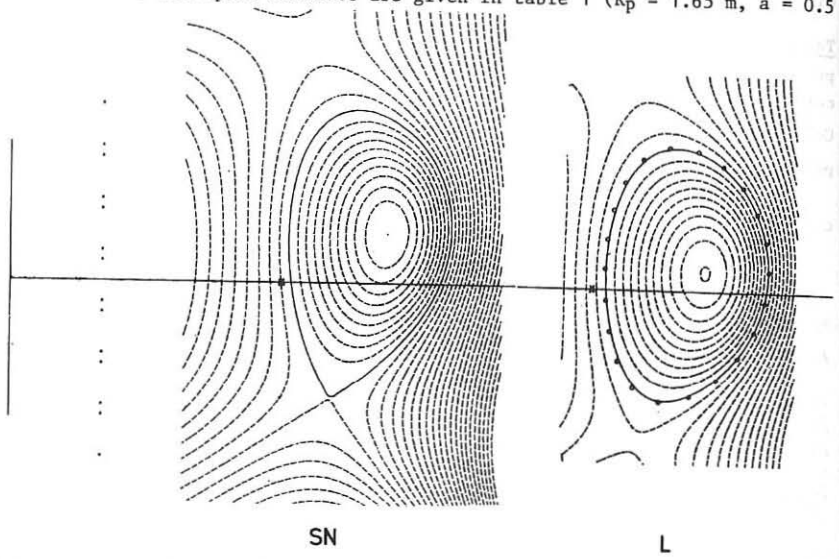

Fig. 2a-b: SN and Pump Limiter Configuration for INTOR (β_p = 2.7, R_p = 5.3 m, a = 1.2 m)

ASYMMETRY OF PLASMA SCRAPE-OFF IN LIMITER AND DIVERTOR TOKAMAKS

U. Daybelge

Marmara Research Institute
Department of Applied Mathematics
P.O.Box 21, Gebze, Kocaeli-TURKEY

1. INTRODUCTION

Plasma scrape-off asymmetries in poloidal divertors such as observed in ASDEX, PDX and T12 are well known /1,2/. They include asymmetry of flow and radiation of plasma onto the target plates and the walls with a concomitant asymmetry in the secondary effects such as sputtering and arcing on the surfaces. In the construction of future generators with divertors prediction of asymmetry effects will become important, due to the higher power densities involved.

The observed asymmetries of the scrape-off plasma in the divertors are a) top-bottom asymmetry with respect to the midplane, and b) inner-outer asymmetry with respect to the vertical axis of the plasma cross-section. Although, the first effect is weaker, it was the less expected one, because of the top-bottom constructional symmetry of the poloidal divertors. It is observed, that for a centred plasma, the average plasma density at the upper divertor is about 20% higher than the value measured at the lower divertor /1/. It is the direction of the toroidal field that determines the preferential loading of the divertors /3/. The asymmetries of the polidal divertors were first anticipated on theoretical grounds in Ref./4/, and they were calculated in Ref./3/.

Although they have remained so far unnoticed, the plasma scrape-off asymmetries can also arise in the ordinary limiter-tokamak experiments, as we shall show in this paper. Their detection, however, should be more difficult, since the ease in positioning and the relative stability of the divertor plasmas are in this case not provided. Here, we shall give a generalization of the drift-kinetic approach of Ref./4/, to describe the plasma asymmetries arising from the interaction with a poloidal limiter. Our main assumption is that the ions in the plasma edge are in the weakly collisional regime, i.e., $\langle \nu_{ii} \rangle \tau_{||} << 1$, whereas the electrons are collisional. With this assumption we can neglect the electric field effects on the drift orbits /4/. Our results will be confined to the lowest order in a/R_o; we shall neglect the banana orbits and consider only the transiting drift orbits.

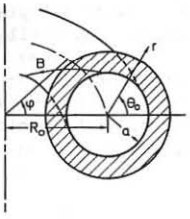

Fig.1. A circular poloidal limiter

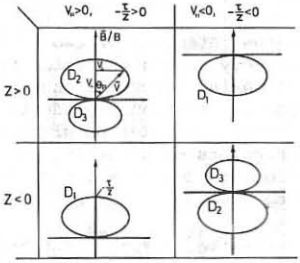

Fig.2. Ion loss regions in the velocity space as a function of the position (shaded regions).

2. KINETIC EQUATION OF THE LIMITER SCRAPE-OFF LAYER

The normalized drift kinetic equation for the limiter scrape-off can be written as /4/,

$$v \sin\theta \frac{1+x^2}{2x} \frac{\partial f}{\partial \tau} + \frac{\partial f}{\partial \theta} + q(a) \frac{\partial f}{\partial \phi} = \delta^2 \frac{C(f)}{Nvx \langle \nu_{ii} \rangle} \qquad (1)$$

where θ is poloidal angle, x is cosine of the pitch angle, τ is radial distance from the limiter edge, $\tau = (r-a) R_o eB_p / aMv_{Ti}$, $q(a) = aB_T/R_oB_p$ is the safety factor which will be taken as a rational number K/N. Further, $\delta^2 = R_oK \langle \nu_{ii} \rangle / v_{Ti} \sim \langle \nu_{ii} \rangle \tau_n/2 \ll 1$, and the Fokker Planck ion-ion collision operator in the weakly collisional limit is

$$\frac{C(f)}{Nvx\langle \nu_{ii} \rangle} \sim \frac{3}{8\pi Nvx} \int_D W^{-1} e^{-V^2} (\overleftrightarrow{I} - \vec{e}_w \vec{e}_w) d^3V : \langle \nabla_v \nabla_v f \rangle \qquad (2)$$

where $W = |\vec{W}| = |\vec{v} - \vec{V}|$, $\vec{e}_w = \vec{W}/W$, and the domain D of the velocity integral is the complementary of the loss regions in the velocity space. The boundaries of the loss regions are determined using the drift orbits /4/

$$\tau = \tau_o - z(\theta_0, \phi)\, s \qquad (3)$$

where $z = \cos\theta - \cos\theta_0$, $\theta = \theta + \phi/q$ and $s = v(1+x^2)/2x$. Here, an initial point of an orbit in the limiter plane is given by $(\phi_0 = o, \tau_0, \theta_0)$. Our assumption of a rational safety factor $q = K/N$ implies that every orbit crosses the limiter plane K times and therefore, it may intersect the limiter surface more than once. Within the collisionless theory, a single intersection readily depletes the orbit. To determine the boundary of the loss region in velocity space at a given point (ϕ, τ, θ) we set in Equ. (3) $\tau_0 = 0$. The resulting equation between $v_\parallel = vx$ and $v_\perp = v\sqrt{1-x^2}$ is an ellipse, i.e., $2v_\parallel^2 + v_\perp^2 - 2\, s^{(k)} v_\parallel = 0$, as shown in Fig.2. Since τ_0 can be set to zero at different $\theta_0^{(k)}$, where integer k is $1 \leq k \leq K$, we obtain a family of internested ellipses. The elliptical boundary to be chosen is the one, which gives a maximal loss region. The discussion given in /4/ for the determination of D can be summarized as follows: A test particle moving with $v_\parallel > 0$ does not collide with particles having $v_\parallel < 0$, as long as $z > 0$, and it collides only with particles whose velocity lie in D_1, the exterior of a well-defined ellipse in the half plane $v_\parallel > 0$. Whenever $z < 0$, on the other hand, the collision partners of the test particle have velocities inside D_2 and D_3, the interiors of two ellipses in the upper and lower half-planes, respectively. Given the velocity of the test particle, the upper ellipse remains an invariant curve. In the case of $z > 0$, however, the resulting lower ellipse is position dependent, its size increasing from zero to infinity. Choosing $v_\parallel > 0$, let us write the radial positions of the consecutive intersection points of an orbit with the limiter plane: Starting the orbit from the limiter edge, i.e., $\tau_0^{(0)} = 0$, and putting $\phi = 2\pi k$, where k is an integer, from Equ. (3) we can write

$$\tau_0^{(k)} = v \frac{1+x^2}{x} \sin(Nk\pi/K) \sin(\theta_0 + Nk\pi/K) \qquad (4)$$

where $k = 0, 1, 2, \ldots K$

If, for example, $\theta_0 = \pi$; then, the initial point is the extreme left point of the orbit. From Equ. (4) we can show /4/, that if $(K-1)\pi/K < \theta_0 < (K+1)\pi/K$, then the orbit is cut only once by the limiter.

Using a magnified radial variable $\xi = \tau_0/\delta$, which measures the distance from the limiter edge, we can reduce the drift-kinetic equation at the inner-limit to a diffusion equation, namely,

$$q \frac{\partial f}{\partial \phi} = \frac{3 z^2}{32\pi N v_1 x_1^5} F(D) \frac{\partial^2 f}{\partial \xi^2} \qquad (5)$$

where $F(D)$ is a position dependent coefficient, which must be evaluated over the existence regions in velocity space and v_1 and x_1 are parameters. Position dependence of $F(D)$ leads to a faster or slower repopulation of the orbits along their sectors, which, as we shall see, is the main reason for top-bottom asymmetries. Transforming to a new toroidal coordinate ζ, such that

$$\frac{d\zeta}{d\phi} = \frac{1}{\gamma} z^2(\phi)\{HF(D_1) + (1-H)[F(D_2)+F(D_3)]\}, \qquad (6)$$

where $H=0$ for $z > 0$, and $H = 1$ for $z < 0$, and only $F(D_3)$ is a function of ϕ. Imposing also the normalization condition $\zeta(\phi=0)=0$ and $\zeta(\phi=2\pi K)=1$, we can write Equ.(6) as

$$\frac{\partial f}{\partial \zeta} = \frac{3\gamma}{32\pi N v_1 x_1^5} \frac{\partial^2 f}{\partial \xi^2} \qquad (7)$$

where γ is the normalization constant, which can be calculated as

$$\gamma = \frac{1}{q} \int_0^{2\pi K} z^2 F(D)\, d\phi \quad .$$

3. MIXED-BOUNDARY-VALUE PROBLEMS FOR THE SCRAPE-OFF LAYER

Within the framework of the foregoing summary of Ref./4/, now we can formulate the mixed-boundary-value problems for the distribution functions $f^{\pm} = f(v_{\parallel} \gtrless 0)$, i.e.,

$$\frac{\partial f^+}{\partial \zeta} = \lambda \frac{\partial^2 f^+}{\partial \xi^2} \quad \text{for} \quad 0 \le \zeta \le 1 \quad \text{and} \quad -\infty < \xi < \infty$$

where $\lambda = 3\gamma / 32\pi N v_1 x_1^5$. The boundary conditions at the limiter plane are

$f^+(\zeta_k, \xi) = 0$ for $\xi > 0$ and $k=0,1,2,..K$ (No emission at the limiter)

$f^+(0,\xi) = f^+(1,\xi)$ for $\xi < 0$ (Periodicity of plasma in the limiter aperture)

Further, we have the radial boundary conditions as

$f^{\pm} \to 0, \quad \xi \to \infty$

$f^{\pm} \to f^{\pm}_{core}, \quad \xi \to -\infty$

In Ref./4/ for simplicity, the discussion was confined to a neighborhood of the equator plane, where the flow of ions along once-cut orbits under the assumption of symmetry was considered. Here, we formulate the general

problem for f^+, for example, in the vicinity of the limiter edge, considering both once and twice-cut orbits and indicate the source for the top-bottom asymmetry. Since the solution of Equ.(8) at some ζ_2 can be written in terms of initial data at ζ_1 as

$$f^+(\zeta_2,\xi)=\int_{-\infty}^{+\infty} d\xi'\; K_{12}(\zeta_{12},|\xi-\xi'|)\; f^+(\zeta_1,\xi'), \qquad (9)$$

where $\zeta_{12}=\zeta_2-\zeta_1$ and $K_{12}=(4\pi\lambda\zeta_{12})^{-1/2}\exp-(\xi-\xi')^2/4\lambda\zeta_{12}$, we can formulate an integral equation for initial f^+ closing the orbit again at the initial point. Let us take $q=3$, i.e., $K=3$.

Case a) Once-cut orbits, $(K-1)\pi/K<\vartheta_0<(K+1)\pi/K$:
Intersection of the orbit and the limiter plane are denoted by dots or squares.

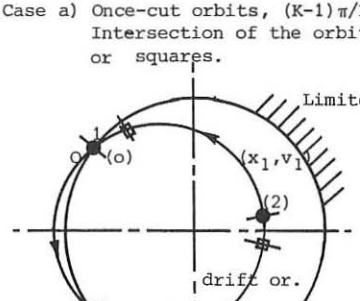

Applying the integral operator consecutively at the symmetric initial po-points 0 and a, we can write

$$f^+(1,\xi)=\int_{-\infty}^{+\infty} K_{a1}\int_{-\infty}^{0} K_{oa}\; f^+(1,\xi') \qquad (10)$$

$$f^+(a,\xi)=\int_{-\infty}^{+\infty} K_{oa}\int_{-\infty}^{0} K_{a1}\; f^+(a,\xi') \qquad (11)$$

Considering the Kernels along orbit segments, we can show, that $f^+(1,\xi)$ decays slower than $f^+(a,\xi)$.

Case b) Twice-cut orbits :

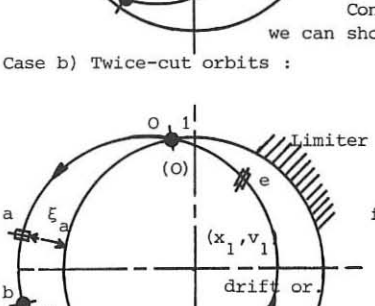

$$f^+(1,\xi)=\int_{-\infty}^{0} K_{c1}\int_{-\infty}^{-\xi_a} K_{bc}\int_{-\infty}^{0} K_{Ob}\; f^+(1,\xi') \qquad (12)$$

$$f^+(c,\xi)=\int_{-\infty}^{-\xi_a} K_{ac}\int_{-\infty}^{0} K_{Oa}\int_{-\infty}^{0} K_{c1}\; f^+(c,\xi') \qquad (13)$$

Since the collisions are more rare outside the limiter aperture, repopulation of the orbits after they hit the limiter surface is slower. These differences in repopulation along various orbit segments are introduced by the Kernels in the integral equations (10)-(13). Again, a qualitative inspection readily indicates that $f^+(1,\xi)$ is larger than $f^+(c,\xi)$.

/1/ M. Keilhacker, paper I.R3 in
M. Keilhacker und U. Daybelge, Proceedings of the IAEA Technical Comm. Meeting on Divertors and Impurity Control, Garching, 6-10 July 1981.
/2/ N.N. Brevnov, ibid, paper I.R4.
/3/ U. Daybelge, Nucl.Fusion, 21 (1981)1589.
/4/ U. Daybelge and B.Bein, Phys.Fluids, 20 (1977) 1777.

ENERGY AND POWER BALANCES IN DITE TOKAMAK

W.H.M. Clark, S.J. Fielding, D.H.J. Goodall, J. Hugill, P.C. Johnson, G.M. McCracken.

Culham Laboratory, Abingdon, Oxon., OX14 3DB, UK
(Euratom/UKAEA Fusion Association)

Introduction

A perennial problem in tokamaks has been an inability to balance the power and energy input to the plasma with the measured losses. By instrumenting all the material surfaces surrounding the plasma it should be possible to obtain a balanced energy inventory, and to identify the distribution of power flow in the various loss channels. Such a method has been used on DITE, with the particular purpose of obtaining accurate data on the power diversion efficiency of the bundle divertor. This paper reports the results.

Energy and Power Measurements

Power losses from radiation and charge exchange (C/X) were measured at one position by a wide angle thin film bolometer, with a response time of 2ms. Toroidal and poloidal variation in these losses, integrated over a discharge, were obtained from measurements of the temperature rises on six of the eight stainless steel bellows, distributed around the torus. The technique is similar to that used on ORMAC /1/. The bellows are 0.5mms thickness, with a thermal diffusion time constant of ~ 0.05s, and in total, comprise ~ 1/4 of the DITE wall surface area. Each of the six bellows is instrumented with up to 9 calibrated miniature thermistors, to give information on the poloidal variation. Temperature rises of up to 5°C have been observed. The total power to the wall is obtained from the bellows measurements, assuming the time variation given by the bolometer.

The two graphite limiters and the graphite divertor target plate are each instrumented with several thermocouples. Instantaneous power to these surfaces was estimated from infrared thermography, using an Aga 780 camera, /2/, modified to give a time response of 20ms. The camera was calibrated by reference to a black body emitter and by comparison of the integrated data with the thermocouple readings. Bolometry in the target chamber indicated that the radiated power loss in the divertor is small (< 30kW) and it has been neglected in the following analysis.

Results

Data from four discharge conditions is prevented: divertor on/off, neutral injection on/off. Divertor action was 'switched on', from 80ms-

200ms, by displacing the magnetic centre of the outer flux surfaces /3/. Plasma currents were in the range 110-140kA and average densities 2.1-3.5.10^{19} m^{-3}. Neutral injection heating, from four beam lines, provided up to 1.5MW of neutrals into the torus, with timing as shown in Figures 4 and 5.

Figure 1 shows the toroidal variation of radiation and C/X energy losses, derived from thermistor data for two ohmic discharges, one with and the other without the divertor. For both discharges the radiation and C/X losses are strongly peaked in the region of the limiters. This is presumably due to a combination of C/X losses from the localised high neutral density associated with particle recycling at the limiters, particle reflection at the limiters on to the walls, and radiation from low ionisation states of impurities released at the limiters. When the divertor is operated the peak at the limiters is reduced, and the highest energy loss is observed at the gas feed. In the case of no divertor a gas feed of ~ 80 amps of neutrals is sufficient to sustain the plasma. When the divertor is used, the gas feed has to be increased to ~ 400 amps giving rise to a much higher local neutral density. Detailed spectroscopic measurements at the gas feed position have failed to show any localised impurity radiation, indicating that the energy peaking in this region is probably due to charge exchange on the gas feed neutrals. A similar effect is observed for the case of injection heated discharges. The large toroidal variations seen in Figure 1 mean that localised bolometry on its own cannot be relied on to give accurate measurements of total radiation and C/X losses.

Figures 2-5 present global power balances for the four different discharge. Estimates have been made of the changes in internal energy in the plasma, derived either from β_θ measurements or profile data, and in all cases these are sufficiently small to be neglected. The results from the two ohmically heated discharges, Figs 2 and 3, show that over 80% of the power and energy input can be accounted for. From Fig 3 it can be seen that up to 70% of the instantaneous power input is observed incident on the divertor target. For the two injection heated discharges, Figs 4 and 5, more than 70% of the energy input can be accounted for, and up to 80% of the power during injection. Up to 15% of the instantaneous power during injection is observed at the divertor target.

It is not obvious whether the unaccounted input energy ($\lesssim$ 30%) is due to statistical or systematic errors in the measurements, or because of local-ised energy losses to uninstrumented surfaces. The measurement errors are difficult to assess but are probably ~ 20%. It should be noted, that for all the discharges analysed the input energy exceeds the measured losses.

by distributed instrumentation of the torus walls, the limiters and the divertor target plate. Radiation and C/X losses exhibit toroidal asymmetries, and are strongly peaked in the region of the limiters, and at the gas feed when the divertor is used.

Global power balances have been made for four sets of discharges, and between 70 and 80% of the power and energy input can be accounted for. The distribution of power in the various loss channels is shown. With diverted discharges up to 70% of the power input for ohmically heated discharges, and ~ 15% for injection heated discharges is observed at the divertor target plate.

Acknowledgements

We gratefully acknowledge the invaluable assistance of W. Millar in collecting the thermal diagnostics data, and Dr. J.W.M. Paul for advice and encouragement.

References

/1/ Edmunds, P.H. and England, A.C. Nuclear Fusion 18 (1978), 23.
/2/ Infrared Systems AB, Box 3, S-18211 Danderyd, Sweden.
/3/ Fielding, S.J., Goodall, D.J.H., Hugill, J., Johnson, P.C. 'Characteristics of the Particle and Energy Exhaust into the DITE Bundle Divertor'. This conference.

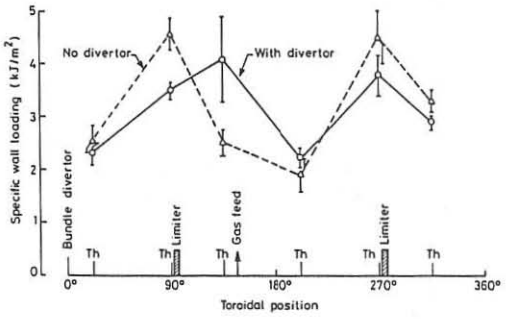

Fig. 1 Toroidal variation of radiation and charge exchange energy losses in ohmically heated DITE discharges. 'Th' symbols refer to the location of instrumental bellows.

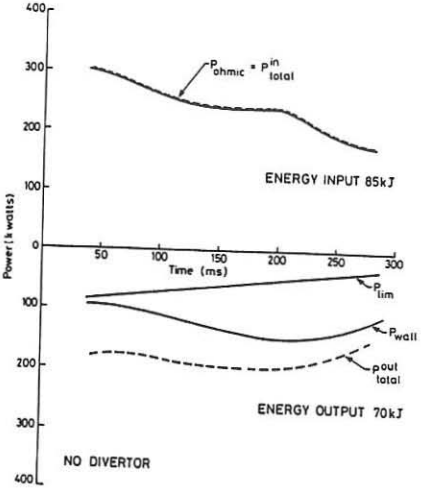

Fig. 2 Global power balance for ohmically heated discharge, no divertor. I_g = 110kA, $B\phi$ = 2T.

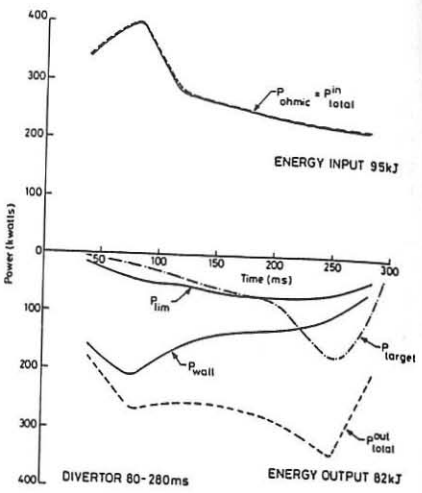

Fig. 3 Global power balance for ohmically heated discharge, divertor on 80-280ms. I_g = 135kA, $B\phi$ = 2.6T.

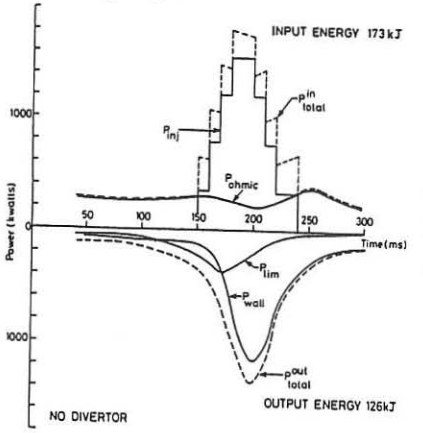

Fig. 4 Global power balance for injection heated discharge, no divertor. I_g = 110kA $B\phi$ = 1.35T.

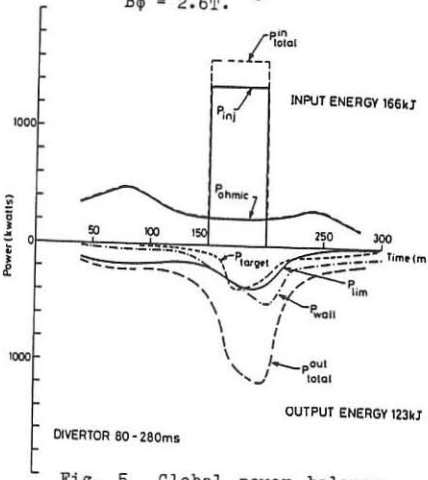

Fig. 5 Global power balance for injection heated discharge, divertor on 80-280ms. I_g = 135kA, $B\phi$ = 2.6T.

CHARACTERISTICS OF THE PARTICLE AND ENERGY EXHAUST INTO THE DITE BUNDLE DIVERTOR

S.J. Fielding, D.J.H. Goodall, J. Hugill, P.C. Johnson.

Culham Laboratory, Abingdon, Oxon., OX14 3DB, England
(Euratom/UKAEA Fusion Association)

Abstract

A simple 0-D model of the particle balance is used to estimate the particle flow into the DITE Bundle Divertor. Simultaneous measurements of the power received by the target and the rate of ionisation in the target chamber indicate that power is convected to the target by a high temperature, low density exhaust plasma.

Discharge Conditions

The measurements were made in the following conditions: toroidal field = 2.6T, plasma current = 140 kA, mean electron density ≈ $3 \times 10^{19} m^{-3}$. The circular carbon limiter radius was 0.26m and the divertor separatrix radius 0.21m. Divertor action was 'switched on' from 80-200ms by displacing the geometrical centre of the outer flux surfaces from a major radius of 1.15m, where the plasma contacts the inner limiter, to 1.17m, where it is centred in the limiter aperture /1/. The torus was conditioned by glow cleaning only, so that the recycling coefficient was comparatively high. The divertor chamber was pumped by a 10^5 ℓs^{-1} cryopump via a 500mm diameter port. This is sufficient to ensure that most particles entering the divertor do not return to the torus. Neutral beam injection heating at a power level up to 1.2MW was applied from 100-150 ms.

Particle Balance

A simple model for the global particle balance is based on the following observations:

(i) In the undiverted discharge a relatively small gas feed rate is sufficient to maintain the density, indicating a high rate of recycling.

(ii) A large increase in the gas feed rate is required to maintain or increase the plasma density when the divertor is 'switched on'. If the gas feed rate is not increased the density falls rapidly.

Figure 1 illustrates a typical diverted discharge.

The particle balance equation is written in simplified form (in amperes equivalent) thus:

$$e\frac{dN}{dt} = S_g + I_B - I_L - I_D \qquad (1)$$

Here, N is the total number of electrons in the discharge calculated from the central channel of a microwave interferometer using model profiles. S_g

is the rate of ionisation due to the cold gas feed. I_B is the particle input by neutral beam injection. I_L is the net loss rate to the limiters and walls of the vacuum vessel due to imperfect recycling. It is estimated from the rate of decay of density when the divertor, gas feed and neutral beams are off. It is small and is assumed to be constant at ~ 20A. I_D is the particle current into the divertor, which is to be found.

We also take $S_g = kH\alpha^{GF}$, where $H\alpha^{GF}$ is the intensity of Hα radiation from the vicinity of the neutral gas input. The calibration factor k is found by plotting edN/dt against $H\alpha^{GF}$ in an undiverted discharge, for which I_B and I_D are zero. A straight line fit to this data has slope k and intercept $-I_L$.

Figure 2(a) illustrates how I_D is calculated from equation (1) for an ohmically heated divertor discharge. Figure 2(b) shows the corresponding intensity of Hα radiation from the target chamber, $H\alpha^D$. I_D and $H\alpha^D$ are obviously strongly correlated.

Power Exhaust

The power flow to one side of the divertor target is estimated from measurements of the evolution of the surface temperature using an infra-red camera. The data are analysed assuming that the diffusion of heat into the target surface can be described by a 1-D diffusion equation. Radiation is neglected. The time resolution is limited by the time required to scan the target area and is approximately 20ms. The power flux to the other side of the target is taken to be the same if the bulk temperature rise is within 10% as measured by thermocouples.

Bolometers placed behind the target area register losses due to radiation and charge exchange from the diverted plasma. Assuming they are 'radiated' isotropically, these losses are several times smaller than the total power flow to the target, P_D. They will be neglected in the following discussion.

Reionisation in the Target Chamber

The intensity of Hα radiation from the divertor target chamber is measured using a narrow band interference filter and photomultiplier, calibrated with a tungsten ribbon lamp. Figure 3 shows the Hα intensity, $H\alpha^D$ normalised to I_D versus the ratio P_D/I_D. The data points are for various times in discharges with ohmic and NBI heating. If the electron temperature in the plasma near the target is $\gtrsim$ 10eV, the rate of Hα radiation puts a limit on the rate of ionisation of neutrals. For the saturated part of the curve in Fig. 3, this amounts to $\lesssim$ 5% of I_D.

Discussion and Conclusions

The rate of reionisation of neutrals recycling from the target plate is too low to support the formation of the cold dense plasma near the

target observed in other experiments /2/. Our data is consistent with power exhaust by convection. The ratio P_D/I_D yields exhaust temperatures in the range 20-150eV, for a heat transport coefficient ≈ 10. The variation of the ratio H_α^D/I_D in Fig. 3 can then be explained by the variation with temperature of the rate of ionisation of neutrals, recycling through an almost transparent plasma of constant density (so far, unmeasured). The variation of P_D with I_D (not shown) is also consistent with this hypothesis.

Acknowledgements

The authors are indebted to the DITE operating team under Mr. R.W. Storey and Mr. R.E. Bradford for machine operations and to the Group Leader, Dr J.W.M. Paul for his support. Dr. P.J. Lomas supervised operation of the neutral beam injection.

REFERENCES

/1/ K.B.Axon et al in Plasma Physics and Controlled Nuclear Fusion Research (Proc.9th Int.Conf.,Baltimore, 1982) Vol.I, IAEA, Vienna (1983).

/2/ M.A.Madavi et al.,Phys.Rev.Lett.41 (1981) 1602.

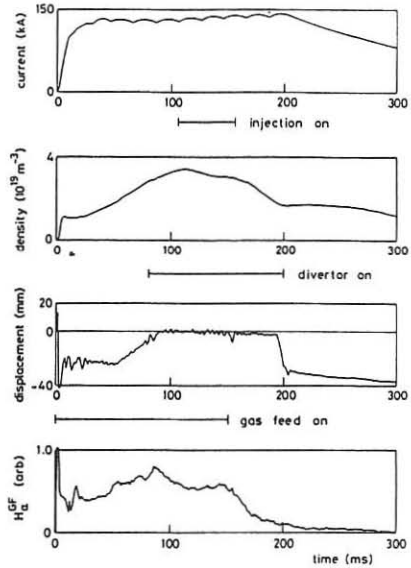

Fig.1 From the top: traces of plasma current, mean density, horizontal displacement of geometric centre from centre of limiter aperture, Hα radiation near gas feed.

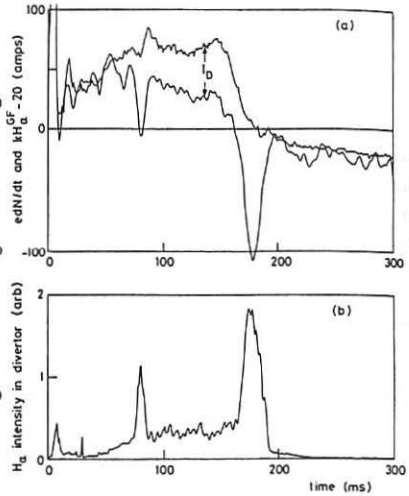

Fig.2 (a) Traces of dN/dt and $KH_\alpha^{GF} - I_L$, showing how I_D is calculated (no NBI, $I_B = 0$).

Fig.2 (b) Corresponding trace of the Hα radiation from the divertor target chamber H_α^D.

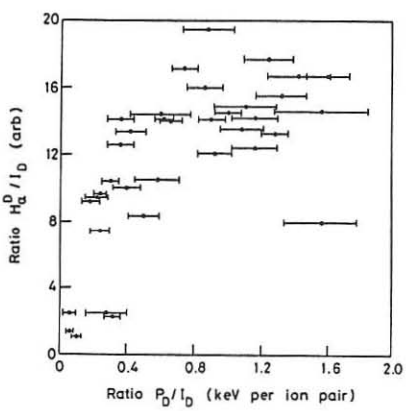

Fig.3 Plot of ratio H_α^D / I_D versus P_D / I_D for various times in discharges with OH and NBI. Vertical error bars are similar to horizontal error bars shown.

Experimental Observation of a Dense and Cold Divertor Plasma in D-III Beam-Heated Divertor Discharges and its Numerical Simulation

M. SHIMADA, S. SENGOKU, T. KOBAYASHI, N. MIYA, M. KASAI and the JAERI team°
C. L. KAHN, K. H. BURRELL and the GA Doublet III Groups†
(° : JAPAN ATOMIC ENERGY RESEARCH INSTITUTE, † : GA Technologies, Inc.)

Introduction

In addition to the good energy confinement capability[1,2], the strong particle shielding of the poloidal divertor results in localized particle recycling near the divertor plate and enhanced radiative cooling[3]. Consequently, the divertor plasma is observed to be dense and cold even in the presence of the neutral beam heating[4] and the heat load of the divertor plate is reduced by the increase of the radiative power in the divertor. The dense and cold plasma negates the wall erosion problem and mitigates helium ash exhaust problem[5] in the fusion reactors. The reduction of the heat load of the divertor plate facilitates heat removal problem. A simple modelling of this dense, cold and radiative divertor plasma is also presented.

Dense and Cold Divertor Plasma[4]

Fig. 1 shows the divertor equilibrium and the diagnostics used in this experiment. 42 Langmuir probes were installed in the divertor plate and the horizontally scanning Langmuir probe measured the electron density and temperature profile across the divertor channel. The vertical profile of the electron density and temperature is shown in Fig. 2. With the increasing plasma density of the main plasma, the electron density of the divertor is observed to increase non-linearly to 2.8×10^{14} cm^{-3} ($n_e = 3.4 \times 10^{13}$ cm^{-3}). Simultaneously, the electron temperature at the divertor plate are reduced to 3.5 eV as the electron density of the main plasma increased. This dense and cold divertor is obtained with $B_T = 20$ kG, $I_p = 290$ kA. Out of the 1.5 MW absorbed power, 0.5 MW is radiated in the main plasma and another 0.5 MW is radiated in the divertor in high density condition.

Reduction of the Heat Load of the Divertor Plate by Remote Radiative Cooling

The power balance of the beam-heated divertor discharge is shown in Fig.3. The radiative power in the divertor increased with the increase of the main plasma density, while the radiative power of the main plasma stayed almost constant over the whole electron density range. As a result, the heat load of the divertor plate was observed to decrease by a factor of two in the high density condition. The heat load of the divertor plate is measured by the 28 thermocouple array embedded in the divertor plate. The reduction of the heat load of the divertor plate was also observed with an infra-red camera and the widening of the divertor channel in high density condition seen in Fig. 2 was also observed. This result was obtained with 2 MW neutral beam injection.

Results with Good Confinement Discharges with 4-5 MW Neutral Beam Injection

With a divertor operation, a high density and high temperature plasma was demonstrated[2] in D-III. In these discharges, The radiative

cooling power was 25-40 % (~30-50 % of the radiative power comes from the divertor) of the heating power and was almost constant over the electron density range investigated. The divertor plate receives 40 -60 % of the heating power (thermocouple measurement). The enhancement of the radiative cooling power in the divertor and the resultant reduction of the heat load have not been observed up to $n_e = 7 \times 10^{13}$ cm^{-3}. This is probably because of the suppressed particle recycling and the high injection power. However, even with 4-5 MW beam injection, the Langmuir probe measurement showed that the plasma near the divertor plate is still dense and cold ($n_e \sim 1 \times 10^{14}$ cm^{-3} and $T_e < 20$ eV).

Numerical Simulation of the Dense, Cold and Radiative Divertor Plasma

To understand the physical mechanism of this dense and cold divertor plasma, a simple divertor modelling code has been developed. Particular attention was taken in physical mechanisms such as remote radiative cooling[3], particle recycling near the divertor plate[6] and particle shielding at the main plasma scrape-off. One-fluid one-dimensional plasma code solves the equations of continuity, momentum and energy. The particle, momentum and energy source/sink terms due to neutral particles are evaluated by a two-dimensional neutral transport code.

The following assumptions are adopted;

- steady state $\dfrac{\partial}{\partial t} = 0$
- $n_e = n_i$, $v_e = v_i$ (charge neutrality)
- fast equipartition $T_e = T_i$
- $\eta_{\parallel} = 0$ (resistivity)
- $m_e = 0$ (electron mass)
- $\pi_{\alpha\beta} = 0$ (viscosity)

Equations solved are :

$$\frac{\partial}{\partial \xi} \Phi = S_n \qquad \text{(equation of continuity)}$$

$$\frac{\partial}{\partial \xi} (p + m v \Phi) = S_p \qquad \text{(momentum flux)}$$

$$\frac{\partial}{\partial \xi} \left(q_e + \left(5 T + \frac{m}{2} v^2 \right) \Phi \right) = S_E \qquad \text{(heat flux)}$$

where suffices e, i denote electron, and ion.

m	:	particle mass
n	:	particle density
v	:	flow velocity
Φ	:	particle flux density ($\Phi = n v$)
S_n	:	particle source density
S_p	:	momentum source density (due to charge-exchange)
S_E	:	energy source density (including radiation loss by oxygen)
q	:	heat codution
P	:	pressure (sum of electron and ion pressure)
T	:	temperature

The neutral transport is solved as follows ;

$$n_p^{(n)} = \frac{1}{4\pi} \iiint \frac{dxdydz}{\delta x^2+\delta y^2+\delta z^2} \frac{\sigma^{(n-1)}}{v}(x,y,z) e^{-\int \frac{ds}{\lambda}}$$

where n_p is the neutral particle density of the n-th generation, $\sigma^{(n-1)}$ is the particle source density due to charge-exchange reaction of the (n-1) generation.

Figure 4 shows the comparison of the calculated electron density, temperature, particle flux and Mach number along the field line with the corresponding experimental results. The values in the middle were obtained with the scanning Langmuir probe. A good fit is obtained with this simple numerical simulation. The radiative cooling power both from hydrogen and oxygen (assumed to be 1 % of the electron density) amounts to 50 % of the power from the main plasma which is also a good agreement with the measured result.

Acknowledgement

The authors would like to express their appreciation to Drs. S. Mori, Y. Iso, K. Tomabechi, Y. Obata and M. Yoshikawa of JAERI and Drs. T. Ohkawa and J. Gilleland of GAC for continuous encouragement throughout this work. This work was performed under a cooperative agreement between the Japan Atomic Energy Research Institute and the United States Department of Energy under DOE Contract No. DE-AT03-80SF11512.

REFERENCE

/1/ WAGNER, F. et al., in Plasma Physics and Controlled Nuclear Fusion Research (Proc. 9th Int. Conf. Baltimore, 1982) Vol. 1, IAEA, Viena (1983) 43.
/2/ NAGAMI, M. et al., this conference.
/3/ SHIMADA, M. et al., Nucl. Fusion 22 (1982) 643.
/4/ SENGOKU, S. et al., JAERI-M 83-008 (1983).
/5/ SHIMADA, M. et al., Phys. Rev. Lett. 47 (1981) 796.
/6/ PETRAVIC, M. et al., Phys. Rev. Lett. 48 (1982) 326.

FIGURE CAPTIONS

Fig. 1. D-III divertor equilibrium and the diagnostics used in this experiment.
Fig. 2. Electron density and temperature profile along the divertor plate.

Fig. 3. Power Balance of the beam-heated divertor discharges. In high density divertor discharges, the increase of the radiative power in the divertor reduced the heat load of the divertor plate.
Fig. 4. Profiles of electron density, temperature, particle flux and Mach number along the field line calculated by a divertor plasma-neutral code. ξ is the coodinate along the field line. The origin (ξ=0) corresponds to the divertor entrance (separatrix null point) and $\xi(B_p/B_T)$ = 0.4 corresponds to the divertor plate. The experimental values are shown with error bars. The electron density at the divertor plate was observed to be (0.8-2.8) x 10^{14} cm^{-3} (not shown in the figure). The particle flux estimated from the ion saturation current agrees with the calculated value within a factor of two at the midst of the divertor channel.

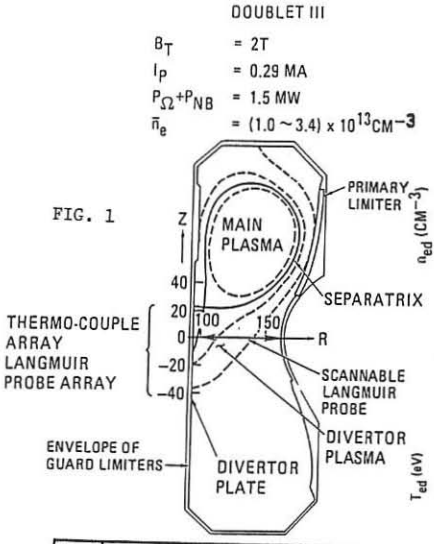

FIG. 1

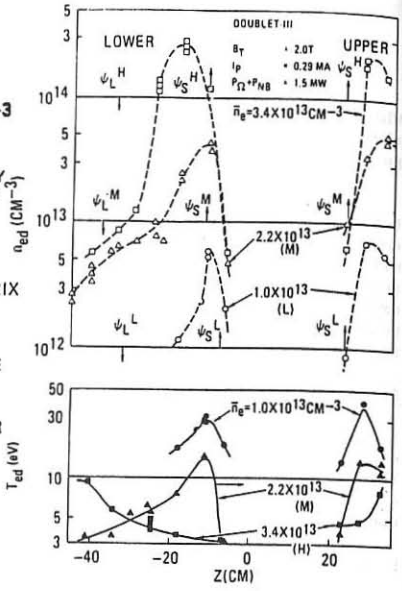

FIG. 2

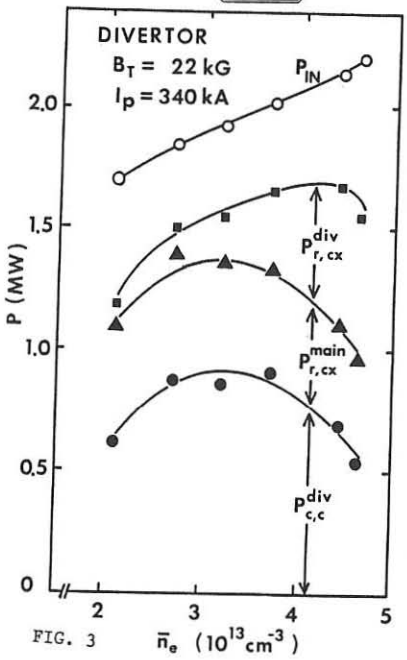

FIG. 3

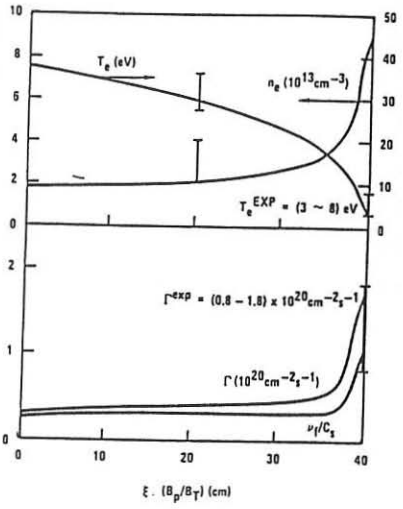

FIG. 4

IMPURITY FLUXES IN THE SCRAPE-OFF LAYER OF THE TCA TOKAMAK: EFFECTS OF RF HEATING

J.K. Gimzewski and S. Veprek
Institute of Inorganic Chemistry, University of Zürich, Winterthurerstr. 190, CH-8057 Zürich, Switzerland.
F. Hofmann, J.B. Lister and A. Pochelon
Centre de Recherches en Physique des Plasmas, Association Euratom-Confédération Suisse, Ecole Polytechnique Fédérale de Lausanne, CH-1007 Lausanne, Switzerland.
P. Groner
Federal Institute for Reactor Research, 5303 Würenlingen, Switzerland.

1. INTRODUCTION

The TCA tokamak (R=0.61m, a=0.18m, B≤1.5T, I≤140kA)/1/ was built with the aim of studying Alfven wave heating at frequencies $\omega < \omega_{ci}$ /2/. Although increases in T_i and T_e of~50% have been observed during rf heating, Bolometric and spectroscopic measurements have shown that large radiation losses, originating primarly from iron impurities, severely limit the maximum heating effect /3/. The present paper concerns the processes of impurity production and transport in the scrape-off layer (SOL) which have been investigated using collection probes and surface analysis by X-ray photoelectron spectroscopy (XPS). The data obtained from an extensive series of experiments has permitted the determination of impurity fluxes, ion energies and sputtering phenomena within the SOL. Particular attention has been given to the effects of rf heating and limiter material.

2. EXPERIMENTAL

The shot duration was 90ms. During this time rf heating could be applied at input power levels of 96-150 kW with a pulse time of 20-40ms. The rf antennas are constructed from stainless steel and are situated in the vicinity of the plasma (20mm behind the limiter); they account for~16% of the total plasma surface area. The wall material is stainless steel. Stainless Steel (SS) or carbon (C) limiters were used during the experiments.

Gold or carbon foil probes, wrapped around a cylinderical rod (Ø=30mm; Length =70mm) were used as collection probes. A tubular shield, with slits of 8 mm width facing the electron- and ion- drift sides in the shadow of the limiter, was fitted to the surface studies port on the TCA vacuum vessel. Four shot sequences could be made on each probe. The entire sequence of exposures, transport and XPS analysis was done under UHV conditions using a portable, ion-pumped, vacuum suitcase which connected, via vacuum locks,to the tokamak- or the XPS vacuum chamber.

A Leybold Heraeus LHS-10 XPS system was used for surface analysis. Selected spectral regions were repetitively scanned and summed in a multichannel scalar. The integrated counts in the photopeak, after a background subtract-

ion routine was used to determine the areal concentrations; a cross-check, using RBS, confirmed that the values determined are very accurate in the absolute sense. Details of the ion energy impact energy determination are reported elsewhere /4/ and in these proceedings.

3. RESULTS

The principal elements retained are Fe and O. The atomic ratio of O/Fe was found to be approximately unity over a wide range of impurity retention levels for carbon probes. This represents a lower limit of the O/Fe ratio because O ions are known to chemically interact with carbon to form CO /5/; also the trapping probability of O is not known.

Impurity Flux Determination. The areal concentration of iron, c_{Fe}, was investigated as a function of both the number of shots, N, and the distance from the plasma edge, d, which we define as the limiter position. A typical example of the experimental data, for a gold probe, is shown in Fig.1. The radial profiles exhibit a complex dependence on N; also impurity retention is non-linear with N. From these and similar data, the impurity flux per shot, Γ_{Fe} and a first order rate constant, k, is obtained from c_{Fe} as a function of N using an iterative least squares fitting routine to the expression,

$$c_{Fe} = (\Gamma_{Fe} / k).(1 - \exp [- k.N] \qquad (1)$$

In general, this expression fits the data well (see Fig.1) and accounts for simultaneous erosion and deposition of impurities on the probe.

Effects of rf Heating. For a SS limiter and a fixed analysis distance (d=20mm) $\Gamma_{Fe} = 1.7 \pm 0.4 \times 10^{14} cm^{-2} shot^{-1}$. In contrast, rf heating at a power level of 108kW and a pulse time, t_{rf}, of 30ms resulted in $\Gamma_{Fe} = 2.5 \pm 0.7 \times 10^{14} cm^{-2} shot^{-1}$. Taking into account that the shot duration is 90ms, the Fe flux increases by a factor of ~2 during rf heating. The increase in Γ_{Fe} as a function of t_{rf} is non-linear (Fig.2a). This behaviour is also evident from Fig. 2b, which shows the % increase in Γ_{Fe} per ms pulse time as a function of rf power. These data may be interpreted in terms of additional sputtering by impurities generated during the rf pulse duration. Other investigations have shown that the Fe

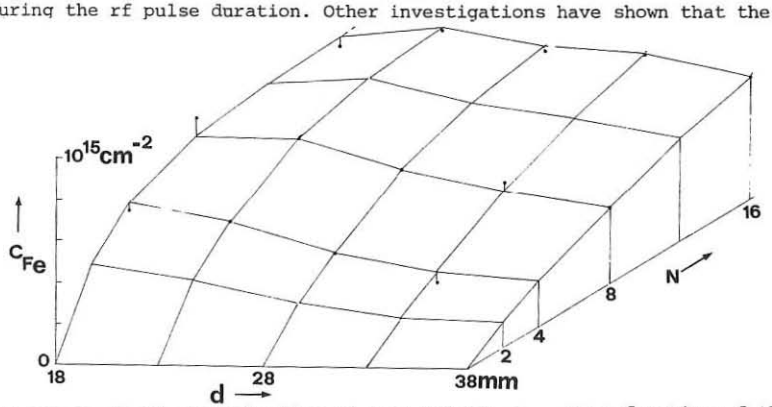

Figure 1. Areal concentration of Fe retained, c_{Fe}, as a function of the number of shots,N, and distance from the plasma edge,d.Limiter=C;Probe=Au.

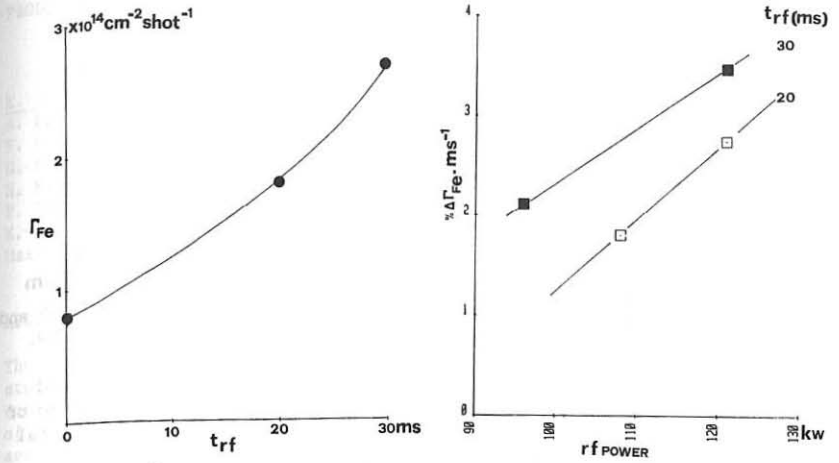

Figure 2. a) Γ_{Fe} as a function of rf pulse time at an rf power of 121kW and b) % increase in Γ_{Fe} as a function of rf power for t_{rf}= 20 and 30ms.

concentration can approach 1% during rf heating /3/.

Effects of rf Heating on Impurity Decay. The measured radial dependence of c_{Fe} as a function of d is a complex function of $\Gamma_{Fe}(d)$, k(d) and N (see Fig. 1). However, the decay of Γ_{Fe} is independent of N. Figure 3 (curves a and b) show the dependences of Γ_{Fe} on d for a SS limiter without and with rf heating. The curves are fitted expodential decay functions, characterized by impurity e'folding lengths, δ. In the absence of rf heating, δ=15mm and with rf heating δ=21mm. This is evident from the increased Fe flux at the wall and antenna regions observed for the rf heating case.

Limiter Material Effects. Replacement of the SS limiter with a C limiter resulted in a considerable reduction in the radiated power loss. However the dominant species responsible is still iron. In Fig.3 (curves b and c), the dependences of Γ_{Fe} upon d are shown for SS and C limiters where rf heating was applied. For the C limiter, δ=12mm, which is markedly lower than that for the SS limiter (δ=21mm). Also it is important to note that the impurity flux in the antenna and wall regions are lower by a factor of 2-4 with the C limiter.

Sputtering Effects. The impact energy of the Fe ions, estimated from their implantation depth in C probes, is 100-180ev /4/. These energies are above the threshold energy for sputtering. The erosion rate constant may be expressed in terms of a linear combination, $k=(\Gamma_{Fe}.S_{Fe}+\Gamma_{O}.S_{O}+\Gamma_{D}.S_{D})/n$, /7/ where Γ and S are the fluxes and sputter yields for the ions indicated in subscript and n is taken to be a monolayer ($n= 2\times10^{15}cm^{-2}$). Empirically we find that k is a function of Γ_{Fe} ($k= \alpha\Gamma_{Fe} + k_0$), where $\alpha= 7\times10^{-16}cm^{-2}$ and k_0=0.06; k_0 is the sputtering due to D ions which might possibly be neglected for shots with high impurity fluxes. Assuming that the O and Fe ions have

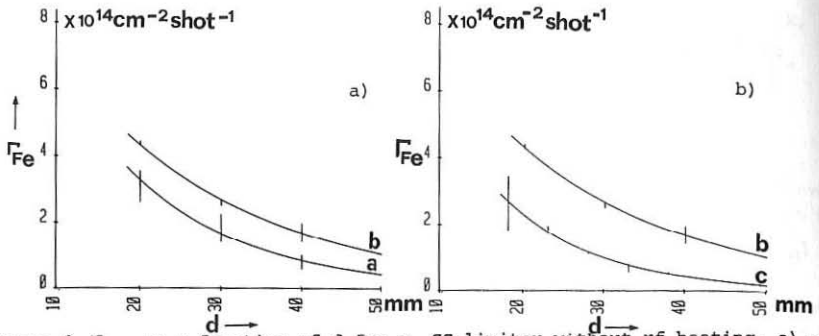

Figure 3. Γ_{Fe} as a function of d for a SS limiter without rf heating, a) and with rf heating and a carbon limiter with rf heating, c). rf power=108 kW.

similar energies (~150eV) then S_{Fe}=0.5 and S_O=0.3. Using these values and measured fluxes of O and Fe, we calculate $\alpha = 7.5 \times 10^{-16}$ for an O/Fe ratio of 3. These results show excellent self consistency and agree also with global estimates of the O and Fe concentrations in TCA /8/.

CONCLUSIONS

The data presented demonstrate that impurity induced sputtering by O and Fe ions account for the principal erosion processes in the scrape-off layer of TCA. The effect of rf heating is to increase the Fe impurity flux by a factor of ~2 However, this flux is reduced considerably by replacing the steel limiter with a carbon one. A global estimate /8/ using the data obtained in these investigations also leads to the conclusion that sputtering by impurities in the scrape-off layer is sufficient to explain the impurity levels observed. Other mechanisms, such as unipolar arcing cannot be excluded as contributing sources to impurity generation also.

Acknowledgements. The partial support of the National Energy Research Foundation (NEFF) and the Swiss National Science Foundation is acknowledged.

REFERENCES

/1/ Cheetham, A.D. et al.: Proc. 11th Symp. Fusion Technol. (1980), Oxford, Pergamon Press 1981, Vol.1, p601.
/2/ de Chambrier, A. et al.: in Plasma Physics and Controlled Nuclear Fusion Research, Proc. 9th Int. Conf. Baltimore, 1982, IAEA-CN-41/J-1-1.
/3/ Stamp, M.F. et al.: Lausanne Report LRP 220/83 (1983).
/4/ Gimzewski, J.K. and Vepřek, S.: J. Vac. Sci. Technol., to be published.
/5/ Hechtl, E., Bohdansky, J. and Roth, J.: J. Nucl. Mater. 103&104 (1981) 333.
/6/ Thomas, E.W., Partridge, J. and Vince, J.: J. Nucl. Mater. 89 (1980) 182.
/7/ Gimzewski, J.K. et al.: Project Report 1982/83, University of Zürich (1983).
/8/ Hofmann, F. et al.: to be presented at the Symp. on Energy Removal and Particle Control in Toroidal Fusion Devices, Princeton, July 1983.

PRODUCTION AND TRANSPORT OF IMPURITIES IN THE ASDEX TOKAMAK PLASMA

K. Behringer, G. Fussmann, W. Poschenrieder, E. Taglauer and K. Bernhardi, A. Eberhagen, O. Gehre, J. Gernhardt, G.v.Gierke, E. Glock, G. Haas, F. Karger, M. Keilhacker, S. Kissel[+], O. Klüber, M. Kornherr, G.G. Lister, G. Lisitano, H.-M. Mayer, K. McCormick, D. Meisel, E.R. Müller, H. Murmann, H. Niedermeyer, H. Rapp, B. Scherzer, F. Schneider, G. Siller, P. Smeulders, F. Söldner, E. Speth, A. Stäbler, P. Staib, G. Staudenmaier, K. Steinmetz, K.-H. Steuer, Z. Szymanski[++], O. Vollmer, G. Venus, F. Wagner
Max-Planck-Institut für Plasmaphysik, EURATOM-Association, D-8046 Garching

ABSTRACT

The correlation of impurity fluxes and impurity densities in the plasma was studied in ASDEX for various elements and discharge parameters. The impurity confinement is well described by a diffusion transport model. With the influx of intrinsic impurities known, conclusions can be drawn on impurity sources and generation mechanisms.

1. INTRODUCTION AND METHOD

The impurity content of tokamak plasmas is measured quite routinely, but little is known about impurity fluxes due to plasma-wall interaction. However, a knowledge of these fluxes is very important for identifying the actual mechanisms and locations of impurity production. In ASDEX the correlation of the impurity density in the plasma and the respective impurity influx was studied in detail for different impurity species and experimental conditions. These are divertor (D) and toroidal limiter (tL) discharges in either H_2 or D_2, with or without neutral injection (N.I.). Since it is often difficult to measure the influx directly, the behavior of impurities was simulated by injecting gases, especially silane (SiH_4). Model calculations describing the measurements very well were also made.

In steady state, the total loss of impurity ions ϕ_i must be balanced by the total neutral influx ϕ_o. This outflux ϕ_i may be characterized by a particle confinement time, defined as $\tau_p = N_i/\phi_o$, where N_i means the total number of impurity ions in the plasma. In the context of a simple diffusion model /1/ the impurity ion flux can be calculated from an anomalous diffusion coefficient D_a and the gradient characterized by the ionization length of the neutrals, λ_{ion}. The particle confinement time is then

$$\tau_p = (\lambda_{ion} \cdot a)/2D_a.$$

λ_{ion} is a function of the neutral velocity v_o and the parameters of the edge plasma; D_a may be derived from transport studies of the plasma. The most accurate measurement in ASDEX by means of a neon-seeded pellet yielded

---

[+] On leave from Massachusetts Institute of Technology, Cambridge, USA
[++] On leave from Institute of Fundamental Technological Research, Warsaw, Poland

$D_a \sim 4000$ cm^2/s for a deuterium and $D_a \sim 6000$ cm^2/s for a hydrogen background plasma.

A more sophisticated model must take into account the presence of parallel flows in the plasma scrape-off and of friction between impurities and the background ions. In the following, measured values of τ_p are compared with calculated values. The latter were obtained by a transport program using the following expression for the flux density of the impurity species i (Ref./2/):

$$\vec{\Gamma}_i = -(D_a \frac{\partial n_i}{\partial r} + 2 \frac{D_a \cdot r}{a^2}) \, e_r$$

with $D_a = 4000$ cm^2/s. In the scrape-off region volume sinks are included to account for parallel transport. This program was also used for evaluating the impurity densities from measured radial profiles of individual spectral lines.

2. IMPURITY CONFINEMENT

2.1 Silane Injection

Silane was injected into ASDEX discharges to simulate wall-produced impurities. For this purpose a flux of about 10^{19} atom/s was puffed through a gas valve in the torus midplane. When this valve is opened, the radiation rises to a plateau value about 200 ms later. After the flux is switched off, the signals disappear. This shows that the processes of deposition and subsequent erosion of Si do not falsify the flux. τ_p can therefore be determined from the gas flux and the Si density in the plasma, as derived from absolute measurement of Si lines.

The results for different experimental conditions and background plasmas are summarized in Table 1. The code calculations in the last column assume that the neutral silicon penetrates the plasma edge at room temperature.

Table 1

type	gas	$\bar{n}_e (10^{13} \text{cm}^{-3})$	τ_p (ms) exp.	τ_p (ms) calculation
divertor	D_2	4.4	1.8	1.8
divertor	H_2	4.4	1.6	1.8
tor. limiter	H_2	3.0	1.2	2.2
tor. limiter + N.I.	H_2	3.0	0.5	1.4

First the experimental results are discussed. A comparison of divertor H_2 and D_2 plasmas shows that the particle confinement times are very similar, though a different diffusion coefficient was previously found. The linear dependence on D_a is probably compensated somewhat by different properties of the H_2 and D_2 edge plasmas. Comparing the limiter and divertor cases, it turns out that the shielding properties of the two discharges are little different; in fact, the limiter boundary results in an even lower impurity confinement time. With neutral injection, τ_p is further reduced owing to a hotter edge plasma. The calculated values (with $D_a = 4000$ cm^2/s may be regarded as agreeing quite well with measurements considering the large uncertainties in the edge plasma parameters. For the N.I. case, an increase of

$D_a \sim 4000$ cm^2/s for a deuterium and $D_a \sim 6000$ cm^2/s for a hydrogen background plasma.

A more sophisticated model must take into account the presence of parallel flows in the plasma scrape-off and of friction between impurities and the background ions. In the following, measured values of τ_p are compared with calculated values. The latter were obtained by a transport program using the following expression for the flux density of the impurity species i:

$$\vec{\Gamma}_i = -(D_a \frac{\partial n_i}{\partial r} + 2 \frac{D_a \cdot r}{a^2} n_i) \vec{e}_r$$

with $D_a = 4000$ cm^2/s. In the scrape-off region volume sinks are included to account for parallel transport. This program was also used for evaluating the impurity densities from measured radial profiles of individual spectral lines.

2. IMPURITY CONFINEMENT

2.1 Silane Injection

Silane was injected into ASDEX discharges to simulate wall-produced impurities. For this purpose a flux of about 10^{19} atom/s was puffed through a gas valve in the torus midplane. When this valve is opened, the radiation rises to a plateau value about 200 ms later. After the flux is switched off, the signals disappear. This shows that the processes of deposition and subsequent erosion of Si do not falsify the flux. τ_p can therefore be determined from the gas flux and the Si density in the plasma, as derived from absolute measurement of Si lines.

The results for different experimental conditions and background plasmas are summarized in Table 1. The code calculations in the last column assume that the neutral silicon penetrates the plasma edge at room temperature.

Table 1

type	gas	$\bar{n}_e (10^{13}\text{cm}^{-3})$	τ_p(ms) exp.	τ_p(ms) calculation
divertor	D_2	4.4	1.8	1.8
divertor	H_2	4.4	1.6	1.8
tor. limiter	H_2	3.0	1.2	2.2
tor. limiter + N.I.	H_2	3.0	0.5	1.4

First the experimental results are discussed. A comparison of divertor H_2 and D_2 plasmas shows that the particle confinement times are very similar, though a different diffusion coefficient was previously found. The linear dependence on D_a is probably compensated somewhat by different properties of the H_2 and D_2 edge plasmas. Comparing the limiter and divertor cases, it turns out that the shielding properties of the two discharges are little different; in fact, the limiter boundary results in an even lower impurity confinement time. With neutral injection, τ_p is further reduced owing to a hotter edge plasma. The calculated values (with $D_a = 4000$cm^2/s) may be regarded as agreeing quite well with the measurements considering the large uncertainties in the edge plasma parameters. For the N.I. case, an increase of

to the spectroscopic measurements the limiter surface is the main source of oxygen, too. No quantitative estimate can be made in this case, but metal oxide and adsorbed water are expected to be responsible for the oxygen contamination.

The iron influx in divertor discharges can readily be explained by sputtering due to charge-exchange neutrals, even if the yield must be strongly reduced to account for surface conditions. This interpretation has already been adopted /4/ owing to the similar time behavior of the high-energy CX flux and Fe density in the plasma. Additional information may be derived from the transition of H_2 to D_2 plasmas. In ASDEX D-discharges a strong increase of the iron content has always been observed during this change of the working gas, while the amount of light impurities remains practically the same. As demonstrated by the silane results, the containment times in H_2 and D_2 are not much different. The higher metal contamination must therefore be due to a higher impurity influx in D_2 compared with H_2, a conclusion which is nicely confirmed by the collecting probe measurements in the divertor chamber. This dependence of the iron flux on the plasma background mass is a further indication of sputtering by CX neutrals.

Information on the oxygen sources is obtained by measuring the gaseous oxygen compounds in the divertor chamber. This indicates that oxygen must originate from the vessel walls at the beginning of the discharge, probably desorbed by low-energy H neutrals (necessary yield $\geq 10^{-3}$). Later, a pressure of H_2O and CO builds up in the divertor chambers which is sufficiently high to explain the measured oxygen flux, i.e. oxygen is just recycling. According to the measurements it is obvious that the vessel walls can build up a few monolayers of water between successive shots. The effective long-term decrease of O is therefore very slow and is determined by the speed of the turbopumps.

The behavior of divertor-produced metallic impurities is still being studied, but is complicated by the fact that the vessel walls are also covered with these materials.

4. DEPOSITION OF MATERIAL ON WALLS AND WINDOWS

ASDEX H_α windows have been regularly analyzed with respect to deposited metals. Layer thicknesses of up to 1 µm and up to 10^4 droplets per mm^2 have been found, the result being strongly correlated with the position of the poloidal limiter /5/. The amount of transported material in this case is much too high to be explained by the above fluxes during discharges and the integrated discharge times. This transport must be due to other processes such as electric arcs, droplets or flakes falling onto the plasma, or occasional melting of the limiter due to local power overload.

References

/1/ Engelhardt, W. and Feneberg, W., J. Nucl. Mat. 76 & 77 (1978) 518.
/2/ Behringer, K., et al., in Proceedings of IAEA Technical Committee Meeting on Divertors and Impurity Control, M. Keilhacker and U. Daybelge (Ed.). Garching 1981, p. 42.
/3/ Vernickel, H., et al., J. Nucl. Mat. 111 & 112 (1982) 317 - 322.
/4/ Keilhacker, M., et al., Physica Scripta T2/2 (1983) 443 - 453.
/5/ Staib, P., et al., J. Nucl. Mat. 111 & 112 (1982) 173 - 176.

A COMPARISON BETWEEN STEEL, CARBON AND TiC-COATED LIMITERS IN THE TCA TOKAMAK

R. Behn, F. Hofmann, Ch. Hollenstein, B. Joye, J.B. Lister,
S. Nowak+, J. O'Rourke and A. Pochelon
Centre de Recherches en Physique des Plasmas
Association Euratom - Confédération Suisse
Ecole Polytechnique Fédérale de Lausanne
21, Av. des Bains, CH-1007 Lausanne / Switzerland

+ University of Fribourg, Switzerland

N.J. Peacock and M.F. Stamp
Culham Laboratory, Euratom - UKAEA Association
Abingdon, OX 14 3DB

ABSTRACT

We present a full analysis of the effects on the plasma purity due to changes in the material and design of the limiters in TCA. Almost identical limiters were constructed from 304 L stainless steel, graphite and TiC-coated graphite, to replace our initial stainless steel bar limiters. The limiters were studied under identical imposed experimental conditions before and during the rf-pulse (2.7 MHz). We correlate the information derived from bolometric, spectroscopic and resistivity measurements as well as residual gas analysis. The insertion of pure carbon limiters led to a large reduction in the radiated power loss and in the intensity of the core iron lines. The TiC-coated graphite limiter led to a further reduction in the radiation, but to a more peaked radiated power profile during the rf-pulse.

LIMITER DESIGN

The initial limiters of TCA were four type 304 SS bar limiters. The observation of important melting of the inner and outer limiters, as well as the increase in iron contamination during the rf-pulse led us to study the influence of limiter design and material on the plasma purity.

Three sets of almost identical limiters were constructed from SS 304, carbon and TiC-coated graphite and compared with the initial steel bar limiters. Figure 1 shows a cross-section of the vacuum vessel with the position of the limiters. The outer limiter, which is not in the same poloidal plane, but 40 ° away toroidally, is movable. The top and bottom limiters are cylindrical. The radius of curvature of the limiters is slightly bigger than the minor radius of the plasma (a = 18 cm). The cross-section in the toroidal direction (Fig. 1 left) is chosen so as to give a constant temperature increase over the whole surface /1/. The toroidal length (12 cm) is sufficient to avoid any melting of the material even if the total plasma energy is deposited on the limiter. Following this design, stainless steel limiters were constructed from SS 304. The graphite (5890 PT from Carbone-Lorraine, France) was machined and cleaned

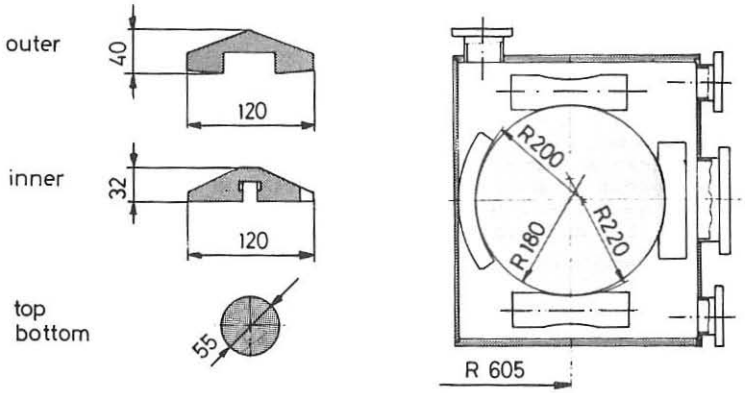

Fig. 1: Cross-section of the vacuum vessel with the limiters (mm)

by ultra-sound in distilled water and then out-gassed at 1200 ° C. Unfortunately, this process produced a slight metallisation of the surface, and an Auger analysis showed 6-8% of metallic impurities (mainly iron and chromium). After being used in the Tokamak for about 1250 discharges, they were polished to remove the impurities, cleaned and out-gassed, and used as a base for the TiC-coating. The 7.5-9 µm TiC-coating was deposited by CVD (LSRH; Neuchâtel/Switzerland) and the limiters were again cleaned and out-gassed at 1000 ° C.

RESULTS

The comparison between the four sets of limiters was made under identical experimental conditions, namely 1.51 Tesla, q_a = 4.3, a = .18 m, n_{eo} = 3×10^{19} m^{-3} and with deuterium as the filling gas. The Alfvén rf-pulse (2.7 MHz) is switched on for 30 ms when the plasma resistance reaches its lowest value. The rf-power is about 80 kW for all cases.

Figure 2 shows the evolution of the radiated power profile during the discharge with the bar limiters. At 45 ms, when the rf-pulse is switched on, the radiation is already peaked on axis (1 W/cm^3). This value can only be explained by the radiation of heavy impurities. A simulation based on a coronal model /2/ gives in this case an iron concentration on axis of about 1%. This high impurity content is the cause of a resistive discharge which needs a loop voltage of 2.4 V. The ratio of radiated power to ohmic power reaches 0.6 in the ohmic phase of the discharge. During the additional heating the increase in the radiation losses is partly explained by the inavoidable density increase (~ 30% of n_e), but the iron concentration also increases. This is shown by spectroscopic measurements on core iron lines (Fe XVI and Fe XVIII), the intensities of which are multiplied by a factor of 2-3 /3/.

We found, surprisingly, no improvement when replacing our old limiters by

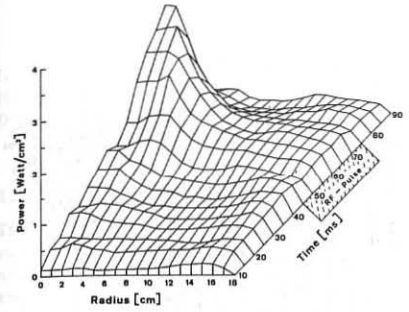

Fig. 2: Radiation profile for bar limiters

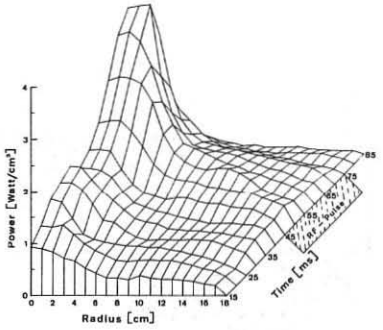

Fig. 3: Radiation profile for SS 304 L limiters

carefully-profiled steel limiters and indeed would infer a degradation. The radiation on the axis reaches a value of about 1.6 W/cm^3 before the Alfvén pulse (Fig. 3). The total radiation losses correspond to 70% of the ohmic power and the resistive voltage reaches 3 V. During the rf-pulse, the huge increase in radiation at the centre is partly due to a bigger increase in density than in the previous case, as well as a larger density peaking factor. Table I summarises the measurements of some impurity lines which show an increase of a factor of 2.5 - 3 for the core iron lines and about 2 for light impurities. We suggest that the increase in the surface area of the limiters increases the sputtering yield by more than the advantage gained from lower surface temperature. Indeed observation of the limiters after about 400 discharges did not reveal any traces of melting and only a very few points of arcing.

The insertion of pure carbon limiters led to a large reduction in the resistive voltage (V_r = 2 V) and in the radiated power (Fig. 4). P_{RAD}/P_{OH} is 0.5 in the ohmic part of the discharge and the radiation on axis does not exceed 1.1 W/cm^3 during the rf-pulse. The fact that we never observed a hollow radiation profile indicates that iron is always the main impurity responsible for the radiation losses at the centre. Table I shows a reduction of about two for the iron lines before, and even more during the rf-pulse, as compared with the stainless steel limiters. The central oxygen emission is seen to be similar to the case with

Limiter material:	304 L	C	TiC
Fe XVIII (974.7 Å)	1.0 (2.6)	0.55 (1.04)	0.33 (1.1)
Fe XVI (360.7 Å)	0.23 (0.62)	0.13 (0.25)	0.08 (0.24)
Ti XIV (2117.1 Å)	--	--	0.2 (0.5)
O VII (1623.7 Å)	1.12 (1.7)	1.2 (2.0)	1.3 (2.5)
C IV (1548.2 Å)	0.19 (0.5)	0.37 (0.79)	0.19 (0.45)

Table I Intensity of impurity lines (arb. units) before and ( ) during the Alfvén rf-pulse

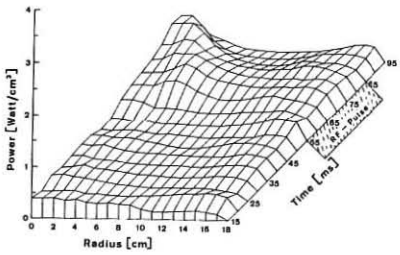

Fig. 4: Radiation profile for C-limiters

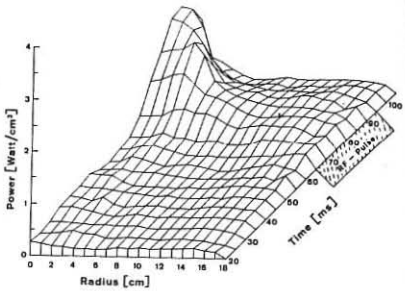

Fig. 5: Radiation profile for TiC-limiters

steel limiters. Typical discharges with carbon limiters had a Z_{eff} value of 3.5. After about 1250 discharges the limiters were practically unchanged in appearance.

With the TiC-coated carbon limiters, the radiated power was still lower (0.3 W/cm^3 on axis, P_{RAD}/P_{OH} = 0.45 before the rf-pulse). The resistive voltage decreases to 1.6 V and Z_{eff} to 2.5. The fact that titanium has a higher nuclear charge than carbon is conteracted by its better sputtering properties. The significant difference between C and TiC limiters is the relative increase in the core iron lines during the rf-pulse. Table I also shows an increase of a factor of 2.5 in the Ti XIV intensity. This increase in heavy ion concentration explains the larger radiated power at the centre during the rf-pulse. The TiC limiters survived some 1300 discharges and the coating was only removed on a small point on the upper part of the inner limiter.

The residual gas measurements after discharges in hydrogen indicated that the chemical reaction between the limiters and the adsorbed gas is comparable with TiC and stainless steel limiters. The CH_4 concentration with carbon limiters was 6 to 10 times bigger.

This work was partly supported by the Swiss National Science Foundation.

REFERENCES

/1/ Equipe TFR; Journal of Nuclear Materials, 105 (1982) 62.

/2/ Post, D.E., Jensen, R.V., Tarter, C.B., Grasberger, W.H., Lokke, W.A.; Atomic Data and Nuclear Data Tables 20, 5 (1977), 397.

/3/ Stamp, M.F., Pochelon A., Peacock, N.J., Lister, J.B., Joye, B., Gordon, H.; Lausanne Report LRP 220/83 (1983).

IMPURITY FLOW IN THE TOKAMAK SCRAPE-OFF LAYER

J. Neuhauser, W. Schneider, R. Wunderlich,
Max-Planck-Institut für Plasmaphysik, EURATOM Association,
D-8046 Garching, Germany.

I. INTRODUCTION AND MODEL

The charge state distribution of impurities in the highly inhomogeneous tokamak boundary depends strongly on the location and composition of the impurity sources and is usually far from local coronal equilibrium. Therefore, a theoretical investigation of the impurity transport requires rather sophisticated models, the dominant physical effects being quite different for different collisionality. In the high recycling regime of present-day tokamaks like ASDEX or of future experiments like INTOR, the mean free path of all relevant particles is small compared with typical system dimensions and a fluid description may be adequate (except for the narrow electrostatic layer at the target plate which enters via boundary conditions). In view of the low impurity content measured in ASDEX /1/ and the small tolerable impurity contamination in future fusion experiments, a test fluid approach seems to be justified. This requires $n_z Z^2 \ll n_e$, where n_e is the electron density and n_z is the density of the Z times ionized impurities. In this limit we may neglect collisions between impurities and also their influence on the background hydrogen plasma.

As a first approximation we consider only the flow parallel to the magnetic field lines. Each ionization stage is then treated as a separate fluid which is coupled to neighbouring states via ionization and recombination and to the hydrogen background plasma via collisions and the ambipolar electric field E ($n_e \cdot e \cdot E = -\partial p_e/\partial s - 0.71 \cdot n_e \cdot \partial(kT_e)/\partial s$, ref. /2/; $p_e = n_e kT_e$, T_e = electron temperature, $e = 1.6 \cdot 10^{-19}$ As). For simplicity, the impurity temperature T_z is assumed to be equal to the hydrogen ion temperature T_i. Then we have to solve the following set of equations:

$$\frac{\partial n_z}{\partial t} + \frac{\partial}{\partial s}(n_z v_z) = S_{z-1} n_{z-1} - (S_z + R_z) n_z + R_{z+1} n_{z+1} + d_z \; ; \qquad (1)$$

$$\rho_z\left(\frac{\partial v_z}{\partial t} + \frac{\partial v_z^2}{2\,\partial s}\right) + \frac{\partial p_z}{\partial s} - n_z Z e E - \rho_z \frac{(v - v_z)}{\tau_z} - \alpha_z n_z \frac{\partial (kT_e)}{\partial s} - \beta_z n_z \frac{\partial (kT_i)}{\partial s}$$

$$= S_{z-1}\rho_{z-1} v_{z-1} - (S_{z-1}\rho_{z-1} + R_{z+1}\rho_{z+1}) v_z + R_{z+1}\rho_{z+1} v_{z+1} - m_z v_z d_z \; ;$$

$$\rho_z = m_z n_z \; , \quad p_z = n_z kT_z \; ; \quad 1 \le Z \le Z_{max} \qquad (2)$$

S/n_e and R/n_e are the ionization and recombination rate coefficients, v_z is the impurity flow velocity and d_z is an externally prescribed impurity source, τ_z the Spitzer slowing-down time /3/. For the electron thermal force coefficient, following the derivation of Braginski /2/, we get $\alpha_z = 0.71\ Z^2$.

For the ion thermal force coefficient β_z, the expression given by Chapman /4/ is used, the asymptotic value for heavy impurities being $\beta_z = 2.65\ Z^2$. The numerical solution of the time-dependent equations is similar to that described in /5/. The rate coefficients are taken from Behringer /6/.

II. RESULTS

The hydrogen background plasma parameters are taken from a one-dimensional hydrodynamic two-fluid model /7/. Typical profiles as calculated for ASDEX, assuming a total loss power of 1 MW and a particle flux of $10^{22}\ s^{-1}$ into the scrape-off are shown in Fig.1. s is the coordinate along field lines from the midplane (s = 0) to the target plates (s = 15). Because of the strong recycling in the divertor chamber ($s \gtrsim 12$m), all parameters vary appreciably along field lines, and the flow outside the divertor is subsonic (Mach number $M_p \approx 0.2$).

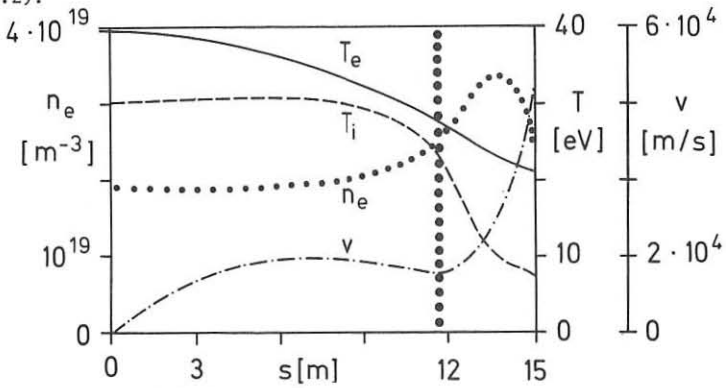

Fig. 1: Variation of the hydrogen plasma parameters along magnetic field lines for an ASDEX-type configuration.
(s=0: midplane; s=15m: target plate; s≈12m: divertor throat).

Assuming that neutral oxygen from the main chamber wall is ionized in the scrape-off near the equatorial plane (O II source around s=0) and that all oxygen ions arriving at the target plate are absorbed, we get the density and velocity profiles for individual charge states shown in Fig. 2 (left-hand side). Oxygen is quickly ionized to intermediate charge states and swept towards the divertor by the frictional drag force. Near the divertor entrance, however, the ion temperature gradient is high, while the hydrogen velocity is still low. Here, the thermal forces, directed towards high temperature, become dominant and the impurity density builds up until the resulting pressure gradient is high enough to overcome the thermal force barrier. The velocity profiles also show clearly the retardation at the divertor entrance. At the target plate, the oxygen ions arrive at nearly hydrogen sound speed and their total kinetic energy including the gain in the electrostatic Debye layer is around 600 eV with obvious consequences for the sputtering of target material.

If the thermal forces are neglected ($\alpha_z = \beta_z = 0$), the pronounced density peak near the divertor throat disappears and the velocity of the most prominent charge states (> III) are close to the background velocity everywhere (Fig. 2, right-hand side).

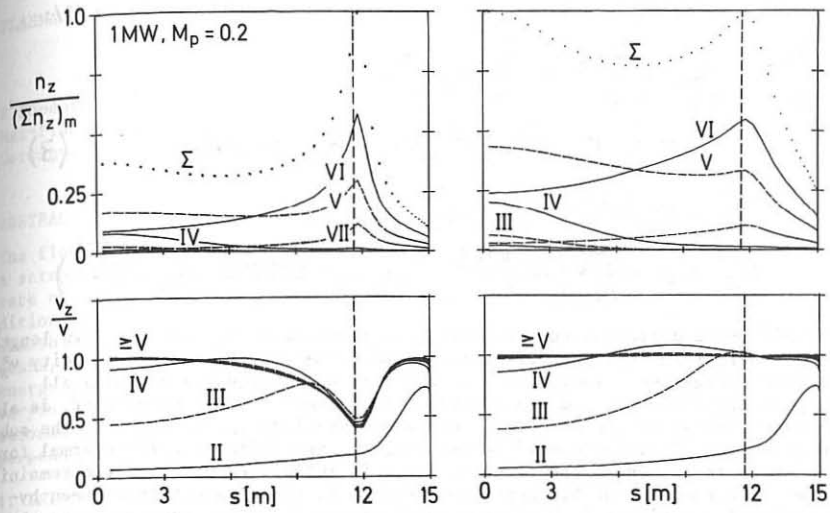

Fig. 2: Normalized density and velocity profiles for individual oxygen charge states along magnetic field lines with (left) and without (right) thermal forces. The total density is denoted by Σ.

Results for the same hydrogen plasma but other impurities (e.g. Fe, C, He) show a qualitatively similar behaviour. Because of the Z^2 dependence of the collision frequency, the accumulation peak near the divertor entrance increases sharply with Z. Changing the hydrogen background, the most important feature is that thermal forces become the more important, the lower the local Mach number is. For very low Mach number even impurity accumulation near the midplane is observed, resulting in a serious deterioration of the impurity pumping. Self-sputtering of target material was studied for iron, showing the importance of the frictional drag in addition to the electrostatic energy gain. The threshold for the onset of a self-sputtering avalanche is not a simple function of the plasma temperature at the target.

DISCUSSION

In the collisional regime, the most significant effect with respect to the impurity flow parallel to the field lines is the occurence of thermal forces. Since these are directed towards the hot central plasma, they may strongly affect the impurity removal. Considering only the collisional momentum transfer between impurities and hydrogen ions (i.e. the frictional drag and the ion thermal force), a simple criterion for impurity flow reversal is obtained: the thermal force dominates, if the local Mach number M becomes smaller than the ratio of the ion mean free path λ_i to the temperature gradient length λ_T, i.e. $M < \lambda_i/\lambda_T$. This criterion agrees roughly with the onset of density accumulation in the numerical calculations.

A simple but more complete formulation is obtained, if the inertia terms in eqs. (1) and (2) are neglected, as might frequently be justified in the subsonic region. A diffusion-drift equation is then obtained of the same form

as used for empirical perpendicular transport in the central plasma /5/:

$$\frac{\partial n_z}{\partial t} - \frac{\partial}{\partial s}\left(D_z^* \frac{\partial n_z}{\partial s}\right) + \frac{\partial}{\partial s}\left(n_z v_z^*\right)$$
$$= S_{z-1} n_{z-1} - (S_z + R_z) n_z + R_{z+1} n_{z+1} + d_z \qquad (3)$$

$$D_z^* = \tau_z k T_z / m_z = \lambda_z^2 / (2\tau_z)$$

$$v_z^* = v - \frac{\tau_z}{m_z}\left(\frac{\partial (kT_z)}{\partial s} - ZeE - \alpha_z \frac{\partial (kT_e)}{\partial s} - \beta_z \frac{\partial (kT_i)}{\partial s}\right)$$

The effective diffusion coefficient D_z^* is governed by the slowing down length λ_z at thermal energy. The difference between the effective drift velocity v_z^* and the background velocity v, i.e. the slip velocity $(v_z^* - v)$ contains all temperature gradients and the electric field, which, to leading order, is also proportional to the electron temperature gradient ($p_e \approx$ const. in the subsonic region /7/). The coefficients, however, are different. The thermal forces scale as Z^2, while the electric field is multiplied by Z and the remaining term is independent of Z. Therefore, at high Z, the slip motion between hydrogen and impurities is dominated by the thermal forces, especially by the ion part. Then, setting $v_z^* \lesssim 0$, we get again the simple criterion for flow reversal mentioned above.

In the collisional regime, where our model is applicable, $\lambda_i / \lambda_T \ll 1$, holds. Therefore, at high Mach number ($M \approx 1$), the impurities are efficiently swept onto the target plates together with the hydrogen. Thermal forces become important, however, for the subsonic flow to be expected in the high recycling regime of future experiments.

REFERENCES

/1/ Engelhardt W. et al., J.Nucl. Mat., 111 & 112, 337 (1982)

/2/ Braginsky, S.I., in Reviews of Plasma Physics, Vol. 1; M.A.Leontovich (Editor); Consultants Bureau, New York, 1965

/3/ Spitzer, L. jr., "Physics of Fully Ionized Gases"; 2nd Edition; Interscience Publishers, New York, 1962

/4/ Chapman, S., Proc. Phys. Soc. 72, 353 (1958)

/5/ Lackner K., Behringer, K., Engelhardt, W., Wunderlich, R., Z.f. Naturforschung 37a, 931 (1982)

/6/ Behringer, K., private communication

/7/ Chodura, R., Lackner, K., Neuhauser, J., Schneider, W., "Plasma Physics and Controlled Nuclear Fusion Research 1982", IAEA Vienna, Vol. I, p. 313 (paper CN-41/D-3-1).

PLASMA TRANSPORT TO THE WALL THROUGH THE ELECTROSTATIC SHEATH

R.Chodura
Max-Planck-Institut für Plasmaphysik, EURATOM Association, D-8046 Garching, Germany.

ABSTRACT

The flow of particles and energy through the presheath and sheath region of a scrape-off plasma is calculated using a kinetic model. For a given input rate of particles and energy into the presheath and a given reflextion condition at the wall the plasma state behind the presheath and ahead of the sheath is determined. Two dimensionless quantities are characteristic for this state, i.e. the ratio of flow velocity to sound speed and the ratio of total energy flux to convected thermal energy flux. Both quantities are derived for varying angles of incidence Ψ of the magnetic field. Electron reflexion by secondary emission from the wall enhances the energy flux ratio for nearly perpendicular field and leaves it unaffected for grazing incidence of the field.

1. INTRODUCTION

Plasma flow along the scrape-off layer to the absorbing wall of a limiter or divertor is adjusted to ambipolarity by an electric field. This field is relatively weak in the so-called presheath region far upstream of the wall and becomes strong in the electrostatic sheath immediately ahead of the wall. While the presheath has large dimensions, is collision-dominated and includes particle sources, for instance by ionization, the electrostatic sheath is small of the order of a Debye - or ion gyro length, and is collision- and source-free. In the latter region the velocity distribution of the plasma is strongly affected by the wall and far from being Maxwellian.

The conditions of the plasma at the transition between presheath and sheath (indicated by the index P in the following), is determined by the sources in the presheath, and by the properties of the wall: The x-component (perpendicular to the wall) of particle flux F_x and the sum of ion and electron energy flux Q_x is given by the production of particles and energy in the presheath. They both are connected (assuming cold ions) by

$$Q^i_{xP} + Q^e_{xP} = \left(\frac{m_i}{2} V_P^2 + \delta T_{eP} \right) F_x \qquad (1)$$

where T_e is the electron temperature and δ a numerical factor with depends on the reflectivity of the wall. For an ion-absorbing wall the flow velocity V_p at the end of the presheath is of the order of the sound speed, i.e.

$$V_P^2 = \gamma T_{eP} / m_i \qquad (2)$$

where γ is a numerical factor. Thus, knowing γ and δ, equs. (1) and (2) determine the electron temperature T_{ep} ahead of the sheath. Finally, the density n_p ahead of the sheath is given by

$$n_P = F_x / (V_P \cos\Psi) . \qquad (3)$$

In the following section a numerical model is presented which describes the particle kinetics in the presheath and sheath region, and allows to determine the numerical factors γ and δ .

2. MODEL

A 1d particle model /1/ is used which follows the collisionless particle orbits in their self-consistent electric field $\underline{E}$ and externally prescribed magnetic field $\underline{B}$ of strength such that $\omega_{ce} = \omega_{pe}$ and arbitrary direction ψ. (Fig. 1). Ions and electrons are borne with the same rate in a localized source to the left, electrons with temperature T_{eo}, ions with $T_{io} = 0$. Electrons reflected by the electric field and passing the plane x = 0 outward are replaced by the same number entering with temperature T_{eo}.

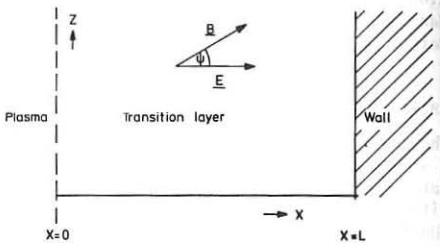

Fig. 1: Geometry of the model.

3. FLOW VELOCITY

Fig. 2a shows the x-profile of the mean flow velocity $\underline{V}$ of ions and electrons for a magnetic field angle $\psi = 70°$. The source to the left (which extends over about 5 Debye lengths λ_D gives rise to the presheath acceleration of the flow to a plateau value $\underline{V}_p$. The acceleration extends over about an ion gyro radius, is quasineutral and aligned with the magnetic field direction. After a plateau, the flow again becomes accelerated in the sheath. At first the flow stays quasineutral over the ion gyro scale length. Ions begin to deviate from the magnetic field lines while electrons stay tied up. Only at the last few Debye lengths also the electrons become decoupled from field lines and are strongly accelerated towards the wall. The flow becomes non-neutral. Fig. 2b gives the plateau value of the flow velocity V_p ahead of the sheath for different magnetic field angles ψ .

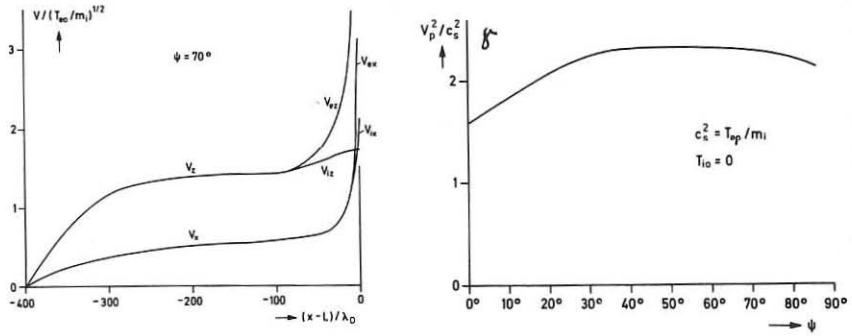

Fig. 2a,b: Flow velocity $\underline{V}(x)$ of ions and electrons and plateau velocity $\underline{V}_p^2$ ahead of the sheath.

4. ENERGY FLOW

In Fig. 3a the energy flux profile Q(x) is plotted for ions and electrons. In the presheath as well as in the sheath electron thermal energy is transformed to ion kinetic energy. Again, the energy flux is aligned to the magnetic field except for the sheath were ion and electron energy flux deviate at the ion-gyro and Debye length respectively. The plateau value of the energy flux after the presheat and ahead of the sheath i.e. the factor δ of eq. (1) is given in Fig. 3b for different angles ψ .

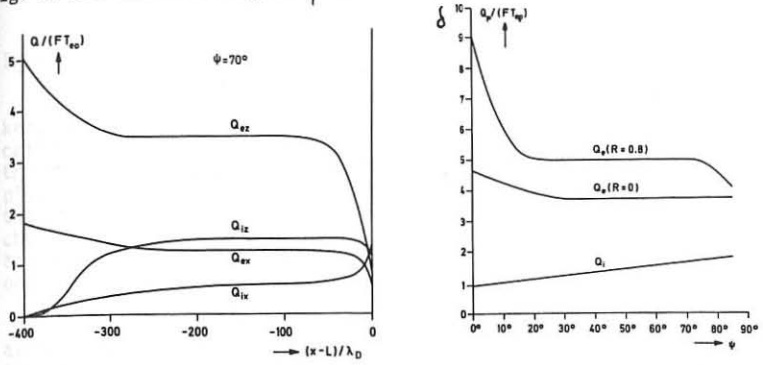

Fig. 3a,b: Energy Flux Q(x) of ions and electrons and plateau values $|Q_P|$ ahead of the sheat.

5. SECONDARY ELECTRON EMISSION

The preceding results were obtained for a completely absorbing wall. If it is assumed that the wall reemits incoming electrons above a small threshold energy as cold ones with a reflexion coefficient R the flow velocity of Fig. 2 and the ion energy flow of Fig. 3 is unchanged while the electron energy flow goes up since for the same absorbed particle flux F_x now more electron energy must be transported to the wall. Fig. 3b shows the plateau value Q_{ep} for R = 0.8. Only for nearly perpendicular magnetic field the electron energy flux is enhanced according to the considerations of /2/. For oblique angles many electrons emitted from the wall reencounter the wall by their gyro motion and are absorbed. For nearly grazing angles ψ nearly no reemitted electrons can escape the wall, therefore Q_e retruns to the value for the completely absorbing wall.

REFERENCES

/1/ R.Chodura: Phys. Fluids 25, 1628 (1982)
/2/ G.D.Hobbs, J.A.Wesson: Plasma Physics, 9, 85 (1967)

Surface Conditioning of the TEXTOR Liner and Limiters by Plasmachemical Carbon Deposition

J. Winter, F. Waelbroeck, P. Wienhold, H.G. Esser, L. Könen, T. Banno, E. Rota
Institut für Plasmaphysik Kernforschungsanlage Jülich GmbH, Association EURATOM/KFA, 5170 Jülich, FRG
and
R.E. Clausing, Oak Ridge National Laboratory, Oak Ridge, Tennessee, USA

Introduction

Several questions regarding the influence of carbon present on the tokamak walls and its role in plasma performance are still open today. Empirically, the results of experiments with additional heating are improved when the limiter material is graphite instead of a metal alloy: low Z carbon replaces then the medium Z metals in the plasma. Problems arise however from the need for a long conditioning of the graphite in the tokamak, from its chemical erosion, hydrogen retention and from the difficulty in designing actively cooled graphite limiters. An alternative way of introducing carbon onto selected areas of a fusion device appears highly desirable.

We have developed a plasmachemical process using the RG (radiofrequency assisted glow) discharge conditioning system /1/. It allows to deposit and to remove in situ thin surface films of carbidic carbon on metal surfaces. Both processes can be controlled accurately and are rapid. By adjusting electrical potentials, a selective deposition on the liner, or the limiter, or on both can be achieved. As shown earlier /1/, the same technique is also useful for the oxygen removal from cold walls.

Experimental

The first wall of TEXTOR is a 1 mm thick liner made of Inconel 625, with a minor radius of 0.55 m and a major radius of 1.75 m. Its inner surface area is about 35 m^2. It can be heated by DC- current to 600 °C. The stainless steel vacuum vessel can be baked up to 300 °C. During the experiments reported here, the liner temperature was 150 °C. The conditioning method applied is the RG-discharge; the technique /1/ and the apparatus /2/ have been described in detail elsewhere.

A hot (150 °C) differentially pumped RGA-system (Balzers 112) was used to monitor the gas species during RG discharges (throttle ratio ~ 100) and immediately after tokamak shots (throttle ratio ~ 5). An Auger spectrometer attached to a sample transfer system /3/ provided data on the surface composition of a liner specimen which was exposed to the RG cleaning discharges. Two optical spectrometers recorded the OVI and CV line radiation during tokamak discharges.

The liner had been thoroughly precleaned by RG-discharges in pure hydrogen for several days. An RG-discharge in H_2 containing 0.85 % CH_4 was then operated for 30 min at a total pressure of 2.5×10^{-3} mbar and at an effective pumping speed of 6.6×10^{3} l/s. The RG discharge was switched off and the vessel evacuated during the night. Tokamak operation started the next morning.

Results and Discussion

The evolution of the partial pressures of CH_4 and CO in the torus before, during and after the RG-discharge is shown in fig. 1. The right hand scale indicates the corresponding flow rates. The lower insert shows the DC-currents applied. The CH_4 pressure is initially 2.15×10^{-5} mbar, representative of its 0.85 % fraction in the hydrogen gas. At t=o the RG-discharge is switched on with a current of 1.14 A. The CH_4 signal decreases immediately to 1.51×10^{-5} mbar. The CO partial pressure rises to 0.7×10^{-5} mbar from its background level. When the current is increased after 9.6 min to 2.48 A, CH_4 decreases to 1.2×10^{-5} mbar and CO increases to 0.70×10^{-5} mbar. When the discharge is switched off after 30 min, CH_4 returns to its initial value; the CO level is slightly lower than before.

The total number of CH_4 molecules which disappeared from the gas during the RG-discharge is obtained by the integration of the flow rate differences before and during the discharge. Their number is 3.2×10^{21}. Some of the carbon atoms (7.3×10^{20}) reappear in the gas phase in the form of CO. 2.5×10^{21} atoms have been deposited onto the wall. This is equivalent to about 3.5 monolayers*. The enhanced CO production corresponds to the removal of about one monolayer oxygen from the surface.

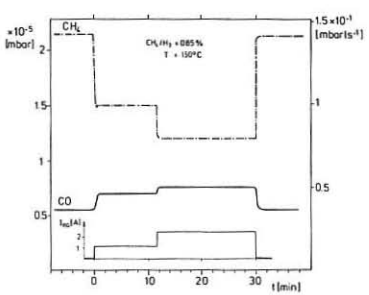

Fig. 1 TEXTOR RG-discharge in a throughflow of H_2 to which 0.85 % CH_4 was admixed. The total pressure is 2.5×10^{-3} mbar. Decrease of the CH_4 partial pressure and increase of the CO partial pressure as a funciton of time and DC-current (lower insert). The right hand scale indicates the flow rates.

Table 1 shows the results of the in situ Auger analysis. The reference state (A) before the carbon deposition is characterized by 3 at % C and 13 at % O on the surface. This was a typical composition of the wall for TEXTOR at that time (leakage rate $\leq 5 \times 10^{-5}$ mbar l/s). It no longer changed significantly when prolonged RG-discharges in pure hydrogen were operated. After the carbon depostion (B), the concentration of C increased to 22 at %, that of oxygen decreased to 8 at %. It is important to note, that the carbon is present on the surface in carbidic form. The fraction of graphitic carbon is too small to be resolved from the Auger signal. Assuming that there was no diffusion of C into the bulk of the sample during the deposition process, one deduces a coverage of about 1 monolayer. Assuming further that the specimen is truly representative of the whole liner, the total number of C atoms on the first wall of TEXTOR is about 8×10^{20}. Since the surface roughness of the liner, the diffusion profile of C and the homogeneity of the depostion are not known, the agreement of the Auger data and that of the RGA particle balance appears reasonable.

On the same basis one evaluates that a total number of about 1.75×10^{20} oxygen atoms were removed from the surface. This is roughly 1/4 of the value from the RGA measurements.

No darkening of windows or other deleterious effects were observed as a consequence of the carbon deposition.

The first tokamak discharges after the carbonization liberated some carbon from the wall. The maximum intensity of the CV radiation increased from 1 unit (arbitrary scale) for the reference state, to 5 units; the OVI intensity decreased from 5 to 2.8 units. These ratios correspond well with those of the Auger analysis. A significant CO release was observed in the RGA after each tokamak shot . It was larger than that of CH_4 and had not been observed to such an extent before. It may well be that H_2O outgassing from hidden surfaces in the machine becomes dissociated, ionized and confined in the plasma. Oxygen ions splash on the first wall at the termination of the tokamak pulse where they meet carbon and form volatile CO. The reoxidation of the surface is thus reduced.

The overall performances of the tokamak discharges were essentially unchanged. The stability of the pulses and their duration (up to 2.5 s) in particular were not affected except for the first five tokamak pulses following the carbon deposition. An increase of T_e and of the electron energy confinement time have been indicated but remain to be rechecked in forthcoming experiments. The influence of carbon on the metal impurity release during tokamak shots could not be studied during this first experiment.

After about 54 tokamak discharges and 16 h RG-cleaning in pure hydrogen the surface composition was checked again by Auger spectroscopy. The oxygen level had returned to its value before the carbon deposition, C decreased to 14 % (row C in table 1). This indicates that only little carbon is lost during the tokamak discharges but that it is mainly redistributed around the torus. The increase of oxygen may be due to the diffusion of C into the bulk in the meanwhile such that it no longer competes with O for surface sites.

RG-discharges in pure hydrogen were run uninterruptedly during the following weekend. They brought the wall back to the initial reference surface composition.

* One monolayer is taken to be 2×10^{15} atoms cm^{-2}.

Table 1:

Surface composition of a liner specimen in at % as measured by in situ Auger spectroscopy

A reference state of the liner, precleaned by RG discharges in hydrogen

B after 30 min RG discharge in H_2 + CH_4 (0.85 %)

C after 54 tokamak discharges and 16 h RG cleaning in hydrogen.

	Cr	Fe	Ni	Mo	C	O	S	N	K	Cl
A	18	5	49	2	3	13	5	4	1	1
B	16	3	41	1	22	8	4	4	-	1
C	18	4	39	-	14	14	5	4	-	1

Conclusion

The information obtained in the first experiment on the reversible plasmachemical deposition of thin carbon films in TEXTOR is still incomplete. Especially a more detailed analysis of the metal impurity concentration before and after the carbonization is required. Nevertheless several conclusions can be drawn:

- the technological feasibility of an in situ deposition of carbon films has been demonstrated;
- only RGA is required for the process control, an attractive feature for large machines with engineering orientation;
- the response of tokamak discharges on the formation of a carbidic wall surface, which results from our method, appears to be favourable;
- no frequent redeposition of C appears to be necessary. If it were the case, the puffing of a little CH_4 at the end of a regular tokamak discharge may suffice /4/.

The time required for the balanced formation of carbide layers on the wall and on limiters may explain the long tokamak conditioning of graphite limiters.

References

/1/ F. Waelbroeck, J. Winter, I. Ali-Khan, P. Wienhold, B. Brandt, K.J. Dietz, Rep. JÜL 1692, Dec. 1980

/2/ J. Winter, F. Waelbroeck, P. Wienhold, Proc. 12th Symposium on Fusion Technology, Jülich 1982, Fusion Technology 1982, p. 369

/3/ R.E. Clausing, L. Heatherly and L.C. Emerson, J. Vac. Sci. Technol. 16(1979)708

/4/ F.G. Waelbroeck, J. Winter, P. Wienhold, L. Könen, T. Banno, L. Grobusch, E. Rota, K.G. Tschersich and TEXTOR-team, review paper IX. Intern. Vacuum Congress, Madrid, Sept. 26 - Oct. 1, 1983

Experiments in TO-2-tokamak with toroidal divertor

I.J.Artemenkov, K.Yu.Vukolov, A.A.Gurov,
J.A.Kovan, S.G.Maltsev, P.J.Melikhov,
P.A.Mukhin, A.P.Popryadukhin, N.N.Schwindt,
K.H.Yusupov
I.V.Kurchatov Institute of Atomic Energy, Moscow, USSR

Studies in the divertor operation at the plasma density 1÷2 . $10^{13}cm^{-3}$ have been carried out. The divertor efficiency for the fluxes of particles ($\eta_p \simeq 85\%$) and for energy ($\eta \simeq 80\%$)have been measured. The divertor layer structure and the plasma parameters in it have been studied. The energy anomality factor is found to be equal: $q = 3$. The absolute concentrations of the main impurities in the tokamak plasma are found by the optical methods. The calculated Z_{eff} on the basis of these measurements exceeds unity by 1%. The burn-out of neutral hydrogen near the walls of the toroidal chamber at a cross-section located far away from the gas feed valve is found by the luminosity of H_β. The power-supply of 1 MW for ICRH has been prepared. The study of wave propagation at a low power level in plasma has been done. It has been shown that a fast magnetosonic wave propagates within a raystrack tokamak, at a field drop by 35% in the divertor zone, in the same manner as in the circular tokamak.

Preliminary Abstract (4-page paper not received in time).

DEUTERIUM AND IMPURITY FLUXES IN THE LIMITER SHADOW OF T-10: INDICATION FOR TIME DEPENDENT LOCAL SOURCES

K.F. Alexander, H. Grote, D. Hildebrandt, M. Laux, P. Pech, H.-D. Reiner, H. Strusny, H. Wolff, E. Kotai[x], A. Manuaba[x], F. Paszti[x]

Zentralinstitut für Elektronenphysik, AdW der DDR, Berlin, GDR

x) Central Research Institute, Hungarian Academy of Sciences, Budapest, Hungary

INTRODUCTION

Using the surface analysis station WASA /1/ time resolved measurements of deuterium and impurity fluxes for both toroidal directions at different radial positions in the near wall region of the limiter shadow of T-10 were carried out.

EXPERIMENTAL

Rotating a deposition probe behind fixed windows particle fluxes to the ion drift side and to the electron drift side were simultaneously detected with a time resolution of about 90 ms. Iron fluxes are routinely collected during single pulses on an Ag evaporation layer and are subsequently in-situ determined by SIMS /2/. The results of about one hundred pulses for three different radial positions are summarized here. Furthermore five shots were superimposed with PAPYEX as the collector material to get quantitative values for the particle densities and to extend the method to light impurities and working gas. The carbon samples were transferred in air and analyzed by RBS and ERD making it also possible to estimate the impact energy of deuterium. The toroidal and poloidal location of the WASA probe and main internal structures (active sector limiter facing the ion drift side of the probe and aperture limiter facing the electron drift side) are shown in Fig. 1.

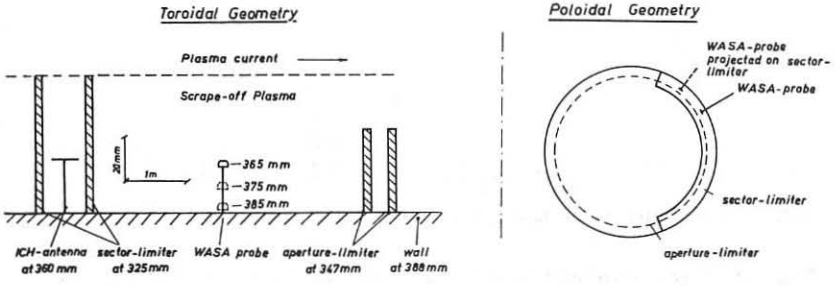

Fig. 1

RESULTS

The presentation of the in-situ iron flux measurements is restricted to the quiet and reproducible plateau phase of normal discharges (without major disruptions). The following statements can be made:

- Time averaged fluxes decay exponentially with the probe position radius r_p. The characteristic lengths are different for both toroidal directions (on the electron side 6 mm and on the ion side 13 mm). Furthermore the ratio between the electron side and ion side signals reverses in the near wall region (near the liner the flux from the ion side is larger but in the middle of the scrape off the electron side flux becomes dominant; Fig. 2).
- Besides obvious similarities the time dependence of the different directed fluxes shows systematic differences (Fig. 3 shows typical examples for the distinct evolution during the plateau phase). The flux difference at 365 mm is caused by a faster rise of the e^--side signal whereas the dominance of the I^+-flux at 385 mm is approximately independent on time.
- There are remarkable fluctuations from shot to shot and a large influence of the plasma column position (see also /3/).

In the experiment with the carbon collector three of the five pulses terminated with a major disruption at 320 ms. The following results are obtained:

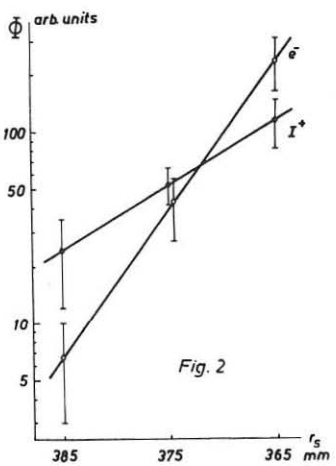

Fig. 2

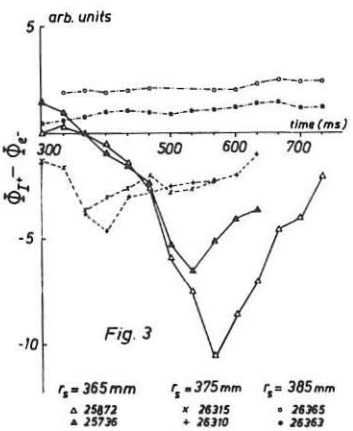

Fig. 3

Fig. 2: Radial dependence of the time averaged Fe-fluxes

Fig. 3: Time evolution of the flux difference during the plateau phase

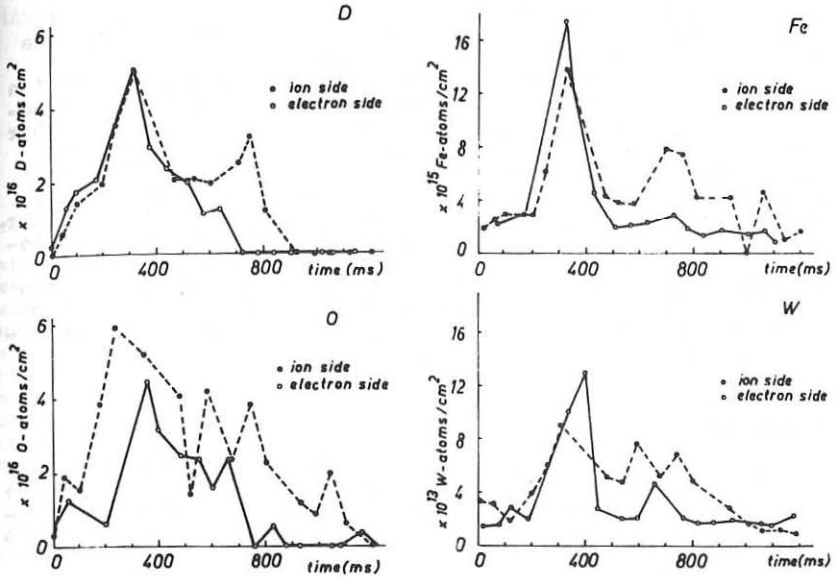

Fig. 4: Time dependences of collected amount of deuterium and impurities

- The impurity level near the wall is very high in all phases of the discharge. In the plateau phase the concentration ratio n_{imp}/n_{deut} is about 0.4 for O, 0.05 for Fe-Cr-Ni and 2.10^{-3} for W.
- The estimated implantation energies of deuterium are about 25 - 40 eV in the plateau phase and larger than 100 eV in the disruptive phases.
- All fluxes show different time evolution for the different flux directions (Fig. 4).

DISCUSSION

The simple model of plasma particle diffusion across the magnetic field lines into flux tubes with free streaming along these tubes /4, 5/ does not explain the different time behaviour of the measured fluxes parallel and antiparallel to the toroidal field. Also the different decay lengths of the fluxes in both toroidal directions are indications against the applicability of the model. There may be two main reasons for these difficulties. Firstly limiter and wall are acting as sources of deuterium and impurities and secondly during the plateau phase a special plasma is built up near the limiter that is much colder and denser than that at other toroidal positions

in the limiter shadow region /6/. Therefore time dependent local sources have to be included especially if the probe is located near the liner and the limiter.
In the PAPYEX experiment the active sector limiter on the ion side of the WASA probe could be a source of deuterium. Whereas the evolution of the electron side flux is similar to that of the line averaged density an additional flux to the ion side at the end of the plateau phase was observed (Fig. 4). A possible explanation could be that due to a plasma limiter contact deuterium was released from the surface and contributed asymmetrically to the toroidal fluxes. If this contact between limiter and main plasma is also a source of neutral iron impurities the characteristic radial length for the ion side fluxes should be approximately equal to the ionisation length and therefore larger than the diffusion length observed on the electron side (Fig. 2).

CONCLUSIONS

From time dependent measurements of deuterium and impurity fluxes in the limiter shadow of T-10 it is concluded that the consideration of time dependent local sources and plasma properties is necessary to explain the particle transport in the near wall region.

ACKNOWLEDGEMENT

The authors wish to thank the T-10 operating team for the continued support.

REFERENCES

/1/ Chicherov, V.M., Hildebrandt, D., Laux, M., Lingertat, J., Lukianov, S.U., Pech, P., Reiner, H.-D., Stepanchikov,V.A., Wolff, H.: Contrib. Plasma Phys. 22 (1982) 207

/2/ Chicherov, V.M., Hildebrandt, D., Laux, M., Lingertat, J., Lukianov, S.U., Pech, P., Reiner, H.-D., Stepanchikov,V.A., Wolff, H.: J. Nucl. Mater. 93/94 (1980) 133

/3/ McCracken, G.M., Partridge, J.W., Erents, S.K., Sofield, C.J., Ferguson, S.M.: J. Nucl. Mater. 111/112 (1982) 159

/4/ Cohen, S.A., J. Nucl. Mater. 76/77 (1978) 68

/5/ Uehara, K., Gomay, Y., Yamamoto, T., Suzuki, N., Maeno,M., Hirayama, T., Shimada, M., Konoshima, S., Fujisawa, N.: Plasma Physics 21 (1979) 89

/6/ Baker, D.R., Snider, R.T., Nagami, M.: Nucl. Fusion 22 (1982) 807

PLASMA EDGE MEASUREMENTS DURING ADDITIONAL HEATING IN THE TFR TOKAMAK

TFR Group
presented by A. Grosman

Association Euratom-CEA sur la Fusion
92260 FONTENAY-AUX-ROSES (FRANCE)

I. Introduction

During last two years, a large part of the experimental work on TFR has been devoted to ion cyclotron resonance heating (ICRH), in view of reducing the large increase of metallic impurities which has been observed in the plasma during the RF pulse /1/. A simple computation of the nickel source (as far as sputtering on the inconel limiter was concerned) gave evidence that we could improve the situation by replacing the inconel limiters by graphite ones (5890-PT of Carbone Lorraine). For the last experiments, the limiter configuration has been as follows : one complete set of poloidal limiters at port P5 (r = 195 mm) the external part of it being a low-field side limiter antenna. An external movable limiter was located at P4 (where a high-field-side antenna was installed) and an internal one at P7.

Using graphite limiters allowed a reduction of the metallic impurities in the discharge by an order of magnitude /2/.

Nevertheless, ICRH is still affected by more metallic impurities than neutral beam injection ($H^\circ \rightarrow D^+$) for which a 600 kW power level has to be reached to yield metallic impurities /3/. In the case of ICRH, metallic impurities radiances grow linearly with the power level, the l.f.s.a yielding 3 times more impurities than the h.f.s.a /4/.

To try to understand these differences, an extended investigation of the scrape-off layer has been undertaken. To that purpose, two Langmuir double probes were used, one in a port next to the l.f.s.a (P6) and one two ports away (P8).

An EXB analyzer /5/ could also be used in the last experiments to mesure the ion parallel velocity. The typical discharge parameters are :
$I_p \sim$ 150-200 kA V_T (loop voltage) $\approx$ 1.5 $\rightarrow$ 2.5 V $\bar{n}_e \simeq$ 3-7 x 10^{13} cm^{-3}
$T_e(o)$ = 1-2 keV

In section 2 we summarize the results of the Langmuir probes. Section 3 is devoted to preliminary results of the EXB analyzer and at last we draw the first conclusions and the prospects of these studies.

II. Plasma edge studies with Langmuir double probes

The main advantage of the double probe is that the interpretation of the results is simple in a "maxwellian" plasma. The probe characteristic is then:

$$I(V) = I^+_{sat} \tanh\left(\frac{eV}{2kT_e}\right) \qquad (1)$$

where the ionic saturation current is : I^+ sat = n A q_i $\left(\frac{kT_e}{2\pi m_i}\right)^{1/2}$
(A being the effective collection area, q_i and m_i the ion charge and mass).

A sweep polarization ($\pm$ 60 V, 80 Hz) provides a characteristic every 6 ms. But is should be reminded that a large uncertainty will remain. It is mainly due to the density fluctuations. The typical error on electron temperature is estimated as 10 % but it may reach 50 % on the density.

A second point to be clarified is the effect of the RF electric field on the probe characteristic, which becomes /6/

$$I(V) = I^{+}_{sat}\ \frac{I_o(X)\ \mathrm{cosh}\left(\frac{eV}{kT_e}\right) - 1}{I_o(X)\ \mathrm{cosh}\left(\frac{eV}{kT_e}\right) + 1} \qquad (2)$$

where $X = \frac{2e\tilde{V}}{kT_e} \sin\frac{\phi}{2}$, I_o being the modified Bessel function, $\tilde{V}$ the amplitude of the RF perturbation and ϕ the phase between the 2 probes. In fact, its main effect is to shift the characteristic towards the negative potential : T_e may still be deduced from the first derivative at the inflexion point.

a) Results obtained during neutral beam injection

Experiments made with NBI heating ($H^{\circ} \rightarrow D^{+}$, 40 keV) were investigated. Even with 300 kW effective power into the plasma, no temperature increase neither density increase could be noticed. The first significant increase of T_e required 600 kW effective power to appear {Additional inflow of metallic impurities occured at the same power level}.

b) Results obtained during the RF pulse

The main results may be summed up as follows {see fig.1 and fig.2}.

- The whole scrape-off layer - i.e. the region between the limiter and the wall - shows an increase of the electron temperature. This effect is likely to be very important in the region r = 22 cm to 26 cm, where the electron temperature reaches and often exceeds 10 eV, which is enough, through the potential drop ($\sim 3\ kT_e$) of an electrostatic sheath, to accele-

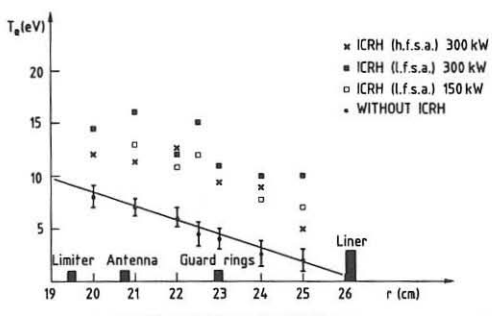

Fig. 1 ELECTRONIC TEMPERATURE PROFILE IN THE SCRAPE-OFF LAYER DURING ICRH WITH DIFFERENT POWER LEVELS AND DIFFERENT ANTENNAS

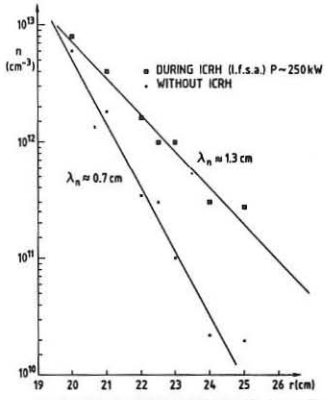

Fig. 2 DENSITY PROFILE IN THE SCRAPE-OFF LAYER DURING ICRH

rate the impinging ions above the sputtering threshold.

- Both double probes gave similar results, which indicates that this effect is not restricted to the vicinity of the antenna.

- This phenomenon is qualitatively independant of the type of antenna used to launch the wave (high-field-side or low-field-side) but also of the heating regime (mode conversion or minority proton heating).

- A very short time (< 200 μs) elapses between the beginning of the RF pulse and the increase of the ion saturation current.

Usually the electron temperature stayed at the same level during the RF pulse and decreases to the preceding level at the end of it.

- As spectroscopic measurements showed that the metallic impurity radiance is a linear function of the RF power level with a given antenna and that the 1.f.s.a yielded more impurities that a h.f.s.a at the same power level, measurements were made with the Langmuir probe in these cases. Although T_e seems to vary similarly (fig.1), the differences are hardly greater than the physical uncertainties.

More convincing results were obtained by increasing the RF power during the pulse. An impressive correlation appears a fig.3 between the evolutions of Te, B Ni XVIII and P_{RF}, during the RF pulse.

- The plasma density shows also a large increase and the effect is stronger in the most peripheral layers where n_e is increased by more than an order of magnitude (at r = 260, i.e. in front of the liner, the density jumps from less than $10^{10}cm^{-3}$ to more than $10^{11}cm^{-3}$). The e-folding length λ_n of the density profile is also slightly greater. λ_n which is usually equal to 0.7-0.95 cm may reach 1.1 to 1.7 cm. If we assume the radial diffusion coefficient in the scrape-off layer to be approximated by half the Bohm diffusion coefficient, then as $D_\perp = \lambda_m^2 / \tau_{//}$ $(\tau_{//} = \frac{4\pi R}{\bar{v}_i}$ where R is the major radius and $\bar{v}_i$ the parallelvelocity component parallel to the magnetic field)

Consequently $$\lambda_m = \left(\frac{4 D_\perp \pi R}{\bar{v}_i} \right)^{1/2} \propto T_e^{1/4}$$

If T_e = 5 eV, $\lambda_n \simeq 0.75$, which is in good agreement. The variations of λ_n corresponded, for a little part to a Te increase and certainly to a large extent to the large increase (∿ 300 %) in wall desorption of hydrogen which led to increased recycling /7/.

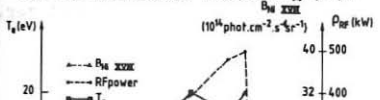

Fig. 3 COMPARATIVE EVOLUTION OF ELECTRONIC TEMPERATURE AND Ni XVIII RADIANCE DURING ICRH WITH VARYING LEVEL (l.f.s.a,r=220mm)

Fig. 4 PARALLEL VELOCITY DISTRIBUTION OF THE O^+ IONS DEDUCED FROM MEASUREMENTS WITH THE EXB ANALYZER

III. Preliminary results of the EXB analyzer

The EXB analyzer is described in ref. 5. Let us recall that through the electromagnetic drift velocity imposed on the D^+ particles, we are able to analyze the parallel velocity distribution of the D^+ ions.

During ohmic discharges, there was a good agreement between the results of the Langmuir probes and the EXB analyzer as far as the electrostatic field E did not go beyond 400 V cm^{-1}.

During the RF pulse, we had to get rid of the impinging electrons, which was not always possible. Nevertheless, the results corroborate Langmuir probes'ones.

The parallel velocity distribution function was assumed to be

$$f(u) = n\left(\frac{m_i}{2\pi kT}\right)^{1/2} \exp - \left(\frac{m_i u^2}{2kT}\right)$$

So $I^+ = q_i A \int u f(u) du$, and $f(u)$ is approximated by $\frac{I^+}{q_i A u \Delta u}$

In fig.4, we show that for different velocity bands, the f(u) approximation seems to induce $T_i \simeq$ 15-20 eV at r = 215 mm during ICRH (1.f.s.a $P \simeq 200$ kW).

IV. Conclusions and prospects

The measurements made in the scrape-off layer of TFR during ICRH prove that an as yet unknown mechanism increases the energy content of the boundary layer. This effect is not local. Furthermore, we gave evidence that both electrons and ions gain energy during ICRH, whereas no increase of Te, Ti and n_e is noticed with NBI at the same power level.

As it appears to be the main reason of the metallic impurity release and of hydrogen desorption, it has to be investigated some more.

At the experimental level, studies will be undertaken on the density and current fluctuations in the scrape-off layer at the ω_{ci} frequency.

Furthermore, special emphasis will be put on the study of the high energy tail of the distribution function of the D^+ ions, thanks to the EXB analyzer.

References

/1/ Equipe TFR, Proc. of the 3rd Varenna-Grenoble Symposium, Vol. 1, p. 225 (Commission of the European Communities).
/2/ TFR Group, Rapport EUR-CEA-FC-1186 (1983).
/3/ TFR Group, Proc. of the 3rd Varenna-Grenoble Symposium, Vol. 3, p. 1177 (C.E.C.).
/4/ TFR Group, presented by J. Adam, These proceedings.
/5/ P. Staib, Journal of Nucl. Mat., 93-94 (1980) 351.
/6/ A. Boschi and F. Magistrelli, Il Nuovo Cimento 29 (1963) 487.
/7/ Equipe TFR, Proc. 9th Int. Vacuum Congress, Madrid Sept. 26, October 1, 1983.

Scaling of plasma scrape-off layers in tokamaks

H.Kever
Inst.f.Plasmaphysik, Association Euratom - KFA
Kernforschungsanlage Jülich

1.Theoretical estimates concerning the scrape-off layer in tokamaks are often based on models which lead to spatially exponential distributions of the relevant plasma parameters. Due to non-linearities in the governing equations evoked through parametric dependances in particular of the diffusion coefficients, the structure of the scrape-off layer must in general be described by solutions of different type. For an assessment of external control measures proposed to improve transport in the scrape-off layer of tokamaks, especially with regard to pump limiter action, the problem of the structure of the boundary layer is reconsidered analytically.

2.The radial distribution of the plasma density n in the scrape-off layer is assumed to be determined by a diffusion equation of the form

$$\frac{\partial n}{\partial t} = \frac{\partial}{\partial x} D \frac{\partial n}{\partial x} - \nu n \qquad (1)$$

Here the loss term is taken to be proportional to the hydrogen component of the plasma density. The magnitude of the inverse particle escape time ν depends in general on several processes : streaming along magnetic field lines,recombination and charge-exchange, and also on ionization, recycling, and additional gas supply.For the purposes intended here,especially with regard to the effect of a pump limiter, the particle streaming term is considered to be the dominant contribution to the losses, i.e. $\nu = v_{\parallel}/L$ where $v_{\parallel}$ is the flow velocity and L a characteristic length denoting the distance to the limiter. The diffusion coefficient D is taken to be of the form

$$D = D_s n_s / n \qquad (2)$$

where D_s and n_s are the values of D and n at the inner boundary of the scrape-off layer; x=0 denotes the position of

the inner boundary adjacent to the plasma of the core. This particular form of D models a space-dependent diffusion coefficient increasing outward which is in accordance with experimental results. In contrast to diffusion coefficients assumed to depend explicitly on the position x , the implicit dependence allows to find solutions analytically resp. to study their behaviour as function of the governing parameters. A variety of particular or approximate solutions of diffusion equations has been discussed recently; the application should be of interest also to the stability problem of the steady state solutions which are discussed in the following.

3.The integral of equ.(1)for the steady state, obtained upon introduction of the variable ϕ through the relation

$$n = n_s \exp(-\phi) \tag{3}$$

is the equation

$$\phi'^2 = \frac{2\nu}{D_s} \exp(-\phi) - \frac{2\nu}{D_s} + \left(\frac{\Gamma_s}{n_s D_s}\right)^2 \tag{4}$$

where Γ_s is the flux density of particles entering the scrape-off layer at x=0. The scaling length corresponding to the one introduced in the case of a constant diffusion coefficient is $\Delta = (D_s/2\nu)^{1/2}$, as is seen from equ.(4) by introducing the normalized coordinate $\xi = x(2\nu/D_s)^{1/2}$. Due to the nonlinearity of the equation, a second dimensionless parameter A determines the width and the structure of the scrape-off layer :

$$A = \frac{\Gamma_s^2}{2\nu n_s^2 D_s} - 1 \tag{5}$$

4.Depending on the sign of A, two qualitatively different types of solutions occur. The limiting case A=0 corresponds to a particular value of the particle flux at the boundary of the scrape-off layer which leads to a density profile of the form

$$n = \frac{n_s}{(1 + x/2\Delta)^2} \tag{6}$$

i.e. an algebraic dependence on x .

For $A > 0$, the solution becomes with $r = A^{1/2}/2\Delta$.

$$n = \frac{An_s}{(A^{1/2}\cosh rx + (1+A)^{1/2}\sinh rx)^2} \qquad (7)$$

Since in this case

$$\frac{\Gamma_s^2}{2\nu n_s^2 D_s} = \frac{\Gamma_s^2 L}{2v_{\parallel} n_s^2 D_s} > 1$$

profiles given by expression (7) occur when the particle flux Γ_s at the separatrix is large and/or the flow velocity $v_{\parallel}$ is low, i.e. for small pumping rates. Compared to the situation with D = const, the width of the scrape-off layer depends also on A, e.g. for large rx

$$n \rightarrow n_s \exp(- A^{1/2} x/\Delta)$$

For $A \rightarrow 0$ and small x, the solution (6) is recovered.

5. If $A < 0$, another solution is found. Rewriting equ.(4)

$$\phi'^2 = \exp(-\phi) - a \qquad (4a)$$

where $a = |A| = 1 - \Gamma_s^2/2\nu n_s^2 D_s$

it is seen by inspection that an upper limit ϕ_c on ϕ exists, for which ϕ' becomes zero. It follows that the solution exists only in a finite range $0 \leq \xi \leq \xi_c$, and that the density has a limit value

$$n_c = n_s \exp(-\phi_c) = a n_s \neq 0 \quad .$$

This solution corresponds to high pumping speeds i.e. when the pumping rate is strong compared to the diffusion rate. The density profile is given by the expression

$$n = \frac{an_s}{(a^{1/2}\cos u + (1-a)^{1/2}\sin u)^2} \quad , \quad u = a^{1/2} x/2\Delta \qquad (8)$$

Here ξ_c is obtained from the condition

$$a^{1/2} \cos u + (1-a)^{1/2} \sin u = 1$$

or

$$\cos(a^{1/2}\xi_c/2) = a^{1/2} \qquad (9)$$

because $n = a\, n_s$ at $\xi = \xi_c$.
For large $v_{\parallel}$, $a \lesssim 1$, ξ_c becomes

$$\xi_c = (\frac{2}{a})^{1/2}(1 - a^{1/2}) \qquad (10)$$

The difference of the two cases $A > 0$ and $A < 0$ is indicated by the behaviour of the solution in the (ϕ,ϕ') - plane. Since $n/n_s = \exp(-\phi) < 1$, it is sufficient to consider the half-plane $\phi > 0$. The line $\phi' = \exp(-\phi/2)$ for A=0 separates the region for which solutions exist which extend to infinity ($n \to 0$) from the ones which are represented by closed curves ($n \to n_c$).

6.The properties of the model equation discussed above should give some insight of the behaviour of more realistic systems used in the numerical simulation of the processes which determine the structure of the boundary layer. The results also indicate options to adjust the width and the structure of the scrape-off layer to variable conditions e.g. when during discharges changes occur in the parameters at the separatrix or inner boundary.

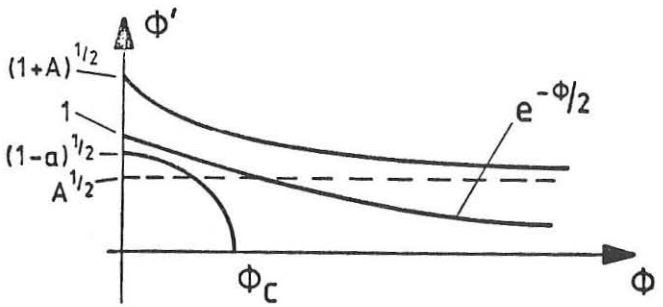

Fig.1 Solutions of equation (4) in the (ϕ,ϕ') - plane

NEUTRAL BEAM INJECTION MODELLING FOR DITE WITH THE MKII BUNDLE DIVERTOR

P.C. Johnson, B.S Mudford, J.G. Cordey*

Culham Laboratory, Abingdon, Oxon., OX14 3DB, England
(Euratom/UKAEA Fusion Association)

*JET Joint Undertaking

Introduction

The motion of fast ions in the magnetic field of a tokamak with a bundle divertor has been discussed in paper /1/. However, the changes in the velocity space boundaries which arise in the presence of a bundle divertor have not been studied, nor have there been any detailed simulations of neutral beam injection into DITE with the MkII bundle divertor. In this paper we will determine the major fast-ion loss mechanism in DITE with a bundle divertor, investigate the velocity space loss region boundaries in the presence of a bundle divertor, and simulate the neutral beam injection (NBI) power deposition of DITE with the MkII bundle divertor.

Loss Region Boundaries

Velocity space loss region boundaries in a tokamak with a bundle divertor are determined by following guiding-centre orbits in a magnetic configuration consisting of an axisymmetric tokamak field plus a set of current-carrying coils representing the bundle divertor. The bundle

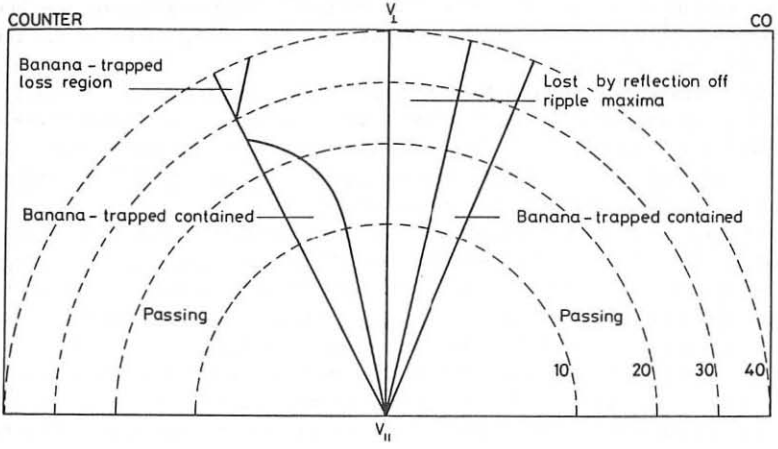

Fig. 1 Velocity space loss region boundaries for particles injected on the flux surface r = .105m. --- contours at 10, 20, 30, 40keV.

divertor ripple is localised about the toroidal position of the bundle divertor, and is composed of a central minimum flanked on each side by local magnetic field maxima. In DITE the peak-to-peak ripple magnitude on the magnetic axis is ~ 5% and rises to 100% at the separatrix radius.

The presence of such a large ripple leads to particle trapping between the 1/R variation of the toroidal magnetic field and the local maxima of the bundle divertor ripple. Once fast ions become trapped in this well they are lost from the plasma by VB-drift, on timescales of the order of the vertical drift time. In a tokamak with a DITE-type bundle divertor this loss mechanism is the dominant loss process, and greatly exceeds both ripple-trapped loss and banana-drift diffusion.

A typical set of velocity space boundaries which arise in a tokamak with a bundle divertor are shown in fig. 1. The loss region covers a large fraction of the banana-trapped region of velocity space. Figure 1 also shows that counter-injection should lead to greater losses than co-injection. These loss region boundaries are in contrast to those found in a tokamak with toroidal field coil ripple /2/, where the banana-trapped region splits into loss bands due to ripple-trapping and banana-drift diffusion.

NBI Power Deposition

NBI heating of diverted discharges on DITE are modelled by using the Monte Carlo fast-ion transport simulation code FREYA /3/. This code models both the neutral beam deposition and the subsequent thermalisation of the fast ions. The majority of the simulation runs have modelled nearly-tangential pencil beam co-injection into plasmas with $T_e = T_i = 800$ eV on axis, and $n_e = n_i = 5 \times 10^{19} m^{-3}$ on axis. Charge-exchange has been neglected, and the effects of the 1/2 and 1/3 energy components of the beam have also been neglected.

For simulations of nearly-tangental 24 keV neutral beam co-injection into DITE it has been found that the fast-ion energy loss from undiverted discharges is negligible. Simulations of diverted discharges have been carried out for a range of injection energies from 5 keV to 100 keV and for a range of plasma currents from 150 kA to 300 kA.

In none of these simulations was the fast-ion energy loss, which includes first orbit losses, greater than 7% of the total injected energy. The variation of fast-ion energy loss with plasma current and injection energy are shown in fig. 2. The turning point in fig. 2(b) is due to the fact that below about 15 keV the time taken to pitch-angle scatter out of the loss region becomes shorter than the vertical drift time to the wall. Although no more than 7% of the injected energy was lost in any simulation run, the proportion of fast ions which were lost was in the range 20%-25%.

The energy and spatial distributions of lost fast ions are determined for each simulation run. Some typical distributions are shown in fig. 3. For 24 keV neutral injection into DITE with a bundle divertor the average energy of the lost ions is about 6.9 keV, which could lead to relatively high sputtering yields. The fraction of ions which are lost is about .22. These ions are lost from the plasma volume in the range of poloidal angles $30^\circ \leq \theta \leq 120^\circ$. There do not appear to be any preferential toroidal angles for which the fast ions are lost. The shape of the loss orbits could lead to a significant particle flux at the fixed limiters. This in turn could produce a very high thermal load, since the particle loss is localised in poloidal angle.

Conclusion

Monte Carlo simulations of nearly-tangential, co-injected NBI heating of DITE-type discharges with a bundle divertor have produced fast-ion energy losses of no greater than 7% for a wide range of injection energies and plasma currents. This level of energy loss should be tolerable. The fast-ion loss is between 20% and 25% of the injected particles. This high level of particle loss poses potentially the most serious problem associated with NBI heating in the presence of a bundle divertor, as the energies of the lost ions are of the correct magnitude to produce relatively large sputtering yields. The energy flux of the lost ions may also be localised on the fixed limiters, and this could produce very high thermal loads.

References

/1/ Hively, L.M., Rome, J.A., Lynch, V.E., Lyon, J.F., Fowler, R.H., Peng, M., and Dory, R.A.: Constrained ripple optimisation of bundle divertors, Nucl. Tech./Fusion 2 (1982) 372-391.

/2/ Tani, K., Azumi, M., Kishimoto, H., and Tamura, S.: Effect of toroidal field ripple on fast ion behaviour in a tokamak, J. Phys. Soc. Japan 50 (1981) 1726-1737.

/3/ Lister, G.G., Post, D.E., and Goldston, R.: Computer simulations of neutral beam injection into tokamaks using Monte Carlo techniques, in 3rd Symp. on Plasma Heating in Toroidal Devices, Varenna, Italy (1976) 303-307.

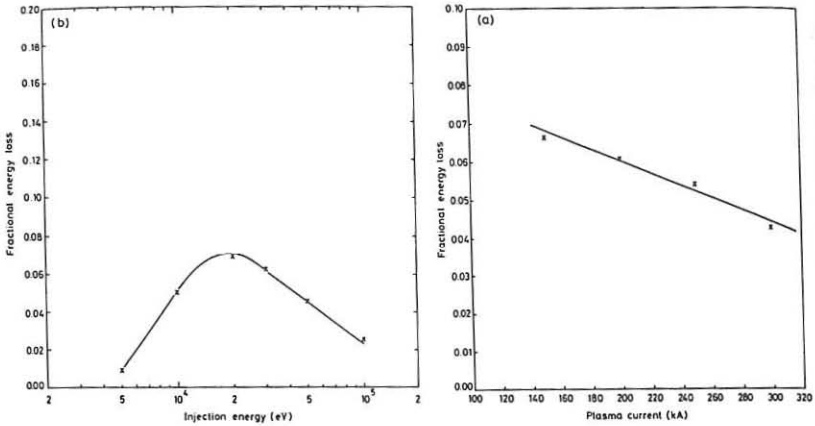

Fig. 2 (a) Fast-ion energy loss versus plasma current; (b) fast-ion energy loss versus injection energy.

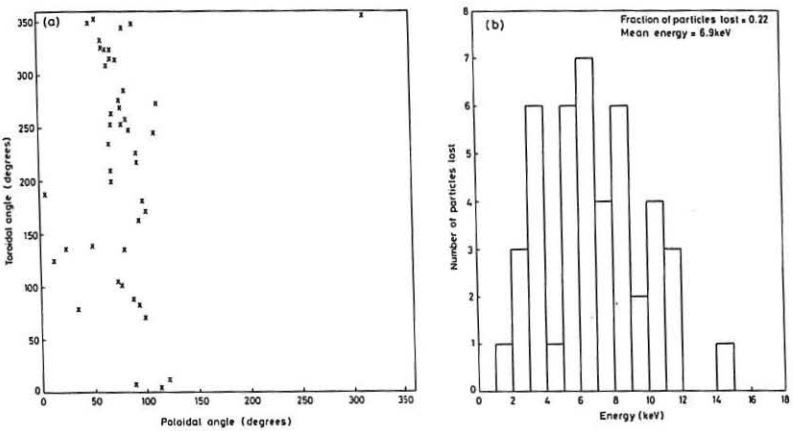

Fig. 3 Simulation runs with I_p = 200kA, B_o = 2.8T, E_o = 24keV; (a) θ, ϕ distribution of lost ions; (b) energy spectrum of lost ions.

Reactor Aspects

D01 - D10

HTMR-A HYBRID TOROIDAL MAGNET TOKAMAK REACTOR STUDY

B. Brunelli, V. Zampaglione
Associazione EURATOM-ENEA sulla Fusione, Centro di Frascati
C.P. 65 - 00044 Frascati, Rome, Italy

P.G. Avanzini, G. Raia, F. Rosatelli
NIRA - C.P. 1166 Genoa, Italy

ABSTRACT

The preconceptual design is presented of a Tokamak reactor with an hybrid toroidal magnet, which can fulfil INTOR-NET objectives with smaller size (R_o = 4.5 m, a = 1 m) and cost, operating at B_o = 6.1 T. Useful ignition margins can be gained by increasing B_o up to 8 T with still an acceptable power consumption in copper toroidal coils.

1. INTRODUCTION

The scope of the paper is to investigate the feasibility of an experimental Tokamak reactor with medium-high toroidal field, viewed as an INTOR-like intermediate step between the present generation of large Tokamaks and the generation of DEMOs [1]. The use of such fields permits achieving ignition with useful margins and demonstrating engineering feasibility of a fusion reactor with reduced size and cost of the facility. Because of present limits on superconducting magnet technology, an attractive solution to obtain medium-high fields is the use of an hybrid superconducting-copper magnet.

In this paper, we present the main features of an hybrid toroidal magnet Tokamak reactor (HTMR) designed for B_o operation up to 8 T. In HTMR (see Table I and Fig. 1), D-T ignition can be achieved for B_o = 6.1 T with a power consumption in copper coils of 30 MW and $V_*^{(HTMR)} \cong 0.6\, V_*^{(INTOR)}$ ($V_* \sim R^2 ak$ is an approximate estimate of the engineered volume, an important cost parameter).

2. PHYSICS BASIS

As in INTOR design study [1], the INTOR-ALCATOR scaling for τ_E has been used as a guideline for HTMR and the scaling $\beta_o^{DT} = 0.2\, a(1+K^2)/2R_o q_I$ for useful beta, together with a safety factor q_I = 2.1, has been assumed.

By increasing B_o, ignition margins can be gained providing safety against uncertainties in τ_E and β_o limit. For instance, degradation of confinement has been observed in a number of auxiliary heating experiments. Moreover, the above scaling for β_o^{DT} should be considered as a β_o limit (β_{max}) and, consequently, a margin should be allowed to compensate for pressure of α-particles and impurities.

3. MACHINE DESIGN GUIDELINES

The main feature of HTMR is the possibility of operating at high toroidal field with a moderate power consumption in the toroidal magnet

Table I - HTMR Parameters

GEOMETRY	
□ Plasma major radius, R_o	4.5 m
□ Plasma minor radius, a	1 m
□ Elongation, K	1.6
PLASMA	
□ Field on plasma axis, B_o	6.1 T
□ Safety factor, q_I	2.1
□ Plasma current, I_p	5.7 MA
□ Useful beta, β_o^{DT}	3.8%
□ Density-average plasma temperature, <T>	10 keV
□ Average plasma density, <n>	$1.75\times10^{20}m^{-3}$
□ Thermonuclear power, P_{th}	570 MW
□ Neutron wall load, P_n	1.7 MW/m^2
□ RF heating power, P_{RF}	45 MW
OPERATION	
□ Burn time	100 s
□ Number of pulses	10^5
SUPERCONDUCTOR SHIELDING	
□ Inboard - Outboard	0.5 m - 0.9 m
BREEDING BLANKET	
□ Material	Li_2O,SS-316,Pb-Bi
□ Breeder temperature	400-800 °C
□ Thickness (inboard) - (outboard)	0.4 m - 0.55 m
□ Breeding ratio	~ 1
□ Tritium recovery	continuous He purge
SUPERCONDUCTING TF COILS	
□ Contribution to B_o	5 T
□ Number of coils	12
□ Clear bore	5.1m × 6.7 m
□ Conductor	NbTi + Nb_3Sn
□ Maximum field	11 T
□ Ampère turns	121 MAT
□ Refrigeration power	5 MW
COPPER INSERT TF COILS	
□ Number of coils	24
□ Clear bore	3.4 m × 5.2 m
□ Ampère turns	25 MAT
□ Current density	850 A/cm^2
□ Resistive power, P_Ω	30 MW
PF COILS	
□ Total flux, Φ	78 V·s
□ Location	external to TF coils
□ Conductor	NbTi
□ Maximum field	8.5 T

made-up by water cooled copper coils inserted in the interior of an INTOR-like superconducting magnet [1]. These coils, besides increasing the toroidal field in the plasma, provide a partial shield for the superconducting magnet against gamma rays, allowing for a reduction of the shield thickness.

The copper coils are included, together with breeding blanket segments, in 24 modules which can be removed for maintenance through the space between adjacent superconducting coils. The power dissipated in the resistive coils for the reference case (B_o = 6.1 T, see Table I) is about 30 MW with a mean copper temperature of 70°C and even for B_o = 8 T this power will be not higher than 220 MW.

In the toroidal superconducting magnet, a maximum field of 11 T has been considered, being compatible with windings of NbTi and Nb_3Sn, thus minimizing the contribution to B_o of the resistive coils. The presence of copper coils between two adjacent superconducting ones allows a reduction, compared to INTOR, of the HTMR superconducting magnet bore to 6.7m × 5.1m without increasing the field ripple (< 1% at the plasma edge).

The total flux swing required for operation at B_o = 6.1 T is about 78 V·s, that can be obtained by a poloidal system with NbTi superconducting coils [1]. Extended performance of the machine, for q_I = 2.1 and B_o up to 8 T, should require either a different design of the transformer or the coupling with a RF current drive system supplementing the transformer flux.

As for as impurity control and ash exhaust are concerned, a preliminary evaluation, based on current models of the plasma edge and scrape-off layer, suggests the use of a removable pumping limiter.

For the first wall we are investigating a closed loop system with an eutectic Pb-Bi alloy as a cooler, which, acting also as a neutron multiplier, increases the breeding ratio. The activated coolant circulates inside the shielding system and exchanges heat with water behind the blanket. Calculations show that, for a suitable design, the MHD pressure drop in the cooling circuit is lower than 2.2 bar/m for $B_o \leq 8$ T, allowing the use of an electromagnetic pump.

Li_2O has been choosen as the reference breeder material, either in slabs cooled by water at high pressure (60 bar) or in cylindrical rods cooled by helium. Tritium recovery is achieved by a low pressure helium stream flowing in voids located inside the Li_2O. In order to facilitate tritium release, the temperature of Li_2O elements should not be lower than 400°C. To obtain a breeding ratio of about one, even the inboard part of the modules is filled with breeder material. Calculations for blanket and shielding optimization are performed by means of an ANISN code with a 100 groups library. The modular structure of the reactor permits, in principle, simultaneous testing of different breeders.

The extraction of each of the 24 modules in the radial direction is achieved by rotating the whole support structure of the superconducting coils and cryogenic system [2] on high-pressure oil hydrostatic bearings. The angular rotation does not exceed 5°. In this way, the gap between superconducting toroidal coils and vacuum chamber is minimized.

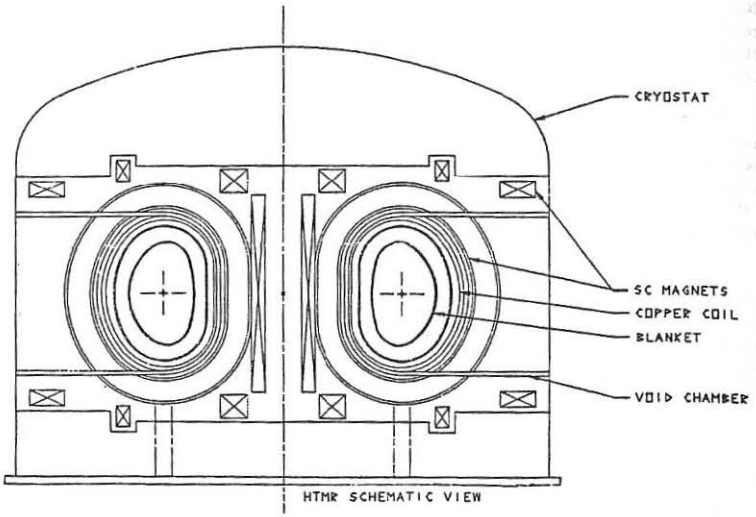

Fig. 1 - Elevation view of HTMR

REFERENCES

[1] INTOR-Phase One -Report of the International Tokamak Reactor Workshop held in Seven Sessions in Vienna during 1980 and 1981, IAEA, Vienna 1982.

[2] Farfaletti-Casali, F.,EURATOM JRC-Ispra, private communication, 1983.

d-d COMPACT REVERSED FIELD PINCH REACTOR TECHNOLOGY ASSESSMENT

A. E. Dabiri and J. E. Glancy
Science Applications, Inc.
La Jolla, California, U.S.A.

ABSTRACT

A quantitative comparison of the technology requirements, safety and cost of a d-d compact reversed field pinch reactor (CRFPR) relative to a d-t/CRFPR has been performed. The first wall/blanket and energy recovery cycle for the d-d reactor is simpler and has a higher efficiency than the d-t reactor. Tritium technology for processing the plasma exhaust is required for d-d reactors, but no tritium containment around the blanket or heat transport system is needed. Safety analysis shows similar consequences of the release of activated corrosion products or activated first wall/blanket structure. Consequences of all postulated d-d accidents for tritium releases are significantly smaller than those from the d-t reactor. Cost studies show that the cost of electricity from a d-d reactor is about 40% higher than that of a d-t reactor.

INTRODUCTION

The advantage of using d-d instead of d-t to fuel fusion reactors is that deuterium is available in nature whereas tritium must be bred in the reactor blanket via neutron-tritium reactions that may require the use of liquid metals and the associated safety hazards. The disadvantages of using d-d instead of d-t are the higher plasma temperature, higher plasma energy confinement requirements, and lower d-d reaction rate that leads to lower power density and, thus, larger reactors for the same net electric power output. However, despite these qualitative differences a quantitative assessment is required if meaningful conclusions are to be reached.

The RFP assessment focuses on a compact reactor because the annual generating cost of electricity for a compact reactor is projected to be lower than that of an equal capacity conventional fusion reactor /1/. Parameter summary for a point design 1000 MWe for compact d-t and d-d reactors is shown in Table 1 /2/.

Table 1. Parameter Summary for 1000 MWe CRFPR Designs.

	d-t	d-d
Major radius (m)	4.3	14.9
Minor radius (m)	.72	.59
Maximum B-field (T)	3.3	6.0
β	.2	.2
Plasma current (MA)	18.5	27.4
Average electron density ($10^{20}/m^3$)	6.7	7.9
Electron temperature (keV)	10.0	28.
Neutron wall load (MW/m^2)	19.5	3
Surface heat load (MW/m^2)	4.87	4.87

TECHNOLOGY ASSESSMENT

The key technology issues are: (1) first wall and blanket; (2) heat transport and energy recovery; (3) tritium containment and recovery, magnet technology; and (5) vacuum technology.

First Wall/Blanket

The requirements on the blanket of a d-d reactor are qualitatively different than for a d-t reactor because no tritium breeding is required. Instead other requirements on the design are high temperature operation for high thermal conversion efficiency, high neutron energy multiplication, longer lifetime and lower cost.

The d-d/CRFPR first wall and blanket design is a water/steam cooled structure that functions as an integrated feedwater heater, boiler, and steam superheater that drives a steam turbine directly. The first wall is a 1.5 mm corrugated high strength copper alloy plate brazed to a flat plate structure that can tolerate a high surface heat load. It is similar to the STARFIRE and WILDCAT limiter designs. The blanket consists of four banks of austenitic steel tubes, 2-2.8 cm o.d., that are separated in the radial direction by layers of graphite. Each bank consists of two rows of tubes which can be connected in series or parallel /3/.

Our assessment shows that a d-d blanket can achieve an efficiency of 37.5% compared with 35% reported for d-t/CRFPR without using advanced technology or incurring high costs /3/. Note that the 35% efficiency has achieved with the use of liquid lithium metal which requires liquid metal technology and the associated safety hazards. The high temperature d-d blanket achieves a neutron energy multiplication of 1.7 compared to 1.1 in the d-t reactor, partially compensating for the lower power density of the d-d fuel.

The blanket lifetime is controlled by total neutron wall load. Based on 10-15 MWy/m^2 neutron wall load limit, the blanket/first wall lifetime is expected to be about 3-5 full power years, compared with less than one full power year in the d-t reactor. This reduces the frequency of first wall/blanket replacement requirements which is a difficult task for the reactor maintenance. Remote repair will still be required in case of a failure, but these systems could be less complex and costly than those required for annual disassembly.

Heat Transport and Energy Recovery

The energy conversion system uses a steam driven turbine generator and is based on a conventional superheat cycle. The cycle requires 1515 kg/sec of superheated steam at 538°C and 6.9 MPa. The turbine is a six flow cross compound unit producing 1370 MWe. Steam is condensed and flows through a series of six feedwater heaters and returns to the reactor at 250°C. Overall efficiency is 37.5%. Pressure lower than the conventional system (16.7 MPa) was used to reduce first wall stress problems. Some of the 6.9 MPa steam is used to reheat the steam exhaust from the intermediate pressure turbine before it flows to the low pressure turbine.

Tritium Containment and Recovery

Tritium is produced and burned by fusion in the plasma at a rate of approximately 50 gr/day for a 1000 MWe d-d reactor and approximately 3 gr/day of tritium is exhausted, purified, separated, and recycled for refueling the reactor. This compares to a refueling flow of approximately 3.1 kg/day of tritium in the d-t reactor and a blanket breeding rate of approximately 370 gr/day. The tritium flows differ by nearly three orders of magnitude. The systems for recovery and containment of tritium in the blanket and heat transport systems are not required in the d-d reactor. We estimate approximately .2 Ci/day of tritium permeates from the plasma into the water coolant through the first wall, and another .8 Ci/day is bred in the water due to the presence of the LiOH corrosion agent. This 1 Ci/day is well within release guidelines of 10 Ci/day and is therefore released across the steam turbines. The "vulnerable" tritium inventory in the d-d reactor is in the cryopumps and refueling system. The pump inventory can be from 0.08 to 1 g depending on the pump cycle time, and the refueling inventory is approximately 3 g. These compare with vulnerable inventories of 80-1000 gr in the d-t reactor cryopumps, depending on the pump cycle time, and approximately 300 g in the refueling system.

Magnet and Vacuum Technologies

Conventional fusion reactor designs are required to use superconducting coils to eliminate unacceptable ohmic losses in the magnet coils. Plasma is contained in the RFP reactors by low magnetic fields. Thus, stored energy and ohmic losses can be made a small fraction of the gross electric power. Based on these facts normal magnets have been proposed for both d-t and d-d reactors /2/. The magnet technology requirements are the same for both reactors. Due to higher magnetic field requirements in the d-d reactor, the total stored energy in the magnets is approximately 18 GJ which is about ten times larger than the d-t magnets /2/.

The d-d reactor vacuum system requirements are more stringent because of the larger volume, higher gas pressure and lower burnup than in a d-t reactor of similar power output. Based on the same gas removal design (equal effective conductances), the gas load on the vacuum system of the d-d reactor is approximately three times as high as on the d-t reactor. The high gas load can be handled by limiter/diverter and vacuum duct designs of higher conductance and the same pumping technology proposed for d-t reactors.

SAFETY AND COST SUMMARIES

Safety of a d-d was compared with safety of a d-t using four types of attributes: (1) source of stored energy, (2) sources of radioactivity, (3) accident scenarios leading to release, and (4) consequences of the most credible accident scenarios. The major sources of radioactivity reside in the activated first wall/blanket structure, activated coolant corrosion products, and tritium inventories of the reactor and the tritium processing facility.

The major sources of energy considered were plasma kinetic energy, decay heat, stored magnet energy and chemical energy of liquid metal reactions for liquid metal d-t blankets. The plasma kinetic energy of the d-d reactor is 10

times as much as the d-t reactor, but it would not cause any damage to the first wall due to possible energy release. There is also about 10 times as much stored energy in the d-d magnets as in d-t magnets. However, credible scenarios for releasing this energy to cause radioactivity dispersal were not identified. The decay heat in the d-d reactor is nearly three times lower than in the d-t reactor, and it would take 15 min before the first wall would begin to melt following a loss of coolant accident compared to 6 min for the d-t reactors. Blanket melting would take much longer.

The accident scenarios identified for the d-d reactor are the same as those that have been identified for the d-t reactor. The liquid metal/oxygen reaction accident that could occur in a liquid lithium breeder d-t reactor don't exist in the d-d reactor.

The consequences of the release of activated coolant corrosion products appear to be similar for d-d and d-t reactors. The most severe accident identified for potential release of the activated first wall/blanket structure through oxidation was a loss of coolant or loss-of-flow accidents. The consequences are sensitive to alloy composition, but appear to be comparable for d-d and d-t reactors, for a given structural material. The consequences of a major tritium release from a d-d reactor is about three orders of magnitude lower than a d-t reactor. A major tritium release in a d-d reactor results in a 50-year population dose commitment of between 0.001-0.01 rem, depending on the vacuum pump regeneration time. A similar release in the d-t reactor would lead to a 50-year dose commitment between 1-10 rem. The NRC guideline is 20 rem total body dose in two hours following an accidental release.

Recommended economic guidelines were used as the basis for the costing framework used in this study /2/. The cost analysis resulted in COE of 52 mills/kWeh for d-d reactor as compared with 37 mills/kWeh for a d-t reactor which the difference is mainly due to the cost of magnets.

ACKNOWLEDGMENT

The authors are grateful to Drs. Husam Gurol and D. Dobrott for their assistance in the preparation of this paper. This work was supported by the U.S. Department of Energy Contract No. DE-AC03-81-ER53113.

REFERENCES

/1/ Krakowski, R. A., Glancy, J. E., and Dabiri, A. E., "Technology of Compact Fusion Reactor Concepts," Presented at the National Science Foundation Workshop, Washington, DC, September 30-October 1, 1982.

/2/ Hagenson, R. L., and Krakowski, R. A., "Compact Reversed-Field Pinch Reactors (CRFPR), Sensitivity Study and Design Point Determination," Los Alamos National Laboratory Report L.A. 9389-MS, July 1982.

/3/ Dabiri, A. E., and Glancy, J. E., "Design of a High Temperature First Wall/Blanket for a d-d Compact Reversed Field Pinch Reactor," Presented at the 5th Topical Meeting of Technology of Fusion Energy, Knoxville, Tennessee, April 1983.

Empirical Determination of the Parameters of Ignition and Reactor Tokamaks

R D Gill
The JET Joint Undertaking, Abingdon, Oxon, UK

ABSTRACT

Recently derived ion and electron energy containment time scaling laws are used to investigate the constraints placed on the design of tokamaks intended to demonstrate ignition and on the parameters of ignited tokamak reactors.

INTRODUCTION

Recent consideration of ohmically and injection heated tokamak experiments /1,2/ has produced empirical scaling laws for the ion energy containment time valid in both the plateau and collisionless regimes, and for the electron containment time including its dependence on temperature. The ion containment time is /2/ (in MKS units with the ion temperature T_i in eV)

$$\tau_{Ei} = 3.5 \times 10^3 \; Ra^2 \; B_\phi^2/T_i^{3/2} \; q_L \sqrt{A_i} \; f(\nu_i^*)$$

where R and a are the tokamak major and minor radii, B_ϕ the toroidal field strength, q_L the safety factor and A_i the ion mass. $f(\bar{\nu}_i^*) = 1$ for $\bar{\nu}_i^* > 3.3$ and otherwise $f(\bar{\nu}_i^*) = 0.46\bar{\nu}_i^{*\,0.65}$ with the mean collisionality parameter

$$\bar{\nu}_i^* = 3.49 \times 10^{-16} \; (R/a)^{3/2} \; (\bar{n}_e \; q_L \; R/T_i^2) \; Z_{ION}$$

with $\bar{n}_e$ the line averaged plasma density and $Z_{ION} \approx (\sqrt{2}Z_{eff} - 0.41)$. The ion losses exceed neoclassical losses by up to a factor of five over the range $0.02 > \bar{\nu}_i^* > 2$. The electron containment time was determined /2) by regression analysis of a data bank and from injection heating data.

$$\tau_{Ee} = 2 \times 10^{-28} R^{1.54} \; a^{0.75} \; \bar{n}_e^{1.33} \; Z_{eff}^{0.35} \left(\frac{T_e}{T_e^p} \right)^{0.75}$$

where T_e is the electron temperature and the peak temperature for ohmically heated discharges is

$$T_e^p = 6.47 \times 10^{-3} \; R^{0.96} \; I^{0.81} \; Z_{eff}^{0.37}/a^{1.24}$$

with I the plasma current. These scaling laws have been used to construct a Ø-D plasma transport model /2/. They are based on both ohmic and injection heated discharges but do not contain data from the recent experiments which show a saturation of β at high injection power levels. (e.g. Ref./4/).

2 IGNITION TOKAMAKS

For a tokamak to achieve ignition both the product $\bar{n}_e \tau_E$ and T_i must exceed certain values which are taken as $1.8 \times 10^{20} m^{-3} s$ and 3×10^4 eV, and where τ_E is the total energy confinement time. The solutions of the model are investigated in a D-T plasma in which the electrons and ions are closely coupled with $T_e \approx T_i$. This condition is fulfilled except at low density in low field machines. The mean plasma density is equated to the maximum value determined from (see Ref. /3/).

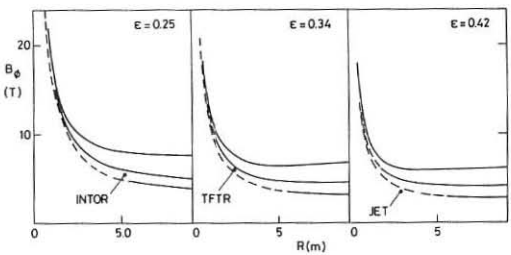

Fig. 1. Minimum toroidal field strength required for ignition as a function of major radius for various values of ε. The curves are for ζ = 1, 0.7, 0.5.

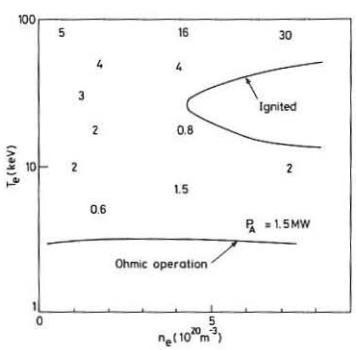

Fig. 2. $T_e - \bar{n}_e$ plot showing values of P_A and the ignited and ohmic regimes. (ε = 0.25).

$\bar{n}_e = 2.3 \times 10^{20} \zeta B_\phi / qR$ with $\zeta \leq 1$ for existing experiments. For a given inverse aspect ratio (ε) and $q_L = 3.0$ the Ø-D model can be solved for $B\phi$ for a particular R, leading to a B_ϕ -R plot (Fig. 1) which shows the minimum sized machine in which ignition can be achieved for a particular value of toroidal field. The curves on Fig. 1 are for various values of

ζ and become broken when $\beta_\theta > R/a$ as these values are generally considered inaccessible on mhd grounds. The rapid rise of B_ϕ at small R makes the construction of ignition machines with very small R unattractive. A conservatively chosen machine intended to demonstrate ignition might have R = 4m, B_ϕ = 6T.

According to Fig. 1 the INTOR machine would ignite, TFTR might just ignite, but JET would not ignite, at least with the circular plasmas to which these calculations pertain.

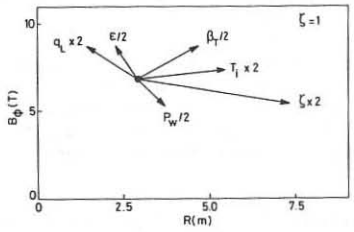

Fig. 3. Effect of changing parameters on B_ϕ and R for an ignited tokamak reactor.

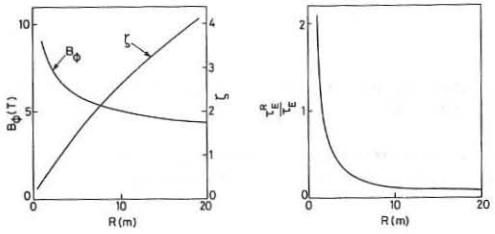

Fig. 4. Variation of (a) B_ϕ and (b) τ_E^R/τ_E for varied ζ.

The additional power requirements needed to achieve ignition from an initial ohmic plasma are investigated with the Ø-D model. Before ignition is achieved, a given set of plasma parameters require additional heating P_A satisfying

$$P_A + P_\Omega + P_N = P_L$$

where the P_Ω is the ohmic power, P_N the nuclear power generated as charged particles and P_L is the plasma power loss. Fig. 2 shows a chart of P_A (in MW) as a function of n_e and T_i for a machine with R = 1.0 m and B_ϕ = 14T. It is clear that to pass from the ohmic to ignited regimes that an additional heating power is required of about 2 MW. If the ohmic heating power is increased to include the effects of trapped electrons /5/

then this machine still does not ignite. However, a 5% increase of B_ϕ would give ohmic ignition. For larger machines with R = 5 m and B_ϕ = 5 T an additional heating requirement of up to 7 MW is calculated.

3 IGNITED TOKAMAK REACTORS

A successful commercial tokamak reactor must operate with a mean plasma $\beta_T \gtrsim 0.05$ and with a reactor wall power loading P_w of the order of a few MW.m^{-2} (P_w = 3.6 is assumed). These conditions, together with the lower limit on $n_e \tau_E^R$, the temperature at ignition and the values ε = 0.25, q = 3 and ζ = 1 then uniquely determine, within the framework of the Ø-D model, values of B_ϕ = 6.9T, R = 2.9 m and τ_E^R = 0.615s. This gives a tokamak of rather small dimensions and the effect on B_ϕ and R of changing the various assumed parameters is investigated in Fig. 3 from which is is seen that a relatively small increase in the value of ζ (up to ζ = 2) leads to possible values of R over the range R = 2.9 - 7.3 with B_ϕ = 7-5.5T. The effect of changing the other parameters (with the exception of the P_w value) is to increase the value of B_ϕ required.

In Fig. 4 the value of B_ϕ as a function of R is shown for various ζ. Also shown is the calculated value τ_E compared with the containment time calculated from the empirical scaling laws. It is seen that, except for very small major radii, the value of τ_E required by the reactor consideration is smaller than τ_E determined by the empirical scaling law by a considerable factor.

4 SUMMARY

(i) The minimum B_ϕ of an ignited tokamak has been determined as a function of major radius.

(ii) It has been shown that the empirical scaling law for τ_E leads to containment times longer than required for an ignited tokamak reactor by a considerable factor.

REFERENCES

/1/ R D Gill, Physics Letters 91A (1982) 407.

/2/ R D Gill, CLM-P681, Culham Lab., UK.

/3/ K B Axon et al, Plasma Physics and Controlled Nuclear Fusion Research 1980, 1 (1981) 413. IAEA, Vienna.

/4/ M Murakami et al, 9th International Conference on Plasma Physics and Controlled Nuclear Fusion Research, Baltimore 1982. Paper IAEA-CN-41/A-4.

/5/ F L Hinton and R D Hazeltine, Rev Mod Phys 48 (1976) 239.

THE MIRROTRON - A COMPACT DISPOSABLE TANDEM MIRROR FUSION REACTOR

A. Sternlieb
Soreq Nuclear Research Centre
Yavne 70600, Israel

ABSTRACT

A preliminary feasibility study of a compact disposable tandem mirror fusion reactor is undertaken. It is suggested that a near term, D-T burning, compact, disposable fusion reactor, based on the thermal barrier axisymmetric Tandem Mirror approach, is scientifically, technically and economically feasible, using current technologies.

1. INTRODUCTION: THE TANDEM MIRROR APPROACH

The tandem mirror confinement scheme has several favorable features as compared to a tokamak /1/:

(a) It can obtain high-β values, enhancing achievable pressures.

(b) It has continuous operation, unlike tokamaks which are operated inductively. These first two points contribute to a greater economical feasibility. RF current drive for steady state tokamaks is still in its infancy.

(c) It is possible to achieve breakeven without going through ignition, by continuously refuelling and heating the plasma. On the other hand, for a ohmically heated tokamak, ignition is absolutely necessary in order to achieve breakeven. Even if ignition is achieved in a tokamak, β-values have to be high enough to make a reactor economical, which is not easy to achieve.

(d) Tandem Mirror devices have simpler, more accessible geometry. The confinement is separated from the refuelling and heating. High temperatures are achieved by neutral beam injection or RF heating (ICRH, ECRH). In addition to the relatively simpler physics involved, the straight geometry is also more suitable to a hybrid fusion-fission reactor, in which a specially designed blanket surrounds the central cell /2/. Calculations have shown that high energy, 1 MeV/amu, $Z \geq 3$ ion beams may be preferable to the difficult to obtain neutral hydrogen beams. Concerning the required RF power, it is hoped that the thermal barrier concept will bring about a significant reduction in the required ECRH power necessary to provide the end plug potentials.

2. CONVENTIONAL TANDEM MIRROR FUSION REACTORS

It has been estimated that a driven tandem mirror reactor of a size not much larger than that of the TMX-U experiment, combined with a breeding and/or power generating blanket, can become economical (Q = 20-30). The TDF /3/

and TASKA /4/ planned designs are of such a size. Because of complexity of shielding and superconducting magnets, even such relatively small fusion devices tend to become very expensive and cumbersome. Therefore, high reliability and relatively long life span are necessary. High power densities, heat and radiation fluxes are not allowed. For these reasons, conventional reactors tend to be oversized, expensive, long term and having high output powers of several gigawatts.

In a conventional fusion reactor the plasma at the center is surrounded by a vacuum region which in turn is surrounded by the blanket. Next comes the shielding which protects the superconducting magnets. The blanket is cooled continuously. It is clear that the design optimization of the blanket serves several purposes: it breeds tritium (from lithium) and fissile material (from fertile material), it generates fission power, it collects neutron energy and transports the heat fluxes outwards. Fission suppressed breeding may be used for maximum fissile fuel production.

There are still scientific and technological problems which require careful solutions. Such issues are: tritium handling and radioactivity of the blanket in a hybrid reactor, optimization of the end plug design, achieving of required neutral beam and RF heating sources. Fusion reactors can be combined with a direct-energy converter from end-less ion flux, for better efficiency. The required RF heating power can be reduced in several ways. Among them are: use of thermal barriers, use of axisymmetric configuration, negative potential operation. It is an accepted view that a combination of a hybrid fusion-fission reactor has a better chance to succeed, than a pure fusion device. However, the complexity and high radioactivity of the blanket are serious disadvantages. Breeding hybrids can operate in conjunction with LWR's. It has been estimated that one hybrid breeder can provide fuel for up to 20 LWR's. There have been various estimates of the necessary Q which will make a driven hybrid device with a fertile blanket, economical. This depends on the price of U_3O_8 / /. However, a Q of 2-5 may be necessary, under the best circumstances. Also they are inferior in environmental safety and simplicity as compared to pure fusion devices; hybrids have the big advantage of combining neutron rich but power poor fusion with power rich but neutron poor fission / /.

3. THE PROBLEMATICS OF COMPACT FUSION REACTORS

A compact fusion reactor can be defined as one which has high power density and, for same total power, is significantly smaller than a conventional magnetic fusion reactor. The difference can be of an order of magnitude (e.g. 0.5 MWt/m^3 for a conventional reactor, vs. 5 MWt/m^3 in a compact reactor), according to existing designs. A common purpose of any compact concept is to reduce the total mass (volume) of the power generating core. This includes the mass of the first wall, blanket, shield, coils and all mechanical support. In the case of a tandem mirror, it does not include the end plugs. This reduction in mass, is also about an order of magnitude. It is reasonable to assume that the cost of the power core is related to the mass involved. On the overall, it has been estimated (considering the other plant components) that the normalized plant cost (per kWe) is approximately halved for a compact reactor as compared to a conventional reactor. The system power densities, and mass efficiency factors of the compact fusion concepts are comparable to today's LWR's. A major goal of compact designs is to reduce the fraction

of total plant costs taken by the fusion power core (from 0.5-0.8, to 0.3). The compact reactor designs use in general copper coils for magnets, instead of superconducting coils which are used in the conventional concepts. This has as an effect the reduction of shielding required to isolate the magnets from the fusion heat and neutron source, and allows placing the coils closer to the fusion plasma. This has the double advantage of permitting higher magnetic field strength at the plasma and smaller, less costly coils. It has the disadvantage of requiring the recirculation of more electricity from the plant to provide current to the coils. It is expected that materials lifetime in the compact designs will be considerably shorter than in conventional concepts because of higher neutron flux which should result in somewhat increased maintenance and replacement costs. An advantage of compact concepts is that, because the fusion power cores would be smaller than for the conventional fusion concepts, the development steps, test reactors, experiments, etc. might also be smaller, and hence both more affordable and quicker to complete. The compact reactors would come naturally in smaller unit sizes, i.e. power capacity, which might make them easier to market. Also, because the fusion power core is a smaller percentage of total plant costs, shortfalls in the physics and engineering performance of the core have less impact on the cost of the plant.

Although compact concepts have many attractive features, it is generally recognized that uncertainties in the performance and development paths are larger than in the case of the conventional reactor. Extrapolations in physical scale laws are larger and there may be new specific physics issues. The main technological problem for compact concepts is expected to be first wall radiation damage and sputter erosion, leading to more frequent wall replacement. The primary issues for fusion reactor economics are size, power density, wall loading, beta, field strength, choice of first wall material, overall efficiency and maintenance. The primary physics-related issues for compact concepts are the assumption made on what plasma beta and confinement times are needed or assumed. The primary technology issues are the performance of first wall materials at high wall loading and the development of maintenance approaches compatible with high availability and short first wall lifetimes. An important motivating factor among compact concept advocates is to produce small unit plant size (e.g. <500 MWe). Smaller unit sizes, if economically competitive, result in more rapid deployment. Modular construction is necessary to keep costs low.

4. THE MIRROTRON - A COMPACT, DISPOSABLE TANDEM MIRROR FUSION REACTOR

In this paper, we propose a new tandem mirror fusion reactor design, which we call the Mirrotron. In this design, the central cell coil magnets are conventional and placed close to the reacting plasma. The special shielding for the superconducting magnets is thus eliminated. The coils can be powered by a motor generator device. This compact tandem mirror design will have a disposable central cell, which will have to be replaced frequently, because of heavy neutron radiation damage. On the other hand, the limited lifetime of the central cell eliminates the need for remote maintenance. The expected power of a driven, disposable compact hybrid tandem mirror reactor will be under 1 GW.

It should be noted that the Mirrotron is similar in its philosophy to the Riggatron TM concept /5/ of INESCO, Inc. The Riggatron is basically an

ohmically heated tokamak, compact and disposable, with or without auxiliary heating (RF, depending on design and scaling law). However, the success of the Riggatron concept depends entirely on achieving ignition during each pulse, which is highly uncertain, because of unknown scaling of resistivity at fusion regime temperatures and possible disruption instability. There are also many technological uncertainties. Moreover, even if ignition is attained, β values high enough for the Riggatron to become economical will be difficult to achieve.

Therefore, the Mirrotron, whose operation is not dependent on achieving ignition and which can easily attain high β values, has both the advantages of the compact, disposable philosophy and the advantages of the mirror approach. Because of the high power and radiation densities, the central cell will have to be replaced at short intervals. It is probable that technology will be taken to its limits (magnetic stress resistance, heat flux removal, power supply, neutron radiation damgage). The central cell can be made modular, with minimum replacement time on site. It is possible to prevent damage of the plug regions, which therefore can be made superconducting. Therefore, replacing central cell modules will be the only major maintenance procedure. It would be desirable to have relatively more RF heating (ECRH, ICRH), and less neutral beams, which tend to be expensive. The conventional proposed tandem mirrors closest to the Mirrotron are the TDF design at Livermore and the TASKA-M concept of Karlsruhe-Wisconsin. However, these two designs are not disposable reactors, but only testing devices, intended for long life-spans. Their Q's are around 20-40% and they use superconducting magnets from the central cell. We expect that the Mirrotron will be a TDF-size device with the proper modifications necessary to make it an economical reactor.

5. SUMMARY

It appears that only steady-state tokamaks and tandem mirror reactor concepts will be at similar stages of development with respect to their potential as conventional reactor candidates, by 1986-1987. At present, the tokamak program has a larger data base, but its continuous operation at high β-values is still uncertain. The opposite is true for the tandem mirror approach. This situation will probably be corrected during the next few years.

In parallel with the conventional approach, it has been instructive during the last few years to consider compact reactor designs. Such a detailed design, called the Riggatron, TM is based on the ohmically heated tokamak. It is suggested in this paper that a similar feasibility study should be undertaken for a compact, disposable design, based on the tandem mirror approach.

6. REFERENCES

/1/ The National Mirror Fusion Program Plan, UCAR-10042-82, 1982.
/2/ Reynolds, J. A.: An Introduction to Hybrid Fusion, CLM-R219, 1982.
/3/ Thomassen, K. I. and Doggett, J. N.: A Technology Demonstration Facility, UCRL-88849, 1983.
/4/ Heinz, W. and Maurer, W.: Studies for a Fusion Technology Device, Nucl. Eng. Design 73 (1982) p. 171.
/5/ Bussard, R. W.: The RIGGATRON™ Tokamak Fusion Demonstration Experiment Program, TANS 39 (1981) 238.

NUCLEAR SPIN DEPOLARIZATION BY CLASSICAL MIXING IN FUSION REACTOR PLASMAS

J.J. Lodder

Association Euratom-FOM, FOM-Instituut voor Plasmafysica "Rijnhuizen", Nieuwegein, The Netherlands

It has been proposed /1,2/ to polarize the nuclear spins of the neutral particles injected in a fusion reactor, which will have various useful effects if the polarization survives on the fusion reaction time-scale. Even if it is true that individual nuclei remain fully polarized, the plasma as a whole does not have to remain polarized sufficiently long since the directions of the individual spins can be mixed classically by the precession of the spin in the complicated fields which are necessary for confinement.

For the present purpose the quantum description of the spin can be replaced by an equivalent classical treatment /3/. The state of the quantum-mechanical spin-half particle can be represented by a state vector in a two-dimensional Hilbert space

$$|\psi> = C_1|\uparrow> + C_2|\downarrow> ; \quad C_1 C_1^* + C_2 C_2^* = 1 , \tag{1}$$

or by the equivalent density operator

$$\rho = |\psi><\psi| ; \quad \mathrm{Tr}\,\rho = 1 . \tag{2}$$

Any density operator for a spin-half particle can be expanded in Pauli matrices

$$\vec{\sigma} = \sigma_x, \sigma_y, \sigma_z ,$$

as

$$\rho = \tfrac{1}{2}(I + \vec{P} \cdot \vec{\sigma}) . \tag{3}$$

Conversely, for a pure state the state vector can be found, up to an irrelevant phase vector, from the polarization vector $\vec{P}$. The polarization vector $\vec{P}$ can be interpreted as the direction in which the spin points since

$$<\vec{\sigma}> = \mathrm{Tr}(\vec{\sigma}\,\rho) = \vec{P} , \tag{4}$$

as one sees from the properties of the Pauli matrices. For an ensemble of spins in states $|\psi>$ with probabilities p_n, the ensemble density operator is $\rho_e = \Sigma\, p_n |\psi_n><\psi_n|$. The polarization vector $\vec{P}_e$ of the ensemble can be found by vectorial averaging of the individual polarization vectors

$$\vec{P}_e = \mathrm{Tr}(\vec{\sigma}\,\rho_e) = \Sigma\, p_n \vec{P}_n . \tag{5}$$

In a magnetic field the equation of motion for the density operator

$$i\hbar \frac{d\rho}{dt} = [H,\rho] = -\tfrac{1}{2}\gamma[\vec{B} \cdot \vec{\sigma}, \rho] \tag{6}$$

translates, by using the properties of the Pauli matrices, into the equation

$$\frac{d\vec{P}}{dt} = \gamma \vec{P} \times \vec{B} \equiv \vec{P} \times \vec{\omega}_L \tag{7}$$

for the polarization vector, which shows that $\vec{P}$ precesses just as a classical magnetic dipole with the same gyromagnetic ratio.

Neglecting spin-orbit coupling the non-relativistic equations of motion for a particle with spin are

$$\frac{d\vec{r}}{dt} = \vec{v}\,, \qquad \frac{d\vec{v}}{dt} = \frac{e}{m}\left(\vec{E}(\vec{r},t) + \vec{v}\times\vec{B}(\vec{r},t)\right)\,, \tag{8}$$

$$\frac{d\vec{P}}{dt} = \gamma\,\vec{P}\times\vec{B}(\vec{r},t)\,. \tag{9}$$

The polarization vector of an ensemble of spins is found by mixing the solutions of (8,9) in accordance with (5). The complicated system of Eqs. (8,9) will have conserved quantities only under special circumstances. It is known however from the classical theory of the top that the average component of $\vec{P}$ parallel to $\vec{B}$ is an adiabatic invariant of the motion. The $\parallel$ component of $\vec{P}$ can be changed only by a rapidly varying perpendicular magnetic field. In a plasma confinement device this is provided by the change in the magnetic field direction over the gyro-orbit of the particle.

For deuterium ions in a tokamak reactor (R = 5 m, a = 1 m, B = 5 T, T = 10 keV) one has

$$\omega_C = 2.5\times10^{8}\ \mathrm{s}^{-1}\,, \qquad r_C = 3\times10^{-3}\ \mathrm{m}\,, \qquad \omega_L = 0.86\ \omega_C = 2.2\times10^{8}\ \mathrm{s}^{-1}. \tag{10}$$

The variation in the magnetic field B_1, perpendicular to the average field over a cyclotron orbit, is of the order

$$B_1 \approx \frac{r_C}{a}\,B_p \approx \frac{r_C}{R}\,B_T \approx 10^{-3}\,B_T\,, \tag{11}$$

which corresponds to a frequency

$$\omega_1 = 10^{-3}\,\omega_L \approx 2\times10^{5}\ \mathrm{s}^{-1}\,. \tag{12}$$

This variation in field direction is seen by the spin as an oscillating field at the gyrofrequency. The solution of (7) in the presence of a rotating perpendicular field is found by transforming to coordinates rotating with angular velocity ω_C around the average field $\vec{B}_o$, which gives

$$\left(\frac{d\vec{P}}{dt}\right)_{rot} = \frac{d\vec{P}}{dt} + \vec{\omega}_C\times\vec{P} = (\vec{\omega}_C - \vec{\omega}_L + \vec{\omega}_1)\times\vec{P} \equiv \vec{\omega}_T\times\vec{P}\,, \tag{13}$$

The vector $\vec{\omega}_T$ doe not depend on time in the rotating coordinates, so the solution of (13) is a precession of $\vec{P}$ around $\vec{\omega}_T$. The angle $\Delta\phi$ between $\vec{\omega}_T$ and $\vec{B}$ is of the order

$$\Delta\phi = \mathrm{arctg}\left(\omega_1/(\omega_C - \omega_L)\right) \approx 10^{-2}\ \mathrm{rad}\,. \tag{14}$$

The direction of $\vec{\omega}_1$ in the rotating coordinates, depends on the relative phase of the perturbing field and the precession motion in the non-rotating coordinates. This phase will be influenced by various processes on different timescales, for instance by the

poloidal motion : time-scale $R/v_{th} \approx 10^{-5}$ s, (15)

drift motions : time-scale $a/v_d \approx 10^{-4}$ s, (16)

field perturbations and waves : time-scale unknown, (17)

collisions : time-scale (collision time) $\tau_C \approx 10^{-2}$ s. (18)

To make an estimate of the combined effect of these perturbations, it is assumed that $\vec{\omega}_1$ is a vector of constant length having a randomly varying direction, with an exponentially decaying autocorrelation function on the scale of the fastest relevant process, which is the poloidal motion. Its power spectrum is then Lorentzian, yielding an estimate

$$\tau_{mix,r} = (R/v_{th})\ \omega_1^2/(\omega_C - \omega_L)^2 \approx 10^{-1}\ s \qquad (19)$$

for the time needed to turn the spin through a significant angle. This time-scale $\tau_{mix,r}$ corresponds to a reversible mixing of the spins.

For collisions it is possible to derive that the power spectrum has a Lorentzian line shape, the width being determined by the collision time τ_C. This implies the appearance of an irreversible mixing over a time

$$\tau_{mix,ir} = \tau_C\ \omega_1^2/(\omega_C - \omega_L)^2 \approx 100\ s\ , \qquad (20)$$

which is of the order of the fusion reaction time.

A more qualitative description of the spin motion is also possible. In co-rotating coordinates the spin motion is a precession around a vector which wanders on a narrow cone (aperture 10^{-2} rad) around the average field direction. Taking this motion to be random leads to a diffusion of the spin direction. The time needed to change the spin direction by this diffusion is of the order

$$t = \left(\frac{1}{\Delta\phi}\right)^2 \Delta t = 10^4\ \Delta t\ , \qquad (21)$$

where Δt is the time for a stochastic step of the precession centre. The estimates (19,20) are recovered by substituting the appropriate time-scales.

The existence of a perturbing field at the gyrofrequency also invalidates the estimates in Refs. 1 and 2 of the effects of waves, field ripple, etc., which are based on the assumption that perturbations have to act with the precession frequency ω_L in order to be effective, while it is sufficient to have the difference frequency $\omega_C - \omega_L$, which is smaller by a factor seven.

It must be appreciated that the precession of the spins in an inhomogeneous magnetic field does not depolarize single spins, but it depolarizes the ensemble of spins, since particles follow different trajectories, so that they experience different fields with correspondingly different rotations. Collisionless mixing is in principle reversible. The mixing becomes irreversible on the time-scale (20) related to collisions. The combined Eqs. (8,9), in principle, give the possibility of calculating (numerically) the actual behaviour of the spin, even in very complicated fields.

For tritium with $\omega_L = 8.94\ \omega_C$ the situation is more complicated than for deuterium. There is a close match between the eighth harmonic of the gyrofrequency and the effective precession frequency $\omega_L - \omega_C = 7.94\ \omega_C$ but the strength of this harmonic will depend on the perturbation of the orbit from a circle, so it does not seem possible to give a simple estimate.

For other confinement schemes, different from a tokamak, the situation can be expected to be similar since inhomogenuous fields with varying direction are necessary for confinement in all cases.

In conclusion it seems unlikely that the requirements to be fulfilled for keeping an ensemble of nuclei polarized for times relevant for fusion applications are compatible with those of plasma confinement. Even if individual nuclei remain polarized for long times, the directions of the individual spins will be randomized by classical mixing of their directions.

Acknowledgement. This work was supported by FOM, ZWO and EURATOM.

References

/1/ Kulsrud, R.M., Furth, H.P., Valeo, E.J., and Goldhaber, M., Princeton University, Plasma Physics Laboratory, Report PPPL 1912, 1982; Phys. Rev. Lett. 49 (1982) 1248.

/2/ Kulsrud, R.M., Furth, H.P., Valeo, E.J., Budley, R.J., Jassby, D.L., Michlich, B.J., Post, D.E., Goldhaber, M., and Happer, W., Proc. Intern. Conf. on Plasma Phys. and Contr. Nucl. Fusion Res., Baltimore, 1982; post deadline paper.

/3/ Merzbacher, E., Quantummechanics, 2nd Ed., Wiley & Sons, New York, 1970.

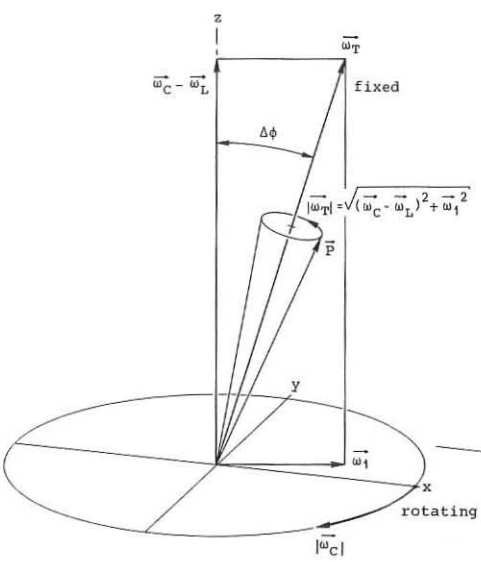

A possible spin motion in rotating coordinates.

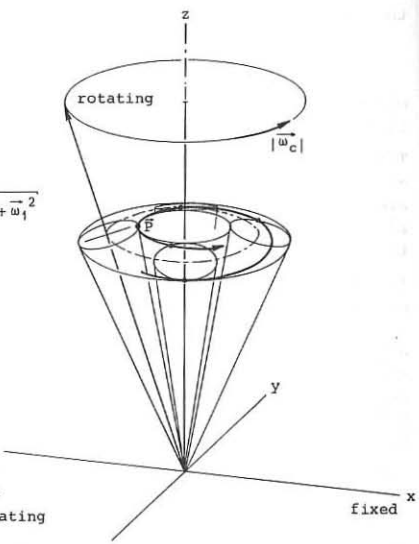

The same motion in stationary coordinates.

PHYSICS AND ENGINEERING CONSTRAINTS ON THE FEASIBILITY OF ADVANCED FUEL FUSION REACTORS[+]

W.Kernbichler, K.Niederl, M.Heindler
Technical University Graz
Petersgasse 16, A-8010 Graz, Austria

INTRODUCTION

The recent attention to engineering problems related to DT fueled fusion reactors has lead to a revival of the interest in advanced fuels (AFs). However, comparative assessments tend to conclude that AF fueled reactors (AFRs) are unattractive if not unfeasible /1/. The following study will first investigate the engineering constraints on AFRs and then some physical aspects concerning the power amplification (ignition) and the resulting operational requirements.

For the study of engineering constraints on AFRs we will follow the considerations by J.R.Roth /1/ except that we assume neither the same temperature for electrons and ions nor the same density for both fuel ion species. The relaxation of these two assumptions will turn out to have an important impact on fusion power densities in an AFR. As a consequence, Roth's assertion that proton based AFs be inconsistent with engineering constraints is shown to be not conclusive.

PLASMA POWER DENSITY IMPOSITIONS

There is general agreement in the literature that the power density in the plasma of a DT burning reactor with magnetic confinement will be not larger than 10 MW/m³ due to first wall and minimum size considerations, and must not be smaller than 1 MW/m³ if there should by any chance at all for economic competitiveness. This power bracket will be designated as "desirable power density regime" and taken as target for AFRs. The associated temperature and fuel mix dependent ion density regime can be derived, for each fuel, from

$$P_{fu} = 1.6\cdot10^{-7} n^2 \varepsilon(\varepsilon+1)^{-2} \langle\sigma v\rangle U \Rightarrow n = n(\varepsilon, kT; P_{fu}) \qquad (1)$$

Here we consider fuels consisting of i and j type ions, mixed according to the density ratio $\varepsilon=n_j/n_i$ at the same temperature $T_j=T_i=T$. The unit convention employed is $P(MW/m^3)$, $\langle\sigma v\rangle(m^3 s^{-1})$, $U(MeV)$, $n(cm^{-3})$, $kT(keV)$, $B(T)$. Furthermore we assume $Z_j>Z_i$ yielding $0<\varepsilon\leq1$ as the range of interest.

+) Work supported by the Steiermärkische Landesregierung, Abteilung für Wissenschaft und Forschung

ENGINEERING CONSTRAINTS: DENSITY LIMITATIONS

Clearly, if the fuel mix ratio is optimized, for fixed total ion density $n=n_i+n_j$, to yield maximum fusion power density, one finds $\varepsilon^{n}_{opt}=1$, as used by /1/. However, in a magnetically confined plasma the achievable total ion density is

$$n(\beta,B) = 2.5\cdot10^{15}\beta B^2(kT)^{-1}H^{-1} \qquad (2)$$

with

$$H = (Z_i+Z_j\varepsilon)\alpha(\varepsilon+1)^{-1}+1;\ \alpha = T_e/T \qquad (3)$$

The associated fusion power density is given by

$$P_{fu}\ (\beta,B) = 10^{24}\beta^2B^4\langle\sigma v\rangle\ U(kT)^{-2}F \qquad (4)$$

with

$$F = \varepsilon\{(1+Z_i\alpha)+(1+Z_j\alpha)\varepsilon\}^{-2} \qquad (5)$$

The ion density ratio can be optimized, for constant β and B, with respect to maximum fusion power density, yielding

$$\varepsilon^{\beta B}_{opt} = (1+Z_i\alpha)/(1+Z_j\alpha) \qquad (6)$$

In Fig. 1 we show the high extent to which the fusion power density can be improved if the fuel mixture is optimized according to Eq. (6), in particular for p based fuels. Note the strong increase of P_{fu} with decreasing electron to ion temperature ratio. The actual α value, to be obtained by self consistent calculations, will be low for these fuels since bremsstrahlung losses increase dramatically with increasing Z. For deuterium based fuels the improvement margin is clearly smaller.

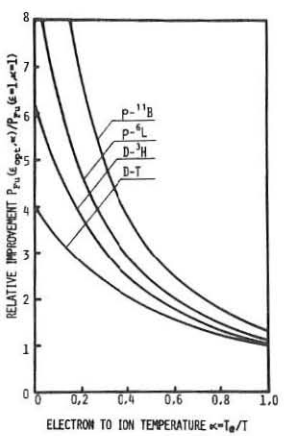

Fig. 1: Improvement of the fusion power density, Eq(4),associated with an electron to ion temperature ratio α and with the optimum ion density ratio ε,Eq(6), relative to $\alpha=\varepsilon=1$.

ENGINEERING FEASIBILITY OF ADVANCED FUELS

Equations (1) to (6) identify, in an ion density vs. ion temperature plot, the desirable fusion power density regime. For fuel mix ratio values between 1 and those obtained from Eq.(6) (e.g. $\varepsilon\beta B_{opt} = 0.52$ for p-11B at $\alpha=0.3$) the desirable power density regime turns out to be insensitive to the actual mix ratio. Therefore the domain displayed in Fig. 2a applies both for the non-optimized case, Ref. /1/, and the optimized one. Fig. 2a also shows the density domain which is actually accessible for given βB, limited by straight lines according to Eq.(2). The position of that limit depends strongly on the ratios ε and α. Using the $\varepsilon=\alpha=1$ line, according to /1/, the desirable regime appears almost inaccessible, whereas for the optimized case, the entire desirable power density regime is accessible over a broad range of temperatures. In each case we have assumed $\beta=1$ and B=8 (T) as in /1/. Under the same conditions a p-6Li fueled reactor reaches a maximum fusion power density of 2.5 MW/m³ at 90 keV; if one includes p chaining /2,3/, results comparable to those for p-11B are obtained.

Clearly, the claim cannot be maintained that p-based fuels cannot even meet engineering constraints. However, the accessibility of high fusion power densities is not the only criterion for the reactor feasibility of a fuel. In the following we address the issue of power amplification in the plasma.

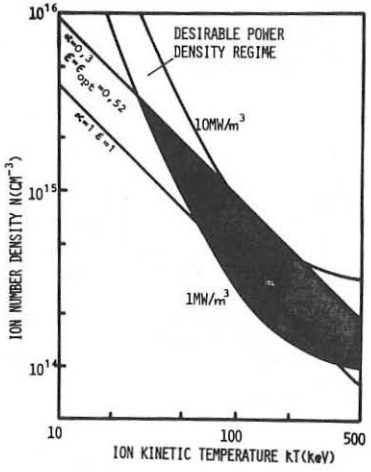

Fig. 2a

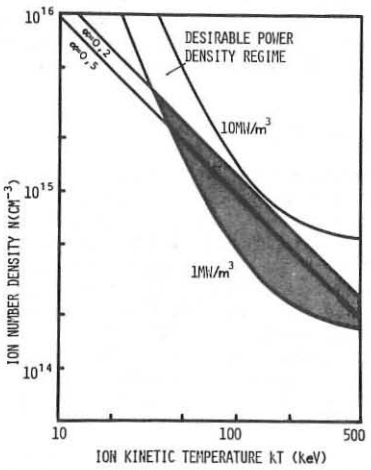

Fig. 2b

Ion number density vs. ion temperature for the desirable power density regime 1 to 10 MW/m³, Eq.(1), and for the βB confined density, Eq.(2), for B=8(T), $\beta=1$ and p-11B reactions. Fig. 2a relates to $\alpha=\varepsilon=1$, Ref /1/, and to $\alpha=0.3$, $\varepsilon=0.52$ (optimum P_{fu} at given n and βB, resp.). Fig. 2b relates to $\alpha=0.5$, 0.2 and $\varepsilon=0.1$ (optimum P_{fu}/P_b ratio). Values for $\langle\sigma v\rangle$ from Ref. /4/.

PHYSICAL CONSTRAINTS: BREMSSTRAHLUNG LIMIT TO Q

Since bremsstrahlung will be important for most AFs we will compare the fusion to bremsstrahlung power densities /5/:

$$P_{fu}/P_b = 3.4\cdot 10^{23} U\langle\sigma v\rangle (\alpha kT)^{-0.5} (1+2\alpha kT/511)^{-1} S^{-1} \quad (7)$$

where

$$S = \{(Z_i+\varepsilon Z_j)(Z_i^2+\varepsilon Z_j^2)+2(Z_i+\varepsilon Z_j)^2\cdot A\}/\varepsilon \quad (8)$$

Optimization of the mix ratio ε with respect to P_{fu}/P_b yields

$$\varepsilon^b_{opt} = (Z_i/Z_j)\sqrt{(Z_i+2A)/(Z_j+2A)}; \quad A=1-(1+\alpha kT/511)^{-2} \quad (9)$$

For this optimum mix ratio values as low as 0.1 to 0.2 are found. For such low concentrations of the high-Z fuel ion species the n-T-plot changes appreciable, Fig.2b. It is apparent that low α ratios are imperative if the engineering constraint is to be met. According to a self consistent solution of the electron energy flux equation, with bremsstrahlung losses only, values for α slightly below 0.5 can be expected. Including other losses and accounting for relativistic effects /6/ α may be as low as 0.2. The pertinent confinement limits are plotted in Fig.2b, showing again the satisfactory performance of p-11B as a reactor fuel.

Investigation of the fusion to bremsstrahlung power ratio for optimum fuel mix indicates that, for α=0.2, values above unity are attained in the ion temperature range of 200 to 550 keV. This defines the ion and electron temperature domain for which ignition against bremsstrahlung can be achieved.

CONCLUSION

Contrary to the conclusions by Roth /1/, neutron lean reactions are shown to be consistent with engineering constraints. The desired power density can be confined in high β devices even if the fuel mix is optimized with respect to energy amplification rather than to fusion power. The pertinent parameter ranges have been identified. The issue of ignition against bremsstrahlung is more delicate since fusion to bremsstrahlung power ratios are found to be at best close to unity, thus suggesting a more careful investigation of the compound influence of chaining, friction of ions on relativistic electrons, nuclear elastic scattering and non-Maxwellian ion distribution functions.

/1/ Roth, J.R., Nuclear Technology/Fusion Vol.2 (1982) 29-42.
/2/ Miley, G.H. in B.Brunelli, G.G.Leotta, Ed.: Unconventional Approaches to Fusion, Plenum Press, New York (1982)
/3/ Hirshfield, J.L., EPRI ER-536-SR (1977) 261-274, Palo Alto
/4/ McNally, Jr. J.R., Rothe, K.E., Sharp, R.D., ORNL/TM-6914, Oak Ridge, USA (1979)
/5/ Dawson, J.M., EPRI ER-536-SR (1977) 403-434, Palo Alto, USA
/6/ Channon, S.R., AEL-report 83-11 (1983), Princeton, USA

BURN OPTIMIZATION IN A THERMONUCLEAR REACTOR

U.Carretta(.), D.Farina, M.Lontano, E.Minardi, R.Pozzoli
Istituto di Fisica del Plasma
Associazione EURATOM-CNR
Milano-Italy.
(.)Centro di Studio sulla Propulsione e l'Energetica
CNR-Politecnico di Milano
Milano-Italy.

1.- Equations and numerical model

The burn control by feedback compression and decompression of the plasma has been investigated by means of a zero-dimensional code which includes the evolution of electrons, deuterons, tritons and thermalized alpha particles, treated as fluid populations, and of the energetic alpha particles, described by their energy distribution.
At any time t, the plasma major radius R(t) is given by the equilibrium (Grad-Shafranov) equation, which is coupled to the transport equations for the plasma components.
We consider the following equations for the different plasma populations, /1/, :
-continuity for the ion components:

$$\frac{dn_i}{dt} + 2\frac{\dot{R}}{R} n_i + \frac{n_i}{\tau_{p,i}} = -n_i n_j S_\alpha$$

where i=D,T; S_α is the α-production rate coefficient; $\tau_{p,i}$ is the particle confinement time.
-Continuity for the thermal α-particles:

$$\frac{dn_\alpha}{dt} + 2\frac{\dot{R}}{R} n_\alpha + \frac{n_\alpha}{\tau_{p,\alpha}} = S_{\alpha t}$$

where the source term $S_{\alpha t}$ is computed by taking into account the evolution of the suprathermal α-population, as described below.
-Energy balance for the ion components:

$$\frac{d}{dt} p_i = -\frac{10}{3}\frac{\dot{R}}{R} p_i - \frac{p_i}{\tau_{\varepsilon,i}} + n_i \sum_q \nu_\varepsilon^{i/q} (T_q - T_i) - n_i T_i n_j S_\alpha + Q_{\alpha_\varepsilon, i}$$

where $\tau_{\varepsilon,i}$ is the energy confinement time, $\nu_\varepsilon^{i/q}$ is the energy exchange collision frequency with the fluid population q, $Q_{\alpha_\varepsilon, i}$ is the power density exchange term with suprathermal alpha particles.
-Energy balance for electrons and thermal α-particles:

$$\frac{d}{dt} p_e = -\frac{10}{3}\frac{\dot{R}}{R} p_e - \frac{p_e}{\tau_{\varepsilon,e}} + n_e \sum_q \nu_\varepsilon^{e/q} (T_q - T_e) - Q_{br} + Q_{\alpha_\varepsilon, e} + \frac{2}{3}\eta J^2$$

$$\frac{d}{dt}p_\alpha = -\frac{10}{3}\frac{\dot{R}}{R}p_\alpha - \frac{p_\alpha}{\tau_{\varepsilon,\alpha}} + n_\alpha \sum_q \nu_\varepsilon^{\alpha/q}(T_q - T_\alpha) + Q_{\alpha\varepsilon,\alpha} + S_{\alpha\varepsilon,\alpha}$$

where ηJ^2 is the ohmic input, Q_{br} the Bremsstrahlung loss, and the source term $S_{\alpha\varepsilon\alpha}$ takes into account the power input due to the thermalization of suprathermal α-particles.
The energetic α-particle population is treated as a discrete ensemble of packets, characterized by their density and energy values, $n_{\alpha\varepsilon,j}$ and ε_j respectively.
Their evolution is given by :

$$\frac{d\, n_{\alpha\varepsilon,j}}{dt} = -2\frac{\dot{R}}{R} n_{\alpha\varepsilon,j} - \frac{n_{\alpha\varepsilon,j}}{\tau_j(\varepsilon_j)} + S_j$$

$$\frac{d\,\varepsilon_j}{dt} = -\frac{4}{3}\frac{\dot{R}}{R}\varepsilon_j - \frac{\varepsilon_j}{\tau_{\varepsilon_j}}$$

where S_j is the source term for the j-th packet, $\tau_j(\varepsilon_j)$ the neoclassical confinement time and $\tau_{\varepsilon j}$ the total time of energy exchange of the α-particles with the plasma populations.
In our model, when the energy of the packet becomes lower than the thermal ion energy, the packet is considered thermalized and its energy spread into a Maxwellian distribution.
In the simulation we assume a modified Alcator scaling, /2/, for $\tau_{\varepsilon,e}$, and neoclassical scaling for $\tau_{\varepsilon,i}$. We put $\tau_{p,j} \sim \tau_{\varepsilon,e}$ for all fluid populations.
The equilibrium condition giving the value of R, under the assumption of constancy for the poloidal and toroidal fluxes, writes:

$$\Lambda(R,\langle p\rangle,B_v) \equiv B_v(R,t) - B_e(R,\langle p\rangle) = 0$$

where B_v is the external field, $\langle p\rangle$ is the mean pressure, B_e is the equilibrium field; B_v is assumed of the form:

$$B_v(R,t) = (R_o/R)^{n_v} \cdot B_o(t)$$

where n_v is the field index.
The equilibrium equation is solved consistently with the above-mentioned set of equations.
The feedback mechanism is simulated by giving the following relation between the vertical field and the total plasma pressure $\langle p\rangle$:

$$B_o(t) = B^* \left(1 + K\,\frac{\langle p\rangle - \langle p\rangle^*}{\langle p\rangle^*}\right)$$

where B^*, $\langle p\rangle^*$ refer to an equilibrium plasma state, and the parameter K determines the strength of the feedback.
It should be observed that even when the profile effects are

taken into account, the controllability of the burn with a vertical field depends on the validity of the zero-dimensional theory. The conditions for this validity were discussed recently, /3/ .
The present paper differs from the recent zero-dimensional treatments of the burn control, /4/, mainly in the consistent treatment of the α-particle dynamics and of the equilibrium equation, avoiding assumptions about the adiabatic behaviour of the plasma.
In addition, this study allows also the investigation of conditions not so close to the ignition, where linear analysis is not applicable.
As a first result, it seems that the energy reservoir of suprathermal α-particles, which is poured continuously into the plasma (we note that the total slowing-down times of α-particles for an INTOR-like plasma are about 0.3 ÷ 0.4 s) acts as an increasing factor in the inertia of the plasma to heating and cooling by compression and decompression.

2.- Preliminary results.

The code has been applied to an INTOR-like ignited plasma, /4/, with the following characteristics: $\langle T \rangle$ = 10 keV, $\langle n \rangle$ = 1.4 10^{14} cm^{-3}, β_p = 2.9, profile index δ = 2.
In absence of the feedback term (i. e. for K=0) the time behaviours of the radius R and of the total pressure are shown in Fig. 1, for field index n_v = 1 and -1.

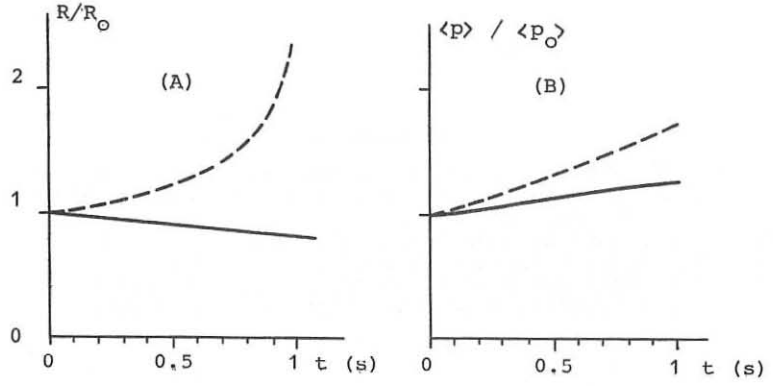

Fig. 1 : time evolution of the plasma major radius R, (A), and of the total plasma pressure $\langle p \rangle$, (B), for values of the field index n_v = 1 (solid line) and n_v = -1 (dashed line). In this case K = 0. R_o and $\langle p_o \rangle$ are the starting values of R and $\langle p \rangle$, respectively.

The results agree qualitatively with those foreseen by linear treatment: the n_v = 1 case is closer to stability than the

physical case $n_v = -1$, even if the chosen starting condition is not close to ignition.
The effect of the feedback is shown in Fig. 2.
In our case, for $K = K^* \sim 0.5$ the radius R is kept fixed by the increasing vertical field and the pressure growth is maximum. Lower K-values make the pressure growth lower, increasing the excursion of R.

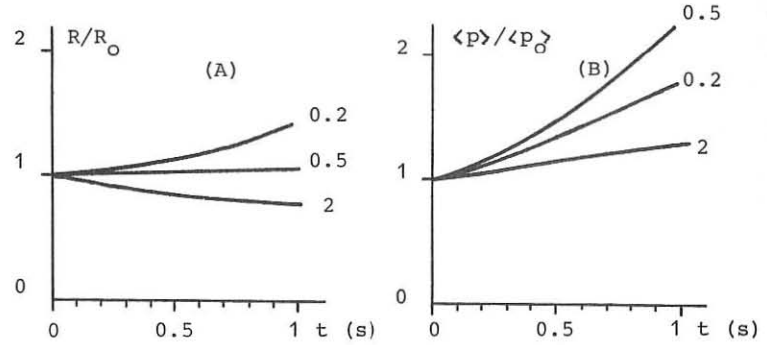

Fig. 2 : the same as in Fig. 1 for $n_v = -1$ and different values of K which are shown on the plots.

REFERENCES

/1/ - U.Carretta, S.Corti, M.Lontano, R.Pozzoli; Proc. 3rd Joint Varenna-Grenoble Int. Symp. on Heating in Toroidal Plasmas, II, 827 (1982).
/2/ - TFR Group; Nuclear Fusion 20, 1227 (1980).
/3/ - E. Minardi; Nuclear Fusion 23, 83 (1983).
/4/ - INTERNATIONAL TOKAMAK REACTOR, Zero Phase, IAEA, Vienna (1980); Phase One, IAEA, Vienna (1982).

SOME ASPECTS OF AN ADVANCED STELLARATOR REACTOR

U. Brossmann, H. Gorenflo, E. Harmeyer,

J. Kisslinger, J. Raeder, F. Rau, H. Wobig

Max-Planck-Institut für Plasmaphysik, EURATOM-Association,
D-8046 Garching, FRG

Abstract: The W VII-AS configuration /1/ is scaled up to reactor dimensions. Available space for a blanket, forces and stresses in the twisted coils are discussed leading to the result that a W VII-AS reactor coil set seems to be feasible. Ignition conditions are studied using a neoclassical transport model. Stable burning points are found with temperatures below 10 keV.

I. Introduction: The basic properties of the W VII-AS configuration /1/ are the reduced neoclassical transport losses, reduced secondary currents as compared with classical stellarators and a modular coil set consisting of 45 twisted coils. This paper concentrates on the problem whether this coil set is feasible under reactor conditions, whether there is enough space for a blanket and discusses the ignition conditions. Questions of MHD-stability and ß-limits are not discussed in this paper.

II. Configuration: Scaling up the W VII-AS configuration to reactor dimensions under the condition of leaving 1.8 m space for a blanket yields a device of 25.5 m major radius and 1.65 m minor plasma radius.

Table I: Average system parameters

	W VII-AS	Ref./2/	AS-reactor
Major radius /m/	2.06	20.6	25.5
Plasma radius /m/	0.2	1.30	1.65
Magnetic field /T/	3.5	5.3	5.3
Rotational transform	0.4	0.48	0.58
Aspect ratio	10	16	16
Coil aspect ratio	4.3	4.3	4.9
Coil current density /MA/m^2	27	13.3	9.8
Maximum field on the coils /T/		9-10	8-9

The coil set of the AS-reactor consists of 50 coils arranged in 5 periods. In reactor dimensions no special coils for neutral beam injection are necessary. One period of the coil set is shown in fig. 1, the contours visualize the current carrying volume. The coils have elliptic poloidal cross sections, see fig.2. There the vacuum magnetic surfaces are also shown for different toroidal angles. The minimum distance between coils and the last magnetic surface is 1.8 m. Thus sufficient space for blanket and shield is provided. The maximum magnetic field on the coils is 8-9 T, depending on the specific coil.

Forces and stresses of this coil set have been calculated using a simple support sheme /2/. Replacing the inner support ring, as described in ref./3/, by an outer ring and employing elastic paddings between the coil and its lateral structure reduces the peak value of the von-Mises stress of the coil compound to an uncritical value of about 70 MPa. Less than 10 coils per period would give better access for maintainance but also would increase

the magnetic field ripple and the ratio B_{max}/B_o (B_o = magnetic field in the plasma).

III. Ignition conditions: A simple transport code is used to calculate temperature and density profiles with α-particle heating as a heating mechanism and neoclassical transport as loss mechanism. In electron heat conduction and particle transport the $1/\nu$ scaling due to trapped particles is taken into account whereas ion heat conduction follows the plateau scaling. This choice is justified in /4 /. The refuelling mechanism is modelled by a given particle deposition profile. Particle influx and deposition profile are the external parameters in order to control the burning plasma.

It is found that neoclassical transport is compatible with an ignited plasma with an average temperature of 6 keV. Increasing the particle input flux ϕ_o leads to higher densities, higher temperatures and higher fusion power output. Fig. 3 summarizes the plasma parameters as a function of the input flux ϕ_o. In this figure particle refuelling peaks in the center of the plasma (λ =0). With refuelling in the outer regions ignition is only possible above T≈ 8keV. Fig. (4) shows plasma parameters under this condition: thermal fusion power is 3.6 GW, $\bar{\beta}$=5.3 %, T_e =12 keV, T_i = 10 keV which is the range of optimum burn temperature. The thermal stability of the ignited plasma is provided by the temperature dependence of the trapped electron losses. If the ion thermal conductivity also follows the $1/\nu$-scaling, ignition is still possible but the required ß-values are above 10 %. These values are above the equilibrium limit of the AS-reactor.

IV. Discussion: Scaling up the W VII-AS configuration to reactor dimensions under the condition of leaving 1.8 m space for a blanket yields a device of 25 m major radius and 1.65 m averaged plasma radius. The maxiumum magnetic field at the coils is 8-9 T. Stress analysis and a proper choice of the support structure demonstrate that a coil set of the AS-type show gross feasibility, for details further engineering studies are required. Ignition in an AS-reactor is possible if the ion thermal losses follow the neoclassical plateau scaling. Stronger trapped ion losses are not tolerable. These calculations do not take into account selfconsistent radial electrical fields. It has to be expected that a radial electrical field contributes to a better confinement of the trapped particles and thus reduces the ion thermal conductivity. The ß-values are only determined by plasma transport, MHD-stability is not considered in this paper. Neoclassical transport allows an ignited plasma at $\bar{\beta}$ = 1.5 %, which could be a stable equilibrium. But the fusion power in this case is too low for a reasonable reactor.The present analysis indicates that the key problems to be addressed of a modular AS-reactor are ß-limits and neoclassical transport rather than the technical feasibility of the modular coil set.

References

/1/ U. Brossmann, W. Dommaschk, F. Herrnegger, G. Grieger, J. Kisslinger, W. Lotz, J. Nührenberg, F. Rau, H. Renner, H. Ringler, J. Sapper, A. Schlüter, H. Wobig, 9th IAEA-CN-41/Q5.
/2/ U. Brossmann, S.B. Mukherjee, J. Sapper, Proc. 12th S.O.F.T Vol. II, 985, Jülich 1982
/3/ U. Brossmann, S. Mukherjee, Proc. 12th S.O.F.T Vol. II, 979, Jülich 1982
/4/ H. Wobig, Z. f. Naturforsch. 37a, 906-911 (1982)

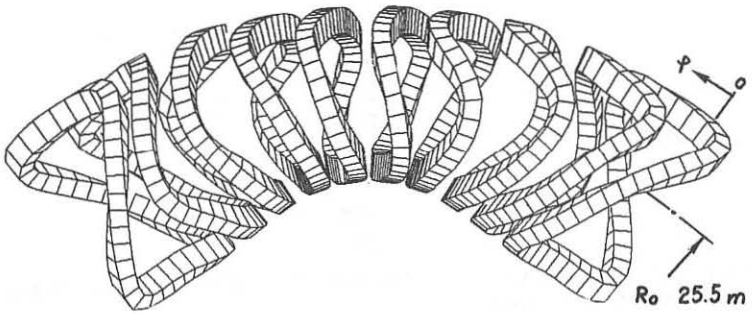

Fig.1 Modular coil arrangement of the AS-reactor, one field period.

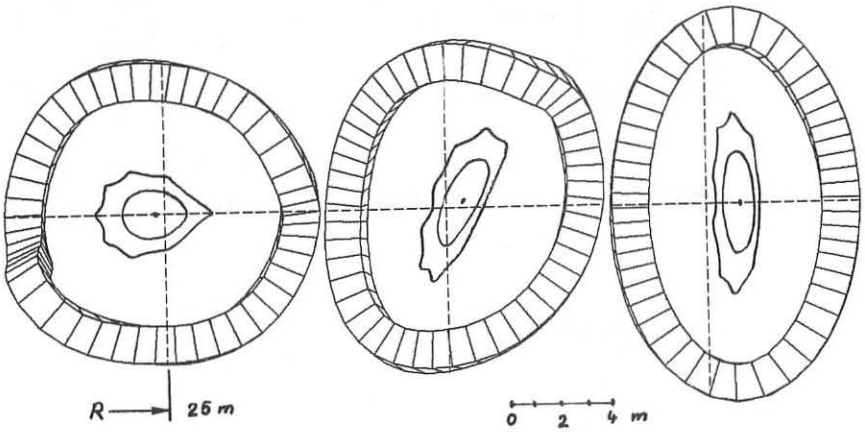

Fig.2 Cross section of magnetic surfaces with adjacent twisted coil, at 0, 1/4, 1/2 field period.

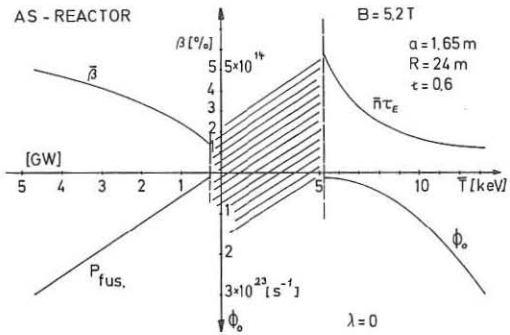

Fig.3 Plasma parameters as a function of refuelling rate Φ_o. Refuelling in the center. ($\lambda = 0$)

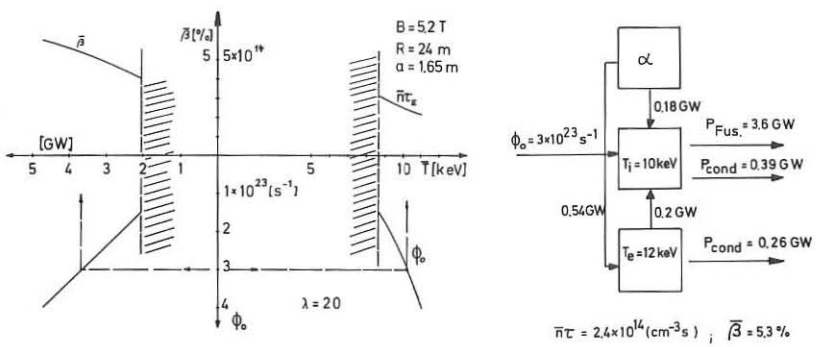

Fig.4 Plasma paramters with refuelling in the boundary region. ($\lambda = 20$)

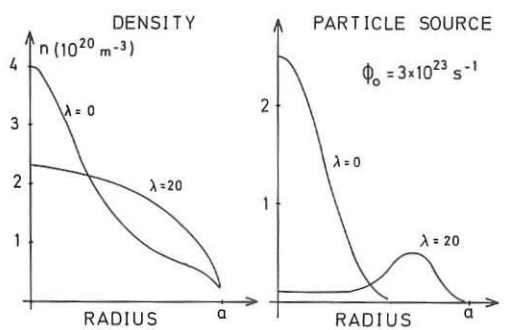

Fig.5 Density profiles and particle deposition profiles. Comparison of central refuelling with boundary refuelling.

PASSIVE STABILIZATION IN INTOR REACTOR

S.Bobbio^, V.Coccorese^, G.Fabricatore^, R.Martone†, G.Rubinacci^†
^ Istituto di Elettrotecnica, University of Naples, Italy
† Dipartimento Elettrico, University of Calabria, Rende, Italy

1. INTRODUCTION

Due to its elongated shape, INTOR plasma is intrinsically unstable with respect to axisymmetric vertical displacements; without any stabilization system, the negative decay index of the vertical field would produce an axisymmetric vertical instability with a characteristic time of the order of few μs. A passive stabilization is then necessary to slow down this instability up to time of the order of few tens of ms, which are required to the active feedback on the external shaping currents to become effective (due to the delay times of the feedback chain and the power limits of the amplifiers involved). In INTOR the problem is solved by means of suitably located saddle coils to be embedded in the blanket structure (being the structure, in itself, not sufficient to provide the required stabilization level).

This paper aims to present some numerical results achieved in studying the efficiency of such system with respect to the main parameters involved, i.e. the plasma equilibrium configuration, the plasma displacement models and the configuration of the Stabilizing Passive Conductors (SPC). These parameters are described in detail in Sect.2, while in Sect.3 we discuss the approach used for the analysis; in Sect.4, the relevant numerical results are presented; finally, Sect.5 is dedicated to the main conclusions.

2. PARAMETERS AFFECTING THE STABILITY PROPERTIES

To show the effect of the plasma equilibrium on the vertical stability two plasma equilibria have been considered and compared each other. The first is the INTOR "reference" equilibrium configuration /1/, where a single null poloidal divertor is foreseen. The second one is a symmetric equilibrium with no divertor; approximately the same plasma shape and destabilizing energy have been assumed to highlight the difference between a solution with divertor and one with limiter.

To tackle the uncertainties concerning the physics of the plasma displacements on the time scale required for passive control, four different models have been considered. The first one (called Model A in the following) assumes that the plasma ring shifts vertically keeping its shape and volume (rigid displacement); it is based on ideal MHD theory and therefore skin currents appear on the plasma surface during its displacement. The second model (Model B) is based also on ideal MHD theory, but any vertical and incompressible displacements are allowed. The third model (Model C) allows rigid displacements only as Model A, but the skin current is suppressed; this model has been introduced to take into account experimental results /2/ showing a negligible effect of the skin current on the time scale required for passive control.

Finally, the fourth model (Model D) allows non rigid plasma displacements like Model B but in addition, no modifications of the plasma current profile are allowed (as Model C). It will be shown that the stabilization efficiency decreases passing from Model A to D.

The stability properties are strongly affected by the configuration of the SPC; in particular, the following parameters should be considered, namely the distance of the conductors from the plasma, the number of toroidal segments, and the number, cross section, shape and resistivity of the SPC. An extensive sensitivity analisys in this respec has been presented elsewhere /3/. Here we shall consider the case of 3 passive toroidal conductors only, placed on the first wall and splitted in 24 saddle coils.

3. STABILITY ANALYSIS

In the framework of MHD ideal theory the stability has been approached by means of the Energy Principle, which in a circuital form gives the terms /3/:

$$\Delta L = \Delta L_d + \Delta L_e + \Delta L_s + \Delta L_i \qquad (1)$$

Here ΔL_d is the work due to the interaction between the external field and the equilibrium plasma current (represented by a set of ideally conducting, flux conserving and mechanically indipendent toroidal rings), and is related to the decay index of the external field; ΔL_e is the work due to the interaction between the external field and the perturbed plasma current, not present in the C and D plasma models, where no modifications of the plasma current profile are allowed. ΔL_s is the work due to the field of the SPC, while ΔL_i gives the work due to relative displacements between the plasma elementary currents. The details of this approach have been reported elsewhere /3/. Here we recall that, after linearization, the work of eq. (1) can be rewritten in a suitable quadratic form $\xi^T W \xi$, where ξ is a vector representing the vertical displacement.

The "worst" displacement is represented by the vector ξ_o, maximizing ΔL in eq. (1), and hence corresponding to the eigenvector of the self-adjoint energy operator W associated with its largest eigenvalue. The sign of ΔL, i.e. of the largest eigenvalue, allows to see whether the worst displacement leads to a stable ($\Delta L < 0$), or to an unstable ($\Delta L > 0$) situation. If $\Delta L < 0$, $|\Delta L|$ is a measure of the "inductive SPC efficiency", proportional to the square of the frequency of the oscillatory plasma motion. Finally, the optimal position for given number of SPC has been found by minimizing the largest eigenvalue of W with respect to the vector x_s, representative of the position of the N SPC.

When resistive SPC are assumed the system is intrinsically unstable. In particular, a slow mode growth (on the time scale of the L/R time of SPC, usually of the order of few tens of ms) appears in the configurations found stable with ideally conducting SPC. This mode is evaluated by means of a procedure based on a mathematical model, where the dynamics of the axisymmetric plasma ring is coupled with a circuital equation of the SPC, for which the actual loop structure is taken into account. The dynamic matrix of the system is then considered, whose positive eigenvalue represents the searched growth rate.

4. RESULTS

First of all, the reference equilibrium with divertor has been compared with a symmetric one. The latter has been evauated by means of a fixed boundary code /4/, whose main feature is to find a plasma equilibrium current profile as "near" as possible to an assigned one; the plasma shape has been chosen to fit the upper shape of the reference equilibrium while the current profile is of the following type:

$$J(\rho) = J_o[1 - (\rho/\rho_o)^2]^\alpha \qquad (2)$$

where J_o is the maximum value of the current density, which arises at $R = R_o$ on the equatorial plane, ρ is a polar coordinate centered in R_o and ρ_o is the value of ρ in corrispondance of the plasma boundary; finally α has been chosen in such a way as to give approximately the same ΔL_d as the reference configuration ($\alpha = 2.5$, whereas $\alpha = 1.4$ in the reference case). For sake of simplicity we have considered the case of 3 SPC only placed on the first wall in an optimized position with respect to the Model B of the reference case. The results are summarized in Table I. One can see, as expected, that the destabilizing terms ΔL_d are approximately the same, together with the stabilizing terms ΔL_s due to SPC. The main differences are in the terms ΔL_e (interaction with the skin currents); in this respect we remind that the skin currents arise to shield field variations due to the vertical displacements. Therefore this skin current is the sum of two opposite contributions; the first one (stabilizing) is the shielding of the external field variation, and the second one (destabilizing) is the shielding of the field due to the currents induced in SPC. For the single null configuration, the derivative $\partial B_r/\partial z$, where B_r is the radial component of the external field, is larger in the lower part of the non symmetric plasma, due to the presence of the divertor, so that the effect of the shielding current is locally more pronounced, justifying the behaviour reported in Table I.

In order to investigate the influence of the non symmetry on the vertical stability properties of the INTOR plasma, work is in progress; preliminarly we have studied the stability of symmetric configurations with respect to different current profiles and triangularities. We have found a stabilizing effect of flatter current profiles and larger triangularities, leading to an improvement of the stability properties of 20%, for current profiles similar to the reference one and with reference to the C and D plasma models.

Finally, in order to illustrate the effect of the configuration of the SPC on the slow mode growth, we refer to Fig.1, where growth rate for the reference case is shown as a function of the SPC cross section, for different plasma models and cross sections of poloidal connections. There 3 SPC located on the first wall and divided in 24 toroidal segments (as in Table I) were chosen.

5. CONCLUSIONS

The results reported show that the choice of the plasma displacement model is a critical issue in evaluating the efficiency of the SPC also with respect to the plasma equilibrium configuration; in particular, we have found that symmetric equilibria are more stable in the models without skin currents,

which appear to be the more realistic ones in the time scale of the slow mode.

6. REFERENCES

/1/ INTOR Phase I Report, IAEA (Vienna) 1982.

/2/ Kuznetsov, Yu.K., Lebed, S.A., Pavlichenko, O.S.: Discharge start-up in a Tokamak with a poloidal divertor, Nucl.Fusion 20 (1980) 123

/3/ Bobbio, S., Coccorese, V., Fabricatore, G., Martone, R., Rubinacci, G., Chapter X, INTOR Phase IIA, Vol. III, Dec. 1982.

/4/ Bobbio, S., Coccorese, V., Martone, R.: A new approach to the analysis of axisymmetric MHD equilibria in non circular plasmas, Alta Frequenza Vol. LI, 2 (1982).

Table I. Comparison between symmetric (S) and non symmetric (NS) equilibria in terms of work ΔL for different plasma models. ΔL in [MJ].

	MODEL A		MODEL B		MODEL C		MODEL D	
	NS	S	NS	S	NS	S	NS	S
ΔL_d	15.6	15.4	10.5	10.9	15.6	15.4	10.0	7.7
ΔL_e	- 4.8	- 1.7	- 8.1	- 1.5	0.0	0.0	0.0	0.0
ΔL_s	-22.8	-22.1	- 8.6	-11.6	-18.3	-18.4	- 7.3	-7.0
ΔL_i	0.0	0.0	0.95	- 0.9	0.0	0.0	- 2.6	-1.8
ΔL	-12.0	- 8.4	- 5.3	- 3.0	- 2.7	- 3.0	0.1	-1.1

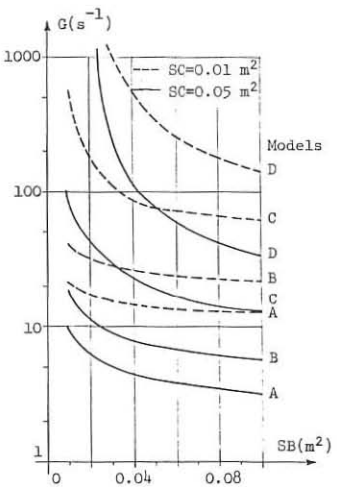

Fig. 1. Slow mode growth rate versus cross section SB of SPC for different cross sections SC of vertical connections. 3 SPC on first wall.

DEPRESSION OF THE NUCLEAR PROPERTIES OF FUSION REACTOR BREEDING BLANKETS BY NONHOMOGENEITIES

J.S. Brozosko*, L. Ingrosso, and B.V. Robouch
Associazione EURATOM-ENEA sulla Fusione, Centro di Frascati,
C.P. 65, 00044 Frascati, Rome, Italy

In recent years numerous designs of fusion reactor blankets (tritium breeders) have been reported. The compilation [1] of the nuclear parameters, mainly obtained through the use of one-dimensional (1-D) transport codes looks very promising: they offer tritium breeding ratios (TBR of up to 1.6, and energy depositions (ED) due to neutrons of up to 22 MeV. A comparision of results obtained using 1-D and three-dimensional (3-D) transport codes has been carried out by the STARFIRE Argonne Group [2] and revealed a decrease of 20% in TBR and ED. More recently, a 3-D investigation of a blanket for a spherical chamber for effects related to neutrons leaking through beam injection ducts, vacuum pump channels, etc...[3] lead to a dramatic decrease in the TBR and ED parameters for a 17Li83Pb breeder and a substantial one for a Li-metal breeder. Also reported [4] that the neutron flux leaking through ports in a toroidal chamber drastically increase the nuclear heating in magnetic coils. All these conflicting predictions as to the design, lead Frascati to start a systematic study of the consequences of blanket nonhomogeneities on the nuclear properties of the blanket.

The calculations are carried out using the VINIA 3DAMTC subroutine complex especially developed for the treatment of fusion reactors on large computers; the first results have recently been presented [5]. The VINIA 3DAMTC is a 3-D analogical Monte Carlo treatment, with a continuous energy and space representation, using different data files (in ENDF/B format) in the point by point representation without group treatment and no truncation introduced on the data of the files! The above subroutine complex in fact follows the history of the neutrons in the blanket, randomly selecting the place and direction of the neutron emission, its consecutive interactions with the constituting nuclei, and accounting for the angular and energy distributions of the reaction products. The one approximation used is the neutron history extinction as the energy falls below a cut-off energy; a sensitivity analysis showed that an energy cut-off of 0.1 eV introduces negligible errors. To study nonhomogeneity effects, the geometrical model of ref.[5] was further extended to include 7 tori zones, 12 toroidal cooling tubes, 24 disks and 24 sectors, typical elements of present day designs.

The aim of the present study is to identify tendencies in the evolution of nuclear parameters as nonhomogeneities are introduced into the blanket. We assumed the main geometrical characteristics of the tori (as size, etc...) from the Argonne Demo design (see Fig. 1), with breeders Li_2O (30% ^6Li enriched, 0.6 TD) or 17Li83Pb (90% ^6Li enriched, 1 TD). A first wall (thickness 1.3 cm AISI-316 55 water cooled, 2/1 by volume) is surrounded by a blanket 66 cm thick. All previously referred to variations (tubes, sectors, etc....) conserved a fixed over all volumetric ratio:

1) Breeder Li_2O 75%, Multiplier Pb or Be 11.5%, AISI-316 SS 9%, water 4.5%.

2) Breeder 17Li83Pb 85%, AISI - 316 SS 10%, water 5%.

The radial gradiant of the water density, when considered, was roughly taken to reproduce that of ref.[6]. The analysis considered the 12 Demo ports, with a port opening corresponding to 10% the inner plasma vessel surface. The ENDF/B-4 file with the $^{7}Li(n,t)$ data updated [7] was used.

The results of the study are schematically reported in fig. 2 and 3, in which the deposited energy excess, EX, (ED - 14.1 MeV of the original neutron) and neutron leak, NL, (through ports and blanket) normalised to one fusion neutron are given with the TBR as the abscissa. The shaded areas represent the field covered by the results of our calculations for different designs.

Observing these figures reveals a number of trends:

1) Our calculations for fully homogeneous toroidal blankets indicate, in agreement with ref. [2], a decrease of 10-20% in TBR and 50-70% for EX as compared to adeguate 1-D transport results.
2) The introduction of ports (see the pairs of similar points in fig. 2) reduces the TBR in a manner similar to that of the spherical case [3], while EX is less drastically reduced.
3) The neutron leak seems to be most dramatic in the case of 17Li83Pb; in Li_2O it is due to ports only. The kinetic energy losses due to leaking is of the order of 1 MeV/fusion neutron. We generally confirm the conclusions of ref.[4] concerning the nuclear heat deposition in the coils.

The general tendency is that the best nuclear properties correspond to Li_2O blankets with Be-multipliers (Pb-multipiers being but slightly worse); the use of 17Li83Pb as a breeder should be taken into consideration with great care.

It is to be noted that the present results correspond to a fixed design orientation. As the influence of ports and other nonhomogeneities are geometry dipendent, detailed calculations must naturally be carried out for every specific reactor design case by case. Yet we feel that a tendency may be inferred from this particulare case.

NOTE AND REFERENCES

* On leave from the Warsaw University, Bialystok Branch (Poland)

[1] Brzosko, J.S., and Robouch, B.V., Proc. of the Workshop on: Fusion Blanket Technology, Erice, June 1983, paper 5
[2] Starfire Design Team: Report ANL/FPP-80-1 (1980) and Report ANL/FPP/TM-154 (1982), Argonne National Lab, Argonne IL - 60439 USA
[3] Meier, W.R., Nucl. Techn. Fusion 3, 385 (1983)
[4] Santoro, R.T., Tang, J.S., Alsmiller, R.G., Barnes, J.M.,: Nucl. Techn. 37, 65 (1978)
[5] Robouch, B.V., Ingrosso, L., and Brzosko, J.S., Proc. of the workshop on Fusion Blanket Technology, Erice June 1983, paper 12
[6] Carre, F., Tilliette, Z., Remoleur, J., and Proust, E.: Proc. of workshop on Fusion Blanket Technology, Erice, June 1983, paper 4, (CEA, Saclay, BP 2, France-91191 gif-sur-yvette Cedex)

[7] Lisken, H. et al: Proc. Intern. Conf. on Nuclear data for Science and Technology, Antwerp (1982)

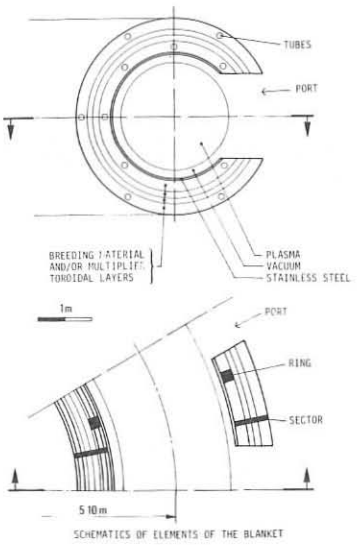

SCHEMATICS OF ELEMENTS OF THE BLANKET

Fig 1

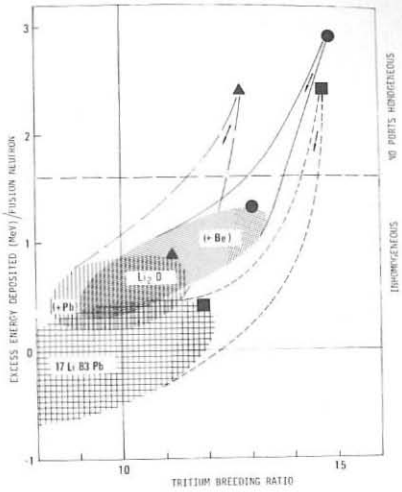

Fig 2

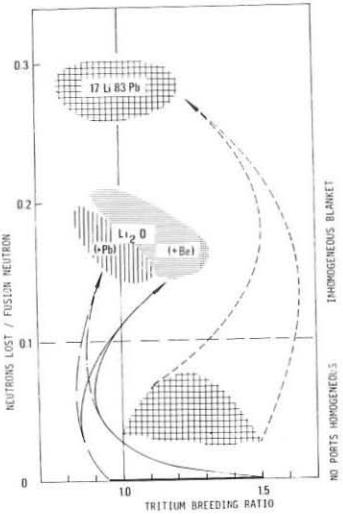

Fig 3

Author Index

Abe Y D 12
Abels van Maanen A. A 15
Abu el Nasr T.Z. D 34
Agapov L.N. O 20
Aikawa H. B 13
Ainsworth N.R. E 26
Airoldi A.C. D 24 / E 18
Alcock M.W. D 28 / E 26
Alexander K.F. C 33
Alikhanov S.G. D 44
Alladio F. E 15 FT Team
Anania G. C 42
Anderson D. C 05 / C 06 / D 50
Anderson D.T. D 15
Anderson F.S.B. D 15
Andersson P. D 49 / E 37
Ando A. B 24
Andreev A.P. A 26
Andryukhina Eh.D. O 20
Angel T. B 13
Antoni V. O 30
Appert K. A 29 / A 30 / B 29
Aragones J.M. B 16
Argenti L. D 24 / D 25
Armentrout C. B 13
Armstrong W.T. O 29
Arnold R. O 07
Arora A.K. C 39
Arroyo R. B 16
Arsenev A.V. D 17
Artemenkov L.J. C 32
ASDEX Team A 05 / A 06 / A 07 / A 14 A 33 / C 27 / O 06
Atkinson D. B 03 / D 28
Atzeni S. E 37
Audenaerde K. D 26
Avanzini P.G. D 01
Avinash K. E 52
Azechi H. E 39

Baity F.W. O 17
Banno T. A 35 / C 31
Barbato E. FT Team / A 25
Bardinov A.A. D 39
Bardotti G. FT Team
Baretich F. E 23
Barnes C.W. O 29
Barnes D.C. O 29
Barrero A. E 43
Barsukov A.G. A 03
Barter J. C 08
Bartiromo R. FT Team
Barth C.J. D 30
Bartsch R.R. O 29
Batanov G.M. O 20
Batyuk V.A. C 14
Bazzo I. E 23
Becker G. A 14
Behn R. A 29 / C 28
Behringer K. ASDEX Team
Behrisch R. A 33
Bein B.K. A 06
Bell J.D. O 01
Bell M. O 10
Bender S.E. B 11 / B 12
Berezhetskij M.S. O 20
Berk H.L. O 13
Bernard L.C. A 09 / O 22
Bernardin M.P. B 44
Bernhardi K. ASDEX Team
Bertalot L. O 25
Besedin N.T. A 17
Besen M. O 02
Bessell W.G. E 07
Besshou S. B 15 / O 19
Betz G. A 42
Bhadra D.K. O 22
Bhatnagar V.P. C 12/ C 13
Bibet P. B 28
Bielik M. O 27
Bird C.R. O 09
Blackfield D.T. D 22
Blanc P. B 28
Blau F. B 13
Blewett S. B 03 / D 28
Blokh M.A. C 14 / C 23/ O 20
Bobbio S. D 09
Bocharov V.N. D 18 / D 19
Boehmer H. C 08
Bogdanov S.D. O 20
Bogen P. A 41
Bol K. O 10
Bombarda F. B O6
Bond D.J. E 07
Bondeson A. D 50
Bonizzoni G. D 25
Bonoli P. O 32
Bornatici M. D 23
Borowiecki M. E 04 / O 27
Bostick W.H. O 28
Bourham M.A. D 34
Boyd D. O 10
Braams B.J. B 34
Bracco G. FT Team
Brambilla M. C 07
Bramson G. B 13
Brau K. O 10
Bravenec R. B 02
Breizman B.N. B 31
Briand P. B 28
Briffod G. B 28
Brooks N.H. B 09 / B 13
Brossmann U. D 08
Brower D.L. B 02
Brown D.A. E 44
Brunelli B. D 01
Brzosko J.S. D 10 / O 26
Buceti G. FT Team
Buchenauer D. O 10
Budny R. O 10
Büchl K. C 02
Buffa A. O 30
Bulyginsky D.G. E 34
Bunting C.A. A 44 / B 32
Buratti P. FT Team
Burchenko P.Ya. D 17
Bures M. A 28
Burrell K.H. A 09 / C 25 / O 03
Burtsev V.A. D 39
Busch G.E. O 09
Bush C.E. O 01

Campbell D.	C 02
Canobbio E.	B 27
Cap F.	E 30
Carnevali A.	O 01
Carolan P.G.	A 44
Carreras B.A.	O 18
Carretta U.	D 07 / D 25
Caruso A.	E 37
Casci F.	B 43
Cassamagnaghi C.	E 23
Cattanei G.	W VII A Team
Cavallo A.	A 26 / O 10
Challis C.D.	E 07
Chance M.S.	C 42 / C 44 / O 12
Chang C.T.	C 03
Charatis G.	O 09
Charlton L.A.	O 18
Chase R.	B 13
Cheetham A.D.	B 04
Chen L.	C 44 / O 12
Cheng C.Z.	C 44
Chirochkin V.S.	O 20
Chistyakov R.R.	D 21
Chkuaseli Z.D.	E 09
Cho T.	B 24
Chodura R.	A 12 / C 30
Chrien R.E.	O 29
Chu M.S.	C 49
Chudin N.V.	B 49
Chyrczakowski S.	E 05
Cima G.	D 25
Cirant S.	D 24 / D 25
Clark W.H.M.	B 39
Clausing R.E.	C 31
Clement M.	B 28
Cobble J.A.	O 17
Coccorese E.	D 09
Cochrane J.C.	O 29
Cohn D.R.	E 21
Colchin R.J.	O 17
Colleraine A.	B 13
Collins G.A.	A 29 / E 26
Collins P.R.	D 28 / E 26
Connor K.A.	E 19
Conrads H.	O 26
Cooper W.A.	O 18
Coppi B.	D 47
Cordey J.G.	C 36
Core W.G.F.	A 18 / D 50
Corti S.	D 25
Couture P.	O 10
Crestani M.	D 23
Crisanti F.	E 15 / FT Team
Croci R.	B 27
Crowley T.	O 10
Czekaj S.	E 03 / E 04 / O 23 / O 27
D III Physics, Operations Neutral Beam and Theory Groups	A 09 / C 25 / O 03
Dabiri A.E.	D 02
Da Costa Cabral J.A.	E 52
Dalton A.	B 03 / D 28
Dandl R.	C 08
Dangor A.E.	E 07 / E 08
Darrrow	O 10
Davis L.G.	B 09
Davis W.A.	O 17
Daybelge U.	B 38
DeAngelis R.	FT Team
DeChambrier A.	A 29
Decker G.	D 37
de Groot B.	D 30
Degtyarev L.M.	O 11
de Kluiver H.	D 30 / D 31
DeLuca F.	D 25
DeMarco F.	FT Team
DeMeio L.	E 46
DePretis M.	FT Team
Denus S.	E 03 / E 04 / O 23 / O 27
Dewar R.L.	O 12
Dimant Ya.S.	E 48
Djachenko V.V.	E 34 / E 35
Dmitrieva M.V.	A 16
Dnestrovskij Yu.N.	B 52 / E 48 / E 49
Dobrokhotov E.J.	O 05
Donskaya N.P.	C 23 / O 20
Dorokhov V.V.	A 31
Dorst D.	W VII A Team
Dory R.A.	O 18
Dremin M.M.	O 05
Dubois M.A.	B 08
Dubovo L.V.	O 20
Düchs D.F.	A 21
Dukov I.V.	D 33
Dunlap J.L.	O 01
Duperrex P.A.	A 29
Duvidzon V.M.	O 20
Dyabilin K.S.	O 20
Dyer G.R.	O 01
Eberhagen A.	ASDEX Team
Edenstrasser J.W.	A 46 / A 48 / D 31
Edlington T.	B 03 / D 28
Edmonds P.H.	O 01
Elfimov A.G.	A 31
El Gamal H.A.	D 34
Ellis J.J.	O 04
Elsner A.	W VII A Team
Englade R.	O 32
Erckmann V.	W VII A Team
Erofeev V.I.	B 31
Ertl K.	A 33
Es'kov A.G.	A 48
Esser H.G.	C 31
Eubank H.	O 10
Evangelidis E.A.	C 37
Evrard M.P.	C 12
Fabricatore G.	D 09
Faillon G.	B 30 / E 29
Fairbanks E.	B 13
Fanchenko S.D.	E 13
Fanegas F.M.	B 16
Farina D.	D 07
Farynski A.	D 36
Fasolo J.	B 13
Faulconer D.W.	C 12 / O 16
Favorsky A.P.	A 16
Favre M.	E 08
Fedorenko S.I.	B 11

Fedorov A.A.	B 12
Fedyanin O.I.	O 20
Ferri P.	D 23
Fidelman G.N.	A 39
Fielding S.J.	B 35 / B 39 / B 40
Filippov V.N.	E 25
Fiore C.L..	O 02 / O 32
Fisher R.K.	B 09 / B 13
Flyagin V.A.	A 26
Fonck R.	O 10
Foord M.	O 02
Forester J.C.	E 19
Forrest M.J.	E 12
Fowler R.H.	O 18
Fraiman A.A.	O 20
Freidberg J.P.	O 15
Freudenberger K.	NI Group, Garching
Frey M.	C 47
Frigione D.	FT Team
FT Team	A 01 / A 02 / A 23 / A 24
Fujita J.	D 16 / O 33
Fujiwara M.	C 22
Funahashi A.	A 08
Funato Y.	D 13
Furth H.P.	O 12
Fußmann G.	ASDEX Team

Gacek A.	D 36
GA Doublet III Groups	C 25
Gago J.A.	B 16
Galvao R.M.O.	B 46
Gambier D.J.	C 11
Gammino G.	E 23
Gandy R.	O 02 / O 32
Garcia L.	O 18
Gardner W.L.	O 01
Garin P.	E 29
Gasparotto M.	FT Team
Gebalski S.	D 41
Gehre O.	ASDEX Team
Geilfus P.	C 13
Gentle K.	B 02
Gernhardt J.	ASDEX Team
Gerver M.	D 22
Ghatak A.K.	E 40
Giannella R.	FT Team
v.Gierke G.	ASDEX Team
Gill R.D.	D 03
Gimblett C.G.	A 45
Gimzewski J.K.	C 26/ E 22
Gippius A.F.	O 20
Gippius E.F.	C 23
Guidicotti L.	O 30
Gladd N.T.	O 29
Glancy J.E.	D 02
Glock E.	ASDEX Team
Glowienka J.C.	O 17
Goedbloed J.P.	B 46 / O 15
Goede H.	C 08
Golant V.E.	B 11/ B 12
Goldsmith P.	B 03 / D 28
Goldston R.	O 10 / O 12
Goncharov S.G.	B 11
Goodall D.H.J.	B 39 / B 40
Gorbulin Yu.M.	E 13
Gordeev E.M.	E 13
Gorenflo H.	D 08
Gormezano C.	B 28
Gornostaev S.V.	B 11 / B 12
Gorshkov A.V.	A 03
Goto Y.	E 39
Goyer J.R.	E 19 / O 17
Grace P.M.V.	E 27
Granetz R.S.	O 02 / O 32
Grauer R.	C 40
Grebenshchikov S.E.	C 14
Greenwald M.	O 02 / O 32
Grek B.	O 10
Grekov D.L.	C 15
Grelot P.	B 28
Grésillon D.	B 07
Gribkov V.M.	C 48
Grieger G.	C 24 / W VII A Team
Grigoriev A.V.	B 11 / B 12
Grigull P.	W.VII A Team
Grimm R.C.	C 42 / O 12
Grolli M.	FT Team
Groner P.	C 26
Grosman A.	C 34
Großmann R.	B 47
Grosso G.	D 25
Grote H.	C 33
Gruber O.	B 37
Gryaznevich M.P.	B 11 / B 12
Gryukanov M.F.	D 43
Gryziński M.	D 40 / D 41
Gülker H.J.	E 17
Gurevich A.V.	E 48
Gurov A.A.	C 32
Gusev V.K.	B 11 / E 34
Gwinn D.	O 02 / O 32

Haas F.A.	E 47/ O 06
Haas G.	ASDEX Team
Hacker H.	W VII A Team
Haines M.G.	B 20
Hall K.	B 03 / D 28
Hallock G.A.	E 19/ O 17
Hamberger S.M.	B 04
Hamnén H.	D 50
Hanatani K.	B 15 / O 19
Hankins O.E.	O 17
Hansen F.R.	A 27
Harbour P.J.	B 33
Harmeyer E.	D 08
Harned D.S.	O 29
Harris J.H.	O 18
Harrison M.F.A.	B 36
Hartfuß J.	W VII A Team
Hasegawa K.	A 08
Hasse O.R.	E 17
Hasselberg G.	D 48 / O 14
Haste G.R.	E 19 / O 17
Heifetz D.	A 34
Heikkinen J.A.	E 38
Heindler M.	D 06 / E 53
v.Hellerman M.	E 17
Helton F.J.	B 09 / C 49 / O 22
Hémon A.	B 07
Hender T.C.	O 18
Hendricks F.B.	D 30
Henins I.	O 29

Herold H.	O 25
Herrnegger F.	B 47
Hess W.	B 28
Hewett D.W.	O 29
Hickok R.L.	E 19
Hicks H.R.	O 18
Hildebrandt D.	C 33
Hillis D.L.	O 17
Hino T.	B 13
Hirano K.	E 06
Hiraki N.	A 04 / D 29
Hiroe S.	O 17
Hirshman S.P.	O 18
Hitchon W.N.G.	B 21 / O 13
Hofmann F.	A 29 / C 26 / C 28
Hogan J.T.	O 01
Hogg G.R.	B 04
Hoida H.W.	O 29
Hollenstein Ch.	A 29 / C 28
Holmes J.A.	O 18
Honda A.	A 08
Hong R.	B 13
Honrubia J.	B 16
Hora H.	E 40
Hoshino K.	A 08 / B 13
Hosokawa M.	C 22
Hotston E.S.	B 36
Houlberg W.A.	O 18
How J.A.	B 04
Howe H.C.	O 01
Hübner K.	A 07
Hugill J.	B 39 / B 40
Husinsky W.	A 42
Hutchinson D.P.	O 01
Hutchinson I.H.	A 43
Huussen F.	D 30
Iacono R.	A 01
Ichtchenko G.	B 28
Igitkhanov Yu. L.	A 36
Iguchi H.	C 22
Iima M.	B 15 / O 19
Iiyoshi A.	B 15 / O 19
Ikegami H.	C 22
Ikezawa S.	D 30 / D 32
Ikonnikov A.O.	A 38
Ilyukhin B.I.	C 23
Ingrosso L.	D 10
Ioffe M.S.	D 21
Irby J.	D 22
Irzak M.A.	E 24
Ishibori I.	A 08
Isler R.C.	O 01
Itoh S.	A 04 / D 28
Ivanov R.S.	A 39
Jaccia A.	D 25
Jacobson A.R.	O 31
Jäckel H.	W VII A Team
Jäger U.	O 25 / D 37
Jaehnig K.	O 10
Jaenicke R.	W VII A Team
JAERI Team	C 25
Jahns G.	B 13
Jankowicz Z.	O 27
Jarboe T.R.	O 29
Jardin S.C.	O 12
Jennings W.C.	E 19
Jernigan T.C.	O 18
Jerzykiewicz A.	O 27
Jitsuno T.	E 39 / O 08
Johnson D.	O 10
Johnson J.L.	C 42
Johnson P.C.	B 39 / B 40 / C 36
Johnson R.R.	O 09
Jones D.A.	E 40
Joye B.	A 29 / C 28
Jüttner B.	A 33
Junker J.	W VII Team / E 33
Kabanov V.N.	A 38
Kadomtsev B.B.	C 48
Kahn C.L.	C 25
Kaita R.	O 10
Kaleck A.	B 43
Kaligin A.G.	A 47
Kalinin Yu.G.	E 13
Kamimura T.	C 22
Kammash T.	C 43
Kamperschroer J.	B 13
Kanaev B.I.	D 21
Kaneko H.	B 15 / O 19
Kantor M.Yu.	E 34
Karger F.	A 10 / ASDEX Team
Karttunen S.J.	E 38
Kasai M.	B 13 / C 25
Kasai S.	A 08
Kashimura T.	A 08
Kashiwa Y.	A 08
Kasperczuk A.	O 23
Kato Y.	E 39 / O 08
Kaw P.K.	C 45
Kawahata K.	D 16 / O 33
Kawakami T.	A 08
Kawashima H.	A 08
Kaye S.M.	O 10
Kazawa M.	A 08
Keilhacker M.	ASDEX Team
Keller R.	A 29
Kernbichler W.	D 06
Kesner J.	D 22
Kever H.	C 35
Kewish R.W.	O 29
Khait V.D.	B 42
Khalilov M.A.	B 11
Khautiev E.Yu.	D 38
Khol nov Yu.V.	O 20
Khrabrov V.A.	E 11
Kick N.	W VII A Team
Kies W.	D 37
Kikuchi K.	A 08
Kikuchi M.	A 04 / D 29
Kim J.	B 13
Kimura H.	A 08
Kindsfather R.R.	O 01
Kirchev S.D.	D 33
Kirk R.E.	E 12
Kirkpatrick R.	C 13
Kislyakov A.I.	B 11
Kisoda A.	O 24
Kissel S.	ASDEX Team

Kisslinger J.	A 12 / D 08
Kitagawa Y.	O 08 / O 24
Kitajima S.	D 13
Kitsunezaki A.	B 13
Kladov S.V.	C 23
Klieb L.	D 45
Klima R.	B 25
Klingner P.L.	O 29
Klinkowstein R.E.	D 22
Klüber O.	A 10 / ASDEX Team
Knox S.O.	O 29
Kobayashi K.	E 06
Kobayashi T.	B 13 / C 25
Koch R.	C 12/ C 13
Kochan W.J.	A 47
Kochanski T.	B 02
Kociecka K.	O 27
Kocinski L.	O 27
Könen L.	C 31
Kolesnikov V.K.	B 42
Kolesnikov V.N.	C 23 / O 20
Kolik L.V.	O 20
Komar W.	E 05
Komissarova I.I.	E 25
Komoshvilli K.G.	A 16
Kondakov A.A.	D 39
Kondo K.	B 15 / O 19
Kondratenko A.N.	D 33
Konkashbaev I.K.	D 42 / D 43
Konoshima S.	B 13
Konstantinov S.G.	D 18/ D 19
Kornherr M.	ASDEX Team
Korshunov V.K.	A 48
Kostomarov D.P.	B 52 / D 49 / E 48
Kotai E.	C 33
Kotsulanov V.D.	D 17
Kovan I.A.	C 14 / C 32
Kovrizhnykh L.M.	B 45
Kovrov P.E.	A 03
Kozhevin V.M.	D 39
Koziarkiewicz W.	E 04
Kratzsch K.A.	C 41
Krauz V.I.	D 38
Kretchuk A.P.	A 47
Krikunov S.V.	B 11 / B 12
Kritz A.H.	B 29
Kroiss H.	W VII A Team
Krüger H.	A 32
Krusch K.	W VII A Team
Krylov S.F.	A 48
Kryuchkov S.P.	O 20
Kubasov V.A.	D 39
Kubo S.	B 24
Kuchinssky A.A.	D 39
Kuciński J.	D 35 / O 27
Kudryavtsev A.M.	D 18 / D 19
Kühner G.	W VII A Team
Kugel H.	O 10
Kukushkin A.S.	A 36
Kuksov P.V.	E 13
Kulaga A.E.	D 17
Kunieda S.	A O8
Kurbatov V.I.	O 20
Kurtmullaev R.Kh.	A 47 / A 48
Kuroda J.	E 39
Kuteev B.V.	A 26
Kuznetsov V.S.	D 39
Kuwahara H.	B 04
Labombard B.	O 02
Lackner K.	A 14/ A 34 / B 37
Lalousis P.	E 40
Lam N.T.	D 26
Lane B.	D 22
Langley R.A.	O 01
Langner J.	D 41
Lao L.L.	O 22
Larionov M.M.	E 34 / E 35
Larionova N.F.	C 14 / C 23 / O 20
Lashkul S.I.	B 12
Laukhin Ya.	A 48
Laux M.	C 33
Lax B.	E 21
Lazar N.	C 08
Lazarus E.A.	O 01
Lebedev A.D.	E 35
Lebedev S.V.	B 11 / B 12
LeBlanc B.	O 10
Lee J.K.	A 09 / C 49
Lehner T.	B 08 / C 16
Lenoci M.	A 24
Leonov V.M.	A 03/ B 01
Levchenko Yu.M.	A 03
Levin L.S.	E 34 / E 35
Lilliequist C.G.	O 29
Lieber A.	B 13
Lietti A.	A 29
Lindmann E.L.	B 20
Linford R.K.	O 29
Lipin B.M.	B 11 / B 12
Lipinski B.	O 27
Lipschultz B.	O 02 / O 32
Lisak M.	C 05 / C 06 / D 50
Lisitano G.	E 23 / ASDEX Team
Lister G.G.	A 20 / ASDEX Team / NI Group
Lister J.B.	A 29 / C 26 / C 28
Litunovskij R.N.	B 11 / B 12
Litunovsky V.N.	D 39
Litvak A.G.	O 20
Lloyd B.	O 02 / O 32
Lodder J.J.	D 05
Lohr J.	B 13
Long J.W.	A 45
Lontano M.	D 07
Lotz W.	A 12
Lozovski S.N.	A 31
Luhmann N.C. Jr.	B 02
Lunin N.V.	C 23
Luxon J.L.	B 09
Lynch V.E.	O 18
Lynov J.P.	A 27
Lyon J.F.	O 18
Lyublin B.V.	D 39
Ma C.H.	O 01
Maaßberg H.	C 21
Machuzak J.	E 21
Maekawa T.	B 24
Maeno M.	A 08

Maevskii V.A.	O 20
Mahdavi M.A.	B 09
Mahn C.	W VII A Team
Malek K.	A 07
Maltsev S.G.	C 32
Malutin A.I.	A 48
Mancuso S.	FT Team
Manickam J.	C 42 / O 12
Manos D.	O 10
Mansfield D.	O 10
Manuaba A.	C 33
Marchington P.S.	E 44
Marklin G.	O 29
Marlier S.	W VII A Team
Marmar E.S.	O 02 / O 32
Martinez Val J.M.	B 16
Martini S.	O 30
Martone R.	D 09
Maschke E.K.	B 51
Masden B.F.	O 18
Mase A.	D 16
Massey R.S.	O 31
Massig J.	A 05
Mateev E.S.	E 08
Mathew J.	E 19
Matoba T.	A 08
Matsuda T.	A 08 / B 13
Matsumoto H.	A 08
Matsuzaki Y.	A 08
Mauel M.E.	D 22
Mazzitelli G.	FT Team
Mazzucato E.	O 10
Mayer H. M.	ASDEX Team
McCann R.	O 10
McColl D.	B 13
McCool S.	O 02 / O 32
McCormick K.	ASDEX Team
McCracken G.M.	B 35 / B 39
McCune D.	O 10
McGuire K.	O 10
McLenithan K.D.	C 24
McKenna K.telli G.	FT Team
Mazzucato E.	O 10
Mayer H. M.	ASDEX Team
McCann R.	O 10
McColl D.	B 13
McCool S.	O 02 / O 32
McCormick K.	ASDEX Team
McCracken G.M.	B 35 / B 39
McCune D.	O 10
McGuire K.	O 10
McLenithan K.D.	C 24
McKenna K.F.	O 29
McVey B.D.	D 22
Meisel D.	ASDEX Team
Melikhov P.J.	C 32
Melin G.	B 28
Mercurio S.	C 04
Merezhkin V.G.	A 03
Meshcheryakov A.I.	C 14
Messiaen A.M.	C 12
Metzler N.	O 07
Meyer ter Vehn J.	O 07
Michelsen P.	A 27
Mikhailov M.I.	C 38
Miklaszewski R.	O 23
Miley G.H.	E 53
Milora S.	O 02
Minardi E.	B 17 / D 07
Minenko V.P.	A 16
Minguez E.	B 16
Minyaev O.A.	B 11 / B 12
Mioduszewski P.K.	O 01
Misaizu H.	E 06
Miura Y.	A 08
Miya N.	B 13 / C 25
Miyamoto K.	O 33
Miyanaga N.	E 39 / O 08
Miyawaki S.	D 12
Mizuuchi T.	B 15 / O 19
Mochizuki T.	E 39
Mohan M.	B 26
Mondt J.P.	O 31
Montgomery D.B.	D 22
Monticello D.A.	O 12
Montvai A.	B 14
Moore R.W.	A 09
Morgan J.G.	B 33
Mori M.	A 08 / E 14
Morimoto S.	B 15 / O 19
Morris A.W.	E 26 / O 04
Morris W.A.	E 26
Morton A.H.	B 04
Mosher D.	E 07
Motojima O.	B 15 / O 19
Moulin B.	B 28
Mourier G.	E 29
Mudford B.S.	C 36
Mueller D.	O 10
Müller E.R.	ASDEX Team
Müller G.	W VII A Team
Muir D.G.	E 12 / A 44
Mukhin P.A.	C 32
Mukhovatov V.S.	A 03
Mulligan W.J.	E 21
Munro J.K.	O 01
Murakami M.	O 01
Murdock A.	O 10
Murmann H.	ASDEX Team
Murray L.E.	O 01
Murusidze I.G.	E 45
Mutoh T.	B 15 / O 19
Mynick H.E.	B 21
Myskin O.K.	D 18 / D 19
Nagami M.	B 13
Nagao A.	A 04 / D 29
Nagao S.	D 12 / D 13
Nagayama Y.	O 33
Nakai S.	E 39
Nakamura H.	A 08
Nakamura K.	A 04 / D 29
Nakamura M.	B 24
Nakamura Y.	A 04 / D 29
Nakao S.	B 24
Nakashima Y.	B 15 / O 19
Nakasuga M.	B 15 / O 19
Nakatsuka M.	E 39 / O 08
Nalesso G.F.	A 46
Nardi V.	O 28
Nedospasov A.V.	A 38 / B 54 / O 21
Neilson G.H.	O 01
Neudatchin S.V.	E 49

Neuhauser J.	A 05 / B 18 / C 29
Neutral Injection Team	A 14
Newton A.A.	A 45
Nguyen K.	C 43
Nicolai A.	A 13 / A 19
Nicolas J.A.	E 42
Niederl K.	D 06
Niedermeyer H.	A 10 / ASDEX Team
Niestadt R.M.	D 30
NI Group.	C 17 / C 18 / C 19 / C 20 / E 24 / E 33
Nikandrov L.B.	D 42
Ninomiya H.	B 13
Nishihara K.	O 08
Nishino N.	B 15 / O 19
Nishizawa A.	D 16
Nocentini A.	E 46
Noda N.	D 16 / O 33
Noll P.	A 21
Novikov V.P.	D 44
Novikova A.V.	O 20
Nowada S.	E 39
Nowak S.	C 28
Nührenberg J.	B 47
Obiki T.	B 15 / O 19
O'Brien M.R.	E 27
Ocana J.L.	B 16
Odajima K.	A 08
Ogawa H.	A 08
Ogawa T.	A 08
Ogura K.	B 24
Ohlendorf W.	W VII A Team
Ohta K.	A 08
Ohtake I.	B 15 / O 19
Ohtsuka H.	A 08
Ohuchi K.	A 08
Okabayashi M.	O 10 / O 12
Okajima S.	D 12
Okano H.	A 08
Okano K.	O 10
Okuda T.	E 31
Olivain J.	C 10
Orefice A.	D 24 / E 18
Orlov V.B.	E 11 / O 20
O'Rourke J.	A 29 / C 28
Ortolani S.	O 30
Ostrovskaya G.V.	E 25
Ott W.	A 20 / NI Group
Ottaviani M.	C 07
Ovsyannikov V.A.	D 39
Owens D.K.	O 10
Oyevaar Th.	A 26 / D 30
Paduch M.	O 23
Panarella E.	E 10
Panasyuk V.M.	D 18 / D 19
Panchenko V.G.	C 16
Panzarella A.	B 28
Pappas D.S.	O 02 / O 32
Paramonov A.V.	C 23 / O 20
Pare V.K.	O 01
Parham B.	B 03 / D 28
Park W.	C 49
Parker J.	O 02
Parker R.R.	O 02 / O 32
Parlange F.	B 28
Pastukhov V.P.	D 21
Paszti F.	C 33
Patel S.	B 23
Pavlenko V.N.	C 16
Pavlichenko O.S.	A 17
Pavlo P.	B 25
Pavlov Yu.D.	O 05
PDX Group	O 10
Peacock N.J.	C 28 / E 12
Pearson D.I.C.	C 12
Pech P.	C 33
Peebles W.A.	B 02
Pegoraro F.	D 45 / D 47
Pellat R.	C 47
Pena J.J.	B 16
Peneva I.H.	D 33
Penningsfeld F.P.	A 20 / NI Group
Perepelkin N.F.	D 17
Pereverzev G.V.	E 49
Pericoli V.	FT Team
Perkins F.W.	O 12
Perlado J.M.	B 16
Perre Y.	E 29
Pesić S.	D 27
Petrasso R.	O 02
Petrov A.E.	O 20
Petrov D.P.	O 05
Petrov V.G.	A 37
Petrzilka V.A.	B 25
Phillips P.	B 02
Piekaar H.W.	A 26 / D 30
Piekoszewski J.	D 41
Pieroni L.	FT Team
Pigarov A.Yu.	A 36
Pistunovich V.I.	A 36
Pitersky V.V.	D 21
Platts D.A.	O 29
Platz P.	B 06
Pochelon A.	A 29 / C 26 / C 28
Pochrybniak C.	D 41
Pócs L.	B 14
Podda S.	FT Team
Pogutse O.P.	B 48 / B 49 / C 48 / D 45
Polevoy A.R.	A 03 / E 49
Politzer P.A.	O 02
Popitaev A.N.	D 39
Popov A.M.	B 52 / O 22
Popov S.N.	O 20
Popryadukhin A.P.	C 32
Porkolab M.	O 02 / O 32
Porrot E.	B 28
Poschenrieder W.	ASDEX Team
Poshekhonov Yu.Yu.	O 11
Pospieszczyk A.	A 41
Post D.	O 10
Post R.S.	D 22
Potok R.	D 22
Powell C.	O 28
Pozzoli R.	D 07
Pribyl P.	O 02 / O 32
Prior W.	O 28
Proshletsov A.P.	A 47
Pross G.	D 37
Psimopoulos M.	E 08
Puiatti M.E.	O 30

PWW Team	A 33 / C 27
Pyatov V.N.	A 17
Rabbett H.	B 03 / D 28
Rabiński M.	D 35
Raeder J.	D 08
Rager J.P.	O 26
Raia G.	D 01
Ramos J.	D 47
Ramponi G.	D 24 / D 25 / E 18
Rapp H.	ASDEX Team
Rasmussen D.A.	O 17
Rau F.	D 08 / A 12 / W VII A Team
Rauh K.G.	A 34
Rawls J.	B 09
Razdobarin G.T.	B 11
Rebhan E.	C 40 / C 41
Reiner H. D.	C 33
Reiter D.	A 13
Rej D.J.	O 29
Rem J.	B 46
Renner H.	W VII A Team
Reusch M.	O 10 / O 12
Revenchuk S.M.	C 16
Rewoldt G.	C 42 / C 44
Rey G.	B 28
Rice J.E.	O 02 / O 32
Richards B.	B 02
Richards R.K.	O 17
Richter B.	A 05 / O 06
Rickard G.	B 20
Riedler J.M.	E 53
Righetti G.B.	FT Team
Ring R.	C 39
Ringler H.	C 17 / W VII A Team
Riviere A.C.	E 28
Robinson D.C.	B 03 / D 28 / E 26
Robouch B.V.	D 10 / O 26
Rockett P.D.	O 09
Rodichkin V.A.	D 39
Rödiger K.	A 32
Rogister A.	D 48 / O 14
Rohatgi R.	O 15
Romanelli F.	FT Team
Romero H.	C 09
Rosatelli F.	D 01
Rosety L.	E 43
Rosenau Ph.	B 50
Rosenbluth M.N.	O 13
Rota E.	A 35 / C 31
Rottler L.	B 13
Rowan W.	B 02
Rozhdestvenskij V.V.	B 11 / B 12
Rubinacci G.	D 09
Rubtsov K.S.	D 17
Ruffina U.	D 23
Rutherford P.H.	O 12
Rybach J.	D 37
Rydygier E.	E 05
Ryltseva T.V.	D 42
Ryzhkov V.N.	E 09
Sadowski M.	D 41 / E 05 / O 27
Safronov V.M.	D 20
Sakai T.	D 16
Sakabe S.	E 39
Sakamoto I.	D 13
Sakanaka P.H.	B 46
Sakharov N.V.	B 11 / B 12
Salomaa R.R.E.	E 38
Salukvadze R.G.	D 38 / E 09
Samain A.	B 53 / C 11
Samec T.	C 08
Samm U.	A 40 / A 41
Sano F.	B 15 / O 19
Sanmartin J.R.	E 42
Sannikov V.V.	A 03
Santicchi S.	E 23
Santini F.	FT Team/ A 25
Santolaya J.M.	B 16
Sanz J.	E 43
Sapozhnikov A.V.	O 20
Saramito B.	B 51
Sardei F.	W VII A Team
Sarhad I.Ibn	D 33
Sarksyan K.A.	O 20
Sasaki A.	B 15 / O 19
Sasaki N.	D 12
Sato M.	B 15 / E 06 / O 19
Savage R	B 02
Savic P.	E 10
Sayed N.	E 44
Sbitnikova I.S.	C 14 / C 23 / O 20
Scarin P.	O 30
Scharer J.E.	C 09 / D 26
Schep T.J.	D 45 / D 46
Scherzer B.	C 27 / O 06
Schmalz R.	O 07
Schmidt G.	O 10
Schmidt H.	O 25
Schmidt R.	O 25
Schneider F.	ASDEX Team
Schneider W.	A 34 / C 29
Schroeder R.J.	O 09
Schüller F.	A 10
Schulz V.	A 32
Schuresko D.	O 02
Schuss J.J.	O 02 / O 32
Schuurman W.	D 31
Schwarzmeier J.L.	O 29
Schwindt N.N.	C 32
Scott S.D.	O 01
Segre S.E.	FT Team
Semenov V.N.	A 48
Sen A.	C 45
Sengoku S.	A 08 / C 25
Seraydarian R.	B 13
Serebreny G.A.	E 34 / E 35
Serrano J.F.	B 16
Sesnic S.	O 10
Seyler C.E.	O 29
Sgro A.G.	O 29
Shafranov V.D.	C 38 / O 11
Shagirov E.A.	B 52
Shaing K.C.	O 18
Shakhatre M.	O 25
Shakhovetz K.G.	B 11 / B 12
Shansky V.T.	D 39
Sharma A.S.	B 26
Sharp L.E.	B 04
Shashkov A.Yu.	E 13
Shcerbak A.F.	O 05

Shchemelinin S.G.	B 11 / B 12
Shchepetov S.V.	B 45
Shedova E.N.	E 25
Sheffield J.	O 18
Shepard C.L.	O 09
Sherwood A.R.	O 29
Sherwood E.G.	O 29
Shestakov A.I.	O 29
Shibata T.	A 08
Shibuya T.	A 08
Shiina T.	A 08
Shimada M.	B 13 / C 25
Shimoda K.	E 06
Shimozuma T.	B 24
Shohet J.L.	C 24 / D 14 / D 15 / O 13
Shoji T.	A 08 / C 22
Sholokhov Yu.I.	D 39
Shustova N.V.	E 34
Shvets O.M.	A 17
Sidnev V.V.	D 20
Sidorov V.P.	A 16
Siemon R.E.	O 29
Sigmar D.J.	O 01
Silagi R.	B 13
Sillen R.M.J.	A 26 / D 30
Siller G.	ASDEX Team
Simm W.	A 29
Simonet F.	B 05
Simpson J.D.	O 09
Sinman A.	E 01 / E 02
Sinman S.	E 01 / E 02
Skladnik Sadowska E.	D 41
Skoblikov S.V.	A 26
Skoryupin V.A.	E 13
Skrzeczanowski W.	E 04 / O 27
Skvortsov Yu.V.	D 20
Slater D.C.	O 09
Slavny A.S.	A 17
Sledzinski S.	O 23
Slusher R.	O 10
Smeulders P.	ASDEX Team
Smirnov A.P.	E 48
Smirnova A.D.	C 23
Smirnova E.A.	E 13
Smith J.	B 13
Smith D.K.	D 22
Smolyakova O.B.	O 20
Snider R.	B 13
Socha R.	E 04
Söldner F.	ASDEX Team
Solensten L.	E 19 / O 17
Sollner T.C.L.C.	E 21
Solntsev A.M.	O 05
Soltwisch H.	A 11 / C 01
Spencer R.L.	O 29
Speth E.	ASDEX Team / A 20 / NI Group
Spigel I.S.	C 14 / C 23 / O 20
Stäbler A.	ASDEX Team
Staib P.	C 27 / O 06
Stambaugh R.D.	A 09 / B 09
Stamp M.F.	C 28
Stampa A.	A 32
Start D.F.H.	E 27
Staudenmaier G.	C 27 / O 06
Stefanovskij A.M.	O 05
Steinmetz K.	O 26 / ASDEX Team
Stepanov K.N.	C 15
Sternlieb A.	D 04 / E 41
Steuer K.H.	ASDEX Team
Stix T.H.	O 12
Storer R.G.	C 46
Stotsky G.J.	A 39
Strachan J.D.	A 11
Strait E.J.	A 09
Strusny H.	C 33
Subbarao D.	E 36
Sudera Y.	E 44
Succi S.	B 29
Suckewer S.	O 10
Sudo S.	B 15 / O 19
Sugai H.	B 32
Sukhodol'skii V.N.	C 14 / O 20
Sullivan D.	O 09
Sund R.	C 09
Sundaram A.K.	C 45
Suprunenko V.A.	D 17
Surko C.	O 10
Suvorov E.V.	O 20
Suzuki K.	A 08
Suzuki N.	A 08
Swain D.W.	O 17
Sykes A.	B 23
Szydlowski A.	E 03
Szymanski Z.	ASDEX Team
Tagger M.	C 47
Taglauer E.	C 27 / O 06
Tajima Y.	A 08
Takahashi H.	O 35
Takamura S.	E 31
Takase Y.	O 32
Takasugi K.	C 22
Takeda S.	D 32
Talapaga	E 40
Rosenberger S.	
Tamai H.	A 08
Tanahashi S.	D 16 / O 33
Tanaka M.	A 04 / C 22
Tanaka S.	B 24
Tanaka Y.	A 08
Tang W.M.	C 44 / O 12
Tani T.	A 08
Taquet B.	B 28
Tartari U.	D 25
Tarvin J.A.	O 09
Tataronis J.A.	B 44
Taylor T.	B 09 / B 13
Tomkin R.J.	E 21
Tendler M.	B 18 / B 19
Tenney F.	O 10
Teplov P.P.	B 01 / B 12
Terebkov A.L.	O 05
Terentiev A.R.	E 11
Ternay F.	B 28
Terry J.L.	O 02 / O 32
Terumichi Y.	B 24
Texter S.	O 02 / O 32
Tetsuka T.	D 16
TFR Group	B 05 / B 06 / B 07 / B 08 / C 10 / C 34
Thomas C.E.	O 01
Thomas P.	A 10

Thyagaraja A.	E 47
Tikhanov E.K.	E 09
Tilinin G.N.	A 03
Tishkin V.F.	A 16
Todd A.	O 12
Todd T.N.	B 03 / D 28 / O 22
Tokar M.Z.	O 21
Tomashevich V.N.	D 39
Tomaszewski K.	E 04 / O 23
Tonetti G.	E 20
Tooker J.	B 13
Towner H.	O 10
Treffert J.D.	D 14
Truc A.	B 08 / C 10
Tselnik F.A.	D 18 / D 19
Tsintsadze N.L.	E 45 / E 46
Tskhakaya D.D.	E 45
Tsuboi F.	C 22
Tsuchidate H.	C 22
Tsuji S.	O 33
Tsukishima T.	D 16
Tsushima A.	C 22
T 1O Group	A 26
Tubbing B.J.D.	D 30
Tuccillo A.	FT Team
Turner M.F.	B 22 / B 23
Tuszewski M.	O 29
Tutter M.	W VII A Team
Uckan T.	O 17
Uesugi Y.	A 08
Uma R.	E 36
Umov A.P.	A 26
Unterseer K.	O 07
Uo K.	B 15 / O 19
Ushigusa K.	E 31
Usov V.G.	A 26 / O 20
Vaclavik J.	A 30 / B 29
Valley J.	O 10
Valyi	B 14
Vance C.F.	B 04
Vandenplas P.E.	C 12
Van der Meiden H.J.	D 30
Van Houtte D.	B 28
Vasilev M.P.	D 17
Vaslov D.	B 13
Velarde G.	B 14 / B 16
Venema M.	D 45 / D 46
Venus G.	ASDEX Team
Veprek S.	C 26 / E 22
Verschuur J.W.J.	D 30
Vertiporokh A.N.	A 03
Viehböck F.	A 42
Villard L.	A 29 / A 30
Vlases G.	C 02
Vlasov S.N.	O 20
Vodo A.M.	A 03
Volkov E.D.	D 17
Vollmer O.	ASDEX Team
Voronov G.S.	C 23 / O 20
Vukolov K.Yu.	C 32
Waelbroeck F.	A 35 / C 31 / O 14
Wagner F.	ASDEX Team
Wahlberg C.	C 39
Waidmann G.	B 10
Watanabe H.	D 13
Watanabe T.	D 29
Watkins M.L.	A 15 / A 21
Watt R.G.	O 31
Watterson R.	O 02 / O 32
Weiland J.	D 51
Weller A.	W VII A Team
Wereszczynski Z.	O 23
Werner Z.	D 41
Wesley J.C.	B 09
Wesson J.A.	B 22
Weynants R.R.	C 12 / C 13
White R.B.	O 12
White T.L.	O 17
Wickham M.	C 08
Wieland R.M.	O 01
Wienhold P.	A 35 / C 31
Wilgen J.B.	O 17
Wing W.R.	O 01
Winter J.	A 35 / C 31
Witkowski J.	O 27
Witkowski S.	O 07
Wobig H.	A 12 / A 22 / C 21 / D 08 / W VII A Team
Wojtowicz S.	B 13
Wolf G.H.	A 19
Wolfe S.M.	O 02 / O 32
Wolff H.	C 33
Wolski J.	O 23
Wooding E.R.	E 44
Wootton A.J.	E 19 / O 01
Woskoboinikow P.	E 21
Wright B.L.	O 29
W VII A Team	C 17 / C 18 / C 19 C 20 / E 24 / E 33
Wuerker R.	C 08
Würsching E.	W VII A Team
Wunderlich R.	B 18 / C 29
Wyndham E.S.	E 07
Wyszynski W.	O 27
Xue M.L.	B 41
Yabe T.	O 08
Yamada Y.	O 24
Yamamoto S.	A 08
Yamamoto T.	A 08 / C 06
Yamamoto Y.	O 24
Yamanaka C.	E 39 / O 08 / O 24
Yamanaka M.	O 24
Yamanaka T.	E 39
Yamauchi T.	A 08
Yanagisawa I.	A 08
Yang T.F.	D 22
Yokokura T.	A 08
Yokomizo H.	B 13
Yokoyama K.	A 08
Yokoyama M.	O 24

Yoshida K	E 39 / O 08
Yousef N.	D 30
Yu C.X.	B 02
Yurchenko E.I.	B 48
Yushmanov E.E.	D 21
Yushmanov P.N.	E 50 / E 51
Yusupov K.H.	C 32

Zadrozny M.	E 04
Zampaglione V.	D 01
Zanza V.	FT Team
Zdanowski K.	D 41
Zebrowski J.	E 05
Zehrfeld H.P.	B 43
Zhang Z.X.	A 22
Zhitlukhin A.M.	D 20
Zhukov A.P.	D 39
Zippe M.	W VII A Team
Zlotnikov D.M.	E 13
Zoletnik S.	B 14
ZT 40 M Team	O 31
Zukakishvili G.G.	E 09
Zushi H.	B 15 / O 19
Zykova N.M.	A 38